

# Synthesis, Properties and Applications of Ultrananocrystalline Diamond

## NATO Science Series

*A Series presenting the results of scientific meetings supported under the NATO Science Programme.*

The Series is published by IOS Press, Amsterdam, and Springer (formerly Kluwer Academic Publishers) in conjunction with the NATO Public Diplomacy Division.

### *Sub-Series*

<b>I. Life and Behavioural Sciences</b>	IOS Press
<b>II. Mathematics, Physics and Chemistry</b>	Springer (formerly Kluwer Academic Publishers)
<b>III. Computer and Systems Science</b>	IOS Press
<b>IV. Earth and Environmental Sciences</b>	Springer (formerly Kluwer Academic Publishers)

The NATO Science Series continues the series of books published formerly as the NATO ASI Series.

The NATO Science Programme offers support for collaboration in civil science between scientists of countries of the Euro-Atlantic Partnership Council. The types of scientific meeting generally supported are "Advanced Study Institutes" and "Advanced Research Workshops", and the NATO Science Series collects together the results of these meetings. The meetings are co-organized by scientists from NATO countries and scientists from NATO's Partner countries — countries of the CIS and Central and Eastern Europe.

**Advanced Study Institutes** are high-level tutorial courses offering in-depth study of latest advances in a field.

**Advanced Research Workshops** are expert meetings aimed at critical assessment of a field, and identification of directions for future action.

As a consequence of the restructuring of the NATO Science Programme in 1999, the NATO Science Series was re-organized to the four sub-series noted above. Please consult the following web sites for information on previous volumes published in the Series.

<http://www.nato.int/science>  
<http://www.springeronline.com>  
<http://www.iospress.nl>



**Series II: Mathematics, Physics and Chemistry – Vol. 192**

# Synthesis, Properties and Applications of Ultrananocrystalline Diamond

edited by

**Dieter M. Gruen**

Argonne National Laboratory,  
Argonne, IL, USA.

**Olga A. Shenderova**

International Technology Center,  
North Carolina, U.S.A.

and

**Alexander Ya. Vul'**

Ioffe Physico-Technical Institute,  
St. Petersburg, Russia



Published in cooperation with NATO Public Diplomacy Division

Proceedings of the NATO Advanced Research Workshop on  
Synthesis, Properties and Applications of Ultrananocrystalline Diamond  
St. Petersburg, Russia  
7–10 June 2004

A C.I.P. Catalogue record for this book is available from the Library of Congress.

ISBN-10 1-4020-3321-4 (PB) Springer Dordrecht, Berlin, Heidelberg, New York  
ISBN-13 978-1-4020-3321-6 (PB) Springer Dordrecht, Berlin, Heidelberg, New York  
ISBN-10 1-4020-3320-6 (HB) Springer Dordrecht, Berlin, Heidelberg, New York  
ISBN-10 1-4020-3322-2 (e-book) Springer Dordrecht, Berlin, Heidelberg, New York  
ISBN-13 978-1-4020-3320-9 (HB) Springer Dordrecht, Berlin, Heidelberg, New York  
ISBN-13 978-1-4020-3322-3 (e-book) Springer Dordrecht, Berlin, Heidelberg, New York

---

Published by Springer,  
P.O. Box 17, 3300 AA Dordrecht, The Netherlands.

*Printed on acid-free paper*

---

All Rights Reserved  
© 2005 Springer

No part of this work may be reproduced, stored in a retrieval system, or transmitted in any form or by any means, electronic, mechanical, photocopying, microfilming, recording or otherwise, without written permission from the Publisher, with the exception of any material supplied specifically for the purpose of being entered and executed on a computer system, for exclusive use by the purchaser of the work.

Printed in the Netherlands.



## TABLE OF CONTENTS

Foreword. ....	ix
 <b>I. New Forms of Nanocarbon. Theory and Observation</b>	
1. <b>Carbon Family at the Nanoscale</b> O.A. Shenderova, Z. Hu, and D. Brenner .....	1
2. <b>Structural and Electronic Properties of Isolated Nanodiamonds: a Theoretical Perspective</b> J.-Y. Raty and G. Galli. ....	15
3. <b>From Nanodiamond to Nanowires</b> A. Barnard. ....	25
4. <b>Quantum Chemical Studies of Growth Mechanisms of Ultrananocrystalline Diamond</b> L.A. Curtiss, P. Zapol, M. Sternberg, P.C. Redfern, D.A. Horner, and D.M. Gruen .....	39
5. <b>Nanodiamonds in the Cosmos</b> <b>Microstructural and Trapped Element Isotopic Data</b> T.L. Daulton .....	49
6. <b>Diamond Molecules Found in Petroleum. New Members of the H-Terminated Diamond Series</b> R.M.K. Carlson, J.E.P. Dahl, S.G. Liu, M.M. Olmstead, P.R. Buerki, and R. Gat .....	63
 <b>II. Ultrananocrystalline Diamond Films</b>	
7. <b>Synthesis of Nanocrystalline Diamond Films in Ar/H<sub>2</sub>/CH<sub>4</sub> Microwave Discharges</b> F. Bénédic, F. Mohasseb, P. Bruno, F. Silva, G. Lombardi, K. Hassouni, and A. Gicquel .....	79
8. <b>Modelling of Ar/H<sub>2</sub>/CH<sub>4</sub> Microwave Discharges used for Nanocrystalline Diamond Growth</b> F. Mohasseb, K. Hassouni, F. Bénédic, G. Lombardi, and A. Gicquel .....	93

9. <b>Nanodiamond Seeding for Nucleation and Growth of CVD Diamond Films</b> V. Ralchenko, A. Saveliev, S. Voronina, A. Dementjev, K. Maslakov, M. Salerno, A. Podesta, and P. Milani. . . . .	109
10. <b>Mechanism and Properties of Nanodiamond Films Deposited by the DC-GD-CVD Process</b> A. Hoffman . . . . .	125
11. <b>Nanodiamond Injection into the Gas-Phase During CVD Diamond Film Growth</b> N.A. Feoktistov, V.G. Golubev, S.A. Grudinkin, A.V. Nashchekin, T.S. Perova, and A.Ya. Vul' . . . . .	145
12. <b>Stabilization of Diamond-Like Nanoclusters by Metallic Atoms and the Epitaxial Growth of Diamond Films: <i>ab initio</i> Simulation</b> V. G. Zavodinsky . . . . .	157
<b>III. Detonation nanodiamond</b>	
<b>III.1 Formation of Detonation Nanodiamond</b>	
13. <b>The Formation Kinetics of Detonation Nanodiamonds</b> V.M. Titov, B.P. Tolochko, K.A. Ten, L.A. Lukyanchikov, and P.I. Zubkov . . . . .	169
14. <b>Nanocarbon Phase Diagram and Conditions for Detonation Nanodiamond Formation</b> V.V. Danilenko. . . . .	181
15. <b>Nanodiamond Graphitization and Properties of Onion-Like Carbon</b> V.L. Kuznetsov and Yu.V. Butenko. . . . .	199
<b>III.2 Modification and Properties of Detonation Nanodiamond</b>	
16. <b>Physical and Chemical Problems of Modification of Detonation Nanodiamond Surface Properties</b> V.Yu. Dolmatov and T. Fujimura . . . . .	217

<b>17. Disintegration and Purification of Crude Aggregates of Detonation Nanodiamond</b> <i>A Few Remarks on Nano Methodology</i>	
E. Osawa . . . . .	231
<b>18. Purification and Functionalization of Nanodiamond</b>	
B.V. Spitsyn, M.N. Gradoboev, T.B. Galushko, T.A. Karpukhina, N.V. Serebryakova, I.I. Kulakova, and N.N. Melnik . . . . .	241
<b>19. Interaction of Carbon Atoms with Nanodiamond Surface</b>	
A.P. Dementjev, K.I. Maslakov, and A. V. Naumkin . . . . .	253
<b>20. Physical and Chemical Properties of Modified Nanodiamonds</b>	
A.P. Puzyr, V.S. Bondar, A.A. Bukayemsky, G.E. Selyutin, and V.F. Kargin . . . . .	261
<b>21. Magnetic Resonance Study of Nanodiamonds</b>	
A.I. Shames, A.M. Panich, W. Kempinski, M.V. Baidakova, V.Yu. Osipov, T. Enoki, and A.Ya. Vul'. . . . .	271
<b>22. Infrared Spectra of Explosion Nanodiamonds: a Comparison with Spectra of Hydrogenated Amorphous Carbon Films</b>	
W.W. Duley, V.I. Grishko, and O.A. Shenderova. . . . .	283
<b>23. Conversion of Elemental Substances and Inorganic Compounds to Carbon Nanostructures</b>	
V.G. Lutsenko . . . . .	289
<b>24. The Fine and Fractal Structure and Protonic Conductivity of Phosphosilicate-Diamond Sol-Gel Nanocomposites</b>	
V.V. Shilov, Yu.P. Gomza, O.A. Shilova, V.I. Padalko, L.N. Efimova, and S.D. Nesin. . . . .	299
<b>III.3 Industrial Production of Detonation Nanodiamonds</b>	
<b>25. Facilities for Ultradisperse Diamond Production</b>	
T. M. Gubarevich, and D.N. Gamanovich . . . . .	311

<b>26. Ultradisperse Diamond Regeneration from Composite Electrolytes of Chromium Plating</b> T.M. Gubarevich, L.E. Chernukho, V.P. Kulik, and R.G. Shtempljuk . . . . .	321
<b>27. Synthesis and Processing of Chelyabinsk Detonation Nanodiamonds</b> I.L. Petrov . . . . .	333
<b>28. Conversion Raw Materials in Industrial Production of Ultradisperse Diamonds</b> T.M. Gubarevich and D.N. Gamanovich . . . . .	337
<b>29. Ultradisperse Diamond Modifications in the Composite Gilding Process</b> T.M. Gubarevich and L.E. Chernukho . . . . .	345

#### **IV. Applications of Nanodiamond**

<b>30. Applying CVD Diamond and Particulate Nanodiamond</b> J. L. Davidson, W. P. Kang . . . . .	357
<b>31. Electronic Properties and Applications of Ultrananocrystalline Diamond</b> O. A. Williams, T. Zimmermann, M. Kubovic, A. Denisenko, E. Kohn, R. B Jackman and D. M Gruen. . . . .	373
<b>32. Thermoelectric Effect in Field Electron Emission from Nanocarbon</b> A.Ya. Vul', E.D. Eidelman, and A.T. Dideikin. . . . .	383
Authors Index . . . . .	395
Subject Index . . . . .	397
List of Workshop Participants . . . . .	399

## FOREWORD

We are pleased to present the Proceedings of the NATO Advanced Research Workshop “Syntheses, Properties and Applications of Ultrananocrystalline Diamond” which was held June 7-10, 2004 in St. Petersburg, Russia.

The main goal of the Workshop was to provide a forum for the intensive exchange of opinions between scientists from Russia and NATO countries in order to give additional impetus to the development of the science and applications of a new carbon nanostructure, called **ultrananocrystalline diamond (UNCD)** composed of 2-5 nm crystallites. There are two forms of UNCD, dispersed particles and films. The two communities of researchers working on these two forms of UNCD have hitherto lacked a common forum in which to explore areas of scientific and technological overlap. As a consequence, the two fields have up to now developed independently of each other. The time had clearly come to remedy this situation in order to be able to take full advantage of the enormous potential for societal benefits to be derived from exploiting the synergistic relationships between UNCD dispersed particulates and UNCD films.

The NATO sponsored ARW therefore occurred in a very timely manner and was successful in beginning the desired dialogue, a precondition for making progress toward the above stated goal.

The discovery of UNCD completes a triad of nanostructured carbons which includes fullerenes and nanotubes. These three forms of carbon are closely related thermodynamically because their free energies of formation differ from one another by only 1-3 kcal/mol compared to graphene sheets consisting of a comparable number of carbon atoms. Kinetic factors therefore play an important role in deciding the outcome of chemical reactions designed to synthesize one or another of these forms. Indeed, reaction conditions can be manipulated in ways so as to synthesize, for example, nanotubes and UNCD simultaneously in the same experiment to produce nanostructured carbon composites. The opportunities for the creation of new and potentially useful carbon materials in this branch of nanoscience are clearly open ended and very promising.

The major topics of the workshop were UNCD particles produced by detonation of carbon explosive materials (characteristic size ~5 nm)

discovered in the USSR in the 1960's and phase-pure UNCD films (grain size 3-5 nm) produced by chemical vapor deposition during the last ten years by Dr. D. M. Gruen and colleagues in his group at the Argonne National Laboratory in the USA.

The scientific program of the Workshop consists of 25 lectures of key speakers, one poster session (22 posters) and three panel discussions "Unsolved Problems for Nanodiamonds", "Critical Issues on UNCD Films and UNCD Particles" and "Market Opportunities for Nanodiamonds". 49 participants took part at the Workshop.

The discussion at the Workshop has clearly shown that both UNCD particles and UNCD films possess unique properties and different niche applications.

UNCD particles produced by detonation synthesis represent new building blocks suitable for making nanocomposites and refrigerating fluid. Besides, they can serve as a source material, for the production of selective adsorbents, as well as for medical and biological applications. Colloidal solutions of UNCD particles are suitable objects for the investigation of physical and chemical properties of dispersions with minimal size particles in solution. The use of UNCD particles considerably improves the properties of microabrasive and polishing materials, lubricating oils, abrasive tools, polymer composites, rubbers, and information-recording media. In addition, UNCD particles can be used for growing nanocrystalline diamond films on various substrates, for making arrays of quantum dots of silicon and as a material for creation of a new generation of cold emission cathodes for vacuum electronics. Thus, it was clearly seen that UNCD particles have many useful applications in electronics, new materials fabrication, industrial and machine application.

UNCD films are superior in many ways to traditional micro- and nanocrystalline diamond films: they are smooth, dense, pinhole free, and phase-pure, and can be coated on a wide variety of materials and high-aspect-ratio structures. The set of unique properties include mechanical, tribological (extremely low friction  $\sim 0.01$ ), transport (tunable electrical conductivity, high thermal conductivity), electrochemical (wide working potential window), and electron emission (low, stable threshold voltage). The UNCD films has been considered for a variety of applications including MEMS and moving mechanical assembly devices, surface acoustic wave (SAW) devices, electrochemical sensors, coatings for field emission arrays, photonic and RF switching, and neural prostheses. Recent achievements in

n-type doping demonstrate the highest carrier concentrations seen for any n-type diamond material to date resulting in several orders of magnitude increase in UNCD films conductivity that promise applications in heterojunction electronic devices.

The contents of the Proceedings can be divided into four parts. The first part related to the last results in theory, computer simulation and experimental observations of isolated nanodiamonds in cosmos and petroleum. Herein calculations of growth mechanisms of UNCD films are presented. In the second part are collected papers related to technology and electronic properties of UNCD films. Third part of the Proceedings is devoted to UNCD clusters produced by detonation method from strong explosives, features of their production, purification and surface modification. At last a reader of the forth part can estimate the progress in the field of application UNCD films and particles.

In conclusion we would like to mention that modern technology is definitely on its way from the world of micrometer sizes to that of nanometers, and the words "nanoworld" and "nanoscience" have become an integral part of scientific terminology in the past two decades. Many international meetings are now using in their titles the word nanotechnology covering nanoelectronics, nanobiotechnologies and the technology of nanosize materials.

Among the latter, nanocarbon clusters - fullerenes, nanotubes and onion-like carbons discovered at the end of the 20th century - are becoming increasingly important and now ultrananocrystalline diamond is full-fledged member of this nanocarbon family.

We believe that the NATO Workshop helped to extend boundaries of our knowledge on this unique material and this Proceeding open this knowledge for scientific community.

As organizers we would like to express our gratitude to the sponsors of the Workshop: the NATO Scientific Affairs Division, Office of Naval Research International Field Office, the Russian Foundation for Basic Research.

We would like to thank Mrs. L.N. Smirnova for her work for improving of English of authors from Russia and CIS.

Dieter Gruen, Olga Shendorova, Alexander Vul'  
Editors

# 1

## CARBON FAMILY AT THE NANOSCALE

O.A. Shenderova<sup>1</sup>, Z. Hu<sup>2</sup>, and D. Brenner<sup>2</sup>

<sup>1</sup> International Technology Center, P.O.Box 13740 Research Triangle Park, NC, 27709, USA

<sup>2</sup> North Carolina State University, Raleigh, NC, USA

**Abstract:** An overview of the relative stability of various carbon structures with characteristic sizes in the nanoscale region is presented with major emphasis on ultrananocrystalline diamond (UNCD), which has very diverse structures at the nanoscale. Heats of formation of nanodiamond particles of different morphologies are reported.

**Keywords:** nanocarbon, ultrananocrystalline diamond, heat of formation, cohesive energy, hydrogenated carbon

### 1. INTRODUCTION

The science of carbon materials is at an important juncture. The historically independent scientific communities studying graphite-based materials, fullerene nanotubes and diamond are merging as their interests overlap at the nanoscale. While the current popularity of carbon nanostructures to a large extent is due to fullerenes and nanotubes, other members of the nanocarbon family are also attracting steadily increasing attention. For confirmation we refer to recent reviews [1–3] and books [4–7] on nanodiamond materials. Accordingly, structures, properties and numerous applications of nanostructured graphite, which belongs to a broad group of so called *new carbon materials*, has been recently summarized in a book by Inagaki [8]. In parallel, new carbon allotropes are being discovered as, for example, carbolite, an esoteric chain-like crystalline form of carbon [9]. Understanding properties of carbon entities at the nanoscale within a unified framework, including the conditions under which one form transforms into another, has become an important issue. An overview of the relative stability of various carbon structures with characteristic sizes in the nanoscale region will be presented in Section 2. The major part of the discussion will be



devoted to the stability of ultra-nanocrystalline diamond particles, which have very diverse structures at the nanoscale.

## 2. CARBON AT THE NANOSCALE

### 2.1 Nanocarbon Classification

In principle, different approaches can be used to classify carbon nanostructures. The appropriate classification scheme depends on the field of application of the nanostructures. For example, a classification can be based on an analysis of the dimensionalities of the structures, which in turn are connected with the dimensionality of quantum confinement and thus is related to nanoelectronic applications. The entire range of dimensionalities is represented in the nanocarbon world, beginning with zero dimension structures (fullerenes, diamond clusters), and including one-dimensional structures (nanotubes, diamond nanorods), two dimensional structures (graphite sheets) and three dimensional structures (nanocrystalline diamond films, agglomerates, fullerite, nanotube ropes). In a different approach, the scale of characteristic sizes can be introduced as the major criterion for classification. This scheme more naturally allows the consideration of complicated hierarchical structures of carbon materials (carbon fibers, carbon polyhedral particles). A summary based on different shapes and spatial arrangements of elemental structural units of carbon caged structures also provides a very useful picture of the numerous forms of carbon structures at the nanoscale [10].

In terms of a more fundamental basis for the classification of carbon nanostructures, it would be logical to use a classification scheme based on existing carbon allotropes that is inherently connected with the nature of bonding in carbon materials. An interesting discussion of carbon allotropy and a scheme for classifying existing carbon forms is provided in [11]. The classification scheme is based on the types of chemical bonds in carbon, with each valence state corresponding to a certain form of a simple substance. Elemental carbon exists in three bonding states corresponding to  $sp^3$ ,  $sp^2$  and  $sp$  hybridization of the atomic orbitals, and the corresponding three carbon allotropes with an integer degree of carbon bond hybridization are diamond, graphite and carbyne [11]. All other carbon forms constitute so-called transitional forms that can be divided into two big groups. The first group comprises *mixed* short range order carbon forms with more or less arranged carbon atoms of different hybridization states, e.g. diamond-like carbon, vitreous carbon, soot, carbon blacks, etc., as well as numerous hypothetical structures like graphynes and ‘superdiamond’. The second group includes

*intermediate* carbon forms with a non-integer degree of carbon bond hybridization,  $sp^n$ . The subgroup with  $1 < n < 2$  includes various monocyclic carbon structures. For  $2 < n < 3$ , the intermediate carbon forms comprise closed-shell carbon structures such as fullerenes, carbon onions and nanotubes, hypothetical tori, etc. The fractional degree of hybridization in this group of carbon structures is due to the curvature of the framework. The value of the suggested scheme is that any form of carbon substance is included in the classification.

A hybridization-based scheme for carbon classification was also suggested by Inagaki [8] considering diamond, graphite, fullerenes and carbyne as four basic carbon forms. In addition, Inagaki's scheme demonstrates interrelations between organic/inorganic carbon substances at the molecule scale and emphasizes the interdisciplinary nature of carbon nanotechnology, which is based on both materials science and chemistry.

The classification schemes outlined above [8,11] were combined to classify carbon nanostructures within the general hierarchy of carbon materials [3] (Figure 1). In comparison to the scheme published in [3], the scheme outlined in Figure 1 has a new and important member – buckydiamond. The scheme is based on two major characteristics: the type of carbon atom hybridization and the characteristic sizes of nanostructures. Starting with a description of the bonding nature of carbon atoms, the idea is to analyze how different classes of carbon networks are formed with the increasing characteristic size of a carbon structure. Starting with small organic molecules (inner circle), the hierarchy of carbon materials can be described as an extension of organic molecular species to bulk inorganic all-carbon materials through a variety of carbon entities in the nanoscopic size range. If we consider fullerenes, nanotubes, graphene of finite size and the currently observed smallest nanodiamond clusters as basic structural units in the carbon nanoworld, prototype molecules can be assigned to these units at the scale of molecules (inner circle). It should be noted, however, this scheme does not mean that these molecules are involved in the synthesis of the units, rather we would emphasize topological similarities between organic species and inorganic materials. While the sizes of representative members of  $sp^2$ - and  $sp^n$  ( $2 < n < 3$ ) families experimentally identified change rather smoothly from the molecular scale (few nanometers) to the scale of nanostructures (tens of nanometers), for  $sp^3$  carbon forms there is currently a gap in sizes between observed molecular forms of the highest diamondoids [12] (~1 nm in size, containing up to 50 carbon atoms) and the smallest nanodiamond particles (~2–3 nm in size, few thousands carbon atoms). Recently, a hybrid form of an entity with a diamond core and fullerene-like outer shells called bucky-diamond has been suggested and experimentally confirmed [13]. The next structural level in Figure 1, with a corresponding

increase of the characteristic sizes, can be considered as consisting of assemblies of the structural units, ranging from simple forms, such as MWNTs or carbon onions to more complicated carbon architectures as carbon black, schwarzites, and agglomerates of nanodiamond particles or ultrananocrystalline diamond films. An example of a carbon structure with a complex architecture combining two structural units are recently discovered graphite polyhedral nano- and microcrystals with axial carbon structures having nanotube cores, nanotube-structured tips, and graphitic faces [14]. Finally, at the upper micro/macroscale scale there is diamond, graphite, carbolite, fullerite and recently discovered SWNT strands of macroscopic sizes [15]. While the described scheme corresponds to the bottom up approach of molecular synthesis, it is also necessary to add to the scheme for completeness nanostructures obtained by top down approaches using different nanopatterning techniques such as, for example, fabrication of diamond nanorods of single crystalline diamond of 50 nm diameter by reactive ion etching combined with microwave plasma treatment of diamond [16]. Obviously, structural units from different families can be combined to form hybrid nanostructures.

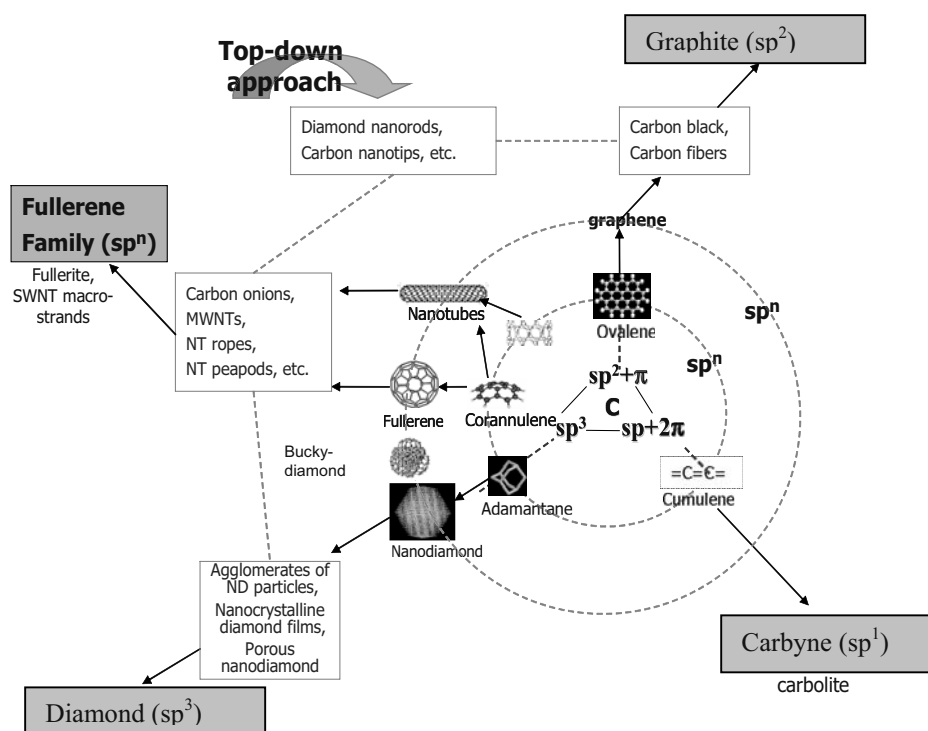


Figure 1. Classification of carbon nanostructures. Mark  $sp^n$ , corresponds to intermediate carbon forms with a non-integer degree of carbon bond hybridization.

## 2.2 Stability of Nanodiamond

Until recently, most of the experimental work dealing with nanodiamond produced by means of detonation described the shape of clusters as being spherical. However, HRTEM images of a single nanodiamond cluster on the surface of a Mo tip clearly indicate the presence of facets at the particle surface, with the cluster resembling a polyhedral shape [17]. The shape of a diamond cluster is inherently connected to its stability, which in turn depends on the state (coordination) of the surface atoms and defects present in the bulk of the particles (for example, twins in particles of pentagonal shape). The stability of nanodiamond particles will also depend on the presence of specific functional groups on a particle surface or on the interface energy between a UNCD particle and surrounding matrix if a particle is incorporated to a matrix (as for example, UNCD grains in CVD films, nanodiamonds surrounded by carbide material during synthesis by a carbide chlorination process, nanodiamond in agglomerates, etc.). In the current study we calculated formation energies and preferred morphologies of hydrogenated diamond clusters. Atomistic simulations were performed using a bond-order interatomic potential for hydrocarbons [18].

Four different morphologies of nanodiamond particles were considered: octahedral, cuboctahedral, spherical and a particle of a pentagonal shape. For analysis of a particle energies, possible reconstructions, and interaction with specific functional groups, it is useful to know the dependence of the number of under-coordinated surface atoms on particle size. Previously, a ‘nanodiamond formula’ for octahedral particles was derived [19]:

$$\begin{aligned}
 N_{C2} &= 6 \\
 N_{C3} &= 4N^2 - 12 \\
 N_{Surface} &= N_{C2} + N_{C3} = 4N^2 - 6 \\
 N_{total} &= N(4N^2 - 1)/3
 \end{aligned} \tag{1},$$

where  $N$  is number of atoms along an octahedron edge, and  $N_{C2}$  and  $N_{C3}$  are the number of 2- and 3-coordinated atoms, correspondingly. For example,  $N = 2$  corresponds to the adamantane molecule. It is also possible to obtain similar equations for cuboctahedra, obtained by truncation of corresponding octahedra. However, the formulas are different for  $N$  odd and even (here again  $N$  is the number of atoms along a corresponding octahedron edge):

$$\begin{aligned}
N_{c2} &= \begin{cases} \frac{3(N^2-1)}{2} & N \text{ is odd} \\ \frac{3N^2}{2} & N \text{ is even} \end{cases} \\
N_{c3} &= \begin{cases} N^2 & N \text{ is even} \\ N^2+3 & N \text{ is odd} \end{cases} \\
N_{total} &= \begin{cases} \frac{1}{12}N(2N+1)(5N+2) & N \text{ is even} \\ \frac{1}{12}(10N^3+9N^2+2N-9) & N \text{ is odd} \end{cases}
\end{aligned} \tag{2}$$

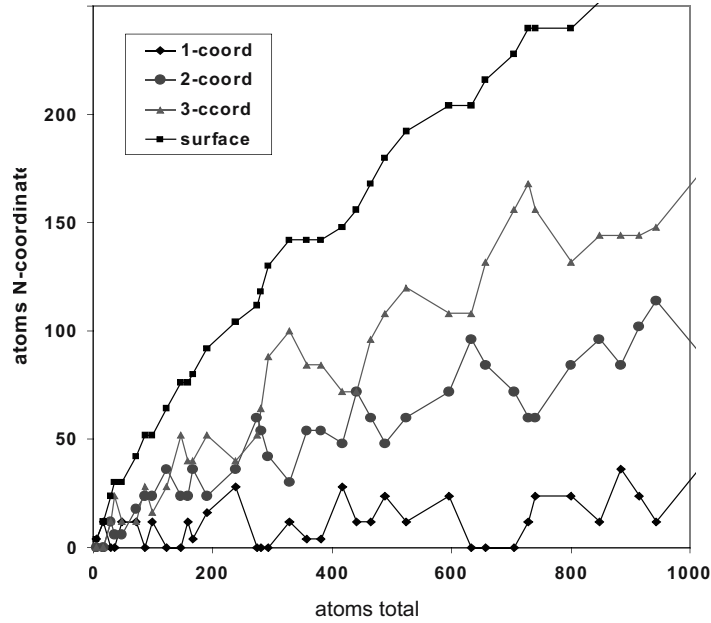


Figure 2. Number of under-coordinated surface atoms of different types for a spherical particle as a function of total number of atoms. Particles are constructed by adding shell-by-shell surface atoms.

Thus gradually increasing  $N$ , a series of self-fashioned particles with a gradually increasing size can be constructed. If in the additional energies of a particular type of surface atom is known from macroscopic surface simulations and it does not sufficiently depend on a particle size, predictions of stability of relatively large particles can be pursued. For a series of

spherical clusters constructed shell-by-shell by gradually adding atoms, it was not possible to derive analytical expressions. Statistics on under-coordinated atoms for series of spherical clusters is illustrated in Figure 2 obtained from atomistic modeling.

To establish if analytic expressions for the number of under-coordinated surface atoms of a certain type can be used in combination with the related local energy per atom, histograms of energy distributions within hydrogenated octahedra and reconstructed (001)2×1 cuboctahedra have been plotted (Figure 3). The possibility of analyzing the distribution of atomic energies within clusters is an advantage of an analytic potential in comparison with more sophisticated methods that typically provide total energies of systems. As is illustrated in Figure 2 (top), specific groups of atoms (on vertices, (111) faces and 4-coordinated atoms in the bulk) have very similar binding energies within every group that are essentially independent of particle sizes. In contrast the local atomic energies are more pronouncedly size-dependent for cuboctahedra clusters (Figure 2, bottom), although specific groups of atoms (on vertices, edges, (111) and (001) faces) can clearly be distinct.

Cohesive energies of octahedra and reconstructed cuboctahedra series have been calculated using Formula (1) and (2), and values for specific surface atoms calculated for (111) and (001) reconstructed macroscopic surfaces (some of the values are provided in the caption for Figure 3. Based on known local atomic energies for specific surface atoms, cohesive energies can generally be described as:

$$E_{ND} = E_{C4} \cdot N_{C4} + E_{C3} \cdot N_{C3} + E_{C2} \cdot N_{C2} + E_{H(C3)} \cdot N_{H(C3)} + E_{H(C2)} \cdot N_{H(C2)}$$

or, similarly (eqs.3):

$$\frac{E_{ND}}{N_C} = E_{C4} + (E_{C3} - E_{C4}) \frac{N_{C3}}{N_C} + (E_{C2} - E_{C4}) \frac{N_{C2}}{N_C} + E_{H(C3)} \frac{N_{H(C3)}}{N_C} + E_{H(C2)} \frac{N_{H(C2)}}{N_C} \quad (3).$$

The latter formula provides more details on the contribution to the cohesive energy of particular types of under-coordinated atoms and their fractions in the particle as compared to the ‘traditional’ equation:

$$\frac{E_{ND}}{N_C} = E_C + E_H \cdot \frac{N_H}{N_C} \quad (4).$$

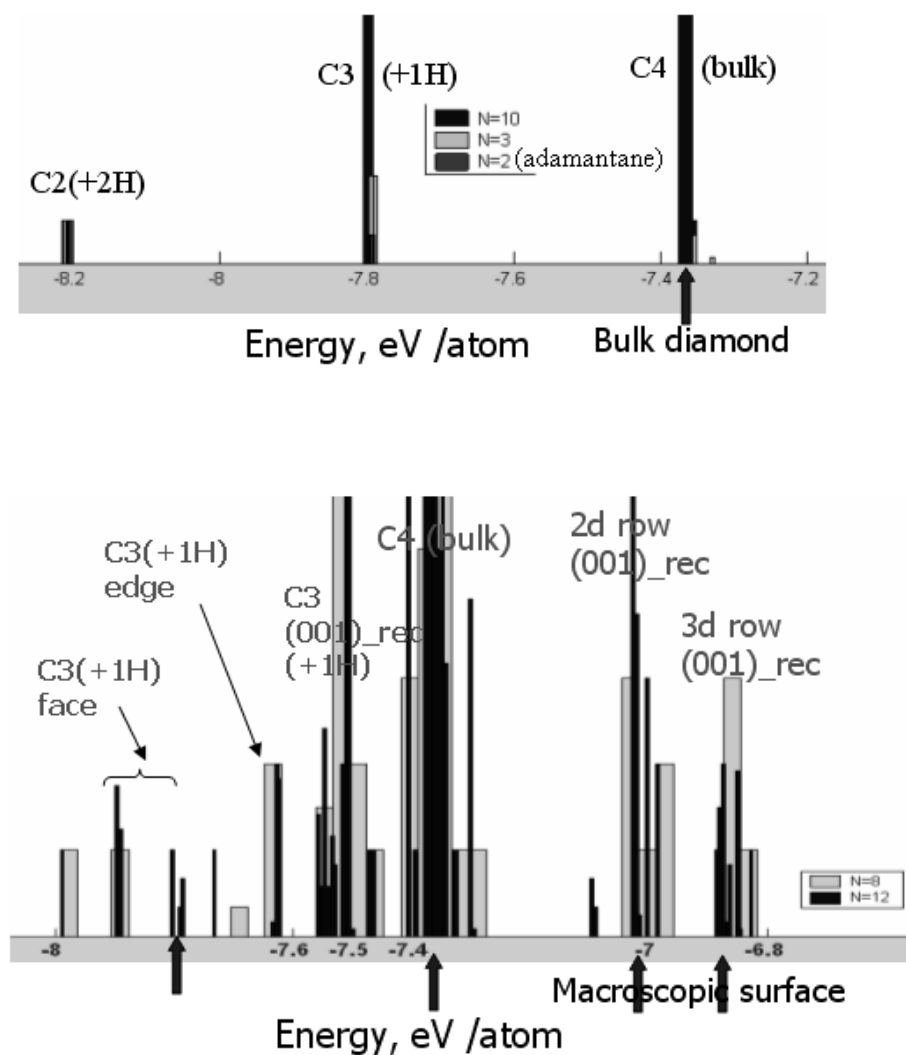


Figure 3. Histograms of atomic energies of carbon atoms for three octahedral particles (top) ( $C_{10}H_{16}$  ( $N=2$ ),  $C_{35}H_{36}$  ( $N=3$ ),  $C_{1330}H_{400}$  ( $N=10$ )) and two cuboctahedral particles (bottom) ( $C_{436}H_{208}$  ( $N=8$ ),  $C_{1550}H_{432}$  ( $N=12$ )). Arrows from the bottoms of the pictures mark energies of carbon atoms in bulk diamond (-7.37 eV) and at the (111) hydrogenated (-7.8 eV) and (100) 2x1 reconstructed (-7.5 for C2+1H, -7 eV for C4-2<sup>d</sup> row and -6.9 eV for the C4-3<sup>d</sup> row) macroscopic surfaces.

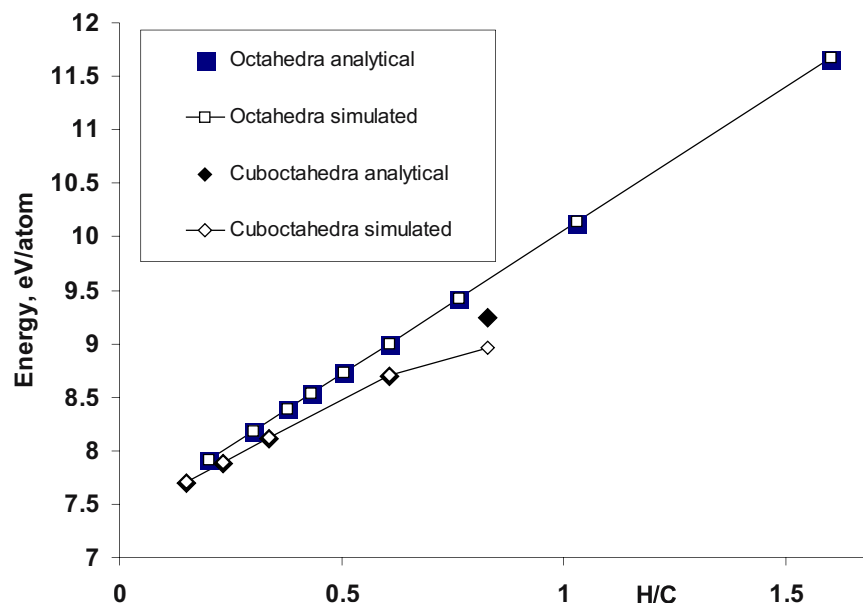


Figure 4. Cohesive energy from simulations with the bond-order potential (open symbols) and predicted analytically (solid symbols).

Results of predictions are illustrated in Figure 4. For comparison, the same clusters had been relaxed using the bond order potential (Figure 4). While for octahedra both analytic and atomic simulation approaches show similar results, for small cuboctahedra there is a difference in the results of the two approaches. Also, for small clusters, the slopes in the energy curves for octahedra and cuboctahedra structures are distinct. The intersection of the curves with the energy axis can be referred as the ‘nanodiamond’ energy, which is different from bulk diamond energy in a case of relaxed all-carbon particles [20], so the accuracy of the slope is important. For our simulations of hydrogenated particles, the intersection points with the ordinate axis for extrapolated octahedral and cuboctahedra curves is the same, -7.37 eV per carbon atom, which is the cohesive energy for bulk diamond.

Using an empirical interatomic potential to analyze the cluster energies allows us to conclude (at least quantitatively) the following: (i) it is not recommended to use small clusters to fit nanodiamond cohesive energies (‘molecules’ and particles should be separated); (ii) it is recommended to use particles from the same series for fitting the nanodiamond cohesive energy. It would be interesting to evaluate nanodiamond cohesive energies for all-carbon clusters [20] taking into account the above considerations. Obviously, corresponding atomic energies for macroscopic surfaces obtained



from *ab initio* calculations can be used for prediction particle energies, and any functional group can be analyzed this way.

Finally, heats of formation have been calculated for several nanodiamond series for particles relaxed with the bond order potential:

$$\Delta H_f^o(ND) = N_C \cdot \Delta H_f^o(C) + N_H \cdot \Delta H_f^o(H) - (E^{at} - E_{zpe})$$

where  $E^{at}$  is the atomization energy obtained from the simulations and  $E_{zpe}$  is the zero point energy [18], which accounted only for small clusters.

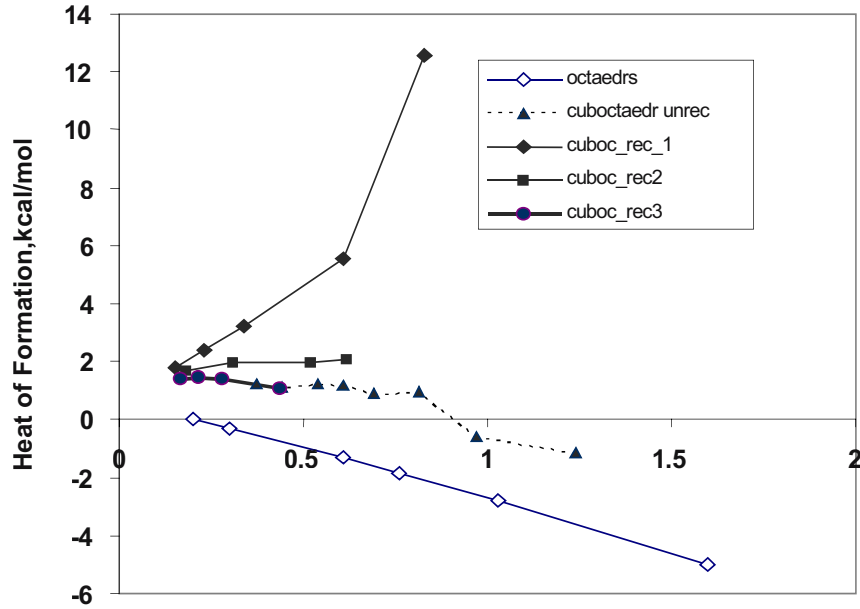


Figure 5. Heats of formation for hydrogenated octahedra ( $\diamond$ ) and cuboctahedra: unreconstructed ( $\blacktriangle$ ); with all atoms on (001) surface reconstructed in  $2 \times 1$  manner ( $\blacklozenge$ ); partially reconstructed ( $\blacksquare$ ).

Results of the calculations for octahedra and several sub-series of cuboctahedra are illustrated in Figure 5. It should be noted that the unreconstructed octahedral cluster becomes structurally unstable for  $N=15$  in simulations with the bond order potential. From Figure 5 it follows that some series become more, some - less stable with increasing size. All of the series are bounded by curves corresponding to hydrogenated octahedra and (001)  $2 \times 1$  reconstructed cuboctahedra. Extrapolated curves intersect the ordinate axis in a point corresponding to the heat of formation of bulk diamond ( $\sim -0.5$  kcal/mol).

In addition to cuboctahedral and octahedral clusters, Figure 6 illustrates heats of formation for spherical particles and pentaparticles. From Figure 6 in general it can be concluded that the most stable morphologies for hydrogenated nanodiamond are octahedra, pentaparticles and groups of spherical particles. Obviously, there are many more series of different nanodiamond morphologies that can be constructed, which, however, will probably be bound by the octahedra / (001)2×1 reconstructed cuboctahedra curves.

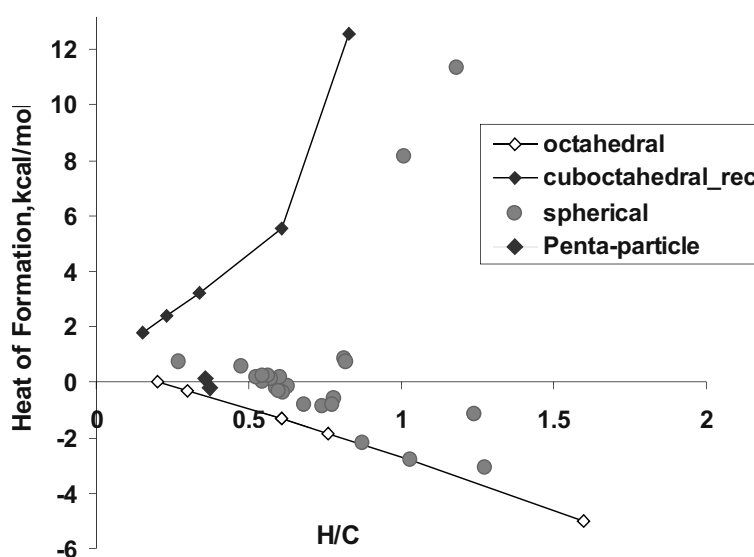


Figure 6. Heats of formation for hydrogenated octahedra ( $\diamond$ ), (001)2×1 reconstructed cuboctahedra (connected  $\blacklozenge$ ); spherical clusters ( $\bullet$ ) and two clusters with pentagonal shape ( $\blacklozenge$ ).

### 2.3 Stability of Nanocarbon

Presently, a relatively large amount of accurate simulation results has been generated in order to create a general concept of stability of carbon forms at the nanoscale. Results on the thermodynamic stability for a variety of all-carbon nanostructures have been summarized in [3]. Recently, Barnard and colleagues included fullerenes, onions and bucky-diamond in the ‘traditional’ analysis of the relative stability of diamond and graphite at the nanoscale and defined size regions of the stability of these structures [21]. According to the results in [21] as the system size for all-carbon structures is increased the most stable carbon form at the nanoscale changes from fullerene - to onions - to buckydiamond- to nanodiamond - to graphite. The

crossover from fullerenes to closed nanotubes had also been analyzed recently [22]. Regarding small carbon clusters, three regions for the stability can be outlined [23]: below 20 atoms, the most stable geometries are one-dimensional ring clusters; between 20 and 28 atoms, clusters with quite different types of geometry have similar energetics; for larger clusters, fullerenes should be more stable. In combination with the above analysis on hydrogenated clusters, the hierarchy of the stabilities of carbon forms at the nanoscale is summarized in Figure 7. The region of the relative stability of different forms of hydrogenated carbon is highlighted in order to emphasize the plurality of possible morphologies for nanodiamond particles that comprise this region as demonstrated above.

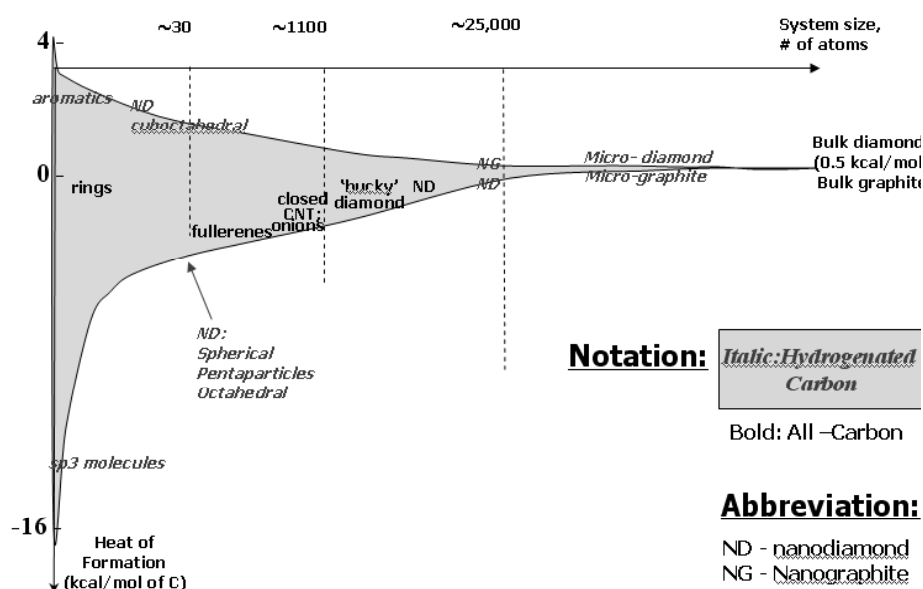


Figure 7. Schematic representation of the most stable carbon phase (all-carbon and hydrogenated species) depending on the size of the carbon structure.

To make the scheme more quantitative, all related simulations need to be done using the same computational approach (of ab initio) level.

This work was supported by the National Science Foundation through grant DMR-0304299.

## REFERENCES

1. D.M. Gruen. Nanocrystalline diamond films. *Annual Rev. Mater. Sci.* **29**, 211-59 (1999).
2. V.Y. Dolmatov. Detonation synthesis ultradispersed diamond: properties and applications. *Russian Chem. Reviews* **70**, 607-26 (2001).
3. O. Shenderova, V. Zhirnov, and D. Brenner. Carbon Materials and Nanostructures. *Critical Reviews in Solid State and Materials Sciences* **27**(3/4), 227-356 (2002).
4. V.Yu. Dolmatov. *Ultradisperse diamonds of detonation synthesis: production, properties and applications*. St. Petersburg: State Polytechnical University, 2003.
5. A.L. Vereschagin. *Detonation Nanodiamonds*. Barnaul, Russian Federation: Altai State Technical University, 2001, (in Russian).
6. V.V. Danilenko. *Synthesis and Sintering of Diamond by Detonation*. Energoatomizdat, 2003, (in Russian).
7. Detonation Nanodiamonds and Related Materials, Bibliography Index, First Issue, Eds. A. Vul, V. Dolmatov and O. Shenderova, "Fizintel", St.Petersburg, Russia, 2003.
8. M. Inagaki. *New carbons*. Elsevier, 2000.
9. *Carbyne and Carbynoid Structures*. Eds. R.B. Heimann, S.E. Evsyukov and L. Kavan, Kluwer Academic Pub., 1999.
10. E. Osawa, M. Yoshida, and M. Fujita. Shape and fantasy of Fullerenes. *MRS Bull.* **19**(11), 33 (1994).
11. R.B. Heimann, S.E. Evsyukov, and Y. Koga. Carbon allotropes: a suggested classification scheme based on valence orbital hybridization. *Carbon* **35**, 1654-58 (1997).
12. J.E. Dahl, S.G. Liu, and R.M.K. Carlson. Isolation and structure of higher diamondoids, nanometer-sized diamond molecules. *Science* **299**(5603), 96-9 (2003).
13. J.-Y. Raty, G. Galli, C. Bostedt, T.W. van Buuren, and L.J. Terminello. Quantum confinement and fullerene-like surface reconstructions in nanodiamonds *Phys. Rev. Lett.* **90** (2003).
14. Y. Gogotsi et.al. Graphite polyhedral crystals. *Science* **290**, 317-20 (2000).
15. H.W. Zhu, C.L. Xu, D.H. Wu, B.Q. Wei, R. Vajtai, and P.M. Ajayan. Direct synthesis of long single-walled carbon nanotube strands. *Science* **296**, 884-86 (2002).
16. E.S. Baik, et al. Fabrication of diamond nanowhiskers. *Thin Solid Films* **377**, 295 (2000).
17. T. Tyler, V. Zhirnov, A. Kvit, D. Kang, and J. Hren. Electron emission from diamond nanoparticles on metal tips. *Applied Physics Letters* **82**, 2904-06 (2003).
18. D.W. Brenner, O.A. Shenderova, J.A. Harrison, S.J. Stuart, B. Ni, and S.B. Sinnott. A second-generation reactive empirical bond order (REBO) potential energy expression for hydrocarbons *J. Phys.: Solid State* **14**, 783-802 (2002).
19. P. Badziag, W.S. Verwoerd et.al. Nanometre-sized diamond is more stable than graphite. *Nature* **343**, 244-45 (1990).
20. A. Barnard, S. Russo, and S. Snook. Ab initio modelling of the stability of nanocrystalline diamond morphologies. *Phil. Mag. Lett.* **83**, 39 (2003).
21. A. Barnard, S. Russo, and S. Snook. Coexistence of bucky diamond with nanodiamond and fullerene carbon phases. *Phys. Rev. B* **68**, 073406 (2003).

22. N. Park, K. Lee, S.W. Han et al. Energetics of large carbon clusters: Crossover from fullerenes to nanotubes. *Phys.Rev.B* **65**, 121405 (2002).
23. D. Tomanek and M.A. Schluter. Growth regimes of carbon clusters. *Phys.Rev.Lett.* **67**, 2331 (1991).

## 2

# STRUCTURAL AND ELECTRONIC PROPERTIES OF ISOLATED NANODIAMONDS: A THEORETICAL PERSPECTIVE

J.-Y. Raty<sup>1</sup> and G. Galli<sup>2</sup>

<sup>1</sup> Université de Liège, Département de Physique, 4000 Sart-Tilman Belgique

<sup>2</sup> Lawrence Livermore National Laboratory, P.O. Box 808, Livermore CA94550 USA

**Abstract:**

Nanometer sized diamond has been found in meteorites, proto-planetary nebulae and interstellar dusts, as well as in residues of detonation and in diamond films. Remarkably, the size distribution of diamond nanoparticles appears to be peaked around 2–5 nm, and to be largely independent of preparation conditions. Using *ab-initio* calculations, we have shown that in this size range nanodiamond has a fullerene-like surface and, unlike silicon and germanium, exhibits very weak quantum confinement effects. We called these carbon nanoparticles *bucky-diamonds*: their atomic structure, predicted by simulations, is consistent with many experimental findings. In addition, we carried out calculations of the stability of nanodiamond which provided a unifying explanation of its size distribution in extra-terrestrial samples, and in ultracrystalline diamond films. Here we present a summary of our theoretical results and we briefly outline work in progress on doping of nanodiamond with nitrogen.

**Keywords:**

*ab-initio* calculation, bucky-diamond, isolated nanodiamond, ultrananocrystalline diamond

## 1. INTRODUCTION

Nanoscale diamonds can have extra-terrestrial as well as terrestrial origins. Extra-terrestrial nanodiamonds have been discovered in 1987 by Lewis et al. [1] in primitive meteorites formed before the solar system. They have later been detected in protoplanetary nebulae [2] and in minute quantities in interplanetary dust originated from comets and asteroids [3]. Recently, nanodiamond vibrational signatures have been indirectly

evidenced in some circumstellar disks [4]. A remarkable feature of extra-terrestrial nanodiamonds is their narrow size distribution: those found in meteorites have a median diameter of 2.6 nm, and a similar size distribution would also explain the absorption signal detected from nebulae.

On earth, nanodiamonds can be produced by detonation and by chemical vapor deposition techniques. Detonation synthesis [5] has been greatly optimized in the last 15 years and nanodiamonds produced in this way are now commercially available. These nanodiamonds are often called ‘Ultra Dispersed Diamond’ (UDD) because of their very narrow size distribution peaked, e.g. around  $\sim 4$  nm. Recently nanodiamonds were produced using Chemical Vapor Deposition (CVD) techniques [6]. Under some specific conditions, including a hydrogen depleted atmosphere, it was shown that CVD deposited carbon films are extremely smooth assemblies of nanometer sized particles rather than microcrystallites. These films have been called “Ultra Nanocrystalline Diamond Films” (UNCD).

The characterization of nanodiamonds from both the sky and the earth has revealed interesting, common features, in particular the presence of graphitic-like sites, possibly at the surface [7]. For example, UNCD films are believed to contain 2–5% of  $sp^2$  bonded carbons, supposedly at grain boundaries and less than 1% hydrogen. Aleksenskii et al. [7] performed a structural study of UDD using X-ray diffraction and small angle X-ray scattering and found that the majority of nanodiamond has a core size of about 4 nm, with a surface covered by a mixture of  $sp^2$  and  $sp^3$  bonded carbon atoms. Recently, we have proposed that nanoscale diamond obtained by detonation as well as found in meteorites indeed has a diamond core with a fullerene-like surface reconstruction and we have called these carbon particles bucky diamonds [8]. We will give a description of bucky diamonds in Section 3, after describing the properties of hydrogenated nanodiamonds smaller than  $\sim 2$  nm in Section 2.

There is a growing interest in producing nanodiamonds in the laboratory, not only to understand their growth and formation in the solar and extra-solar systems, but also for their potential technological applications [9,10]. It has been proposed that nanodiamonds could be used to produce bright, low voltage (cold) cathodes and light- emitters, if nitrogen doped. The exceptional hardness, fracture strength, and inertness of UNCD films, together with their smooth surface make them unique materials for miniaturized mechanical systems and devices (MEMS), such as cantilevers and gears [9]. In addition, surface hydrophobicity makes UNCD films ideal for support of biological molecules, such a DNA [10], thus providing a material to integrate biological systems with electronic devices. Even at the molecular level, the recently discovered ‘diamondoids [11]’, which are

composed of a few linked adamantane cages, are considered possible building blocks of future diamond-based nanotechnological applications.

In spite of numerous studies of diamond at the nanoscale, the observed size distribution and stability of diamond nanoparticles has long remained an intriguing property. Recently we have carried out an investigation of the ultradispersivity of diamond at the nanoscale using first principles calculations [12]. We have studied the relative stability of nanodiamonds as a function of size and of the surface hydrogen coverage. Our results show that as the size of diamond is reduced to about 3 nm, it is energetically more favorable for this material to have bare, reconstructed surfaces than hydrogenated surfaces. This inability to retain hydrogen at the surface may then prevent the growth of larger grains. These results are summarized in Section 4 of this paper. Finally, we present our conclusions in Section 5.

## 2. HYDROGENATED DIAMOND NANOPARTICLES

Silicon and Germanium nanoparticles are known to show quantum confinement effects up to 5–7 nm and it is interesting to consider whether such effects could appear in nanodiamond as well. An early XANES study of CVD deposited diamond films [13] suggested that in diamond quantum confinement effects persist up to sizes much bigger than those of Si and Ge nanoparticles, that is up to about 27 nm.

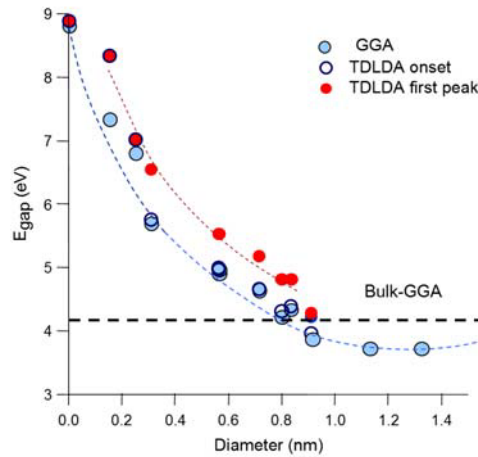


*Figure 1.* Calculated energy gap [ $E_{\text{gap}}$ ] of hydrogenated diamond nanoparticles using Density Functional Theory in the Gradient Corrected Approximation (GGA) and Time dependent Density Functional Theory (TDLDA), as a function of the nanoparticle diameter. The lines are guides to the eye. (See Ref. [8].)



The fit to XANES spectra reported in Ref.[13] and used to substantiate the claim of quantum confinement was later questioned by L. Ley et al. [14]. In addition, recent NEXAFS measurements [15] on nanodiamond films prepared by hot-filament CVD showed quantum confinement effects much smaller than those reported in Ref. [13].

In order to address the question of quantum confinement in diamond, we carried out a combined theoretical and experimental investigation of crystalline nanodiamonds and found that quantum confinement effects are smaller than in Si and Ge, i.e. they persist up to much smaller sizes [8]. The results of our first principles calculations are reported in Figure 1 where we show that for hydrogenated diamond nanoparticles of 1 nm or bigger, the optical gap is the same as in bulk diamond. These theoretical findings are consistent with emission and absorption measurements on soot samples, showing that at  $\sim 4$  nm quantum confinement effects are not present. We note that a key difference between the measurements reported in Ref. [8] and Ref. [13] is the sample crystallinity.

In our calculations we found that the surface structure and hydrogen composition can strongly affect the electronic and optical properties of hydrogenated nanodiamonds. For example, reconstructions of the type of those reported in Figure 2 for a 66 C atom cluster can considerably lower the value of the gap below that of bulk diamond, as shown for sizes larger than 1 nm in Figure 1.

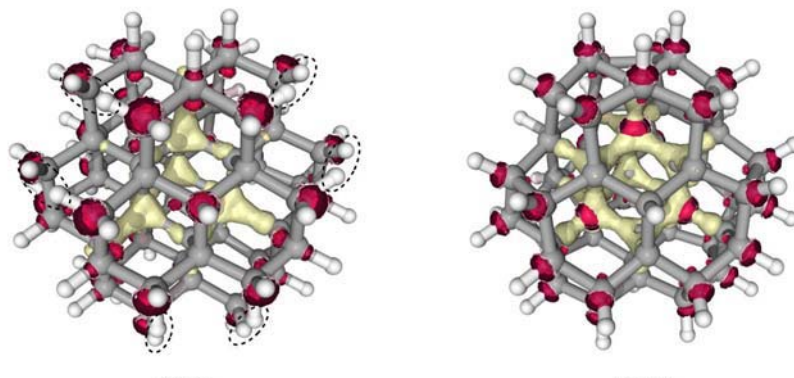


*Figure 2.* Ball and stick representation of the atomic structure of fully hydrogenated  $C_{66}H_{64}$  (left hand side) and  $C_{66}H_{40}$  with reconstructed surfaces (right hand side). Grey and white spheres represent Carbon and Hydrogen atoms, respectively. Contour plots around the atoms represent the squared amplitude of the highest occupied molecular state of the clusters. The reconstruction is initiated by removing pairs of hydrogen atoms, which are circled by dashed lines on the left panel.

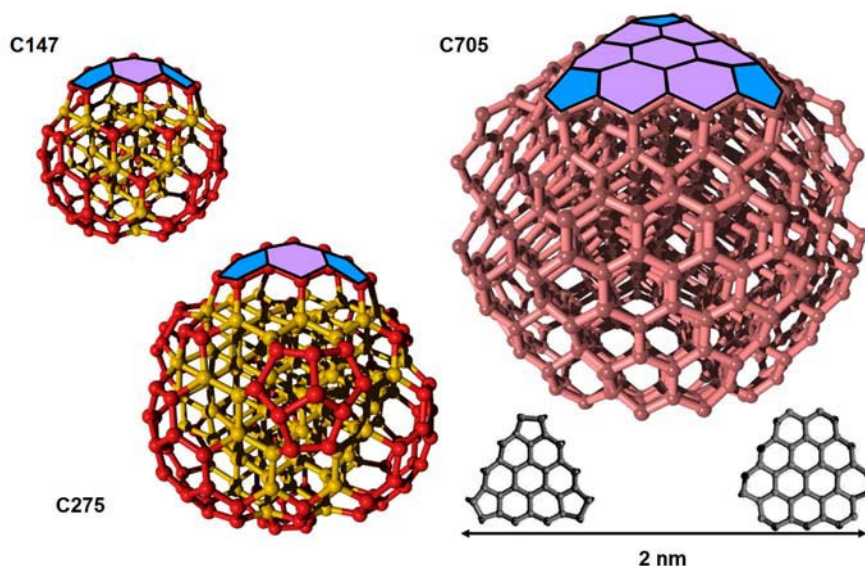


Figure 3. Ball and stick representation of bare nanodiamonds (bucky-diamonds). Reconstructed facets (some of the highlighted for clarity) consists of a mixed pentagons/hexagons network, as represented on the lower right inserts. (See text and Ref. [8])

### 3. BARE NANODIAMONDS

When all hydrogen is removed from the surface of nanodiamond, an interesting surface reconstruction is observed in our *ab-initio* molecular dynamics simulations at room temperature: a fullerene-like cap is formed on the diamond core, yielding a hybrid fullerene-diamond at the nanoscale, which we have called bucky-diamond. The reconstruction occurs spontaneously at room temperature. The atomic structure of two bucky-diamonds obtained using *ab-initio* simulations ( $C_{147}$  and  $C_{275}$ ) and that of larger ones studied with semi-empirical tight-binding methods is reported in Figure 3.

X-ray emission and absorption measurements on soot samples have confirmed that indeed small nanodiamonds have a diamond core and a fullerene like reconstructions, thus also confirming previous measurements and the interesting models developed in Ref. [7].

#### 4. ULTRADISPERSITY AT THE NANOSCALE

Having established the atomic and electronic structure of both hydrogenated and bare nanodiamonds, we studied the relative stability of nanoparticles with the same carbon content but different hydrogen coverage, as a function of size, using a grand canonical formalism. The formation energy of a carbon particle is defined as:

$$E_{\text{formation}} = E_{\text{total}} - \mu_C N_C - \mu_H N_H - E_{\text{vib}}$$

Here  $N_x$  are the numbers of C or H atoms and  $\mu_x$  is their respective chemical potential;  $E_{\text{vib}}$  and  $E_{\text{total}}$  are the vibrational and the total energy of a nanoparticle, respectively, obtained within Density Functional Theory. The formation energy thus expresses the difference in energy between a nanoparticle and a reservoir of carbon and hydrogen atoms whose energy is  $\mu_x$ . In our calculations, we considered five core sizes containing 29, 66, 147, 211 and 275 C atoms and for all of them we found that the stability sequence of the particles with different surface structures is the same as a function of  $\mu_H$ . In all the five cases, in going from the  $\text{CH}_4$  chemical potential to lower values, the stable structures are, in order of increasing stability, nanoparticles with fully hydrogenated surfaces, those with (111) reconstructed, hydrogenated surfaces and those with bare, reconstructed surfaces. Our results for the formation energy of two specific diamond clusters (with 66 and 275 C atoms, respectively) as a function of the hydrogen chemical potential are shown in Figure 4. This figure indicates that the difference in formation energy between particles with hydrogenated surfaces and those with bare surfaces is rapidly decreasing as the size of the nanoparticle is increased. This suggests that there exist a size in the nanometer range where a reversal of stability between hydrogenated and bare nanoparticles will occur and bucky diamonds (or parent structures) will become more stable than diamond nanoparticles with hydrogenated, reconstructed surfaces.

The computed difference in formation energy ( $\Delta$ ) between the stable hydrogenated structure and the bare diamond nanoparticle as a function of size is shown in Figure 5, where we assumed that Delta is dependent only on the number of surface carbon atoms. With this assumption

$$\Delta = E_{\text{formation, bare}}^{3/2} - E_{\text{formation, stable}}^{3/2}$$

is almost linear with the particle diameter. Our results show that for all values of the  $H$  chemical potential,  $\Delta$  becomes *negative* when the diameter of the nanoparticle is comprised between 2 and 3 nanometers. In other words,  $\Delta$  does not depend in any significant way on the hydrogen chemical

potential, and thus to a large extent on different experimental synthesis conditions.

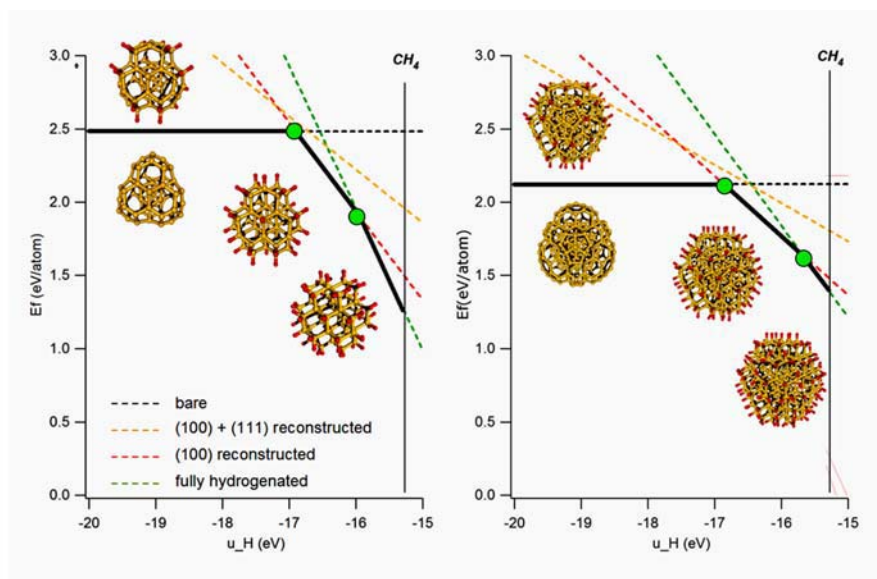


Figure 4. Formation energy of nanodiamonds with different hydrogen coverage and different core sizes (66 Carbon atom and 275 Carbon atoms on the left and right hand sides, respectively), as a function of the hydrogen chemical potential, which mimic different experimental preparation conditions.

Our calculations show that between 2 and 3 nm, it is energetically more favorable for nanodiamond to have a bucky diamond-like structure and bare unreconstructed surfaces than having hydrogen at the surface. The presence of hydrogen is a necessary condition for the growth of diamond; therefore the release of surface hydrogen from growing nanodiamonds should result in the premature end of the growth of bulk samples between 2 and 3 nm. These findings help explain why nanodiamond size distributions are peaked around the same size, about 3 nm, irrespective of the preparation method used to generate the nanoparticles. Although our calculations cannot establish the exact size at which the crossover between hydrogenated and bare, reconstructed surfaces occur, they provide a robust, qualitative explanation of why the crossover occurs in the few nanometers range, and why it is the same irrespective of preparation conditions.

Based on the simple thermodynamic mechanism presented here, one might argue that it would be impossible to grow diamond on a micro- or macroscopic scale. To address this issue, it is necessary to compare the

formation energies of nanodiamonds of various sizes with those of flat diamond surfaces. This comparison indicates that at the highest values of the H chemical potential (-15.5 eV) considered in our study, the infinite (100) surface is more stable than any nanodiamond, while at lower chemical potential, there exist a critical diameter above which the nanodiamond clusters are the most stable structure. For instance at a chemical potential value of -16.5 eV, if the particle grows to a diameter larger than 2.5 nm, then it becomes more stable than a bulk surface. These numerical results help explain how, by varying the hydrogen pressure (and thus the hydrogen chemical potential) in a CVD reactor, one can deposit either microcrystalline or ultrananocrystalline diamond films.

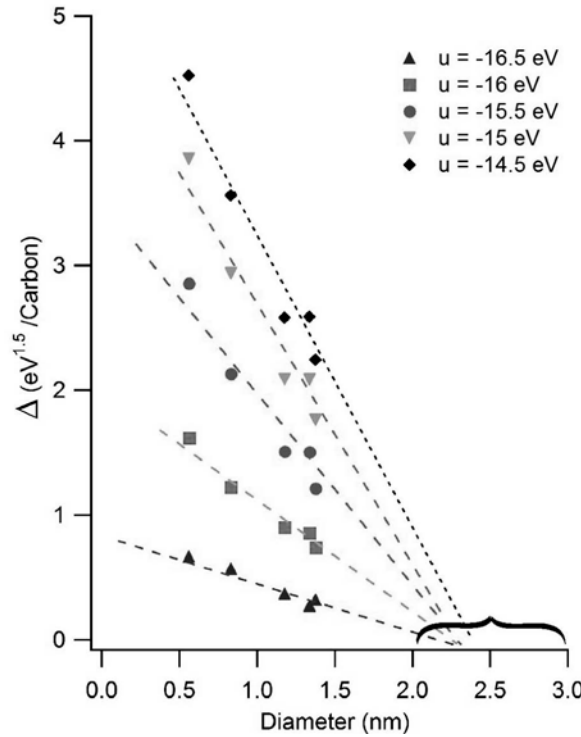


Figure 5. Difference in formation energy between nanodiamonds with fully reconstructed surfaces and the most stable structure found for a given value of the hydrogen chemical potential ( $u$ ), as a function of the nanoparticle size.

## 5. CONCLUSIONS

In summary, using *ab-initio* methods with no adjustable parameters, we have proposed an explanation for the ultradispersity of diamond at the nanoscale which relies on simple thermodynamic arguments. We have shown that depending on the temperature and pressure of the hydrogen and carbon gases used in diamond growth processes, diamond will grow into nanoparticles with reconstructed, non hydrogenated surfaces of about 3 nm or into microcrystallites, if the typical conditions of diamond CVD growth are met. Our results, together with the proposed geometry of bucky diamond will help build structural models of UNCD and UDD films which can be used to study mechanical properties of these systems, as well as their interfaces with biological molecules.

Work is in progress to study doping of nanodiamond, which is a very promising area for technological applications. In this area the research has been focused on nitrogen doping, where the general goal is to introduce carrier levels into the (nano)-diamond gap (this level is located 1.7 eV below the conduction band minimum in bulk diamond) and thus increase the conductivity and lower the electron emission voltage threshold. Calculations are under way to compute optical gaps of both bare and hydrogenated nanodiamonds with nitrogen impurities at the surface, as a function of size.

## Acknowledgements

The authors would like to acknowledge Prof. A. Vul' and Dr. M. Baidakova for useful discussions. This work was performed under the auspices of the U.S. Dept. of Energy at the University of California/LLNL under contract no. W-7405-Eng-48. JYR acknowledges support from the FNRS and the NOMADE- Region Wallonne contract.

## REFERENCES

1. R.S. Lewis, M. Tang, J.F. Wacker, E. Anders, and E. Steel. Interstellar diamonds in meteorites. *Nature* **326**, 160-62 (1987).
2. H.G. Hill, A.P. Jones, and L.B. d'Hendecourt. Diamonds in carbon-rich proto-planetary nebulae. *Astron. Astrophys.* **336**, 41-4 (1998).
3. Z.R. Dai, J.P. Bradley, D.J. Joswiak, D.E. Brownlee, H.G.M. Hill, and M.J. Genge. Possible in situ formation of meteoritic nanodiamonds in the early solar system. *Nature* **418**, 157-59 (2002).
4. C. Van Kerkhoven, A.G. Thielens, and C. Waelkens. Nanodiamonds around HD 97048 and Elias 1. *Astron. Astrophys.* **384**, 568-84 (2002).
5. N.R. Greiner, D.S. Philips, J.D. Johnson, and F. Volk. Diamonds in detonation soots. *Nature* **333**, 440-42 (1988).

6. S. Jiao, A. Sumant, M.A. Kirk, D.M. Gruen, A.R. Krauss, and O. Auciello. Microstructure of ultrananocrystalline diamond films grown by microwave Ar-CH<sub>4</sub> plasma chemical vapor deposition with or without H<sub>2</sub>. *J. Applied Physics* **90**, 118-22 (2001); A.R. Krauss, O. Auciello, M.Q. Ding, D.M. Gruen, Y. Huang, V.V. Zhirnov, E.I. Givargizov, A. Breskin, R. Chechen, E. Shefer, V. Konov, S. Pimetov, A. Karabutov, A. Rakhimov, and N. Suetin. Electron field emission for ultrananocrystalline diamond film. *J. Applied Physics* **89**, 2958-67 (2001).
7. A.E. Aleksenskii, M.V. Baidakova, A.Ya. Vul', and V.I. Siklitskii. The structure of diamond nanoclusters. *Physics of the Solid State* **41**, 668 (1999) and references therein.
8. J.-Y. Raty, G. Galli, A. Van Buuren, and L. J. Terminello. Quantum confinement and fullerene-like surface reconstructions in nanodiamonds. *Phys. Rev. Lett.* **90**, 037401 (2003).
9. A.R. Krauss, O. Auciello, D.M. Gruen, A. Jayatissa, A. Sumant, J. Tucek, D.C. Mancini, N. Moldovan, A. Erdemir, D. Ersoy, M.N. Gardos, H.G. Busmann, E.M. Meyer, and M.Q. Ding. Ultrananocrystalline thin films for MEMS and moving mechanical assembly devices. *Diam. and Rel. Mater.* **10**, 1952-61 (2001).
10. W. Yang, O. Auciello, J.E. Butler, W. Cai, J.A. Carlisle, J.E. Gerbi, D.M. Gruen, T. Knickerbocker, T.L. Lasseter, J.N. Russel, L.M. Smith, and R.J. Hamers. DNA modified nanocrystalline diamond thin-films as stable, biologically active substrates. *Nature Materials* **1**, 253-57 (2002).
11. J.E.P. Dahl, S.G. Liu, and R.M.K. Carlson. Isolation and structure of higher diamondoids, nanometer-sized diamond molecules. *Science* **299**, 96-9 (2003).
12. J.-Y. Raty and G. Galli. Ultradispersity of diamond at the nanoscale. *Nature Materials* (2003).
13. Y.K. Chang, H.H. Hsieh, W.F. Pong, M.H. Tsai, F.Z. Chien, P.K. Tseng, L.C. Chen, T.Y. Wang, K.H. Chen, D.M. Bhusari, J.R. Yang, and S.T. Lin. Quantum confinement effect in diamond nanocrystals studied by X-ray-absorption spectroscopy. *Phys. Rev. Lett.* **82**, 5377 (1999).
14. L. Ley, J. Ristein, and R. Graupner. Comment on Quantum Confinement Effect in diamond nanocrystals studied by X-ray-absorption spectroscopy. *Phys. Rev. Lett.* **84**, 5679 (2000).
15. Y.H. Tang, X.T. Zhou, Y.F. Hu, C.S. Lee, S.T. Lee, and T.K. Sham. A soft X-ray absorption study of nanodiamond films prepared by hot-filament chemical vapor deposition. *Chem. Phys. Lett.* **372**, 320 (2003).



# 3

## FROM NANODIAMOND TO NANOWIRES

A. Barnard

Center for Nanoscale Materials, Argonne National Laboratory, 9700 South Cass Ave,  
Argonne, IL, 60439, USA

**Abstract:** Recent advances in the fabrication and characterization of semiconductor and metallic nanowires are proving very successful in meeting the high expectations of nanotechnologists. Although the nanoscience surrounding  $sp^2$  bonded carbon nanotubes has continued to flourish over recent years the successful synthesis of the  $sp^3$  analogue, diamond nanowires, has been limited. This prompts questions as to whether diamond nanowires are fundamentally unstable. By applying knowledge obtained from examining the structural transformations in nanodiamond, a framework for analyzing the structure and stability of diamond nanowires may be established. One possible framework will be discussed here, supported by results of *ab initio* density functional theory calculations used to study the structural relaxation of nanodiamond and diamond nanowires. The results show that the structural stability and electronic properties of diamond nanowires are dependent on the surface morphology, crystallographic direction of the principal axis, and the degree of surface hydrogenation.

**Keywords:** diamond, nanodiamond, nanowire, morphology, *ab initio*, density functional theory

### 1. INTRODUCTION

The study of nanocarbon in its various forms [1] has grown into an almost autonomous field of materials science [2]. The science and technology of fullerenes and carbon nanotubes has continued to expand and these materials show great promise for future nanodevices. Diamond has also been observed at the nanoscale, with a number of forms of nanodiamond (polycrystalline clusters, nanocrystalline thin films and monodispersed nanodiamond particles) being synthesized using various techniques. Isolated diamond nanoparticles (ultradispersed diamond (UDD) or detonation diamond [3]) are synthesized during high energy exothermic



detonations, whereas ultrananocrystalline diamond (UNCD) thin films are grown using chemical vapor deposition with varying pressure and plasma chemistry [4–6].

In addition to the numerous possible applications of nanocrystals, quasi-one dimensional nanostructures are also becoming important components in nanotechnology. Carbon nanotubes have already been applied to various applications, and nanowires are also expected to play an integral part in the design and construction of both electronic and optoelectronic nanodevices [1]. Still, successes in the fabrication of diamond nanowires to date have been few. Since the  $sp^3$  analogue of carbon nanotubes, diamond nanowires, are isolated structures they are expected to have more in common with UDD diamond nanoparticles than UNCD films. Thus, a rudimentary understanding of the stability of diamond nanowires may begin by considering isolated diamond nanocrystals.

The structure and stability of nanocrystalline diamond is far from trivial. It has been found that upon heating to 1200–1800K, nanodiamonds transform into onion-like carbon (OLC). The transition occurs from the surface inward, with the transformation temperature being dependent on the size of the particle. This transformation has been observed in high temperature annealed 2–5 nm nanodiamond [7,8] involving the partial or complete transformation of the nanodiamonds into OLC. The reverse phenomena involving the transformation of OLC into nanodiamond has also been observed experimentally [9], under electron irradiation. The OLC underwent self-compression at the centre, decaying into diamond nuclei [10] that grew to become single or polycrystalline nanodiamond as the irradiation continued [11].

The creation of stable one-dimensional diamond nanostructure appears also to be non-trivial. Aligned diamond nanowhiskers (a term used to describe tapered nanowires) have been formed using air plasma etching of polycrystalline diamond films [12]. Dry etching of the diamond films with molybdenum deposits created well-aligned uniformly dispersed nanowhiskers up to 60 nm in diameter with a density of  $50/\mu\text{m}^2$ . These diamond nanowhiskers showed well-defined characteristics of diamond. Diamond nanocylinders with a diameter of approximately 300 nm have been reported [13], and most recently nano-rods of single crystalline diamond have been grown [14].

Theoretical methods have also been used to research diamond nanowires as a function of size and morphology [15–17]. Using *ab initio* techniques to study the structural relaxation of diamond nanowires, it was found that the stability of a diamond nanowire was dependent on both the surfaces and the crystallographic direction of the principal axis. Dodecahedral and cubo-dodecahedral morphologies were found to retain the diamond structure

and remain stable upon relaxation, but diamond nanowires with octahedral surface facets exhibited delamination of octahedral surfaces parallel to the nanowire axis; forming hybrid structures known as bucky-wires [18].

In this article an overview of the relationship between the structural properties of nanodiamonds and diamond nanowires examined using *ab initio* computational methods is presented. In particular, the effects of surface hydrogenation on the stability and the electronic properties will be highlighted.

## 2. *Ab initio* TECHNIQUES

The first principles calculations presented herein have been carried out using Density Functional Theory (DFT) within the Generalized-Gradient Approximation (GGA), with the exchange-correlation functional of Perdew and Wang (PW91) [19]. This has been implemented via the Vienna *ab initio* Simulation Package [20,21], which spans reciprocal space with a plane-wave basis. In this case a basis was used up to a kinetic energy cutoff of 290 eV. The Linear Tetrahedron Method (LTM) has been used for Brillouin zone integration with a 4×4×4 Monkhorst-Pack *k*-point mesh. Although this choice of *k*-mesh resulted in superfluous *k*-points in the non-periodic directions, inclusion of these *k*-points was found to assist in convergence of the systems.

The electronic relaxation is performed with an efficient matrix diagonalization routine based on a sequential band-by-band residual minimization method of single-electron energies [22,23], with direct inversion of the iterative subspace, whereas the ionic relaxation involves minimization of the Hellmann- Feynman forces. The relaxations and the final static single point energy calculations used to characterize the final structures employed gradient-corrected Vanderbilt-type pseudopotentials (US-PP) [24,25].

## 3. NANODIAMOND

The transformation of nanodiamonds into OLC mentioned above has been modelled theoretically using various methods [8,26], although most previous studies focussed on spherical nanoparticles [27,28]. To further investigate the importance of geometry and morphology on the equilibrium structure of nanocarbon particles, a broad study has been previously undertaken [29–32], examining nanodiamond structures of octahedral,

cuboctahedral and cubic morphologies of various sizes up to approximately 2 nm in diameter.

Three octahedral nanodiamonds,  $C_{35}$ ,  $C_{84}$  and  $C_{165}$ , were terminated in all directions with  $C(111)(1\times 1):1db$  surfaces (one dangling-bond surfaces), but the structure was found to alter significantly upon relaxation. The smallest  $C_{35}$  nanocrystal adopted a more ‘rounded’ appearance, but retained the  $sp^3$  diamond structure throughout [31]. The  $C_{84}$  octahedral nanodiamond was also found to adopt a rounded appearance but the 74 surface atoms delaminated from the ten atom inner core forming an octahedral OLC structure. The shell-core separation distance was found to be approximately 2.25 Å. The relaxation of the  $C_{165}$  atom octahedral carbon nanocrystal (the centre structure in Figure 1) showed a similar transformation. In this case the 130 surface atoms separate from the 35 atom core cluster, also forming an octahedral nanoparticle with a  $sp^2$  bonded outer shell and a  $sp^3$  core known as a bucky-diamond [28,33], also with the shell-core separation distance of approximately 2.25 Å [31].

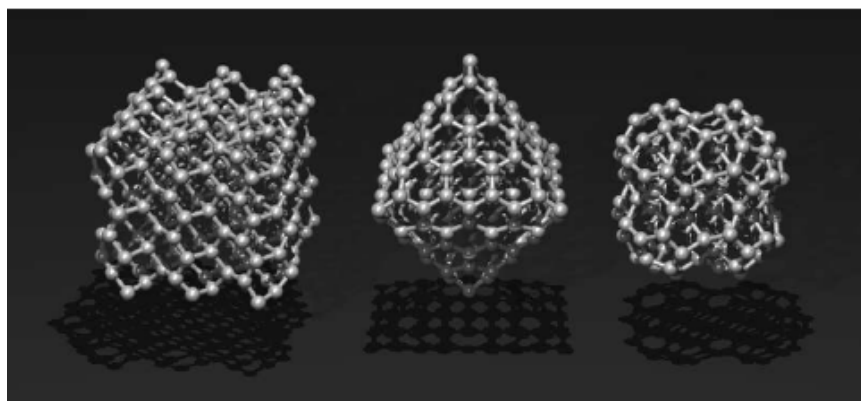


*Figure 1.* Examples of relaxed dehydrogenated nanodiamonds with (left) cubic, (center) octahedral and (right) cuboctahedral morphology. The octahedral and cuboctahedral particles exhibit delamination of the  $C(111)$  surface facets, forming structures known as bucky-diamonds.

Three structures were considered with cuboctahedral morphology, with a surface area comprising 40%  $C(111)$  and 60%  $CC(100)$  surface area. The smallest cuboctahedral nanodiamond considered, the  $C_{29}$  structure, was found to transform into the  $C@C_{28}$  endo-fullerene carbon atom upon relaxation [29]. A larger cuboctahedron with 142 atoms also exhibited a structural transition (as shown to the right of Figure 1). The  $C(100)$  surfaces initially reconstructed, followed by a delamination of the  $CC(111)$  facets to form the curved fullerene ‘cages’ or ‘bubbles’ on the surface. The same

effect was, however, less pronounced in the  $C_{323}$  structure, where only the central region of the C(111) surface formed fullerenic cages [30,31].

Finally, the three cubic nanodiamonds were included in the study (the  $C_{28}$ ,  $C_{54}$  and  $C_{259}$  structures) with C(100)(1×1):2db and C(110)(1×1):1db surfaces. In each case, the initial step of the relaxation process involved the reconstruction of the C(100) surfaces to the (2×1) structure [34]. Upon relaxation the smallest cubic nanodiamond decayed to a tetrahedral amorphous structure, even though the most energetically favorable structure for 28 carbon atoms is known to be the  $C_{28}$  fullerene. The two larger cubic nanodiamonds were found to have surface reconstructions and relaxations comparable to bulk diamond [32] and to be almost entirely comprised of  $sp^3$  carbon. Minor changes in the bonding did occur in the newly formed (2×1) dimers and at the corners of the nanocrystals. The relaxed  $C_{259}$  structure is shown to the left of Figure 1.

These results clearly demonstrate the preferential exfoliation of the C(111) surfaces over the lower index C(100) and C(110) surfaces.

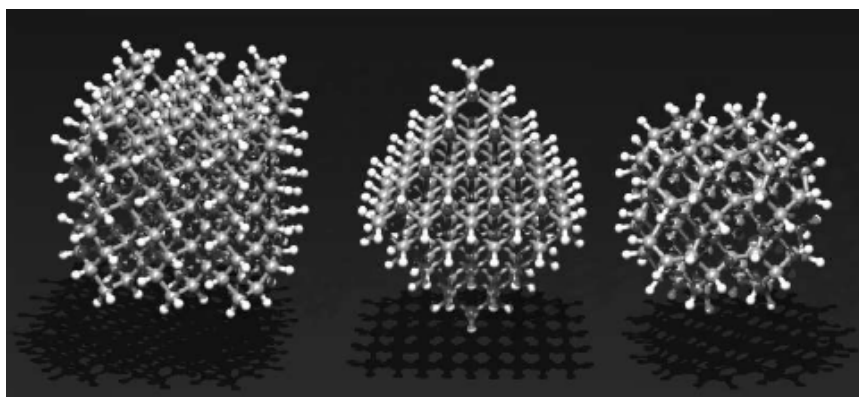


Figure 2. Examples of relaxed hydrogenated nanodiamonds with (left) cubic, (center) octahedral and (right) cuboctahedral morphology. No delamination of the C(111) surfaces is observed.

### 3.1 Hydrogen Induced Stability

Although the studies outlined above show that the surfaces of dehydrogenated nanodiamonds are structurally unstable, it has been found that surface hydrogenation may induce stability [26,31,35,36]. By comparing the displacements of the carbon atoms in the relaxed dehydrogenated and hydrogenated version of the same nanodiamonds [31] it was confirmed that

the transformation to OLC or bucky-diamond can be eliminated, and a more bulkdiamond like surface structure obtained [32].

This was also verified via calculation of Wannier functions [35], which are local bond centred functions (rather than atom centred). The Wannier function calculations illustrate that while the dehydrogenated structures contain distorted  $\sigma$  and  $\pi$ -bonds, the hydrogenated counterparts were found to be entirely  $\sigma$ -bonded. The surface structure of dehydrogenated and hydrogenated C(100) nanodiamond surface has also been analyzed (and compared to bulk diamond) [32], and confirmed that surface hydrogenation of nanodiamond structures serves not only to passivate the surfaces, but also to stabilize the crystal and enforce a bulk diamond-like structure.

In addition to the stabilizing of the surfaces, hydrogenation of nanodiamond surfaces was also found to reduce the full-crystal relaxations that result in the expansion and contraction of nanodiamond lattices. More than just volume changes due to the relaxation of surface layers, full-crystal relaxations involve all the atomic layers, right into the center of the nanocrystal. Such effects are peculiar to nanostructures, with no corresponding effects in bulk diamond. The full-crystal relaxations were identified by considering the changes in the volume of the nanocrystal in conjunction with changes in the total surface area.

### 3.2 Quantum Confinement in Nanodiamonds

Finite size effects have been found to affect more than just the structural stability of nanocrystalline diamond. Chang *et al.* [37] measured the x-ray absorption spectra of a series of nanodiamond thin films with grain diameters ranging from 3.5–5 nm at the C K-edge using a sample drain current mode at room temperature. Resonance peaks resembling the C 1s core exciton were observed, and the results of the C K-edge XANES spectra of nanodiamonds showed that the exciton state and conduction band edge shift to higher energies with the decrease of the crystallite size. They attributed this finding to effects of quantum confinement. Their results also showed that the crystallite size strongly influences the exciton binding energies [37].

Later, Raty *et al.* [28] presented results of XANES experiments and *ab initio* calculations showing that the size of carbon diamond must be reduced to at least 2 nm, in order to observe an increase of its optical gap. The experiments were performed on samples of  $4 \pm 1$  nm in size, and their results predicted that quantum confinement has no appreciable effect on the optical gap of diamond clusters for diameter larger than 1 nm. The nanodiamond K-edge absorption and emission showed the same spectral

features as bulk diamond, and the authors did not observe any blue-shift in the position of nanodiamond conduction and valence band edges (compared to bulk diamond). In addition to this, the core exciton feature clearly observed in the K-edge absorption of bulk diamond was broadened in the nanodiamond spectra, an effect that was attributed to the decrease in lifetime of the core-hole excitation due to confinement of the electron and core hole in the small diamond nanoparticles [28].

#### 4. DIAMOND NANOWIRES

Using knowledge gained from information on the stability of nanodiamond, a methodical approach to the study of diamond nanowires has been devised. Since the C(111) surfaces are unstable on diamond nanocrystals it is reasonable to assume that *stable* diamond nanowires may be bounded exclusively by C(100) and C(110) surfaces. Meeting this criteria three dehydrogenated nanowire morphologies with increasing average diameter have been examined, characterized by pure dodecahedral forms and combinations of cubododecahedral forms. The dodecahedral nanowires were bounded by C(110) surfaces, with a square cross-section and had a [100] principle axis. One cubododecahedral group was termed ‘cubic’ due a square (or rectangular) cross-section, and the other ‘cylindrical’ due a quasi-circular cross-section. The cubic diamond nanowires were bounded by two C(100) surfaces and two C(110) surfaces with a [110] principle axis; whereas the cylindrical nanowires were bounded by four C(100) surfaces and four C(110) surfaces with a [100] principle axis. This choice of morphologies succeeded in avoiding the problematic octahedral surfaces, while still offering a range of cross-sections and surface structures [15,17]. All of the diamond nanowires were periodic along the principle axis, thereby creating infinite structures in one dimension.

An example of the final dodecahedral diamond nanowires is shown to the left in Figure 3. In this case the outer most atomic layer was found to contract inwards, but no surface reconstruction or buckling occurred. This contraction was however more pronounced at the nanowire edges, causing the {110} surfaces to become slightly convex in shape. Both types of cubo-dodecahedral diamond nanowires underwent a two-stage relaxation, involving the reconstruction of the C(100) surfaces to form the (2×1) surface structure, followed by further relaxation of the entire nanowire [15]. Upon relaxation a cubic diamond nanowire with a diameter of < 0.5 nm transformed into a ‘non-classical’ single-walled nanotube; a transition which involved the dissociation of dicarbon molecules from the surface. This type

of transition was not observed in cubic nanowires with a diameter  $> 0.6$  nm. An example of a larger, structurally stable cubic diamond nanowires is shown to the right in Figure 3. This 0.81 nm structure adopted a slightly tapered cross-section, with  $(2\times 1)$  dimers comparable to bulk-diamond surfaces [16]. In contrast final relaxed cylindrical nanowires also retained the diamond  $sp^3$  bonding, but full-wire relaxations resulted in twisted rope-like structures (centre of Figure 3).

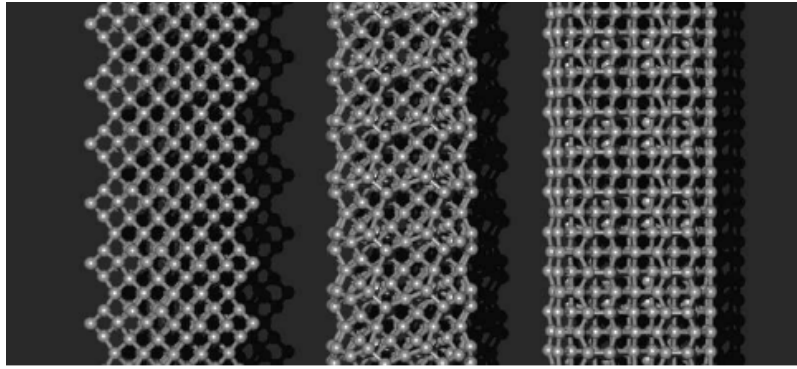


*Figure 3.* Examples of stable dehydrogenated diamond nanowires with (left) dodecahedral, (center) ‘cylindrical’ and (right) ‘cubic’ morphology. These structure are 0.72, 0.84 and 0.81 nm in diameter (respectively), with the (periodic) principle axes aligned top to bottom.

It is important to note that none of the surfaces exfoliated as observed in the  $\{111\}$  nanodiamonds [15]. In general, the diamond bonding was preserved in all of the dodecahedral and cubo-dodecahedral structures upon relaxation for all nanowires over approximately 0.6 nm in diameter. Full-wire relaxations (involving changes in the cross-sectional area and simulation segment length) diminished with increasing nanowire diameter, and the relative stability of the diamond nanowires was found to be dependent on both the surface morphology and the crystallographic direction of the principle axis [15].

#### 4.1 Hydrogenated Diamond Nanowires

As described above, surface hydrogenation has been found to be useful not only in stabilizing the delamination of the C(111) surface of diamond nanocrystals [31], but also promoting a more bulk-diamond like surface structure [32,35]. Similarly, it has been found that surface hydrogenation of diamond nanowire surfaces also promotes a more bulk-diamond like surface structure [16] and reduces the full-wire expansions and contractions [15].



Examples of the hydrogenated diamond nanowires are shown in Figure 4, and more information on the effects of surface hydrogenation on the structure of diamond nanowires may be found in references [16] and [15].

## 4.2 Quantum Confinement in Diamond Nanowires

In addition to structural applications diamond nanowires may also find their way into electronic nanodevices [14]. Like diamond nanocrystals, the surface structure will be central to the electronic properties of diamond nanowires and variations in the surface structure [16] are likely to be important. Quantum confinement effects and the introduction of surface states into the band gap will make the band structure of diamond nanowire differ from that of bulk diamond. Therefore, the electronic density of states (EDOS) in the vicinity of the band gap was investigated for a number of stable diamond nanowires, with both clean and hydrogenated surfaces.

Ten dehydrogenated and nine hydrogenated diamond nanowires with both [100] and [110] orientations and a range of sizes were included in this part of the study [38]. In order to obtain reasonable electronic properties of the diamond nanowires a  $16 \times 4 \times 4$  Monkhorst-Pack  $k$ -point mesh was used, where the increased  $k$ -points correspond to the direction of the principle axes. Although the DFT GGA method may not be considered by some to be the ‘ideal’ method for calculating band gaps, higher levels of theory were found to be too computationally expensive (making the investigation of the larger diameter nanowires unviable). Also, the use of DFT GGA facilitated direct comparison of the nanowire results with the band gaps of bulk diamond and bulk diamond surfaces obtained by other research groups [39,34].

The results of the EDOS of the dehydrogenated dodecahedral nanowires showed additional peaks in the band gap, due to unoccupied C(110)(1 $\times$ 1) surface states, which merge with the valence band maximum and narrow the band gap. The dehydrogenated cubic and cylindrical nanowires also exhibited significant band gap narrowing due to the introduction of unoccupied C(100)(2 $\times$ 1) and C(110)(1 $\times$ 1) states above the valence band maximum. In some instances the band gap (of the cubic nanowires) was found to be zero and the density of states finite at the Fermi level, indicating a semimetal. However, in the case the cylindrical nanowires the unoccupied C(100)(2 $\times$ 1) and C(110)(1 $\times$ 1) states are higher than the valence band maximum and were closer to the conduction band minimum, indicating a semiconductor [38].

The hydrogenated diamond nanowires also exhibited band gap narrowing (irrespective of morphology) due to the occupied C(110)(1 $\times$ 1):H and



C(100)(2×1):H states merging with the conduction band minimum. This narrowing was more pronounced in the larger nanowires even though the surface to volume ratio is lower, but was less significant than that observed in the dehydrogenated nanowires. This highlights that surface hydrogenation also influences the electronic as well as the structural properties [38] of diamond nanowires.

The reduction of the band gap of both dehydrogenated and hydrogenated structures was found to be dependant upon the nanowire diameter (a nanoscale phenomena that can not be predicted from knowledge of bulk diamond surfaces), and the presence of C(110) surfaces. By comparing like-morphologies (both dehydrogenated and hydrogenated versions), the effective band gap was found to decrease with increasing nanowire diameter. By comparing likediameters (across morphologies) the nanowires with a higher fraction of C(110) surface bonds were found to have a lower band gap than those with a higher fraction of C(100) surface bonds. The dehydrogenated nanowires with  $> 50\%$  C(110) surface bonds were semimetals in this size range, whereas dehydrogenated nanowires with  $< 50\%$  C(110) surface bonds were semiconductors [38].

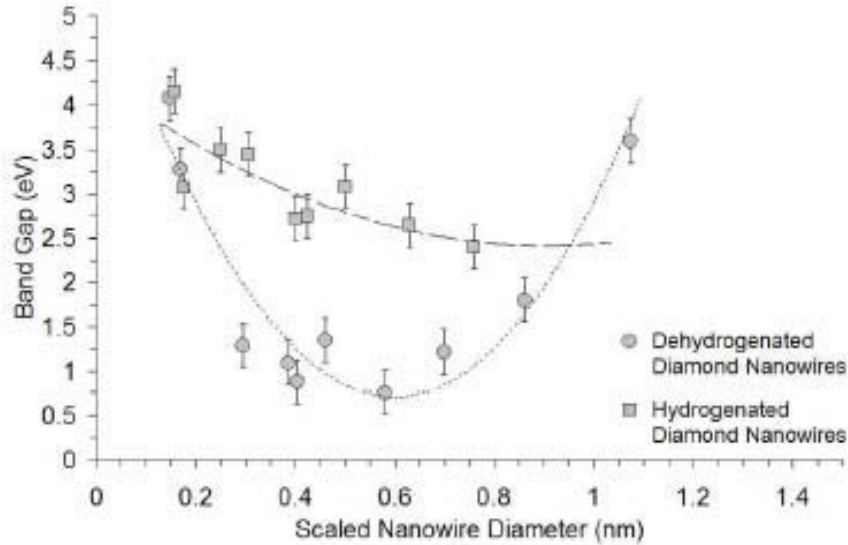


Figure 5. The electronic band gap versus nanowire diameter scaled by the fraction of C(110) surface bonds for the dehydrogenated and hydrogenated diamond nanowires. The quadratic fits are shown to guide the eyes.

Therefore, assuming that the nanowire diameter and the fraction of C(110) surface area are the primary factors influencing the band gap, all of

the data was combined. The band gaps for the dehydrogenated and hydrogenated nanowires were plotted as a function of the average diameter of each nanowire, scaled by the fraction of C(110) surface area [38]. These plots are shown in Figure 5. The dispersion in these results has been attributed to variations in the surface structure of the nanowires, especially in the vicinity of the edges [16]. In each case the empirical best fits were found to be quadratic, with a minima at a diameter of  $\sim 1.22$  nm for the dehydrogenated nanowires and of  $\sim 1.81$  nm for the hydrogenated nanowires (assuming that a general nanowire may be synthesized with 50% C(110) surface area). At these sizes the band gaps were predicted to be  $\sim 0.45$  and  $\sim 2.42$  eV, respectively. Although still under investigation, it is thought that the band gap minimum is due to the unoccupied surface and edge states in the gap. The increase in the gap of nanowires with a larger diameter may be due to the decrease in the dispersion induced by the nanowire edges (and their proximity to one another), whereas the increase in the band gap of nanowires with a smaller diameters may be due to quantum confinement effects.

## 5. CONCLUSIONS

These theoretical results indicated that, like nanodiamond crystals, certain morphological criteria are required to achieve structural stability of diamond nanowires[15–17]. The work of experimentalists has shown that a number of possible synthesis routes exist depending upon the type of structures required [12–14], and that the shape and orientation of these diamond nanomaterials maybe controlled [12,14]. It is apparent however that in order to reliably obtain diamond nanowires with structural properties analogous to bulk diamond, surface hydrogenation is a necessity. The need for consistency and predictability in wide band gap nanomaterials for electronic devices also advocate the need for H-terminated surfaces. The results presented here show that the band gaps of diamond nanowires with diameters less than  $\sim 1.8$  nm are significantly smaller than bulk diamond; and may be semiconducting to semimetallic depending upon the nanowire diameter, surface morphology and degree of surface hydrogenation. Although experimental characterization of the electronic and optoelectronic properties of the various nanowhiskers and nanowires have not yet been reported, these theoretical results suggest that is may be possible to tailor the band gap of diamond nanowires via skillful manipulation of structural parameters. Given the apparent relationship between the structural properties of nanodiamond and diamond nanowires, perhaps the feasibility of this

suggestion may be investigated by first engineering the electronic properties of nanodiamonds.

## Acknowledgments

I would like to thank Ian Snook and Salvy Russo for their valued collaboration, Larry Cutriss for assistance with this article, the Victorian Partnership for Advanced Computing and the Australian Partnership for Advanced Computing supercomputer centre for support during the project. This work was supported in part by the U.S. Department of Energy's Office of Basic Energy Sciences, Division of Materials Science, under contract no. W-31-109-ENG-38.

## REFERENCES

1. O.A. Shenderova, V.V. Zhirnov, and D.W. Brenner. Carbon Nanostructures. *Critical Reviews in Solid State and Material Sciences* **27**, 227 (2002).
2. Y. Gogotsi Perspective, Designing Carbon Crystals for Nanotechnology Applications. *Crystal Growth & Design* **1**, 179 (2001).
3. N.R. Greiner, D.S. Phillips, J.D. Johnson, and F. Volk. Diamonds in detonation soot. *Nature* **333**, 440 (1998).
4. D.M. Gruen. Nanocrystalline diamond films. *Annual Reviews of Material Science* **29**, 211 (1999).
5. T. Sharda and T. Soga. A different regime of nanostructured diamond film growth. *Journal of Nanoscience and Nanotechnology* **3**, 521 (2003).
6. T. Wang, H.W. Xin, Z.M. Zhang, Y.B. Dai, H.S. Shen. The fabrication of nanocrystalline diamond films using hot filament CVD. *Diamond and Related Materials* **13**, 6 (2004).
7. V.L. Kuznetsov, A.L. Chuvilin, Y.V. Butenko, I.Y. Mal'kov, and V.M. Titov. Onion-Like carbon From ultra-disperse diamond. *Chemical Physics Letters* **222**, 343 (1994).
8. V.L. Kuznetsov, I.L. Zilberberg, Y.V. Butenko, A.L. Chuvilin, and B. Seagall, Theoretical study of the formation of closed curved graphite-like structures during annealing of diamond surface. *Journal of Applied Physics* **86**, 863 (1999).
9. F. Banhart and P.M. Ajayan. Carbon onions as nanoscopic pressure cells for diamond formation. *Nature* **382**, 433 (1996).
10. M. Zaiser and F. Banhart. Radiation-induced transformation of graphite to diamond. *Physical Review Letters* **79**, 3680 (1997).
11. F. Banhart. The transformation of graphitic onions to diamond under electron irradiation. *Journal of Applied Physics* **81**, 3440 (1997).
12. E.-S. Baik, Y.-J. Baik, and D. Jeon. Aligned diamond nanowhiskers. *Journal of Materials Research* **15**, 923 (2000).
13. H. Masuda, T. Yanagishita, K. Yasui, K. Nishio, I. Yagi, T.N. Rao, and A. Fujishima. Synthesis of well-aligned diamond nanocylinders. *Advanced Materials* **13**, 247 (2001).
14. Y. Ando, Y. Nishibayashi, and A. Sawabe. 'Nano-rods' of single crystalline diamond. *Diamond and Related Materials* **13**, 366 (2004).

15. A.S. Barnard, S.P. Russo, and I.K. Snook. Ab initio modelling of diamond nanowire structures. *Nano Letters* **3**, 1323 (2003).
16. A.S. Barnard, S.P. Russo, and I.K. Snook. Surface Structure of Cubic Diamond Nanowires. *Surface Science* **538**, 204 (2003).
17. A.S. Barnard, S.P. Russo, and I.K. Snook. From nanodiamond to diamond nanowires. Structural properties affected by dimension. *Philosophical Magazine* **84**, 899 (2004).
18. A.S. Barnard, S.P. Russo, and I.K. Snook. Bucky-wires and the instability of diamond (111) surfaces in one-dimension. *Journal of Nanoscience and Nanotechnology* **4**, 151 (2004).
19. J. Perdew and Y. Wang. Accurate and simple analytic representation of the electron-gas correlation-energy. *Physical Review B* **45**, 13244 (1992).
20. G. Kresse and J. Hafner. Ab initio molecular dynamics for liquid metals. *Physical Review B* **47**, RC558 (1993).
21. G. Kresse and J. Furthmüller. Efficiency of ab-initio total energy calculations for metals and semiconductors using a plane-wave basis set. *Physical Review B* **54**, 11169 (1996).
22. G. Kresse and J. Furthmüller. Efficiency of ab-initio total energy calculations for metals and semiconductors using a plane-wave basis set *Computational Materials Science* **6**, 15 (1996).
23. D.M. Wood and A. Zunger. A new method for diagonalising large matrices. *Journal of Physics A* **18**, 1343 (1985).
24. D. Vanderbilt. Soft self-consistent pseudopotentials in a generalized eigenvalue formalism. *Physical Review B* **41**, 7892 (1990).
25. G. Kresse and J. Hafner. Norm-conserving and ultrasoft pseudopotentials for first-row and transition-elements. *Journal of Physics Condensed Matter* **6**, 8245 (1994).
26. N.W. Winter and F.H. Ree Kinetics and thermodynamic behavior of carbon clusters under high pressure and high temperature. *Journal of Computer-Aided Materials Design* **5**, 279 (1998).
27. F. Fugaciu, H. Hermann, and G. Seifert. Concentric-shell fullerenes and diamond particles, A molecular-dynamics study. *Physical Review B* **60**, 10711 (1999).
28. J.Y. Raty, G. Galli, C. Bostedt, T.W. Buuren, and L.J. Terminello. Quantum confinement and fullerene-like surface reconstructions in nanodiamonds. *Physical Review Letters* **90**, 37402 (2003).
29. A.S. Barnard, S.P. Russo, and I.K. Snook. Ab initio modelling of stability of nanodiamond morphologies. *Philosophical Magazine Letters* **83**, 39 (2003).
30. A.S. Barnard, S.P. Russo, and I.K. Snook. Structural relaxation and relative stability of nanodiamond morphologies. *Diamond and Related Materials* **12**, 1867 (2003).
31. A.S. Barnard, S.P. Russo, and I.K. Snook. First principles investigations of diamond ultrananocrystals. *International Journal of Modern Physics B* **17**, 3865 (2003).
32. S.P. Russo, A.S. Barnard, and I.K. Snook. Hydrogenation of nanodiamond surfaces, Structure and effects on crystalline stability. *Surface Review and Letters* **10**, 233 (2003).
33. A.S. Barnard, S.P. Russo, and I.K. Snook. Coexistence of bucky diamond with the nanodiamond and fullerene carbon phases. *Physical Review B* **68**, 73406 (2003).
34. J. Furthmüller, J. Hafner, and G. Kresse. Dimer reconstruction and electronic surface states on clean and hydrogenated diamond (100) surfaces. *Physical Review B* **53**, 7334 (1996).
35. Barnard A.S., N.A. Marks, S.P. Russo, and I.K. Snook. Hydrogen stabilization of 111 nanodiamond. *Materials Research Society Symposium Proceedings* **740**, 69 (2003).

36. J.Y. Raty and G. Galli. Ultradispersity of diamond at the nanoscale. *Nature Materials* **2**, 792 (2003).
37. Y. K. Chang, H.H. Hsieh, W.F. Pong, M.-H. Tsai, F.Z. Chien, P.K. Tseng, L.C. Chen, T.Y. Wang, K.H. Chen, D.M. Bhusari, J.R. Yang, and S.T. Lin. Quantum confinement effect in diamond nanocrystals studied by X-ray-absorption spectroscopy. *Physical Review Letters* **82**, 5377 (1999).
38. A.S. Barnard, S.P. Russo, and I.K. Snook. Electronic band gaps of diamond nanowires. *Physical Review B* **68**, 235407 (2003).
39. G. Kern and J. Hafner. Ab initio calculations of the atomic and electronic structure of clean and hydrogenated diamond (110) surfaces. *Physical Review B* **56**, 4203 (1997).

# 4

## QUANTUM CHEMICAL STUDIES OF GROWTH MECHANISMS OF ULTRANANOCRYSTALLINE DIAMOND

L.A. Curtiss<sup>1</sup>, P. Zapol<sup>1</sup>, M. Sternberg<sup>1</sup>, P.C. Redfern<sup>1</sup>, D.A. Horner<sup>1,2</sup>, and D.M. Gruen<sup>1</sup>

<sup>1</sup> Argonne National Laboratory, Argonne, IL 60439 USA

<sup>2</sup> North Central College, Naperville, IL 60540 USA

**Abstract:** Computational studies of growth mechanisms on diamond surfaces based on C<sub>2</sub> precursor have been reviewed. The investigations have postulated reaction mechanisms with diamond growth occurring by insertion of C<sub>2</sub> into the C-H bonds of the hydrogen-terminated diamond surface or into  $\pi$ -bonded carbon dimers on dehydrogenated diamond surfaces. Reaction barriers for both growth and renucleation at (011) and (100) diamond surfaces had been calculated using quantum chemistry approaches. Preliminary results on growth mechanism involving CN precursors are also reported.

**Keywords:** diamond, surface reactions, growth mechanisms, quantum chemical calculations, CN precursor

### 1. INTRODUCTION

Diamond films grown by the conventional plasma CVD methods from hydrogen/hydrocarbon mixtures typically have a microstructure with micron-size crystallites. The fraction of atoms in the grain boundaries relative to the bulk in the case of microcrystalline diamond is extremely small. In contrast, diamond films grown from hydrogen poor argon/fullerene or argon/methane microwave plasmas are characterized by a microstructure consisting of crystallites with an average size of 3–10 nm [1]. The latter films are called ultrananocrystalline diamond (UNCD). Use of hydrogen-poor growth conditions produces uniform films with controlled grain size in the few nanometer range and with thicknesses up to several tens of microns.

The growth mechanism for diamond films grown from hydrogen poor argon/fullerene or argon/methane microwave plasmas is significantly different than that in hydrogen rich plasma since the latter depends on hydrogen abstraction by the hydrogen present in the plasma. The carbon dimer has been proposed as the principal growth species in hydrogen poor plasmas used to grow diamond [2].

This paper summarizes our previous computational studies of  $C_2$  growth mechanisms on diamond surfaces and presents some new results for CN adsorption on diamond surfaces. A more detailed review of the diamond growth mechanism involving  $C_2$ ,  $C_2H_2$ , and  $CH_3$  precursors has been presented elsewhere [3]. The investigations involving  $C_2$  have postulated reaction mechanisms with diamond growth occurring by insertion of  $C_2$  into the C-H bonds of the hydrogen-terminated diamond surface or into  $\pi$  bonded carbon dimers on dehydrogenated diamond surfaces. The results for  $C_2$  addition are summarized in Section 3. Similar reactions can be expected for CN adsorption and preliminary results are given in Section 4. Implications for ultrananocrystalline thin film growth involving CN and  $C_2$  precursors are summarized in Section 5.

## 2. THEORETICAL METHODS

Energy calculations were carried out using a variety of methods including *ab initio* molecular orbital theory [4,5], density functional theory [6], and density-functional-based tight binding (DFTB) [7]. The *ab initio* molecular orbital calculations were carried out at the MP2(full)/6-31G(d) and G3 [8] levels of theory. Density functional calculations were carried out using the B3LYP density functional method with the 6-31G(d) basis set (B3LYP/6-31G(d)). Spin-unrestricted methods were used for radicals, and spin-restricted methods for closed-shell species. For gas phase reactions involving  $C_2$ , all calculations were done on the closed-shell  $^1\Sigma_g$  ground electronic state, although the low-lying  $^3\Sigma_u$  state is also accessible at the *ca.* 1000K temperatures typical of CVD experiments.

Application of computational chemistry to study diamond surface reactions requires that a representative model for the surface be chosen. In the work reported here we have considered the four different diamond surfaces (110) 1 $\times$ 1:H, clean (110), (100)2 $\times$ 1:H, and clean 100) illustrated in Figure 1. For a typical surface study two types of models are used: (1) a finite cluster of atoms such as shown in Figure 2 and (2) a periodic slab with a unit cell that is repeated in all directions. Most of the computational studies reported here use one of these two types of models. The cluster model

includes a finite number of carbon atoms that are terminated by hydrogen. The hydrogens replace carbons at the cluster surface, but with normal C-H distances. The number of carbons in the clusters used to model a diamond surface ranges from two to as many as about 60 atoms. An important consideration is the amount of geometry relaxation of the clusters used in calculations.

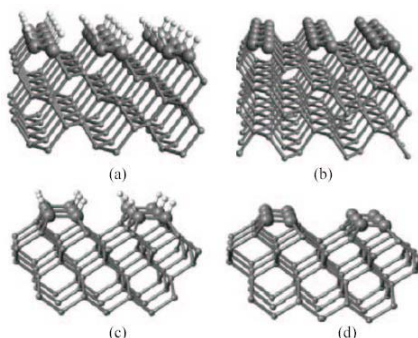


Figure 1. Illustration of diamond surfaces: (a) 110 1 $\times$ 1:H; (b) clean 110; (c) 100 2 $\times$ 1:H; (d) clean 100

The periodic models used for surface studies have translational symmetry in two directions parallel to the surface. In the periodic slab model, translational symmetry is also applied in the third direction, however, the basis vector is chosen to be significantly larger than the slab thickness to avoid interactions between repeating slabs. The periodic slab model is a convenient tool for surface calculations, since many codes that have only 3D periodic boundary conditions implemented can be used for surface studies.

### 3. CARBON DIMER ADDITION TO DIAMOND SURFACES

#### 3.1 (110) 1 $\times$ 1:H Surface

A thorough quantum chemical study of C<sub>2</sub> addition to the hydrogenated diamond (110) surface has been carried out using molecular orbital and density functional methods and reported previously [9]. Hydrogen-terminated diamond-like clusters were used to represent the (110) diamond surface. In a stepwise mechanism, one C<sub>2</sub> unit adds to the surface by inserting itself into first one C-H bond and then a second, producing an adsorbed ethylene-like structure. A second C<sub>2</sub> can then insert itself into two other C-H bonds to produce a surface with two adjacent ethylene-like



groups. Formation of a C-C single bond between adjacent ethylene-like groups can produce a new layer on the diamond surface. All of these steps were examined as well as a concerted addition step in which the  $C_2$  molecule inserts into two C-H bonds simultaneously. Compared to previous mechanisms proposed for diamond growth under CVD conditions, this mechanism was unique in that it was not dependent upon the abstraction of hydrogen atoms from the surface.

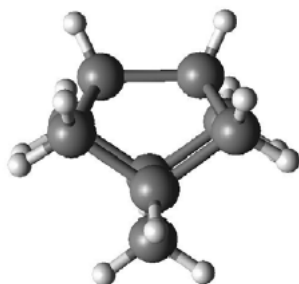


Figure 2. Illustration of  $C_9H_{14}$  cluster that is often used for modeling the (100)  $2\times 1$  diamond surface

In this study the (110) surface of diamond was modeled using 18- and 48-atom carbon clusters, with dangling bonds terminated by hydrogens. Calculations on these two clusters indicated that addition of a  $C_2$  to the diamond (110) surface is favorable, with energy lowerings of about 150–180 kcal/mol per  $C_2$ , respectively. The barriers for addition of  $C_2$  are small. The two-step addition of  $C_2$  to the C-H bonds on the surface has a barrier only 5 kcal/mol and a single-step concerted mechanism for  $C_2$  addition has no barrier. Adjacent  $C_2$  moieties on the (110) surface, adsorbed in ethylene-like arrangements, can be connected via a radical mechanism involving initiation by hydrogen atom addition to the double bond of one ethylene-like group. Calculations indicate that there is little or no energy barrier for this reaction. A path for linking adjacent surface ethylene-like species directly, without the assistance of hydrogen addition, also exists. The barrier for this process is ca. 2 kcal/mol and corresponds to the linking of the first two ethylene-like units to form a singly-bonded diradical structure. The completion of a new surface layer via formation of single bonds between radical structures and ethylene-like groups results in an energy lowering of about 20 kcal/mol.

### 3.2 Clean (110) Diamond Surface

A density functional based tight binding study has been reported by Sternberg et al. [10] of growth steps involving addition of  $C_2$  on a clean

diamond (110) surface (Figure 1). The surface was simulated using a two-dimensional slab geometry with six to eight carbon monolayers. The calculations indicated that initial  $C_2$  adsorption onto a clean (110) surface proceeds with small barriers (2–4 kcal/mol) into a lattice site. The adsorption energy for one  $C_2$  is about 180 kcal/mol. The reaction pathway and energetics of this insertion are very similar to that on the hydrogenated surface (see above). It was found that the addition of more carbon dimers near the first one, leads to  $C_{2n}$  chains along the [110] direction on the surface. The adsorption energies are in the range 160–230 kcal/mol per  $C_2$  at adsorption sites that lead to chain growth and slightly smaller 115–160 kcal/mol for sites that do not result in chain continuation, i.e. defect sites. The barriers for additional  $C_2$  insertion are small (0–12 kcal/mol). The calculations indicate that the  $C_2$  chain addition mechanism eventually leads to coalescing chains with broken backbonds on either side. Relaxation was carried out on a model in which every other trough along the [110] direction was covered with a contiguous chain. This results in a  $C(110):2\times 1$  reconstruction that has multiple bent graphene segments along the [110] direction. The bending direction is that of a carbon nanotube of the (n,n) type, i.e. the armchair tube. Continued addition of  $C_2$  in the valley between the two arches revealed that it was possible, without barrier, to cause the  $sp^2$ -like carbons near the adsorbate to return to an  $sp^3$  configuration and rebond in the diamond structure.

### 3.3 (100) $2\times 1:H$ Diamond Surface

The (100) diamond surface is the slowest growing surface and thus plays an important role in the growth mechanism. Under growth conditions used to grow diamond films with the  $C_2$  dimer, it is likely that the (100) surface has a substantial fraction (0.1–1%) of sites devoid of hydrogen [1]. We have reported investigations [11] of  $C_2$  insertion reactions on the (100)  $2\times 1:H$  surface using density functional theory. A small cluster ( $C_9H_{14}$ ) was used to model the initial steps of the reaction of  $C_2$  with the surface. The initial step is reaction of  $C_2$  with two C-H bonds to form a monosubstituted vinylidene intermediate as illustrated in Figure 3. Reaction paths from this structure lead to either carbene-like or cyclobutene-like structures.

The carbene-like structure results from rearrangement of the intermediate so that one end of the  $C_2$  is attached to one carbon on the top of the  $C_9H_{14}$  cluster (sticking upwards). It is about 32 kcal/mol higher in energy than the cyclobutene-like structure as shown in Figure 4 resulting from rearrangement of the  $C_2$ . The energy barrier between the initial intermediate and the carbene-like structure is about 60 kcal/mol higher than the barrier

along the path from this intermediate to the cyclobutenelike product. Thus, reaction of  $C_2$  to form a cyclobutene-like structure is favored on the monohydrided surface. Starting from the cyclobutene-like structure, formation of a new layer of the existing monohydrided surface proceeds readily.

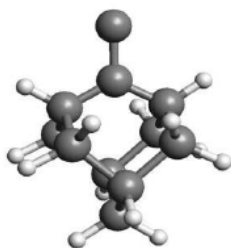


Figure 3. Illustration of initial structure resulting from insertion of  $C_2$  to form a vinylidene-like intermediate.

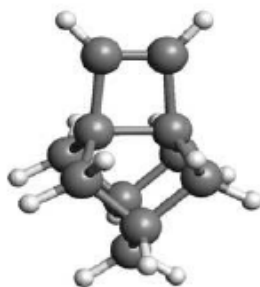


Figure 4. Illustration of cyclobutene-like structure.

### 3.4 Clean (100) 2x1 Diamond Surface

We have reported studies of  $C_2$  insertion reactions on the clean (100) 2x1 using density functional theory with a small cluster ( $C_9H_{12}$ ). The calculations indicated that insertion of  $C_2$  into a carbon-carbon double bond leads to an energy lowering of about 120 kcal/mol for this cluster. The insertion occurs with no energy barrier and results in a carbene-like structure as shown in Figure 5. In a subsequent study [12,13] we reported a densityfunctional based tight binding (DFTB) study of diamond growth by  $C_2$  on a clean (100) surface modeled using a supercell containing 16 atoms per layer and 8 carbon monolayers. The most stable structure is a bridge structure between two adjacent surface dimers along a dimer row with an adsorption energy of 159 kcal/mol. This structure was not found in the cluster study [11] due to the small cluster size used. A barrier of ~28 kcal/mol must be overcome to

reach it from a higher energy corresponding to the carbene-like structure. The barriers to diffusion were found to be very high (40–60 kcal/mol) effectively precluding diffusion on the surface at experimental growth temperatures. The results of the latter study indicate that the clean (100) surface provides sites for both growth and re-nucleation. In contrast  $C_2$  addition on the hydrogenated (100) surface was found to lead to growth [11]. Because only a small fraction of the (100) surface sites are unhydrided, most  $C_2$  insertion events likely lead to growth, with only a few leading to re-nucleation. This can be used in a kinetics analysis to explain the small grain size observed in ultrananocrystalline diamond [14].

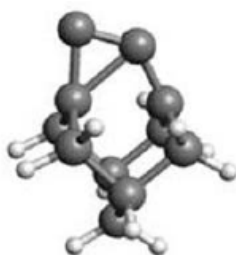


Figure 5. Structure of carbenelike structure resulting from addition of  $C_2$  to a dimer bond on a  $C_9H_{12}$  cluster.

#### 4. CYANOGEN ADDITION TO DIAMOND SURFACE

Nitrogen impurities dramatically alter the properties of UNCD films. For example, diamond films deposited from hydrogen-poor fullerene/argon<sup>15</sup> or methane/argon mixtures [16,17] have 2–5 nm grain sizes and 0.3–0.4 nm-thick grain boundaries, but UNCD films synthesized from gas mixtures containing more than about 5%  $N_2$ , i.e.  $CH_4(1\%)/N_2(> 5\%)/Ar$ , exhibit both increased grain size (*ca.* 12 nm) and grain boundary thickness (*ca.* 1.5 nm) [18]. The increase in grain size that accompanies the introduction of nitrogen into the feed gas suggests that a nitrogen-containing species enhances diamond growth or inhibits nucleation. Appreciable amounts of CN radical and  $C_2$  are found in the microwave plasma, and the concentrations of both increase substantially as  $N_2$  gas is added to the mixture [18].

We have investigated the binding of CN radical to a  $C_9H_{12}$  model (Figure 2) of the unhydrided, reconstructed diamond (100)–(2×1) surface. The energies for the adsorption of CN on this cluster in various configurations are listed in Table 1, and illustrated in Figure 6. A comparison of the binding energies of different structures shows that when CN binds

through one end, the carbon end binds more strongly than nitrogen. Further, CN is adsorbed more strongly by binding to only one carbon of the dimer than by inserting into the  $\pi$  bond to form a three- or four-membered ring. In the most stable structure, 5, with a B3LYP/6-31G(d) reaction energy of -4.51 eV, CN is bound through the C to one carbon, and a Mulliken population analysis locates the unpaired electron on the  $\beta$  carbon. The binding of CN across two adjacent dimers is less stable, by ca. 1.6 eV, than binding to a single dimer through the CN carbon atom. The CN bond length is essentially unchanged when CN forms a single bond to ethene, remaining at 1.17 Å, but lengthens by up to 0.10 Å when CN forms two bonds to the dimer.

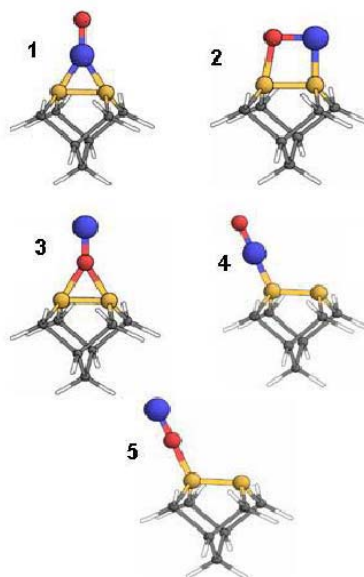


Figure 6. Structures of CN adsorbates on a  $C_9H_{12}$  cluster. (Nitrogen is represented by the large sphere).

Table 1. Energies,  $\Delta E_e$ , of CN addition to cluster model of the reconstructed diamond (100) surface. Energies in eV.

Product	Cluster	HF/6-31G	B3LYP/6-31G
1	$C_9H_{12}$	-1.16	-1.28
2	$C_9H_{12}$	-2.88	-2.96
3	$C_9H_{12}$	-3.17	-3.21
4	$C_9H_{12}$	-4.06	-3.60
5	$C_9H_{12}$	-4.84	-4.51

The results of this study suggest that CN addition to the (100) surface will block potential nucleation sites for  $C_2$  addition and is not likely to be a nucleation site itself because the nitrogen site in structure 5 will not be reactive. This provides a possible explanation of the larger grain size observed experimentally in  $N_2$  plasma. A more detailed study of CN adsorption on the (100) surface will be published elsewhere [19] that includes studies of co-adsorption of  $C_2$  and CN. The results of this more detailed study confirm this conclusion.

## 5. CONCLUSIONS

We have reviewed computational studies of  $C_2$  growth mechanisms on diamond surfaces. These investigations have postulated reaction mechanisms with diamond growth occurring by insertion of  $C_2$  into the C-H bonds of the hydrogen-terminated diamond surface or into  $\pi$  bonded carbon dimers on dehydrogenated diamond surfaces. Quantum chemical calculations of  $C_2$  addition to the diamond (110) surface showed that  $C_2$  can add easily to the surface by inserting itself into first one C-H bond and then a second C-H bond producing an adsorbed ethylene-like structure. A second  $C_2$  can then insert itself into two other C-H bonds to produce a surface with two adjacent ethylenelike groups. Formation of a C-C single bond between adjacent ethylene-like groups can produce a new layer on the diamond surface. This mechanism was found to have only very small reaction barriers and a large energy lowering. Quantum chemical calculations of the clean (100) surface indicate that it constitutes sites for both growth and renucleation. In contrast  $C_2$  addition on the hydrogenated (100) surface was found to lead to growth. Because only a small fraction of the (100) surface sites are unhydrided, most  $C_2$  insertion events likely lead to growth, with only a few leading to renucleation. This may explain the small grain size observed in ultra-nanocrystalline diamond. Finally, the adsorption of CN on a (100) surface is found to be exothermic by about 4.5 eV. CN forms a bond to a single surface atom, with the nitrogen end directed outward.

## Acknowledgements

This work is supported in part by the U.S. Department of Energy, BES-Materials Sciences, under Contract W-31-109-ENG-38.

## REFERENCES

1. D.M. Gruen. Nanocrystalline diamond films. *Annu. Rev. Mater. Sci.* **29**, 211-59 (1999).
2. D.M. Gruen, S. Liu, A.R. Krauss, J. Luo, and X. Pan. Fullerenes as precursors for diamond film growth without hydrogen or oxygen additions. *Appl. Phys. Lett.* **64**, 1502-04 (1994).
3. P. Zapol, L.A. Curtiss, H. Tamura, and M.S. Gordon. Theoretical Studies of Growth Reactions on Diamond Surfaces. In: *Computational Materials Chemistry*, in press
4. W.J. Hehre, L. Radom, J.A. Pople, and P.v.R. Schleyer. *Ab Initio Molecular Orbital Theory*. New York:Wiley, 1987.
5. M. J. Frisch et al. *Gaussian 98*. Pittsburgh: Gaussian, Inc., 1998.
6. W. Kohn, A. D. Becke, and R. G. Parr. Density functional theory of electronic structure. *J. Phys. Chem.* **100**, 12974-80 (1996).
7. Th. Frauenheim, G. Seifert, M. Elstner, T. Niehaus, C. Kohler, M. Amkreutz, M. Sternberg, Z. Hajnal, A. Di Carlo, and S. Suhai. Atomistic simulations of complex materials: ground-state and excited-state properties. *J. Phys. Cond. Matter* **14**, 3015-47 (2002).
8. L.A. Curtiss, K. Raghavachari, P.C. Redfern, V. Rassolov, and J.A. Pople. Gaussian-3 (G3) theory for molecules containing first and second-row atoms. *J. Chem. Phys.* **109**, 7764-76 (1998).
9. P.C. Redfern, D.A. Horner, L.A. Curtiss, and D.M. Gruen. Theoretical studies of growth of diamond (110) from dicarbon. *J. Phys. Chem.* **100**, 11654-63 (1996).
10. M. Sternberg, M. Kaukonen, R.M. Nieminen, and Th. Frauenheim. Growth of (110) diamond using pure dicarbon. *Phys. Rev. B* **63**, 165414 (2000).
11. D.M. Gruen, P.C. Redfern, D.A. Horner, P. Zapol, and L. Curtiss. Theoretical studies on nanocrystalline diamond: nucleation by dicarbon and electronic structure of planar defects. *J. Phys. Chem. B* **103**, 5459-67 (1999).
12. M. Sternberg, P. Zapol, and L. Curtiss. Carbon dimers on the diamond (100) surface: Growth and nucleation. *Phys. Rev. B* **68**, 205330 (2003).
13. M. Sternberg, P. Zapol, T. Frauenheim, J. Carlisle, D. M. Gruen, and L. A. Curtiss, Density functional based tight binding study of C2 and CN Deposition on (100) diamond surface. *Mat. Res. Soc. Symp. Proc.* **675**, W12.11.1 (2001).
14. P. Zapol and M. Sternberg, to be published.
15. D. M. Gruen, S. Liu, A. R. Krauss, and X. Pan. Buckyball microwave plasmas: Fragmentation and diamond-film growth. *J. Appl. Phys.* **75**, 1758-63 (1994).
16. D. Zhou, T. G. McCauley, L. C. Qin, A. R. Krauss, and D. Gruen. Synthesis of nanocrystalline diamond thin films from an Ar-CH<sub>4</sub> microwave plasma. *J. Appl. Phys.* **83**, 540-43 (1998).
17. D. Zhou, D. M. Gruen, L. C. Qin, T. G. McCauley, and A. R. Krauss. Control of diamond film microstructure by Ar additions to CH<sub>4</sub>/H<sub>2</sub> microwave plasmas. *J. Appl. Phys.* **84**, 1981-89 (1998).
18. S. Bhattacharyya, O. Auciello, J. Birrell, J. A. Carlisle, L. A. Curtiss, A. N. Goyette, D. M. Gruen, A. R. Krauss, J. Schlueter, A. Sumant, and P. Zapol. Synthesis and characterization of highly-conducting nitrogen-doped ultrananocrystalline diamond films *Appl. Phys. Lett.* **79**, 1441-43 (2001).
19. M. Sternberg, D. A. Horner, P. C. Redfern, P. Zapol, L. A. Curtiss, to be published.

# 5

## NANODIAMONDS IN THE COSMOS

### *Microstructural and Trapped Element Isotopic Data*

T.L. Daulton

*Naval Research Laboratory, Marine Geoscience Division, Stennis Space Center, MS 39529, USA*

**Abstract:** Interstellar molecular clouds exhibit infrared emission features characteristic of C-H stretching bands that are attributed to dust grains of hydrogen terminated diamond. Within our solar system, primitive chondritic meteorites (among the most well preserved, least altered, and least metamorphosed material that initially formed in our solar system) have been found to contain pristine dust grains that predate the formation of the solar system. Nanometer-sized diamonds are ubiquitous in primitive chondrites at 1–1400 ppm, often representing a significant component of carbon in the matrices of these meteorites. The astronomical sources, which produced the nanodiamonds, and the relative contribution of the sources to the nanodiamond population have not been fully established. The presence of trapped Xe with specific isotopic anomalies (characteristic of explosive nucleosynthesis) in nanodiamond isolates from meteorites suggests at least a subpopulation of the nanodiamonds formed in association with supernovae. However, all attempts to isolate that subpopulation have failed and the exact nature of the Xe carriers is not known. Asymptotic giant branch (AGB) carbon stars are a likely source of presolar nanodiamonds based on their pervasive dust production, however the available isotopic evidence can neither support nor eliminate AGB stars as sources. Similarly, the solar nebula should not be neglected as a possible source since the available isotopic evidence cannot exclude it. Regardless of source, comparative microstructural studies indicate the majority of the nanodiamonds formed by low-pressure vapor condensation. Microstructural and trapped element isotopic data on meteoritic nanodiamonds are discussed in terms of the origin and formation mechanisms of the nanodiamonds.

**Keywords:** presolar nanodiamonds, meteoritic nanodiamonds, star dust, circumstellar grains, CVD nanodiamonds, detonation soot nanodiamonds, twin microstructures, dislocations, lonsdaleite, 2H polytype



## 1. INTRODUCTION

The solar system formed from the collapse of an interstellar gas cloud containing presolar dust that originated in a variety of stellar environments. During the evolution of the solar nebula, a significant fraction of the presolar dust was reprocessed into new minerals and its original form destroyed. The resulting (solar) material experienced extensive thermal, irradiative, and chemical processing. No presolar grains are expected to have survived in large accreted bodies that experienced high temperatures and pressures, such as the sun, planets, and their moons. Nevertheless, sufficiently small accreted bodies should contain surviving presolar grains. In particular, presolar grains are found in the least metamorphosed meteorites, chondrites, which have experienced only modest thermal alteration since their accretion as asteroids. A number of presolar grain species have been isolated from primitive meteorites: diamond [1], SiC (3C and 2H polytypes) [2,3], graphite [4], carbide solid solutions of Ti, V, Fe, Zr, Mo, and Ru [5–8], kamacite (FeNi) [7], corundum ( $\text{Al}_2\text{O}_3$ ) [9], spinel ( $\text{MgAl}_2\text{O}_4$ ) [10], titanium oxide [11], hibonite [12], and silicon nitride [13]. Among these presolar minerals, the origins of the most abundant by mass, diamond, remains largely enigmatic.

Nanometer-sized diamonds are present in primitive chondrites at concentrations (1–1400 ppm) inversely proportional with the degree of metamorphic alteration exhibited by the host meteorite [14]. Nanodiamonds are isolated from these meteorites as a colloid by multi-step acid dissolution [15]. In basic solution, the nanodiamonds remain in colloidal suspension presumably because of acidic carboxyl groups ( $-\text{COOH}$ ) on their surface [16].

## 2. ISOTOPIC COMPOSITIONS OF PRIMARY AND TRAPPED ELEMENTS

As our protosolar nebula evolved, much of its presolar material, possessing widely ranging isotopic compositions reflecting nucleosynthetic processes that occurred in the different star types at various stages of stellar evolution, was extensively mixed and reprocessed. The resulting solar material became isotopically homogeneous as evident by the uniform isotopic compositions in a large number of elements measured in terrestrial, lunar, martian, and many meteoritic rocks, as well as in the solar photosphere. Therefore, mineral grains that have isotopic compositions distinct from the mean compositions of the solar system in a manner that cannot be produced by mass fractionation, cosmic-ray-induced spallation

reactions, or by radioactive decay *in situ* subsequent to the formation of the solar system can be identified as presolar.

The isotopic composition of primary and trapped elements is the only physical characteristic that can definitively identify sources of mineral grains (i.e. asymptotic giant branch (AGB) stars, supernovae, or solar nebula). Since isotopic compositions of individual, meteoritic nanodiamonds cannot be measured, measurements must be made on bulk nanodiamond separates. The  $^{13}\text{C}/^{12}\text{C}$  compositions of nanodiamond separates from acid dissolution residues of primitive carbonaceous chondrites fall within the range of the solar mean. The likely explanation is that individual nanodiamonds possess diverse  $^{13}\text{C}/^{12}\text{C}$  compositions and their ensemble average from all sources mirrors the solar mean. Nonetheless, meteoritic nanodiamond separates are linked to various isotopic anomalies in Xe [1], Te [17], Sr [18], N [19], Ba [18], and H [20]. The anomalous Xe is associated with supernovae, and is often taken as the strongest isotopic evidence for a presolar origin for at least a subpopulation of the diamonds. This is because the anomalies in Ba and Sr are three orders of magnitude smaller than Xe and are somewhat marginal. Isotopic measurements of Te are limited. Furthermore, H is not a reliable indicator of origin because it is loosely bound to diamond surfaces and can be readily altered. Lastly, N isotopic compositions, although anomalous compared to solar, cannot be readily attributed to a particular stellar source.

Xenon occurs in three trapped gas components (termed P3, HL, and P6) that contain all five stable noble gases [21]. Isotopically anomalous Xe occurs in the HL component, and is substantially enriched (by factors of 2) in both its heaviest (Xe-H:  $^{134}\text{Xe}$  and  $^{136}\text{Xe}$ ) and lightest (Xe-L:  $^{124}\text{Xe}$  and  $^{126}\text{Xe}$ ) isotopes with respect to solar Xe [21,22]. The Xe-L and Xe-H isotopes are believed to form in supernova by nucleosynthesis through the *p*-process (photodisintegration or proton capture) and a mechanism similar to the *r*-process (rapid neutron capture), respectively [23,24]. There is no evidence for the presence of *s*-process (slow neutron capture) Xe (Xe-S) which has been observed in presolar SiC [25]. The Xe-S isotopes show an enrichment of even-numbered middle isotopes ( $^{128}\text{Xe}$ ,  $^{130}\text{Xe}$ , and  $^{132}\text{Xe}$ ) and depletion of the odd ones ( $^{129}\text{Xe}$ ,  $^{131}\text{Xe}$ ), and are thought to be produced in AGB stars [26]. Since nanodiamonds likely originate from many different sources, this implies that only those nanodiamonds associated (in whatever way) with supernovae acquire Xe in measurable quantity [27]. In other words, the mechanism in which diamond acquires Xe apparently occurs only in association with the relatively rare supernovae.

The concentration of Xe-HL in the diamond separates is  $15 \times 10^{-8}$  ml/g ( $4 \times 10^{12}$   $^{136}\text{Xe}$ -HL-atoms/g-diamond) [28]. With mean diamond diameters of 2.6 nm (Murchison) and 2.8 nm (Allende) [29], this corresponds to one  $^{136}\text{Xe}$ -HL atom per  $\sim 10^6$  meteoritic nanodiamonds. The high mineral purity

of the nanodiamond separates (>98%), ability to oxidize the carrier, high levels of trapped noble gases (1 noble gas atom per 10 diamonds, that cannot all reside in a trace mineral) coupled with the inseparability of Xe from the other noble gases, and inseparability of the Xe-H and Xe-L components from the separates suggest that diamonds are the Xe carriers [21]. However, all attempts to isolate the Xe carrier have failed and the exact nature of the carrier remains unknown.

Two mechanisms have been proposed for the incorporation of noble gases into meteoritic nanodiamonds: entrapment during condensation and ion implantation. The relatively low abundance of  $^{129}\text{Xe}$  relative to other Xe isotopes in nanodiamond separates suggests Xe was acquired by a chemically non-selective process such as ion implantation [30]. This hypothesis is based on the fact that  $^{129}\text{Xe}$  is produced exclusively from radioactive decay of  $^{129}\text{I}$  (16.4 Myr half life) which is normally an abundant *r*-process product. If the trapping mechanism was chemically selective,  $^{129}\text{Xe}$  should be greatly enriched over other Xe isotopes because the efficiency of trapping chemically active elements like iodine are far greater than noble gases [24]. It is possible that chemically selective trapping occurred only after the  $^{129}\text{I}$  had decayed to negligible levels while yet, in the intervening time, the Xe-HL escaped dilution by non *r*- and *p*-process Xe isotopes, however this is thought to be an unlikely scenario [30].

Low-energy (700 eV) ion irradiation of  $\sim 4$  nm diameter ultradispersed detonation diamonds (UDDs) was shown to implant mixed noble gases (He, Ar, Kr, and Xe) at a yield of 0.1 the ion dose [31]. Thermal release profiles of implanted gases in UDD exhibited a bimodal release similar to those observed in meteoritic nanodiamonds [31]. In meteoritic nanodiamonds this has been attributed to the presence of a noble gas component with nearly-solar isotopic composition (P3) released only at low temperature (200–900°C, presumably from surface sites) [21] and a clear presolar component (HL) released only at high temperature (1100–1600°C, presumably from bulk sites). A minor gas component of nearly-solar isotopic composition (P6), released at slightly higher temperatures than HL, is not completely separated by stepped pyrolysis from HL [21,22]. The relative levels of P3 to HL gases decrease with increased metamorphic grade of the host meteorite [22].

The bimodal release pattern exhibited by irradiated UDD might result from ion-range effects and nature of the irradiated target. The UDDs were irradiated as a deposited thin film and the ion ranges were calculated by TRIM simulation to be of the order of the mean grain radius [31]. However, it is difficult to accurately predict ranges of low-energy ions in solids, let alone in nanocrystals (i.e., 4 nm diameter diamonds have 45% of their C atoms within one unit cell of the surface), and simulated ranges are only an

order of magnitude approximation. Thus, it is possible the bimodal release reflects bulk implantation in the topmost UUD layer and near-surface implantation in the underlying layer. Also, depending on energy, an ion with non-center-of-mass incidence into a nanodiamond could implant near the surface of that crystal or the surface of an adjacent crystal. In contrast, presolar diamonds, if implanted, were likely implanted as individual grains suspended in supernova outflows, complicating their comparison with ion-irradiated UDDs.

For implantation to occur in diamond, a large ion like Xe must disrupt many strong carbon  $sp^3$  bonds and displace many lattice atoms along its trajectory, requiring at least several hundred eV of energy. Nearly all of this energy (minus that dissipated by possible sputtered C atoms) would be deposited into a small nanometer system ( $\sim 2000$  C atoms per mean sized grain), substantially heating the diamond. Therefore, Xe implantation should produce heavy lattice damage in nanodiamonds if not partially or fully transform the grains. Microstructural studies of low-energy ion irradiated UDD are presently underway by the author.

### 3. MICROSTRUCTURE

Several mechanisms have been proposed for nanodiamond formation in supernovae. These include formation by low-pressure condensation similar to chemical vapor deposition (CVD) in expanding gas envelopes [32], shock metamorphism of graphite or amorphous-carbon grains driven by high-velocity (grain-grain) collisions in interstellar shock waves [33], annealing of graphite particles by intense UV radiation (in type II supernova) [34], and irradiation-induced transformation of carbonaceous grains by energetic ions [35]. In circumstellar atmospheres of carbon stars, nanodiamond condensation by CVD has been proposed [1]. Nanodiamond formation in the solar nebula [36], presumably by CVD, has been also proposed.

Product microstructures of nanocrystals depend on the growth mechanisms and conditions during formation. Therefore, to evaluate several of the formation theories for meteoritic nanodiamonds, high-resolution transmission electron microscopy (HR-TEM) compared nanodiamonds synthesized by shock metamorphism and CVD to those isolated from the Allende and Murchison carbonaceous chondritic meteorites [29]. Shock-synthesized diamonds were produced from mixtures of high explosives TNT (trinitrotoluene  $C_7H_5N_3O_6$ ) and RDX (cyclotrimethylene-trinitramine  $C_3H_6N_6O_6$ ) detonated in Ar-filled chambers [37]. The CVD nanodiamonds were synthesized in a substrate-free microwave plasma CVD flow reactor by

nucleation and homoepitaxial growth directly from the vapor phase[38]. Although changes in experimental conditions can result in a range of growth features and affect the proportion of nanodiamonds synthesized by any given process, microstructural features should exist that are uniquely characteristic of specific formation mechanisms exclusive to either condensation or shock metamorphism. In fact, such features were identified in the synthesized nanodiamonds, and when compared to the microstructures of nanodiamonds from Allende and Murchison indicated that the predominant mechanism for meteoritic nanodiamond formation is that of vapor condensation [29].

### 3.1 Twin Microstructures

In cubic diamond, twinning along  $\{111\}$  planes is common and results when the stacking sequence of  $\{111\}$  planes is abruptly reversed, e.g.  $\{AaBbCcBbAa\}$ . In coincident site lattice (CSL) notation, this twin structure is described as a first order  $\Sigma=3$   $\{111\}$  twin. The interface at a  $\Sigma=3$  twin boundary is one of the lowest-energy lattice defects. As a result, cubic nanocrystals can form  $\Sigma=3$  twin structures relatively easily to accommodate growth constraints. Thus,  $\Sigma=3$  twin microstructures should provide a diagnostic indicator for different nanodiamond formation mechanisms.

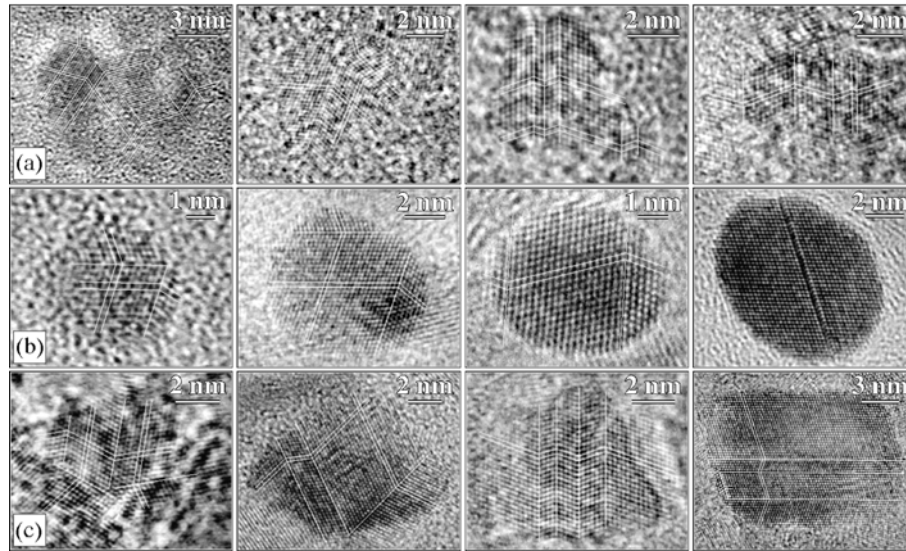


Figure 1. Multiply-twinned microstructures in meteoritic (row a), CVD (row b), and detonation (row c) nanodiamonds.

Multiple  $\Sigma=3$  twins are relatively common microstructures in nanodiamonds and occur in two configurations. The first type (linear) exhibits parallel  $\Sigma=3$   $\{111\}$  twin boundaries that terminate at the crystal surface (Figure 1). The second type (non-linear) is characterized by oblique  $\Sigma=3$   $\{111\}$  twin boundaries (Figure 1) that terminate either at crystal surfaces, twin boundary intersections, or both.

Important differences become apparent when the relative abundances of twin microstructures are compared in the synthesized diamonds (Figure 2). Firstly, the ratio of single crystals to twinned crystals in shock-synthesized diamonds differs from those synthesized by CVD. There is a smaller proportion of single crystals in the detonation soot residues. Since re-entrant corners of twinned crystals are associated with increased growth rates over single crystals [39], this suggests that the mean growth rate for shock-synthesized diamonds is greater than the mean growth rate of CVD-synthesized diamonds. Nanodiamonds present in the detonation soot residues must have experienced rapid thermal quenching to escape graphitization after the passage of the shock front. Those nanodiamonds that survived must have experienced high growth rates. The abundance of single crystals relative to twinned crystals in the meteoritic residues suggests growth rates similar to those of the CVD-synthesized diamonds.

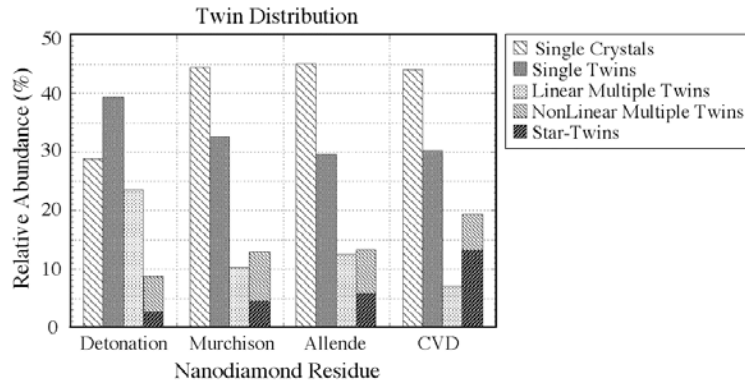


Figure 2. Normalized distribution of  $\Sigma=3$  twin microstructures for nanodiamonds in each residue. Unobstructed and isolated nanodiamonds exhibiting clear cross-lattice fringes were classified by their twin type. Statistics are based on 209 (detonation), 372 (Murchison), 257 (Allende), and 130 (CVD) individual nanodiamonds; a total of 968 nanodiamonds.

Secondly, linear features dominate in shock-synthesized nanodiamonds. During detonation synthesis of nanodiamonds, large, highly anisotropic shock pressure gradients would momentarily exist. Following a shock-induced carbonaceous grain-grain collision, partially molten material would



rapidly solidify behind planar shock fronts. Further, any potential nanodiamond condensation at high-pressure shock fronts would occur within highly anisotropic conditions. In both cases, crystallization should occur along planar growth fronts producing microstructures dominated by parallel twin boundaries. Consistent with this interpretation, the shock-synthesized nanodiamonds display a distribution of multiple twins dominated by parallel twin boundaries. The direction of growth is presumably related to the geometry of the shock front and direction of the pressure gradients. In sharp contrast, the CVD-synthesized nanodiamonds are dominated by non-linear multiple twins indicative of isotropic growth. The multiply twinned structures of meteoritic nanodiamonds more closely resemble CVD nanodiamonds.

The most striking non-linear, multiply-twinned configurations correspond to multiply-twinned particles (MTPs). The most common MTPs are decahedra (five slightly distorted tetrahedra with a common  $[110]$  edge,  $D_{5h}$  point group symmetry) and icosahedra (twenty slightly distorted tetrahedra sharing a common apex,  $I_h$  symmetry). The CVD nanodiamonds, synthesized by direct nucleation and homoepitaxial growth from the vapor phase, have a large abundance of decahedra MTPs (Figure 3b). Icosahedra MTPs were also observed. Unlike decahedra MTPs (star twins), icosahedra MTPs do not exhibit well-defined lattice fringes because their arrangement of overlapping tetrahedral twin domains produces complex moiré patterns. Icosahedra MTPs are excluded in the twin distributions of Figure 2 because the selection criteria used to generate the statistics only accepted nanodiamonds with well-defined  $\langle 111 \rangle$  cross-lattice fringes.

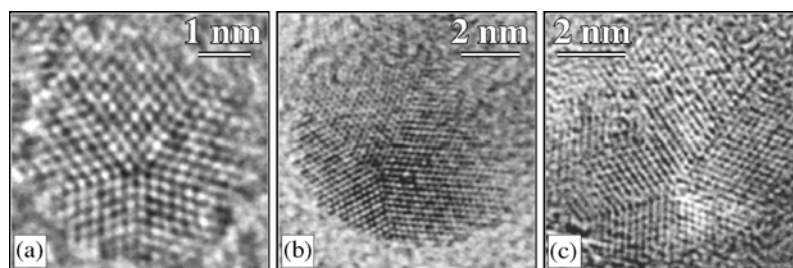


Figure 3. Star twin microstructure (i.e. decahedra multiply-twinned particle) in a) meteoritic (Allende), b) CVD-synthesized, and c) shock-synthesized nanodiamonds.

Similar to CVD residues, star twins are relatively common growth features in the meteoritic residues (Figure 3a). In contrast, star twins (Figure 3c) are relatively rare in detonation soot residues with an abundance at least a factor of two less than in the meteoritic residues (Figure 2). The

coherent twin boundaries present in the star twins are indicative of radial (isotropic) growth as would be possible from the direct nucleation and homoepitaxial growth from a locally uniform supersaturated gas such as in a CVD-type process. Star-twin microstructures would not be expected from the highly anisotropic shock-induced metamorphism of carbonaceous grains. The non-linear multiple-twin crystals (including MTPs) observed in detonation soot residues might have formed by a less efficient mechanism occurring within the rarefaction wave of the expanding shock front. Vaporization of a fraction of the precursor carbonaceous material in the shock heating event could supersaturate the partially ionized gas in carbon. Given favorable conditions, vapor condensation might occur after the passage of the shock front leading to nanodiamond nucleation and growth.

### 3.2 Dislocation Microstructure

Dislocations represent relatively high-energy defects because their cores contain disrupted nearest-neighbor bonds and significant bond distortion. In comparison to the formation of twins and stacking faults, which is influenced by low-energy processes, formation of dislocations requires relatively high-energy processes. This is especially the case for diamond with strong  $sp^3$  carbon bonds. For example, epitaxial dislocations are common in CVD diamond films and result from strain induced at the substrate interface and at interfaces where two growing crystals impinge at an arbitrary angle. High dislocation densities also develop in natural diamond to accommodate lattice distortions around mineral inclusions and plastic deformation caused by shear stresses in the upper mantle.

The very nature of martensitic-type mechanisms occurring behind shock fronts can leave a high density of residual dislocation defects in the transformation product. A small population of nanodiamonds containing dislocations with disorder were observed in the detonation soot residue (Figure 4). In sharp contrast, dislocations are not expected to form in nanometer grains that nucleated directly from the vapor phase, and indeed, no such defect structures were observed in the CVD-synthesized nanodiamonds.

No analogous dislocations were observed in the meteoritic nanodiamonds. It is possible that the dislocations could have been removed by thermal processing prior to or following accretion of the meteorite. However, the temperatures required to anneal dislocations would be sufficient to desorb surface hydrogen. On the contrary, a significant amount of presolar (surface-bound) H is retained by the meteoritic nanodiamonds [40]. Alternatively, dislocations might preferentially etch under chemical



attack. However, it is unlikely that the chemical isolation destroyed meteoritic nanodiamonds with dislocations. Detonation soot residues were subjected to acid treatments, although not as extensive as the meteorites, and still retain nanodiamonds with dislocations. Thus, the lack of dislocation microstructures suggests that the majority of meteoritic nanodiamonds did not form by shock metamorphism.

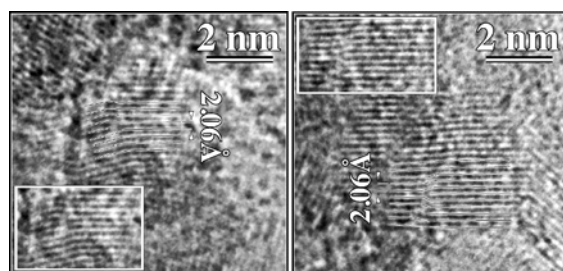


Figure 4. Shock-synthesized nanodiamonds containing dislocations. The superimposed lines illustrate the missing  $\langle 111 \rangle$  half planes. Insets display non-annotated dislocation images.

### 3.3 Polytype Variations

In analogy to the twin and dislocation microstructures which correlate with different formation processes, polytype modifications could provide indicators of particular formation mechanisms. The rare 2H polytype of diamond (lonsdaleite) has been observed together with cubic (3C) diamond in the highly metamorphosed Canyon Diablo iron meteorite and Goalpara achondrite meteorite [41,42]. Analyses of the coexisting minerals in these meteorites indicate that they experienced high levels of shock [43,44]. Furthermore, macroscopic diamond present in Novo-Urei and Goalpara ureilites have preferred orientations with respect to the meteorite matrix, indicative of an anisotropic formation process such as shock [44]. Although Greiner *et al.* [37] did not report any X-ray diffraction lines of lonsdaleite in their detonation soot residues, HRTEM images reveal a small amount ( $<$  several percent by number) of 2H diamond (Figure 5a,b). Nanocrystals with cross-lattice fringes similar to those of the [100] zone of lonsdaleite were observed in the CVD residue; however their small size ( $<$  1.2 nm) and low contrast made it difficult to accurately measure their lattice spacings. As such they are only plausible candidates for lonsdaleite.

The meteoritic nanodiamond separates contained a few nanocrystals exhibiting cross-lattice fringes consistent with the [100] zone axis of lonsdaleite. Furthermore, a nanodiamond from Allende exhibiting a homoepitaxial intergrowth of the 2H and 3C polytypes was observed

(Figure 5c). The  $\{111\}$  cubic-diamond plane is identical to the  $\{001\}$  (2H) lonsdaleite plane, and therefore, the interface between the two polytypes is coherent. The 2H region displays some disorder and may reflect the relative instability of lonsdaleite with respect to 3C diamond. Allende has suffered negligible shock deformation and Murchison is a breccia composed of minerals exhibiting slight to moderate shock. Since neither experienced the shock levels necessary to produce lonsdaleite, lonsdaleite must have formed prior to the accretion of those parent bodies.

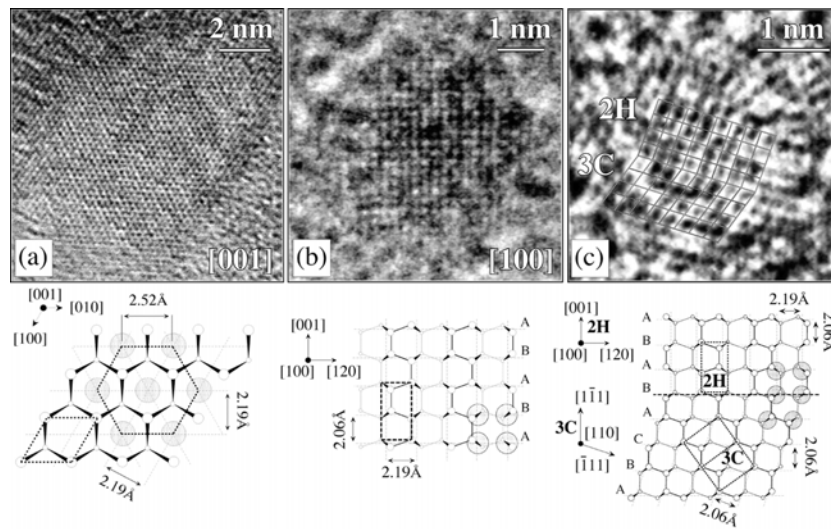


Figure 5. Nanocrystals of the 2H polytype of diamond (lonsdaleite) from a-b) detonation soot and c) meteoritic (Allende) residues.

Synthesized lonsdaleite in the detonation soot residues differs from the natural lonsdaleite in the meteoritic residues in several respects. Shock-synthesized lonsdaleite crystals are generally larger, more ordered, and more numerous than in meteoritic residues. These differences could point to a mechanism other than shock for the formation of meteoritic lonsdaleite. For example, low-pressure synthesis of several hexagonal polytypes of diamond, including 2H, have also been reported in microwave plasma CVD flow reactors [45] and in thermal plasma CVD reactors [46]. Nevertheless, meteoritic diamonds represent an ensemble average of many different astrophysical sources and therefore shock formation of a subpopulation is not inconsistent with the other microstructural data. However, if supernova products of shock metamorphism contribute to the population of nanodiamonds in meteorites, then certainly they represent a minor

subpopulation since the majority of the meteoritic nanodiamonds do not exhibit microstructures indicative of anisotropic shock.

#### 4. CONCLUSIONS

Presolar grains are direct specimens from distant stellar environments, recording valuable information about the physical and chemical conditions where the grains formed. In addition, alteration structures of presolar minerals provide important information about the early evolution of our solar system and the metamorphic processes that occurred on the meteorite parent bodies. Nanoscale characterization of the microstructures of presolar and extraterrestrial minerals represents a new direction in astronomy that can provide important geochemical information which otherwise would be difficult, if not impossible, to obtain.

Nanodiamonds, likely originating from several sources, are present in primitive meteorites at significant concentrations. At least a subpopulation of meteoritic nanodiamonds, if not all, predate the formation of the solar system. Presolar origin is suggested by trace levels of trapped Xe of supernova origin (Xe-HL) in the bulk meteoritic nanodiamond separates. However, the Xe carrier has never been isolated and directly identified. Although the sources and their relative contribution to the population of meteoritic nanodiamonds remain to be established, microstructural studies provide sufficient evidence to indicate that the majority of the meteoritic nanodiamonds formed by low-pressure condensation similar to the CVD process.

#### Acknowledgements

This material is based upon work partially supported by NASA under contract W-10246 issued through the Office of Space Science.

#### REFERENCES

1. R.S. Lewis, M. Tang, J.F. Wacker, E. Anders, and E. Steel. Interstellar diamonds in meteorites. *Nature* **326**, 160-62 (1987).
2. T. Bernatowicz, G. Fraundorf, M. Tang, E. Anders, B. Wopenka, E. Zinner, and P. Fraundorf. Evidence for interstellar SiC in the Murray carbonaceous meteorite. *Nature* **330**, 728-30 (1987).
3. T.L. Daulton, T.J. Bernatowicz, R.S. Lewis, S. Messenger, F.J. Stadermann, and S. Amari. Polytype distribution in circumstellar silicon carbide. *Science* **296**, 1852-55 (2002).
4. S. Amari, E. Anders, A. Virag, and E. Zinner. Interstellar graphite in meteorites. *Nature* **345**, 238-40 (1990).

5. T.J. Bernatowicz, S. Amari, E.K. Zinner, and R.S. Lewis. Interstellar grains within interstellar grains. *Astrophys. J.* **373**, 73-6 (1991).
6. T.J. Bernatowicz, R. Cowsik, P.C. Gibbons, K. Lodders, B. Fegley Jr., S. Amari, and R.S. Lewis. Constraints on stellar grain formation from presolar graphite in the Murchison meteorite. *Astrophys. J.* **472**, 760-82 (1996).
7. T. Bernatowicz, J. Bradley, S. Amari, S. Messenger, and R. Lewis. New kinds of massive star condensates in a presolar graphite from Murchison. *Lunar Planet. Sci.* **30**, 1392 (1999).
8. K. Croat, T. Bernatowicz, F.J. Stadermann, S. Messenger, and S. Amari. Coordinated isotopic and TEM studies of a supernova graphite. *Lunar Planet. Sci.* **33**, 1315 (2002).
9. I.D. Hutcheon, G.R. Huss, A.J. Fahey, and G.J. Wasserburg. Extreme  $^{26}\text{Mg}$  and  $^{17}\text{O}$  enrichments in an Orgueil corundum: Identification of a presolar oxide grain. *Astrophys. J.* **425**, 97-100 (1994).
10. L.R. Nittler, C.M. O'D. Alexander, X. Gao, R.M. Walker, and E.K. Zinner. Interstellar oxide grains from the Tieschitz ordinary chondrite. *Nature* **370**, 443-46 (1994).
11. L.R. Nittler and C.M. O'D. Alexander. Automatic identification of presolar Al- and Ti-rich oxide grains from ordinary chondrites. *Lunar Planet. Sci.* **30**, 2041 (1999).
12. B.-G. Choi, G.J. Wasserburg, and G.R. Huss. Circumstellar hibonite and corundum and nucleosynthesis in asymptotic giant branch stars. *Astrophys. J.* **522**, 133-36 (1999).
13. P. Hoppe, R. Stöbel, P. Eberhardt, S. Amari, and R.S. Lewis. Evidence for an interstellar nitride grain with highly anomalous isotopic compositions of C, N and Si. *Lunar Planet. Sci.* **25**, 563-64 (1994).
14. G.R. Huss and R.S. Lewis. Presolar diamond, SiC, and graphite in primitive chondrites: Abundances as a function of meteorite class and petrologic type. *Geochim. Cosmochim. Acta* **59**, 115-60 (1995).
15. S. Amari, R.S. Lewis, and E. Anders. Interstellar grains in meteorites: I. Isolation of SiC, graphite, and diamond; size distributions of SiC and graphite. *Geochim. Cosmochim. Acta* **58**, 459-70 (1994).
16. R.S. Lewis, E. Anders, and B.T. Draine. Properties, detectability and origin of interstellar diamonds in meteorites. *Nature* **339**, 117-21 (1989).
17. S. Richter, U. Ott, and F. Begemann. Tellurium-H in interstellar diamonds. *Lunar Planet. Sci.* **28**, 1185 (1997).
18. R.S. Lewis, G.R. Huss, and G. Lugmair. Finally, Ba & Sr accompanying Xe-HL in diamonds from Allende. *Lunar Planet. Sci.* **22**, 807-8 (1991).
19. J.W. Arden, R.D. Ash, M.M. Grady, I.P. Wright, and C. T. Pillinger. Further studies on the isotopic composition of interstellar grains in Allende: 1. Diamonds. *Lunar Planet. Sci.* **20**, 21-2 (1989).
20. A. Virag, E. Zinner, R.S. Lewis, and M. Tang. Isotopic composition of H, C, and N in C $\delta$  diamonds from the Allende and Murray carbonaceous chondrites. *Lunar Planet. Sci.* **20**, 1158-59 (1989).
21. G.R. Huss and R.S. Lewis. Noble gases in presolar diamonds. I. Three distinct components and their implications for diamond origins. *Meteoritics* **29**, 791-810 (1994).
22. G.R. Huss and R.S. Lewis. Noble gases in presolar diamonds. II. Component abundances reflect thermal processing. *Meteoritics* **29**, 811-29 (1994).
23. D. Heymann and M. Dziczkaniec. Xenon from intermediate zones of supernovae. *Proc. Lunar Planet. Sci.* **10**, 1943-59 (1979).
24. D.D. Clayton. Origin of heavy xenon in meteoritic diamonds. *Astrophys. J.* **340**, 613-19 (1989).

25. R.S. Lewis, S. Amari, and E. Anders. Interstellar grains in meteorites. II. SiC and its noble gases. *Geochim. Cosmochim. Acta* **58**, 471-94 (1994).
26. B. Srinivasan and E. Anders. Noble gases in the Murchison meteorite: Possible relics of *s*-process nucleosynthesis. *Science* **201**, 51-6 (1978).
27. T.J. Bernatowicz. In: *From Stardust to Planetesimals*. Eds. Y.J. Pendleton and A.G.G.M. Tielens, ASP Conference Series, San Francisco, pp. 227-51 (1997).
28. E. Anders, in *Meteorites and the Early Solar System*, edited by J. Kerridge (University of Arizona Press, Tucson, 1988), pp. 927-55.
29. T.L. Daulton, D.D. Eisenhour, T.J. Bernatowicz, R.S. Lewis, and P.R. Buseck. Genesis of presolar diamonds: Comparative high-resolution transmission electron microscopy study of meteoritic and terrestrial nano-diamonds. *Geochim. Cosmochim. Acta* **60**, 4853-72 (1996).
30. R.S. Lewis and E. Anders. Isotopically anomalous xenon in meteorites: A new clue to its origin. *Astrophys. J.* **247**, 1122-24 (1981).
31. A.P. Koscheev, M.D. Gromov, R.K. Mohapatra, and U. Ott. History of trace gases in presolar diamonds inferred from ion-implantation experiments. *Nature* **412**, 615-17 (2001).
32. D.D. Clayton, B.S. Meyer, C.I. Sanderson, S.S. Russell, and C.T. Pillinger. Carbon and nitrogen isotopes in type II supernova diamonds, *Astrophys. J.* **447**, 894-905 (1995).
33. A.G.G.M. Tielens, C.G. Seab, D.J. Hollenbach, and C.F. McKee. Shock processing of interstellar dust: Diamonds in the sky. *Astrophys. J.* **319**, L109-113 (1987).
34. J.A. Nuth III and J.E. Allen Jr. Supernovae as sources of interstellar diamonds. *Astrophys. Space Sci.* **196**, 117-23 (1992).
35. M. Ozima and K. Mochizuki. Origin of nanodiamonds in primitive chondrites: (1) Theory. *Meteoritics* **28**, 416-17 (1993).
36. Z.R. Dai, J.P. Bradley, D.J. Joswiak, D.E. Brownlee, H.G. M. Hill, and M.J. Genge. Possible *in situ* formation of meteoritic nanodiamonds in the early solar system. *Nature* **418**, 157-59 (2002).
37. N.R. Greiner, D.S. Phillips, J.D. Johnson, and F. Volk. Diamonds in detonation soot. *Nature* **333**, 440-42 (1988).
38. M. Frenklach, W. Howard, D. Huang, J. Yuan, K.E. Spear, and R. Koba. Induced nucleation of diamond powder. *Appl. Phys. Lett.* **59**, 546-48 (1991).
39. J.C. Angus, M. Sunkara, S.R. Sahaida, and J.T. Glass. Twinning and faceting in early stages of diamond growth by chemical vapor deposition. *J. Mater. Res.* **7**, 3001-09 (1992).
40. W. Carey, E. Zinner, P. Fraundorf, and R.S. Lewis. Ion probe and TEM studies of a diamond bearing Allende residue. *Meteoritics* **22**, 349-50 (1987).
41. C. Frondel and U.B. Marvin. Lonsdaleite, a hexagonal polymorph of diamond. *Nature* **214**, 587-89 (1967).
42. R.E. Hanneman, H.M. Strong, and F.P. Bundy. Hexagonal diamonds in meteorites: Implications. *Science* **155**, 995-97 (1967).
43. M.E. Lipschutz and E. Anders. The record in the meteorites -IV Origin of diamonds in iron meteorites. *Geochim. Cosmochim. Acta* **24**, 83-105 (1961).
44. M.E. Lipschutz. Origin of diamonds in the Ureilites. *Science* **143**, 1431-34 (1964).
45. M. Frenklach, R. Kematich, D. Huang, W. Howard, K.E. Spear, A.W. Phelps, and R. Koba. Homogeneous nucleation of diamond powder in the gas phase. *J. Appl. Phys.* **66**, 395-99 (1989).
46. K. Maruyama, M. Makino, N. Kikukawa, and M. Shiraishi. Synthesis of hexagonal diamond in a hydrogen plasma jet. *J. Mater. Sci. Lett.* **11**, 116-18 (1992).

# 6

## DIAMOND MOLECULES FOUND IN PETROLEUM

### *New Members of the H-Terminated Diamond Series*

R.M.K. Carlson<sup>1</sup>, J.E.P. Dahl<sup>1</sup>, S.G. Liu<sup>1</sup>, M.M. Olmstead<sup>2</sup>, P.R. Buerki<sup>3</sup>, and R. Gat<sup>4</sup>

<sup>1</sup> *MolecularDiamond Technologies, ChevronTexaco Technology Ventures, P.O. Box 1627, Richmond, CA 94802, USA*

<sup>2</sup> *Department of Chemistry, University of California, One Shields Ave., Davis, CA 95616, USA*

<sup>3</sup> *Scripps Institution of Oceanography, Geosciences Research Division, Dept. 0244, University of California San Diego, 9500 Gilman Drive, La Jolla, CA 92093-0244, USA*

<sup>4</sup> *Coating Technology Solutions Inc, 36 Munroe St #1, Somerville, MA 0214, USA*

#### **Abstract:**

We recently reported [1,2] the discovery and isolation of new members of the hydrogen-terminated diamond series, ~1 to ~2 nm sized higher diamondoids from petroleum. Crystallographic studies [1,2] revealed a wealth of diamond molecules that are nanometer-sized rods, helices, discs, pyramids, etc. Highly rigid, well-defined, readily derivatizable structures make them valuable molecular building blocks for nanotechnology. We now produce certain higher diamondoids in gram quantities. Although more stable than graphite particles of comparable size, higher diamondoids are extraordinarily difficult to synthesize. Attempts to synthesize them were abandoned in the 1980's. We examined extracts of diamond-containing materials synthesized by CO<sub>2</sub> laser-induced gas-phase synthesis [3] and commercial CVD in an attempt to detect diamantane to undecamantane. However, high-sensitivity GCMS detected no diamondoids in these materials.

#### **Keywords:**

diamondoids, polymantanes, adamantane, CO<sub>2</sub> laser, CVD, nanotechnology

## 1. INTRODUCTION

We begin this paper by examining the enormous size range of hydrogen-terminated diamond crystals, focusing on the tiniest possible ultranano-

crystals of cubic diamond. We next discuss how structures of the diamond series are conceptually built-up from the smallest member to give the lower diamondoids. We then describe the newly discovered higher diamondoids, and show how they differ from the lower diamondoids. This includes a discussion of the many interesting structural features of higher diamondoids pertinent to the emerging field of nanotechnology. We briefly review past efforts to synthesize higher diamondoids by synthetic organic chemists (efforts ending in the 1980's), and discuss the surprising occurrence of higher diamondoids in petroleum. Finally, we describe our (unsuccessful) attempts to detect the formation of diamondoid hydrocarbons by two methods used to produce synthetic diamond, and discuss possible implications of these findings to the formation of higher diamondoids.

## 2. THE SMALLEST ULTRANANOCRYSTALLINE DIAMOND

Ultrananocrystalline diamonds possess a myriad of interesting and useful properties, as the proceedings of this conference readily attest. With modern technologies pushing the size of diamond crystals needed in newer applications to smaller and smaller ranges, it is worthwhile reexamining the limits of this miniaturization progression. This is particularly true with the growing interest in the fields of nanotechnology and nanomaterials. These fields aim to “engineer” and “build” structures and devices using components having nanometer dimensions [4]. Moreover, there is a fundamental understanding that diamond is a prized material for such applications [5–7].

The well-known unit cell of cubic diamond [8] is shown in Figure 1*a*. The 10-carbon cage, characteristic of the cubic diamond structure, is shown excised from the lattice in Figure 1*b*. When dangling carbon bonds are terminated with hydrogen atoms, this 10-carbon diamond crystal cage becomes a molecule of adamantane, the  $C_{10}H_{16}$  hydrocarbon (molecular weight, MW 136). Adamantane is in the  $T_d$  point group. Octahedral symmetry is displayed by the spatial relationship of its secondary carbon atoms, Figures 1*c* and 1*d*. The faces of the adamantane octahedron (Figure 1*c*) correlate with the (111) lattice faces of larger octahedral diamond crystals (e.g., the 455-carbon octahedral diamond drawn in Figure 2). The vertices of the octahedron in adamantane, and a perfect H-terminated macroscopic octahedral diamond crystal (if such a thing existed), as well as all of the intermediate members of the diamond



octahedral crystal series (e.g., Figure 2), are secondary carbon atoms. Adamantane is the smallest crystal of H-terminated cubic diamond [9,10].

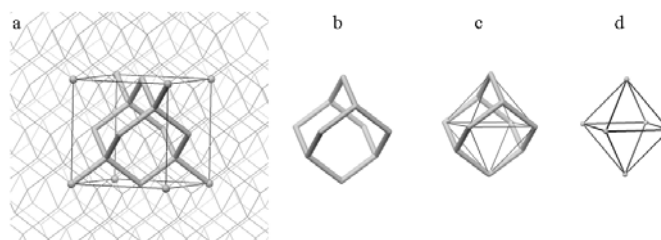


Figure 1. *a)* Unit cell of cubic diamond superimposed on the diamond crystal lattice with the 10-carbon “adamantane” cage emphasized. *b)* “adamantane” cage excised from the diamond lattice. *c)* Octahedral symmetry within  $T_d$  adamantane shown by lines connecting its six secondary carbon atoms. *d)* Octahedron shown separate from adamantane.

Adamantane has many unusual chemical and physical properties, as might be expected for the smallest member of the H-terminated diamond molecular series [11]. It also has applications in pharmaceuticals [12], polymers [13], and numerous other industries [14,15]. Adamantane can be prepared using classical synthetic organic chemistry and is often referred to as a “diamondoid” hydrocarbon [11].

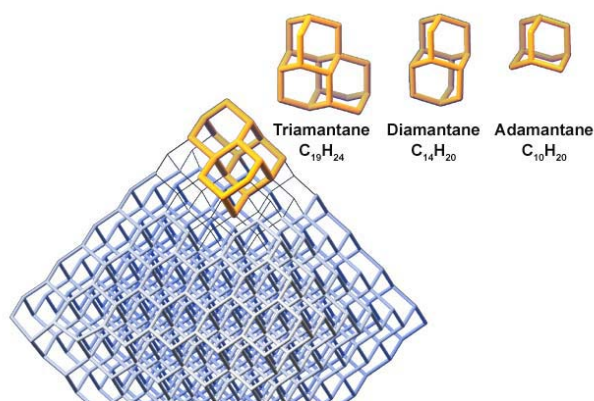


Figure 2. The triamantane carbon framework shown superimposed on a 455-carbon diamond lattice, along with separate representations of the carbon frameworks of adamantane, diamantane, and triamantane, the lower diamondoid hydrocarbons.

While diamond gemstones are macroscopic molecules, adamantane crystals are billions of trillions of diamondoid molecules held together by



weak van der Waals forces in a lattice having 4 adamantane molecules per unit cell. Adamantane in fact has two crystalline forms (tetragonal and cubic) [16] punctuated by an interesting solid-phase “plastic” transition at  $-64^{\circ}\text{C}$  [17]. Adamantane crystals melt at  $270^{\circ}\text{C}$  (extremely high for a  $\text{C}_{10}$  hydrocarbon), but vibrational spectroscopy shows little difference in the intramolecular diamond-like structure of its molecules in either phase [18]. Macroscopic diamond crystals “melt” at  $>3550^{\circ}\text{C}$ , but this involves breaking of the C-C  $sp^3$  diamond framework.

## 2.1 Lower Diamondoids: the Smallest Members of the H-Terminated Diamond Series

It is possible to imagine building-up the diamond structure by adding diamond crystal cages to an adamantane molecule. If an additional diamond cage is face-fused to the 10-carbon adamantane structure, a molecule of diamantane ( $\text{C}_{14}\text{H}_{20}$ , MW 188,  $\text{D}_{3d}$ ) is formed. Face fusing of diamond cages is easy to do when drawing chemical structures on paper. However, the difficulties associated with the synthesis of the face-fused diamond-cage structure of diamantane is an entirely different matter, as will be discussed in Section 3 of this paper. Like adamantane, the carbon framework of diamantane is directly superimposable on the diamond crystal lattice (Figure 2). It is important to note that adding the second cage to any of the four faces (all of which are cyclohexane rings in the “chair” configuration) of an adamantane molecule yields the same structure: there is only one diamantane structure (it has no isomers). This is also true of triamantane ( $\text{C}_{18}\text{H}_{24}$ , MW 240,  $\text{C}_{2v}$ ), which consists of three face-fused diamond cages, and has only a single structural form, Figure 2.

## 2.2 Higher Diamondoids: New Members of the H-Terminated Diamond Series

A new structural group within the H-terminated diamond series arises with the addition of a fourth cage to form the tetramantanes ( $\text{C}_{22}\text{H}_{28}$ , MW 292). An additional cage can be face-fused to any of the eight external cage faces of the triamantane structure, giving rise to four different tetramantane isomers with shapes that are significantly different from each other (Figure 3). A cage can be face-fused to either end of the long-axis of the triamantane molecule generating a rod-like structure, named [121] tetramantane ( $\text{C}_{2h}$ ) in Balaban-Schleyer nomenclature [19]. It is possible to image the progression (fusing cages to the ends of the long axis of each

successive “rod”) to give a series of rod-like [1212] pentamantane (Figure 4,  $C_{2v}$ ), [12121] hexamantane (Figure 5,  $C_{2h}$ ), etc.: a higher diamondoid series with members of alternating  $C_{2v}$  and  $C_{2h}$  symmetry.

Diamond crystal cages can also be added to four faces of triamantane to form a right- or left-handed spiral, generating the first unsubstituted chiral diamond molecules, P[123] and M[123] tetramantane (Figure 3). These are higher diamondoids with rare primary helical structure, which we have been able to resolve using chiral chromatography [1]. They are members of the helical structural series including [1234] pentamantane (Figure 4), [12341] hexamantanes (Figure 5), and so on, all with  $C_2$  symmetry.

Finally, a cage can be added to triamantane in either of two ways to generate the disc-shaped [1(2)3] tetramantane molecule with  $C_{3v}$  symmetry (Figure 5).

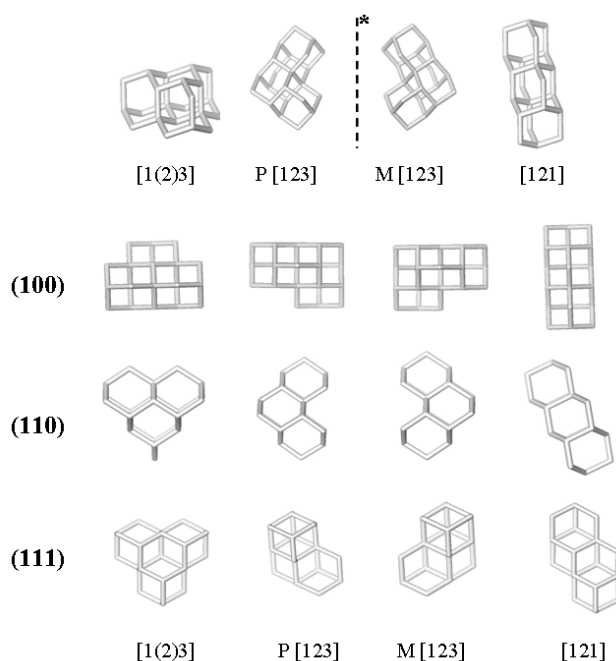


Figure 3. The four tetramantane carbon framework structures shown in perspective and parallel to their low-index diamond lattice faces. Higher diamondoids found in petroleum [1].

Because there are four tetramantanes (of differing symmetries) each with ten external cage faces, face-fusing the next adamantane cage gives rise to 10 different pentamantane structures. Nine of these structures are isomers with MW 344: three chiral pairs and three symmetrical achiral structures, Figure 4. As discussed above, some of these pentamantane isomers fall into

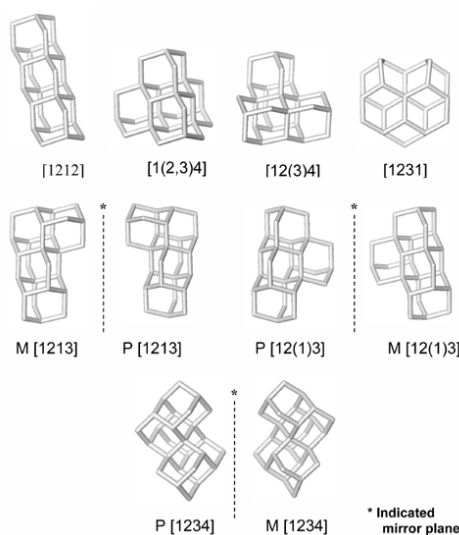


Figure 4. The pentamantanes (nine 344 MW and one 330 MW) shown in carbon framework. Higher diamondoids found in petroleum [1].

previously discussed series: rod-like [1212] pentamantane, or the helical **P** & **M** [1234] pentamantanes, Figure 4. However, other shapes also arise in the 344 MW pentamantanes, e.g., [1(2,3)4] pentamantane which is a perfect tetrahedral pyramid (Figure 4,  $T_d$ ). It is interesting that there is only one way to draw this pentamantane structure by face-fusing cages to the tetramantanes (and that only using the [1(2)3] tetramantane structure), whereas each of the two enantiomeric [12(1)3] pentamantane structures can be drawn in three different ways, and by face-fusing a cage to [121], [1(2)3], or the corresponding enantiomer of the [123] tetramantane structure. In the tenth pentamantane, the cage is added to either of the [123] tetramantane enantiomeric structures forming a circular pattern of fused cages. This allows sharing of carbons forming fused cage faces, reducing the molecular weight of this [1231] pentamantane to 330. In [1231] pentamantane (Figure 4) the circular pattern of fused cages is incomplete, causing steric compression of two adjacent hydrogens resulting in low-stability. This splitting of the pentamantanes into two molecular weight members is the beginning of an expanding progression that continues in the hexamantanes (with three MW families, 396, 382, 342), heptamantanes (with four MW families, 448, 434, 420, 394), octamantanes (with five MW families, 500,

486, 472, 446, 432), and so on. Each additional cage generates a new MW family.

This increasing number of MW families compounds the overall complexity of higher diamondoids. However, it also offers some simplification in that each newly arising MW family has a small number of members. For example, there are twenty-eight 396 MW hexamantanes (related to the 344 MW pentamantanes, i.e.,  $C_{4n+6}H_{4n+12}$ , where  $n$  is the number of cages in the family), but only one 342 MW hexamantane ([12312] hexamantane, Figure 5,  $C_{4n+2}H_{4n+6}$ ). A cage can be added to the disc-shaped [12312] hexamantane molecule in only two ways. Therefore, there are only two 394 MW heptamantanes, whereas over a hundred heptamantanes with MW 448 exist. There are only 18 octamantane members of this same continuing structural family, six chiral pairs and six symmetrical achiral structures with MW 446.

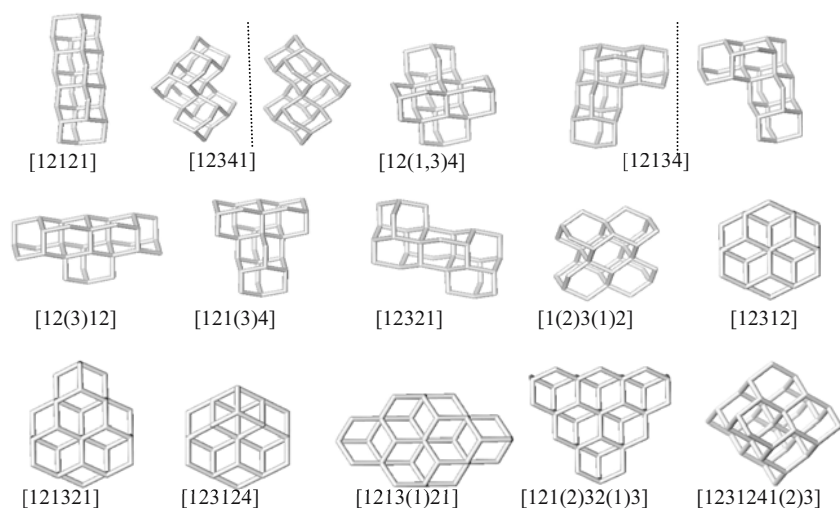


Figure 5. Selected hexamantanes, heptamantanes, octamantane, nonamantane and decamantane found in petroleum [1,2].

Decamantane has seven molecular weight families, but only one member exists in the  $C_{35}H_{36}$  family, [1231241(2)3] decamantane, MW 456 (Figure 5,  $T_d$ ). This decamantane is the 35-carbon member of the octahedral H-terminated diamond series discussed in Section 2.

The range of lengths and atom-fraction hydrogen contents of the higher diamondoids are bounded by the elongated rod-shaped [1212--] and compact octahedral diamond molecular series. These two properties are graphed

versus higher diamondoid carbon atom content in Figures 6a and 6b. The wedges in Figure 6a and 6b define the range of possible sizes and hydrogen content for the higher diamondoids.

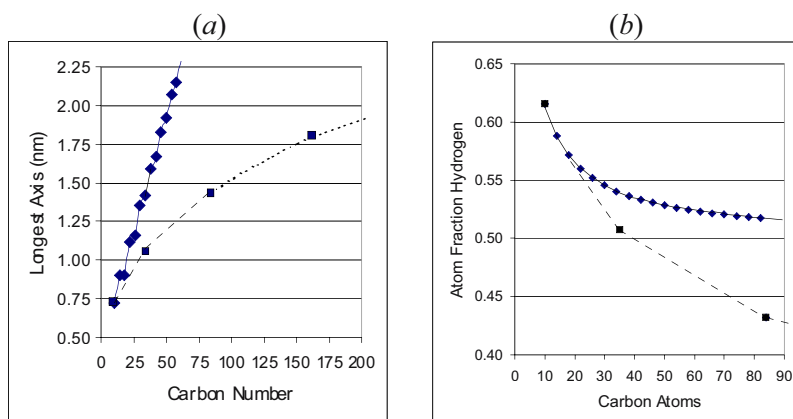


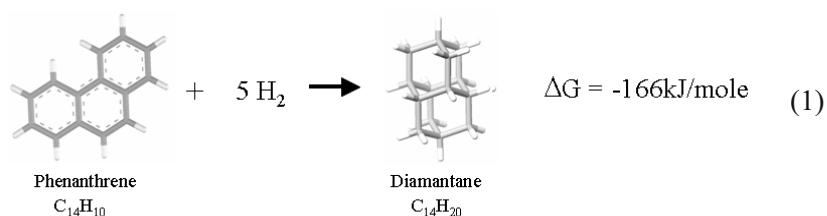
Figure 6. a). Length of the longest molecular axis (H van der Waals surfaces) versus carbon number. b) Atom-fraction hydrogen content versus carbon number. Rod-shaped diamondoids [121---] (diamond-shaped symbols), octahedral diamondoids (squares),  $C_{10}$ ,  $C_{35}$ ,  $C_{84}$ ,  $C_{165}$ .

Higher diamondoids have *knowable* diamond structures. This means that we can isolate and crystallize pure materials and determine their precise molecular structures by single crystal x-ray diffraction (Sec. 4). Knowing the exact structures of the higher diamondoids, and having them in pure form, makes possible their use in rational, reproducible “construction” at the nanometer scale, a primary objective of nanotechnology that is difficult to achieve with many nanomaterials. Also, diamond molecules of this size may show interesting and useful properties, such as quantum confinement [20].

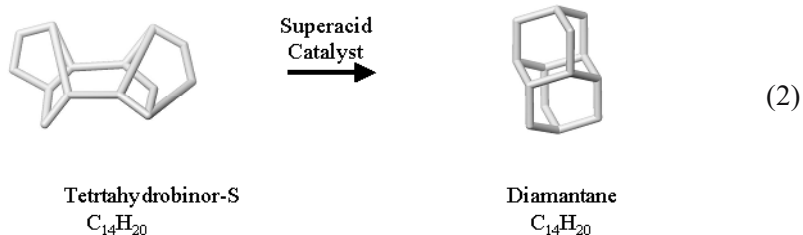
As the size, and numbers of possible isomers and molecular weight classes explode with increasing carbon numbers for larger and larger diamond molecules/particles (Figure 6), a point will be reached where precisely knowable diamondoid/diamond structures are no longer possible (at least with current technology). Our work demonstrates that, at least through undecamantane (an 11-cage higher diamondoid), *knowable* diamond structures can be isolated [1,2].

### 3. BUILDING DIAMOND FROM THE BOTTOM UP: LIMITS TO THE RATIONAL SYNTHESSES OF DIAMONDROID MOLECULES

Thermodynamic calculations [21–23], and recent experimental results [24] show that H-terminated nanodiamonds are more stable than H-terminated graphitic particles up to a size of ~5 nm. This relationship has been illustrated by the change in free energy for the transformation of phenanthrene to diamantane (Eq. 1) [25].



Classical synthetic chemical attempts at the preparation of diamondoids have a considerably different history than Eq. 1 might suggest. An alternative name for diamantane is “congressane” because its synthesis was posed as a worthy challenge to chemists at the Nineteenth Congress of the International Union of Pure and Applied Chemistry. The first synthesis of adamantane was an arduous task with a yield of 0.16% [26]. However, Schleyer discovered that adamantane can be formed from  $\text{C}_{10}$  tricyclic intermediates by carbocation-mediated thermodynamically controlled equilibration reactions [27]. His research group used this method to synthesize diamantine [28].



The overall reaction of a strained  $\text{C}_{14}\text{H}_{20}$  polycyclic isomer, e.g., tetrahydrobisnor-S, to yield diamantane by the carbocation-mediated equilibration is easy to write down (Eq. 2.) However, this simplicity belies the staggering complexity of the underlying thousands of reaction pathways.

Graphical analysis of the mechanisms for adamantane formation from endo-tetrahydrodicyclopentadiene shows an amazing 2897 different pathways [29]. Representations of this complex system of intermediates and pathways has been dubbed “adamantaneland” or the “Whitlock-Siefkin mechanism,” many of the details of which have now been verified [30].

Graphical analyses have also been performed for carbocation equilibration reactions leading to the diamondoids methyladamantane [31] and diamantine [32]. Limited analysis of the heptacyclooctadecane (triamantane) system suggests the existence of at least  $10^5$  intermediates [33]. Although these equilibration reactions have great complexity, they can show good efficiencies for synthesis of the lower diamondoids [34].

The situation changes as we cross over to the higher diamondoids. Substantial efforts by outstanding synthetic organic chemists have demonstrated that formation of higher diamondoids by the superacid-carbocation equilibration method does not work [35]. Accordingly, another property that distinguishes the lower diamondoids from the higher ones is that lower diamondoids can be synthesized by carbocation equilibration reactions while higher diamondoids can not [36]. Only one of the higher diamondoids, [121] tetramantane has been synthesized, and this by a complex, low-yielding, gas-phase double homologation of diamantine [37].

Osawa *et al.* assessed the future of higher diamondoid synthesis in 1980, concluding that prospects were dim because of a lack of large polycyclic precursors, increasing problems with rearranging intermediates becoming trapped in local energy minima, rising potential for disproportionation reactions leading to unwanted side products, and rapidly expanding numbers of isomers as carbon numbers of target higher diamondoid products increase [38]. With the failure to implement carbocation mediated syntheses of higher diamondoids, the field waned in the earlier 1980's.

#### **4. SURPRISING OCCURANCE OF HIGHER DIAMONDIDS IN PETROLEUM**

The lower diamondoid, adamantane, was discovered in petroleum in 1933 [39]. Diamantane has also been isolated from petroleum [40]. Lower diamondoids occur in most petroleum, and have been shown to be useful geochemical indicators of thermogenic gas formation [41]. Petroleum source beds contain clay minerals capable of catalyzing carbocation reactions, and it has been suggested that these minerals participate in the formation of lower diamondoids by the carbocation equilibration mechanisms discovered by

Scheyler [42]. However, as discussed in the previous section, structurally complex higher diamondoids could not be synthesized by such processes.

The presence of higher diamondoids in petroleum had been suspected [43], but prior to our work no isolations or definitive structural assignments had been reported. We have described how vacuum distillate fractions of certain petroleum were found to contain high molecular weight hydrocarbons resilient to pyrolytic treatments at 450°C (a property consistent with diamondoid structures), how combined size and shape-selective high performance liquid chromatographic (HPLC) techniques were used to isolate them and subsequent crystallization and single crystal x-ray diffraction studies proved their structures [1]. We have demonstrated that tetramantanes, pentamantanes, hexamantanes, octamantanes, nonamantanes, decamantanes, and undecamantanes are present in petroleum, and have shown that chiral HPLC is effective at resolving [123] tetramantane enantiomers [1,2]. We have now used these methods to isolated gram quantities of the tetramantanes, and [1(2,3)4] pentamantane.

Higher diamondoid molecules crystallize into a variety of crystal systems [1]. For example, crystals of [1(2,3)4] pentamantane are orthorhombic (space group  $Pnma$ ), crystals of [1213] pentamantane are triclinic (space group  $P-1$ ), and crystals of [12(3)4] pentamantane are monoclinic (space group  $P2_1/n$ ). Rod-shaped [1212] pentamantane molecules form orthorhombic crystals (space group  $P2_12_12_1$ ), Figure 7, in which they align themselves parallel to their long axis,  $\sim$ perpendicular to their diamond (110) lattice faces.

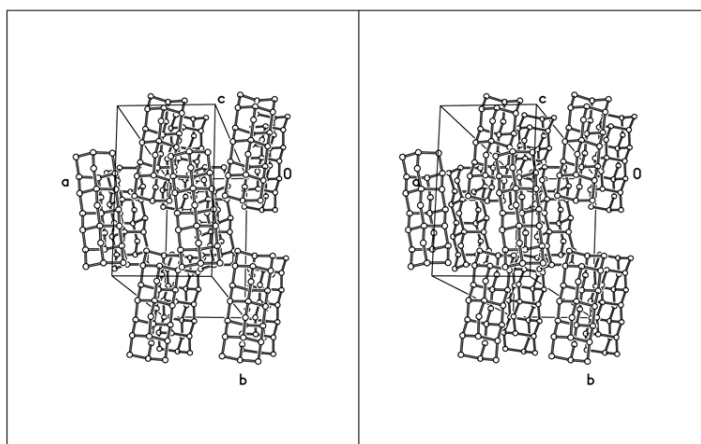


Figure 7. Stereogram of the crystal structure of [1212] pentamantane.



## 5. ATTEMPT TO DETECT FORMATION OF DIAMONDROID HYDROCARBONS BY PROCESSES KNOWN TO PRODUCE SYNTHETIC DIAMOND

Although attempts to synthesize higher diamondoids were abandoned in the 1980's, their thermodynamic stabilities are high relative to other hydrogenated carbon particles of comparable size. Furthermore, we have now proven their existence in petroleum. Therefore, we decided to attempt to determine if higher diamondoids might be formed during processes known to produce larger diamond materials. These diamond-forming processes involve free-radical reaction mechanism [44], unlike the synthetic chemical approaches just discussed which employ carbocation reaction mechanisms.

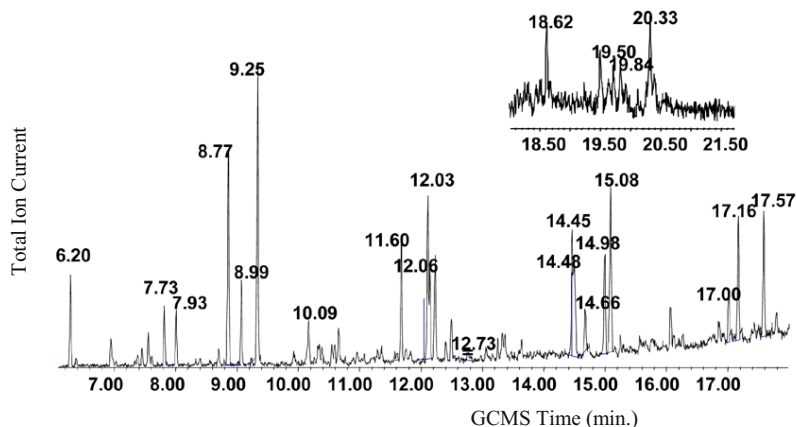


Figure 8. Aromatics formed during CO<sub>2</sub>-laser-induced gas-phase synthesis of diamond. Numbers above peaks are GC retention times in minutes. GCMS column and operating conditions are documented in the supporting on-line material to Ref. 1. The peak at 6.20 min. is anthracene (MW 178) [47,48].

Diamond particles ranging in diameter from  $\sim 6$  nm up to several micrometers can be formed by a CO<sub>2</sub>-laser-induced gas-phase synthetic method [3,45]. Previous studies of this system provided samples in which diamond was synthesized under a range of conditions [3,45,46]. Diamond-containing materials from these studies were thoroughly extracted using warm cyclohexane and ultrasonic agitation and analyzed by gas chromatography-mass spectrometry (GCMS) [47]. GCMS data were examined for traces of lower diamondoids (diamantane and triamantane) and higher diamondoids (tetramantanes through undecamantane), but no traces of diamondoids were found. The extracts, which had a deep yellow to orange color, were all shown to contain similar profiles of unalkylated polynuclear

aromatic hydrocarbons with 3 to 6 aromatic rings [48]. Figure 8 shows the total ion chromatogram for the extract of sample CD2 [47].

It is interesting that polynuclear aromatic hydrocarbons rather than diamondoids were formed by the CO<sub>2</sub>-laser method. Anthracene and phenanthrene rather than diamantane are present in its reaction products, apparently defying Eq.1 in Sec. 3. Perhaps insufficient hydrogen was available at the reaction site, or perhaps the temperatures were high enough to initiate the stripping of surface hydrogens from the forming diamondoids, a process which computational studies indicate should induce graphitization (aromatization) [49]. Alternatively, mechanistic difficulties might block diamondoid formation in this system (as in the synthetic systems discussed in Sec.3), but how such difficulties are overcome for diamond particles of ~ 6 nm diameter and larger is unclear.

Diamond samples produced by commercial chemical vapor deposition (CVD) were also extracted, concentrated, and analyzed by GCMS using the same methods described above. For this limited sample set neither diamondoids nor polynuclear aromatic hydrocarbons were detected in the extracts. This could have been a problem of formation mechanisms or detection limits, and warrants further study.

## 6. CONCLUSIONS

Ultrananocrystalline diamond is an attractive material for modern technological applications in fields such as nanotechnology. Higher diamondoids are an important group of ~1 to ~2 nanometer-sized members of the H-terminated diamond series. They offer many advantages in terms of diverse, well-defined, derivatizable 3-D geometries, features not found in larger members of the diamond series. Petroleum is our source for these new materials, and we can now produce tetramantanes and one of the pentamantanes in gram quantities. Attempts to synthesize them using synthetic organic chemistry were abandoned decades ago. Our initial studies indicate that higher diamondoids are not formed during processes used to produce diamond films and particles. It is possible that geologic time frames associated with petroleum and natural gas generation are a key element of higher diamondoid formation.

## Acknowledgments

We thank John Fetzer for helpful discussions concerning PAHs, and Michael Cheng for phenanthrene co-injection results.

## REFERENCES

1. J.E. Dahl, S.G. Liu, and R.M.K. Carlson. Isolation and structure of higher diamondoids, nanometer-sized diamond molecules. *Science* **299**, 96-9 (2003).
2. J.E.P. Dahl, Moldowan J.M., T.M. Peakman, J.C. Clardy, E. Lobkovsky, M.M. Olmstead, P.W. May, T.J. Davis, J.W. Steeds, K.E. Peters, A. Pepper, and R.M.K. Carlson. Isolation and structure proof of the large diamond molecule, cyclohexamantane, C<sub>26</sub>H<sub>30</sub>. *Angew. Chem. Internat.* **42**, 2040-44 (2003).
3. P.R. Buerki and S. Leutwyler. CO<sub>2</sub>-laser-induced gas-phase synthesis of micron-sized diamond powders: recent results and future developments. *Diamond and Related Materials* **2**, 174-82 (1993).
4. G. Timp. *Nanotechnology*. New York: Springer-Verlag, 1999.
5. K.E. Drexler. *Nanosystems: Molecular Machinery, Manufacturing, and Computation*. New York: Wiley, 1992.
6. T.Cagin, J. Che, M.N. Gardo, A. Fijany, and W.A. Goddard. Simulation and experiments on friction and wear of diamond: a material for MEMS and NEMS application. *Nanotechnology* **10**, 278 (1999).
7. D.W.Brenner, O.A. Shenderova, D.A. Areshkin, J.D. Schall, and S.-J.V. Frankland. *Comput. Model. Engin. Sci.* **3**, 643 (2002).
8. W.H.Bragg and W.L. Bragg. The structure of diamond. *Nature* **91**, 557 (1913).
9. T.R. Anthony. Synthesis of metastable diamond. *Mat. Res. Soc. Symp. Proc.* **162**, 61-3 (1990).
10. W. Piekarczyk. Crystal growth of CVD diamond and some of its peculiarities. *Cryst. Res. Technol.* **34**, 553-63 (1999).
11. R.C. Fort. *Adamantane, the chemistry of diamond molecules*. New York: Dekker, 1976.
12. R.S. Schwab, D.C. Poskanzer, A.C. England, and R.R. Young. Amantadine in the treatment of Parkinson's disease. Review of more than two years' experience. *J. Amer. Med. Assoc.* **222**, 792-95 (1972).
13. M.A. Meador. Recent advances in the development of processable high temperature polymers. *Annu. Rev. Mater. Sci.* **28**, 599 (1998).
14. A.P. Marchand. Polycyclic Cage Compounds: Reagents, Substrates, and Materials for the 21st Century. *Aldrichimica Acta* **28**, 95 (1995).
15. K. Tominaga and M. Haga. Next generation fine chemicals raw material - adamantane. *Chem. Econ. Eng. Rev.* **17**, 23 (1985).
16. C.E. Nordman and D.L. Schmitkons. Phase transition and crystal structures of adamantane. *Acta Cryst.* **18**, 764-7 (1965).
17. C.G. Windsor, D.H. Suanderson, J.N. Sherwood, D.Taylor, and G.S. Pawley. Lattice dynamics of adamantane in the disordered phase. *J. Phys. C: Solid State* **11**, 1741-59 (1978).
18. T.E. Jenkins and J.A. Lewis. Raman study of adamantane (C<sub>10</sub>H<sub>16</sub>), diamantane (C<sub>14</sub>H<sub>20</sub>) and triamantane (C<sub>18</sub>H<sub>24</sub>) between 10K and room temperatures. *Spectrochim. Acta* **36A**, 259-64 (1980).
19. A.T. Balaban and P. von R. Schleyer. Systematic classification and nomenclature of diamond hydrocarbons. *Tetrahedron* **34**, 3599-609 (1978).
20. J.Y. Raty, G. Galli, C. Bostedt, T.W. van Buuren, L.J. Terminello. Next generation fine chemicals raw material - adamantane. *Phys. Rev. Lett.* **90**, 037401 (2003).
21. P. Badziag, W.S. Verwoerd, W.P. Ellis, and N.R. Greiner. Nanometer-sized diamonds are more stable than graphite. *Nature* **343**, 244-5 (1990).
22. A.S. Barnard, N.A. Marks, S.P. Russo, and I.K. Snook. Hydrogen Stabilization of the (111) Nanodiamond. *Mat. Res. Soc. Symp. Proc.* **740**, I3.4.1-I3.4.6 (2003).

23. N.W. Winter and F.H. Ree. Carbon particle phase stability as a function of size. *J. Computer-Aided Materials Design*, **5**, 279-94 (1998).
24. S. Prawer, J.L. Peng, J.O. Orwa, J.C. McCallum, D.N. Jamieson, and L.A. Bursill. Size dependence of structural stability of nanocrystalline diamond. *Phys. Rev. B.*; **62**, R16 360-3 (2000).
25. J.C. Angus. *Thermodynamic and kinetic issues of metastable diamond growth. In Properties, Growth and Applications of Diamond*, M. H. Nazaré , A. J. Neves, Ed., London: Inspec, pp. 256-61, 2001.
26. V. Prelog and R. Seiwerth. Synthesis of adamantane. *Ber.* **74B**, 1644 (1941).
27. P.v.R. Schleyer. A simple preparation of adamantane. *J. Am. Chem. Soc.* **79**, 3292 (1957).
28. C. Cupas, P.v.R. Schleyer, and D.J. Trecker. Congressane. *J. Am. Chem. Soc.* **87**, 917 (1965).
29. H.W. Whitlock and M.W. Siefkien. Tricyclo[4.4.0.03,8]decane to adamantane rearrangement. *J. Am. Chem. Soc.* **90**, 4929-39 (1968).
30. R.P. Kirchen, T.D. Sorensen, and S.M. Whitworth. A mechanistic study of the carbocation route from tetrahydrodicyclopentadiene to the adamantane ring. *Can. J. Chem.* **71**, 2016-27 (1993).
31. E. Osawa, K. Algami, N. Takaishi, Y. Inamoto, Y. Fujikura, Z. Majerski, P.v.R. Schleyer, E.M. Engler, and M. Farcasiu. The mechanism of carbonium ion rearrangements of the tricycloundecanes elucidated by empirical force field calculations. *J. Am. Chem. Soc.* **99**, 5361-73 (1977).
32. T.M. Grund, P.v.R. Schleyer, P.H. Gund, and W.T. Wipke. Computer assisted graph theoretical analysis of complex problems in polycyclic hydrocarbons. The mechanism of diamantane formation from various pentacyclotetradecanes. *J. Am. Chem. Soc.* **114**, 497-505 (1975).
33. F.S. Hollowood and M.A. McKervey. Synthesis of triamantane. *J. Org. Chem.* **45**, 4954 (1980).
34. O. Farooq, S. Morteza, F. Farnia, M. Stephenson, and G. Olah. A Superacid-Catalyzed Near Quantitative Isomerization of  $C_{4n+6}H_{4n+12}$  ( $n = 1-3$ ). *J. Org. Chem.* **53**, 2840-43 (1988).
35. P.v.R. Schleyer, E. Osawa, and M. Drew. Nonacyclo[11.7.1.12,18.03,16.04,13.05,10,06,14.07,11,015,20]docosane, a bastard tetramantane. *J. Am. Chem. Soc.* **90**, 5034-36 (1968).
36. M.A. McKervey. Synthetic Approaches to large diamondoid hydrocarbons. *Tetrahedron* **36**, 971-92 (1980).
37. W. Burns, T.R.B. Mitchell, and M.A. McKervey. Gas-phase Reactions on Platinum. Synthesis and Crystal Structure of *anti*-Tetramantane, A Large Diamondoid Fragment. *J. Chem. Soc., Chem. Commun.*, 893 (1976).
38. E. Ozawa, A. Furusaki, N. Hashiba, T. Matsumoto, V. Sing, Y. Tahara, E. Wiskott, M. Farcasiu, T. Iizuka, N. Tanaka, T. Kan, and P.v.R. Schleyer. Thermodynamic Rearrangements of larger polycyclic hydrocarbons. *J. Org. Chem.* **45**, 2985-95 (1980).
39. S. Landa. The isolation of several hydrocarbons from Hodonin crude oil, especially adamantane. *Chem. Listy* **27**, 415 (1933).
40. S. Hala and S. Landa. Isolation of tetracyclo[6.3.1.02,6.05,10]dodecane and pentacyclo[7.3.1.14,12.02,7.06,11]tetradecane (diamantane) from petroleum. *Angew. Chem. Internat. Edit* **5**, 1045 (1966).
41. J.E. Dahl et al. Diamondoid hydrocarbons as indicators of natural oil cracking. *Nature* **399**, 54-7 (1999).

42. P.v.R. Schleyer. *Cage Hydrocarbons*, G.A. Olah ed. NY. USA: Wiley, pp. 1-38, 1990.
43. R. Lin and Z. Wilk. Natural occurrence of tetramantane ( $C_{22}H_{28}$ ), pentamantane ( $C_{26}H_{32}$ ) and hexamantane ( $C_{30}H_{36}$ ) in a deep petroleum reservoir. *Fuel* **74**, 1512-20 (1995).
44. J.E. Butler and R.L. Woodin. Thin film diamond growth mechanisms. In *Thin film Diamond*, A. Lettington, J.W. Steeds, eds., London: Chapman & Hall, pp. 15-30 (1994).
45. P.R. Buerki and S. Leutwyler.  $CO_2$ -laser-induced vapor-phase synthesis of HN-diamond nanoparticles at 0.6 – 2 BAR. *Nanostructured Materials* **4**, 577-82 (1994).
46. P.R. Buerki and S. Leutwyler. Homogeneous nucleation of diamond powder by  $CO_2$ -laser-driven gas-phase reactions. *J. Appl. Phys.* **69**(6), 3739-44 (1991).
47. Four samples of diamond materials C7, CH8, CD2, and CD7 were analyzed in this study. Sample C7 was synthesized by  $CO_2$  laser photolysis of pure  $C_2H_4$  gas at 1800 mbar; sample CH8 was synthesized by  $CO_2$  laser photolysis of a  $C_2H_4$  /  $H_2$  mixture (81.2 and 18.8 vol.%, respectively) at 2000 mbar; sample CD2 was synthesized by  $CO_2$  laser photolysis of  $C_2H_4$  gas saturated with cis-decalin at 800 mbar; and sample CD7 was synthesized by  $CO_2$  laser photolysis of  $C_2H_4$  gas saturated with cis-decalin at 1800 mbar. The synthesis conditions, diamond size distributions, and TEM images of diamonds from sample CD2 are published in ref. 3. All samples consisted mostly of soot- and tar-like reaction products that were previously not analyzed in detail, and traces of diamond particles. Samples of the materials on cellulose filters were each separately extracted with 35 mL of Fisher Scientific HPLC-grade cyclohexane. Filter material was broken-up and each flask was sonicated for 20 min. in a Branson Ultrasonic Cleaner Model B-220 at 37°C. Extracts were evaporated under a stream of dry nitrogen, taken-up in a minimum volume of cyclohexane, transferred to micro-vials, volumes reduced to ~10  $\mu$ L and analyzed by gas chromatography–mass spectroscopy (GCMS). GCMS analyses were performed using the instrumentation and methods described in the Supporting On-line material published in our Science publication [1]. Calibration of our GCMS system showed a detection limit of ~0.2 ng [121] tetramantane per 1 microliter injection.
48. The following is the listing of GCMS retention times grouped by molecular ions and polynuclear aromatic hydrocarbon assignments for Figure 8: 6.20 min. ( $M^+$  178, anthracene –positively identified by GCMS co-injection with an authentic standard, phenanthrene is the small unlabeled peak eluting immediately after anthracene), 7.73 min. (phthalate impurity, plasticizer), 7.93 min. ( $M^+$  204, dihydropyrene or dihydroacephenanthrylene), 8.77, 8.99, and 9.25 min. ( $M^+$  202, pyrene and three-ring aromatics with cyclopentano ring closure), 10.09 ( $M^+$  216), 11.60, 12.03 min. ( $M^+$  226, benzo[ghi]-fluoranthrene and cyclopenta[cd]pyrene), 12.06 min. ( $M^+$  228, four-ring aromatic) 12.73 min.(impurity, dioctyl phthalate plasticizer from PE storage bag), 14.45, 14.48, 14.66, 14.98, 15.08 min. ( $M^+$  252, four-ring aromatic with cyclopentano ring closure), 17.00, 17.16, 17.57 min. ( $M^+$  276, five-ring aromatic with cyclopentano ring closure), 18.61 ( $M^+$  288, unknown), 19.49, 19.72 ( $M^+$  302, six-ring aromatic with cyclopentano ring closure), 19.83, 20.32 min. ( $M^+$  300, six-ring aromatic with cyclopentano ring closure).
49. A.S. Barnard, S.P. Russo, I.K. Snook. Ab initio modeling of the stability of nanocrystalline diamond morphologies. *Philosoph. Mag. Lett.* **83**, 39-45 (2003).

# 7

## SYNTHESIS OF NANOCRYSTALLINE DIAMOND FILMS IN Ar/H<sub>2</sub>/CH<sub>4</sub> MICROWAVE DISCHARGES

F. Bénédic, F. Mohasseb, P. Bruno, F. Silva, G. Lombardi, K. Hassouni, and  
A. Gicquel

*Laboratoire d'Ingénierie des Matériaux et des Hautes Pressions, UPR 1311 CNRS, 99 av.  
J.B. Clément, Université Paris 13, 93430 Villetaneuse, France*

**Abstract:** This work deals with the investigation of the microwave plasma assisted CVD process employed for nanocrystalline diamond (NCD) deposition, using an Ar/H<sub>2</sub>/CH<sub>4</sub> feed gas. The different steps required in order to insure the process control and optimization are considered. The stable process parameters providing the discharge stability and reproducibility are first determined. Then, the influence of the growth parameters on the film characteristics is examined. In particular, the effect of the surface temperature is probed combining both *in-situ* and *ex-situ* measurements. Finally, the potentiality of NCD films for the achievement of high frequency surface acoustic wave devices is illustrated.

**Keywords:** nanocrystalline diamond, microwave plasma, CVD process control, film characterization, pyrometric interferometry, surface acoustic waves

### 1. INTRODUCTION

Nano-crystalline diamond (NCD) films have been the subject of a large interest since the demonstration of the feasibility of their deposition ten years ago [1]. This interest was motivated by the fact that, in addition to some physical properties similar to those of poly-crystalline diamond (PCD), NCD films possess typical properties related to their nanometer-scale grain size and to the particular nature of their grain boundaries [2]. Especially, NCD films have an extremely low thickness-independent surface roughness suitable for some tribological and electronic applications that often require very smooth films.

The synthesis of NCD film have been demonstrated using various and quite different processes, such as DC arc plasma [3], hot filament CVD [4], DC magnetron sputtering [5], inductively coupled plasma [6] or microwave plasma assisted CVD [2]. Diverse environments can also be employed and many papers reported the use of gas mixtures formed for instance of  $H_2/CH_4$  with high  $CH_4$  concentration [7],  $H_2/CH_4/O_2$  [8],  $Ar/C_{60}$  [1],  $Ar/CH_4$  [9] or  $Ar/H_2/CH_4$  [10]. Whatever the technique employed, the reproducible elaboration of NCD films with properties suitable for specific applications requires the control and the optimization of the growth process. For this purpose, different steps must be necessarily accomplished: determination of stable process parameters insuring the reproducibility of growth conditions, investigation of the influence of the growth parameters on the film characteristics in correlation with plasma features, and assessment of the film properties for the envisaged applications.

In this paper we illustrate the development allowing the production of functional NCD layers in the case of the microwave plasma assisted chemical vapor deposition (MPACVD) process making use of  $Ar/H_2/CH_4$  gas mixture, that is the most common technique employed for NCD growth. We summarize the investigations that enabled us to control the growth conditions and the film properties and give an example of film application concerning NCD-based surface acoustic wave (SAW) devices.

## 2. EXPERIMENTAL SETUP

The deposition experiments were performed in a MPACVD device commonly used for NCD and PCD synthesis, that has been described in previous works [11]. It mainly consists of a quartz bell jar low-pressure chamber inserted in a resonant cavity (Figure 1).

The dimensions of the microwave cavity have been chosen in order to favor the  $TM_{01}$  mode of 2.45 GHz frequency electromagnetic wave. The plasma discharge is ignited in the microwave cavity in an  $Ar/H_2/CH_4$  gas mixture, just above a 5 cm diameter molybdenum substrate holder held in the center of the chamber, with a 1200 W, 2.45 GHz microwave power supply. An additional heating system located in the substrate holder enables us to control the substrate temperature independently of the other growth parameters.

For all the experimental investigations presented in this paper, the total gas flow rate was maintained at 250 sccm, whereas the value of the gas pressure, input microwave power (MWP), substrate temperature ( $T_s$ ) and gas ratios (%Ar, % $H_2$ , and % $CH_4$ ) was varied in order to study the influence of all these parameters on the plasma and film characteristics.



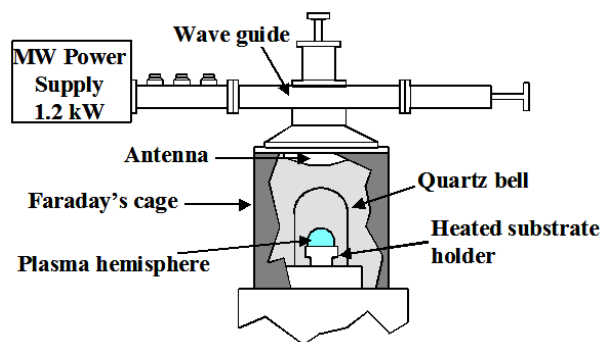


Figure 1. Schematic of the MPACVD apparatus used for NCD deposition.

### 3. CONTROL OF PROCESS PARAMETERS

In this part, we present the investigations carried out in order to determine process parameter windows insuring the Ar/H<sub>2</sub>/CH<sub>4</sub> microwave discharge stability and reproducibility. We discuss in particular the feed gas composition and the role of molecular hydrogen.

According to the literature, a suitable gas mixture that may be employed for the synthesis of NCD is simply composed of argon and small amounts of methane [9]. In the case of the bell jar reactor, the use of such a feed gas leads in most of experimental conditions to the formation of incandescent particles at the plasma edges, that correspond to soot particles present in the plasma and cause the deposition of black deposits on the quartz bell.

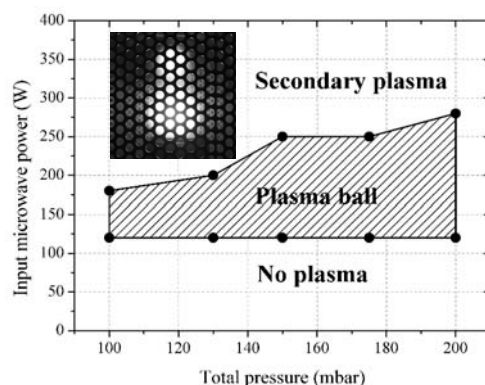


Figure 2. MWP/total pressure domains obtained for an Ar/CH<sub>4</sub> (99:1) microwave discharge.



Besides this phenomenon, unfavorable to plasma stability, the process parameter window that permits to form a plasma ball is quite narrow as shown in Figure 2 presenting the different MWP/total pressure domains obtained in the bell jar reactor for an Ar/CH<sub>4</sub> (99:1) discharge. This figure shows that, for a given pressure, under a lower limit MWP-value no plasma can be ignited, whereas above an upper limit MWP-value a secondary plasma ball located at the top of the bell is created. In the latter configuration a significant amount of the input MWP is dissipated far from the substrate and does not act in the deposition process, and the secondary plasma ball may cause the destruction of the quartz dome.

These drawbacks can be overcome by adding small amounts of molecular hydrogen in the feed gas in substitution of argon. Indeed, Figure 3 demonstrates that 2% H<sub>2</sub> causes an enlargement of the stability domain where an hemispherical plasma located just above the substrate holder and apparently free of soot formation can be switched on. Moreover, an increase of the H<sub>2</sub> concentration in the feed gas from 2 to 7% leads to a further broadening of the stability channel and to a shift towards greater MWP.

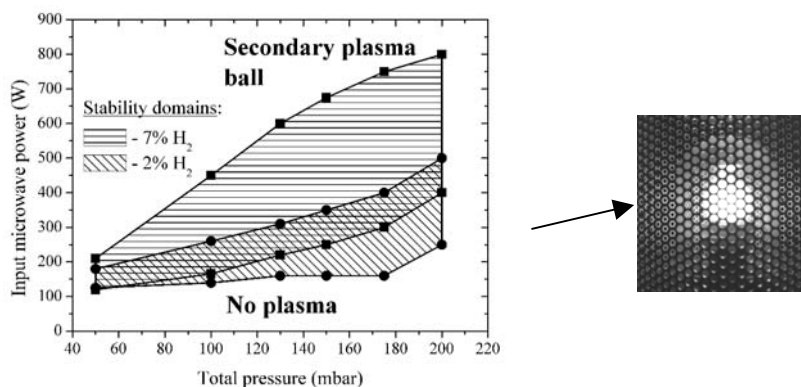


Figure 3. MWP/total pressure domains obtained for Ar/H<sub>2</sub>/CH<sub>4</sub> microwave discharges with 97:2:1 and 92:7:1 gas ratios.

Thus, the introduction of molecular hydrogen in the gas mixture is advantageous in terms of process flexibility and plasma reactivity. Nevertheless, only small amounts must be introduced in order to maintain the nanocrystalline features of diamond films [10].

Other investigations were lead with the aim of finding experimental parameters insuring the reproducibility and the stability of growth conditions, especially avoiding soot particle formation. Results show that it can be fulfilled for process parameter windows corresponding to 1–2% CH<sub>4</sub> and 2–7% H<sub>2</sub> in the gas mixture, a total pressure between 100 and 200 mbar,

a microwave power between 200 and 800 W depending on the gas composition and pressure, and a substrate temperature above 700K. Also, a precise deposition protocol must be followed, including the obtaining of a secondary vacuum before each synthesis experiment and the cleaning of the reactor in H<sub>2</sub> or H<sub>2</sub>/O<sub>2</sub> low-pressure discharges after each plasma treatment.

#### 4. GROWTH AND CHARACTERIZATION OF NCD FILMS

The first step of the process control being completed, our studies were focused on the influence of growth conditions on the properties of elaborated films. Parametric studies were then conducted by varying each growth parameter in the stability domains determined previously.

In this part, we report as an illustrative example the investigations carried out in order to study the influence of the substrate temperature on NCD growth. In addition to conventional *ex-situ* characterization techniques (SEM, Raman spectroscopy, TEM and XRD), *in-situ* monitoring was performed by using pyrometric interferometry (PI) technique. Based on the measurement of the film/substrate apparent temperature during the growth employing a pyrometer, this technique allows the estimation of some parameters related to the growth mechanisms and film properties: incubation time, growth rate and film optical constants [12,13]. In the following, we will focus in particular on the estimation of the NCD film extinction coefficient from PI data obtained with an infrared bichromatic pyrometer working at wavelengths of 1.52 and 1.64  $\mu\text{m}$ .

Two series of samples were completed. For the first series, the gas ratios were maintained at %Ar:%H<sub>2</sub>:%CH<sub>4</sub> values of 96:3:1 and the surface temperature  $T_s$  was varied in the range 880–1280K. For the second series,  $T_s$  ranged from 1050 to 1380K, while setting the gas ratios at 92:7:1. In all the synthesis experiments, the MWP, the total gas pressure and the deposition time were set at 600 W, 20000 Pa, and 4.0 hrs, respectively. Prior to deposition, the (100)-oriented silicon wafers of 1 inch diameter used as substrates were ultrasonically abraded in a suspension of diamond powder in order to enhance diamond nucleation.

Figure 4 presents the apparent temperature data corresponding to samples deposited under 92:7:1 gas ratios for a moderate  $T_s$  value ( $T_s = 1160$  K, Figure 4a) and a high  $T_s$  value ( $T_s = 1380$  K, Figure 4b). Both curves present oscillations that get progressively attenuated as the film becomes thicker. The oscillatory behavior is attributed to the variations of the film/substrate thermal emissivities at the two working wavelengths as the film grows,

whereas the damping phenomenon is attributed to the non-transparent compounds within the films and is linked to its extinction coefficient. The figure shows obviously the considerable difference that exists between the two signals as regards the signal attenuation. Indeed, for the sample realized at high temperature, the oscillation attenuation occurs rapidly (Figure 4b), whereas the signal corresponding to the lower  $T_s$  value is slowly damped (Figure 4a). A comparable behavior was also noticed for the other series of samples deposited for a 96:3:1 gas ratio set.

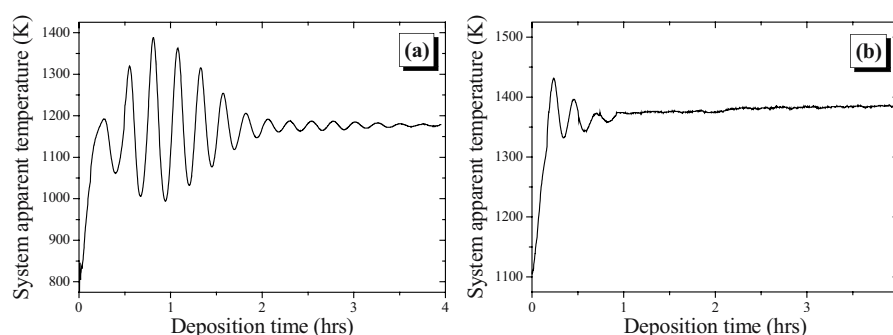


Figure 4. Experimental data of the apparent temperature measured as a function of the deposition time for samples elaborated under Ar/H<sub>2</sub>/CH<sub>4</sub> (92:7:1) microwave discharge at different surface temperatures: (a)  $T_s = 1160\text{K}$ ; (b)  $T_s = 1380\text{K}$ .

This means that the extinction coefficient is expected to be much higher for the films elaborated at high  $T_s$  values than for the other conditions considered, that should be attributed to the raise of non-diamond absorbent phases, particularly  $sp^2$ -hybridized compounds, with the substrate temperature.

More quantitative investigations were conducted in order to estimate the values of the film extinction coefficient from the best fit of the apparent temperature data with a theoretical curve. Figure 5 presents the extinction coefficient thus estimated for the considered sample series as a function of the surface temperature. Both curves show that the extinction coefficient remains approximately constant in the range 0.1–0.2 for low and moderate temperatures and drastically increases to 0.6–0.7 at high temperatures. This confirms that the formation of absorbent non-diamond phases is strongly enhanced at high  $T_s$ . In order to support this behavior further *ex-situ* characterizations were carried out.

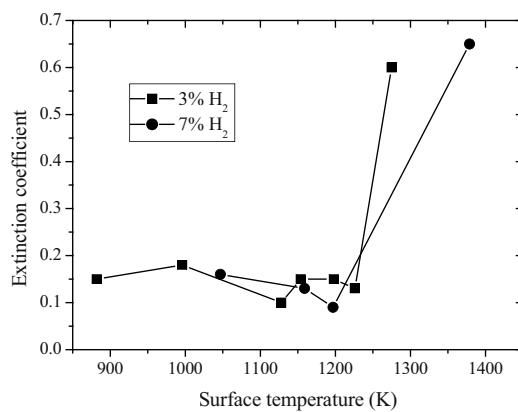


Figure 5. Extinction coefficient determined from the best fit of the apparent temperature measured for the samples elaborated under Ar/H<sub>2</sub>/CH<sub>4</sub> microwave discharges with 96:3:1 and 92:7:1 gas ratios as a function of the surface temperature.

A selection of SEM micrographs covering the entire ranges of temperatures explored for the two sample series is given in Figure 6.

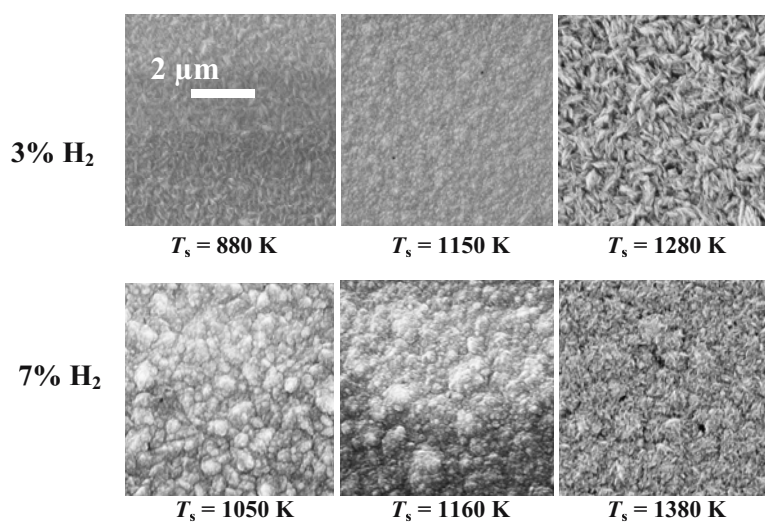


Figure 6. SEM micrographs of the samples elaborated under Ar/H<sub>2</sub>/CH<sub>4</sub> microwave discharges with 96:3:1 and 92:7:1 gas ratios at different surface temperatures  $T_s$ .

For both gas compositions, the morphology of the films elaborated at low and moderate  $T_s$  is characterized by relatively smooth surfaces typical of the diamond layer nanostructure, where no emerging crystallized grains can be noticed. The film surface obtained for the highest surface temperature is characteristic of ballas-like morphology containing graphitic lamellae [14]. This means that the deposition of  $sp^2$ -hybridized carbon atoms is enhanced while increasing the surface temperature, which supports the pyrometric observations.

UV-Raman spectroscopy was completed using a 363.8 nm laser excitation in order to enhance the scattering signal coming from  $sp^3$  phases with respect to  $sp^2$  bondings. Some selected spectra obtained for the sample series corresponding to 96:3:1 gas ratios are presented in Figure 7.

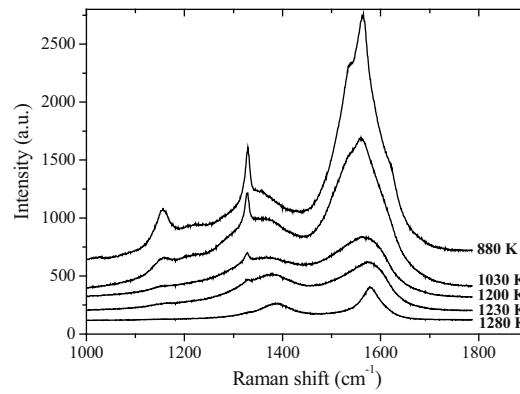


Figure 7. UV-Raman spectra of the samples elaborated at different surface temperatures under Ar/H<sub>2</sub>/CH<sub>4</sub> microwave discharge with 96:3:1 gas ratios.

A Raman spectra representative of the NCD features is characterized by bands around 1140 and 1470 cm<sup>-1</sup> typical of trans-polyacetylene, graphite D and G bands around 1350 and 1580 cm<sup>-1</sup>, respectively, and a broad diamond peak at 1332 cm<sup>-1</sup> [15,16]. These attributes are well-observed in Figure 7 at low surface temperature. While  $T_s$  is raised, the intensity of the diamond peak and trans-polyacetylene bands hugely decreases. The Raman spectra evolves then towards a structure where only the graphite D and G bands are mainly distinguished, that is typical of important graphitic contents in the films [14]. Note that this trend was also observed for the other sample series.

TEM was performed on the sample achieved under 96:3:1 gas percentages at a moderate surface temperature  $T_s = 1150\text{K}$  (Figure 8). The layer is composed of clusters containing diamond grains with a size in the

nanometer-scale, separated by amorphous grain boundaries. Diamond (111) lattice planes are clearly identifiable on Figure 8 through the distance between two successive fringes estimated at approximately 0.205 nm.

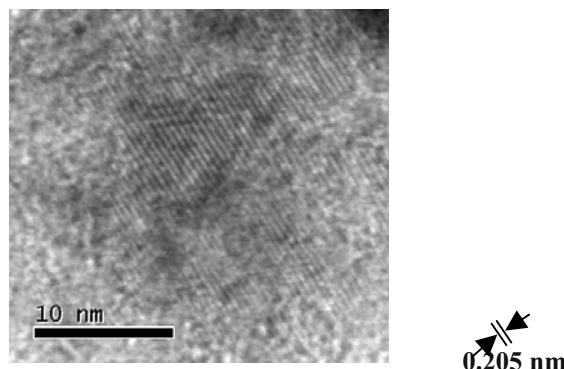


Figure 8. High resolution TEM micrograph of the sample elaborated under Ar/H<sub>2</sub>/CH<sub>4</sub> (96:3:1) microwave discharge at a surface temperature  $T_s = 1150\text{K}$ . The lattice fringes correspond to the diamond (111) planes.

Thus, even if the diamond contribution is widely reduced as  $T_s$  is raised in the Raman spectra of Figure 7, the films elaborated at low and moderate temperatures are always mainly composed of nanocrystalline diamond grains. Consequently the changes in the film structure are actually limited for restrained temperature variations, which is consistent with the roughly constant extinction coefficient values estimated at low and intermediate surface temperatures (see Figure 5).

Finally XRD characterizations were performed on the samples using the CuK $_{\alpha 1}$  radiation ( $\lambda = 1.54056\text{ nm}$ ) with an incident X-ray angle of  $10^\circ$ . All the XRD spectra of the deposited films are dominated by the  $\langle 111 \rangle$ ,  $\langle 220 \rangle$  and  $\langle 311 \rangle$  diamond diffraction peaks that give evidence for the presence of crystalline diamond within the films whatever the surface temperature. Using the Scherrer formula applied to the  $\langle 111 \rangle$  diffraction peak, the grain size was estimated in the ranges 10–20 nm and 15–45 nm for the 96:3:1 and 92:7:1 sample series, respectively, depending on  $T_s$  values. These measurements are in good agreement with the film nanocrystalline structure observed by TEM.

Figure 9 shows that the XRD spectrum of samples synthesized under Ar/H<sub>2</sub>/CH<sub>4</sub> (96:3:1) microwave discharge at high surface temperature ( $T_s = 1280\text{K}$ ) contains an unambiguous contribution of graphite through the broad  $\langle 002 \rangle$  diffraction peak located at  $2\theta = 26.4^\circ$  (JCPDS No. 41-1487), that not occurs at moderate temperature ( $T_s = 1150\text{K}$ ). This definitely proves that microcrystalline graphite is formed at high surface temperatures for the

experimental conditions considered in this work. Consequently, only low and moderate surface temperatures should be used for NCD growth in order to avoid the film graphitization.

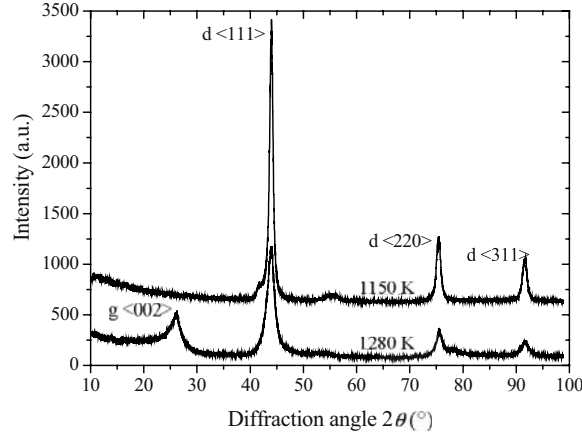


Figure 9. XRD patterns of the samples elaborated under Ar/H<sub>2</sub>/CH<sub>4</sub> (96:3:1) microwave discharge at surface temperatures  $T_s = 1150\text{K}$  and  $T_s = 1280\text{K}$ . The diamond and graphite diffraction peaks are indexed by ‘d’ and ‘g’, respectively.

The entire deposition experiments realized permits to conclude that the best combination of NCD film properties (grain size below 10 nm, surface roughness around 20–25 nm, growth rate at approximately 1  $\mu\text{m/h}$ , satisfactory purity) is obtained for low CH<sub>4</sub> and H<sub>2</sub> concentrations (1% and 2–3%, respectively), high pressure (200 mbar), moderate surface temperature (1100–1200K) and maximum microwave power value that can be injected (500–600 W). The growth conditions being optimized, the feasibility of some applications was then considered.

## 5. SAW DEVICE ACHIEVEMENT

Surface acoustic wave devices are critical components for wireless communication systems. The increasing demand for large volume data transmission requires devices operating in high frequencies (GHz range). As the center frequency  $f_0 = v_\phi/\lambda$  is determined by the phase velocity ( $v_\phi$ ) and the wavelength ( $\lambda$ ), diamond, which possesses the highest acoustic phase velocity, is a very promising substrate for SAW application when combined with piezoelectric material.



High frequency SAW devices in the GHz range based on PCD were recently successfully achieved [17]. However the grow-side of diamond is quite rough and must be smoothed by mechanical polishing in order to favor the wave propagation and to fulfill the requirements of the photolithographic process. Recent works proposed an alternative method for SAW device achievement that consists in using the smooth unpolished nucleation side of freestanding diamond layers [18], but this solution requires up to 100  $\mu\text{m}$ -thick films.

Owing to the high smoothness of their grow-side surface, as-grown NCD films may represent a good alternative to PCD for SAW application. Indeed, their use would permit to avoid the polishing step or the growth of thick films, which are time-consuming processes.

We present here the successful fabrication of SAW filters based on AlN/NCD/Si layered structure. NCD deposition was achieved in a 96:3:1-500 W Ar/H<sub>2</sub>/CH<sub>4</sub> discharge under 200 mbar total pressure and 250 sccm total gas flow rate, while maintaining the substrate temperature around 1170K. Various deposition times, ranging from 4.0 to 24.0 h, were explored in order to obtain different thickness. Aluminum inter-digital transducers (IDTs) of 16 and/or 32  $\mu\text{m}$  wavelengths ( $\lambda$ ) were developed on AlN/NCD/Si and AlN/Si structures by photolithography technique. The number of IDTs pairs fingers, the IDTs aperture length (W) and inter-IDTs distance (Gap) were set to 50 mm, 2 mm and 1 mm, respectively. DC planar magnetron sputtering was employed in optimized conditions in order to deposit c-oriented AlN layers [19]. Figure 10 shows a schematic diagram of the resulting NCD-based SAW device.

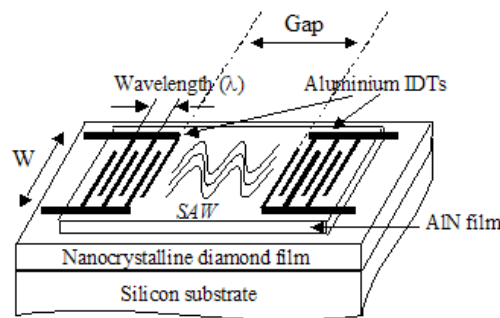


Figure 10. Schematic diagram of NCD-based SAW device showing the AlN/NCD/Si layered structure (not to scale).

An example of the frequency response measured with a network analyzer for both wavelength values with SAW one-port resonators achieved on an AlN/NCD/Si structure is shown in Figure 11.



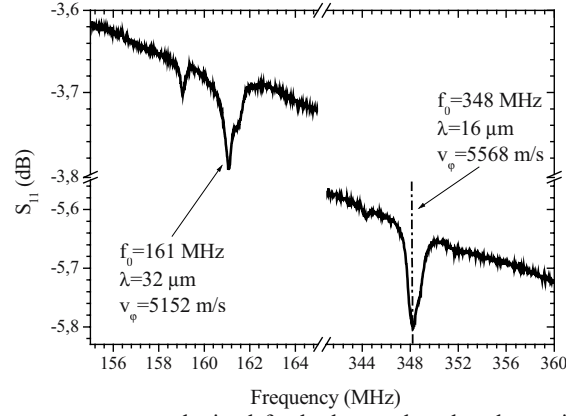


Figure 11. Frequency responses obtained for both wavelength values with SAW one-port resonators achieved on an AlN/NCD/Si structure consisting of 2.4  $\mu\text{m}$ -thick NCD film (4.0 hrs of growth) and 1.5  $\mu\text{m}$ -thick AlN layer.

The Table 1 summarizes the thickness ( $h$ ) of NCD and AlN layers, the wavelengths ( $\lambda$ ) of IDTs, and the acoustic velocity ( $v_\phi$ ) deduced from the center frequency  $f_0$  for all the SAW devices achieved.

Table 1. NCD thickness, AlN thickness, wavelength and resulting acoustic velocity of layered structures achieved on the samples investigated.

Structure	$h_{\text{NCD}}$ ( $\mu\text{m}$ )	$h_{\text{AlN}}$ ( $\mu\text{m}$ )	$\lambda$ ( $\mu\text{m}$ )	$v_\phi$
AlN/Si	0	2	16	5098
			32	5088
AlN/NCD/Si	2.4	1.5	16	5568
			32	5152
AlN/NCD/Si	4.6	2	32	5700
AlN/NCD/Si	18.9	4	32	9472

This table points out that the phase velocity obtained for AlN/NCD/Si structure is higher than that obtained for AlN/Si structure, that makes evidence for the positive influence of high-velocity NCD layer. Also, the effect of the wave penetration depth in the layered structure (typically of the order of magnitude of the wavelength) is illustrated by considering the raising of  $v_\phi$  when  $\lambda$  is reduced from 32 to 16  $\mu\text{m}$  and when the thickness of the NCD film increases [20]. The increase of  $v_\phi$  is due to the decrease of the contribution of the low-velocity silicon substrate as the wave penetrates less deeply within the structure. Finally, a phase velocity of almost  $10^4$  m/s was measured for the structure completed with 4- $\mu\text{m}$  AlN, almost 19- $\mu\text{m}$  NCD films and  $\lambda = 32$   $\mu\text{m}$ , which is comparable to the value measured for AlN/PCD structure [21]. Consequently, low surface roughness as-grown

NCD films offer a very promising alternative for high velocity/high frequency SAW devices conception.

## 6. CONCLUSION

In this paper we presented the different steps that must be accomplished to control and optimized the MPACVD process of NCD layers using Ar/H<sub>2</sub>/CH<sub>4</sub> gas mixture. The determination of stable process parameters insuring the reproducibility of growth conditions and the study of the influence of the growth parameters on the film properties were carried out in order to produce functional films suitable for high velocity/high frequency SAW devices.

We are now working on different solutions allowing the improvement of the deposition process by further decreasing the diamond grain size, keeping stable and reproducible discharges, especially without significant soot particle production. Concerning AlN/NCD/Si SAW devices, we are working on the obtaining of very high operating frequency by diminishing the IDT wavelength and optimizing the NCD film thickness that should permit to limit the penetration depth of the acoustic wave in the low-velocity silicon substrate.

## Acknowledgements

The authors are grateful to O. Elmazria, M.B. Assouar, P. Alnot and L. Bouvot from the University Henri Poincaré (Nancy, France) for the realization and characterization of SAW devices and valuable discussions.

## REFERENCES

1. D.M. Gruen, X. Pan, A.R. Krauss, S. Liu, J. Luo, and C.M. Foster. Deposition and characterization of nanocrystalline diamond films. *Journal of Vacuum Science and Technology A* **12**, 1491 (1994).
2. D.M. Gruen. Nanocrystalline diamond films. *Annual Review of Materials Science* **29**, 211 (1999).
3. V.I. Konov, A.A. Smolin, V.G. Ralchenko, S.M. Pimenov, E.D. Obraztsova, E.N. Loubnin, S.M. Metev, and G. Sepold. DC arc plasma deposition of smooth nanocrystalline diamond films. *Diamond and Related Materials* **4**, 1073 (1995).
4. T. Lin, G.Y. Yu, A.T.S. Wee, Z.X. Shen, and K.P. Loh. Compositional mapping of the argon-methane-hydrogen system for polycrystalline to nanocrystalline diamond film growth in a hot-filament chemical vapor deposition system. *Applied Physics Letters* **77**, 2692 (2000).

5. S.N. Kundu, M. Basu, A.B. Maity, S. Chaudhuri, and A.K. Pal. Nanocrystalline diamond films deposited by high pressure sputtering of vitreous carbon. *Materials Letters* **31**, 303 (1997).
6. K. Okada, T. Aizawa, R. Souda, S. Komatsu, and S. Matsumoto. Vibrational studies of microcrystalline diamond and diamond-like carbon by high resolution electron energy loss spectroscopy. *Diamond and Related Materials* **10**, 1991 (2001).
7. L.C. Chen, P.D. Kichambare, K.H. Chen, J.-J. Wu, J.R. Yang, and S.T. Lin. Growth of highly transparent nanocrystalline diamond films and a spectroscopic study of the growth. *Journal of Applied Physics* **89**, 753 (2001).
8. D.M. Bhusari, J.R. Yang, T.Y. Wang, K.H. Chen, S.T. Lin, and L.C. Chen. Effects of substrate pretreatment and methane fraction on the optical transparency of nanocrystalline diamond thin films. *Journal of Materials Research* **13**, 1769 (1998).
9. D. Zhou, T.G. McCauley, L.C. Qin, A.R. Krauss, and D.M. Gruen. Synthesis of nanocrystalline diamond films from an Ar-CH<sub>4</sub> microwave plasma. *Journal of Applied Physics* **83**, 540 (1998).
10. D. Zhou, D.M. Gruen, L.C. Qin, T.G. McCauley, and A.R. Krauss. Control of diamond film microstructure by Ar addition to CH<sub>4</sub>/H<sub>2</sub> microwave plasmas. *Journal of Applied Physics* **84**, 1981 (1998).
11. K. Hassouni, T.A. Grotjohn, and A. Gicquel. Self-consistent microwave field and plasma discharge simulations for a moderate pressure hydrogen discharge reactor. *Journal of Applied Physics* **86**, 134 (1999).
12. F. B  n  dic, M. Belmahi, T. Easwarakhanthan, and P. Alnot. In-situ optical characterization during MPACVD diamond film growth on silicon substrates using a bichromatic infrared pyrometer under oblique incidence. *Journal of Physics D: Applied Physics* **34**, 1048 (2001).
13. P. Bruno, F. B  n  dic, F. Mohasseb, F. Silva, and K. Hassouni. Effects of substrate temperature on nanocrystalline diamond growth: an in-situ optical study using pyrometric interferometry, *Thin Solid Films*, in press.
14. R. Haubner and B. Lux. Deposition of ballas diamond and nano-crystalline diamond. *International Journal of Refractory Metals and Hard Materials* **20**, 93 (2002).
15. A.C. Ferrari and J. Robertson. Origin of the 1150 cm<sup>-1</sup> Raman mode in nanocrystalline diamond, *Physical Review B: Condensed Matter* **63**, 121405(R) (2001).
16. R. Pfeiffer, H. Kuzmany, N. Salk, and B. G  nther. Evidence for trans-polyacetylene in nanocrystalline diamond films from H-D isotropic substitution experiments. *Applied Physics Letters* **82**, 4149 (2003).
17. H. Nakahata, S. Fujii, K. Higaki, A. Hachigo, H. Kitabayashi, S. Shikata, and N. Fujimori. Diamond-based surface acoustic wave devices. *Semiconductor Science and Technology* **18**, S96-S104 (2003).
18. V. Mortet, O. Elmazria, M. Nesladek, M.B. Assouar, G. Vanhoyland, J. D'Haen, M. D'Olieslaeger, and P. Alnot. Surface acoustic wave propagation in aluminum nitride-unpolished freestanding diamond structures. *Appl. Phys. Letters* **81**, 1720 (2002).
19. M.B. Assouar, O. Elmazria, L. Le Brizoual, P. Alnot. Reactive DC magnetron sputtering of aluminum nitride films for surface acoustic wave devices. *Diamond and Related Materials* **11**, 413 (2002).
20. F. B  n  dic, M.B. Assouar, F. Mohasseb, O. Elmazria, P. Alnot, and A. Gicquel. Surface acoustic wave devices based on nanocrystalline diamond and aluminium nitride. *Diamond and Related Materials* **13**, 347 (2004).
21. H. Nakahata, H. Kitabayashi, T. Uemura, A. Hachigo, K. Higaki, S. Fujii, Y. Seki, K. Yoshida, and S. Shikata. Study on surface acoustic wave characteristics of SiO<sub>2</sub>/interdigital-transducer/ZnO/diamond structure and fabrication of 2.5 GHz narrow band filter. *Japanese Journal of Applied Physics* **37**, 2918 (1998).

# 8

## MODELLING OF Ar/H<sub>2</sub>/CH<sub>4</sub> MICROWAVE DISCHARGES USED FOR NANOCRYSTALLINE DIAMOND GROWTH

F. Mohasseb, K. Hassouni, F. Bénédic, G. Lombardi, and A. Gicquel  
*Laboratoire d'Ingénierie des Matériaux et des Hautes Pressions, UPR 1311 CNRS, 99 av.  
J.B. Clément, Université Paris 13, 93430 Villetaneuse, France*

**Abstract:** This work deals with the modelling of Ar/H<sub>2</sub>/CH<sub>4</sub> microwave discharges used for nanocrystalline diamond film deposition. Two thermochemical models are developed and used in order to estimate the discharge composition, the gas temperature and the average electron energy in the frame of a quasi-homogeneous plasma assumption. The first one takes into account the formation of hydrocarbons containing up to two carbon atoms, while in the second heavier aliphatic molecules and poly-aromatic hydrocarbons are considered along with soot particle nucleation.

**Keywords:** nanocrystalline diamond, microwave plasma, modeling, poly-aromatic hydrocarbons, soot particles

### 1. INTRODUCTION

Usually, Ar/H<sub>2</sub>/CH<sub>4</sub> gas mixture characterized by low H<sub>2</sub> and CH<sub>4</sub> concentrations [1] is employed for nano-crystalline diamond (NCD) film synthesis by microwave plasma assisted chemical vapor deposition (MPACVD) process. The control and optimization of NCD deposition requires the understanding of the main phenomena that govern the growth process. Only few studies were reported on experimental investigations of the considered discharges and especially the measurements of the C<sub>2</sub> dimer density and of the gas temperature. C<sub>2</sub> is indeed assumed to be the growth precursor, while the gas temperature is a key-parameter for the plasma chemistry [2–4]. The few measurements performed so far give only partial information on the plasma features, and almost no data exists on the other plasma parameters. More detailed characterization of these discharges could

be obtained through plasma modelling supported by spectroscopic diagnostics.

The work presented in this paper deals with the modelling of moderate pressure Ar/H<sub>2</sub>/CH<sub>4</sub> discharges ignited in a microwave cavity system and used for nanocrystalline diamond film deposition. These discharges are characterized by a H/C ratio which typically ranges between 8 and 18. For these H/C values, heavy hydrocarbons and soot particles may be formed for some conditions depending on pressure and input microwave power (MWP) values. Thus, in order to describe the plasma chemistry, two thermochemical models were developed. In the first one, the formation of hydrocarbons with more than 2 carbon atoms and of poly-aromatic hydrocarbon (PAH) molecules is neglected, while in the second these along with soot particle nucleation are taken into account. These plasma models were developed and used in order to estimate the discharge composition, the gas temperature and the average electron energy in the frame of a quasi-homogeneous plasma assumption.

## 2. INVESTIGATED PLASMA REACTOR

The thermochemical models were developed for a MPACVD device commonly used for poly-crystalline diamond (PCD) and NCD film deposition and extensively described in previous publications [5]. It mainly consists of a quartz Bell-Jar low-pressure chamber placed inside a resonant microwave cavity (Figure 1).

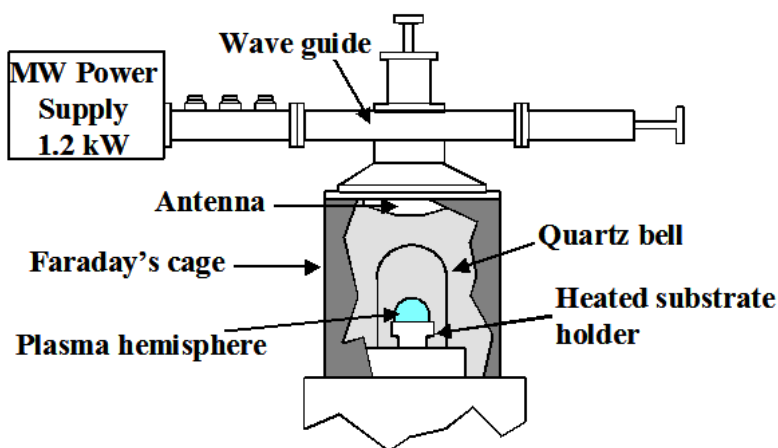


Figure 1. Schematic of the MPACVD apparatus used for NCD deposition.

The gas is activated by a 1200 W, 2.45 GHz microwave power supply. Optimal deposition conditions are achieved when the plasma volume ignited in the reaction chamber is hemispherical and located just above a 2 inches diameter silicon substrate on which diamond is deposited. The substrates are heated by the plasma and by an additional heating source that enables to control the substrate temperature. For standard growth conditions, the total gas flow rate is maintained at 250 sccm and the total gas pressure at 20000 Pa [6]. The models developed in this work were used to investigate Ar/H<sub>2</sub>/CH<sub>4</sub> discharges corresponding to feed gas composition with H<sub>2</sub> concentration (%H<sub>2</sub>) that varies between 2 and 7% and a constant methane concentration (%CH<sub>4</sub>) of 1%. The amount of argon (%Ar) was chosen in such way to keep the feed gas flow constant. A parametric study of the input MWP values was systematically performed for each gas composition.

### **3. MODERATE PRESSURE AR/H<sub>2</sub>/CH<sub>4</sub> PLASMA MODELS**

#### **3.1 Thermochemical Model**

Since the Ar/H<sub>2</sub>/CH<sub>4</sub> microwave discharges are characterized by a strong thermal and chemical non-equilibrium, the model distinguishes two different energy modes: the heavy species translation-rotation (t-r) characterized by the gas temperature  $T_g$ , and the electron translation mode (e), the distribution of which may significantly deviates from a Maxwellian [7]. Due to the relatively high pressure used in the reactor, a thermal equilibrium was assumed between the vibrational modes of molecular species and the 't-r' mode.

#### **3.2 Chemical Models**

One of the main objective behind the chemical kinetics investigation of the considered discharges is to analyze the thermochemical properties of the plasma in NCD deposition conditions and to study the possibility of PAH formation and soot particle nucleation under various conditions (gas composition and input microwave power). For this purpose, we developed two kinetic models with different degrees of complexity:

First, the description of the kinetic was focused on conditions where the formation of heavy hydrocarbons and soot particles is limited and may be neglected [8]. In these situations the gas temperature is higher than 2000K, which corresponds to the conditions met in the plasma bulk under growth conditions. Consequently, only species containing up to 2 carbon-atoms

were considered in a first numerical model (denoted 2C-model). This permitted to understand the main energetic characteristics of the investigated plasma and to evaluate the population of active species.

In order to analyze the soot particle formation, this numerical model was extended taking into account the formation of PAHs through a radical mechanism. This model (denoted A4-model) takes into account large neutral PAHs up to 4 aromatic rings from which the soot particle nucleation was assumed to take place. This study was performed in such a way to investigate the whole temperature domains that characterize the plasma bulk, the plasma/substrate boundary layer and the plasma edge.

### 3.2.1 2C-Model

The 2C-model is an extension of the kinetic model that was previously developed to describe the chemical kinetics of moderate pressure  $H_2/CH_4$  microwave discharges used for the deposition of PCD films [9]. This model takes into account molecular and atomic hydrogen and their ions, the first two excited states of H-atom, neutral hydrocarbon species with up to two carbon atoms ( $C_{1-2}H_{0-6}$ ), the most significant hydrocarbon ions ( $C^+$ ,  $CH_3^+$ ,  $CH_4^+$ ,  $CH_5^+$ ,  $C_2H^+$ ,  $C_2^+$ ,  $C_2H_2^+$ ,  $C_2H_3^+$ ,  $C_2H_4^+$ ,  $C_2H_5^+$  and  $C_2H_6^+$ ), the singlet state of methylene  $^1CH_2$  and the electrons. These species are linked by chemical reactions that include electron-impact dissociation and ionization of hydrogen and hydrocarbon species, thermal chemistry that only involves heavy species and leads to  $H_2$  dissociation and hydrocarbons conversion, a large number of ion conversion processes that favor the formation of some hydrocarbon ions even for low methane concentration in the feed gas and dissociative recombination processes for  $H_3^+$  and hydrocarbon ions. The present model takes into account the argon based compounds Ar, Ar\*, Ar<sup>+</sup>, ArH<sup>+</sup> and ArH<sup>+</sup>\*, along with the reactions describing their chemistry [10]. The production of Ar<sup>+</sup> and Ar\* species is due to the electron impact ionization and excitation of argon. ArH<sup>+</sup> is obtained through ion conversion process that involve Ar<sup>+</sup> and  $H_2$ . Note also that in the presence of hydrocarbons, Ar<sup>+</sup>-ion will tend to undergo charge transfer reactions with hydrocarbon molecules that leads to a significant amount of hydrocarbon ions even at the low methane percentage that characterizes the investigated discharges. The 2C-model takes into account 38 species involved in a 147 chemical reaction mechanism. Note that this model is only suitable for describing the discharge conditions where the formation of large hydrocarbons is negligible.

### 3.2.2 A4-Model

In this model the reactions describing the formation of large aliphatic and aromatic neutral hydrocarbons were included. This group of reactions is essentially thermal in nature and does not include electron impact process. It is derived from the work of Wang and Frenklach [11] on soot formation in flames. The only difference with the literature is that we did not consider the reactions containing oxygen, as it was not used in our feed gas mixture.

The species added to the 2C-model are the aliphatic hydrocarbons containing 3 to 6 carbon atoms with an hydrogen content varying from 2 to 8 (C<sub>3-6</sub>H<sub>2-8</sub>) and the PAHs containing up to 4 aromatic rings. The details of the species nomenclature can be found in literature [12]. For instance, a PAH containing *q* fused rings are specified by A<sub>q</sub>, *e.g.* A<sub>2</sub> for the naphthalene. The first aromatic ring (benzene) is produced by the recombination of C<sub>4</sub>H<sub>5</sub> with C<sub>2</sub>H<sub>2</sub> or by the reaction between two C<sub>3</sub>H<sub>3</sub> radicals. Then the production of larger aromatic compounds proceeds through the Hydrogen Abstraction Carbon Addition (HACA) mechanism [11]. This mechanism is illustrated in Figure 2 where is presented the production of naphthalene from benzene.

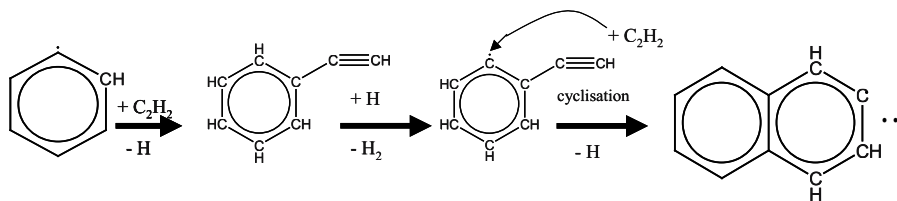


Figure 2. HACA mechanism.

In the present model soot nucleation is assumed to result from the condensation of two large PAH molecules. This nucleation mechanism is still subject to a large controversy [13] since the formation of two-PAH complex is insured by Van der Waals type bonds which requires very large PAHs (*i.e.* to insure a large surface attraction and therefore strong enough Van der Waals bonds) to be stable at temperatures as high as those encountered in our discharges. Nevertheless, we assumed here that the nucleation mechanism occurs from the condensation of two pyrene (A<sub>4</sub>) molecules in order to determine the main qualitative features of soot nucleation:  $A_4 + A_4 \rightarrow (A_4==A_4)_s$ . The nucleation rate constant was thus derived from the A<sub>4</sub> concentration and the condensation reaction rate constant. The A<sub>4</sub>-model takes into account 101 species linked by 356 reactions. The aerosol dynamics and soot growth, coagulation and aggregation are not considered in the present model which only yields information on the soot particle nucleation rate.



### 3.3 Quasi-Homogeneous Plasma Model

The thermochemical models discussed above were used to describe the investigated discharges under the assumption of quasi-homogeneous plasmas. The details of the model based on this assumption were described elsewhere [14] and we will only summarize its main features here. In the quasi-homogeneous plasma approximation we assume that the discharge is made of a homogenous plasma volume, where all the plasma characteristics are constant, and of a thin boundary layer, where species density and plasma temperature vary linearly (Figure 3).

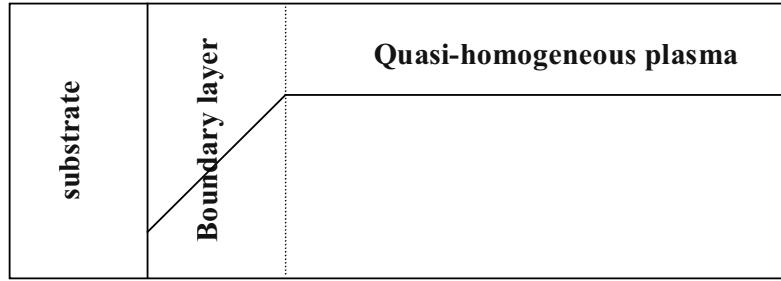


Figure 3. Schematic principle of a quasi-homogeneous plasma model.

Under this assumption, the time-evolution of the species density in the bulk of the discharge are governed by a set of ordinary differential equations. According to previous study, for moderate pressure discharges the electron-heavy species reaction rate constants only depend on the average electron energy and the knowledge of the whole electron energy distribution function is not required to estimate these rate constants [9]. Thus, instead of coupling the electron Boltzmann's equation to the species equation, an electron average energy equation may be considered. The dependence between the rate constants and the average electron energy is then determined independently by using an offline Boltzmann solver. The heavy species-heavy species reaction rate constants depend on the gas temperature. This is determined by coupling to the species and electron energy equations a total energy equation.

For a given discharge conditions, *i.e.* microwave power density, pressure and feed gas composition, the steady state plasma composition is calculated by time-integrating the coupled set of species and energy balance equations. The integration starts from a plasma composition corresponding to a cold gas with a very small electron density. The absorption of the microwave power induces an electron heating that leads to a strong ionization and dissociation kinetics, a gas heating and an enhanced thermal chemistry. The integration is

stopped once the species densities and the electron and gas temperature reach the steady state. The numerical algorithm makes use of fully implicit backward difference formulae (BDF).

## 4. RESULTS AND DISCUSSION

### 4.1 2C-Model

The model calculations were performed for 2, 3, 5 and 7% H<sub>2</sub> by varying the microwave power from 250 W to the maximum values that can be experimentally injected, *i.e.* 500, 600, 700 and 800 W, respectively.

Figure 4 shows that the gas temperature  $T_g$  strongly increases with the input MWP from 3100K for 2% H<sub>2</sub> and 250 W to 4400 K for 7% H<sub>2</sub> and 800 W.

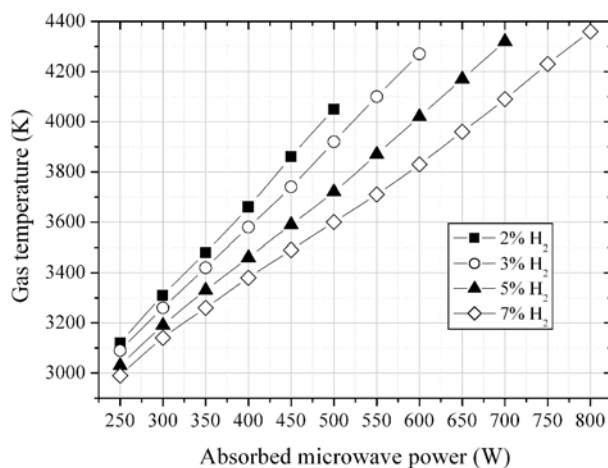


Figure 4. Gas temperature  $T_g$  calculated in the Ar/H<sub>2</sub>/CH<sub>4</sub> microwave discharges under 200 mbar as a function of the absorbed MWP and for different %H<sub>2</sub>.

The  $T_g$ -values obtained for the Ar/H<sub>2</sub>/CH<sub>4</sub> discharges are then much higher than those obtained in H<sub>2</sub>/CH<sub>4</sub> discharges used for the deposition of PCD films. Indeed, for the latter  $T_g$  is around 2200 K for 25 mbar and 600 W discharge conditions [15]. Furthermore, for a given MWP,  $T_g$  tends to decrease while increasing the hydrogen concentration in the feed gas (Figure 4). This behavior, as well as the high  $T_g$ -values typically above 3000K, are due to the difference between the thermal conductivities of hydrogen and argon. The higher thermal conductivity of H<sub>2</sub>, which exceeds the argon thermal conductivity by more than one order of magnitude, insures

an enhanced thermal transfer to the substrate surface and reactor walls, which leads to a lower gas temperature in  $\text{H}_2/\text{CH}_4$  discharges and when the  $\text{H}_2$  ratio is increased in  $\text{Ar}/\text{H}_2/\text{CH}_4$  discharges. Note that the theoretical values obtained for the maximum MWP value investigated for each % $\text{H}_2$  are in satisfactory agreement with experimental measurements reported elsewhere [16].

The variation of atomic hydrogen mole fraction  $X_{\text{H}}$  as a function of the absorbed MWP and for different % $\text{H}_2$  in the feed gas is given in Figure 5. This shows that the mole fraction of H-atom increases with both MWP and % $\text{H}_2$ . For 2%  $\text{H}_2$ ,  $X_{\text{H}}$  varies from  $4 \times 10^{-2}$  to  $7.5 \times 10^{-2}$ , while MWP increases from 250 to 500 W. For 7%  $\text{H}_2$ , the H-atom mole fraction increases from  $5 \times 10^{-2}$  to 0.16 whereas MWP varies from 250 to 800 W.

As a matter of fact, H-atom mole fraction values thus obtained are very high compared to those calculated in  $\text{H}_2/\text{CH}_4$  discharges used for PCD deposition [9]. As an example a 1.99–600 W  $\text{H}_2/\text{CH}_4$  microwave discharge under 25 mbar is characterized by a  $X_{\text{H}}$  of approximately 0.01, which yields a H-atom density of  $10^{15} \text{ cm}^{-3}$ . For the  $\text{Ar}/\text{H}_2/\text{CH}_4$  discharges obtained under the same absorbed MWP, the H-atom mole fraction ranges between 0.09 and 0.15, which corresponds to a density between  $3 \times 10^{16}$  and  $6 \times 10^{16} \text{ cm}^{-3}$ , with only 3 to 7% hydrogen in the feed gas.

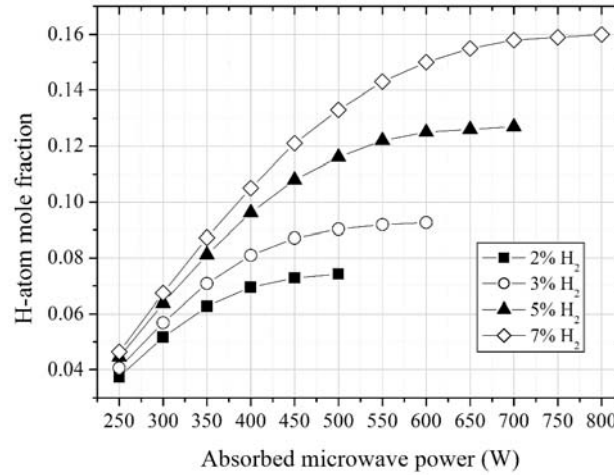


Figure 5. H-atom mole fraction calculated in the  $\text{Ar}/\text{H}_2/\text{CH}_4$  microwave discharges under 200 mbar as a function of the absorbed MWP and for different % $\text{H}_2$ .

The  $\text{Ar}/\text{H}_2/\text{CH}_4$  discharge conditions corresponding to NCD film deposition are therefore characterized by a large amount of H-atom that probably play a key-role in the growth process by insuring an enhanced

etching of the non-diamond phases. The very high H-atom mole fractions result from the strong thermal dissociation and conversion of H<sub>2</sub> and CH<sub>4</sub>.

As far as hydrocarbon species are concerned, results of simulations show that C<sub>2</sub>H<sub>2</sub> is the major species at low MWP and that its concentration strongly decreases when the MWP increases (Figure 6a). This trend is due to an efficient C<sub>2</sub>H<sub>2</sub> → C<sub>2</sub> conversion which leads to the increase of the C<sub>2</sub> mole fraction up to a maximum value (Figure 6b). The value and the position of this maximum depend on the hydrogen amount in the feed gas. When the MWP is further increased C<sub>2</sub> is converted to atomic carbon (Figure 6c) and its density decreases (Figure 6b). The atomic carbon becomes then the major carbon containing species. This C<sub>2</sub>H<sub>2</sub> → C<sub>2</sub> → C conversion channel is mainly driven by thermal chemistry.

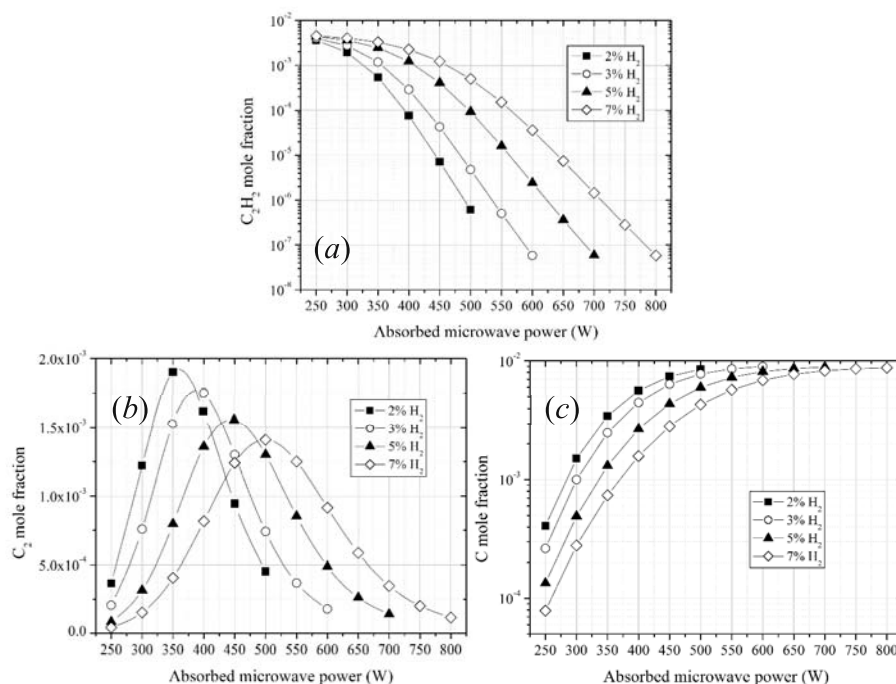


Figure 6. Mole fractions of the predominant hydrocarbon species calculated in the CH<sub>4</sub>/H<sub>2</sub>/Ar microwave discharges under 200 mbar as a function of the absorbed MWP and for different %H<sub>2</sub>: (a) C<sub>2</sub>H<sub>2</sub>; (b) C<sub>2</sub>; (c) C.

For the conditions corresponding to the maximum MWP value absorbed for each %H<sub>2</sub>, the calculated C<sub>2</sub> mole fraction slightly decreases from 4.5 × 10<sup>-4</sup> to 10<sup>-4</sup> (Figure 6.b), when %H<sub>2</sub> and MWP are simultaneously increased. This mole fraction variation corresponds to a density decrease from 2 × 10<sup>14</sup> to 4 × 10<sup>13</sup> cm<sup>-3</sup>. These values are in good agreement with those

experimentally determined through absorption measurements carried out on the  $C_2$  Mulliken system [16], which also show a decreasing tendency with values varying from  $9 \times 10^{13}$  to  $1.5 \times 10^{13} \text{ cm}^{-3}$ .

The predominance of C-atoms and  $C_2$ -radicals in the investigated discharges represents another significant difference between the presently investigated NCD deposition discharges and the  $H_2/CH_4$  plasmas used for PCD deposition where  $C_2H_2$  is the predominant hydrocarbon species [9]. Also in the present work the values determined for the  $C_2$  density between  $10^{13}$  and  $10^{14} \text{ cm}^{-3}$  are much greater than those estimated in other works, where density-values in the range  $10^{10}$ – $10^{12} \text{ cm}^{-3}$  were reported [2,4]. This difference in  $C_2$  density is consistent with the much higher gas temperature obtained in the discharges investigated in this work. The gas temperature reported in the literature for the discharges used for NCD deposition ranges indeed between 1450 and 1600K.

## 4.2 A4-Model

The simulations were performed for a feed gas composition of 1%  $CH_4$ , 2%  $H_2$  and 97% argon at a pressure of 20000 Pa and input MWP values ranging between 10 and 500 W. The investigation of several power values enabled us to analyze the effect of the gas temperature on the PAH formation and soot particle nucleation. Each value of the input power corresponds to a steady state gas temperature that characterizes a different discharge region (either the bulk or the edge of the plasma). The dependence between input MWP and  $T_g$  is presented in Figure 7 showing that the gas temperature vary between 1200K and 4000K in the investigated MWP domain.

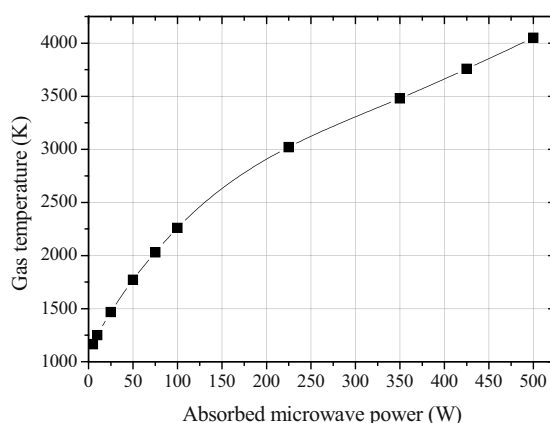


Figure 7. Evolution of the gas temperature in the Ar/ $H_2$ / $CH_4$  microwave discharges under 200 mbar as a function of the input microwave power.

For high MWP, the A4-model predicts high temperature values between 3500 and 4000K. These values are in good agreement with those calculated by the 2C-model and are representative of the plasma bulk for NCD deposition conditions. The  $T_g$ -values obtained at low MWP range between 1000 and 2500K and characterize the temperature at the plasma edges. In the following, the calculation results will be discussed as a function of the gas temperature in order to describe these two plasma regions.

The evolution of H<sub>2</sub> and H-atom mole fractions as a function of the gas temperature is given in Figure 8. At low MWP the molecular hydrogen is almost not dissociated and H-atom mole fraction is below  $10^{-3}$ . When the power increases, the H<sub>2</sub> dissociation is enhanced and almost all the hydrogen is in the atomic form.

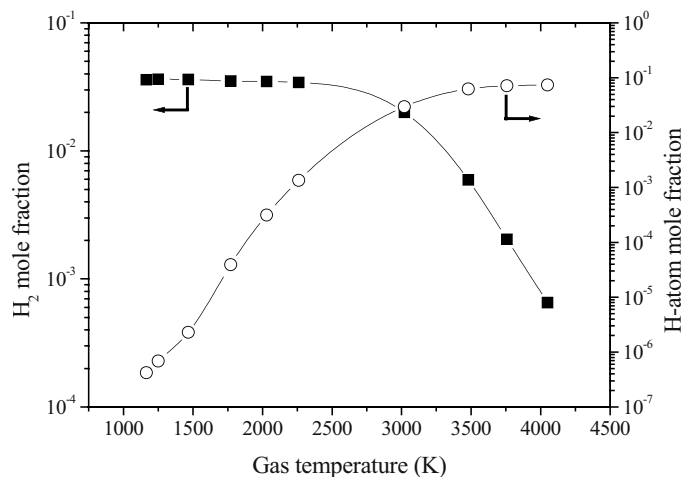


Figure 8. Evolution of H<sub>2</sub> and H-atom mole fractions in the Ar/H<sub>2</sub>/CH<sub>4</sub> microwave discharges under 200 mbar as a function of the gas temperature.

As previously described a fraction of H-atom present in the discharge comes also from the conversion of CH<sub>4</sub>. Finally both 2C- and A4-models lead to the same values for H<sub>2</sub> and H-atom mole fractions.

The mole fractions of the major hydrocarbon species containing up to 2 carbon atoms (CH<sub>4</sub>, C, C<sub>2</sub>H<sub>4</sub>, C<sub>2</sub>H<sub>2</sub> and C<sub>2</sub>) are shown in Figure 9 as a function of  $T_g$ .

Up to a gas temperature around 1500K, CH<sub>4</sub> remains the major hydrocarbon species. At higher  $T_g$  the methane is converted to acetylene that becomes the major species up to 3500K. Above this temperature, C<sub>2</sub>H<sub>2</sub> is converted to C<sub>2</sub> and C, which remain the only significant carbon-containing species when the MWP is further increased. At high  $T_g$ , the A4-model provides the same mole fraction values as the 2C-model, whereas at low  $T_g$

the small aliphatic molecules do not contain all the carbon atoms present in the feed gas.

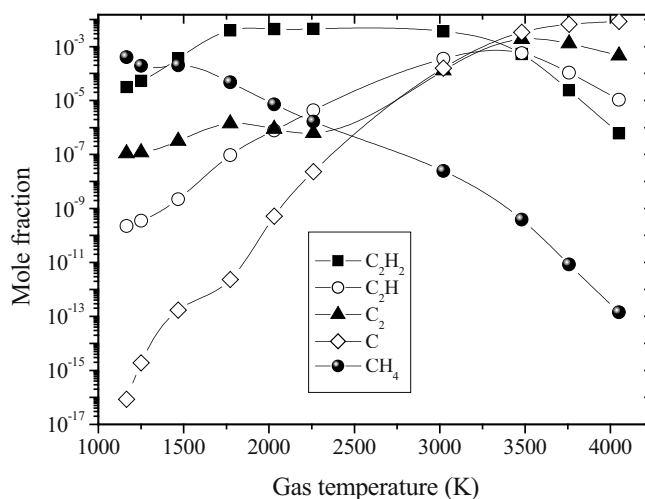


Figure 9. Evolution of the C<sub>2</sub>H, C<sub>2</sub>H<sub>2</sub>, C<sub>2</sub>, CH<sub>4</sub> and C mole fractions in the Ar/H<sub>2</sub>/CH<sub>4</sub> microwave discharges under 200 mbar as a function of the gas temperature.

Figure 10 shows that a large fraction of the carbon atoms of the feed gas participate to the formation of PAH molecules at low temperature. The benzene (A1) is always the major aromatic species and reaches a mole fraction of 10<sup>-4</sup> at low temperatures. The other PAH densities are significant only for temperatures below 1500K and show mole fraction values roughly one or two orders of magnitude less than that of benzene. At high temperature values, the PAH mole fractions decrease significantly and becomes negligible while C<sub>2</sub> and C becomes the major carbon-containing species.

Finally, Figure 11 presents an estimation of the soot particle nucleation rate as a function of  $T_g$ . The nucleation rate is quite high for gas temperatures between 1200K and 1500K and strongly decreases for higher  $T_g$ . Therefore, the A4-model points out that the homogenous nucleation mechanism, involving only neutral chemistry and more specifically the HACA mechanism, may explain the formation of soot particles for gas temperatures below 1500K. Actually, these temperatures characterize the cold regions of the discharges used for NCD deposition. These cold regions correspond to the plasma edge and to the boundary layer between the plasma and the substrate surface.

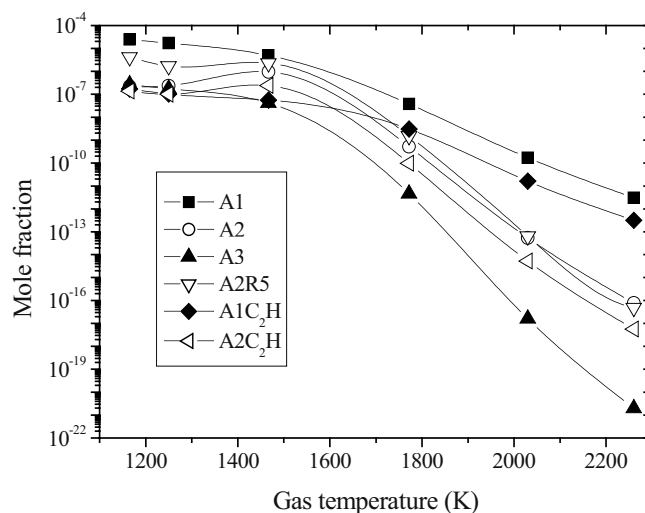


Figure 10. Evolution of predominant PAH mole fractions in the Ar/H<sub>2</sub>/CH<sub>4</sub> microwave discharges under 200 mbar as a function of the gas temperature.

It is important to note that other nucleation sources such as heterogeneous soot formation on the substrate surface and the reactor walls, or homogenous nucleation through condensation of charged species may also be significant but were not considered in the present model.

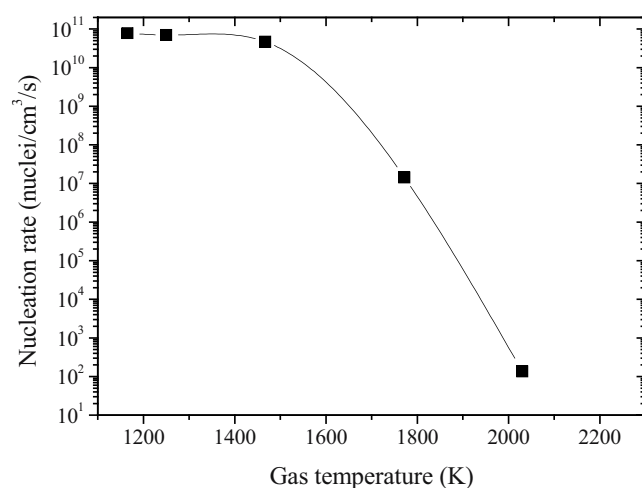


Figure 11. Evolution of the soot nucleation rate in the Ar/H<sub>2</sub>/CH<sub>4</sub> microwave discharges under 200 mbar as a function of the gas temperature.



However, the A4-model allows to estimate first-hand values of the nucleation rate and to probe the possibility of soot formation through a radical mechanism in Ar/H<sub>2</sub>/CH<sub>4</sub> microwave discharges.

## 5. CONCLUSION

In this paper Ar/H<sub>2</sub>/CH<sub>4</sub> microwave discharges used for nanocrystalline diamond deposition in a Bell-Jar cavity reactor were characterized by modelling investigations under quasi-homogeneous plasma assumption.

The 2C-model, that neglects PAH formation and soot particle nucleation, enabled us to probe the main characteristics of the considered discharges. Simulations yield gas temperature values ranging between 3000 and 4000K and C<sub>2</sub> density values between 10<sup>13</sup> and 10<sup>14</sup> cm<sup>-3</sup>, depending on the investigated conditions. These values are relatively high compared to those reported in literature. The calculation results indicate also that the predominant carbon-containing species are C<sub>2</sub>H<sub>2</sub>, C<sub>2</sub> and C at low MWP, C<sub>2</sub> and C at moderate MWP and C at high MWP. Besides, the H-atom density in Ar/H<sub>2</sub>/CH<sub>4</sub> discharges is very high with a mole fraction ranging between 5 and 15%. This amount of H-atom is greater than that encountered in H<sub>2</sub>/CH<sub>4</sub> microwave discharges suitable for polycrystalline diamond growth. This surprising result is due to an enhanced thermal chemistry and should be taken into account in the investigation of the surface chemistry leading to NCD formation.

The A4-model was developed on the basis of 2C-model in order to investigate the formation of large aliphatic and aromatic hydrocarbons in the considered discharges and the possibility of soot particle nucleation. The results show that a significant production of PAHs and soot particles can occur when the gas temperature is lower than 1500K. Under such conditions, the molecular hydrogen is almost not dissociated and acetylene and methane are the major hydrocarbon species in the discharge. Although the present model makes use of a quasi-homogenous plasma assumption and give information only on the bulk of the discharge, it may give some additional qualitative information with respect to soot formation under NCD deposition discharge conditions. The model particularly shows that for high power density discharges actually used for NCD deposition, the soot cannot be formed in the bulk of the discharge. The only reactor regions where homogeneous nucleation, based on the HACA mechanism, may take place are the cold region located just above the substrate surface and at the edge of the discharge zone. The fact that nuclei may form just near the growing film may have a significant effect on the deposition process and should be considered more thoroughly in the frame of process optimization.

Forthcoming works will deal with the development of one dimensional models making possible to follow the plasma composition and temperatures in the reacting boundary layer. The development of such a model and its validation through spatially-resolved spectroscopic measurements would be of great interest for further understanding of the main phenomena that govern NCD deposition. Also, more quantitative conclusions concerning the soot formation require an improvement of the A4-model by coupling the aerosol dynamics, including growth, aggregation and transport of particles, and by taking into account the soot formation through an ionic mechanism.

## REFERENCES

1. D. Zhou, D.M. Gruen, L.C. Qin, T.G. McCauley, and A.R. Krauss. Control of diamond film microstructure by Ar addition to CH<sub>4</sub>/H<sub>2</sub> microwave plasmas. *Journal of Applied Physics* **84**, 1981 (1998).
2. A.N. Goyette, J.E. Lawler, L.W. Anderson, D.M. Gruen, T.G. McCauley, D. Zhou, and A.R. Krauss. Spectroscopic determination of carbon dimer densities in Ar-H<sub>2</sub>-CH<sub>4</sub> and Ar-H<sub>2</sub>-C<sub>60</sub> plasmas. *Journal of Physics D: Applied Physics* **31**, 1975 (1998).
3. W.S. Huang, T.A. Grotjohn, and J. Asmussen. Plasma diagnostic measurements of argon-hydrogen-methane discharges used for ultra-nanocrystalline diamond deposition in a microwave CVD system. Proceeding of the 27<sup>th</sup> IEEE International Conference on Plasma Science (Piscataway: IEEE, NJ) pp. 180 (2000).
4. A.N. Goyette, J.E. Lawler, L.W. Anderson, D.M. Gruen, T.G. McCauley, D. Zhou, and A.R. Krauss. C<sub>2</sub> Swan band emission intensity as a function of C<sub>2</sub> density. *Plasma Sources Science and Technology* **7**, 149 (1998).
5. K. Hassouni, T.A. Grotjohn, and A. Gicquel. Self-consistent microwave field and plasma discharge simulations for a moderate pressure hydrogen discharge reactor. *Journal of Applied Physics* **86**, 134 (1999).
6. F. Mohasseb, G. Lombardi, F. Bénédict, K. Hassouni, F. Silva, and A. Gicquel. Characterization of MPACVD process suitable for nanocrystalline diamond film deposition. In: *Progress in Plasma Processing of Materials*, edited by P. Fauchais and J. Amouroux (Begell House, New York, Wallingford, UK), p. 689 (2003).
7. K. Hassouni, C.D. Scott, S. Farhat, A. Gicquel, and M. Capitelli. Non-Maxwellian effect on species and energy transport in moderate pressure H<sub>2</sub> plasmas. *Surface and Coatings Technology* **97**, 391 (1997).
8. S.L. Girshick, C. Li, B.W. Yu, and H. Han. Fluid boundary layer effects in atmospheric-pressure plasma diamond film deposition. *Plasma Chemistry and Plasma Processing* **13**, 169 (1993).
9. K. Hassouni, O. Leroy, S. Farhat, and A. Gicquel. Modeling of H<sub>2</sub> and H<sub>2</sub>/CH<sub>4</sub> moderate-pressure microwave plasma used for diamond deposition. *Plasma Chemistry and Plasma Processing* **18**, 325 (1998).
10. G. Lombardi, K. Hassouni, F. Bénédict, F. Mohasseb, J. Röpcke, and A. Gicquel. Spectroscopic diagnostics and modelling of Ar/H<sub>2</sub>/CH<sub>4</sub> microwave discharges used for nanocrystalline diamond deposition. *Journal of Applied Physics*, accepted.

11. H. Wang and M. Frenklach. A detailed kinetic modeling study of aromatics formation in laminar premixed acetylene and ethylene flames. *Combustion and Flame* **110**, 173 (1997).
12. M. Frenklach, D.W. Clary, T. Yuan, W.C. Gardiner, and S.E. Stein. Mechanism of soot formation in acetylene-oxygen mixtures. *Combustion Science and Technology* **50**, 79 (1986).
13. H.F. Calcote. Mechanisms of soot nucleation in flames - a critical review. *Combustion and Flame* **42**, 215 (1981).
14. K. Hassouni, X. Duten, A. Rousseau, and A. Gicquel. Investigation of chemical kinetics and energy transfer in a pulsed microwave  $H_2/CH_4$  plasma. *Plasma Sources Science and Technology* **10**, 61 (2001).
15. A. Gicquel, K. Hassouni, Y. Breton, M. Chenevier, and J.C. Cubertaon. Gas temperature measurements by laser spectroscopic and optical emission spectroscopy. *Diamond and Related Materials* **5**, 336 (1996).
16. G. Lombardi, F. Bénédict, F. Mohasseb, K. Hassouni, and A. Gicquel. Determination of gas temperature and  $C_2$  absolute density in  $Ar/H_2/CH_4$  microwave discharges used for nanocrystalline diamond deposition from  $C_2$  Mulliken system. *Plasma Sources Science and Technology* **13**, 375 (2004).

# 9

## NANODIAMOND SEEDING FOR NUCLEATION AND GROWTH OF CVD DIAMOND FILMS

V. Ralchenko<sup>1</sup>, A. Saveliev<sup>1</sup>, S. Voronina<sup>1</sup>, A. Dementjev<sup>2</sup>, K. Maslakov<sup>2</sup>, M. Salerno<sup>3</sup>, A. Podesta<sup>3</sup>, and P. Milani<sup>3</sup>

<sup>1</sup> *A.M. Prokhorov General Physics Institute RAS, Vavilov str. 38, Moscow 119991, Russia*

<sup>2</sup> *IRTM, RRC "Kurchatov Institute", Kurchatov square, Moscow 123182, Russia*

<sup>3</sup> *INFN-Dipartimento di Fisica, Università di Milano, Via Celoria 16, 20133 Milano, Italy*

**Abstract:** Detonation nanodiamonds are shown to be effective seeds for growth of CVD diamond films as they provide high nucleation density on a substrate and can be placed on shaped surfaces and even into porous materials. XPS, AES and TEM analyses give useful information on the early stage of diamond growth. The transfer molding technique for manufacturing various diamond shapes is described. As the nucleation side of free-standing films produced by molding is the “working” surface, emphasis is placed on the study of its properties, such as topography, impurity contamination, thermal conductivity, and wettability. Diamond items grown directly on patterned Si templates are illustrated.

**Keywords:** detonation nanodiamond, CVD diamond film, nucleation, XPS, XAES, patterning, molding

### 1. INTRODUCTION

Spontaneous nucleation of diamond on a foreign substrate in a CVD process has a low probability; for example, the nucleation density is typically of the order of  $10^4$  nuclei/cm<sup>2</sup> on silicon. A much higher density of nucleation centers must be achieved to produce thin continuous films or conformal diamond coatings on surfaces with intricate shape. Therefore, diamond seeds for further growth must be placed on the substrate before or during diamond deposition. If the nucleation density is  $10^8$ – $10^{10}$  cm<sup>-2</sup>, grains of 1.0–0.1  $\mu$ m in size are formed on the substrate, evolving into columnar crystallites with their size gradually increasing with the film thickness. The surface relief of the bottom (nucleation) side of a free-standing film

separated from the substrate is a replica of the substrate relief; the quality of the replica improves with the nucleation density. Since the processing of diamond, in particular polishing, is a difficult and tedious procedure, it is a great advantage that the nucleation side of the film can be made smooth enough (when grown on a polished substrate) to be immediately used without pretreatment for fabrication of, say, surface acoustic wave devices or heat spreaders for electronic devices [1]. Alternatively, various diamond microstructures can be directly produced by a molding technique, i.e. by growing the film on a patterned substrate, followed by the substrate removal (see [2,3] for a review). A better quality of replicas is achieved by depositing a nanocrystalline diamond layer [4,5] on the film/substrate interface by an appropriated seeding/growth process. Here we consider the diamond film deposition in microwave plasma CVD (MPCVD) and direct current (DC) plasma CVD reactor, using nanodiamond particles for seeding on flat and patterned Si substrates. The focus is on the properties of the nucleation surface of the films; examples of diamond shapes produced by the transfer molding technique are presented.

## 2. SUBSTRATE SEEDING

A number of seeding procedures are available to strongly enhance diamond nucleation. A simple mechanical abrasion of the substrate with a diamond grit promotes the nucleation (other hard grits, like c-BN, give no positive effect [6]). However, the surface damage due to the arising defects and scratches may not be tolerable. This drawback can be by using a bias-enhanced nucleation (BEN) that does produce a high (up to  $10^{12} \text{ cm}^{-1}$ ) nucleation density. The BEN process involves the substrate biasing at a negative DC voltage (typically  $-150 \div -200 \text{ V}$ ) at the beginning of diamond deposition [7] to generate nuclei in a carbonaceous layer by bombardment with accelerated ions. The spin-off coating on the substrate with a photoresist containing diamond particles [8] is a seeding technique compatible with standard microelectronic technology. Another approach uses the printing of seeds by a stamp brought in contact with the substrate [9]. All the seeding methods work well mostly for flat substrates but may be ineffective for intricate surfaces. For instance, the nucleation by BEN can be incomplete on a patterned surface with undercut structures (because of a shadow effect) or on a porous substrate. The seeding by ultrasonic treatment in a suspension of diamond powder in an appropriate liquid (acetone, alcohol, etc) is free from the latter limitation. The suspension of detonation nanodiamond powder has proved to provide the highest nucleation density ( $>10^{10} \text{ cm}^{-2}$ ) as compared with the ultrasonic treatment with a grit of larger

size [10,11]. It is important that the seeding with nanodiamond causes no surface damage. Moreover, nanoscale seeds can penetrate with the liquid into very small pores, allowing the diamond deposition inside [12,13].

In the experiments described here, the seeding was performed by treating Si substrates in a alcohol suspension of 4–6 nm diamond, placed in an ultrasonic bath typically for 15–30 minutes. The nanodiamonds were produced by a detonation technique [14] at the Russian Federal Nuclear Center (Snezhinsk).

### 3. DIAMOND DEPOSITION SYSTEMS

Two types of CVD diamond reactors were used for diamond growth on seeded Si substrates. The DC plasma CVD reactor was described elsewhere [5,11,15]. The substrate was placed on a substrate holder (anode), while a glassy carbon or tantalum carbide rode served as the cathode. A DC discharge at the current 1.8–2.2 A provided the diamond deposition in CH<sub>4</sub>-H<sub>2</sub> mixtures (100 sccm flow rate, 2–10% methane concentration) with a growth rate up to 10 μm/hour over a 10×10 mm<sup>2</sup> area at a substrate temperature close to 800°C. The thickness of the diamond thin films was determined *in situ* by a laser interferometric technique [10,15] based on measuring the intensity evolution of a He-Ne laser beam (633 nm wavelength) reflected from the growing film.

Large area (50–75 mm diameter) deposition was carried out using microwave CVD reactors ASTeX PDS 19 [16,17] and the DF-100 model recently designed at the GPI. Both systems operate at 5 kW maximum power at 2.45 GHz frequency. The techniques allow the growth of high quality thick diamond wafers in CH<sub>4</sub>-H<sub>2</sub> mixtures under the typical conditions: the methane content of 1–5%, the gas flow rate 1000 sccm, the pressure 100 Torr, and the substrate temperature 700–800°C, providing the growth rate in the range of 1–5 μm/h.

### 4. THE EARLY STAGE OF DIAMOND GROWTH

Transmission electron microscopy (TEM) used to examine a seeded polished Si substrate before growth in a DC plasma revealed nanodiamond particles agglomerated in clusters of 40–50 nm in size [15]. The density of the particles within the agglomerates was of the order of 10<sup>12</sup> cm<sup>-2</sup>. After 1 min deposition, the crystallite size increased to 50–70 nm, which corresponds to the growth rate of about 1 nm/sec, and their number density

was found to be of the order of  $10^{10} \text{ cm}^{-2}$  (Figure 1a). The presence of many multiply twinned particles was revealed at higher magnification. A twinned (bi-crystal) particle is illustrated in Figure 1b. Note that in contrast to nanodiamond seeds, which are spherical, these tiny CVD crystallites are well faceted, suggesting good abrasive properties with a size small enough for superpolishing applications. Potentially, the production of abrasive ultrafine grit by CVD using a detonation nanodiamond powder as the starting material could be economically viable. As the surface of the faceted particles is H-terminated, it would be chemically inert, and, hopefully, a deleterious effect of particle aggregation characteristic for nanometric detonation synthesis diamond could be reduced.

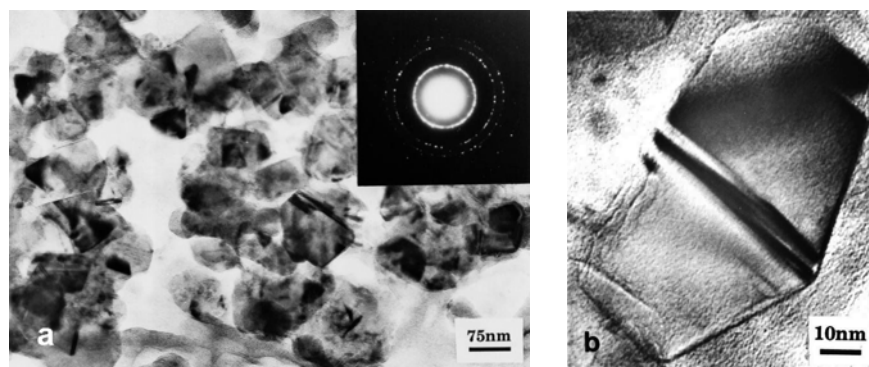


Figure 1. (a) TEM image of diamond crystallites deposited by DC plasma CVD for 1 min at 5%  $\text{CH}_4$  concentration in  $\text{H}_2$  on a Si substrate seeded with detonation nanodiamonds; (b) a faceted 50 nm particle (bi-crystal) grown in the same run [15].

The surface of diamond films deposited onto a Si substrate during the initial growth in a DF-100 MPCVD reactor was studied by X-ray-excited Auger electron spectroscopy (XAES) and X-ray photoelectron spectroscopy (XPS). The combination of XAES, electron energy loss spectroscopy (EELS) and valence band (VB) XPS is useful since these methods have different information depths of 1–2 monolayer (ML), 5–7 ML and 10–12 ML, respectively [18], and are sensitive to  $sp^2$  and  $sp^3$  bonds.

The XPS and XAES spectra were registered by a MK II VG scientific spectrometer with a non-monochromatized Al  $K\alpha$  X-ray source (1486.6 eV) at the base pressure of  $5 \cdot 10^{-10}$  mbar [19,20]. All the spectra were charge-referenced to the C1s XPS peak (284.8 eV). The position of the C1s line was determined with respect to the Ar  $2p_{3/2}$  XPS peak at 241.3 eV after low dose  $\text{Ar}^+$  implantation in the diamond sample. The X-ray excitation of Auger emission has a great advantage over  $e$ -excitation, as it allows a reduction in

the surface damage and, at the same time, obtaining XPS data. Only the  $N(E)$  CKVV spectra were used because the  $dN(E)/dE$  CKVV spectrum practically carries no information about the chemical interaction.

After ultrasonic seeding, the Si substrate was placed in a CVD chamber heated in a pure H plasma for 10 min, then methane was supplied for 4 min to grow a diamond film at the following parameters: MW power 3.2 kW,  $\text{CH}_4$  content 4%, pressure 80 Torr, substrate temperature  $T = 740^\circ\text{C}$ . After the growth termination by shutting down the methane flow, the sample was kept in the hydrogen plasma for 3 min, then it was cooled to room temperature for 7 min such that the film surface could be assumed to be H-terminated.

Figure 2a shows a wide-scan XPS spectrum of the “4 min” film. The strong C1s peak dominates, while the Si peaks are weak, indicating that the carbon film almost entirely covers the substrate. We estimated the film thickness from the measured growth rate of thicker (*ca.* 10  $\mu\text{m}$ ) films and found it to be about 100. In addition, a small oxygen contamination was found on the surface.

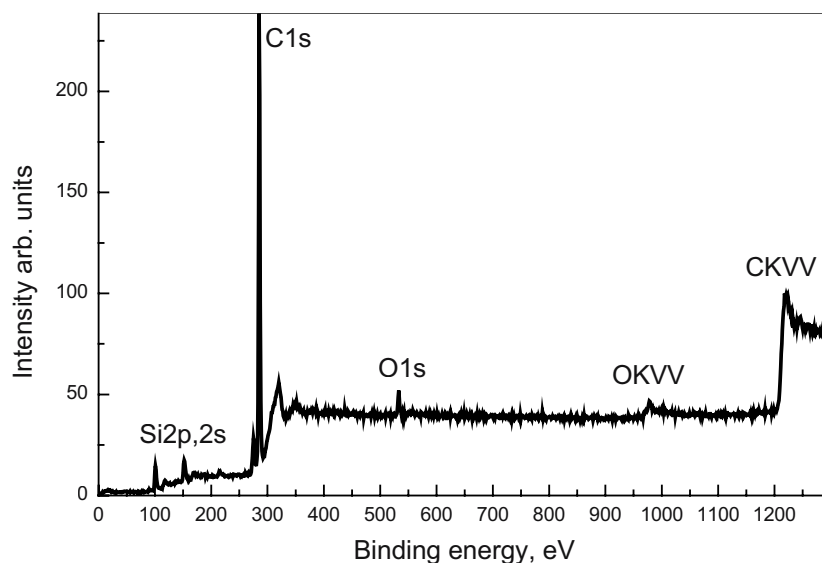


Figure 2a. The survey XPS spectrum of diamond deposited on Si. Growth time 4 min.



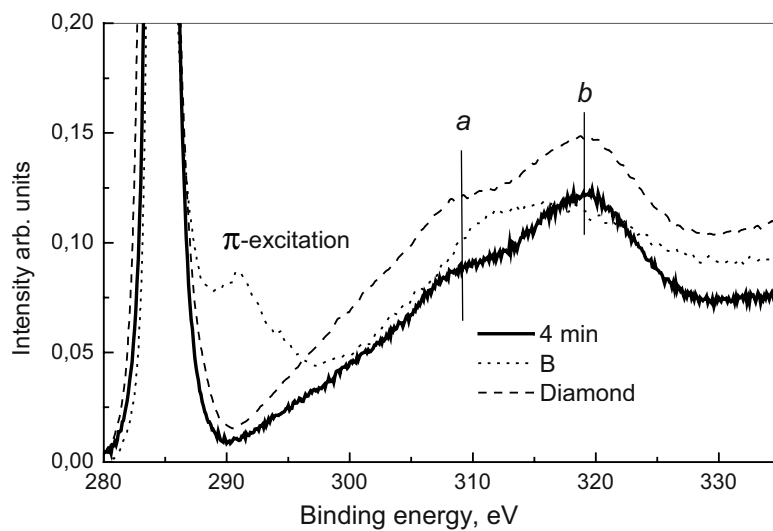


Figure 2b. The XPS EELS spectrum of the C1s region for a diamond film on Si (solid line). Growth time 4 min. Surface and bulk plasmons labelled as *a* and *b* are characteristic for the diamond. The spectra for reference single crystal diamond (dashed line) and HOPG (dotted line) are shown for comparison.

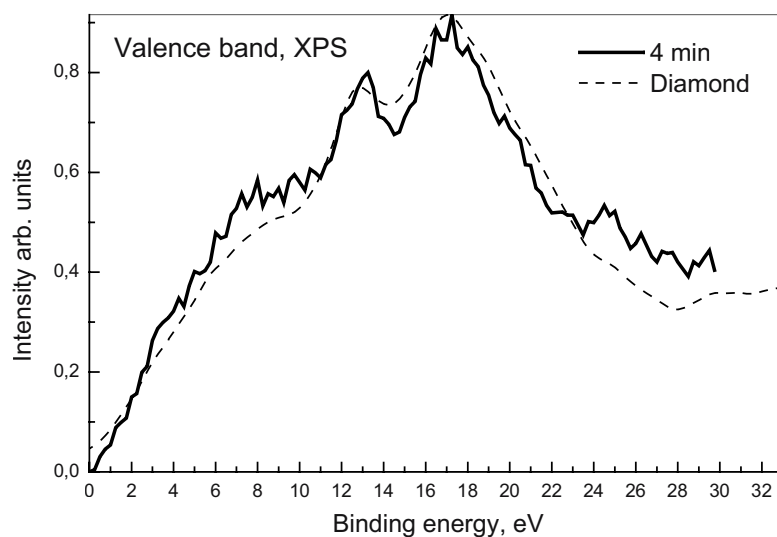


Figure 2c. The XPS valence band of the film after 4 min growth (solid line) and reference single crystal diamond (dashed line). The spectral similarity indicates the diamond position within the 10-12 ML probed layer.

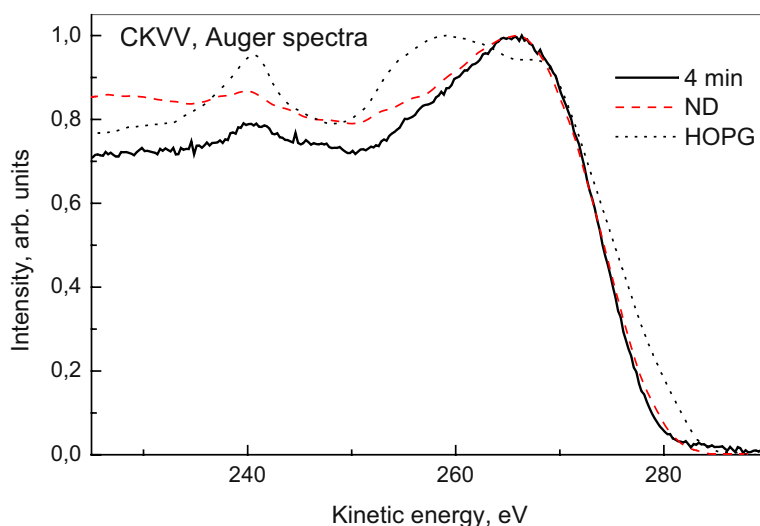


Figure 2d. The XAES spectra of a diamond film after 4 min growth (solid line). The spectra for detonation nanodiamond (ND) powder (dashed line) and HOPG (dotted line) are shown for comparison. The information depth is 1–2 ML only.

The characteristic electron energy loss spectrum shows two peaks of the surface plasmon at 24 eV and the bulk plasmon at 34 eV to the higher binding energy of the C1s line (Figure 2b) reliably indicating the diamond structure. The EELS spectrum is identical to that for the reference natural single crystal diamond. The spectrum for highly oriented pyrolytic graphite (HOPG) given for comparison shows the presence of the  $\pi$ -plasmon at 6 eV (Figure 2b).

Also, the valence band XPS spectrum of the film is quite similar to that for natural diamond (Figure 2c). However, the XAES analysis giving information only about the top 1–2 monolayers, did not reveal the purely  $sp^3$  state of the surface. Figure 2d compares the CKVV AES spectra for this film, for detonation nanodiamond and graphite. The slope of the right side of the spectrum is for the film and it is to be close to that for polyethylene [19] - the reference  $sp^3$  material - but different from the slope for graphite. On the other hand, the specific energy peaks for the diamond film cannot be attributed simply to  $sp^3$  but rather to the  $\pi$ -bonds of the dimers on the reconstructed diamond surface [19,21]. Interestingly, the Auger spectrum for H-terminated diamond is identical to that for nanodiamond (see Figure 2d) [19,20]. According to [22], the carbon atoms in this chemical state have the same electronic configuration as in graphite but with the

$\pi$ -level displaced by 1 eV below the Fermi level. It might, however, be that H atoms were desorbed by X-ray photons during the registration of the XEAS spectra, followed by the surface reconstruction and the  $\pi$ -bond formation, and the XAES data do not refer to the initially H-terminated surface.

The Raman spectrum taken at 488 nm excitation wavelength on the “4 min” sample displays (Figure 3) a peak near  $1145\text{ cm}^{-1}$ , which is typically observed for nanocrystalline diamond films [5]. It is likely to originate from transpolyacetylene contamination at the grain boundaries [23]. There are also two other broad peaks at  $1340$  and  $1580\text{ cm}^{-1}$ , which are due to disordered  $sp^2$  bonded (graphitic) carbon, and a weaker peak at  $1500\text{ cm}^{-1}$  presumably also related to transpolyacetylene. The diamond peak at  $1332\text{ cm}^{-1}$  is hardly visible against the background of disordered graphite. The laser beam probes the entire film thickness (the Raman peak from the Si substrate has been observed but is not shown here). As the Raman scattering cross-section is two orders of magnitude larger for  $sp^2$  bonds than for the diamond phase, one cannot conclude about graphitic carbon being dominant in the film structure.

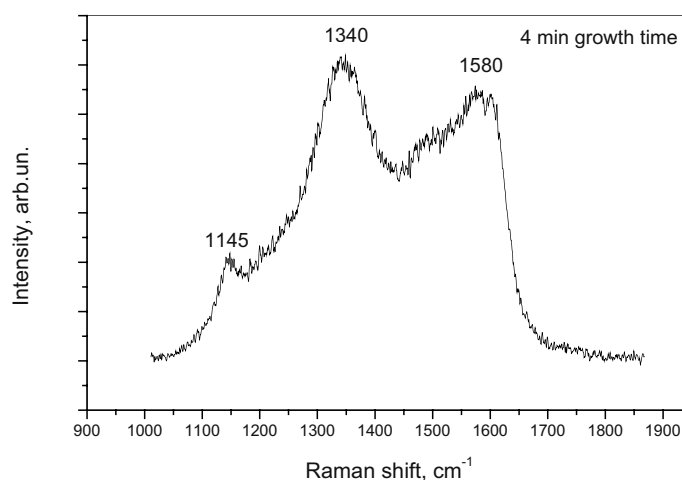


Figure 3. The Raman spectrum of a MPCVD diamond film grown on Si for 4 min.

## 5. PROPERTIES OF THE NUCLEATION SIDE

Generally, the nucleation side of the film mimics the surface relief of the substrate; in particular, in the case of a polished Si substrate the nucleation side may look mirror-like. A closer inspection, however, reveals a specific

grain structure. Figure 4 shows the surface relief of the nucleation side of a MPCVD diamond film with a relatively low nucleation density, as indicated by AFM data (Digital Nanoscope IIIA). The grains with a typical size of  $2\ \mu\text{m}$  have pits between them and an elevation away from the grain center (nucleation site) towards the edges. The formation of concave grains is illustrated in Figure 5. At the early stage of diamond growth, before the separate crystals merge, the uncovered silicon surface is subjected to etching by hydrogen plasma. So a particular grain extending laterally contacts locally the *inclined* etched Si surface. The resulting slope is constant if the Si etching rate and the diamond growth rate are assumed to be constant. When the faceted grains coalesce, some gaps may arise between them. After the substrate removal, the nucleation side replicates the etched silicon. As the nucleation site is preserved from the etching the grain center on the nucleation side is the lowest point (Figure 4).

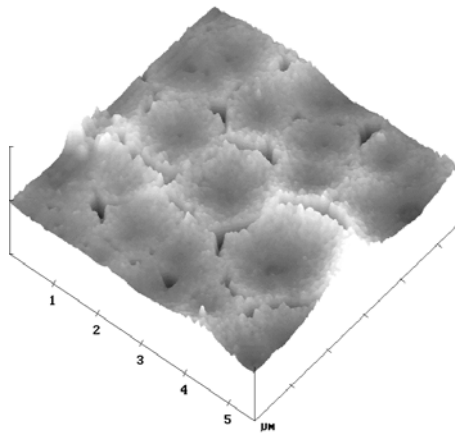


Figure 4. A 3D surface relief measured with AFM on the nucleation side of a diamond film with relatively low nucleation density. The grain boundaries (light contrast) are elevated relative to the grain center. The image area is  $5.6 \times 5.6\ \mu\text{m}^2$ .

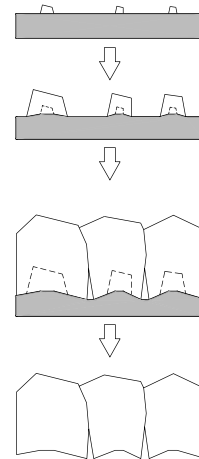


Figure 5. Schematic development of the surface relief on the nucleation side due to the Si substrate etching by H plasma.

This is more clear from a representative surface profile over several grains (Figure 6). The pits as deep as 100 nm can be observed. For a particular grain (the boundaries are shown by arrows), the elevation of the edges relative to the grain center is 37 nm due to the Si etching for about 30 min, and the slope is almost constant. Much smaller (40–100 nm) grains were observed on the nucleation side of films deposited at relatively low

temperatures of 690–710°C, the surface roughness  $R_a$  being as small as 5–9 nm (as measured with AFM across on area of  $5 \times 5 \mu\text{m}$ ).

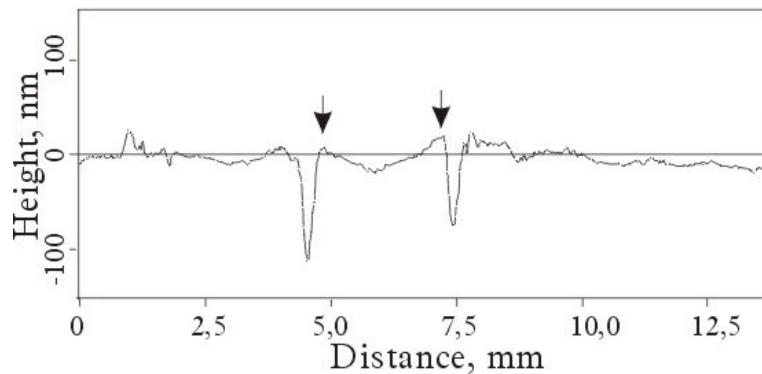


Figure 6. The surface profile on the nucleation side. Pits between concave grains are seen. Arrows show the elevated edges of a grain.

Since the diamond growth proceeds in a hydrogen-rich ambient, the hydrogen is a major impurity in CVD diamond; its concentration ranges from a few tens ppm for high quality films with large grains to 20,000 ppm for thin nanocrystalline films [24]. Hydrogen is distributed nonuniformly across the film thickness, typically a 20–50  $\mu\text{m}$  thick fine-grained layer adjacent to the substrate is rich in hydrogen by an order of magnitude greater than the film bulk [25]. The hydrogen decorates the defects and grain boundaries, so its local concentration should roughly follow the defect depth profile. An enhanced optical absorption [26] and a lower thermal conductivity [27,28] on the nucleation side have been reported. To illustrate, thermal conductivities of 20.0 W/cmK and 7.4 W/cmK have been determined for a 450  $\mu\text{m}$  thick translucent diamond film in 30  $\mu\text{m}$  thick layers adjacent to the growth and the nucleation side, respectively [28]. Several tens of microns of the defect material on the nucleation side should be removed to improve the optical, thermal and electronic properties of a free-standing film.

Silicon is another impurity that accumulates at the film bottom [3]. The contamination occurs during the Si substrate etching in a hydrogen plasma at initial stage of the deposition, followed by the Si incorporation from the plasma into the growing film. When the substrate is completely covered with a thin diamond film, the silicon etching stops. The higher is the nucleation density, the smaller is the thickness of the layer enriched with Si. The silicon in diamond can be detected locally by micro-photoluminescence (PL)

spectroscopy with a resolution of several microns, because a Si-vacancy defect center in diamond gives the PL line at 737 nm [29]. In this way, the Si depth profiles typically extending to 20-60  $\mu\text{m}$  from the interface into the film have been traced [3].

The Si contamination affects the wettability of the nucleation side. The wetting of thick diamond films with a polished growth side and a virgin nucleation side was examined using a sessile drop (water) method by Ostrovskaia *et al.* [30]. After hydrogenation in a microwave plasma, the growth side was hydrophobic with the contact angle as large as  $\theta = 93^\circ$ , but it changed to a hydrophilic one ( $\theta = 42^\circ$ ) after oxidation (Figure 6). The nucleation side showed a similar tendency under these treatments; yet it was more hydrophilic (the contact angle varied between  $65^\circ$  and  $32^\circ$ ) presumably due to Si impurity.

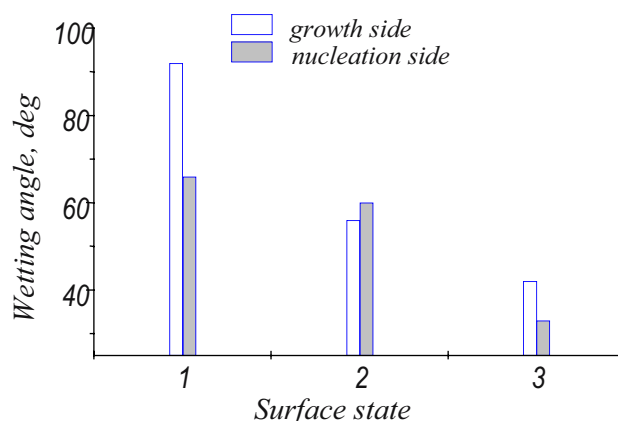


Figure 7. The contact angle for water on the growth (white bar) and nucleation (grey bar) surfaces of a diamond film in three states: (1) hydrogenization in a microwave  $\text{H}_2$  plasma at  $700^\circ\text{C}$  for 5 min, (2) naturally oxidized surface (aging), and (3) oxidation at  $500^\circ\text{C}$  in air for 30 min [30].

## 6. DIAMOND STRUCTURES DIRECTLY GROWN BY A MOLDING TECHNIQUE

The extreme chemical stability and hardness of diamond make its shaping and the fabrication of diamond items difficult. Diamond micromachining with laser beams or reactive ion etching [3] can be effective. For instance, diffractive CVD diamond cylindrical and Fresnel lenses [31] and antireflective periodic surface structures [32] have been

produced by laser engraving. Yet, the geometry of the patterns thus produced and their definition has a limitation. A promising approach is a direct growth of CVD diamond components [2] to minimize the surface treatment and to extend the variety of 2D and 3D structure designs.

Transfer molding is based on diamond deposition on a patterned substrate, followed by the substrate removal to obtain the replica of the master structure on the nucleation side of a free-standing film. The diamond nucleation density must be very high to get a high quality replica.

A large variety of diamond structures produced by this method have been demonstrated. Selected examples include pyramidal arrays for field electron emission cathodes [33–35], diamond optics with antireflective "moth eye" surface structures [13,36], lenses [37], microfluidic cooling systems and optical microelectromechanical systems (MEMS) [38,39], boron-doped MEMS [40], microspheres [41], cantilevers and sharp tips for scanning probe microscopy [3,42], microchannels (vias) with a very high aspect ratio [43], three-dimensional diamond replicas of porous opal [12], and flow controller micronozzles [44].

The sequence of operations for the production of diamond microstructures is shown schematically in Figure 8 [41]. First, a Si substrate is patterned by conventional photolithography and appropriate etching. Then the patterned surface is seeded with nanodiamonds in an ultrasonic bath to provide a high nucleation density and is placed in a CVD reactor. After the diamond deposition, the silicon is etched away with a mixture of hydrogen fluoride and nitric acids to obtain a replica.

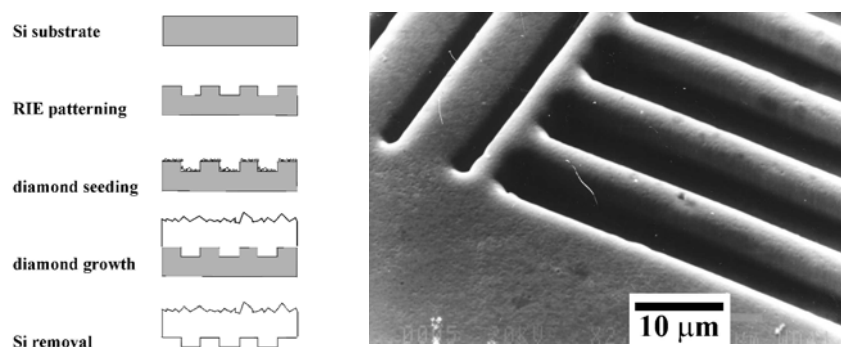


Figure 8. The fabrication of a diamond replica using a Si template (left); a diamond replica with a series of microtrenches, grown in a DC CVD reactor (right).

Subwavelength "moth-eye" periodical structures on a diamond surface form a kind of gradient refraction index layer such that they can essentially

increase the optical transmission of diamond optics, which normally has a high (30%) reflection loss [13, 36]. Regular micron-scale pyramids with periods of 4.5 and 12  $\mu\text{m}$  have been fabricated on Si patterned with inverted pyramids produced by anisotropic etching (Figure 9). Their infrared transmission increased to 78% from the normal 71% for polished surfaces, which is not bad considering that the pyramids were grown principally on one side only. Similar pyramids were used in field emission studies.

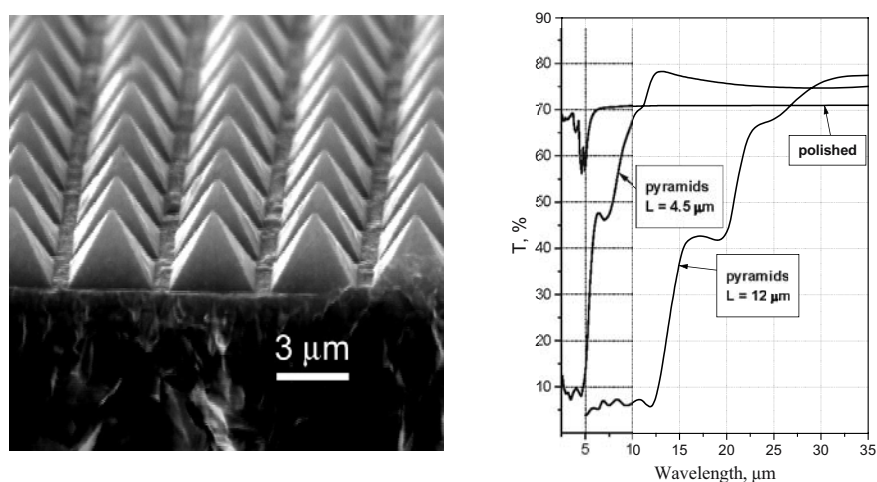


Figure 9. An array of diamond micropyramids on a Si patterned template (left); IR optical transmission spectra of CVD diamond surfaces with pyramids with the periods  $L = 4.5 \mu\text{m}$  and  $12 \mu\text{m}$  (right) [36]. The spectrum of a polished  $160 \mu\text{m}$  thick film is shown for comparison.

Not only microstructures but also macroscopic diamond components, e.g. X-ray lenses of a few centimeters long [45], can be grown using an appropriate template. Why should not we expect in the future even art pieces made from CVD diamond by this molding technique?

## 7. CONCLUSION

Nanodiamond particles seeded on a substrate provide densely arranged nucleation centers for CVD diamond growth. This technique is very useful for the deposition of submicron continuous coatings and very smooth nucleation sides in thick films. Nanodiamond seeding allows the growth of high quality patterned diamond structures for many applications by a replica



(molding) technique. This approach seems to be a promising alternative to conventional diamond shaping by post-growth processing.

## Acknowledgements

The authors are thankful to I.Vlasov for measuring the Raman spectra, S. Lavrishev for making the SEM pictures, and to A. Popovich for the help in preparation of the manuscript.

## REFERENCES

1. *Low-Pressure Synthetic Diamond: Manufacturing and Applications*. Eds. B. Dischler and C. Wild, Berlin: Springer, 1998.
2. V. Ralchenko. Nano- and microstructural features in CVD diamond growth. In: *Nanostructured Carbon for Advanced Applications*. Eds. G. Benedek, et al. Dordrecht: Kluwer, 2001, pp. 27-52.
3. V. Ralchenko, I. Vlasov, V. Frolov, D. Sovyk, A. Karabutov, K. Gogolinsky, and V. Yunkin. Nano- and microcrystalline CVD diamond films on surfaces with intricate shape. Proceedings of the NATO-Russia Advanced Research Workshop on Nanostructured Thin Films and Nanodispersion Strengthened Coatings, 2003 December 8-10, Moscow, Russia, Dordrecht: Kluwer (in press).
4. D.M. Gruen. Nanocrystalline diamond films. *Ann. Rev. Mater. Sci.* **29**, 211-59 (1999).
5. L.C. Nistor, J. Van Landuyt, V.G. Ralchenko, E.D. Obraztsova, and A.A. Smolin, Nanocrystalline diamond films: transmission electron microscopy and Raman spectroscopy characterization. *Diamond Relat. Mater.* **6**, 159-68 (1997).
6. W.A. Yarbrough. A chemical perspective on the nucleation and growth of diamond from hydrocarbons. In: *Proc. Applications of Diamond Films and Related Materials*. Eds. Y. Tzeng et al. Amsterdam: Elsevier, 1991, p. 25-34.
7. S. Yugo, T. Kanai, T. Kimura. A new method for generation of diamond nuclei by plasma CVD. *Diamond Relat. Mater.* **1**, 388-91 (1992).
8. V.G. Ralchenko, K.G. Korotoushenko, A.A. Smolin, and V.I. Konov. Patterning of diamond films by direct laser writing: selective-area deposition, chemical etching and surface smoothing. In: *Advances in New Diamond Science and Technology*. Eds. S. Saito et al.. Tokyo: MYU, 1994, pp. 493-96.
9. K. Higuchi and S. Noda. Selected area diamond deposition by control the nucleation sites. *Diamond Relat. Mater.* **1**, 220-29 (1992).
10. A.A. Smolin, V.G. Ralchenko, S.M. Pimenov, T.V. Kononenko, and E.N. Loubnin. Optical monitoring of nucleation and growth of diamond films. *Appl. Phys. Lett.* **62**, 3449-51 (1993).
11. V.I. Konov, A.A. Smolin, V.G. Ralchenko, S.M. Pimenov, E.D. Obraztsova, E.N. Loubnin, S.M. Metev, and G. Sepold. D.C. arc plasma deposition of smooth nanocrystalline diamond films. *Diamond Relat. Mater.* **4**, 1073-78 (1995).
12. A.A. Zakhidov, R.H. Baughman, Z. Iqbal, C. Cui, I. Khayrullin, S. Dantas, J. Marti, and V.G. Ralchenko. Carbon structures with three-dimensional periodicity at optical wavelengths. *Science* **282**, 897-01 (1998).

13. V. Ralchenko, A. Khomich, L. Butvina, I. Vlasov, V. Konov, L. Schirone, and G. Sotgiu. CVD diamond optics with moth-eye antireflective surface structures produced by molding technique. *New Diamond and Frontier Carbon Technology* **10**, 109-19 (2000).
14. V.V. Danilenko. Synthesis and sintering of diamond by explosion technique. Moscow: Energoatomizdat, 2003 (in Russian).
15. L.C. Nistor, J. Van Landuyt, V.G. Ralchenko, E.D. Obratsova, K.G. Korotushenko, and A.A. Smolin. Structural studies of diamond thin films grown from d.c. arc plasma. *J. Mater. Res.* **12**, 2533-42 (1997).
16. V.G. Ralchenko, A.A. Smolin, V.I. Konov, K.F. Sergeichev, I.A. Sychov, I.I. Vlasov, V.V. Migulin, S.V. Voronina, and A.V. Khomich. Large-area diamond deposition by microwave plasma. *Diamond Relat. Mater.* **6**, 417-21 (1997).
17. V. Ralchenko, I. Sychov, I. Vlasov, A. Vlasov, V. Konov, A. Khomich, and S. Voronina. Quality of diamond wafers grown by microwave plasma CVD: effects of gas flow rate. *Diamond Relat. Mater.* **8**, 189-93 (1999).
18. C.J. Powell and A. Jablonski. NIST Electron Inelastic-Mean-Free-Path Database-Version 1.1, NIST, Gaithersburg, MD, 2000.
19. P.I. Belobrov, L.A. Bursill, K.I. Maslakov, and A.P. Dementjev. Electron spectroscopy of nanodiamond surface states. *Appl. Surf. Sci.* **215**, (2003) 169-77.
20. A.P. Dementjev, K.I. Maslakov, and A.V. Naumkin. Interaction of carbon atoms with nanodiamond surface. Proceedings of the NATO ARW on Synthesis, properties and applications of ultrananocrystalline diamond. St. Petersburg, Russia, June 7-10, 2004; Kluwer (in press).
21. K.C. Pandey. New dimerized-chain model for reconstruction of the diamond (111)-(2x1) surface. *Phys. Rev. B* **25**, 4338 (1982).
22. A.P. Dementjev and K.I. Maslakov. Chemical state of carbon atoms on the surface of nanodiamond particles. *Physics of Solid State* **46**, 678-80 (2004).
23. R. Pfeiffer, H. Kuzmany, P. Knoll, S. Bokova, N. Salk, and B. Guenther. Evidence for trans-polyacetylene in nano-crystalline diamond films. *Diamond Relat. Mater.* **12**, 268-71 (2003).
24. V. Ralchenko, A. Khomich, R. Khmel'nitskii, and A. Vlasov. Hydrogen incorporation in CVD diamond films. In: *Hydrogen Materials Science and Chemistry of Metal Hydrides*. Eds. N. Veziroglu et al. Kluwer, 2002, pp. 203-12.
25. S.M. Pimenov, V.V. Kononenko, V.G. Ralchenko, V.I. Konov, S. Gloor, W. Luthy, H.P. Weber, and A.V. Khomich. Laser polishing of diamond plates. *Appl. Phys. A* **69**, 81-8 (1999).
26. E. Woerner, C. Wild, W. Mueller-Sebert, R. Locher, and P. Koidl. Optical and thermo-optical properties of chemical vapor deposited (CVD) diamond. In: *Diamond Films, 9<sup>th</sup> CIMTEC'98 - Forum on New Materials, Symp. IV-Diamond Films*, Ed. P. Vincenzini, Techna Srl (1999), pp.305-16.
27. J.E. Graebner, J.A. Mucha, and F.A. Baiocchi. Sources of thermal resistance in chemically vapor deposited diamond. *Diamond Relat. Mater.* **5**, 682-87(1996).
28. V.G. Ralchenko, A.V. Vlasov, E.V. Ivakin, A.V. Sukhadolau, and A.V. Khomich. Measurements of thermal conductivity of undoped and boron-doped CVD diamond by transient grating and laser flash techniques. Proceedings of the 7th Applied Diamond Conference/3<sup>rd</sup> Frontier Carbon Technologies Joint Conference (ADC/FCT 2003), MNASA/CP-2003-212319 (2003), pp. 309-14.
29. C.D. Clark and C.B. Dickerson. The 1.681 eV centre in polycrystalline diamond. *Surf. Coat. Technol.* **47**, 336-43 (1991).

30. L. Ostrovskaya, V. Perevertailo, V. Ralchenko, A. Dementjev, and O. Loginova. Wettability and surface energy of oxidized and hydrogen plasma-treated diamond films. *Diamond Relat. Mater.* **11**, 845-50 (2002).
31. V.V. Kononenko, V.I. Konov, S.M. Pimenov, A.M. Prokhorov, V.S. Pavelyev, and V.A. Soifer. CVD diamond transmissive optics for CO<sub>2</sub> lasers. *New Diamond and Frontier Carbon Technology* **10**, 97-107 (2000).
32. T.V. Kononenko, V.V. Kononenko, V.I. Konov, S.M. Pimenov, S.V. Garnov, A.V. Tischenko, A.M. Prokhorov, and A.V. Khomich. Formation of antireflective surface structures on diamond films by laser patterning. *Appl. Phys. A* **68**, 99-102 (1999).
33. K. Okano, K. Hoshina, M. Ida, S. Koizumi, and T. Inuzuka. Fabrication of diamond field emitter array. *Appl. Phys. Lett.* **64**, 2742-44 (1994).
34. W.P. Kang, J.L. Davidson, M. Howell, B. Bhuvu, D.L. Kinser, D.V. Kerns, Q. Li, and J.F. Xu. Micropatterned polycrystalline diamond filed emitter vacuum diode arrays. *J. Vac. Sci. Technol. B* **14**, 2068-71 (1996).
35. A.V. Karabutov, V.G. Ralchenko, I.I. Vlasov, R.A. Khmelnitsky, M.A. Negodaev, V.P. Varnin, and I.G. Teremetskaya. Surface engineering of diamond tips for improved field electron emission. *Diamond Relat. Mater.* **10**, 2178-83 (2001).
36. V.G. Ralchenko, A.V. Khomich, A.V. Baranov, I.I. Vlasov, and V.I. Konov. Fabrication of CVD diamond optics with antireflective surface structures. *Phys. Stat. Sol.(a)* **174**, 171-76 (1999).
37. E. Woerner, C. Wild, W. Mueller-Sebert, and P. Koidl. CVD-diamond optical lenses. *Diamond Relat. Mater.* **10**, 557-60 (2001).
38. H. Bjorkman, P. Rangsten, P. Hollman, and K. Hjort. Diamond replicas from microstructured silicon masters. *Sensors and Actuators A* **73**, 24-9 (1999).
39. H. Bjorkman, P. Rangsten, and K. Hjort. Diamond microstructures for optical micro electromechanical systems. *Sensors and Actuators A* **78**, 41-7 (1999).
40. K.C. Holms, A. Wisitsora-at, T.G. Henderson, J.L. Davidson, W.P. Kang, and V. Pilugurta. Microstructures in diamond for "DMEMS", diamond micro electromechanical systems. Proceedings of the 6<sup>th</sup> Int. Symp. on Diamond Materials, The Electrochemical Soc., Pennington, USA, **99-32**, 360-68 (2000).
41. V. Ralchenko, L. Schirone, G. Sotgiu, A. Zakhidov, R. Baughman, A. Khomich, M. Nunuparov, I. Vlasov, V. Frolov, and A. Karabutov. Direct growth of diamond components. Proceedings of the 6<sup>th</sup> Int. Symp. on Diamond Materials, The Electrochemical Soc., Pennington, USA, **99-32** (2000) 72-79.
42. E. Oesterschulze, W. Scholz, Ch. Mihalcea, D. Albert, S. Sobisch, and W. Kulisch. Fabrication of small diamond tips for scanning probe microscopy. *Appl. Phys. Lett.* **70**, 435-37 (1997).
43. V.G. Ralchenko and E.I. Givargizov. Fabrication of very-high-aspect-ratio microchannels in CVD diamond by a molding technique. Proceedings of the 7<sup>th</sup> Applied Diamond Conference/3<sup>rd</sup> Frontier Carbon Technologies Joint Conference (ADC/FCT 2003), M. Murakawa et al. (Eds), NASA/CP-2003-212319 (2003), pp. 540-43.
44. S. Silva, M.C. Salvadori, K. Kawakita, M.T. Pereira, W. Rossi, and M. Cattani, Fabrication of diamond flow controller micronozzles. *Diamond Relat. Mater.* **11**, 237-41 (2002).
45. A. Snigirev, V. Yunkin, I. Snigireva, M. Di Michiel, M. Drakopoulos, S. Kouznetsov, L. Shabel'nikov, M. Grigoriev, V. Ralchenko, I. Sychov, M. Hoffmann, and E. Voges. Diamond refractive lens for hard X-ray focusing, in Design and Microfabrication of Novel X-Ray Optics. *Proceedings of SPIE* **4783**, 1-9 (2002).

# 10

## MECHANISM AND PROPERTIES OF NANODIAMOND FILMS DEPOSITED BY THE DC-GD-CVD PROCESS

A. Hoffman

*Department of Chemistry, Technion - Israel Institute of Technology, Haifa 32000, Israel*

### Abstract:

Nanocrystalline carbon film of a prevailing diamond character can be deposited by direct current glow discharge (DC GD) chemical vapor deposition (CVD) from a methane-hydrogen mixture. The growth of a nanodiamond film by the DC GD CVD process occurs on top of a hydrogenated  $sp^2$ -coordinated carbon precursor (graphitic-like) as confirmed by near-edge x-ray adsorption fine structure (NEXAFS) and transmission electron microscopy (TEM). No surface pretreatment is necessary in order to induce film growth and the thickness of the precursor layer is  $\sim 200$  nm. By high resolution TEM and x-ray diffraction (XRD) it has been established the nanocrystalline nature of the films and that the average size of the diamond crystallites is about 5 nm. Preferential vertical alignment of the basal planes in the precursor was determined by cross-section HR TEM as well as by angle-resolved NEXAFS. Electron energy loss spectroscopy (EELS) demonstrated the  $sp^2$ -coordinated character of the nanodiamond films surface. Secondary ion mass spectroscopy (SIMS) established a drastic increase in the adsorbed hydrogen content accompanying the nanodiamond formation. Whereas the hydrogen concentration in the precursor layer is only a few percent it increases to  $\sim 15$ – $20$  at.% in the nanodiamond film. Density measurements X-ray reflection (XRR) of the films increases with thickness as expected from the phase composition of the films determined from the spectroscopic methods. From a microscopic perspective nanodiamond film and growth is explained as a sub-surface process in terms of a four step cyclic process: (i) Formation of a dense, hydrogenated  $sp^2$  carbon coordinated oriented layer; (ii) precipitation of  $sp^3$  clusters in this graphitic phase, (iii) growth of nanodiamond particles up to  $\sim 5$  nm in size by energetic species bombardment of the diamond/hydrogenated carbon - interface. It involves preferential displacement of  $sp^2$  carbon coordinated carbon atoms leaving  $sp^3$  coordinated carbon atoms intact, leading to expansion of the diamond phase, (iv) frustration of growth of the diamond particles and (v) growth of the film formed of an agglomerate of nanodiamond particles by a cyclic process which involves process 2–4. From a macroscopic perspective nanodiamond formation is suggested to be associated with a sub-surface

nano-graphite – nanodiamond phase transition triggered by stress relaxation.

**Keywords:** nanodiamond, mechanism of formation, hydrogen content

## 1. INTRODUCTION

Carbon is a unique element in the variety of its structures. The carbon science and technology has develop extensively in the last few decades due to discoveries of various poly-crystalline and nanocrystalline diamond films deposition methods, synthesis of nano-tubes, fullerenes and carbon fibers, etc. Nanocrystalline diamond films represent a new remarkable material that attracts a lot of attention of the scientific world due to its promising potential in many possible applications, such as tribology [1–2], field emission [3–4], electrochemistry [5–6], protective optical windows [7–8], as well as its unique ability to incorporate *n*-type dopants [9], compared to polycrystalline and single crystal diamond.

A quest for an efficient method of nanocrystalline diamond film deposition has lead to development of the direct-current glow-discharge (DC GD) deposition technique from a methane/hydrogen mixture strongly depending on deposition temperature and without need of any surface pre-treatment [10]. Whereas at a deposition temperature of  $\sim 880^\circ\text{C}$  the films display a predominant diamond character at lower and higher temperatures the deposited films are graphitic. This paper is dedicated to summarize some aspects of our research activity on the formation mechanism and properties of the nano diamond films deposited by DC GD CVD.

The phase-composition, morphology and structural evolution and properties of the DC GD nanodiamond was comprehensively explored by a number of complementary techniques. The hydrogen content and its role in nanodiamond film formation was assessed. The experimental methods used in this studied comprise near edge X-ray adsorption fine structure (NEXAFS) to prove the short range coordination of the carbon films and indirectly their phase composition. By X-ray diffraction (XRD) the crystalline nature of the films and the diamond particle size were determined. By atomic force microscopy (AFM) the morphology evolution of the films surface was measured. The surface and grain boundary phase composition were investigated by a combination of electron energy loss spectroscopy (EELS) measured as a function of incident electron energy and hydrogen etching experiments. By transmission electron microscopy (TEM) the micro-structural evolution and their visualization were achieved. The

density evolution of the films was determined by X-ray reflectivity (XRR). The hydrogen content and distribution in the films was studied by secondary ion microscopy spectroscopy (SIMS). Finally our present understanding of the mechanism of formation and growth of nanodiamond films deposited by the DC GD is presented.

## 2. EXPERIMENTAL DETAILS

Carbon films were synthesized by direct-current glow discharge chemical vapor deposition (DC GD CVD) from a methane-hydrogen mixture (9%  $\text{CH}_4$ :91%  $\text{H}_2$ ) in a home-build reactor [10]. The deposition temperatures investigated in our studies are in the 800–950°C range. At 880°C the films display their maximal diamond character and therefore films deposited at this temperature were mostly analyzed. *P*-type boron-doped Si (001) wafers were used as substrates. The silicon substrate was grounded during the plasma deposition while the other electrode was under 500 Volts bias. A schematic picture of the deposition system is shown in Figure 1.

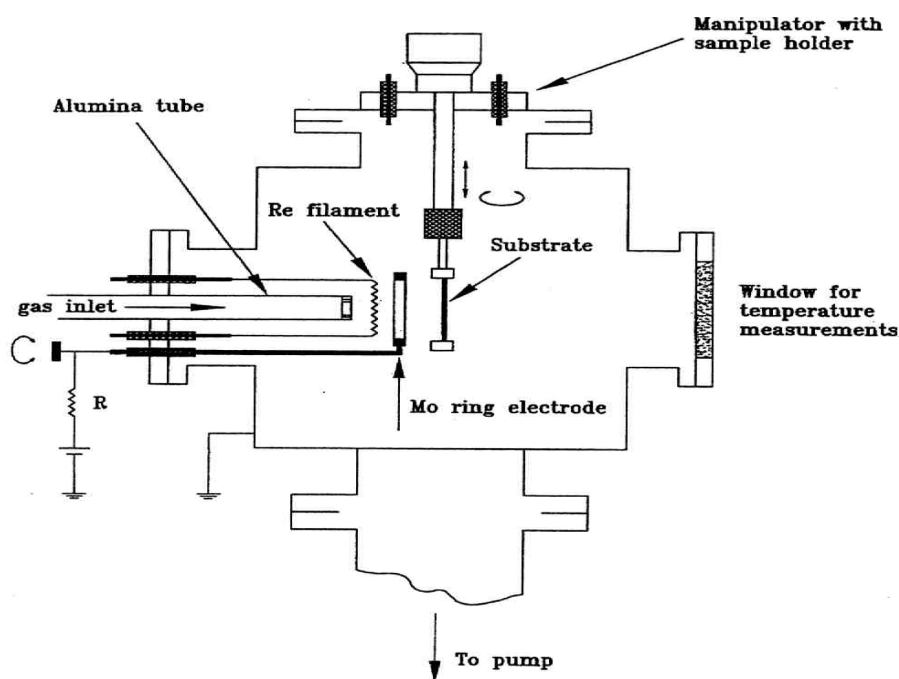


Figure 1. Schematic picture of the deposition system used for nanodiamond deposition by the DC-GD CVD method.

NEXAFS measurements were carried out on the SA72 beam line (150–600 eV photon energy range, 135 mm spot size) using synchrotron radiation from Super-Aco at LURE, Orsay, France. The monochromator resolution was about 0.1 eV in the region close to the carbon *K* edge. The spectra were recorded by measuring intensity of 8 eV secondary electrons. The angle-resolved (AR) NEXAFS measurements were carried out in the total electron yield (TEY) mode recording the sample electron current to the ground. XRD analysis was performed in a Bede D<sup>3</sup> diffractometer combined with 18 kV Rigaku rotating anode generator that produced monochromatized Cu K $\alpha_1$  radiation. The measurements were done under grazing angle configuration, *i.e.* the angle between the incident beam and the immobile sample surface was 3.5° while a 2 $\Theta$  scan of the reflected intensity was performed with a 0.2 mm receiving slit in front of the detector. With this system the X-ray reflectivity were carried out as well. Cross section high resolution TEM measurements of the films were conducted in a Philips CM200 microscope for structural imaging (point resolution 0.19 nm) and a Gatan parallel electron energy loss (PEEL) spectrometer. The samples were thinned by mechanical grinding, polishing, and ion milling (4.5 keV, Ar<sup>+</sup> ion beam in a liquid nitrogen cooling stage) to electron transparency. Non-contact AFM analysis was carried out on a Topometrix 2010 AFM, using pyramidal Si<sub>3</sub>N<sub>4</sub> tips with an aspect ratio of 2:1. The curvature radii were 10 nm. Electron energy loss spectroscopy (EELS) analysis of the samples was carried out in a SPECS ultrahigh vacuum experimental system equipped with a hemispherical electron analyzer. SIMS analysis was performed in a dynamic mode in a Cameca IMS4f ion microscope. The samples were irradiated by 14.5 keV Cs<sup>+</sup> ion beam. The sampling area was about 64  $\mu\text{m}^2$ . The basic chamber pressure was  $8 \times 10^{-10}$  Torr, while the ion current was about  $1 \times 10^{-8}$  A.

### 3. RESULTS

#### 3.1 Evolution and Properties of the Films Studied by NEXAFS: Coordination and Orientation

The films deposited by DC GD were extensively explored by NEXAFS spectroscopy. This technique is a very powerful spectroscopic method for analysis of the phase composition of the nanocrystalline carbon structures. Unlike Raman spectroscopy, NEXAFS has a similar cross section to different carbon allotropes and it is sensitive to local chemical bonding, which enables analysis of nano-sized carbon materials. Furthermore in the



case of an-isotropic materials angle resolved measurements can provide information about preferred growth orientation.

The phase composition of the films was found to be strongly dependent on deposition temperature. NEXAFS spectra of films deposited at temperatures between 800 and 950°C clearly showed that at a deposition temperature of 880°C the predominant phase of the films is diamond. The evolution of the films as a function of deposition time was accomplished by carrying out NEXAFS measurements as a function of film thickness. Figure 2 shows NEXAFS spectra of the films deposited at 880°C for different deposition times and reference materials (CVD diamond and glassy carbon). The spectroscopic features used for determination of the phase composition of the carbon films are well known [11-15]. As can be observed in this figure, the DC GD films are  $sp^2$ -bonded up to deposition time of 15 minutes. The prominent spectroscopic features of  $sp^2$ -coordinated carbon materials include a  $C(1s)-\pi^*$  resonance at about 285.5 eV and the onset of  $C(1s)-\sigma^*$  transition at 291 eV. However, the films deposited for 30 minutes possess a dominant diamond character, as obviously follows from their spectra, which demonstrate a  $C(1s)$  absorption edge associated with the  $C(1s)-\sigma^*$  transition of  $sp^3$ -bonded carbon at about 289 eV and the large dip at 302.4 eV associated with the second absolute band gap of the crystalline diamond electronic structure. Thus, it can be concluded that the DC GD nanocrystalline diamond film develop from the graphitic precursor after deposition time of about half an hour. The presence of the  $C(1s)-\pi^*$  resonance in the films deposited for longer than 30 minutes demonstrates that this film is actually a composite material. Comparison of the normalized intensity of this peak with the reference spectrum of GC established that the  $sp^2$  phase represents ~ 20% of the material in the near-surface region [16].

The possibility that the hydrogenated graphitic layer precursor to nanodiamond formation display some preferred orientation was investigated by angle resolved NEXAFS (AR-NEAFS). Due to the two-dimensional structure of HOPG,  $\pi^*$  electronic states are directed perpendicular to its surface and therefore it is possible to selectively excite final states of this symmetry using polarized light [17,18]. The  $\sigma^*$  states, on the other hand, have been demonstrated to be insensitive to the changes of the incident angle. Based on this analysis the percent of the orientated basal planes was estimated and found that the fraction of alignment of the graphitic carbon in the precursor material is about 42%. A similar percent of ordered graphitic carbon that reached 50% was estimated to be in the samples grown by MW-activated BEN from a methane/hydrogen mixture [19]. This value is smaller in the 950°C 15 minute film (about 34%) and it is equal to 19% in the 800°C 60 minute specimen [20]. The main origin of such



thermodynamically unstable vertical alignment of the basal planes is proposed to be associated with the stresses developing in the film. Moreover, the highest content of the orientated planes was in the films deposited at 880°C, i.e. in the graphitic precursor to the nanodiamond phase. The consequent conclusion is that the highest stresses develops in the film deposited at 880°C [21].

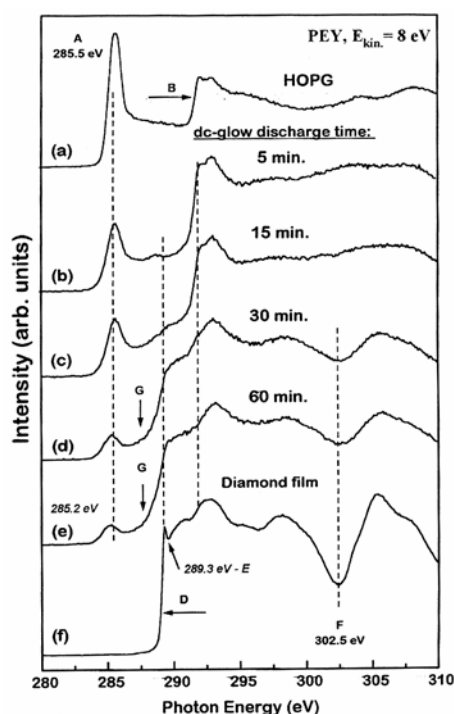


Figure 2. NEXAFS spectra recorded in the 280–310 eV photon energy range in the PEY mode collecting 8 eV electrons of glassy carbon, a CVD diamond film, and the DC GD films deposited at 880°C for various deposition times.

### 3.2 Crystalline Structure of the Films by XRD

Examination of the 880°C film by NEXAFS clearly shows that the carbon atoms in the films display a predominant  $sp^3$  coordination and strongly suggest the diamond nature of these films. By XRD we unambiguously determined the nano crystalline nature of the films. In Figure 3 diffraction patterns of the DC GD carbon films deposited at 880°C as well as of the standard materials are shown. Due to the glancing angle configuration, the (311) Si substrate diffraction peak at  $2\Theta = 56.12^\circ$

dominates in all the diffraction patterns. Diffraction patterns of the films grown at 880°C for 1 hour did not exhibit crystalline peaks. The films grown at 880°C for longer than one hour deposition demonstrate a diamond structure with a prominent diamond (111) peak at 43.9°. The (111) diamond peak in the diffraction patterns of the films deposited at 880°C is broadened as a result of the nanocrystalline structure of these films. The size,  $D$ , of diamond particles could be evaluated by the Scherrer formula,

$$D = 0.89\lambda / (B \cos \Theta)$$

where  $\lambda = 1.5406 \text{ \AA}$  is the X-ray wavelength,  $B$  is the half-width of the diffraction peak, and  $\Theta$  is the Bragg's angle. The instrumental peak width was subtracted from the measured  $B$  values. After this correction, the grain size was estimated to be about 5 nm [21].

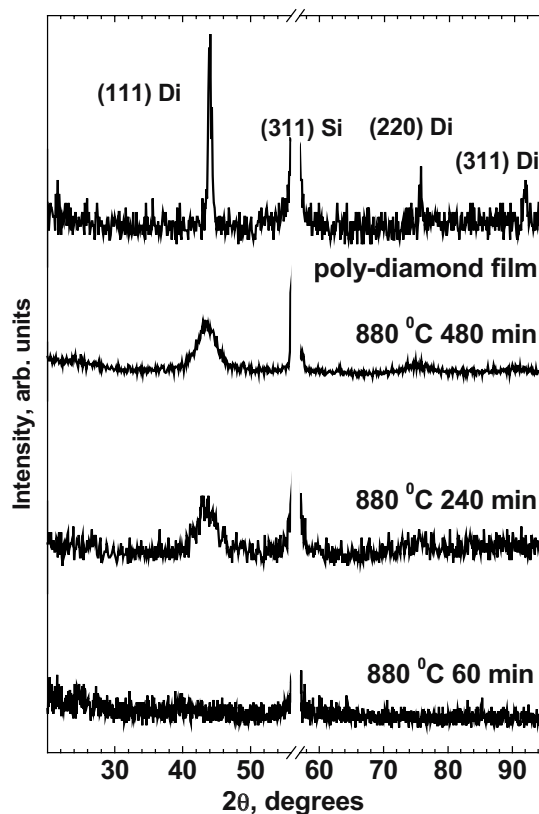


Figure 3. XRD patterns of DC GD carbon films deposited at 880°C for various deposition times, and of reference glassy carbon and of a polycrystalline HF CVD diamond film.

### 3.3 Morphological Evolution of the Films by AFM

AFM topographic analysis of the film surfaces established a strong roughening effect that accompanies formation of the nanodiamond phase [20]. The average film roughness increased from 2.9 nm in the graphite-like film deposited for 15 minutes to 33.5 nm in the film deposited for 30 minutes (more than 10 times). Increase of surface roughness connected with the stress development is a well-known phenomenon in thin-film deposition of semiconductors [22] and metals [23]. Spaepen has demonstrated that an increase of the surface roughness can lead to the stress relaxation when the roughness amplitudes approximate the average size of grain sizes on the surface [24]. Given the very high values of the measured roughness and the nano-sized grain boundaries, stress relaxation via a drastic roughness increase is a plausible mechanism of the stress relaxation for the carbon films deposited by DC GD.

### 3.4 Surface and Grain Boundaries Phase Composition Studied by EELS

The surface and grain boundaries phase composition of the nanodiamond films were explored by EELS measured at different primary electron energies and exploring the effect of micro wave (MW) hydrogenation on the films. Figure 4(a) shows EELS of a nanodiamond film grown at 880°C for 60 minutes using primary electron energies in the 500–2000 eV range. The position of the losses, used in our analysis, was determined by second-order derivatives of the measured EEL spectra [20].

In EEL spectra recorded using higher primary electron energies, the features in the loss spectrum are outweighed by excitations localized in deeper regions compared to spectra recorded using lower primary energy. For primary electron energy of 500 eV, loss peaks at 6 and 27 eV are prominent. These losses are characteristic to graphite-like carbon and they are associated with  $\pi$ - $\pi^*$  interband transition and the excitation of the  $(\pi+\sigma)$  plasmon, respectively. For primary electron energies higher than 1500 eV, the dominant loss peaks are located at 34 and 24 eV. These losses are assigned to diamond bulk and surface plasmons, respectively. The nature of the peak in the 15–18 eV range is less clear. It is known that an interband transition at about 15 eV appears in EEL spectra of diamond [25]. It can also be represented by a surface plasmon of amorphous carbon that is present in the near-surface area in significant amounts (about 20% by NEXAFS measurements) and its energy will be equal approximately to 19 eV (27 (energy of the bulk plasmon of  $sp^2$  carbon) divided by

$\sqrt{2} \approx 19$  eV). Therefore these results strongly suggest that the upper surface of the films is composed of a  $sp^2$  coordinated carbon layer.

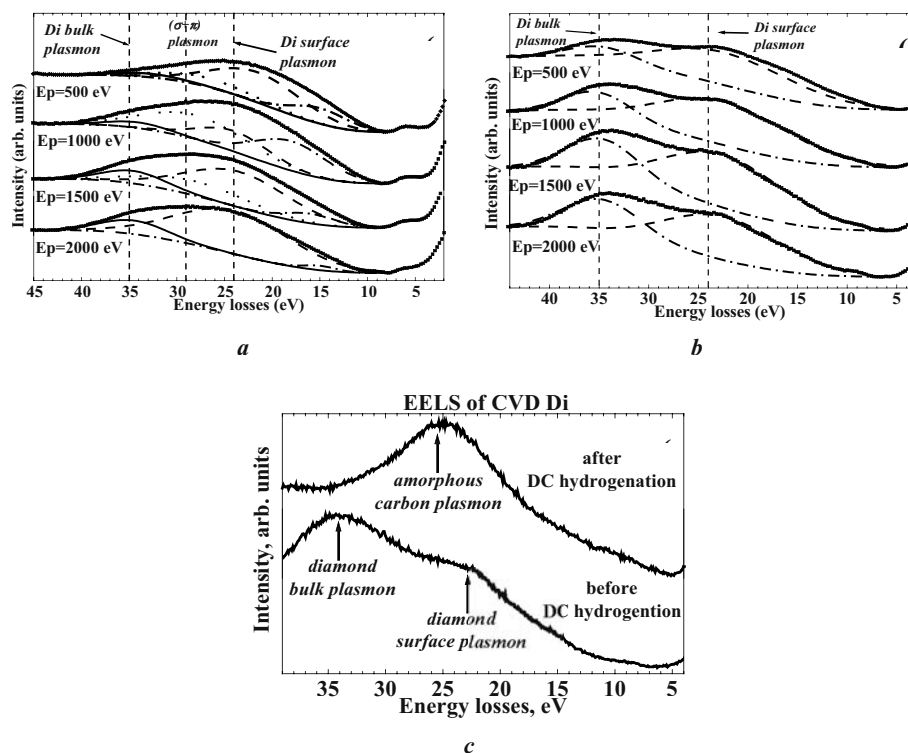


Figure 4. (a) EEL spectra of a nano- diamond film (880°C) for different incident electron energies; (b) EEL spectra for different incident electron energies of a nanodiamond film (880°C) after 30-minute hydrogen MW plasma; (c) EEL spectra of a HF CVD diamond film before and after hydrogenation in the DC GD plasma. Primary electron energy is equal to 2000 eV.

To study the nature of the grain boundaries between the nanodiamond particles, the films were exposed to 30-minute treatment in hydrogen MW plasma. It is well known that hydrogen MW plasma etches graphite at a much higher rate than that of diamond. If  $sp^2$  coordinated carbon (whose presence in the films is determined by NEXAFS - Figure 2) is distributed homogeneously throughout the nanodiamond particles, the EEL spectrum is expected to be similar to that measured before hydrogen MW plasma etching. The EELS at primary electron energies in the 500–2000 eV range of the film deposited at 880°C for 60 min followed by its exposure to hydrogen MW plasma for 30 minutes are shown in Figure 4(b). As seen from this

figure the EELS spectrum is dominated by diamond features including bulk and surface plasmon at 34 and 23 eV, respectively, for the whole range of the primary energies. Therefore, the  $sp^2$ -hybridised carbon is located mostly at the grain boundaries between the nanodiamond particles and not within the particles themselves.

MW hydrogen plasma etches very efficiently  $sp^2$ -bonded carbon. At correct conditions (in fact very similar to those used for polycrystalline diamond CVD but without methane and using pure hydrogen) this treatment was found to result in the production of highly ordered single crystal diamond surfaces as determined by LEED and STM. The influence of the DC-GD hydrogen plasma utilized for nanodiamond deposition on the diamond surface was examined. A polycrystalline diamond film grown by HF CVD underwent 30-minute hydrogen plasma treatment in the DC GD reactor. Figure 4(c) demonstrates EEL spectra of the sample before and after the hydrogenation. Upon the DC-GD plasma hydrogenation, the diamond features at about 33 and 23 eV that belong to diamond bulk and surface plasmons are smeared out. The measured spectrum possesses resemblance with EEL spectra of hydrogenated diamond-like carbon (DLC) films with a prominent ( $\pi+\sigma$ ) plasmon at 25 eV. These results show that the role of activated hydrogen in the formation of nanodiamond by the DC GD method developed in our laboratory is different from that in the growth of microcrystalline diamonds by CVD methods. It can be concluded that the activated hydrogen by the DC-GD has sufficient energy to amorphize the upper surface structure of diamond. This effect bears great importance to understand the mechanism of nanodiamond formation by DC GD CVD.

### 3.5 Hydrogen Content in the Films by SIMS and ERD

Hydrogen content in the deposited films was determined by Secondary Ion Mass Spectroscopy (SIMS). As such analysis is complicated by the presence of background hydrogen, the samples were grown from a  $CD_4/D_2$  gaseous mixture for analysis of the deuterium content [31]. In Figure 5 deuterium profile of a DC GD nanodiamond sample grown at 880°C for 60 minutes is shown. This figure demonstrates that the hydrogen concentration in the film is not constant, it obtains a maximal value of ~19 at.% in the diamond region and decreases in the graphitic region. Such large concentrations makes accurate quantitative analysis of hydrogen by SIMS quite uncertain as the linear calibration of the measured intensity signal is valid up to about 1 at.%. These results clearly show that the nucleation and growth of nanodiamond is accompanied by intensive adsorption of hydrogen in the deposited film. The absolute maximal

hydrogen concentration was determined by elastic recoil detection (ERD) analysis [27,31].

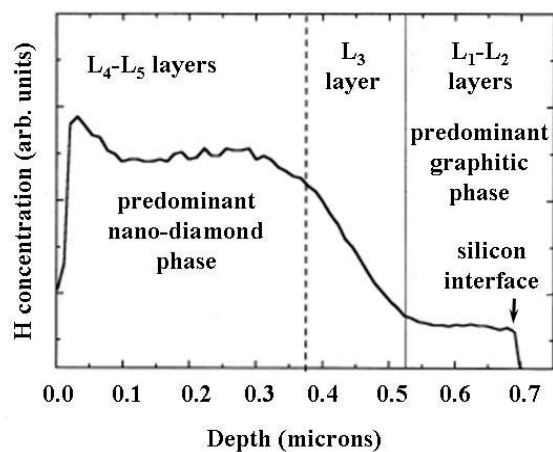


Figure 5. SIMS depth profile of deuterium in a nanodiamond film grown from a 9% CD<sub>4</sub>/91% D<sub>2</sub> mixture at 880°C for 60 minutes.

### 3.6 Visualization and Evolution of the Films Studied by HR TEM

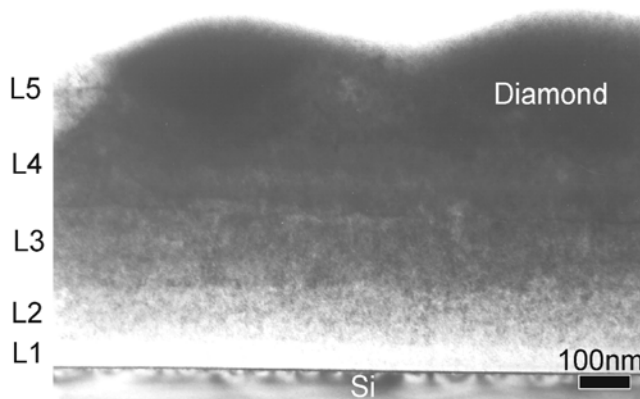
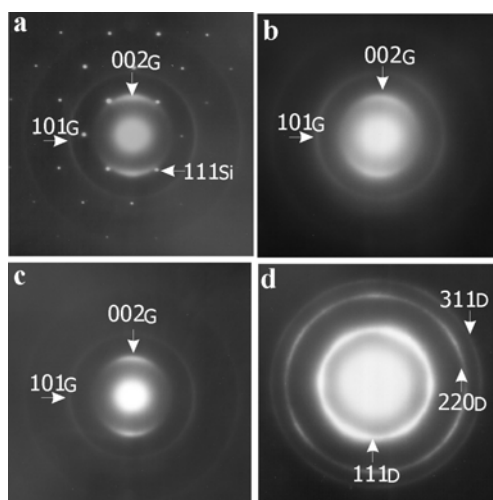
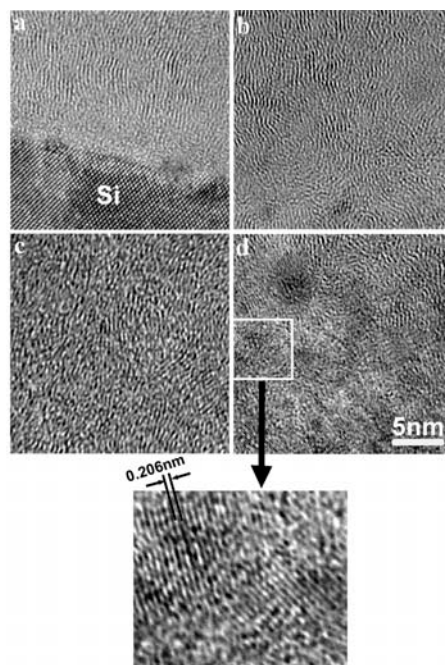


Figure 6. Low-magnification cross-sectional TEM image of the nanodiamond (880) film. A layered structure consisting of five layers with increasing density (deduced from the darkening of each layer with respect to the previous one) is observed on the Si substrate.

TEM analysis was carried out on a film grown at 880°C for 60 minutes. The low-resolution cross-sectional TEM image of the sample is shown in Figure 6. As seen from this figure the density of the film increases with film thickness. The higher the density, the darker the layer is. To guide the eye the film was divided in five layers and higher resolution examination was carried out on each of these layers. The SAED (Figure 7) of the first four layers is graphitic. The partial first and third graphitic rings observed are due to a preferred orientation of the graphitic basal planes in a direction perpendicular to the substrate, as seen from the relative position of the rings with respect to the silicon substrate spots. This is in agreement with the AR-NEXAFS described above. The SAED of the fifth layer shows diamond rings with some preferred orientation (evident by different intensities in different directions) and the first graphitic ring is absent. HRTEM (Figure 8) confirms the previous observations. The first four layers consist of oriented graphitic planes perpendicular to the substrate. The fifth layer is comprised of a large number of 2–5 nm sized crystallites with a spacing of 2.06 Å dispersed in a graphitic matrix.



*Figure 7.* Small area electron diffraction (SAED) pattern of the different layers of the nanodiamond film in figure 1. a- interface between Si substrate and layer 1; b- layer 3; c- layer 4; d- layer 5. Layers 1-4 are graphitic with an oriented structure (only partial rings). The relative orientation of the rings with respect to the Si indicates the graphitic basal planes are perpendicular to the Si surface. The rings in layer 5 are diamond rings which indicate preferred orientation (they are more intense in certain directions with symmetry similar to that of the cubic diamond lattice).



*Figure 8.* Cross-sectional high-resolution TEM (HRTEM) imaging of the five layers of the nanodiamond film in figure 1. a- interface between Si substrate and layer 1; b- layer 1; c- layer 4; d- layer 5. The graphitic fringes are perpendicular to the Si surface. The films look denser as the layer develops from 1 to 4. Layer 5 shows 2–5nm diamond crystallites embedded in a graphitic matrix. The marked region in d is enlarged to show the crystallites more clearly.

### 3.7 Density evolution of the films examined by XRR

In Figure 9 XRR measurements of a diamond single crystal, a polycrystalline diamond film deposited by filament CVD and a film grown by DC GD CVD at 880°C as a function of desption time (converted to film thickness) are shown. As seen from this figure the density measured for the polycrystalline diamond was constant with film thickness. However for the 880 C DC-GD film the density was measured to increased with thickness from  $\sim 2.4\text{--}2.5\text{ g}\cdot\text{cm}^{-3}$  in the first two layers through 2.6 to 2.8  $\text{g}\cdot\text{cm}^{-3}$  in the third and fourth layers to 3  $\text{g}\cdot\text{cm}^{-3}$  in the fifth layer. These results are in qualitative agreement with the phase evolution of the films from a graphitic like nature (low density) to a diamond like one (higher density).



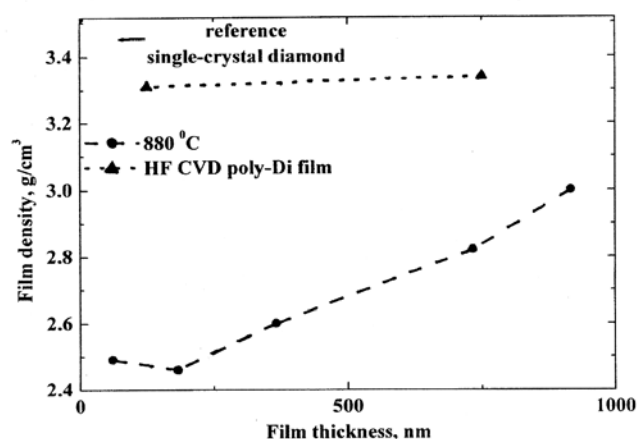


Figure 9. X-ray reflectivity measurements of the density of films with different thickness deposited at 880°C corresponding to the layers indicated in the cross-sectional image of Figure 1. The density increases from 2.4–2.5 g·cm<sup>-3</sup> in layers 1 and 2, to 2.6 g·cm<sup>-3</sup> in layer 3, 2.8 in layer 4, and 3 in the diamond layer.

#### 4. DISCUSSION

As was demonstrated throughout the analysis of the films deposited by the DC GD CVD, the mechanism of the nanodiamond film formation by this method differs from the one of polycrystalline diamond films growth by other CVD techniques. It was also shown that the DC GD hydrogen plasma exposure does not result in preferential etching of the graphite phase, as such plasma severely damaged pre-deposited polycrystalline diamond. This shows that the activated hydrogen is sufficiently energetic to induced displacement of  $sp^3$  coordinated carbon atoms in the upper surface region of the films. The strong dependence of the films on deposition temperature shows that the hydrogen content in the films has an important role for the stabilization and formation of the nanodiamond particles. There is also no need for any preliminary treatment of the substrate prior to deposition to enhance nucleation or growth. The interface between the nanodiamond films and the silicon substrates consists of a hydrogenated graphitic-like precursor with a preferred vertical orientation. Diamond nucleation is accompanied by an increase in density of the films and retention of hydrogen. The increase in density was found to correlated to an increase in stress in the graphitic film. A schematic cartoon of the structure of the nanodiamond films produced by the DC-GD CVD method is shown in Figure 10.

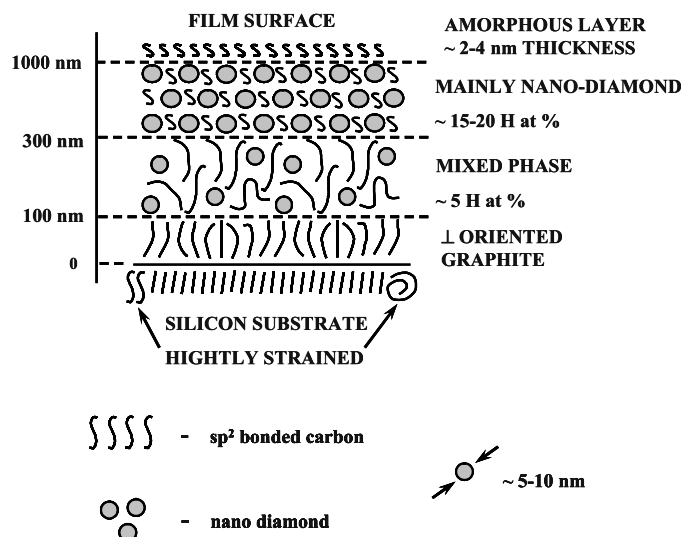


Figure 10. Schematic cartoon picture of the nanodiamond film deposited by the DC-GD CVD method.

From a macroscopic-thermodynamic perspective the nanocrystalline diamond formation can be viewed associated to a nano-graphite - nanodiamond phase transformation promoted by stress build-up or densification of the graphitic layers in the presence of hydrogen. The stresses accumulating in the deposited films at 880°C relaxes through several processes: (i) nano-graphite – nanodiamond phase transformation, this is favoured by the presence of hydrogen; (ii) surface roughening that accompanies the nanodiamond phase nucleation observed by the AFM measurements; and (iii) creation of defects in the silicon substrate established by cross-sectional TEM. Badziag et al. [28], demonstrated that hydrogenated nano-meter sized diamonds are energetically favored over graphite, even without requiring the high pressures or extreme kinetic conditions usually associated with diamond growth. Similar conclusion on thermodynamic stability of nanocrystalline diamond over graphite were obtained by Gamarnik as well [29].

Hydrogen is expected to influence the stress level in the graphitic layer as well. This occurs due to relaxation of distortions of the inter-atomic bonds, formation of micro-voids, and termination of dangling bonds. Therefore it can be concluded that for a given methane concentration, temperatures lower than required for the nanodiamond formation lead to higher hydrogen concentration in the deposited films and to the following relaxation of the stresses. Then the films maintain a graphitic-like structure. Nucleation of the

nanodiamond particles at temperatures above  $\sim 920^\circ\text{C}$  is prevented by a higher rate of hydrogen desorption from the sample. Such desorption makes the hydrogen content in the deposited film insufficient for the stabilization of the nanodiamond phase [30].

From a microscopic perspective the mechanism of nanodiamond film formation as it occurs in the films deposited at  $880^\circ\text{C}$  may be explained as a sub-surface process in terms of a four step cyclic process:

1. Formation of a dense, hydrogenated  $sp^2$  carbon coordinated oriented layer.
2. Precipitation of  $sp^3$  C clusters in this graphitic phase.
3. Growth of nanodiamond particles up to  $\sim 5$  nm in size by energetic species bombardment of the diamond/hydrogenated carbon - interface. It involves preferential displacement of  $sp^2$  carbon coordinated carbon atoms leaving  $sp^3$  coordinated carbon atoms intact, leading to expansion of the diamond phase.
4. Frustration of growth of the diamond particles.
5. Growth of the film formed of an agglomerate of nanodiamond particles by a cyclic process which involves process 2-4.

The basic mechanism responsible for the formation of the films by the DC GD is subplantation [32,33], i.e. a shallow implantation in which the carbon and hydrogen species penetrate to subsurface layers and densification occurs by the balance between trapping (densification) and detrapping (density relaxation) processes. Deposition of films by a mixture of energetic particles containing hydrogen and carbon the film grows through several concurrent competing processes [33]: (1) penetration of energetic H and C atoms to subsurface layers and trapping at the end of their trajectory, (2) thermal migration of atoms to the surface, (3) release of excess hydrogen, (4) chemical etching of carbon by atomic hydrogen and release of volatile hydrocarbon molecules. The growth thus involves simultaneous deposition and etching. The etching rate of some carbon forms (e.g.  $sp^2$  bonded carbon) might be much larger than that of other carbon forms (e.g. diamond). Most of hydrogen atoms (more than 90%) are not trapped in the evolving film, since the H atomic concentration is  $\sim 0\text{--}20\%$  while the H/C atomic ratio in the plasma is 24 (for  $9\%\text{CH}_4/91\%\text{H}_2$ ).

We now address the evolution of the hydrogenated graphitic layers, characterized by graphitic planes perpendicular to the surface. A similar growth was already reported [34,35] for subplantation of energetic (120–1000 eV) mass-selected carbon ions at elevated temperatures (200–300°C). The energetic bombardment induces local stress, but the elevated temperature allows for modification of the evolving phase to the most favorable thermodynamic configuration. The basal planes grow perpendicular to the stress (and to the substrate) which is the most

compressible way possible. Indeed the first layer is characterized by such orientation with a regular graphitic density. Once the graphitic orientation develops and the amount of amorphous material decreases (second layer), this ordered structure offers channels for the more energetic part of the hydrogen and carbon species to penetrate and be trapped between the planes. This enables a density increase (carbon incorporation) and hydrogen concentration increase observed in layers three and four. The density increase from 2.4–2.5 to 2.8 g·cm<sup>-3</sup> indicates about 15–20% carbon incorporation between the graphitic planes. A similar amount of hydrogen (15–20% of the carbon atom density) is also trapped between the planes. The increased density and hydrogen bonding to the additional carbon atoms account for the higher trapping efficiency of hydrogen in the evolving matrix. Evidence for the formation of trans-para-acetylene configurations [36] is provided by Raman which shows two characteristic peaks around 1480 and 1140 cm<sup>-1</sup> that are missing in the spectrum of the first two layers [21].

We now address the diamond nucleation occurring in the fifth layer. Our recent molecular dynamics (MD) calculations show [37] that once the graphitic phase incorporates ~ 20% of hydrogen and carbon species and its density reaches a value of ~ 3 g·cm<sup>-3</sup> 100% *sp*<sup>3</sup> hydrogen-carbon clusters precipitate and the hydrogen decorates the surface of these clusters. We suggested that a very small fraction (say 10<sup>-5</sup>–10<sup>-6</sup>) of these clusters is made of perfect diamond clusters [37]. Once they are formed they are stabilized by the boundary conditions imposed by the dense matrix. Our calculations show [37] that faulty clusters can be annealed by incorporation of carbon interstitials and by hydrogen termination. MD calculations by others showed [38] that graphitic edges may serve as sites for diamond nucleation, enhancing the nucleation probability. This was indeed verified for cubic boron nitride (cBN) nucleation [39]. We did observe the association of oriented graphitic planes with diamond nucleation, but failed to find evidence in our HRTEM images for a preferred nucleation of diamond on graphitic edges with the graphitic basal planes parallel to diamond (111) planes. The SAED pattern nevertheless gives some indication of preferred orientation of diamond nanocrystals (the diffraction rings are stronger in certain directions).

The last issue is the growth of the diamond clusters to the dimensions observed in our HRTEM images (~ 2–5 nm). The experimental conditions leading to the diamond growth involve bombardment with energetic species (~ 100–200 eV), which mostly contain hydrogen. We suggest [37] that the hydrogen atoms preferentially displace the loosely bonded carbon atoms at the  $\alpha$ -C:H/diamond interface, leaving the diamond atoms intact. Each loosely bonded carbon atom is preferentially displaced many times, and has a

considerable probability of occupying a diamond position. The diamond interface thus expands, consuming  $\alpha$ -C:H atoms. This is in accord with the work of Banhart et al. [40] who observed the expansion of diamond interface when a diamond/graphite interface was bombarded by 1.25 MeV electrons. Then the size of the nanodiamond particles is expected to be determined by the range of the energetic ions and atoms involved in the preferential growth of nanodiamond particles. The displacement energy of carbon atoms in the diamond structure is  $\sim 50$  eV and that in a graphitic-like structure is  $\sim 20$  eV (approximate values). Whilst the ion energy is larger than the displacements energy of diamond an amorphous structure is produced. As the ion slows down as it penetrates through the film surface into the sub-surface within an energy window between the displacement energy of graphite and diamond preferential growth of the nanodiamond particles takes place. Frustration of the growth process occurs once the distance between the diamond particle and the surface is larger than the projective range of ions that at such distance do not have sufficient energy to induce preferential displacement of  $sp^2$  coordinated carbon atoms. Nucleation and growth of new diamond particles occurs in a cyclic process resulting in the formation of the nanodiamond film.

## Acknowledgements

The financial support by the Israeli Academy of Science and the Technion Fund for promotion of research for carrying out this work is greatly acknowledged.

## REFERENCES

1. S.Y. Luo, J.-K. Kuo, B. Yeh, J.C. Sung, C.-W. Dai, and T.J. Tsai. The tribology of nanocrystalline diamond. *Mater. Chem. Phys.* **72**, 133-35 (2001).
2. L.Y. Huang, K.W. Xu, J. Lu, and B. Guelorget. Analysis of nano-scratch behavior of diamond-like carbon films. *Surf. Coat. Technol.* **154**, 232-36 (2002).
3. N. Jiang, K. Eguchi, S. Noguchi, T. Inaoka, and Y. Shintani. Structural characteristics and field electron emission properties of nanodiamond/carbon films. *J. Cryst. Growth* **236**, 577-82 (2002).
4. K. Wu, X.R. Wang, S. Liu, E.G. Wang. Bistable characteristic and current jumps in field electron emission of nanocrystalline diamond films. *J. Appl. Phys.* **90**, 4810-14 (2001).
5. N.G. Ferreira, L.L.G. Silva, and E.J. Corat. Electrochemical activity of boron-doped diamond electrodes grown on carbon fiber cloths. *Diam. Relat. Mater.* **11**, (2002) 657-61.

6. Q. Chen, D.M. Gruen, A.R. Krauss, T.D. Corrigan, M. Witek, and G.M. Swain. The structure and electrochemical behavior of nitrogen-containing nanocrystalline diamond films deposited from  $\text{CH}_4/\text{N}_2/\text{Ar}$  Mixtures *J. Electrochem. Soc.* **148**, E44 (2001).
7. J. Li, D. He, W. Guo, J. Zhang, Y. Sun, O. Lei, and X. Gao. Nanocrystalline diamond thin films as infrared optical protective coatings. *Int. J. Mod. Phys. B* **16**, 1013-17 (2002).
8. W.B. Yang, F.X. Lu, Z.X. Cao. Growth of nanocrystalline diamond protective coatings on quartz glass. *J. Appl. Phys.* **91**, 10068-73 (2002).
9. S. Bhattacharyya, O. Auciello, J. Birrell, J.A. Carlisle, L.A. Curtiss, A.N. Goyette, D.M. Gruen, A.R. Krauss, J. Schlueter, A. Sumant, and P. Zapol. Synthesis and characterization of highly-conducting nitrogen-doped ultrananocrystalline diamond films. *Appl. Phys. Lett.* **79**, 1441-43 (2001).
10. I. Gouzman, I. Lior, and A. Hoffman. Formation of the precursor for diamond growth by *in situ* direct current glow discharge pretreatment. *Appl. Phys. Lett.* **72**, 296-98 (1998).
11. D.M. Gruen *et al.* Characterization of nanocrystalline diamond films by core-level photoabsorption. *Appl. Phys. Lett.* **68**, 1640-42 (1996).
12. M.M. Garc'a, I. Jimenez, L. Vazquez, C. Gomez-Aleixandre, J.M. Albella, O. Sanchez, T.J. Terminello, and F.J. Himpsel. X-ray absorption spectroscopy and atomic force microscopy study of bias-enhanced nucleation of diamond films. *Appl. Phys. Lett.* **72**, 2105-07 (1998).
13. L. Coffman, R. Cao, P. A. Pianetta, S. Kapoor, M. Kelly, and L. J. Terminello. Near-edge x-ray absorption of carbon materials for determining bond hybridization in mixed  $sp^2/sp^3$  bonded materials. *Appl. Phys. Lett.* **69**, 568-70 (1996).
14. J. Nithianandam, J.C. Rife, and H. Windischmann. Carbon *K* edge spectroscopy of internal interface and defect states of chemical vapor deposited diamond films. *Appl. Phys. Lett.* **60**, 135-37 (1992).
15. P.R. Bressler, M. Lubbe, D.R.T. Zahn, and W. Braun. X-ray absorption spectroscopy study of different solid carbon modifications. *J. Vac. Sci. Technol. A* **15**, 2085-87 (1997).
16. I. Gouzman, A. Hoffman, G. Comtet, L. Hellner, G. Dujardin, and M. Petravic. Nanosize diamond formation promoted by direct current glow discharge process: Synchrotron radiation and high resolution electron microscopy studies. *Appl. Phys. Lett.* **72**, 2517-19 (1998).
17. R.A. Rosenberg, P.J. Love, and V. Rehn. Polarization-dependent *C(K)* near-edge x-ray-absorption fine structure of graphite. *Phys. Rev. B* **33**, 4034-37 (1986).
18. H. Windischmann. An intrinsic stress scaling law for polycrystalline thin films prepared by ion beam sputtering. *J. Appl. Phys.* **62**, 1800-07 (1987).
19. M.M. Garcia, I. Jimenez, O. Sanchez, C. Gomez-Aleixandre, and L. Vazquez. Model of the bias-enhanced nucleation of diamond on silicon based on atomic force microscopy and x-ray-absorption studies. *Phys. Rev. B* **61**, 10383-87 (2000).
20. A. Heiman, I. Gouzman, S.H. Christiansen, H.P. Strunk, A.G. Comtet, L. Hellner, G. Dejardin, R. Edrei, and A. Hoffman. Evolution and properties of nanodiamond films deposited by direct current glow discharge. *J. Appl. Phys.* **89**, 2622-30 (2001).
21. A. Heiman, E. Lakin, E. Zolotoyabko, and A. Hoffman. Microstructure and stress in nanocrystalline diamond films deposited by DC glow discharge CVD. *Diam. Relat. Mater.* **11**, 601-07 (2002).
22. D.E. Jesson. Morphological evolution of strained semiconductor films. *Ser. Dir. Condens. Matter Phys.* **14**, 195-212 (1998).

23. B. Warot, E. Snoeck, P. Baules, J.-C. Ousset, M.-J. Casanove, S. Dubourg, J.F. Bobo. Growth and stress relaxation of Co/NiO bilayers on MgO(001). *J. Appl. Phys.* **89**, 5414-20 (2001).
24. F. Spaepen. Interfaces and stresses in thin films. *Acta Mater.* **48**, 31-42 (2000).
25. F.R. McFeely, S.P. Kowalczyk, L. Ley, R.A. Pollak, and D.A. Shorley. X-ray photoemission studies of diamond, graphite, and glassy carbon valence bands. *Phys. Rev. B* **9**, 5268-78 (1974).
26. S. Praver, K.W. Nugent, D.N. Jamieson, J.O. Orwa, L.A. Bursill, J.L. Peng. The Raman spectrum of nanocrystalline diamond. *Chem. Phys. Lett.* **332**, 93-7 (2000).
27. A. Heiman, I. Gouzman, S.H. Christiansen, H. P. Strunk, A. Hoffman. Nanodiamond films deposited by direct current glow discharge assisted chemical vapor deposition. *Diamond Relat. Mater.* **9**, 866-71 (2000).
28. P. Badziag, W.S. Verwoerd, W.P. Ellis, N.R. Greiner. Nanometre-sized diamonds are more stable than graphite. *Nature* **343**, 244-45 (1990).
29. M.Y. Gamarnik. Energetical preference of diamond nanoparticles. *Phys. Rev. B.* **54**, 2150-56 (1996).
30. A. Hoffman, A. Heiman, and S.H. Christiansen. Mechanism of nanodiamond film formation by stress relaxation on a preferentially oriented vertical basal plane graphitic precursor. *J. Appl. Phys.* **89**, 5769-73 (2001).
31. A. Hoffman, A. Heiman, R. Akhvlediani, E. Lakin, E. Zolotoyabko, and C. Cytermann. Hydrogen content and density in nanocrystalline films of a predominant diamond character in the formation of nanocrystalline diamond in carbon films grown by DC glow discharge CVD. *J. Appl. Phys.* **4**(7), 4589-95 (2003).
32. Y. Lifshitz, S.R. Kasi and J.W. Rabalais. Subplantation model for film growth from hyperthermal species: Application to diamond. *Phys. Rev. Lett.* **62**, 1290-93 (1989).
33. Y. Lifshitz, S.R. Kasi, J.W. Rabalais, and W. Eckstein. Subplantation model for film growth from hyperthermal species. *Phys. Rev. B* **41**, 10468-80 (1990).
34. J. Kulik, G. Lempert, E. Grossman, and Y. Lifshitz. Structure and bonding in mass-selected ion-beam deposited carbon films. *Proceedings of MRS 1999 Fall Meeting, MRS Proc.* **593**, 305 (2000).
35. H.Y. Peng, N. Wang, Y.F. Zheng, Y. Lifshitz, J. Kulik, R.Q. Zhang C.S. Lee, and S.T. Lee. Smallest diameter carbon nanotubes. *Appl. Phys. Lett.* **77**, 2831-33 (2000).
36. A.C. Ferrari and J. Robertson. Origin of the 1150-cm<sup>-1</sup> Raman mode in nanocrystalline diamond. *Phys. Rev. B* **63**, 121405 (2001).
37. Y. Lifshitz, Th. Köhler, Th. Frauenheim, I. Gouzman, A. Hoffman, R.Q. Zhang, X.T. Zhou, and S.T. Lee. The Mechanism of Diamond Nucleation from Energetic Species. *Science* **297**, 1531-33 (2002).
38. W.R. Lambrecht et al. Diamond nucleation by hydrogenation of the edges of graphitic precursors. *Nature* **364**, 607-10 (1993).
39. P.B. Mirkarimi, K.F. McCarty, and D.L. Medlin. Review of advances in cubic boron nitride film synthesis. *Mater. Sci. Eng. R* **21**, 47-100 (1997).
40. F. Banhart. Irradiation effects in carbon nanostructures. *Rep. Progr. Phys.* **62**, 1181-1221 (1999).



# 11

## NANODIAMOND INJECTION INTO THE GAS-PHASE DURING CVD DIAMOND FILM GROWTH

N.A. Feoktistov<sup>1</sup>, V.G. Golubev<sup>1</sup>, S.A. Grudinkin<sup>1,2</sup>, A.V. Nashchekin<sup>1</sup>,  
T.S. Perova<sup>2</sup>, and A.Ya. Vul<sup>1</sup>

<sup>1</sup>*Ioffe Physico-Technical Institute, St. Petersburg, 194021, Russia*

<sup>2</sup>*Department of Electronic & Electrical Engineering, University of Dublin, Trinity College,  
Dublin 2, Ireland*

**Abstract:** We describe a way of combining, in the same technological cycle, the nanodiamond particle injection from a suspension and the growth of diamond films by microwave plasma chemical vapor deposition (MPCVD). The breaking of injected nanodiamond aggregates into particles of about 100 nm in size when they hit a substrate provides a nucleation density over  $10^{10} \text{ cm}^{-2}$ . The films produced from a  $\text{CH}_4+\text{H}_2$  mixture with a periodic injection of ND particles during the film growth are found to consist of diamond nanocrystallites with the traces of  $sp^2$ -hybridized carbon on them.

**Keywords:** nanocrystalline diamond films, nanodiamond, CVD, nucleation density

### 1. INTRODUCTION

The technology and investigation of nanocrystalline diamond (NCD) films have become a subject of special interest in the past decade. In contrast to microcrystalline diamond, NCD films with a characteristic grain size of a few dozens of nanometers possess a smaller surface roughness and friction coefficient but a greater hardness [1,2]. These properties make it possible to use NCD films as protective coatings for optics, wear-resistant coatings, and masks for X-ray lithography [3,4]. Besides, NCD is a promising material for making field electron emitters [5].



A necessary stage in the NCD CVD technology is the substrate pretreatment for increasing the nucleation density. There are several ways to do this [6], but the use of detonation nanodiamonds (ND) is becoming more common [7]. The substrate may be pretreated simply by evaporating the nanodiamond suspension deposited on it [7,8] or by treating it with ultrasound in the suspension [9]. Some researchers have reported the ND deposition from a suspension using electrophoresis [10]. All of these techniques require a direct contact of the substrate with a liquid suspension, which separates the substrate pretreatment stage from the film growth in the gas-phase. The application of detonation NCD can provide a nucleation density of  $10^{11} \text{ cm}^{-2}$  [11]. Such a high density can also be achieved by bias-enhanced nucleation (BEN) [12].

The above methods have been used to produce nucleation centers either prior to or during the initial film growth. However, the NCD film growth requires a continuous formation of secondary nucleation centres on the growing film. Usually, this is achieved by choosing the proper deposition parameters; for example, the authors of [13] reported a continuous BEN at higher methane concentrations than those used for microcrystalline diamond films. On the other hand, the BEN method makes it difficult to use dielectric substrates. NCD films were produced in [14] by hot filament CVD at a low reactor pressure and a high methane concentration in the gas mixture. At these parameters, the concentration and the mean free path of carbon-containing radicals increased, enhancing the bombardment of the substrate and stimulating the formation of secondary nucleation centres. The possibility of growing NCD films by microwave plasma CVD in an Ar+C<sub>60</sub> plasma was demonstrated in [15]. The films had a nanometer surface roughness and a small friction coefficient. The authors of [6] pointed out that the parameters optimal for the diamond nucleation at CVD process might not be optimal for the growth of films with a high diamond content, which is indicated by an increased non-diamond phase and a higher defect concentration in the film.

Therefore, it seemed important to suggest an effective technique for stimulating secondary diamond nucleation, combined with the CVD film growth, which would not require a radical change of the technological parameters. We thought that the detonation diamond would be a suitable material for nucleation if it could be injected from a suspension into the gas directly during the CVD growth. It was suggested that this procedure could provide a higher nucleation density during the initial growth and that the CVD deposition from a hydrogen-methane mixture could be combined with the deposition by ND injection.

Note that some attempts have recently been made to introduce ND particles into the gas phase. For example, it is reported in [16] that diamond

particles were carried by an air flow out of a suspension, passed through driers, charged in a high electric field and delivered onto a substrate. However, the authors do not present data on the deposition density or the initial film growth, so it is hard to get an idea about the ND deposition efficiency and the nucleation density. In [17], a mixture of ND particles in argon was supplied into a growth reactor and the plasma with the particles was then accelerated electromagnetically towards a substrate. As a result, the nanodiamonds transformed to carbon onions and were deposited on the substrate. But no attempt was made in this work to use ND particles as presursors of diamond film growth.

Here we describe our results on combining, in the same technological cycle, a periodic injection of ND particles into the growth chamber of a MPCVD reactor and the growth of NCD films. The injection of ND particles prior to the growth has been used to increase nucleation density on the substrate. The structure of the NCD films obtained by MPCVD from a  $\text{CH}_4 + \text{H}_2$  mixture was examined in a continuous alternation of the injection events during the growth and in the absence of injection.

## 2. EXPERIMENTAL TECHNIQUES

The initial material for an ND suspension was detonation carbon produced by a commercial synthesis from a trinitrotoluene-hexogen mixture in the proportion 60:40 [18]. The ND powder was separated by etching the non-diamond material with nitric acid at 200–230°C. The size of the coherent scattering region (CSR) of the powder to be used for making the suspension was about 4.5 nm, and the powder concentration in suspension was varied from 0.003 to 3 wt.%.

The experimental reactor is shown schematically in Figure 1. The ND suspension was placed above a diaphragm, which separated the injector vessel into two parts and had a hole of 1.5 mm in diameter. A hydrogen flow was supplied from this vessel at such a pressure that the injector vessel pressure was set at 500–600 Torr when the electromagnetic valve connecting it to the reactor was opened. The suspension was delivered in a pulse mode (~50 ms) by the carrier hydrogen flow, which picked up the suspension droplets containing ND particles. The liquid containing ND particles was evaporated when the droplets passed through a heater. Then the flow of hydrogen and vapour with ND particles was passed into the reactor towards the substrate. The time interval between the injection pulses varied from 1 to 10 sec. The particle injection could be made together with a microwave discharge or without it.

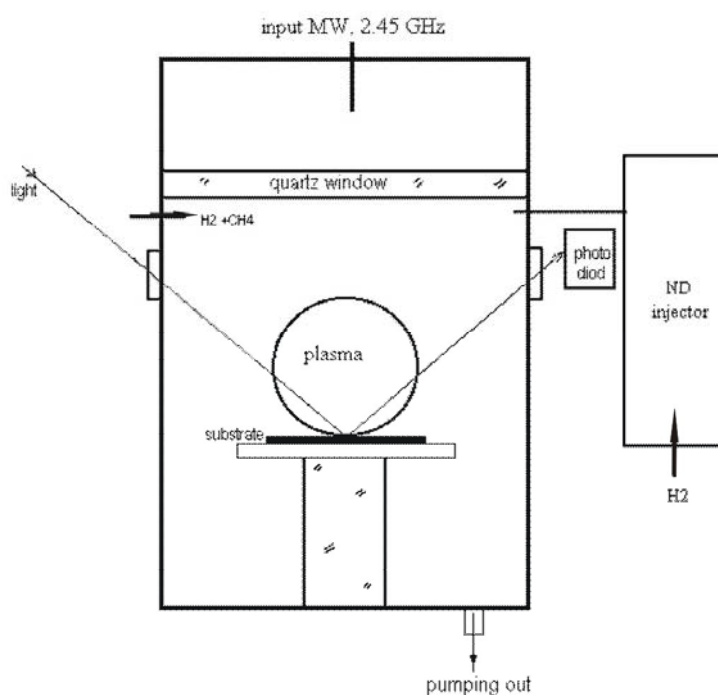


Figure 1. A schematic of MPCVD reactor with an injector.

To control the optical characteristics of the deposited films, the light reflection from the substrate was registered during the growth [19]. When the particle concentration in the suspension was higher than 0.1 wt.%, the ND deposition on the substrate was controlled by measuring the light reflection, but when the particle concentration was lower, the detectable change in the reflection (in the spectral range of 0.45–1  $\mu\text{m}$ ) was less than 1% over the total injection time of 10–60 min.

The substrates used were optically polished silicon wafers of the *n*-type (100) orientation and fused silica. Diamond films were grown from a hydrogen-methane mixture with the methane concentration of 1–3% by MPCVD technique. The hydrogen flow rate was 250 sccm, the pressure was 10–30 Torr, and the substrate temperature was  $\sim 700^\circ\text{C}$  at the microwave discharge power  $\sim 300\text{--}500$  W. The film growth rate was found to be 0.1–0.4 microns per hour. The substrate temperature was controlled by a Pt-PtRh thermocouple inserted into the substrate holder.

The nucleation density of the diamond islands formed after the initial stage of growth was taken to be the criterion for the injector efficiency. It was evaluated from the light reflection and electron microscopic data.

The relative content of the diamond phase in the films was found from Raman spectroscopic data using a Renishaw 1000 Micro-Raman System. The excitation was performed by an argon laser at  $\lambda = 514$  nm. The laser spot on the sample was about 10  $\mu\text{m}$  in size and the radiation power was less than 10 mW.

The structural perfection of the films was characterized by X-ray diffractometry. The measurements were made by a Siemens D-500 X-ray diffractometer in the  $(\theta, 2\theta)$ -geometry, using  $\text{CuK}\alpha$  radiation at the wavelength  $\lambda = 0.15418$  nm.

### 3. RESULTS AND DISCUSSION

Figure 2 illustrates the time dependence of the light reflection from a fused silica substrate with a growing film. The variable parameter is the concentration of ND particles deposited on the substrate from a suspension prior to the growth. The ND concentration on the substrate was defined by the injection time, with the MPCVD parameters remaining unchanged.

Obviously, the scattering by individual particles (growth islands) must decrease the reflection. However, the first interference extremum to appear with the formation of a continuous film should be a peak because the refractivity of quartz is lower than that of diamond, so the reflection must increase. One should recall that the first interference extremum for the growth on a silicon substrate, whose refractivity is higher than that of a growing diamond film, should be a valley; therefore, the reflection due to both the increasing film thickness and the greater scattering should decrease simultaneously. In that case, it would be difficult to separate the contributions of the two processes.

The lower reflection intensity during the initial stage of growth shown in Figure 2 is likely to be due to a greater scattering [19] when isolated diamond seeds grow on ND particles. Indeed, when the density of ND particles is low, the decreased reflection has a larger amplitude and takes a longer time. The change from the initial reflection decrease to its increase results from the formation of a continuous film. The reflection intensity is determined by the interference in the film-substrate system and reaches its first peak when the film thickness becomes equal to  $\lambda/4n$  ( $n$  - reflection index of diamond). One can also see that the initial reflection decrease at high injected ND densities takes from 1/4 to 1/5 of the time necessary for the first

peak to appear, which corresponds to the increase in the film thickness by  $\lambda/4n$ , found to be equal to  $\sim 90$  nm in this experiment.

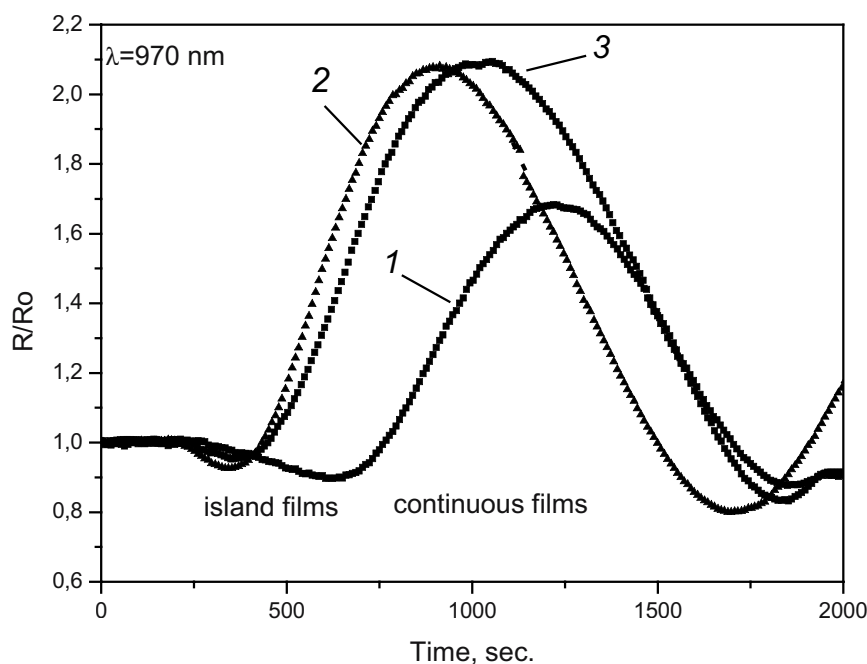


Figure 2. The normalized growth time dependence of the NCD film reflectivity for a fused silica substrate with ND particles injected prior to the growth. The duration of the ND injection: 1 - 15 sec., 2 - 150 sec., 3 - 800 sec. The time interval between the injections is 5 sec and the ND concentration in the suspension is 1%.

The nucleation density can be estimated on the assumption that the growth rate of the diamond islands is isotropic, i.e., the islands are hemispherical. If we also assume that a continuous film starts to form at the island height of 90 nm, the nucleation density will be about  $10^{10} \text{ cm}^{-2}$ . It has been found that the nucleation density rises with the ND concentration in the suspension.

A possible reason for increasing nucleation density may be the substrate “scratching” by the injected particles. But when the particles were removed mechanically from the substrate, the nucleation density decreased by nearly 3 orders of magnitude. This suggests that a diamond film grows on ND particles rather than on mechanical defects of the substrate.

Figure 3 shows representative SEM images of a silicon substrate immediately after the ND injection prior to the growth (*a*) and after 20 min of the film growth (*b*). It is seen that in the latter case a continuous film is formed with a characteristic grain of  $\sim 100$  nm and that the island density is much greater than density of the ND particles resolved in Figure 3*a*. The estimation of the island density presented in Figure 3*b* gives a nucleation density value consistent with that obtained from the light reflection data,  $10^{10} \text{ cm}^{-2}$ .

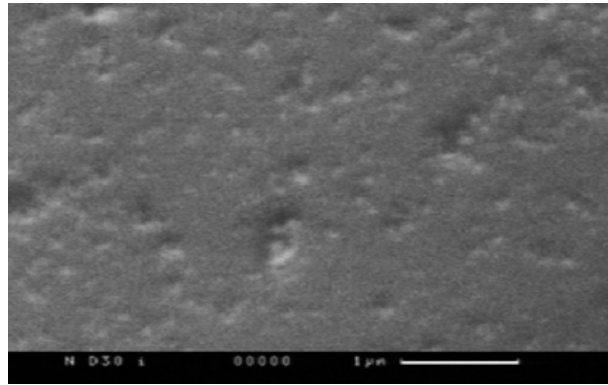
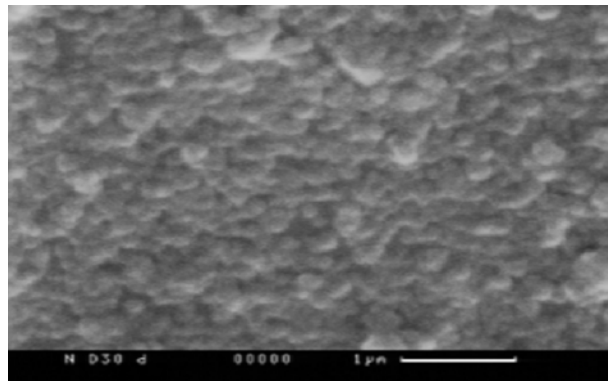
*a**b*

Figure 3. SEM images of a silicon substrate after the ND injection prior to the growth (*a*) and after a 20 min growth by MPCVD (*b*).

Note that SEM images similar to those in Figures 3*a* and 3*b* were registered at various deposited ND densities. This means that the island density is much higher than the observable density of the injected particles. This fact is an evidence for the presence of a large amount of particles with

the size less than 100 nm, while their average size found from the deposition time in the Stokes approximation, assuming the particles to be spherical, was  $\sim 300$  nm. The high density of particles of  $< 100$  nm can be accounted for by a large size dispersion of the suspension particles and by a possible breaking of large ND aggregates when they hit against the substrate at near-sound velocities.

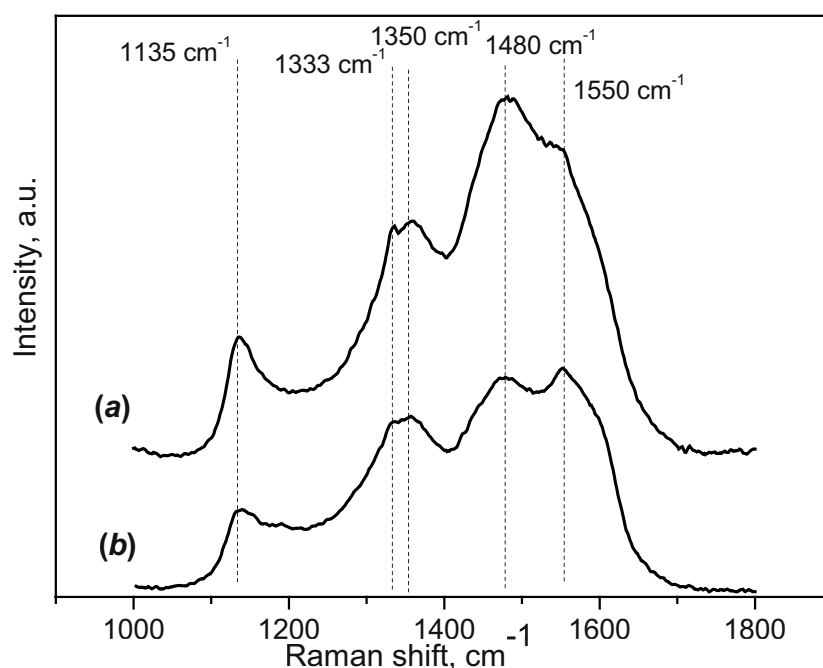


Figure 4. Raman spectra of MPCVD films on silicon substrates with ND particles injected prior to the growth for: (a) a periodic alternation of injection events during the growth and (b) without periodical injection.

Figure 4 illustrates the Raman spectra of NCD films grown on a silicon substrate with ND particles injected prior to the growth in a continuous mode (a) and in the mode of periodic alternation of injection and growth in a methane-hydrogen plasma (b). The spectra show resolvable lines at  $1135\text{ cm}^{-1}$ ,  $1333\text{ cm}^{-1}$ ,  $1350\text{ cm}^{-1}$ ,  $1480\text{ cm}^{-1}$ , and  $1550\text{ cm}^{-1}$  similar to those for MPCVD NCD films [13,20]. A weak band at  $1333\text{ cm}^{-1}$  indicates the presence of crystalline diamond in the film [14]. The lines at  $1350\text{ cm}^{-1}$  and  $1550\text{ cm}^{-1}$  correspond to the well-known D- and G-modes which are due to

$sp^2$ -hybridized carbon [5,14]. The  $1480\text{ cm}^{-1}$  line is due to the presence of amorphous  $sp^2$ -hybridized carbon [21]. Note that the cross section of the Raman scattering by  $sp^2$ -carbon is about 50 times larger than that for  $sp^3$ -carbon.

At present, there are different opinions concerning the origin of the  $1135\text{ cm}^{-1}$  line. Most researchers compare its position with the single phonon density of the diamond states and attribute it to the presence of nanocrystalline diamond in the film. The authors of [23] believe that the  $1135\text{ cm}^{-1}$  line is due to transpolyacetylene inclusions at the boundaries of diamond crystallites.

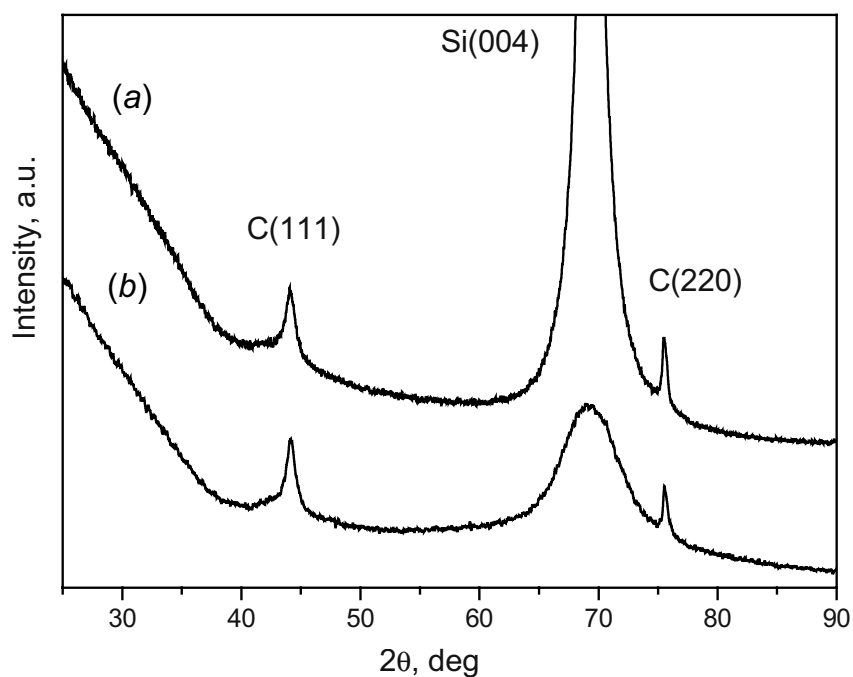


Figure 5. The X-ray diffraction pattern for MPCVD NCD films on silicon substrates ND particles injected prior to the growth for: (a) a periodic alternation of injection events during the growth and (b) without periodical injection.

The X-ray diffraction curves for the diamond films are presented in Figure 5. The diffraction patterns show distinct peaks reflections from the (111) and (220) surfaces of a cubic lattice with the constant



$a_0 = 0.3567 \pm 0.0001$  nm corresponding to the diamond lattice. The background in the range of  $2\theta = 25^\circ - 30^\circ$  is due to the X-ray scattering by the material fixing the sample to the holder in the XRD experiment. No traces of graphite were detected.

The CSR sizes of films grown on ND particles with a periodic injection and in a continuous mode were calculated for the (111) response, using Scherer's formula; they were found to be approximately the same of 10 nm.

We can conclude from the Raman spectroscopic and X-ray diffractometric data that the NCD films grown in the alternating injection mode consist of diamond nanocrystallites with traces of  $sp^2$ -carbon on them. The supply of the excess of oxygen during the periodic injection of an aqueous ND suspension did not lead to a noticeable etching of the film. No essential difference in the structure of the films grown in the two modes was observed.

#### 4. CONCLUSION

This study has demonstrated the possibility of combining, in the same technological cycle, the nanodiamond injection from a suspension and the growth of nanocrystalline diamond films in the MPCVD process. The breaking of injected ND aggregates to a size of about 100 nm when they strike the substrate can provide a nucleation density over  $10^{10} \text{ cm}^{-2}$ . The films produced from a  $\text{CH}_4 + \text{H}_2$  mixture by a periodic injection of ND particles during the growth are found to consist of diamond nanocrystallites with traces of  $sp^2$ -hybridized carbon on their surface.

This work was supported by the Russian Ministry of Education and Science (Contracts N 40.700.12.0117 and N 40.012.11.1147) and by the Presidium of the Russian Academy of Science under the Project "Quantum Nanostructures".

#### REFERENCES

1. N. Jiang, K. Eguchi, T. Inaoka, Y. Shintani, H. Makita, A. Hatta, and A. Hiraki. Reducing the grain size for fabrication of nanocrystalline diamond films. *Journal of Crystal Growth* **222**, 591 (2001).
2. T. Wang, H.W. Xin, Z.M. Zhang, Y.B. Dai, and H.S. Shen. The fabrication of nanocrystalline diamond films using hot filament CVD. *Diamond and Related Materials* **13**, 6 (2004).

3. D. Zhou, A.R. Krauss, L.C. Qin, T.G. McCauley, D.M. Gruen, T.D. Corrigan, R.P.H. Chang, and H. Gnaser. Synthesis and electron field emission of nanocrystalline diamond thin films grown from  $N_2/CH_4$  microwave plasma. *J. Appl. Phys.* **82**, 4546 (1997).
4. A.K. Pal, K.K. Chattopadhyay, S. Chaudhuri, K. Chakrabarti, and R. Chakrabarti. Nano-diamond films produced from CVD of camphor. *Diamond Relat. Mater.* **7**, 845 (1998).
5. M. Hiramatsu, C.H. Lau, A. Bennett, and J.S. Foord. Formation of diamond and nanocrystalline films by microwave plasma CVD. *Thin Solid Films* **407**, 18 (2002).
6. H. Liu and D.S. Dandy. Studies on nucleation process in diamond CVD: an overview of recent developments. *Diamond Relat. Mater.* **4**, 1173 (1995).
7. D. Guerin and S. Ismat Shah. Enhanced nucleation and growth of diamond thin films using a nanodiamond monolayer. *J. Matter. Sci. Lett.* **16**, 476 (1997).
8. A. Hiraki. Low-temperature (200°C) growth of diamond on nano-seeded substrate. *Appl. Surf. Sci.* **326**, 162-63 (2000).
9. A. Eliyahu, J. Buehler, M. Ben-Chorin, H. Cohen, and Y. Prior. Nano-particles seeding and its characterization by X-ray photoelectron spectroscopy (XPS). *Diamond Relat. Mater.* **8**, 146 (1999).
10. A.N. Alimova, N.N. Chubun, P.I. Belobrov, and V.V. Zhirnov. Electrophoresis of nanodiamond powder for cold cathode fabrication. *J. Vac. Sci. Technol. B* **17**, 715 (1999).
11. H. Makita, K. Nishimura, N. Jiang, A. Hatta, T. Ito, and A. Hiraki. Ultrahigh particle density seeding with nanocrystal diamond particles. *Thin Solid Films* **281-282**, 279 (1996).
12. M.J. Chiang and M.H. Hon. Enhanced nucleation of diamond films assisted by positive dc bias. *Thin Solid Films* **389**, 68 (2001).
13. T. Sharda, M.M. Rahaman, Y. Nukaya, T. Soga, T. Jimbo, and M. Umeno. Structural and optical properties of diamond. *Diamond and Related Materials* **10**, 561 (2001).
14. T. Wang, H.W. Xin, Z.M. Zhang, Y.B. Dai, and H.S. Shen. The fabrication of nanocrystalline diamond films using hot filament CVD. *Diamond and Related Materials* **13**, 6 (2004).
15. A. Erdemir, C. Bindal, G.R. Fenske, C. Zuiker, A.R. Krauss, and D.M. Gruen. Friction and wear properties of smooth diamond films grown in fullerene + argon plasmas. *Diamond and Related Materials* **5**, 923 (1996).
16. A.P. Malshe, R.A. Beera, A.A. Khanolkar, W.D. Brown, and H.A. Naseem. Initial results of a novel pre-deposition seeding technique for achieving an ultra-high nucleation density for CVD diamond growth. *Diamond and Related Materials* **6**, 430 (1997).
17. A.V. Gubarevich, J. Kitamura, S. Usuba, H. Yokoi, Y. Kakudate, and O. Odawara. Onion-like carbon deposition by plasma spraying of nanodiamonds. *Carbon* **41**, 2601 (2003).
18. A.E. Aleksenskii, M.V. Baidakova, A.Ya. Vul', V.Yu. Davydov, and Yu.A. Pevtsova. Diamond-graphite phase transition in ultradisperse-diamond clusters. *Phys. Solid State* **39**, 1007 (1997).
19. A.A. Smolin, V.G. Ralchenko, S.M. Pimenov, T.V. Kononenko, and E.N. Loubnin. Optical monitoring of nucleation and growth of diamond films. *Appl. Phys. Lett.* **62**(26), 3449 (1993).
20. T. Xu, S. Yang, J. Lu, Q. Xue, J. Li, W. Guo, and Y. Sun. Characterization of nanocrystalline diamond films implanted with nitrogen ions. *Diamond and Related Materials* **10**, 1441 (2001).

21. R.E. Shroder, R.J. Nemanich, and J.T. Glass. Analysis of the composite structures in diamond thin films by Raman spectroscopy. *Phys. Rev. B* **41**(6), 3738 (1990).
22. R.J. Nemanich, J.T. Glass, G. Lucovsky, and R.E. Shroder. Raman scattering characterization of carbon bonding in diamond and diamond-like thin films. *J. Vac. Sci. Technol. A* **6**(3), 1783 (1988).
23. A.C. Ferrari and J. Robertson. Origin of the 1150  $\text{cm}^{-1}$  Raman mode in nanocrystalline diamond. *Phys. Rev. B* **63**, 121405 (2001).

# 12

## STABILIZATION OF DIAMOND-LIKE NANOCLUSTERS BY METALLIC ATOMS AND THE EPITAXIAL GROWTH OF DIAMOND FILMS: *ab initio* SIMULATION

V.G. Zavodinsky

*Institute for Materials Science, the Far East Branch of the Russian Academy of Sciences,  
153 Tikhookeanskaya, Khabarovsk, 680042, Russia*

**Abstract:** The density functional theory and non-empirical pseudopotentials were implemented to study the stabilization of ultra nanoclusters ( $C_6$  and  $C_8$ ) of diamond by alkali (Li and K) and noble (Cu, Ag and Au) metals. It has been shown that copper is the best candidate to keep the diamond-like cluster geometries. Calculations show that epitaxial diamond films can be grown on copper substrates with geometry parameters closed to those of bulk diamond. The mean cohesive energy for the C(100) films is larger than that for the C(111) films; however, the C(100) films are more stable against the separation from the copper substrate. The latter fact explains why the preferable observed orientation of diamond microcrystallites on copper is the  $\langle 111 \rangle$  direction.

**Keywords:** diamond, nanostructure, epitaxial films, *ab initio* simulation

### 1. INTRODUCTION

Some metals are known to stimulate the formation of diamond nanoparticles at low temperatures, but the nature of their catalytic activity is still poorly understood. This effect has been observed with copper in [1], and the authors suggest that Cu nanoclusters ( $\sim 3$  nm in size) can play a catalytic role in the nucleation of diamond nanoparticles. If this is true, the formation of nanodiamond can be considered as its epitaxial growth on Cu nanocrystallites. The epitaxy of diamond on copper is a well-known

phenomenon [2–10], which is due to a slight mismatch between the copper and diamond lattices and a poor copper-carbon affinity. However, one can imagine another mechanism of nanodiamond nucleation. It was stated in [11] that the formation of diamond nanoclusters in a hydrogen atmosphere might be attributed to the saturation and stabilization of the edge carbon  $sp^3$ -bonds by H atoms. We showed earlier [12,13] that Cu atoms could saturate carbon dangling bonds quite effectively. One can assume, therefore, that the mechanism underlying the Cu catalytic activity is the same as that in the C-H system, i.e. the saturation of the edge dangling  $sp^3$ -bonds. Single copper atoms are shown to interact with carbon like univalent atoms, in a way similar to H atoms. However, when a Cu atom interacts with another Cu atom, the  $d$ -electrons also become involved in this interaction. So it would be interesting to compare the Cu-C systems not only with the H-C systems but also with the K-C, Li-C, Ag-C, and Au-C ones.

Here we report on our study of both mechanisms: the dangling  $sp^3$ -bond stabilization and the epitaxial growth.

## 2. METHODS OF COMPUTATIONS

The computations were performed using the FHI96md simulation code [14] based on the density functional theory, the pseudopotential method, and the plane wave basis set. We used the Perdew-Wang generalized gradient approximation (PW91) [15] for the exchange and correlation of functional and fully separable Troullier-Martins pseudopotentials [16]. The latter were constructed using the FHI98pp code [17]; they were verified to avoid ghost states and to describe the basic experimental characteristics of the bulk materials (lattice constants and elastic modules). I used only one gamma point for the  $k$ -space integrations; the energy cut-off of 40 Ry was applied in all the computations.

## 3. STABILIZATION OF DIAMOND NANOCCLUSERS

To study the ability of K, Li, Cu, Ag, and Au atoms to stabilize diamond-like carbon structures, I used two types of carbon nanoclusters,  $C_5$  and  $C_8$  (Figure 1), assuming that every outer bond was saturated with one metal atom. All the atoms of the structure were free to move to their equilibrium positions; therefore, the total equilibrium energies could be found self-consistently. The structure optimization procedure was continued until the maximum forces on the atoms were less than 0.01 eV/Å.

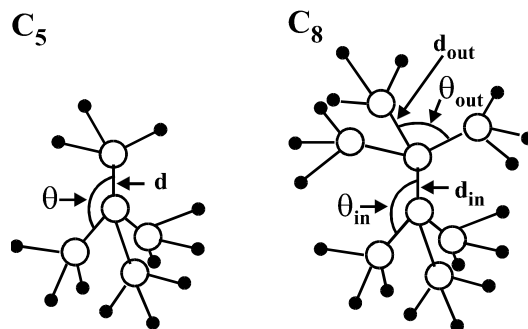


Figure 1. Schematic diamond-like carbon nanoclusters: white circles for carbon atoms and black circles for metal or hydrogen atoms.

The diamond structure is characterized by an equidistant four-atomic coordination and tetragonal bond-bond angles  $\theta$  equal to  $109.47^\circ$ . The bulk C-C distance in diamond ( $d_{\text{bulk}}$ ) is  $1.544 \text{ \AA}$ . Our test computations gave the equilibrium C-C bulk distance of  $1.55 \text{ \AA}$ .

First, I studied  $C_5$  and  $C_8$  clusters terminated by hydrogen. The geometrical parameters of a  $C_5H_{12}$  cluster were found to be very close to those of bulk diamond, namely,  $d = 1.55\text{--}1.56 \text{ \AA}$  and  $\theta = 109.1\text{--}110.1^\circ$ . The geometry of a  $C_8H_{18}$  cluster, however, was not as close to that of bulk diamond. In particular, the internal C-C distance  $d_{\text{in}}$  was equal to  $1.62 \text{ \AA}$ , while the outer C-C bond had the length  $d_{\text{out}}$  of  $1.54 \text{ \AA}$ . To be sure that this result was not an artifact of my approach, I analyzed the  $C_8H_{18}$  cluster using two other procedures: the unrestricted Hartree-Fock (UHF) method with a triple zeta valence basic set and the semi-empirical PM3 method, both implemented in the GAMESS code [18]. The UHF computations yielded  $d_{\text{out}} = 1.54 \text{ \AA}$  and  $d_{\text{in}} = 1.59 \text{ \AA}$ , while the PM3 method gave  $d_{\text{out}} = 1.53 \text{ \AA}$  and  $d_{\text{in}} = 1.57 \text{ \AA}$ . Thus, a non-equivalence of the inner and outer C-C bonds in the  $C_8H_{18}$  cluster seems to be a realistic feature of the H-termination.

The details of the  $C_5H_{12}$  and  $C_8H_{18}$  geometries are listed in Table 1 and compared with those of the  $C_5Me_{12}$  and  $C_8Me_{18}$  systems, where Me stands for Li, K, Cu, Ag or Au. The  $C_5$  clusters terminated by Li, K, and Ag are dimerized. This means that two carbon atoms form a C-C dimer with a length of  $1.31\text{--}1.36 \text{ \AA}$ . The dimerization leads to a significant change in the bond-bond angles. The angles opposed to the dimers become smaller ( $\sim 50^\circ$ ) while the other angles become as large as  $118\text{--}120^\circ$ . Copper and gold retain the diamond-like structure of the  $C_5$  cluster in a similar way. However, the parameters ( $d = 1.51 \text{ \AA}$  and  $\theta = 109.06^\circ$ ) for the copper case are slightly closer to the diamond bulk parameters ( $d = 1.55 \text{ \AA}$  and  $\theta = 109.47^\circ$ ) than those for Au ( $d = 1.44 \text{ \AA}$  and  $\theta = 110.41^\circ$ ).

Table 1. Geometrical parameters ( $d$ ,  $d_{in}$ ,  $d_{out}$ ,  $\theta$ ,  $\theta_{in}$ ,  $\theta_{out}$ ) of  $C_5$  and  $C_6$  diamond-like clusters terminated by H, Li, K, Cu, Ag or Au.

Cluster	Parameter	H	Li	K	Cu	Ag	Au
$C_5$	$d$ , Å	1.55	1.54	1.55	1.51	1.45	1.44
			1.36 (dimer)	1.34 (dimer)		1.31 (dimer)	
	$\theta$ , degree	109.50	118.01	120.96	109.06	117.98	110.41
			51.39 (dimer)	47.45 (dimer)		45.39 (dimer)	
$C_8$	$d_{in}$ , Å	1.62			1.50	2.40	2.20
	$d_{out}$ , Å	1.54			1.51	1.42	1.46
	$\theta_{in}$ , degree	111.95	unstable	unstable	110.02	100.10	106.15
	$\theta_{out}$ , degree	107.48			109.14	117.46	113.22

The  $C_8$  clusters terminated by Li and K are marked as "unstable" in Table 1. This means that their initial diamond-like structure is drastically reconstructed: two C-C dimers are formed in both systems and the other bonds are buckled and twisted. In the case of K, a number of metallic atoms are detached from the carbon cluster to form their own agglomerates (triangles, linear chains, and so on). The Ag (Au)-terminated  $C_8$  clusters are significantly extended. The distance between the inner C atoms is equal to 2.4 (2.2) Å, while the outer C atoms are 1.42 (1.46) Å away from the inner atoms. As a result, the  $\theta_{in}$  angles are smaller and the  $\theta_{out}$  angles are larger than the bulk value of 109.47°. The best result is with the Cu termination:  $d = 1.50$ -1.51 Å and  $\theta = 109.14$ -110.04°, which are quite similar to the bulk diamond values. It is remarkable that the Cu termination leads to even better diamond-like geometries than the H saturation.

It is of interest to compare the energy characteristics of carbon clusters with different terminations, such as the energy of adhesion ( $E_{adh}$ ) for metal (or hydrogen) atoms which saturate the edge carbon bonds:

$$E_{adh} = \frac{E(\text{system}) - E(\text{carbon}) - E(\text{Me or H})}{N(\text{Me or H})},$$

where  $E(\text{system})$  is the energy of the total relaxed system made up of a carbon nanocluster and a metal or hydrogen termination;  $E(\text{carbon})$  and  $E(\text{Me or H})$  are the energies of the detached carbon nanocluster and the group of terminating atoms, whose geometries are taken from the above relaxed system;  $N(\text{Me or H})$  is the number of metallic or hydrogen atoms involved in the termination.

The results of this comparison are summarized in Table 2. The analysis shows that hydrogen atoms have a maximal adhesion to diamond-like carbon nanoclusters. It seems that such large values of the adhesion energy (4–6 eV) can prevent the diamond-like nanoclusters from subsequent growth at low temperatures. On the other hand, the adhesion energies of metals are lower than 1.5 eV. Therefore, additional carbon atoms can easily substitute the metallic atoms at the carbon cluster border, and the growth of a diamond-like particle may go on.

Table 2. The adhesion energy (eV) for various atoms.

	H	Li	K	Cu	Ag	Au
$C_5$	-6.35	-1.32	-0.35	-1.30	-0.62	-1.29
$C_8$	-3.99	1.31	-0.59	-1.24	-0.92	-1.04

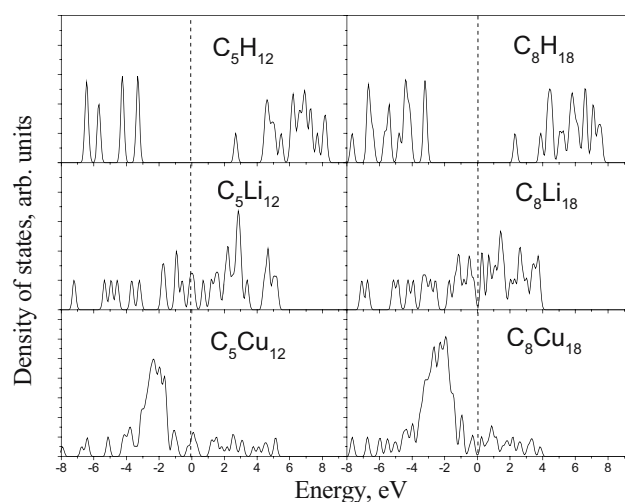


Figure 2. The densities of states in carbon nanoclusters terminated by H, Li or Cu. Vertical dotted lines are the Fermi level.

One of the key characteristics of diamond is its forbidden band gap. In bulk materials, the observation of the band gap may be taken as a sign of the presence of the diamond phase. So I have compared the electronic structure of carbon clusters terminated by hydrogen and by various metals. The densities of states for the H, Li and Cu terminations are presented in Figure 2. One can see that the potassium case is quite similar to the Li case, while the Ag and Au cases are similar to the Cu one. It is only the hydrogen termination that leads to the insulator-type forbidden band gap. All of the metal-terminated systems have non-zero densities of states at the Fermi



level. The reason is that the average distance between the terminating atoms is about 3 Å. This value is quite close to the interatomic distances in bulk metals but much larger than the H-H distance in an H<sub>2</sub> molecule. Therefore, the Li or Cu (as well as K, Ag or Au) wave functions cross over rather well and the metal-like states are formed, but the H wave functions remain localized and saturate the carbon covalent bonds. Clearly, the zero forbidden gap should not be regarded as an unambiguous evidence for the absence of a diamond-like phase when carbon nanoclusters are grown in the presence of a metal.

#### 4. DIAMOND EPITAXY ON A COPPER SURFACE

Thin diamond films have been grown on nondiamond substrates by a number of techniques. Nondiamond substrates can be classified into two large categories: (1) carbide-forming materials and (2) materials with no affinity for carbon. Copper seems to be a promising candidate for a substrate material in the epitaxy growth of diamond films. First, its lattice parameter (3.608 Å) is similar to that of diamond (3.567 Å). Second, it has no carbon affinity. There has been much experimental work on this subject [2–10] with the major result that diamond crystallites grown on polycrystalline copper may be as thick as 20 µm with the preferable orientation of <111>. To our knowledge, however, there is still no theoretical support to such experiments.

The possibility of epitaxial diamond growth on a copper substrate has been studied for the Cu(100) and Cu(111) surfaces. I have simulated the initial epitaxy, from a monatomic deposition to 13-monolayer films. The (111) and (100) surfaces of Cu were five-layer slabs with the 2×2 surface unit cell separated by a 20 Å vacuum space, and only the first layer Cu atoms were relaxed. I used a dipole correction [19] to avoid an artificial electrostatic dipole field, which arises from the slab asymmetry, and the (0.25;0.25;0.00) point for the *k*-space integrations, whereas the gamma point was employed in bulk computations.

In order to compare the energetic preferences of different carbon phases and carbon-copper systems, I found the mean cohesive energy per carbon atom,  $E_{\text{coh}}(\text{mean})$ :

$$E_{\text{coh}}(\text{mean}) = E(C_a) - \frac{E(\text{Cu}-\text{C}) - E(\text{slab})}{N_C},$$

where  $E(\text{Cu}-\text{C})$  is the energy of the Cu-C system consisting of a Cu-slab and  $N_C$  atoms of carbon;  $E(\text{slab})$  is the energy of the Cu slab;  $E(C_a)$  is the energy

of an isolated C atom. For comparison, I calculated the cohesive energies of bulk graphite and diamond: 8.74 eV and 8.55 eV, respectively. These values overestimate the experimental data of 7.37 eV for graphite and 7.35 eV for diamond [20]. This is a usual overestimation of DFT LDA and GGA computations for carbon materials [21–24]. The calculated C-C bond distances are 1.43 Å for graphite and 1.55 Å for diamond, with the respective experimental values of 1.42 Å and 1.53 Å.

The mean cohesive energy  $E_{\text{coh}}(\text{mean})$  includes deposits from the internal, surface and interface carbon atoms. Obviously, the internal bonds must be more like the bulk bonds than like any others. In order to compare the C-C bonding in the internal atomic layers of an epitaxial film and that in bulk diamond, I calculated the internal cohesive energy  $E_{\text{coh}}(\text{internal})$ , using the following expression:

$$E_{\text{coh}}(\text{internal}) = \frac{E(\text{Cu}-\text{C})_L - E(\text{Cu}-\text{C})_{L+2} + 2 \times N_{\text{C}}(\text{layer}) \times E_{\text{C}}}{2 \times N_{\text{C}}(\text{layer})},$$

where  $N_{\text{C}}(\text{layer})$  is the number of carbon atoms in a monatomic layer.

## 5. EPITAXIAL DIAMOND FILMS

To study the geometry and the energy characteristics of epitaxial diamond growth on copper surfaces, I constructed  $L$ -monolayer diamond films ( $L$  was varied from 2 to 13) contacting the Cu(100) and Cu(111) surfaces, respectively (Figures 3 and 4). In the (111) case, the atoms of the bottom C layer occupied the  $T_3$  positions, whereas in the (100) case they were positioned at the  $T_2$  bridge sites. It was found that all the films preserved their diamond-like atomic geometry with the tetrahedral bonding, and their surface reconstructions and relaxations were similar to those of free diamond surfaces. The surface of the (100) film was dimerized, and the dimer length was 1.38–1.41 Å, a value close to 1.37 Å obtained for the bulk diamond (100)- $2 \times 1$  surface by the LDA [25] and quasi-particle [26] computations. As for the (111) relaxed surface, I found the C-C distance  $d(\text{C}-\text{C})_{12}$  to be 1.50–1.51 Å and the undersurface C-C distance  $d(\text{C}-\text{C})_{23}$  to be 1.70–1.72 Å, which are close to the values of 1.46 Å and 1.68 Å reported by Kern *et al.* [25] for the bulk diamond (111) surface. Detailed results on the interatomic distances and tetragonal angles  $\theta$  are presented in Tables 3 and 4. One can see that the geometry of diamond films is in reasonable agreement with that of bulk diamond, especially in the (111) case.

Table 3. The geometrical parameters of the C(100)/Cu(100) epitaxial system.

The number of carbon atomic layers, L	2	4	6	8	10	12
$d(\text{C-Cu})$ , Å	1.90	1.95	1.95	1.94	1.94	1.94
$d(\text{C-C})_{\text{inside}}$ , Å	—	1.56	1.58	1.57	1.56	1.56
$d(\text{C-C})_{\text{dimer}}$ , Å	1.41	1.40	1.39	1.38	1.38	1.38
$\theta$ , degree	—	122.0	112.3	110.1	109.8	109.7

Table 4. The geometrical parameters of the C(111)/Cu(111) epitaxial system.

The number of carbon atomic layers, L	3	5	7	9	11	13
$d(\text{C-Cu})$ , Å	1.94	1.97	1.95	1.94	1.94	1.94
$d(\text{C-C})_{\text{inside}}$ , Å	—	1.57	1.56	1.56	1.55	1.55
$d(\text{C-C})_{12}$ , Å	1.50	1.50	1.50	1.51	1.51	1.50
$d(\text{C-C})_{23}$ , Å	1.55	1.72	1.71	1.70	1.70	1.70
$\theta$ , degree	104.2	109.6	109.4	110.2	109.9	109.6

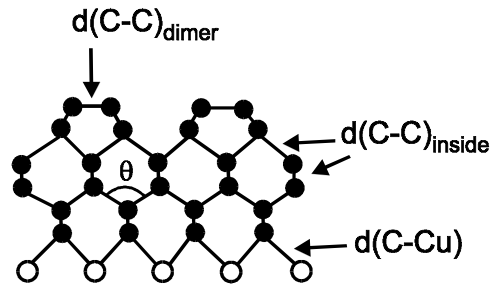


Figure 3. A schematic atomic structure of an epitaxial diamond film on the Cu(100) surface.

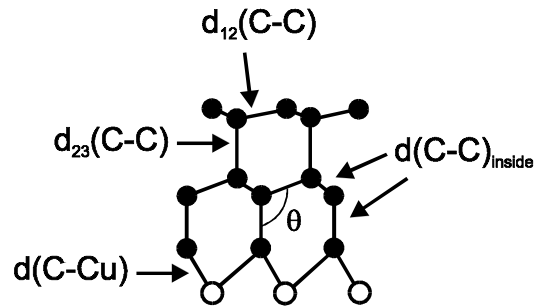


Figure 4. A schematic atomic structure of an epitaxial diamond film on the Cu(111) surface.

The calculated cohesive energies  $E_{\text{coh}}(\text{mean})$  and  $E_{\text{coh}}(\text{internal})$  for C(100) and C(111) films grown on the Cu(100) and Cu(111) surfaces are plotted in Figure 5. One can see that  $E_{\text{coh}}(\text{internal})$  tends to the calculated cohesive energy for diamond (8.55 eV) much better than  $E_{\text{coh}}(\text{mean})$ .

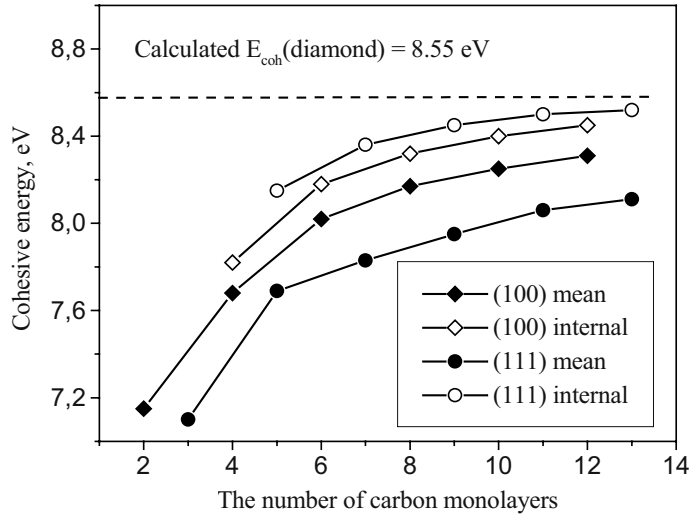


Figure 5. The cohesive energy (mean and internal) for C(100) and C(111) epitaxial films as a function of the number of carbon monolayers.

To study the stability of the film-substrate bonding, I have calculated the film-substrate adhesion energy  $E_{\text{adh}}$ :

$$E_{\text{adh}} = \frac{E(\text{Cu} - \text{C}) - [E(\text{slab})_{\text{frozen}} + E(\text{film})_{\text{frozen}}]}{N_{\text{C}}(\text{interface})},$$

where  $N_{\text{C}}(\text{interface})$  is the number of the interface carbon atoms. The energies of the separated Cu slab ( $E(\text{slab})_{\text{frozen}}$ ) and of the C film ( $E(\text{film})_{\text{frozen}}$ ) were found for the same atomic geometries as in the respective carbon/copper systems.

The  $E_{\text{adh}}$  values characterize the bonding between the carbon film and the copper substrate when they are in contact. However, if we want to understand the energetics of the film-substrate separation, we need to take into account the film and slab relaxations after the separation. The energy difference (per interface atom) between the epitaxial carbon-copper system and the relaxed separated carbon film and the relaxed copper slab can be termed the *separation energy*  $E_{\text{sep}}$ :

$$E_{\text{sep}} = \frac{E(\text{Cu} - \text{C}) - [E(\text{slab})_{\text{relaxed}} + E(\text{film})_{\text{relaxed}}]}{N_{\text{C}}(\text{interface})}$$

It should be emphasized that the positive values of  $E_{\text{sep}}$  correspond to the energetic advantage of the diamond film for the separation from the copper substrate.

The variation of  $E_{\text{adh}}$  and  $E_{\text{sep}}$  with the number of carbon monolayers is plotted in Figure 6 for both C(100)/Cu(100) and C(111)/Cu(111) systems. One can see that the absolute energy of the diamond film bonding to the copper substrate ( $E_{\text{adh}}$ ) increases with the film thickness and tends to the value of  $-2.55$  eV for the C(100) films and  $-2.0$  eV for the C(111) films. However, the stability of the film-substrate system characterized by  $E_{\text{sep}}$  is not such a simple matter. Figure 6 demonstrates that diamond layers thicker than 8 ML are unstable on the Cu(100) substrate ( $E_{\text{sep}} > 0$ ), i.e., thick diamond films cannot grow on this surface. But the films formed on the Cu(111) surface show a tendency for stability when their thickness exceeds 9 monolayers ( $E_{\text{sep}} < 0$ ). These results are consistent with the experimental data of [9,10] showing that diamond microcrystallites grown on copper polycrystalline substrates largely have the (111) orientation.

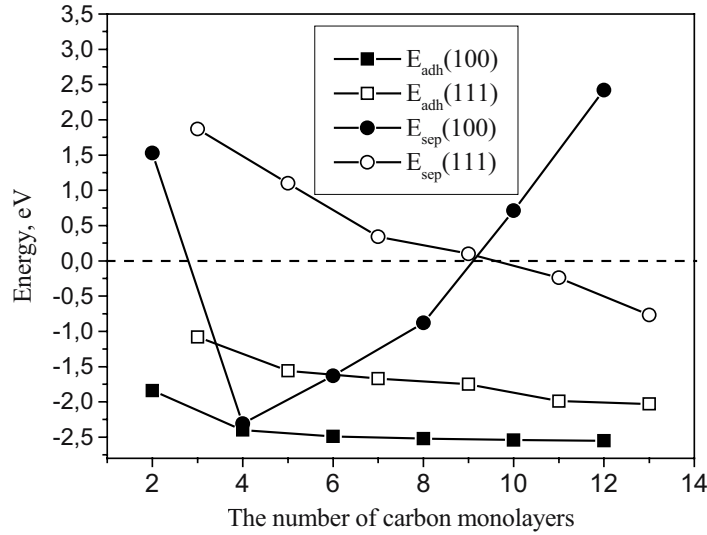


Figure 6. The adhesion and separation energies of epitaxial diamond films grown on Cu(100) and Cu(111) substrates.

## 6. SUMMARY

Our computations have shown that copper atoms can stabilize the diamond-like geometry of carbon ultrananoclusters even better than the terminating hydrogen atoms. Each copper atom terminates one covalent bond of the edge atom in a carbon cluster. The Cu-C bonding is much weaker than the H-C bonding; therefore, additional carbon atoms can easily substitute the Cu atoms, and the growth of a diamond-like particle may go on at low temperatures.

*Ab initio* calculations show that epitaxial diamond films can be grown on copper substrates with geometrical parameters similar to those of bulk diamond. The mean cohesive energy of the C(100) films is larger than that of the C(111) films, but the former are more stable to the separation from the copper substrate. This fact explains why the preferable orientation of diamond microcrystallites on copper is the  $\langle 111 \rangle$  direction.

This work was supported by the Fundamental Research Program of the Russian Academy of Sciences ("Fundamental Problems of Physics and Chemistry for Nanosized systems and Nanomaterials", 2004) and by the Ministry of Education of the Russian Federation (Grant # 16-11, 2003-2004).

## REFERENCES

1. V.I. Ivanov-Omsky and S.G. Yastrebov. The copper induced formation of diamonds in amorphous carbon. *Physics of the Solid State* **41**, 1711-14 (1999).
2. M.L. Hartsell and L.S. Plano. Growth of diamond films on copper. *J. Mater. Res.* **9**, 921-26 (1994).
3. J. Narayan, V.P. Godbole, G. Matera, and R.K. Singh. Enhancement of nucleation and adhesion of diamond films on copper, stainless steel, and silicon substrates. *J. Appl. Phys.* **71**, 966-79 (1992).
4. T.P. Ong, F. Xiong, R.P.H. Chang, and C.W. White. Nucleation and growth of diamond on carbon-implanted single crystal copper surfaces. *J. Mater. Res.* **7**, 2429-39 (1992).
5. R. Ramesham, F.M. Rose, and A. Allerman. Selective diamond seed deposition using electroplated copper. *Diamond Relat. Mater.* **1**, 907-10 (1992).
6. S.I. Ojika, S. Yamashita, K. Kataoka, and T. Ishikara. Diamond grain growth on Cu substrate. *Jpn. J. Appl. Phys.* **32**(Part 2), L1681-87 (1993).
7. S.D. Wolter, B.R. Stoner, and J.T. Glass. The effect of substrate material on bias-enhanced diamond nucleation. *Diamond Relat. Mater.* **3**, 1188-95 (1994).
8. Q.H. Fan, J. Gracio, and E. Pereira. Free-standing diamond film preparation using copper substrate. *Diamond Relat. Mater.* **6**, 422-25 (1997).
9. M. Sommer, R. Haubner, and B. Lux. Diamond deposition on copper treated hardmetal substrates. *Diamond Relat. Mater.* **9**, 351-57 (2000).
10. N. Ali, Q.H. Fan, W. Ahmed, I.U. Hassan, C.A. Rego, and I.P. O'Hare. Role of surface pre-treatment in the CVD of diamond films on copper. *Thin Solid Films* **355-356**, 162-66 (1999).

11. A.E. Aleksensky, M.V. Baidakova, A.Ya. Vul', A.T. Dideikin, V.I. Siklitsky, and S.P. Vul'. Effect of hydrogen on the structure of ultradisperse diamond. *Physics of the Solid State* **42**, 1575-78 (2000).
12. A.P. Kuz'menko, M.P. Leonov, B.A. Groshev, A.V. Kaminsky, and V.G. Zavodinsky. Effect of voltage arising in the copper - ultra dispersed graphite system formed by electrochemical method. Proceedings of the X APAM Topical Seminar and III Conference "Materials of Siberia: Nanoscience and Technology", 2003 June 2-6, pp. 324-25; Novosibirsk, Russia: Siberian Branch of the Russian Academy of Sciences, 2003.
13. A.P. Kuz'menko, V.G. Zavodinsky, A.V. Siarg, M.P. Leonov, V.I. Savchenko, V.A. Groshev, A.V. Kaminsky, E.S. Astapova, and E.B. Pivchenko. Voltage arising in the copper - graphite system formed by electrochemical method. *Zhurnal Strukturnoy Khimii*, in press (in Russian).
14. M. Bockstedte, A. Kley, J. Neugebauer, and M. Scheffler. Density-functional theory calculations for poly-atomic systems: electronic structure, static and elastic properties and *ab initio* molecular dynamics. *Comp. Phys. Commun.* **107**, 187-22 (1997).
15. J.P. Perdew and Y. Wang. Accurate and simple density functional for the electronic exchange energy: Generalized gradient approximation. *Phys. Rev. B* **33**, 8800-02 (1986); J.P. Perdew, J.A. Chevary, S.H. Vosko, K.A. Jackson, M.R. Pederson, D.J. Singh, and C. Fiolhais. Atoms, molecules, solids, and surfaces: Applications of the generalized gradient approximation for exchange and correlation. *Phys. Rev. B* **46**, 6671-87 (1992).
16. N. Troullier and J.L. Martins. Efficient pseudopotentials for plane-wave calculations. *Phys. Rev. B* **43**, 1993-2006 (1991).
17. M. Fuchs and M. Scheffler. Ab initio pseudopotentials for electronic structure calculations of poly-atomic systems using density-functional theory. *Comp. Phys. Commun.* **119**, 67-98 (1999).
18. M.W. Schmidt, K.K. Baldridge, J.A. Boatz, S.T. Elbert, M.S. Gordon, J.H. Jensen, S. Koseki, N. Matsunaga, K.A. Nguyen, S.J. Su, T.L. Windus, M. Dupuis, and J.A. Montgomery. General atomic and molecular electronic structure system. *J. Comput. Chem.* **14**, 1347-63 (1993).
19. J. Neugebauer and M. Scheffler. Adsorbate-substrate and adsorbate-adsorbate interactions of Na and K adlayers on Al(111). *Phys. Rev.* **46**, 16067-80 (1992).
20. CRC Handbook of Chemistry and Physics 65<sup>th</sup> Edition, Weast, R. C., (Ed.) CRC Press, Inc., Boca Raton, 1984-1985, p. D58.
21. H.J.F. Jansen and A.F. Freeman. Structural and electronic properties of graphite via an all-electron total-energy local-density approach. *Phys. Rev. B* **35**, 8207-14 (1987).
22. L.H. Li and J.E. Lowther. Plane-wave pseudopotential calculations of intrinsic defects in diamond. *J. Phys. Chem. Solids* **58**, 1607-10 (1997).
23. B. Farid and R.J. Needs. Energies of atoms and solids within the local-density approximation. *Phys. Rev. B* **45**, 1067-73 (1992).
24. J. Chelikowsky and S.G. Louie. First-principles linear combination of atomic orbitals method for the cohesive and structural properties of solids: Application to diamond. *Phys. Rev. B* **29**, 3470-81 (1984).
25. G. Kern, G.J. Hafner, J. Futhmüller, and G. Kresse. (2x1) reconstruction and hydrogen-induced de-reconstruction of the diamond (100) and (111) surfaces. *Surf. Sci.* **352-354**, 745-49 (1996).
26. C. Kress, M. Fiedler, V.G. Schmidt, and F. Bechstedt. Quasi-particle band structure of C(111) 2x1 and C(100) 2x1 surfaces. *Surf. Sci.* **331-333**, 1152-56 (1995).

# 13

## THE FORMATION KINETICS OF DETONATION NANODIAMONDS

V.M. Titov<sup>1</sup>, B.P. Tolochko<sup>2</sup>, K.A. Ten<sup>1</sup>, L.A. Lukyanchikov<sup>1</sup>, and  
P.I. Zubkov<sup>1</sup>

<sup>1</sup> *Lavrentev Institute for Hydrodynamics SB RAS, 5 Lavrentev Av., Novosibirsk, 630090, Russia;*

<sup>2</sup> *Institute for Solid State Chemistry and Mechanochemistry SB RAS, 18 Kutateladze Av., Novosibirsk, 630128, Russia*

### Abstract:

We report experimental data on small angle X-ray scattering behind the detonation wave front in the high pressure zone, obtained using synchrotron radiation. A series of detonation experiments with ultradisperse diamond in oxygen and oxygen-free media have led us to the conclusion that diamond cannot be produced immediately behind the wave front. We believe that here there is a diamond-free zone and zones of diamond formation. Additional information on this region was derived from the electrical conductivity measurements. It was found that the time (as well as the site) of nanodiamond nucleation coincided with the beginning of unloading. The shock compression initiates the adamantan-diamond transition. These findings indicate that it is the C-H bonds, rather than the C-C bonds, which break up in the adamantan structure and that there is a fast diffusion of hydrogen through adamantan and explosives. A new model of detonation nanodiamond formation is suggested on the basis of our experimental results.

### Keywords:

nanodiamonds, SAXS, synchrotron radiation, conductivity, detonation, adamantan, shock wave, dynamic high pressure

## 1. INTRODUCTION

In order to understand the kinetics of ultrananocrystalline diamond (UNCD) formation, it is necessary to have information about the conditions in which UNCD is formed and its ambient. Naturally, we should know where the construction material for diamonds comes from and what conversions they undergo. It is also important to understand the mechanism, through which diamond is formed (Figure 1). There are still no exact



answers to these questions. In our experiments, we obtained data which can elucidate some of the principal aspects of the UNCD formation kinetics.

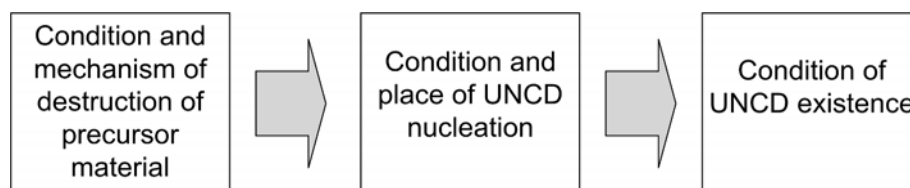


Figure 1. The idea underlying the UNCD nucleation and growth experiments.

## 2. *In situ* SAXS EXPERIMENT

The Synchrotron Radiation (SR) Small Angle X-ray Scattering (SAXS) technique was used to obtain data on UNCD nucleation and growth behind the detonation wave front. We reported earlier on SAXS signals detected during the explosion of different materials [1]. Here we describe SAXS experiments using a position-sensitive X-ray detector for imaging of explosion (DIMEX) [2] (Figure 2) and discuss the time variation of the SAXS signals during the explosion. The composite explosive trinitrotoluene–hexogen (TH) was used in the 50:50 ratio. The samples were cylindrical and had a diameter of 7, 12.5 and 19 mm. They were placed in an explosion chamber and exposed to a synchrotron radiation (beam line # 0-*b*) of a VEPP-3 storage ring in a single bunch mode at  $E = 2$  GeV,  $I = 150$  mA, and the wiggler field  $H = 2$  T. The experiments were performed at the Institute of Nuclear Physics (the Siberian Branch of the Russian Academy of Sciences).

The beam angle was varied from  $0.0068^\circ$  to  $0.84^\circ$  and the energy range used was 20–30 keV. The delay time of the first SAXS frame relative to the wave front was 1–500 ns and the subsequent frames had a 500 ns delay. The exposure time was 1 ns. The dynamics of the SAXS signal is shown in Figure 3. One can see that the signal intensity increases sharply and the curves become steeply inclined

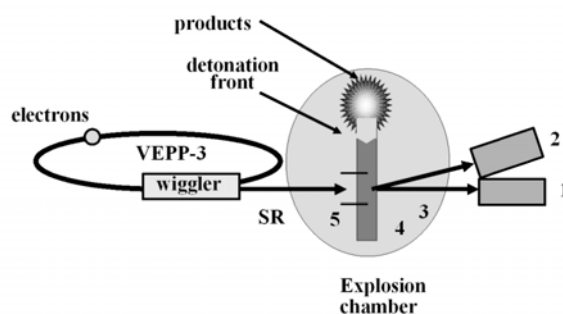


Figure 2. The setup for *in situ* SAXS experiments: 1- absorption detector, 2 - SAXS one-coordinate DIMEX detector, 3 - SR scattered and transmitted beams, 4 - explosive, 5 - wire contact detector for synchronization of DIMEX and explosion.

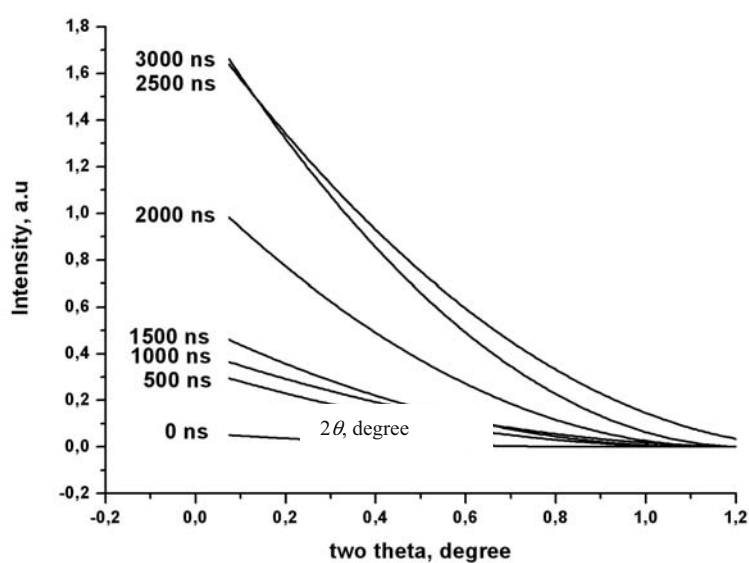


Figure 3. The time dependence of the SAXS signals behind the detonation wave front (trotyl-hexogen in 50:50 ratio, a 19 mm explosive charge). The increasing intensity indicates a growing amount of UNCD; the slopes give information about the average UNCD size.

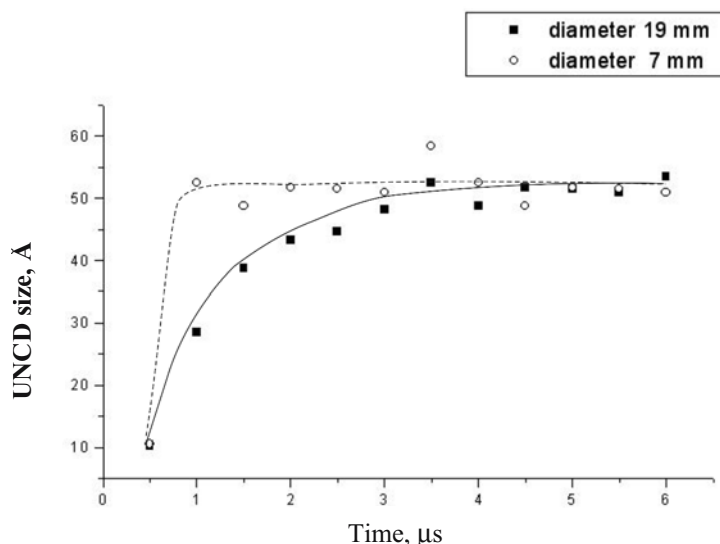


Figure 4. The formal kinetics (one dimensional model) of the UNCD size in the 7 and 19 mm explosive samples.

The SAXS data were processed using the Guinier formula [3]; the results of formal kinetics (from one dimensional model) are presented in Figure 4. It seems rather strange: (1) the average UNCD sizes were found to be the same (50 Å) after the explosion of charges with different diameters; (2) the 7 mm charge produced the 50 Å particles with a  $\sim 500$  ns delay relative to the wave front but the 19 mm charge gave the same size with a 3  $\mu$ s delay. Obviously, the real kinetic of UNCD grows is the same for explosives of all diameters. The formal kinetics may be corrected allowing for 3-dimensional geometric factor.

### 3. MODEL EXPERIMENTS

A series of model experiments were made reproducing the same pressure, temperature and the ambient characteristics, which actually exist behind the detonation wave front. The aim of the shock impact experiment was to try to understand in what ambient UNCD can exist and when it cannot exist at all. In the experiments with adamantan, we tried to follow the crystal structure dynamics and the behavior of different chemical bonds affected by the shock wave. The electrical conductivity was studied to get information about the

ion generation and annihilation behind the shock front and the electron scattering by the nucleated diamond.

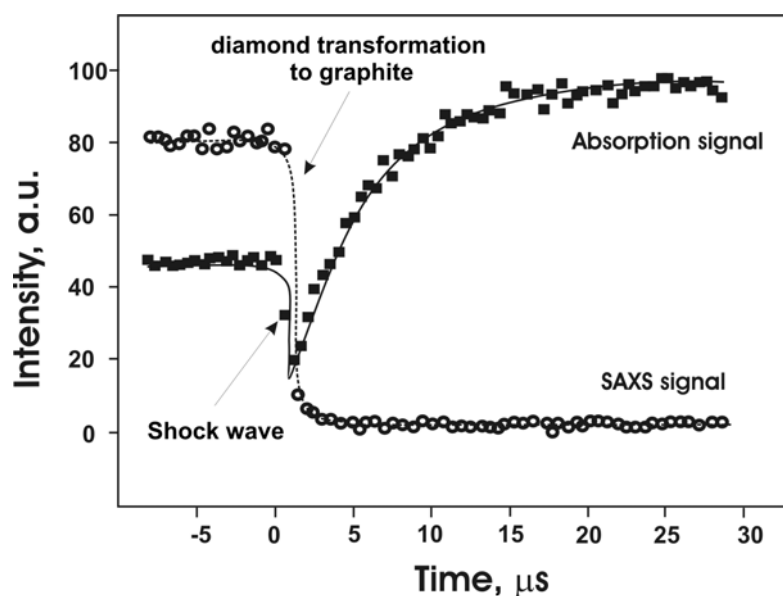


Figure 5. Fast decrease of the SAXS signal amplitude to zero at the moment the shock front reaches the UNCD powder.

### 3.1 Nanodiamond Behavior behind the Detonation Front

The UNCD powder was subjected to shock waves and detonation with the same parameters as in the 50:50 TH experiment for producing UNCD. The powder was placed in different ambient such air, water, benzene, and explosives (trinitrotoluene and others). The SAXS registration was made simultaneously with the absorption measurements. In air, we observed a fast decrease in the SAXS signal amplitude, which turned to zero when the shock front reached the UNCD powder (Figure 5). In water, the time behavior of the SAXS signal was quite different: it did not change at the moment the wave front reached the powder. When the experimental medium was benzene or explosives, the time dependence of the SAXS signal was more complicated: its amplitude first decreased and then increased, and the degree of this change varied with the oxygen–carbon ratio. We think that if diamonds had nucleated immediately behind the wave front, they would have burned down in the oxygen evaporated from the explosives.

These data indicate that UNCD cannot be formed until all the oxygen contained in the explosives is used up by the chemical reactions. The estimation from the conductivity measurements shows that this time is about 100 ns.

### 3.2 Measurements of Electroconductivity

The electrical conductivity was measured during the explosion of trinitrotoluene and other explosives used for UNCD production. Such experiments helped us to understand the processes of decomposition of explosives and nucleation of the solid phase. Immediately behind the detonation front, conductivity is growing rapidly in all explosives (Figure 6).

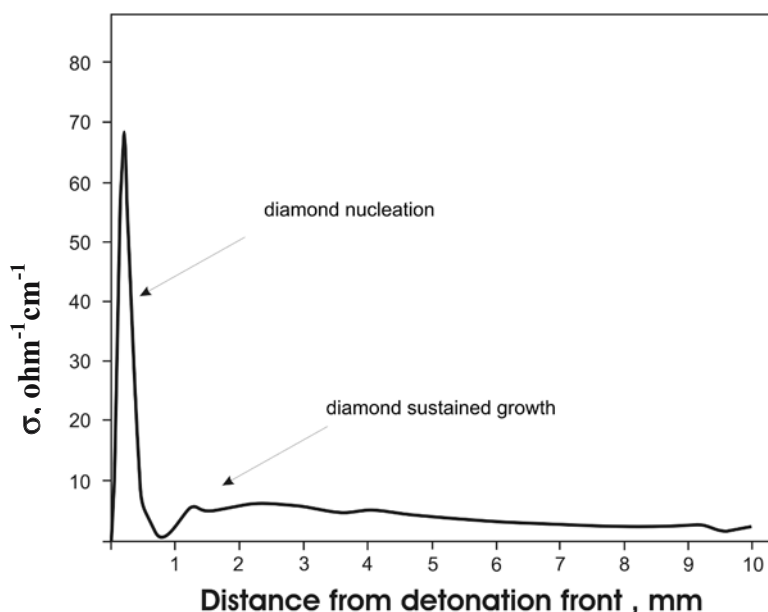


Figure 6. The electrical conductivity of TNT behind the shock front.

The conductivity may be ionic or electronic. The conductivity increase may be due to the effect of the shock wave and the heat on the explosives. As a result, the explosive is decomposed producing a lot of hydrogen, oxygen, nitrogen and carbon ions. The conductivity peak practically disappears in 500 ns due to the reduction in the concentration of charge carriers which are utilized to form the reaction products. However, no solid

particles are produced; instead, there are neutral molecules and individual atoms. This conclusion is based on the fact that the electron wavelength is much larger than the size of a molecule. Therefore, the electrons cannot be scattered by the molecules and the resistance does not rise.

The situation changes radically when solid nanoparticles are formed with a size exceeding the electron wavelength. The electrons are scattered intensively by the particles, leading to a sharp reduction in the electrical conductivity. The most amazing thing is that this happens at the moment of unloading, independent of the explosive sample diameter.

### **3.3 Shock Compression of Adamantane**

Adamantane [4] is a tricyclic bridge hydrocarbon with composition  $C_{10}H_{16}$ . This molecule is hard but not stressed. It includes three condensed cyclohexane rings in conformation of the chair and possesses a high symmetry. The chair conformation is the conformation with the lowest energy, and is therefore the most stable conformation. The carbon skeleton of adamantane at a temperature of 20°C has a face-centered cubic lattice, similar to diamond one.

A shock compression of adamantane gives rise to UNCD particles. We observed an amazing thing: the compression did not change the shape of the initial adamantane particles, but their chemical composition was changed - adamantane transformed to diamond. The degree of transformation to diamond in a crystal was close to 30% (Figure 7, 8).

The diamond produced in this way represents a conglomerate of UNCD particles with their number close to several thousands. However, only a small fraction of an adamantane single crystal is generally transformed to UNCD. The UNCD conglomerate is surrounded by conglomerates of graphite and amorphous carbon.

What is the mechanism of the adamantane--diamond transition? It is generally believed that UNCD particles are produced from the carbon contained in individual particles of the reagents (explosives), as shown in experiments with isotope exchange [5]. Probably, this is not true of adamantane, because carbon atoms do not migrate from one crystal to another. Therefore, the phase transition occurs only within the carbon skeleton, and hydrogen atoms are the only atoms that leave the crystal intensively during the detonation shock.

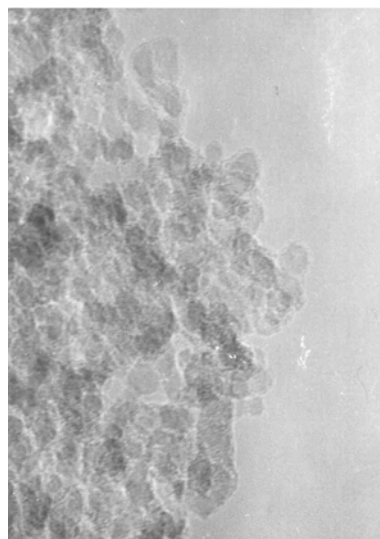


Figure 7. The UNCD conglomerate in the adamantane crystal after the shock compression.



Figure 8. The electron diffraction pattern of the UNCD conglomerate in the adamantane crystal.

One can conclude from these data that the C-H bonds are the first to be broken by the shock and then the breaking of the C-C bonds occurs. This statement contradicts the conclusion drawn by the authors of the work [6]. During the destruction of adamantane, the hydrogen ions begin to diffuse (Figure 9).

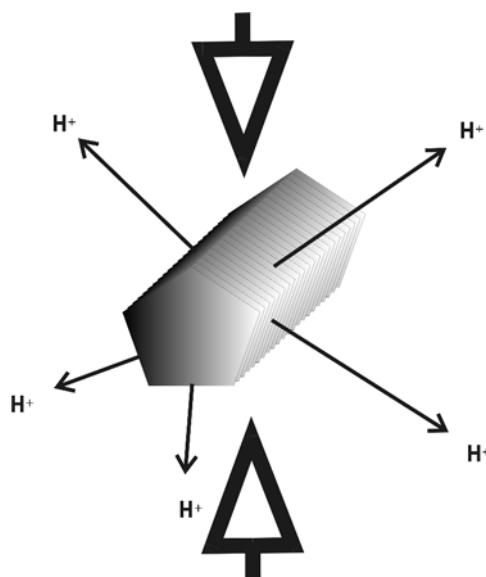


Figure 9. Schematic shock compression of adamantane and H ion behavior

The diffusion was measured in the electroconductivity experiments. Hydrogen ions diffuse through the adamantane single crystal, trying to leave it. The high pressure of hydrogen gas that arises in the micro porous and defects destroys the crystal into small fragments.

#### 4. RESULTS AND DISCUSSION

The principal findings from our experiments are as follows. First, we have found that the electroconductivity behaves nonmonotonically behind the shock front. Second, the size of the UNCD particles is independent of the diameter of the explosive charge. Third, there is no small angle X-ray scattering from large particles during the first nanoseconds after the passage of the shock front.

These data contradict the conclusion of some researchers [5] that diamonds are nucleated immediately behind the detonation front in a short time of about 100 ns. Our estimations show that diamonds appear along the axis of a 19 mm explosive charge (Figure 10, direction 3) only two microseconds later.



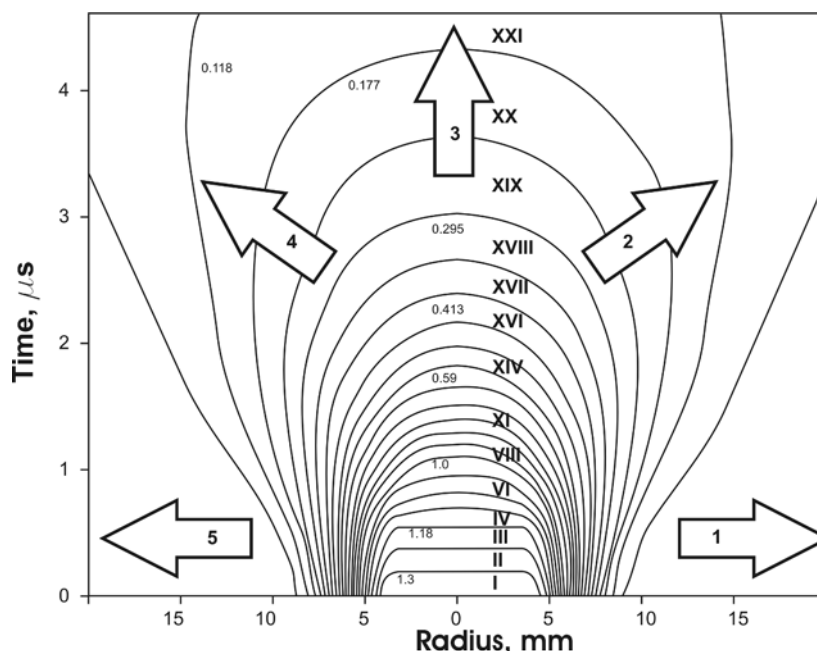


Figure 10. The distribution of the density zones behind the detonation wave front. The arrows are shows the directions of carbon atoms movement.

Our experimental observations with using formal kinetic also show that the UNCD particle size in 19 mm explosive samples increases monotonically, while their size in 7 mm explosives increases abruptly, for 500 ns. We observed no SAXS signal immediately behind the wave front. The electrical conductivity in this region is found to be high.

These findings indicate the existence of a diamond-free zone immediately behind the wave front. This does not exclude a possible formation of a diamond core of less than 10 Å in size, which does not scatter the conductivity electrons. From these conclusions, we have constructed a model of UNCD formation during the explosion. The model uses a cylindrical symmetry of the explosives and can be described only in a three-dimensional space. We use a 3D distribution of the product mass density behind the shock front, measured experimentally (Figure 10).

Analyzing the map of the mass density of the explosion products behind the detonation wave front, it is reasonable to assume that the directions of the mass flow in laboratory system coincide with the density gradient vector. One can choose arbitrarily 5 directions of the density gradient vector, while in reality the density gradient changes continuously from the first to the fifth vector.

The experimental data allow one to draw a mass density map and to divide it arbitrarily into zones of equal densities with some lines. Obviously, during the explosion the matter moving along the density gradient vector crosses the zone boundaries. It is also clear that all the processes involving the matter have several stages of transformation, and each stage can coincide with one of the zones being passed by the material at a particular moment of time. Our model assumes that there is compressed hot plasma consisting of various ions and fragments of the initial explosive material in density zones I and II. One might conclude from thermodynamic simulations that diamonds may be nucleated in these zones. Our data, however, show that if diamonds were nucleated, they would break up here.

The pressure, temperature and mass density decrease in zones III – VI, and there are conditions here for a steady growth and preservation of the nucleated diamonds. The arrows (Figure 10) show the directions of carbon atoms movement. When carbon atoms reach zone III (in all directions) the UNCD sustained nucleation process starts, but the start time for each direction is different. For directions denoted I, V the start time is equal 500 ns and it is equal 3000 ns for direction III. This is a main reason for smoothing of the real sharp kinetics to smooth one for explosive with 19 mm diameter. The kinetic for each direction approximately is the same as for explosive with diameter 7 mm (Figure 4).

## **5. CONCLUSION**

Synchrotron radiation is a powerful tool for the study of fast processes such as the production of UNCD by the explosion method. We have used this technique to obtain data on small angle X-ray scattering in the high pressure zone behind the detonation wave front. The experiments with ultradisperse diamond were varied out in oxygen and oxygen-free atmospheres. Our findings show that nanodiamonds cannot be nucleated immediately behind the shock front. The electroconductivity measurements were used to evaluate the nucleation time, which coincided with the unloading time. We observed the adamantane - diamond transition under the shock compression and made the conclusion about the breakup of the C-H bonds, rather than the C-C bonds, in the adamantane structure. Hydrogen is suggested to diffuse fast through adamantane. Our data also indicate that there is a diamond-free zone and zones of diamond formation behind the wave front. We have obtained data on the dynamics of the size distribution of diamond throughout the zone of detonation products.

## Acknowledgments

This work was supported by RFBR Grants # 02-03-32837, 03-03-32376, and 04-02-16903.

We would like to express special thanks to the staff of the Budker Institute of Nuclear Physics and Institute of Solid State Chemistry and Mechanochemistry (Novosibirsk, Russia): G.N.Kulipanov, V.M.Aulchenko, V.V.Zhulanov, L.I.Shekhtman, M.A.Sheromov, S.I.Mishnev, I.L.Zhagin, O.V.Evdokov, B.B.Bokhonov, M.R.Sharafutdinov for the help during experiments preparation and for discussion.

## REFERENCES

1. A.N. Aleshaev, P.I. Zubkov, G.N. Kulipanov et al. Application of Synchrotron Radiation for Studying Detonation and Shock-Wave Processes. *Combustion, Explosion and Shock Waves* **37**, 585-93 (2001).
2. V. Aulchenko, P. Papushev, S. Ponamarev, L. Shekhtman, and V. Zhulanov. Development of a one-dimensional detector for the study of explosion with a synchrotron radiation beam. *J. Synchrotron Radiation* **10**, 361-65 (2003).
3. A. Guinier. Small-angle Scattering. In: *International Tables for X-ray Crystallography*. Birmingham: The Kynoch Press. **3**, 324-30 (1968).
4. V.M. Titov, V.F. Anisichkin, and I.Yu. Malkov. Study of the process of synthesis of the ultra dispersed diamond in detonation waves. *Physics of Combustion and Explosion* **35**, 117-26 (1989).
5. A.N. Dremin, S.D. Savrov, V.C. Trofimov, and K.K. Shvedov. *The detonation waves in condense matters*. Moscow: Nauka, p. 392 (1970) (in Russian).
6. A.P. Ershov. Simulation of synchrotron diagnostics of explosion. *Technical Physics Letters*, **27**, 841-43 (2001).

# 14

## NANOCARBON PHASE DIAGRAM AND CONDITIONS FOR DETONATION NANODIAMOND FORMATION

V.V. Danilenko

*Joint Stock Company "ALIT", Kiev, 03067, Ukraine*

**Abstract:** To analyse the process of detonation nanodiamond (UDD) synthesis, the positions of the melting and phase equilibrium curves in the carbon phase diagram were calculated for UDD particles of 1–10 nm in size. We also found the position of a set of triple points in the ranges of  $P = 13.5\text{--}16.5$  GPa and  $T = 2210\text{--}4470$  K. This set of points indicates the area of liquid nanocarbon. The diamond area in the phase diagram was subdivided into three regions, depending on the nature of the nanoparticles: UDD and diamond, liquid nanocarbon, and amorphous nanoparticles. The  $C\text{--}J$  parameters of explosives used in the UDD synthesis are found to lie within the liquid nanocarbon region. Therefore, the reaction zone of the detonation wave is the site of formation of carbon nanodroplets, which then crystallize to form UDD particles along a segment of the isotropic line of the detonation product spreading through the UDD area at  $P = 16\text{--}10$  GPa and  $T = 3400\text{--}2900$  K. The curve for the detonation rate vs. the density of the explosive charge exhibits breaks that can be interpreted as being due to the onset and termination of nanocarbon melting rather than to UDD formation in the reaction zone.

**Keywords:** detonation nanodiamond, nanocarbon, nanoparticles, melting, thermodynamic balance, phase diagram, detonation wave, Chapman – Jouguet, non-ideal detonation, explosive charge, detonation soot, graphitization

### 1. INTRODUCTION

The process of carbon condensation during the detonation of an explosive with a negative oxygen balance is still poorly understood. The major reasons are the high temperatures and pressures, a short duration and an extremely nonequilibrium nature of the process, as well as the inapplicability of

conventional steady state, equilibrium models using an equation of state. The condensation characteristics are largely manifested in the final result, namely, as the formation of nanodiamond or ultradisperse diamond (UDD) [1–7]. It is generally believed that UDD is produced in the chemical reaction zone of the detonation wave [4,8,9,11,12]. This conclusion is based on the following observations.

1. The phase diagram for carbon shows that the pressure and temperature of the Chapman-Jouguet plane (further, the  $C-J$  parameters) lie in the diamond region.
2. The time for UDD formation found from the variation in the electrical conductivity of the detonation products (DP) is about  $0.5 \mu\text{s}$  [10], that value agrees with the chemical reaction time [4].
3. The particle size is independent of the mass of the explosive charge or the time of the chemical reaction [4]. This was concluded from experimental data on explosion of charges of 0.1–1 kg only.
4. For explosives with a negative oxygen balance, the experimental curve for the detonation rate vs. the charge density,  $D(\rho)$ , has breaks that can be attributed to the formation of diamond at densities above  $1.3\text{--}1.55 \text{ g/cm}^3$  and of graphite at lower densities [11,12].

However, each of these statements can be questioned or refuted with the following arguments.

1. The electrical conductivity of DP may vary not only due to UDD formation but also to the transformation of soot to liquid carbon in the reaction zone. The correlation between the conductivity variation with density, as well as with the DP temperature and carbon concentration in the DP, is appreciable [12].
2. The measured time of the DP conductivity variation is 2–5 times greater than the reaction time in high density charges [13]. We produced UDD by detonation of the explosives HMX/TNT 70/30 and HMX/TNT 90/10 with the reaction time of  $0.07 \mu\text{s}$  and the reaction zone width of  $0.37 \text{ mm}$  [13]. It is very unlikely that carbon, which is condensed during the reaction, could crystallize for a time shorter than  $0.1 \mu\text{s}$  in an explosive layer of  $< 0.5 \text{ mm}$  thick. Besides, the crystallization of clusters requires their cooling, which does not happen in the reaction zone.
3. The energy release goes on beyond the  $C-J$  plane; this is not due to the reaction termination but rather to the condition  $D = u + c$ , where  $D$  is the detonation rate,  $u$  is the mass, and  $c$  is the sound velocity [13]. The carbon coagulation and crystallization can occur along the isotropic line of the DP expansion. This is supported by our data on the effects of the charge mass and water shell on the UDD size [5]. For example, when the charge was

increased from 0.6 to 10 kg and a water shell was used, the specific surface of the particles was reduced by half, from 400 to 200 cm<sup>2</sup>/g [5].

4. The breaks in the  $D(p)$  curve may be due to the melting of carbon. Similar breaks were observed after a shock compression of chemically inactive materials [14]. The first break occurs at the melting start and the second one at its end. The liquid phase always shows a smoother  $D(p)$  curve, as is typical of all explosives with a negative oxygen balance [11,12].

The direct measurements of graphite temperature made under the conditions of a fast energy supply (for about 1.5  $\mu$ s, like under the detonation conditions) are quite interesting [15]. The  $T(E)$  curve ( $E$  is the input energy) shows clearly the melting onset (at 4800K) and its completion. The  $dT/dE$  slope is smoother for liquid carbon than for graphite, which may be accounted for by a greater calorific capacity of liquid.

5. In addition to the pressure and temperature, the phase diagrams for ultradisperse systems contain a third parameter - the particle size [16,17]. The surface energy of nanoparticles makes the phase diagram different from that for most single crystals. The boundaries of the liquid phase and thermodynamic equilibrium for polymorphic transformations are changed. It is known that the melting point of ultradisperse particles remarkably decreases for smaller particles, for example, by 25% for  $\sim 4$  nm particles [16,17]. So the available phase diagram for bulk carbon is unsuitable for the analysis of UDD production.

The effect of carbon dispersion due to detonation on the graphite-diamond transition was analyzed in [8,9]. The authors of [8] tried to understand how the phase diagram would change when the size and shape of diamond and graphite particles were varied. The estimated value of the transition pressure was found to agree with experiment data (18–20 GPa measured in [18,5]) and increased with the particle size. These calculations were made for prismatic diamond and graphite, whereas UDD particles are globular and are always covered with a shell of non-diamond carbon [19]. This requires a separate determination of the diamond and amorphous carbon (soot) interaction.

A fairly rough three-dimensional phase diagram was suggested for ultradisperse carbon in [20] but it is unsuitable for the analysis of UDD synthesis.

Interesting information was obtained from the simulation of molecular dynamics during the coagulation of carbon particles at high temperature and density in the reaction zone [21]. Particles of  $< 3$  nm in size interact in a way similar to liquid droplets. At constant temperature, the degree of melting of the particles is known to increase with decreasing of their size. The coagulation of nanoparticles goes on for 1 ns and results in a considerable

temperature rise ( $\Delta T = 4000 N^{-1/3}$ , where  $N$  is the number of atoms), which promotes melting.

A direct Monte-Carlo simulation [22] indicates that carbon is in the liquid state in the reaction zone and its melting point is related to the particle size. However, the authors do not present the initial computation parameters or the conditions for measuring the UDD melting points.

Earlier, we suggested a general scenario of UDD formation due to crystallization along the isotropic line of spread of liquid clusters produced in the reaction zone. Here, we substantiate this hypothesis with our calculations of the positions of UDD melting and thermodynamic equilibrium curves in the carbon phase diagram with a detailed analysis of the pressure-temperature conditions in the detonation wave.

## 2. UDD MELTING

Depending on the particle size  $d$ , the melting temperature  $T_d$  can be found from the expression [16]

$$T_d / T_\infty = T' = 1 - 6 \sigma_{s-f} v_f / \lambda_d d, \quad (1)$$

where  $T_\infty$  is the melting point of a single bulk crystal,  $\lambda_d$  is the melting heat,  $v_f$  is the specific volume of the liquid phase, and  $\sigma_{s-f}$  is the surface energy of the solid-liquid interface.

Let us estimate these quantities for diamond, using the following parameters of a triple point:  $P = 13.5$  GPa,  $T_\infty = 4470$ K, the slope of the melting curve  $10.2$  K/GPa [23],  $v_d = 0.295$  cm<sup>3</sup>/g (see Table 1),  $v_f = 0.311$  cm<sup>3</sup>/g [24], and  $\Delta v = v_f - v_d = 0.016$  cm<sup>3</sup>/g. To find  $\sigma_{s-f}$ , we used an expression from [25]:

$$\sigma_{s-f} = 2 (v_f - v_s) \sigma_s / 3 v_f \quad (2)$$

For octahedral diamond facets,  $\sigma_d$  was found in [26] to be  $5 \cdot 10^{-4}$  J/cm<sup>2</sup> at 3000K. Taking  $\sigma_d$  and  $v_f - v_s$  to be constant, we get  $\sigma_{s-f} = 0.172 \cdot 10^{-4}$  J/cm<sup>2</sup>.

Table 1. Melting points of UDD particles ( $P = 20$  GPa).

$d$ , nm	1.0	1.2	1.5	2	3	4	6	$\infty$
$T_d$ , K	2270	3190	3580	3870	4120	4230	4340	4536
$T_d / T_\infty$	0.50	0.70	0.79	0.85	0.91	0.93	0.95	1.00

The melting heat is  $\lambda = T\Delta S$ , where  $\Delta S$  is the entropy change during the melting. The value of  $\Delta S = 1.6$  J/g K can be found from the triple point parameters, using the Clausius- Clapeyron formula. So for the triple point we get  $\lambda_{\infty} = 7.2$  kJ/g. For comparison, we give some parameters of graphite melting ( $T = 4800$ K,  $P = 1$  GPa [15]):  $\Delta S = 2.08$  J/gK,  $v_f - v_s = 0.028$  cm<sup>3</sup>/g and  $\lambda_{\infty} = 10$  kJ/g.

After the transformation of Eq. (1)

$$T' = 1 - 4 \sigma_d \Delta v / (\Delta S T' T_{\infty} d),$$

we get

$$T' = 0.5 + (0.25 - 4 \sigma_d \Delta v / \Delta S T_{\infty} d)^{0.5} \quad (3).$$

Therefore, there is a minimum particle size  $d_{\min}$ , for which  $T_{\min} = 0.5$ :

$$d_{\min} = 16 \sigma_d \Delta v / \Delta S^* (1/T_{\infty})$$

For UDD, we have

$$d_{\min} = 17.9 \Delta v / \Delta S \quad (4).$$

The experimental minimum size of a UDD particle was found to be 1.8 nm [4].

We take into account that every UDD particle is covered with a shell of amorphous carbon of thickness  $\delta$  [19]. So we get  $1.8 = d_{\min} + 2\delta$ . The authors of [19] give  $\delta < 0.5$  nm. We used  $\delta = 0.4$  nm to obtain  $d_{\min} = 1$  nm and found  $\Delta v / \Delta S = 0.056$  from Eq. (4). Then for  $\Delta v = 0.016$  cm<sup>3</sup>/g, we obtained  $\Delta S = 0.286$  J/gK. The values of  $\Delta S$  and  $\Delta v$  were assumed to be constant in the size range from 1 to 10 nm. Hence, the initial slope of the melting curve is  $dT/dP = 56$  K/GPa at  $P = 13.5$  GPa. The value of  $\Delta v$  decreases with pressure more rapidly than that of  $\Delta S$  [14], so the melting slope decreases with the pressure rise. We could not calculate the change in the slope and assumed  $dT/dP = \text{const} = 10.2$  K/GPa (as for the triple point).

Within the framework of these assumptions, Eq. (3) takes a simple form:

$$T' = 0.5 + \{0.25 (1 - 1/d)\}^{0.5}, \quad (5)$$

where  $d$  is the diameter of the diamond core of a UDD particle measured in nanometers.

In our calculations made for the ranges of  $P = 10$ – $30$  GPa,  $T = 2000$ – $4500$ K, and UDD sizes of 1–10 nm, we assumed the following parameters to be constant: the ratio  $\Delta v / \Delta S = 0.056$ ,  $v_f = 0.311$  cm<sup>3</sup>/g,



$T_{\infty} = 4470 + 10.2 (p - 13.5)$ ,  $\sigma_d = 5 \cdot 10^{-4} \text{ J/cm}^2$ , and UDD melting slope  $dT/dp = 10.2 \text{ K/GPa}$ . The results of the calculation of  $T_d$  at  $p = 20 \text{ GPa}$  are presented in Table 1 and Figure 1.

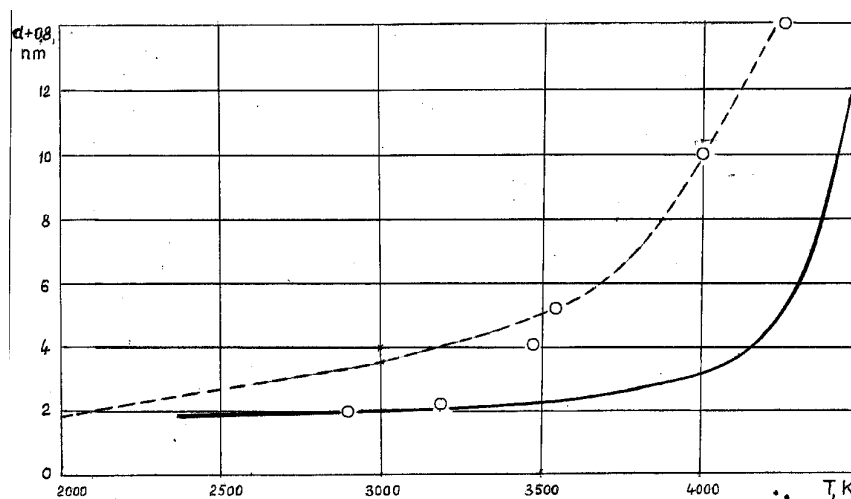


Figure 1. The relation between the melting points and the UDD particle size ( $d + 0.8 \text{ nm}$ ) at  $P = 20 \text{ GPa}$ .

----- calculation [22];  
o - o experiment [22].

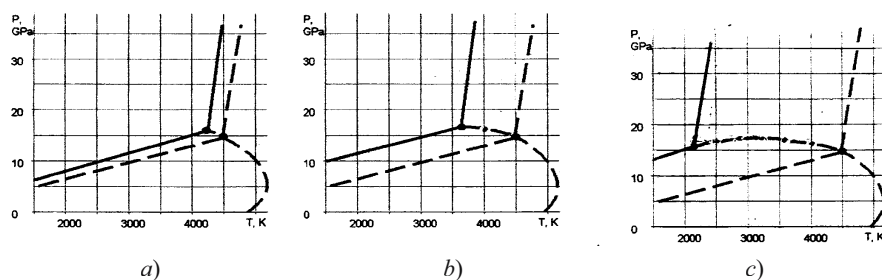


Figure 2. The thermodynamic equilibrium and melting curves for UDD particles of the sizes: 6 nm (a), 1.5 nm (b) and 1 nm (c). Dotted lines - the phase diagram for bulk crystals. Dot-and-dash lines - sets of triple points.

The diamond core of  $d = 1 \text{ nm}$  in the smallest particle of 1.8 nm measured in the UDD synthesis [4] seems to be extremely small, because the volume of smaller particles it is not large enough to form a diamond lattice. It is clear from Table 1 that the melting point of minute UDD particles is twice as

low as for a single crystal. The melting points decrease slowly at  $d \geq 4$  nm and quickly at  $d \leq 2$  nm (Figures 1 and 2).

### 3. UDD-SOOT PHASE EQUILIBRIUM CURVES

With the surface energy of nanoparticles, the transition pressure increases by  $P_s$ :

$$P_d = P_\infty + P_s \quad (6)$$

In a linear approximation with the triple point coordinates, the phase equilibrium curve at zero surface effect can be described as

$$P_\infty = 0.6 + 2.9 \cdot 10^{-3} T, \text{ (GPa)} \quad (7)$$

The value of  $P_s$  is

$$P_s = (dP/d\Delta F) \cdot E_s, \quad (8)$$

where  $dP/d\Delta F$  is a derivative found along the thermodynamic equilibrium curve (with  $\Delta F = 0$ ) and the binding energy (a differential of the thermodynamic potentials  $\Delta F$ ) and pressure. The thermodynamic calculations of  $\Delta F$  [27] yield the following temperature dependence of  $dP/d\Delta F$ :

$$dP/d\Delta F = 0.3 - 10^{-5} T \text{ (GPa/kJ/mol)} \quad (9)$$

The surface energy at the interface,  $E_s$ , for a spherical particle is

$$E_s = S \Delta \sigma, \quad (10)$$

where  $S = 6v_d/d$  is the specific surface area and  $d$  is the diamond core diameter.

Similarly, we transform Eq. (2), where  $\Delta \sigma = 2(v_s - v_d)\sigma_d/3v_s$  is the specific surface energy of the diamond-soot interface (we regard the diamond-soot transition as pseudo-melting of diamond) and  $v_s$  is the specific volume of soot. Then Eq. (6) to be used for the calculations takes the form:

$$P_d = 0.6 + 2.9 \cdot 10^{-3} + 184(0.3 - 10^{-5} T)(v_s - v_d)dv_d/v_s, \quad (11)$$

where  $P_d$  is expressed in GPa and  $d$  in nanometers.

The specific volumes  $v_s$  and  $v_d$  varying with  $P$  and  $T$  were found from the state equations for soot and diamond [27].

For soot, we have

$$P = 0.0746 (\delta^6 - 1) + (-0.2267 + 0.2712\delta) T + 0.0358\delta^{0.5}T^2, \quad (12)$$

with  $\delta = v_0/v$ ,  $v_0 = 0.556 \text{ cm}^3/\text{g}$ ,  $P$  expressed in Mbar, and  $T = T \text{ K} / 11600$ .

For diamond, we get

$$v = v_0(1 + \alpha T)(1 - \beta P), \quad (13)$$

with  $v_0 = 0.284 \text{ cm}^3/\text{g}$ ;  $\alpha = 2.54 \cdot 10^{-6} \text{ c}_v^{-1}/\text{K}$ , ( $c_v$  - specific heat) and  $\beta = 0.16 \cdot 10^{-8} \text{ cm}^2/\text{H}$ .

Some of the results obtained from Eqs. (12) and (13) are presented in Table 2 and those from Eq. (11) in Table 3. The  $P_d(T)$  curves are practically parallel to the  $P_\infty(T)$  equilibrium line, since the values of  $P_s$  vary slightly with temperature and intercept the melting curves at the triple points (Figure 3). So, the effect of the surface energy considerably increases the thermodynamic equilibrium pressure (by a factor of two at  $d = 1 \text{ nm}$ ) with decreasing UDD size. Note that the thermodynamic equilibrium curves do not coincide with the kinetic curves.

Table 2. Calculated specific volumes of soot and diamond ( $\text{cm}^3/\text{g}$ )

$P$ , GPa	Temperature, K				
	2000	2500	3000	3500	4000
10	0.5358	0.5467	0.5587	0.5720	0.5870
	0.2800	0.2887	0.2913	0.2938	0.2964
13.5	0.5098	0.5179	0.5267	0.5364	0.5470
	0.2785	0.3896	0.2896	0.2922	0.2947
15	0.5008	0.5082	0.5161	0.5247	0.5341
	0.2778	0.2864	0.2889	0.2914	0.2940
17	0.4903	0.4968	0.5038	0.5113	0.5195
	0.2769	0.2854	0.2879	0.2905	0.2930
20	0.4770	0.4825	0.4885	0.4948	0.5015
	0.2755	0.2840	0.2865	0.2890	0.2916

Note: The first values of specific volume are for soot, the second ones for diamond.

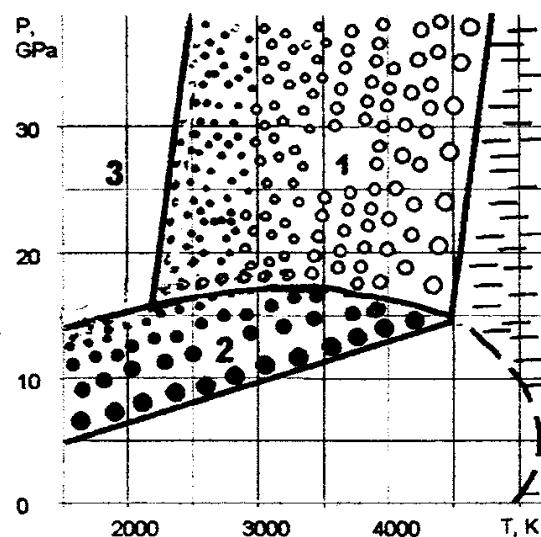


Figure 3. Regions of nanocarbon states in the phase diagram: 1 – liquid nanocarbon (nanodroplets); 2 – diamond and UDD; 3 - amorphous nanocarbon. The direction of decreasing particle size is schematic.

Table 3. Calculated equilibrium pressure for UDD (GPa).

$d$ , nm	Temperature, K				
	2000	2500	3000	3500	4000
1	14.7 (8.3)	16.0 (8.1)	17.2 (7.9)	18.5 (7.8)	19.8 (7.6)
1.2	13.4 (7.0)	14.5 (6.8)	15.9 (6.6)	17.3 (6.5)	18.8 (6.4)
1.5	12.0 (5.6)	13.2 (5.4)	14.6 (5.3)	16.0 (5.2)	17.3 (5.1)
2	10.7 (4.3)	12.1 (4.2)	13.4 (4.1)	14.8 (4.0)	16.1 (3.9)
3	9.3 (2.9)	10.7 (2.9)	12.1 (2.8)	13.5 (2.7)	14.9 (2.7)
4	8.7 (2.3)	10.1 (2.3)	11.5 (2.2)	12.9 (2.1)	14.2 (2.0)
6	8.0 (1.6)	9.4 (1.6)	10.8 (1.5)	12.2 (1.4)	13.6 (1.4)
$\infty$	6.4	7.85	9.3	10.75	12.2

Note: the values of  $P_s$  are given between the brackets.

#### 4. THE CARBON PHASE DIAGRAM FOR UDD

In addition to the pressure and temperature, the phase diagram of a disperse system should contain a third parameter - the particle size  $d$ , such that it becomes three-dimensional. But in practice, it is more convenient to use a conventional 2D diagram with  $d$  as an additional parameter. The phase diagrams for carbon, built from the computations in the temperature range of 2000–4500K and the diamond core diameters  $d = 1\text{--}6$  nm, are presented in Figures 2, 3, and 4. The interceptions of the melting and equilibrium curves for particles of different sizes form a set of triple points, considerably increasing the liquid nanocarbon region at low temperatures. The line of the triple points as a function of the particle size lies within the ranges of  $P = 13.5\text{--}16.5$  GPa (Figures 2, 3, and 4) and  $T = 4470\text{--}2210$ K and seems to be an extension of the graphite melting curve into the diamond region. One can see that the region of liquid nanocarbon becomes larger with decreasing particle size, while that of UDD becomes smaller at lower pressures. The coordinates of the triple points for UDD are given in Table 4.

Table 4. Coordinates of triple points in the UDD phase diagram.

$D$ , nm	1	1.2	1.5	2	3	4	6	$\infty$
$P$ , GPa	15.2	16.5	16.1	15.6	15.2	14.8	14.5	13.5
$T$ , K	2210	3160	3550	3820	4090	4190	4300	4470

If we assume that  $d = 1$  nm is the minimum possible size of a UDD particle, all the diamond region can be subdivided into three regions in terms of the nature of the nanoparticles: UDD and diamond, liquid nanocarbon, and amorphous particles with  $d < 1$  nm (Figure 3). The melting curve at  $d = 1$  nm can be regarded as the line of liquid-to-amorphous nanocarbon transformation.

The real UDD size  $d_{\text{UDD}}$  in Figures 2, 3, and 4 can be found as  $d_{\text{UDD}} = d + 2\delta$  with the shell thickness  $\delta = 0.3\text{--}0.5$  nm. We believe that the origin of amorphous shell on diamond core after purification attributed to the fact that its inability to build the not covered diamond shell on a spherical surface with a large curvature (in the case the sphere radius is about of the diamond lattice parameter).

## 5. THE DETONATION CONDITIONS

The detonation conditions, especially the pressure, determine the extent of the carbon-to-UDD transition. So the optimization of UDD synthesis requires an understanding of the reasons for the detonation pressure reduction for a variety of explosives. The detonation pressure and temperature are maximum in the  $C$ - $J$  plane and then decrease fast on the unloading of the detonation products. The detonation pressure and rate have been measured quite accurately but the temperature could not be measured or calculated as precisely. The theoretical temperatures vary with the equations of state (ES) used. To illustrate, the calculation with ES BKW underestimated the temperature [28], whereas the ES WCA4 computations [29] showed a better agreement with measurements. Some results on the theoretical pressure and temperature in the  $C$ - $J$  plane are presented in Table 5 [28,31]. Note that the highest  $P$  and  $T$  values were obtained assuming the DP carbon to be graphite; the lowest  $P$  and  $T$  values are derived from the assumption that the carbon is present as diamond.

Table 5. Parameters of a perfect detonation in the  $C$ - $J$  plane.

Explosive, density, g/cm <sup>3</sup>	$P$ , GPa, $T$ , K	Experimental Dates	Calculated values
TNT, $\rho = 1.64$	$p$ $T$	19 3700 ( $\rho = 1.51$ )	18.3–20.1 3500–3618
RDX, $\rho = 1.8$	$p$ $T$	34.7 4500 ( $\rho = 1.66$ )	34.7–35 4200
64/36 RDX/TNT, $\rho = 1.713$	$p$ $T$	29.4 -	27.4–29.3 3931–4063
50/50 RDX/TNT, $\rho = 1.67$	$p$ $T$	24.6 -	24.4 3225–3900
Tetryl, $\rho = 1.7$	$p$ $T$	28.3 3700–4300	23.9–25.4 3991–4063

The calculated  $C$ - $J$  parameters in Table 5 are the highest possible values describing a perfect detonation, in which a chemical reaction leads to an equilibrium composition of the DP. Practically, most of the available explosives produce an imperfect, unsteady detonation with uncompleted reactions, providing lower pressures and temperatures than those necessary for UDD synthesis. According to [28], for example, a 50% efficiency of the

reaction provides only  $P_{50}/P_{100} = 0.337$  and  $T_{50}/T_{100} = 0.546$ . This happens for the following reasons [30–32].

1. The side and back unloading of the reaction zone. One example is the detonation of a cylindrical charge with a diameter smaller than the limit for a particular explosive. The reaction cannot practically start in the outer charge layer, whose thickness is approximately equal to the half of the critical diameter, because the unloading is too fast.

2. Low pressure for the explosion start. In this case a shock wave propagates through the explosive charge, followed by a detonation wave at a depth of several millimeters.

3. A spherical detonation wave is produced by an initiator of small diameter (a “dot”), say, by a detonator. The velocity  $D_R$  of this wave increases with the wave radius  $R$  [31] as

$$D_R = D_\infty (1 - 3.5 a/R), \quad (17)$$

where  $D_\infty$  is the velocity of a theoretical plane wave and  $a$  is the reaction zone width. Then we have

$$\Delta D_R = D_\infty 3.5 a / R; \Delta p_R = 2 \Delta D_R = 7 D_\infty a / R; p_R = p_{00} - \Delta p_R$$

Table 6 summaries the results of  $p_R$  calculations for some explosives, using Eq.(17) at  $R = 10, 20$ , and  $30$  mm on the assumption of  $a = \text{const}$ . The reduction of pressure is maximum for TNT and TATB because of large  $a$  values.

Table 6. The C–J pressure in a propagating detonation wave.

Explosives	TNT cast	TNT press.	50/50 RDX/TNT	60/40 RDX/TNT	RDX	TATB
$a$ , mm	1.36	0.87	0.64	0.50	0.36	1.56
$D_\infty$ , km / s	6.94	6.94	7.65	7.85	8.67	7.86
$P_\infty$ , GPa	19.0	19.0	25.0	28.0	34.5	31.5
$P_R$ , GPa $R = 10$ mm	12.4	15.8	21.6	25.3	32.3	22.9
$P_R$ , GPa, $R = 20$ mm	15.7	16.9	23.3	26.6	33.4	27.2
$P_R$ , GPa, $R = 30$ mm	16.9	17.6	23.9	27.1	33.8	28.6

Imperfect detonation decreases the propellant capacity of the explosive, which represents the integral energy release or the DP momentum [32]. For example, the measured loss of the propellant capacity of a 10 mm TNT layer is 25% for a “dot” initiation [32], which is consistent with the calculated pressure drop in the detonation wave. Therefore, the UDD yield should be

expected to be zero at the initiation point because of the effect of the charge shape on the yield of UDD. Our experiments have shown that an elongated cylinder is an optimal design [1,5], since it provides a minimum relative volume of the explosive at the initiator.

To reduce imperfect detonation, it is useful to initiate the explosion by a flat shock wave with a pressure equal to  $p_{C-J}$  and to put the charge into a massive water shell. The DP temperature drops due to the conversion of the thermal energy of the detonation products to the kinetic energy of the shell of optimal mass [5,33]. Then UDD can be produced even if the explosion occurs in air, and the shell material and density, as well as the heat capacity of the gas in the blast chamber, do not affect the UDD yield [1,5].

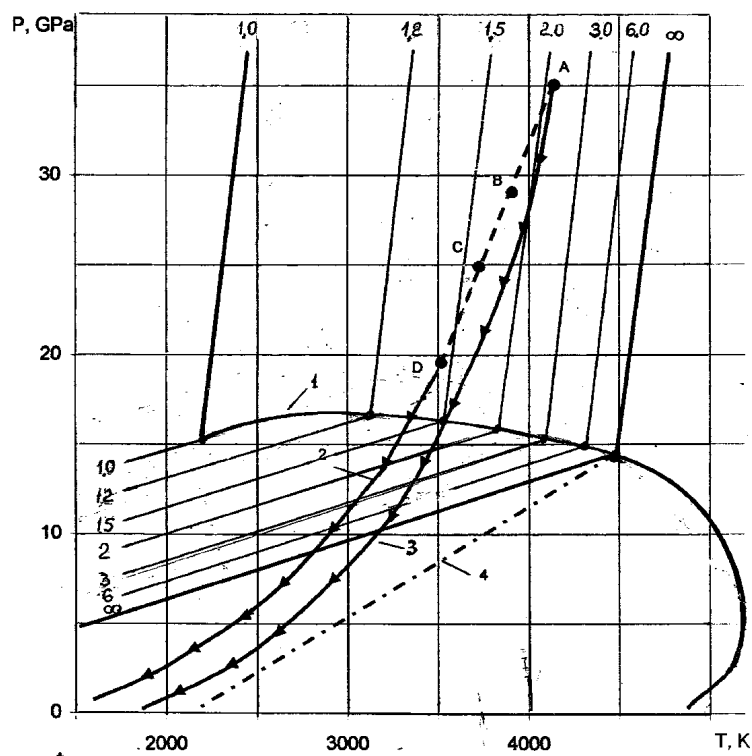


Figure 4. The phase diagram of nanocarbon and detonation parameters. A, B, C, and D are the  $C-J$  parameters for RDX, RDX/TNT 64/36, RDX/TNT 50/50 and TNT, respectively; 1 - line of triple points; 2 - isotropic line of the product spread for TNT; 3 - the same for RDX; 4 - line of instantaneous diamond graphitization. Digits at the melting and thermodynamic equilibrium lines indicate the size of the diamond core in a UDD particle in nanometers.



The  $C$ - $J$  parameters also are affected by the explosive porosity. The pressure continuously decreases with growing porosity, and the temperature rises at first (owing to “hot” pores) and then drops because of the decreasing detonation heat [30]. Besides, high porosity makes the segment of the DP isotropic line going through the diamond region shorter, increasing the temperature at the beginning of the isotropic line in the graphite region. This line can intercept the curve for instantaneous volumetric graphitization, along which the time of a 50% graphitization is zero [5] (Figure 4). Below the line, the diamond completely loses its metastability, making its existence impossible. This happens, for example, when the DP unloading in the  $C$ - $J$  plane is performed at  $P \leq 20$  GPa and  $T \geq 4000$  K. Obviously, it is necessary to use explosives with minimum porosity.

Finally, imperfect detonation and porosity decrease the amount of free carbon in the DP [5,29–31], reducing the UDD yield.

Thus, the detonation of real explosives is characterized by some effective values of the  $C$  –  $J$  parameters integrated over the volume of the explosive of a given geometry and initiation technique. Usually, these values are smaller than the available references.

## 6. DISCUSSION

The nanocarbon phase diagram to be used for the analysis of UDD formation should contain the  $C$ - $J$  parameters of a perfect detonation of TNT, 50/50 RDX / TNT, 64/36 RDX / TNT, and RDX (Figure 4). For these explosives, the  $C$ - $J$  data lie in the straight line in the liquid carbon region with the particle size greater than  $1.2 + 2 \delta$  nm. The higher are the pressure and temperature in this series of explosives, the larger is the size of the nanodroplets in the  $C$ - $J$  plane.

The  $C$ - $J$  parameters for TNT with the density of  $1.55 \text{ g/cm}^3$  lie practically in the line of triple points. Therefore, the break in the  $D(\rho)$  curve observed at this density [11,12] is due to the onset of soot transition to liquid nanocarbon, whose entropy is higher than that of soot, so we observe a smoother  $D(\rho)$  curve after the second break.

The highest  $C$ - $J$  characteristics of a perfect TNT detonation are hardly above the line of triple points. For real detonation, one should expect the carbon in the reaction zone to consist of a mixture of sooty and liquid nanoparticles even at the highest TNT density. Complete melting cannot be achieved, so the  $D(\rho)$  curve for TNT not have the second break, indicating that condensed carbon consists totally of nanodroplets and therefore the UDD yield is maximum. The  $C$ - $J$  parameters for RDX/TNT alloys and tethyl are located far in the region of liquid nanocarbon. As a result, the detonation

analysis of explosives with a various degree of porosity reveals both breaks in the  $D(\rho)$  curve [11,12].

The positions of the isotropic lines of the DP spread for TNT and RDX are shown in Figure 4 [30]. One can identify the following three segments in them.

1. The segment between the  $C$ - $J$  line and the line of triple points indicates a fast carbon coagulation (for  $\sim 1$  ns [22]) and the formation of nanodroplets (in a cluster-cluster mode), whose size varies with the time of the DP spread in this segment and the DP characteristics (the carbon concentration, density, and temperature).

2. The segment between the line of triple points and the lines of thermodynamic equilibrium for UDD particles of different sizes indicates the crystallization of nanodroplets and UDD formation following the well-known sequence (vapor-liquid-crystal [16]) at pressures 16–10 GPa and temperatures 3400–2900K. Therefore, it is only this segment which is characterized by the minimum DP spread rate because of a larger charge mass and a massive water shell. At the DP-water interface, the pressure rises from 8 to 18 GPa [1]; these values practically fit into this segment. The gain in the UDD yield and particle size can, therefore, be attributed to the use of a water shell. Thus, the scale factor, which influences the UDD characteristics, is valid only along segments 1 and 2.

3. The segment of complete DP spread from the pressure equilibrium to the zero point shows the presence of free soot particles and UDD-bound soot. A complete amorphization of supercooled nanodroplets, which had not enough time or temperature to be crystallized within the segment, produces free and partly bound soot. Besides, the carbon atoms and clusters are deposited as soot on the UDD surface. Note that the amorphization temperature of nanodroplets rises as the particles become smaller [16]. So, the free DP soot does not result from UDD graphitisation.

None of the above explosives with a negative oxygen balance has an isotropic line intercepting the line of instantaneous graphitization (Figure 3), and the temperature of completely unloaded RDX DP is found to be 850K [30]. This reduces the graphitization starting at 1300K; however, the temperature of the UDD particles is always higher than that of the DP. Evidently, we should not totally discard the possibility of graphitization along the isotropic line. UDD oxidation is quite likely to start at 650K, which is most important for making the UDD intact during the synthesis.

## 7. SUMMARY

The positions of the melting and thermodynamic equilibrium curves in the carbon phase diagram have been calculated as a function of the diamond core size in UDD particles with  $d = 1\text{--}10$  nm. We determined the position of a set of triple points for  $P = 13.5\text{--}16.5$  GPa and  $T = 2210\text{--}4470$  K and identified the region of liquid nanocarbon, or nanodroplets (Figures 1–4). The diamond region in the phase diagram is subdivided into three subregions of nanoparticles of different nature: UDD and diamond, liquid nanocarbon and amorphous nanoparticles with  $d < 1$  nm, as shown in Figure 3. The melting curve at  $d = 1$  nm can be described as the line of liquid-to-amorphous nanocarbon transition.

We have analysed the detonation conditions for explosive used to synthesize UDD. It is shown that the  $C\text{--}J$  parameters for these explosives lie within the region of liquid nanocarbon (Figure 3). Therefore, the carbon nanodroplets which produced in the reaction zone of the detonation wave, then crystallize to form UDD along the isotropic segment of the curve for the DP spread through the UDD region at  $P = 16\text{--}10$  GPa and  $T = 3400\text{--}2900$  K (Figure 4). This accounts for the experimentally observed effect of the explosive charge mass [5] and the water shell on the UDD synthesis, making the unloading slower. Besides, the use of a water shell decreases the temperature of the detonation products by half [33] and reduces the UDD yield due to the conversion of the product thermal energy to the kinetic energy of water.

Thus, UDD formation follows the well-known scenario: vapor-fluid-crystal [16], accompanied by the cooling of inactive and turbulent detonation products. Soot is produced at pressures and temperatures below the above ranges along the isotropic line. As the density of the explosive increases, the  $C\text{--}J$  parameters become higher and go into the liquid nanocarbon region at the some density. Therefore, the observable breaks in the  $D(\rho)$  curve are related to the beginning and termination of the nanocarbon melting, rather than to the UDD formation in the reaction zone.

## REFERENCES

1. V. Volkov, V.V. Danilenko, and V.I. Elin. Synthesizing of diamond from carbon of products of a detonation of explosives. *Fizika Goreniya i Vzryva* **26**, 123-25 (1990) (in Russian).
2. N.R. Greiner, D.S. Phillips, and F.J.D. Johnson. Diamonds in detonation soot. *Nature* **333**, 440-42 (1988).
3. A.I. Ljamkin, E.A. Petrov et al. Deriving of diamonds from explosives. *Doklady AN SSSR* **302**, 611-13 (1988) (in Russian).

4. V.M. Titov, V.P. Anisichkin, and I.Yu. Malkov. Study of synthesis of ultra dispersed diamond in detonation waves. *Fizika Goreniya i Vzryva* **25**, 117-25 (1989) (in Russian).
5. V.V. Danilenko. *Synthesizing and sintering of diamond by explosion*. Moscow: Energoatomizdat, 2003 (in Russian).
6. B.A. Vyskubenko, V.V. Danilenko, E.E. Lin et al. Influence of scale factors on a size and output of diamonds under denonation synthesis. *Fizika Goreniya i Vzryva* **28**, 108-9 (1992) (in Russian).
7. V.Yu. Dolmatov. *Ultra dispersed diamonds of detonation synthesizing*. St.Petersburg: Publisher St.Petersburg State University, 2003 (in Russian).
8. S.A. Gubin, V.V. Odintsov, V.I. Pepekin, and S.S. Sergeev. Influencing of the shape both size of crystals of graphite and diamond on phase equilibrium and arguments of a detonation of explosive. *Physicheskaya Khimiya* **9**, 401-17 (1990) (in Russian).
9. M. van Thiel and F.H. Ree. Properties of carbon clusters in TNT detonation products. Graphite - diamond transition. *J. Appl. Phys.* **62**, 1761-67 (1987).
10. A.M. Staver, A.P. Ershov, and A.I. Lyamkin. Study of detonation transformation of condensed explosives of methods of electrical conductivity. *Fizika Goreniya i Vzryva* **20**, 79-82 (1984) (in Russian).
11. S.V. Pershin. About formation of diamond at a detonation of a trinitrotoluene. Proceedings of the IV All Union. Sympos. on Detonation. **1**, 1-5 (1988) (in Russian).
12. S.V. Pershin, D.N. Tsaplin, and A.G. Antipenko. About possibility of formation of diamond at a detonation of tetryl. Proceedings of V All Union. Symposium on Detonation. **2**, 233-36 (1991) (in Russian).
13. B.G. Loboiko and S.N. Lyubyatinski. Zones of reacting of detonating solid explosives. *Fizika Goreniya i Vzryva* **36**, 45-64 (2000) (in Russian).
14. S.B. Kormer, M.V. Sinitzyn, G.A. Kirilov, and V.D. Urlin. The experimental definition of temperatures of shock compressed NaCl and KCl and their fusible curves up to pressure 700 kbar. *Journal of Experimental and Theoretical Physics* **48**, 1033 (1965) (in Russian).
15. V.N. Korobenko and A.I. Savvatimskiy. Blackbody design for high temperature (1800 to 5500 K) of metals and carbon in liquid states under fast heating. *Temperature: Its Measurement and Control in Science and Industry* **7**, 783-88 (2003).
16. I.D. Morokhov, K.I. Trusov, and S.P. Chizhik. *UltraDispersed Metal Media*. Moscow: Atomizdat, 1977 (in Russian).
17. Yu.I. Petrov. *Physics of small particles*. Moscow: Nauka, 1982 (in Russian).
18. S.V. Razorenov, G.I. Kanel, and A.A. Ovchinnikov. Registration of shock waves by manganin sensors and pressure of transferring graphite - diamond at heightened temperature. Detonation: Proceedings of the II All Union Symposium on Detonation. Chernogolovka, Issue 2, 70-2 (1981) (in Russian).
19. A.E. Aleksenski, M.V. Baydakova, A.Ya.Vul', and V.J. Siklitski. Structure of diamond nanocluster. *Phys.Solid.State.* **41**, 668-71 (1999).
20. A.L. Vereshagin. About the phase diagram of ultra dispersed carbon. *Fizika Goreniya i Vzryva* **38**, 119-20 (2002) (in Russian).
21. A.L. Kupershtoch, A.P. Ershov, and D.A. Medvedev. Model of coagulation of carbon clusters at high densities and temperatures. *Fizika Goreniya i Vzryva* **34**, 102-09 (1998).
22. Huang Fenglei, Tong Yi, and Yun Shourong. Synthesis mechanism and technology of ultrafine diamond from detonation. *Physics of Solid State* **46**, 601-04 (2004).

23. M. Togaya. Thermophysical properties of carbon at high pressure. Advanced Materials ' 96: Proceedings of the 3<sup>rd</sup> NIRIM Intern. Symp. on Advanced Materials (ISAM ' 96 Tsukuba, Japan, 1996 March 4-8, p. 251-56 (1996).
24. A.M. Molodets. Isochoric - isothermal potential of diamond. *Fizika Goreniya i Vzryva* **34**, 94-101 (1998) (in Russian).
25. S.N. Zadumkin. About value of interphase surface energy of metal on boundary crystal – fusion. *Doklady. AN USSR* **130**, 4 (1960) (in Russian).
26. *Diamond*. Ed. D.F. Fedoseev, N.V. Novikov, A.S. Vishevski et al. Kiev: Naukova Dumka (1981) (in Russian).
27. V.V. Danilenko. Thermodynamics of transformation graphite - diamond. *Fizika gorennya i vzryva* **5**, 137-42 (1988).
28. S.L. Mader. *Numerical modeling of explosives and Propellants*. 2<sup>nd</sup> Edition. N.Y.: CRC Press, 1998.
29. J. Bante, R. Chirat. Which equation of state for carbon in detonation products? The 8<sup>th</sup> Symposium (Intern) on Detonation. 1985, New Mexico. Preprint, p. 287-95.
30. *Physics of detonation*. Second Edition. Ed. K.P. Stanyukovich. Moskow: Nauka, 1975 (in Russian).
31. *Physics of detonation*. Third Edition. Ed. L.P. Orlenko. v.1. Moskow: Fizmatlit, 2002 (in Russian).
32. V.V. Danilenko and Yu.M. Pachurin. Influencing non-ideal of a detonation of explosive charges on energy of accelerated plates. *Fizika Goreniya i Vzryva* **1**, 46-9 (1987) (in Russian).
33. V.A. Mazanov. Macrokinetic of saving of condense carbon and detonation nanodiamond in germetic explosion chamber. *Physics of the Solid State* **46**, 614-20 (2004).

# 15

## NANODIAMOND GRAPHITIZATION AND PROPERTIES OF ONION-LIKE CARBON

V.L. Kuznetsov and Yu.V. Butenko

*Boriskov Institute of Catalysis, Lavrentieva 5, Novosibirsk, 630090, Russia*

**Abstract:** Nanodiamond (ND) reactivity and the ease of graphitization limits the temperature range where it may be effectively used. At the same time new nanocarbons (NC) can be produced using controlled ND graphitization (namely: onion-like carbon (OLC),  $sp^2/sp^3$  nanocomposites, and nanographite). Here we briefly review data on the graphitization of diamond with emphasis on the low temperature graphitization at 1370–1870K and the properties of OLC.

**Keywords:** diamond, nanodiamond, graphitization, onion-like carbon

### 1. INTRODUCTION

The graphitization of diamond has long been a subject of considerable interest from both basic scientific and practical points of view [1,2]. Clearly the subject relates to the stability of diamond under different conditions. This is especially important in the case of ND, because the ease of graphitization limits the temperature range where ND may be effectively used. Previously, we have found that the low temperature (1400–1900K) diamond graphitization is followed by the thermal elimination of all surface species. It was shown that OLC is formed during the annealing of ND [3,4,5], with intermediate products being represented by particles with a diamond core covered by closed curved graphitic shells (graphite/diamond nanocomposites). The annealing of micron-sized diamond produces closed curved graphite-like structures (CCGS: nanotubes, nanofolds etc.) [6,7,8]. In this paper an overview of ND graphitization and properties of annealing

products (OLC,  $sp^2/sp^3$  nanocomposites) is presented. Potential applications of new nanocarbons are also briefly considered.

## 2. SURFACE CHEMISTRY OF NANODIAMONDS

The surface chemistry of ND is of primary importance for their stability and applications. From theoretical considerations it is clear that stability of a clean diamond surface is significantly less than that terminated with different surface groups (containing hydrogen, oxygen and other elements) [9,10]. The composition of diamond surface groups was extensively studied by the FTIR spectroscopy, XPS and temperature programmable desorption (TPD) in numerous papers [11–16]. It has been shown that surfaces of oxidized ND isolated from detonation soot are covered with different oxygen-containing groups: -COOH (carboxylic), -C-O-C=O (lactone), >C=O (carbonyl), -C-O-C- (ether), -OH (hydroxyl). For such samples, the ratio of oxygen to surface carbon atoms is close to 0.5 [17]. The oxygen- and hydrogen-containing groups on diamond surfaces saturate the dangling bonds of surface carbon atoms and stabilize the diamond surfaces, thereby preventing surface graphitization. FTIR spectroscopy combined with TPD study demonstrates that concentration and type of diamond surface groups can be influenced by thermal treatment. Thus, Figure 1 shows the changes of FTIR spectra of ND heated up to 840K. The TPD data correlate with IR spectra recorded after thermal treatment of ND in vacuum (see Figure 2) and provide information on the temperature regions of the decomposition of the diamond surface groups.

Diamond surfaces include a wide spectrum of functional chemical groups, the composition of which can be varied via chemical pretreatments and thermal annealing in controlled conditions. This opens great possibilities for chemical functionalization of diamond surfaces. The creation of specific surface sites on ND for selective molecular attachments is considered a promising approach for their applications in nanofabrication, self-assembly, bioprobes, nanosensors, drug delivery, pigments, etc. [18,19,20].

Note that the hydrogen desorption from diamond surfaces at 1070–1420K in vacuum (see Figure 2) coincides with the graphitization of the diamond surfaces observed with the use of HRTEM [4,5,21] and XPS [22]. At these temperatures the formation of closed curved graphite-like shells on the diamond surfaces of micron-sized diamond was observed [6,7,8]. Partial graphitization of ND opens an additional way for modification of the diamond surface properties and synthesis of new type of carbon/diamond nanocomposites ( $sp^2/sp^3$  nanocomposites). In Figure 3, HRTEM micrographs of different stages of the ND graphitization (ND

treatment at different temperatures for 1 hour) are presented [21,23]. The XPS study demonstrates that ND preliminary purified by boiling in a mixture of  $\text{HClO}_4$  and  $\text{H}_2\text{SO}_4$  and heated up to 1170K in vacuum for 1 hour does not contain a pronounced  $sp^2$  component [22].

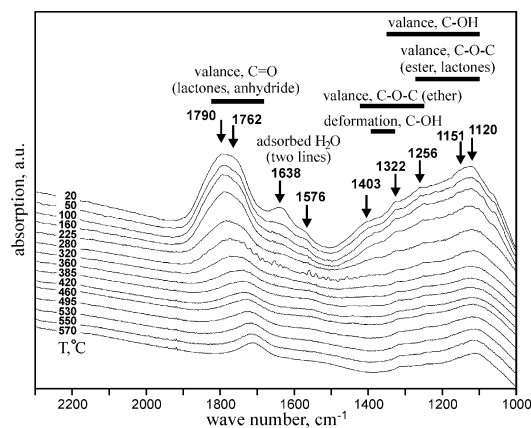


Figure 1. FTIR spectra of surface groups of ND heated at different temperatures (as shown on the figure). The characteristic ranges of vibrations of the surface groups are presented (FTIR spectra were recorded by Prof. E.A. Paukshtis).

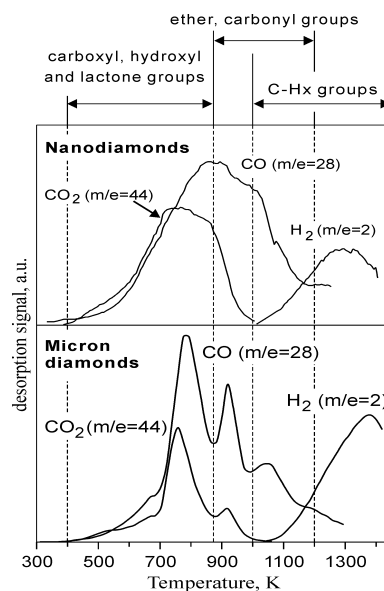


Figure 2. TPD spectra of surface functional groups of ND and micron size diamond powders pretreated by a mixture  $\text{HClO}_4$  and  $\text{H}_2\text{SO}_4$ . The temperature regions of the decomposition of the diamond surface groups are presented [18].



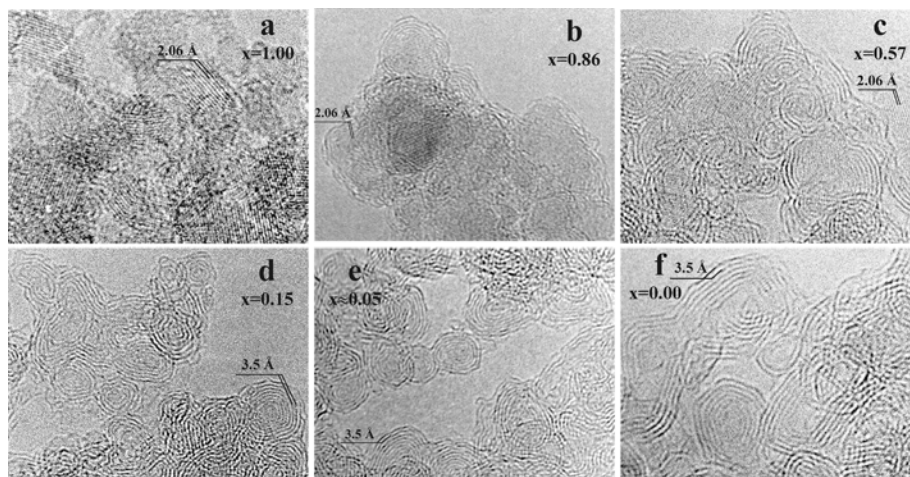


Figure 3. HRTEM micrographs of a ND sample annealed under vacuum conditions at (a) 1170, (b) 1420, (c) 1600, (d) 1800, (e) 1900, (f) 2140K. Exposure time at each temperature is 1 hr. The dark straight contrast lines in micrographs (a), (b) and (c) correspond to the (111) crystallographic diamond layers. The distance between these lines is 2.06 Å. The dark lines in Figures (d), (e) and (f) correspond to the (0002) crystallographic graphite layers. The distance between these lines is 3.5 Å. The diamond weight fractions ( $x$ ) of the samples are also presented within each image [23].

Graphitic carbon can be clearly observed in the C1s photoemission spectra of ND annealed at 1420K in vacuum for 1 hour. The XPS study [22] also revealed the formation of oxygen-containing groups in samples annealed at 1420 and 1600K in vacuum and then exposed to air indicates the presence of the edges in graphitic layers in these samples. Such oxygen-containing groups were not detected in samples annealed at 1800, 1900 and 2140K in vacuum and then exposed to air. Therefore, one can suggest that annealing at temperatures higher than 1600K results in the full closure of the outer fullerene-like shells of OLC.

### 3. PRINCIPAL FEATURES OF LOW TEMPERATURE DIAMOND GRAPHITIZATION

Analysis of HRTEM images provide us information on the intermediate products produced during the annealing of the diamond surfaces [4,5,7,21]. The most important observations from this analysis are as the following:

1. The graphitization proceeds from the surface to the bulk. The temperature at the beginning of the graphitization of approximately ~1170K corresponds to the temperature at which various oxygen-containing groups stabilizing the surface are completely removed (see Figure 2).

2. The transformation rate of the (111) diamond planes to graphite-like sheets is higher than those of other planes.

3. The edges of exfoliated graphite-like sheets merge with the upper untransformed diamond planes.

4. The distance between the inner graphite-like sheet and the upper untransformed diamond layer does not exceed 0.35 nm, indicating an interaction between the diamond and graphite layers.

5. Later, we found that the annealing of micron size diamond produces closed curved graphite-like (or fullerene-like) structures at the interface between the diamond and the evolving graphite. The formation of two curved graphite sheets from three (111) diamond planes was observed [6,7].

After the complete transformation of the diamond core, the annealing products are represented by a) quasi-spherical particles with closed concentric graphitic shells, b) polyhedron particles with closed shells, c) elongated particles with linked external graphite-like layers and closed quasi-spherical shells. The formation of the latter can be explained in terms of the existence of ND as stable agglomerates of small primary particles (2–10 nm). Thus, the annealing of contacting primary ND particle induces the formation of agglomerated OLC particles. The number of neighbors of each carbon onion is likely to be equal to the number of neighbors of the pristine ND. Nevertheless, the Raman study [24,25] demonstrates that some part of OLC particles have very regular structure with specific vibration characteristics, corresponding to a high degree of structural perfection of graphitic network within the shells (see later).

It is interesting to mention that, while we observed OLC formation during ND annealing under vacuum, Enoki *et al.* [26–29] demonstrated possibility of producing of nanographites after ND annealing in argon flow. The principal differences in reaction products can be understood in terms of carbon transport reactions, which occur at high temperature in presence of reactive gases. We have shown that even small quantities of water, carbon oxides or oxygen initiate their reversible reactions with carbon. This leads to carbon redistribution with reactive erosion of nanocarbon materials, and formation of bigger graphitic particles with relatively low surface energy [30]. Therefore, traces of oxygen and/or water could be responsible for the formation graphitic particles. At the same time vacuum annealing allows for the reproducible production of OLC materials in other research groups also [31–35].

#### 4. KINETICS OF ND GRAPHITIZATION

A study of the kinetics of diamond graphitization in the temperature range 1370–2000K has been undertaken [21]. This was achieved by determining the changes in the densities and diamond content in ND samples annealed at different temperatures. The study is facilitated by the rather large difference in the density of carbon in its diamond and graphitic forms. The kinetic parameters describing the graphitization of ND in the temperature range 1370–1860K; the activation energy  $E = 45 \pm 4$  kcal/mol and pre-exponential factor  $A = 74 \pm 5$  nm/s, were obtained. These parameters yield rates which agree well with the HRTEM data related to the graphitization of submicron diamond at 1890K. This suggests that the kinetic parameters of the ND graphitization can be used to estimate rates for the graphitization of larger diamonds. However, the kinetic parameters for the temperatures region of 1370–1860K differ significantly from those obtained by Davies

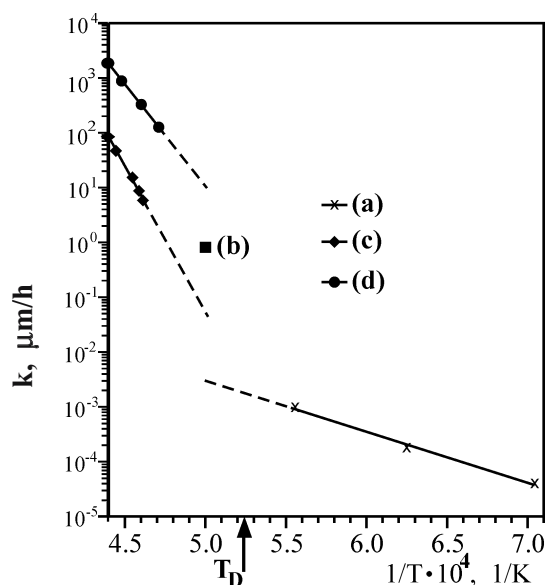


Figure 4. The rates of interface migration for the ND (a) and submicron size particles (b) obtained in this work and for the {111} (c) and {110} (d) faces of macroscopic diamonds determined by Davies and Evans [1,2]. The dashed lines are extrapolations of the Arrhenius expression fits to the “low” and “high” temperature rates. It is inferred that different graphitization mechanisms are operative at and above 2000K and below 1800K. These temperatures bracket the Debye temperature,  $T_D \cong 1910\text{K}$ , which can be taken as the boundary between the two regimes [21].

and Evans for the graphitization of diamond in the 2100–2300K range (see Figure 4) [1,2]. We conclude that there are at least two temperature regions where the graphitization occurs by different mechanisms. The Debye temperature for diamond, 1910K, appears to serve as the boundary between these regions. At and above this temperature all oscillating freedom degrees of the diamond are excited. In the temperature range 1370–1860K, graphitization proceeds from the surface towards the diamond particle bulk. Knowledge gained regarding the graphitization of diamond, and the determination of the kinetic, parameters can help one control the modification of the diamond surface via the growth of fullerene-like carbon states on it. These carbon states are of interest for carbon chemistry (the chemistry of non-planar carbon materials).

It should be mentioned that ND graphitization and the closure of graphitic shells are different processes. The formation OLC fine structure is not possible while a diamond core exists because of significant “bulking” of growing OLC structure. Another important observation concerns the increase of specific surface area of OLC by almost 1.5 times that of pristine ND (from 340 up to 570 m<sup>2</sup>/g) [21]. We will discuss the mechanism of OLC formation from ND after the consideration of OLC properties.

## 5. STRUCTURE AND PROPERTIES OF ND ANNEALING PRODUCTS

Knowledge of the kinetics of ND graphitization provides us with the opportunity of producing diamond/nanographite nanocomposites with variable ratio of diamond carbon (diamond cores) and defective curved graphitic shells. In Figure 5 we present the general scheme of production of OLC and nanocomposites with different fractions of diamond and nanosized graphitic sheets. The scheme demonstrates that the ND annealing at moderate temperatures makes it possible to produce carbon nanocomposites with controlled ratio of  $sp^2/sp^3$  states. At 1800–1900K OLC can be effectively produced. Heating at higher temperatures leads to the formation of hollow OLC.

All these materials are under intensive studies. They were characterized with HRTEM [4,5,7,21], Raman spectroscopy [24,25], XRD [24,33,36], XPS [22], EELS [31], ESR [32], X-ray emission spectroscopy [37] and the electrical resistivity and magnetoresistivity measurements [23,38]. It has been shown that due to an efficient optical limiting action of OLC, they are good candidates for photonic applications [39].

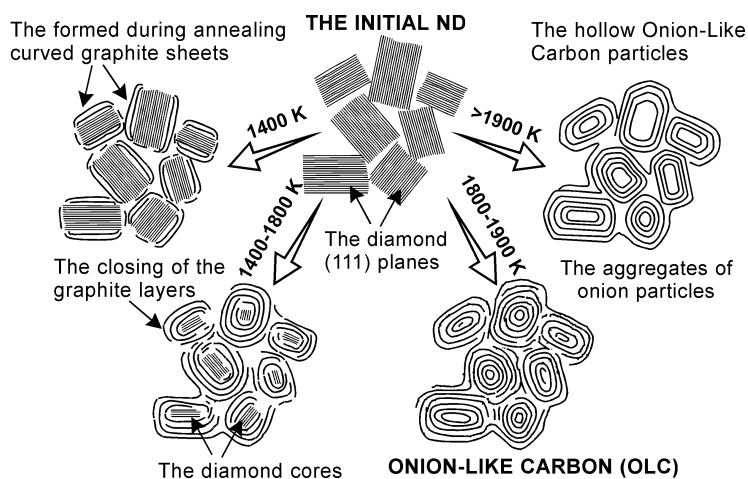


Figure 5. Scheme of  $sp^2/sp^3$  nanocomposites and Onion-Like Carbon production [23].

These structures are related to the interstellar dust problem, and could (at least) contribute to large UV adsorption band at the 217.5 nm wavelength [40,47]. OLC are potentially perfect solid lubricant as hollow  $WS_2$  nanoparticles, and also show high selectivity and catalytic activity in the oxidative dehydrogenation of ethyl benzene to styrene [41]. The last example demonstrates that OLC like ND can be incorporated into chemical reactions and, thus, an onion's surface may be functionalized allowing their further incorporation in biosystems. For the purposes of conciseness, we will discuss only the principal results of these investigations.

## 5.1 Raman Spectroscopy Study of ND Annealing Products

Raman spectroscopy study of ND annealing products [24,25]. According to HRTEM study, the first traces of OLC were observed after ND annealing at 1400K [21]. This sample showed the Raman spectrum of disordered carbon particles ("D" band) together with the remaining ND signal and the broad Raman band at  $1600\text{ cm}^{-1}$  ("G" graphitic peak) (see Figure 6). At 1800K almost all ND particles transform into OLC. This sample showed a specific Raman band at  $1572\text{ cm}^{-1}$ , being approximated as a summary signal from the six- or seven-shell onion. Taking to account HRTEM data the observation of the band at  $1572\text{ cm}^{-1}$  can be attributed to the existence well ordered onion-like particles besides onion agglomerates with joint graphitic shells combining several onion-like cores. The downshift of this mode from the position typical for planar graphite ("G" band) is attributed to the influence

of the bond bending due to the shell curvatures. The narrowness of the band (FWHM=15  $\text{cm}^{-1}$ ), and the dominance of the only band in the second order Raman spectrum at 2712  $\text{cm}^{-1}$ , indicate a high degree of perfection of the crystalline lattice in the spherical carbon shells. After treatment at 1800–2100 K the spherical onions anneal into polygonized particles with hollow centers as well as graphite-like ribbons with parallel graphitic planes. Their Raman spectra are similar to those of glassy carbon.

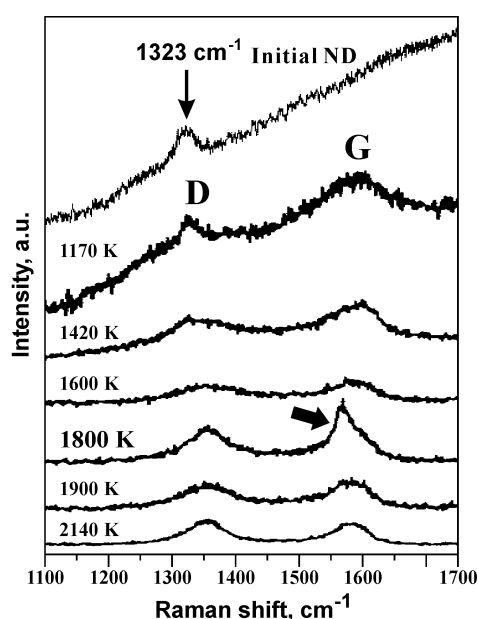


Figure 6. The Raman spectra of the ND powder and the products obtained by annealing at the different temperatures. The spectrum of the initial ND consists of a relatively narrow single Raman band at 1323  $\text{cm}^{-1}$  on the strong photoluminescence background. The Raman spectra of the annealed samples differ from the initial ND by the appearance of two wide Raman bands at 1350  $\text{cm}^{-1}$  (“D” disorder-induced peak) and at 1600  $\text{cm}^{-1}$  (“G” graphitic peak). The spectrum of the sample annealed at 1800 K contains a specific Raman signal at 1572  $\text{cm}^{-1}$  (shown by the arrow) of the fullerene shells of the six or seven shell carbon onions [24,25].

It should be mentioned that carbon onions, produced with different methods, are characterized by a number of parameters; namely primary particle size, number of closed shells, presence of different defects, and the size of agglomerates. Two different types of OLC carbon can be produced by the methods mentioned above: one contains spherical shells another one consists of polygonized shells. It was proposed that the latter onions contain fullerene like spheres with twelve pentagons, which are preferentially

responsible for the formation of polygonized structure. The method of production is therefore crucial for the structure of onions. The perfect spherical onions are produced with electron irradiation of ND [42] and carbon soot [43–46].

Therefore, spherical onions can be formed preferentially via ND heat treatment at temperatures lower than 1900K. At the same time polygonized OLC is usually formed after high temperature treatment ( $> 2000\text{K}$ ) of carbon soot [47] or spherical OLC [21,37].

To explain the sphericity of onions formed under electron beam irradiation of carbon [46] the structural models containing combinations of pentagons and octagons have been proposed by Terrones [48]. However, real OLC are usually imperfect and contain high concentration of defects. Thus, particles show the extensive regions in which graphene network is either missing or highly distorted. In general, defects of all kinds occur and a detailed study of real carbon particles result in more rounded forms.

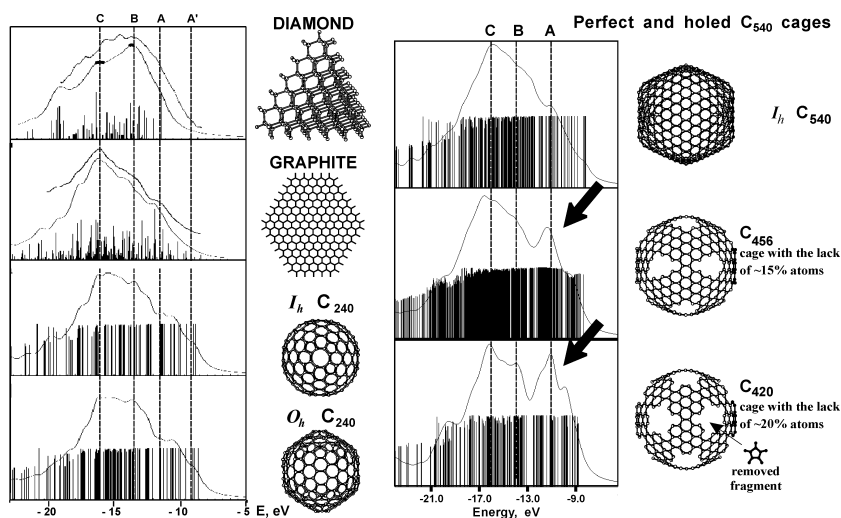


Figure 7. C K $\alpha$  spectra calculated for different carbon clusters. The arrows indicate the increase of the high-energy maximum that may be caused by the defect structure of graphitic networks and corresponded holed defects in fullerene-like shells [37,49].

## 5.2 X-ray Emission Spectroscopy

X-ray emission spectroscopy study of ND annealing products (see the scheme in the Figure 7) detects the difference in the electronic state between carbon shells generated below 2100 K and both graphite and diamond



particles [37,49]. The intensive maximum that found in the high-energy region of the C  $K\alpha$  spectrum indicates significant localization of weakly bonding electrons in OLC. It was proposed that this localization might result from defects in the curved graphitic networks, namely, the holes, which appear through a deficit of surface diamond atoms during ND annealing that are required to form an ideal spherical shell. Quantum-chemical calculations on the holed cage (see Figure 7, which presents the calculated of C  $K\alpha$  spectra for different type of naocarbon cluster) explain the increase in high-energy intensity by the additional contribution of the electrons from dangling bonds on the zigzag edges. The relative chemical inertness of such bonds may be explained by steric problems occurring when reagents penetrate deep into the OLC through the rather small size of holes. The proposed formation of OLC with a holed structure is in a good agreement with the ESR study [32] of similar samples. Thus, 10 unpaired electrons per one carbon onion were registered in [32], where onions were prepared at temperature lower than 2100K. The holed structure of onions can be annealed at temperatures higher than 2100K, however this procedure leads to the formation of bigger polygonized hollow onions.

### 5.3 Resistivity Measurements of OLC and $sp^2/sp^3$ Nanocomposites

Resistivity measurements of OLC and  $sp^2/sp^3$  nanocomposites demonstrate electrical properties that differ from properties of well-known graphite materials [23]. For typical graphite materials (carbon black, graphitized soot, and graphite powder) 3-dimensional electrical conductivity is usually observed. The common graphite materials usually exhibit metallic conductivity, which decreases with increasing temperature. At the same time OLC and intermediate samples of annealed ND demonstrate a variation in the electrical conductivity dimensionality from 0.5 to 1.5. The corresponding temperature dependence of electrical resistivity is typical for systems with variable hopping-length hopping conductivity. This can be explained by a specific type of the composite structure formed with highly curved graphene sheets, carbon onions and diamond core.

Figure 8 illustrates a hierarchical scheme of OLC forming aggregates that result in their unique electrical characteristics. Here, OLC aggregates are obtained by annealing of nanodiamond aggregates. Within the aggregates onions are linked to each other with defect graphite-like sheets and C-C bonds. Some parts of the onions are represented by elongated particles, with linked external graphitic layers and closed quasi-spherical shells. The conduction carrier concentration  $n$  for OLC samples was estimated within



the framework of the theory of negative magnetoresistance in semiconductors in the hopping conduction region (with the proposition  $n \sim n_c$ ,  $n_c$  is critical concentration). The parameters are estimated to be  $n \sim 8 \cdot 10^{21} \text{ cm}^{-3}$  for OLC prepared at 1800K and  $n \sim 3 \cdot 10^{21} \text{ cm}^{-3}$  for OLC prepared at 2140K [38]. The free path length of electrons within OLC particles is comparable with the size of graphitic fragments within holed structure of a single onion ( $1 \sim 12 \pm 2 \text{ \AA}$ ). When the holed structure is further annealed to produce hollow polygonized structures the free path length of the electron increases up to  $18 \pm 2 \text{ \AA}$ . The size localization length (60–100 nm) of current carriers is comparable with the size aggregates of OLC particles. Means to control sizes of ND aggregates are known, so that size of OLC aggregate obtained by annealing of ND can be controlled accordingly.

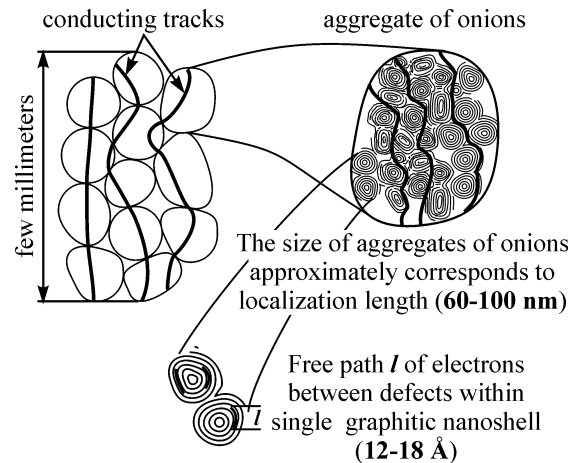


Figure 8. The scheme of three scales of OLC particle organization. The hard solid lines correspond to current conduction tracks [50].

## 6. MODEL OF ND ANNEALING AND FORMATION OF OLC HOLED STRUCTURE

The presented results allow for the proposal of a mechanism of OLC formation via ND annealing. During initial stages of nanodiamond annealing curved graphite like sheets are formed via exfoliation from diamond particles.

Closure of these sheets leads to the formation of spiral-like multishell particles, and finally OLC forms. The formation of relatively high concentration of unsaturated carbon occurs before closure of graphitic shells.

To elucidate the reasons leading to the formation of holed structure of OLC we have performed a computer modeling of ND annealing. Density functional theory (DFT) studies of annealing small ND clusters are known [9,51,52]. However in these papers due to the limitations of number of atom in model the size of diamond clusters could not be big enough to understand the mechanism of defect formation.

We have used a combination of molecular dynamics (MD) calculations that use forces computed by standard semi-empirical quantum mechanics (MNDO, AM1, PM3) with further molecular mechanics models. The initial ND cuboctahedral cluster contained 4490 carbon atoms.

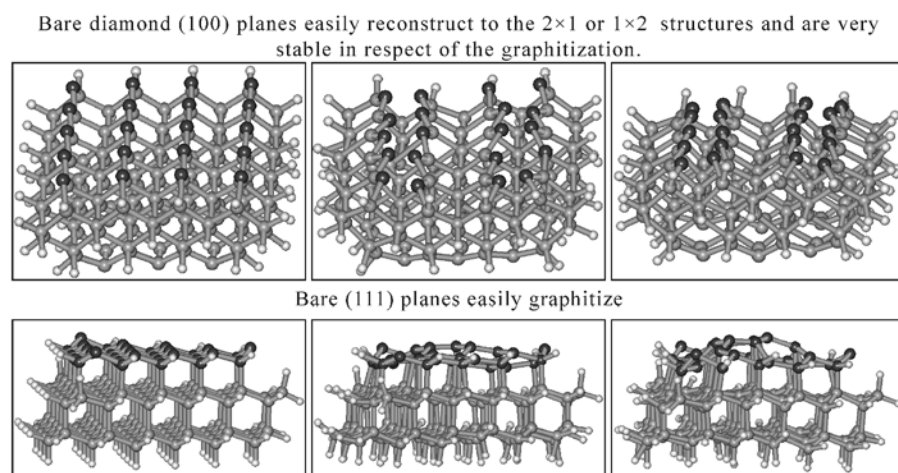


Figure 9. Results of molecular dynamics study (standard semi-empirical method PM3) of bare surface annealing of diamond clusters with different crystallographic planes. (a) Reconstruction of (100) planes ( $2\times 1$  structure formation at 1500K); (b) Successive graphitization of (111) planes with exfoliation of (002) graphitic planes (0.4 ps, 150K).

Figure 9 presents the principal results of MD study of annealing of bare (100) and (111) diamond planes. One can see that annealing of the (100) surface results in  $2\times 1$  surface reconstruction stable up to very high temperatures (1200–1500K), while in the case of cluster with the (111) surface the graphitization occurs at low temperatures. This is in good agreement with experimental results [53] and computer simulation of diamond clusters annealing [9,10,52].

We have used the results regarding the relative stability of different diamond planes to construct sequence of MM models reflecting the successive steps of graphitization of an isolated ND particle. In accord with our experimental data and MD simulation the diamond transformation occurs mainly via the graphitization of (111) planes. At the same time reconstructed (100) planes graphitized only at the cross-sections with transformed (111) planes (see Figure 10).

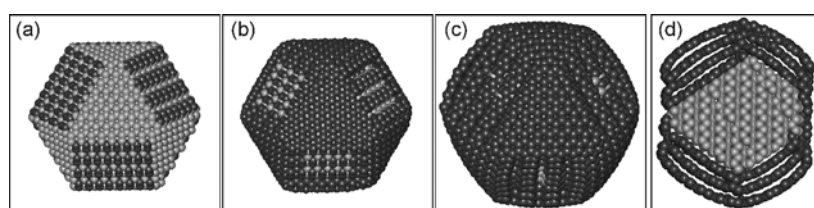


Figure 10. Molecular mechanics models of the successive graphitization of a cuboctahedral diamond cluster. (a) (100) planes only reconstructed into  $2 \times 1$  structures; (b) and (c) graphitization occurs via the transformation of (111) planes; (d) a cross section of the particles (c).

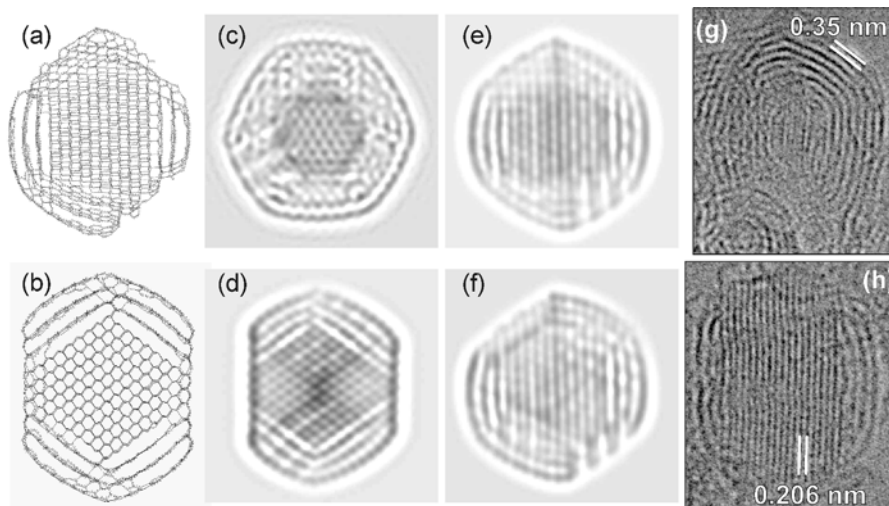


Figure 11. The comparison of the molecular mechanics model of partially graphitized diamond particles (a, b) and their electron microscopy images calculated after the orientation of the model at different angles with electronic beam (c,d,e,f) and experimental electron microscopy images of intermediates of ND annealing products (g,h). (The electron microscopy images were calculated by Dr. A.L. Chuvilin).

Comparison of the model electron microscopy images calculated with the MM model are in good agreement with the experimental ones (see Figure 11). Thus, one can see that graphene-like sheets initially formed mainly after transformation of (111) planes. Closure of graphene sheets leading to OLC formation meets with high deficit of carbon atoms in the regions of pristine (100) planes leading to the formation of holed defects in OLC shells. Annealing of these holes can start only at temperature higher than 1900–2000K, due to lower mobility of carbon atoms at lower temperatures. Experimentally we have observed formation of hollow onions and annealing defects after heating OLC at temperature higher than 2100K. Therefore, the origin of defects accompanying the OLC formation can be explained in terms of deficit of diamond carbon atoms in the graphite/diamond interface to form perfect fullerene-like shells.

## 7. CONCLUSION

ND graphitization has been systematically investigated. ND annealing products (OLC,  $sp^2/sp^3$  nanocomposites) present new nanocarbon materials with some specific properties (namely small size of curved graphitic shells, the presence of interface between nanosize diamond cores and graphitic shells, and high concentration of defects stabilized within nanoparticle volume), which can cause the unusual properties of carbon materials (electronic, magnetic and optical properties). However, the applications of OLC properties are poorly studied, mainly due to their low experimental availability. In spite of that, these materials stimulate a great interest, and extensive experiments for the preparation of narrow fraction of onions and their functionilization are required. At present ND production has been commercialized in Russia, Ukraine, Belarus and China (several hundreds of kilograms). This makes the production of OLC in large quantities by ND annealing more economically feasible than other advanced nanocarbon constituents such as carbon nanotubes and fullerenes, which remain prohibitively expensive for large-scale applications.

## Acknowledgements

This work was supported by the RFBR (02-03-32296) and CRDF and the Department of Education of RF (No 008-X1). We would like to thank Dr. Amanda Barnard for her kind help in the preparation of the paper.

## REFERENCES

1. G. Davies and T. Evans. Graphitization of diamond at zero pressure and a high pressure. *Proc. R. Soc. Lond. A* **328**, 413-27 (1972).
2. T. Evans. Changes produced by high temperature treatment of diamond. In: *The properties of diamond*. Ed. J.E. Field. London, New York, San Francisco: Academic Press, pp. 403-24 (1979).
3. V.M. Titov, I.Yu. Malkov, V.L. Kuznetsov, and A.L. Chuvilin. Method of production of onion-like carbon particles. Russian Patent 209370 (October 19, 1993).
4. V.L. Kuznetsov, A.L. Chuvilin, Yu.V. Butenko, and V.M. Titov. Onion-like carbon from ultra-disperse diamond. *Chem. Phys. Lett.* **222**, 343 (1994).
5. V.L. Kuznetsov, I.Yu. Malkov, A.L. Chuvilin, E.M. Moroz, V.N. Kolomiichuk, Sh.K. Shaichutdinov, and Yu.V. Butenko. Effect of explosions on the structure of detonation soots: ultradisperse diamond and onion carbon. *Carbon* **32**, 873 (1994).
6. V.L. Kuznetsov, A.L. Chuvilin, Yu.V. Butenko, A.K. Gutakovskii, S.V. Stankus, and R.A. Khairulin. Closed Curved Graphite-Like Structures Formation on Micron-Size Diamond, *Chem. Phys. Lett.* **289**, 353 (1998).
7. V.L. Kuznetsov, I.L. Zilberberg, Yu.V. Butenko, A.L. Chuvilin, and B. Segall. Theoretical study of the formation of closed curved graphite-like structures during annealing of diamond surface. *J. Appl. Phys.* **86**, 863 (1999).
8. V.L. Kuznetsov, A.L. Chuvilin, Yu.V. Butenko, I.Yu. Malkov, A.K. Gutakovskii, S.V. Stankus, and R.A. Khairulin. In: *Science and Technology of Fullerene Materials*. Ed. P. Bernuer, D.S. Bethune, L.Y. Chiang, T.W. Ebbesen, R.M. Metzger, and J.W. Minmire. *Mater. Res. Soc. Proc.* **359**. Pittsburgh Materials: Research Society, p. 105, 1995.
9. J.-Y. Raty and G. Galli. Structural and electronic properties of isolated nanodiamonds: a theoretical perspective, this Proceedings, p. 15-24.
10. A.S. Barnard. From nanodiamond to nanowires, this Proceedings, p. 25-38.
11. V.Yu. Dolmatov. Ultradispersed diamond from detonation synthesis: properties and applications. *Uspekhi Khimii* **70**(7), 687 (2001) (in Russian).
12. V.Yu. Dolmatov *Ultradispersed diamond from detonation synthesis*. St. Petersburg: State Polytechnic University, St. Petersburg (2003) (in Russian).
13. A.L. Vereschagin *Detonation Nanodiamonds*. Barnaul, Russian Federation: Altai State Technical University (2001).
14. E. Mironov, A. Koretz, and E. Petrov. Detonation synthesis ultradispersed diamond structural properties investigation by infrared absorption. *Diam. Relat. Mater.* **11**, 872-76(2002).
15. V.L. Kuznetsov, M.N. Aleksandrov, I.V. Zagoruiko, A.L. Chuvilin, E.M. Moroz, V.N. Kolomiichuk, and V.A. Sakovitch. Study of ultradispersed diamond powders obtained using explosion energy. *Carbon* **29**, 665 (1991).
16. Y.W. Zhu, X.Q. Shen, B.C. Wang, X.Y. Xu, and Z.J. Feng. Chemical mechanical modification of nanodiamond in an aqueous system. *Phys. Solid. State* **46**(4), 681 (2004).
17. V.L. Kuznetsov, M.N. Aleksandrov, I.V. Zagoruiko, A.L. Chuvilin, E.M. Moroz, V.N. Kolomiichuk, and V.A. Sakovitch. Study of ultradispersed diamond powders obtained using explosion energy, *Carbon* **29**, 665 (1991).
18. V.L. Kuznetsov and Yu.V. Butenko. Synthesis and properties of nanostructured carbon materials: nanodiamond, onion-like carbon and carbon nanotubes. In: *Nanostructured materials and coating for biomedical and sensor applications*. Ed. Y.G. Gogotsi and I.V. Uvarova, NATO Science Series, Kluwer Academic Publishers, p. 187 (2003).

19. V.S. Bondar and A.P. Puzyr. Nanodiamonds for Biological Investigations. *Physics of the Solid State* **46**(4), 716-19 (2004).
20. A. Härtl, E. Schmich, J.A. Garrido, J. Hernando, S.C.R. Catharino, S. Walter, P. Feulner, A. Kromka, D. Steimüller, and M. Stutzmann. Protein-modified nanocrystalline diamond thin films for biosensor applications. *Nature Materials* **3**, 736 (2004).
21. Yu.V. Butenko, V.L. Kuznetsov, A.L. Chuvilin, V.N. Kolomiichuk, S.V. Stankus, R.A. Khairulin, and B. Segall. The kinetics of the graphitization of dispersed diamonds at 'low' temperatures. *J. App. Phys.* **88**, 4380 (2000).
22. Yu.V. Butenko, S. Krishnamurthy, A.K. Chakraborty, V.L. Kuznetsov, V.R. Dhanak, M.R.C. Hunt, and L. Šiller Photoemission study of onion-like carbons produced by annealing nanodiamonds, accepted for publication in *Phys. Rev. B*.
23. V.L. Kuznetsov, Yu.V. Butenko, A.L. Chuvilin, A.I. Romanenko, and A.V. Okotrub. Electrical resistivity of graphitized ultra-disperse diamond and onion-like carbon. *Chem. Phys. Lett.* **336**, 397 (2001).
24. E.D. Obratsova, S.M. Pimenov, V.I. Konov, M. , Fujii S. Hayashi, V.L. Kuznetsov, Yu.V. Butenko, A.L. Chuvilin, and E.N. Loubnin. Raman investigation of onion-like carbon. *Molecular Materials* **10**(1-4), 249 (1998).
25. E.D. Obratsova, M. Fujii, S. Hayashi, V.L. Kuznetsov, Yu.V. Butenko, and A.L. Chuvilin. Raman identification of onion-like carbon. *Carbon* **36**, 821 (1998).
26. T. Enoki. Diamond-to-graphite conversion in nanodiamond and the electronic properties of nanodiamond-derived carbon system. *Phys. Solid. State* **46**(4), 651 (2004).
27. A.M. Affoune, B.L.V. Prasad, H. Sato, T. Enoki, Y. Kaburagi, and Y. Hishiyama. Experimental evidence of a single nano-graphene. *Chem. Phys. Lett.* **348**, 17 (2001).
28. O.E. Andersson, B.L.V. Prasad, H. Sato, T. Enoki, Y. Hishiyama, Y. Kaburagi, Yoshikawa, M. and S. Bandow. Structure and electronic properties of graphite nanoparticles. *Phys. Rev. B* **58**, 16387 (1998).
29. B.L.V. Prasad, H. Sato, T. Enoki, Y. Hishiyama, Y. Kaburagi, A.M. Rao, K. Oshida, and M. Endo. Heat-treatment effect on the nanosized graphite pi-electron system during diamond to graphite conversion. *Phys. Rev. B* **62**, 11209 (2000).
30. V.L. Kuznetsov, Yu.V. Butenko, V.I. Zaikovskii, and A.L. Chuvilin. Carbon redistribution processes in nanocarbons. *Carbon* **42**, 1057 (2004).
31. S. Tomita, M. Fujii, S. Hayashi, and K. Yamamoto. Electron energy-loss spectroscopy of carbon onions. *Chem. Phys. Lett.* **305**, 225 (1999).
32. S. Tomita, T. Sakurai, H. Ohta, M. Fujii, and S. Hayashi. Structure and electronic properties of carbon onions. *J. Chem. Phys.* **114**, 7477 (2001).
33. S. Tomita, A. Burian, J.C. Dore, D. LeBolloch, M. Fujii, and S. Hayashi. Diamond nanoparticles to carbon onion transformation: X-ray diffraction study. *Carbon* **40**, 1469 (2002).
34. S. Tomita, S. Hayashi, Y. Tsukuda, and M. Fujii. Ultraviolet-visible absorption spectroscopy of carbon onions. *Phys. Solid State* **44**, 450 (2002).
35. J.B. Donnet, Le Moigne, T.K. Wang, M. Samirant, and A. Eckhardt. Onion-like and equilibrium structure of carbon. *CR ACAD SCI II C* **1**(7), 431 (1998).
36. M.V. Baidakova, Yu.V. Butenko, V.L. Kuznetsov, A.Ya. Vul', M.A. Yagovkina. X-ray Diffraction Study of Low Temperature Graphitization of Diamond, International Symposium, Detonation Nanodiamonds: Technology, Properties and Applications, St Petersburg, Russia July 7-9 2003, p 77 (2003).
37. A.V. Okotrub, L.G. Bulusheva, V.L. Kuznetsov, Yu.V. Butenko, A.L. Chuvilin, and M.I. Heggie. X-ray emission studies of valence band of nanodiamonds annealed at different temperatures. *J. Chem. Phys. A* **105**, 9781 (2001).



38. A.I. Romanenko, O.B. Anikeeva, A.V. Okotrub, L.G. Bulusheva, V.L. Kuznetsov, Yu.V. Butenko, A.L. Chuvilin, C. Dong, and Y. Ni. The temperature dependence of the electrical resistivity and the negative magnetoresistance of carbon nanoparticles. *Phys. Solid. State* **44**(3), 487 (2002).
39. E. Koudoumas, O. Kokkinaki, M. Konstantaki, S. Couris, S. Korovin, P. Detkov, V. Kuznetsov, S. Pimenov, and V. Pustovoi. Onion-like carbon and diamond nanoparticles for optical limiting. *Chem. Phys. Lett.* **357**, 336 (2002).
40. Ph. Lambin, L. Henrard, A.A. Lucas, and Th. Cabioch. Optical properties of the carbon onions, in G. Benedek, P. Milani, and V.G. Ralchenko (eds.), *Nanostructured Carbon for Advanced Applications*. Dordrecht: Kluwer Academic Publishers, pp. 273-84 (2001).
41. N. Keller, N.I. Maksimova, V.V. Roddatis, M. Schur, G. Mestl, V.L. Kuznetsov, Yu.V. Butenko, and R. Schlögl. The catalytic use of onion-like carbon materials for Styrene Synthesis by oxidative dehydrogenation of ethylbenzene. *Angew. Chem. Int. Ed.* **41**(11), 1885 (2002).
42. V.V. Roddatis, V.L. Kuznetsov, Yu.V. Butenko, D.S. Su, and R. Schlögl. Transformation of diamond nanoparticles into carbon onions under electron irradiation. *Phys. Chem., Chem. Phys.* **4**, 1964 (2002).
43. D. Ugarte. Curling and closure of graphitic networks under electron beam irradiation. *Nature* **359**, 707 (1992).
44. F. Banhart. Irradiation effects in carbon nanostructures. *Rep. Prog. Phys.* **62**, 1181 (1999).
45. M. Zaiser, Y. Lyutovich, and F. Banhart. Irradiation-induced transformation of graphite to diamond: A quantitative study. *Phys. Rev. B* **62**(5), 3058 (2000).
46. F. Banhart, T. Fuller, Ph. Redlich, and P.M. Ajayan. The formation, annealing and self-compression of carbon onions under electron irradiation. *Chem. Phys. Lett.* **269**, 349 (1997).
47. W.A. De Heer and D. Ugarte. Carbon onions produced by heat treatment of carbon soot and their relation to the 217.5 nm interstellar adsorption feature. *Chem. Phys. Lett.* **207**, 480 (1993).
48. M. Terrones and H. Terrones. The role of defects in graphitic structures. *Full. Sci. and Tech.* **4**, 517 (1996).
49. L.G. Bulusheva, A.V. Okotrub, V.L. Kuznetsov, A.L. Chuvilin, Yu.V. Butenko, and M.I. Heggie. Topology and electronic structure of onion-like carbon and graphite/diamond nanocomposites. In: S. Komarneni, J.-I. Matsushita, G.Q. Lu, J.C. Parker, R.A. Vaia (eds.), *Nanophase and Nanocomposite Materials* **703**, Mat. Res. Sym. Proc., Material Research Society, Pittsburgh, pp. 381-86 (2002).
50. A.I. Romanenko, O.B. Anikeeva, A.V. Okotrub, V.L. Kuznetsov, Yu.V. Butenko, A.L. Chuvilin, C. Dong, and Y. Ni. Temperature dependence of electroresistivity, negative and positive magnetoresistivity of carbon nanoparticles. In: S. Komarneni, J.-I. Matsushita, G.Q. Lu, J.C. Parker, R.A. Vaia (eds.), *Nanophase and Nanocomposite Materials* **703**, Mat. Res. Sym. Proc., Material Research Society, Pittsburgh, pp. 259-64 (2002).
51. J.-Y. Raty, G. Galli, C. Bostedt, T.W. van Buuren, and L.J. Terminello. Quantum confinement and fullerene-like surface reconstructions in nanodiamonds. *Phys. Rev. Lett.* **90**, 037401 (2003).
52. F. Fugaciu, H. Hermann, and G. Seifert. Concentric-shell fullerenes and diamond particles: A molecular-dynamics study. *Phys. Rev. B* **60**, 10711 (1999).
53. B.B. Pate. The diamond surface - atomic and electronic-structure. *Surf. Sci.* **165**, 83 (1986).

# 16

## PHYSICAL AND CHEMICAL PROBLEMS OF MODIFICATION OF DETONATION NANODIAMOND SURFACE PROPERTIES

V.Yu. Dolmatov<sup>1</sup> and T. Fujimura<sup>2</sup>

<sup>1</sup> *Diamond Centre, Sovetskii prospect 33A, St.Petersburg 193076, Russia*

<sup>2</sup> *Kyobashi Kimpodo B/D, 7<sup>th</sup> Floor, 2-8-21, Kyobashi, Chuo-ku, 104-0031, Tokyo, Japan*

**Abstract:**

A wide application of detonation nanodiamonds is hampered by their low purity and difficulties of making stable nanodiamond suspensions. These problems have not been adequately dealt with in available publications. Here we present an integrated conception of the nanodiamond structure and offer a practical solution to some of these problems. A detailed description and a schematic illustration of the detonation nanodiamond structure are presented. The structure-forming effect of nanodiamond particles on the ambient is interpreted. The pH of an aqueous suspension of nanodiamonds is determined and their behavior as a function of the pH is shown. We also analyse the mechanism of a prolonged water washing to remove excessive acidity, a factor determining the chemical purification time. A method is offered to improve essentially the quality of nanodiamonds and the stability of their aqueous suspensions by treating them with ammonia water (to an alkaline medium), followed by heating to 200–240°C under pressure (so called “thermolysis”).

**Keywords:**

detonation nanodiamond structure, chemical purification, surface modification, ammonia water treatment, thermolysis

### 1. PHYSICAL AND CHEMICAL PROPERTIES OF NANODIAMONDS

Detonation nanodiamond (ND) is a very complex object having, at least, a three-layered structure. Purified and dried ND is a cluster carbon diamond-containing material made up of aggregates of rounded or irregular particles with an average diameter of 10 nm and less.



As part of an aggregate, every particle (cluster) represents a structure containing the following constituents:

- a core of carbon atoms ( $sp^3$ -hybridization) making up a cubic crystal lattice typical of diamond; it includes 70–90% of carbon atoms and has a size of 40–60 Å, as evidenced by X-ray data.

- an intermediate 4–10 Å shell of X-ray amorphous carbon around the core, which may include 10–30% of carbon atoms. The shell is made up of  $sp^2$ -hybridization carbon and is inhomogeneous. It has been suggested in [1] that its inner surface immediately adjacent to the diamond core consists of continuous layers of onion-like carbon (groups of 6 carbon atoms in  $sp^2$ -hybridization, or a hexagon); over them there are fragmentary graphite-like monolayers located within the same shell. The amorphous carbon shell has a porous structure; it contains numerous defects and individual carbon areas; it can also incorporate some heteroatoms during the detonation synthesis;

- a surface layer containing other heteroatoms in addition to carbon, producing a wide variety of functional groups; the number of heteroatoms may be quite large, about 10% of the particle mass, and most of them are oxygen atoms. There are some hydrogen and nitrogen atoms present in the functional groups; the major groups (hydroxylic, carboxylic, ketonic, lactonic, and others) contain oxygen.

A schematic illustration of a ND particle, designed by O.Shenderova (Computational Materials Science & Device Modeling Group, International Technology Center, USA), is given in Figure 1.

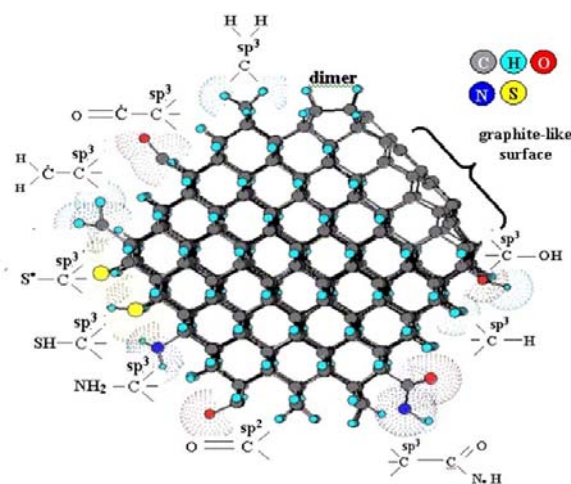


Figure 1. A schematic nanodiamond particle with different surface groups and reconstructions. The structure is optimized by the semi-empirical quantum chemical PM3 method (O. Shenderova, USA).

Since the core and its shell are nearly totally composed of carbon atoms, most heteroatoms are located in the surface layer, occupying about half of it. In other words, ND does not represent a purely carbon material but rather a combination of its structural modifications, including pure diamond. The quantitative parameters characterizing the size and composition of the layers can be changed by varying the production conditions and the extraction technology.

The structural and other quantitative characteristics of the core and the carbon shell arise during the detonation synthesis. The outer shell governs the interrelation between a ND cluster and the ambient; the shell forms the interface and interacts with the latter. The shell structure and composition strongly depend on the methods of ND purification and storage. The minute particle size greatly increases the contribution of the interface interaction, but they govern only the ND macrocharacteristics and their consumer quality. The presence of highly polar reactive groups on the surface underlies a profound ND effect on the ambient medium.

The current ND production techniques are based on detonation synthesis providing only a primary carbon material, the so called "diamond blend" (DB) with diamond fragments. In addition, the DB includes graphite-like structures, broken amorphous chains of carbon atoms combined with numerous functional groups arising from an incomplete oxidative destruction of organic products. Of course, there are also man-caused impurities (metals and their derivations - carbides, oxides) and the components of the production medium (fixed gases, liquids). On the other hand, the chemical methods of ND separation and purification from the primary carbon stimulate the formation of a new surface layer.

The available techniques for separation of graphite impurities and other non-diamond carbon are based on their selective oxidation, when the diamond core is unaffected, whereas the weaker C-C bonds are broken on the surface. It is natural that oxygen-containing groups should prove to be dominant but their qualitative and quantitative composition should strongly depend on the oxidation method used. There are many groups of impurities: metals, non-diamond carbon, inorganic products such as oxides and carbides, reagents used for ND purification, and occasional mechanical impurities.

Within the above model, it would be reasonable to consider ND as a three-dimensional rigidly structured polymer, rather than as a small crystal with a defective surface. Then the inner polymer framework should be formed by saturated carbon bonds and the surface should be saturated with highly polar groups. The three-dimensional framework allows a large quantity of organic fragments to accumulate in a very small volume, providing a structure-forming effect of ND particles. ND is a unique

substance due to its inorganic-organic transition, so it ranks among very special ultradisperse materials like fullerenes, nanotubes, and carbines.

An effective and highly productive technology of chemical purification of detonation nanodiamonds (like ultradisperse diamonds, UDD) is the treatment of DB with dilute nitric acid at a pressure of 100 atm and a temperature of 240–260°C [2]. In that case, the ND purity may be as high as 99 wt.% if the DB is allowed to stay in the high pressure - high temperature zone for 30–40 min. We have successfully introduced this technology in Russia, Byelorussia, and China. But in spite of a high ND quality and reactor productivity, the final, seemingly simple stage - the removal of acid and soluble impurities by washing – still remains a problem. This process lasts for 4–5 days, appreciably decreasing the productivity of the purification stage as a whole.

## **2. PROBLEMS OF ND PURIFICATION**

When we consider the problems of the ND washing to remove water soluble impurities and the control of the washing efficiency and aggregation, we should keep in mind a fairly high intrinsic ND acidity due to the presence of carboxyl groups on the surface.

An aqueous suspension of pure ND cannot be neutral but it has an acidic reaction (Figure 2). We must know the number of the acid groups and their contribution to the total acidity of the medium under different conditions. The sedimentation stratifies a ND suspension into two layers: a bottom thickened layer and a clarified layer at the top (water free from ND), which differ in acidity. The bottom layer acidity depends on the total effect of the acid groups in the ND, as well as on the acidic and alkaline agents dissolved in the water, while the top layer acidity varies only with the acid dissolved.

After the decantation of the top layer, the pH measurement and titration provide information on the contents of acidic and alkaline impurities. From the difference in the acid contents in the two layers, one can estimate the ND contribution to the total medium acidity.

At  $\text{pH} < 1$ , the acid content in the clarified layer of the initial aggregation-stable suspension is nearly the same as that in the thickened layer after a period of setting. However at  $\text{pH} > 3$ , the contribution of the nitric acid on ND particles becomes essential. For example, as much as 95% of nitric acid is found to be on ND and only 5% in water at  $\text{pH} = 4$ . The nitric acid diffusion from the ND surface is very slow because of strong adsorption properties of ND.

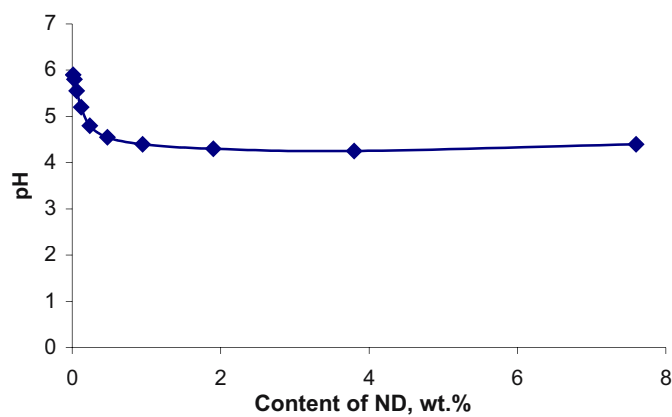


Figure 2. The pH of a washed ND suspension versus the ND content.

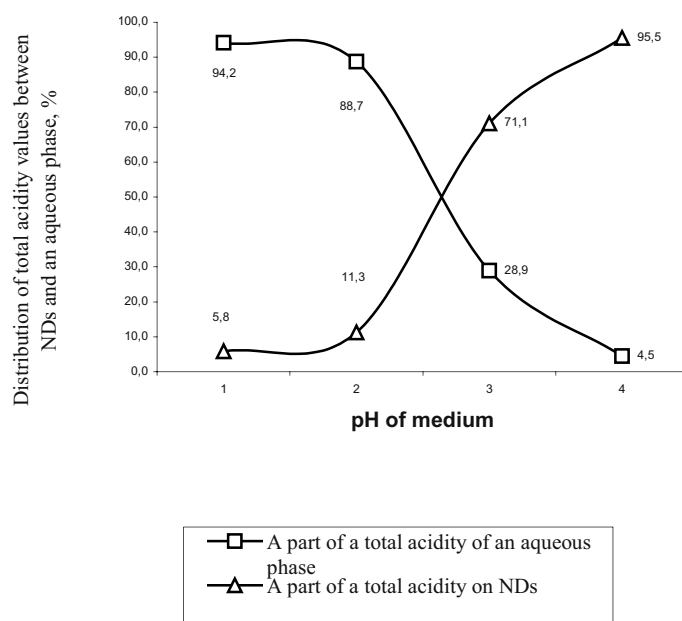


Figure 3. The distribution of the total acidity of a ND suspension between the ND and the aqueous phase at different pH values.

Therefore, the ND particles must behave in water like a non-readily soluble weak organic acid, and this can be observed in practice. Hence, one cannot make a neutral ND suspension without using a neutralizing alkaline agent. But formally, the parameter  $\text{pH} = 7$  can convey nothing about the state of the ND particles because they can be involved in the acid-base equilibrium, acting either as an acidic agent or an alkaline one, depending on the partner's acidity.

The acidic properties are often important in the study of aggregative and sedimentative stability of aqueous suspensions. This issue is equally important for the ND purification technology since all of its available modifications involve the treatment with strong acids. Acids are usually removed by water washing. Free sedimentation of a ND suspension during the washing from acids or ammonia water (in the case of acid neutralization) produces a 5–7% thickening of the suspension, so in the absence of large amounts of salt-forming impurities, further sedimentation is practically stopped, at least, it seems so.

The sedimentation rate in diluted suspensions (Figure 4) is similar to that of particles of about  $1\ \mu\text{m}$  size. It takes 12–24 hours for most ND particles to sediment, producing a thick aqueous suspension at  $\text{pH} < 2$ .

The concentration of ND particles at a maximum 5–7% thickening is well reproduced. The interface between the thickened layer and the clarified layer is well-defined. The mass is mobile, and its thickened portion can be separated. Then water is added the suspension, suspension is agitated, allowed to settle down and the process is repeated. A diluted suspended ND solution is obtained and again thickened to the above value. So the value of 5–7 wt.% seems to be quite representative. At this concentration in the dense suspension, the water is physically in the zone of the structure-forming effect of ND particles. As a result, water forms hydrospheres, which gather around the ND particles or their aggregates and stay in the small vicinity of the particles. The ionic mechanisms and hydrogen bonds seem to play a vital role in the structure-forming effect. It is quite likely that the mechanism of formation of primary hydrospheres determines the level of subsequent agglutination of ND particles or their aggregates with dense slowly moving hydrospheres, which aggregate to form complexes having a common outer hydrosphere behaving as a large particle on sedimentation. This is observed in acidic media at  $\text{pH} < 2$  and in alkaline media at  $\text{pH} > 8$ ; within this range,  $\text{pH}$  depends but little on the concentration of acidic and alkaline agents.

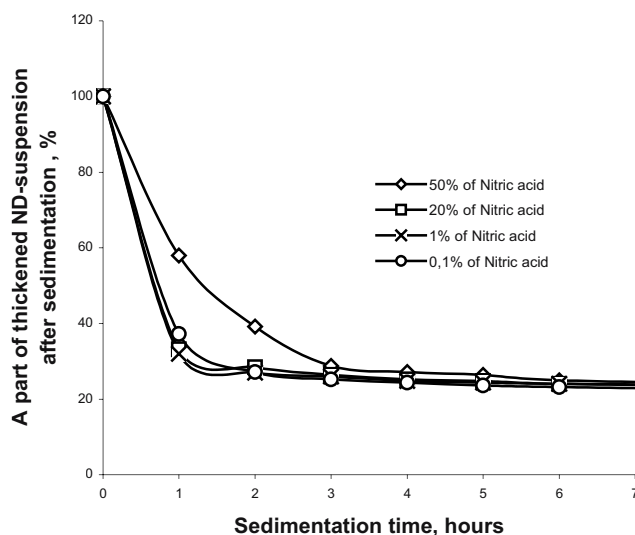


Figure 4. The variation of the sedimentation rate of a 1% ND suspension with the nitric acid concentration in the water phase.

In aqueous suspensions, ND particles are known to have a negative surface charge in the absence of foreign impurities, which is determined by a large number of oxygen-containing polar groups, primarily hydroxyl and carboxyl ones. But in strong acid solutions, e.g. nitric acid solutions, the ND surface must have a positive charge due to the chemical and physical sorption of hydroxonium ions.

A similar situation is observed in alkaline media, e.g. in an ammoniac one. The addition of ammonium ions at the acid sites again makes the surface charge positive, and the presence of highly mobile ions in the diffusive layer initiates an interaction via the ionic mechanism.

As the concentration of ammonia water or nitric acid in the medium decreases during the washing, which can be well controlled by the pH-values, there is a decrease in the thickened layer density, and the interface between the clarified and thick layers becomes smeared (Figure 5). The interface smearing indicates the beginning of a «hovering» phenomenon, which results from decreasing amount of electrolyte (acid, alkaline or salt) in the aqueous suspension.

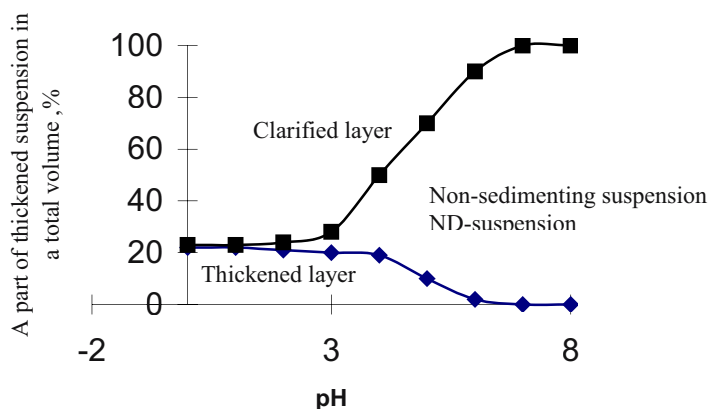


Figure 5. Stratification of a ND suspension during sedimentation as a function of the medium pH. Sedimentation time 24 hours, the initial concentration of the suspension 1%.

The result is a partial disintegration of large associates. In that case, residual ions are accumulated mostly in the ND hydrospheres. Visually, this appears as a decreasing thickening and as the interface smearing (Figure 5). At still lower concentrations of strong acids or bases, a practically complete disintegration of the associates occurs and the system returns to the state complete “hovering”.

The use of centrifugation promotes the ND aggregation in the thickened layer (to 12–14% at  $\text{pH} < 2$ ); it is effective for strong acid media. At pH close to 7, the aggregation effectiveness drops sharply, and the “hovering” suspension cannot be clarified completely. The experience of using ultracentrifuges at Russian plants has shown their low efficiency because of their short lifetime in strong acid media, a factor raising the cost of the ND purification technology and the ND prices.

### 3. THERMOLYSIS

We have shown that if the ratio of the thickened layer volume to the amount of fresh water is kept constant at 1:4, the concentration of nitric acid in the suspension decreases to 0.18–0.25 wt.% ( $\text{pH} = 1.8\text{--}2.0$ ) after the fourth washing run; after the fifth run, the acidic ND concentration is in the range of 0.07–0.10 wt.% ( $\text{pH} = 2.2\text{--}3.0$ ). Further washing seems unreasonable because the suspension becomes “hovering”, the sedimentation time greatly increases while the productivity drops.

To control the “hovering” at pH = 1.5–2.5, one should neutralize the acid residual in the solution and on the ND surface by sharply increasing the amount of ammonia water to change the medium pH from acidic (nitric acid is 0.1–0.3 wt.%) to alkaline (pH = 9–10). Even at pH = 10, the residual ammonia water is only 0.025 wt. %.

Ammonia water treatment has the following advantages. First, the ammonium salts of nitric and nitrous acids dissolve readily in water and can be removed (for 1–2 washing runs) together with the clarified water from the thickened suspension. Second, the residual ammonia water can be easily distilled as a gas. Third,  $\text{NH}_4^+$  ions possessing the smallest radius among alkaline agents penetrate into the medium-sized pores and micropores of the ND aggregates, thereby neutralizing the traces of mineral acids there.

Note that a long-term storage of ND suspensions slightly decreases their pH, e.g., a 21 day storage will decrease pH from 7.2 to 6.7. This is due to the following reasons. The presence of ammonia water in the suspension makes  $\text{HNO}_3$ ,  $\text{HNO}_2$  and nitrogen oxides diffuse faster out of the ND micropores, acidifying the suspension. The ND particles themselves have a weakly acidic reaction in an aqueous suspension. The salts of a weak base ( $\text{NH}_4\text{OH}$ ) and a strong acid ( $\text{HNO}_3$ ,  $\text{HNO}_2$ ) have a weakly acidic reaction in an aqueous solution.

The presence of excessive ammonia water or ammonium salts (electrolyte) in the suspension promotes an alkaline reaction, accelerating the stratification to 2–3 washing runs. The ND layer thickening at the bottom increases to ~ 8 wt.%, sometimes, to 12 wt. %.

However, neither chemical purification nor the treatment of well-washed ND with ammonia water under normal conditions can change the concentration of nitrogen oxides in the medium-sized pores or micropores of the ND aggregates. In order to solve this problem and also to decrease the aggregate sizes, it is necessary to warm up the weakly acidic suspension (neutralized with ammonia water) to 200–240°C for 30 min. [3]. A higher temperature (and pressure) promote the following processes in the medium.

(1) The salts formed on the surface, e.g.  $\text{NH}_4\text{NO}_3$  and  $\text{NH}_4\text{NO}_2$ , readily diffuse into the solution.

(2)  $\text{NH}_4\text{NO}_3$  and  $\text{NH}_4\text{NO}_2$  begin to decompose violently at 200–240°C to produce gaseous products and water, as in reactions (1) and (2) (see below). Nitrous oxide produced from reaction (1) is then decomposed to give nitrogen, as in reaction (3), whereas nitrogen oxides which come in contact with excessive ammonia water form nitrogen and water, as in reaction (4):







(3) Due to a violent gassing, 350–500 nm aggregates break into smaller ones with a size of 10–100 nm. Then the harmless products, such as nitrogen and water, can be removed.

(4) When hydrolyzed, nitrogen oxides are rapidly and nearly completely desorbed from the ND surface (especially, from the inner pores) to form  $\text{NH}_4\text{NO}_3$  and  $\text{NH}_4\text{NO}_2$ . It was shown earlier that nitrogen oxides sorbed by the ND surface could not be readily removed, especially from the micropores, when common water was used even on heating to higher temperatures.

(5) After the cooling and 2 or 3 washing runs to remove residual ammonium salts and water, we obtain a stable colloidal highly concentrated ND suspension. Its storage time without losing its properties is practically unlimited. Besides, such a suspension is a high-tech product possessing a low viscosity and a high mobility in spite of the high ND concentration of 10–12 wt.%.

(6) The final ND purity is very high, about 99.5 wt.%, owing to the effective desorption of organic and inorganic impurities from the surface in the presence of ammonia water at high temperature and pressure, as well as to the finalizing washing.

To illustrate, a well-washed (7 runs) ND sample (UDD-STW) has the total content of incombustible impurities of 0.95 wt.%, while the same ND sample neutralized with ammonia water to  $\text{pH} = 7.3$  and thermolyzed at  $230^\circ\text{C}$  with 2 additional washing runs (UDD-TAH) contains only half of that value, 0.4 wt.% (Table 1).

Since the thermolysis leaves some ammonia water ( $\text{pH} > 7$ ) and ammonium salts, the ND suspension is not sedimentation-stable. This can be achieved by double and triple water washing. The sedimentation gives a clear boundary between the clarified and thickened layers. The thermolysis slightly decreases the medium pH, e.g. from 8.0 to 7.95, from 9.0 to 8.7; and from 10.0 to 9.75, etc.

However, the thermolytic technique has certain limitations. To decompose ammonium salts nearly completely, it is necessary to add a precisely calculated quantity of ammonia water to get  $\text{pH} = 7.0\text{--}7.5$ , which is an optimal pH range for the decomposition (Figure 6). If pH is higher than 8, some amount of salts is decomposed into gases. It is quite likely that the ND surface rich in functional groups has an inhibiting effect on the salt decomposition because in the absence of ND a complete decomposition is known to occur at  $\text{pH} > 8$  under the same conditions. In principle, a

complete decomposition of ammonium salts is not of great importance since they are basically in the water but not on the ND surface and can be easily washed out.

Table 1. Contents of incombustible elements in ND samples (atomic emission spectroscopy data)

ELEMENT	Contents of elements in ND, wt.%		
	Production of SCTB "Technolog"		Production of RFNC-VNIITF
	Aqueous suspension of NDs, sort UDD-STW according to Specifications TU 05121441-275-95	Aqueous suspension of NDs, sort UDD-TAH according to Specifications TU 05121441-275-95	Standard NDs
Iron	0.15	0.1	0.1
Chromium	0.07	0.05	0.5
Silicon	0.3	0.1	0.15
Aluminium	0.005	0.001	0.01
Sodium	0.03	0.003	0.05
Potassium	0.002	0.002	0.002
Copper	0.005	0.002	0.003
Calcium	0.002	0.002	0.01
Magnesium	0.005	0.003	0.005
Manganese	0.001	No at detectivity of $5 \cdot 10^{-4}$ wt.%	0.001
Titanium	0.01	0.005	0.002
Lead	0.001	0.001	0.001
$\Sigma$	0.58	0.27	0.84
Incombustible residuum, %	0.95	0.4	1.4

If a 2.5% ND suspension with pH = 1.35 (the nitric acid content found by titration is 0.57 wt.%) is treated with ammonia water to pH = 7.2, purified with nitric acid, washed 4 times and then subdivided into three portions, one can use one of the three variants of thermolysis:

(1) If the ND suspension is heated to 190°C for 30 min. but the amount of salts (determined from the  $\text{NO}_3^-$  content) does not decrease or even increases from 0.42 to 1.83 wt.%, i.e. over 4 times, this is due to the desorption of nitrogen oxides from the medium-sized pores and micropores, the hydrolysis of nitrogen oxides in water and the neutralization of slightly decomposed ammonium salts of nitric and nitrous acids with ammonia water. If this suspension with pH = 7.2 is then subjected to thermolysis at 230°C for 30 min., the content of salts (from  $\text{NO}_3^-$ ) decreases by a factor of 26, from 1.83 to 0.07 wt.% (Figure 6). In that case the medium pH decreases from 7.2 to 6.1.

(2) If some ammonia water is added to the suspension with pH = 7.2 to get pH = 8 and the thermolysis is performed in a stepwise mode (at 190°C for 30 min., then at 230°C for 30 min.), the salt content (from  $\text{NO}_3^-$ ) will decrease to 0.44 wt.% (Figure 6), or 4 times (from 1.83 to 0.44 wt.%). In that case the medium pH decreases from 8.0 to 7.95.

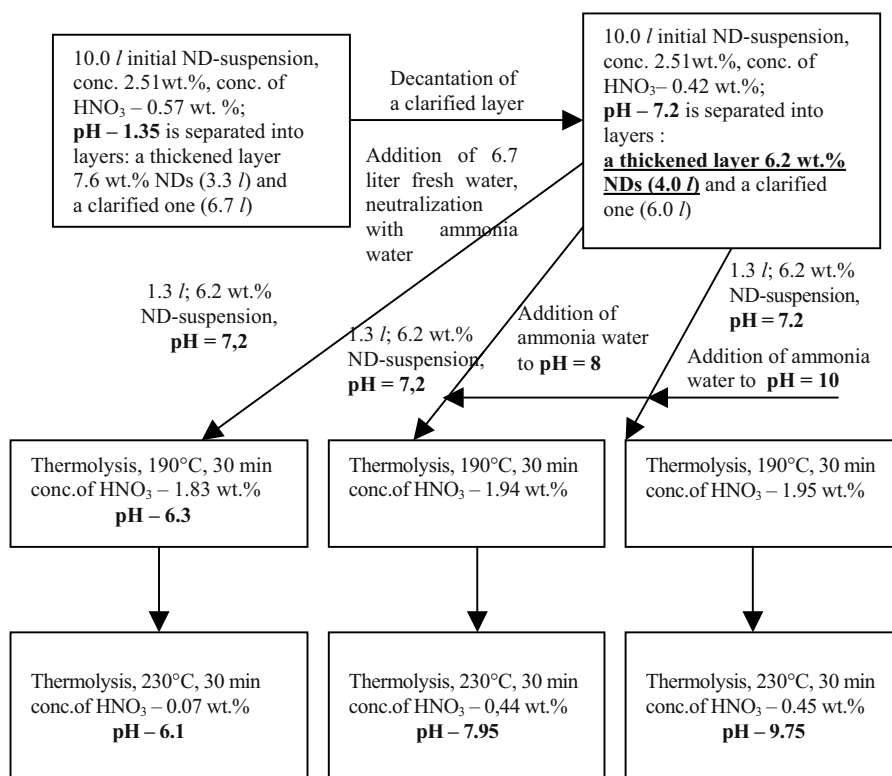


Figure 6. Variants of thermolysis of aqueous ND suspensions at different pH (ammonia treatment).

(3) If the suspension pH is raised to 10.0 by adding some ammonia water and the stepwise thermolysis is used (at 190°C for 30 min., then at 230°C for 30 min.), the salt content (from  $\text{NO}_3^-$ ) will be 0.45 wt.%, (variant 2), decreasing the medium pH from 10.0 to 9.75.

But irrespective of the variant used and the quantity of ammonium salts, the latter can be easily removed, together with the ammonia water excess, by 2 or 3 washing runs to a “hovering” state of pure ND. The final suspension can be stored for years, but the medium pH will gradually decrease to 4.5, a

value for pure ND. Moreover, the size of ND aggregates increases on storage from 10–100 nm to 150–300 nm.

The application of ND in various “delicate” processes, like superpolishing, electronics, oil colloidal compositions, and others, etc., requires that the size of ND aggregates in the suspension should be 100 nm or less. This can be achieved by diluting the suspension to a ND concentration lower than 0.1 wt.%, which is normally unattainable in an actual technological process. Ultrasonic treatment can help grind the ND aggregates but usually for a short time. From a 3.5 wt.% ND suspension, ultracentrifugation can give a sedimentation-stable suspension with a concentration of about 0.7 wt.% with an average aggregate size of 40–85 nm, depending on the centrifugation rate (Figure 7).

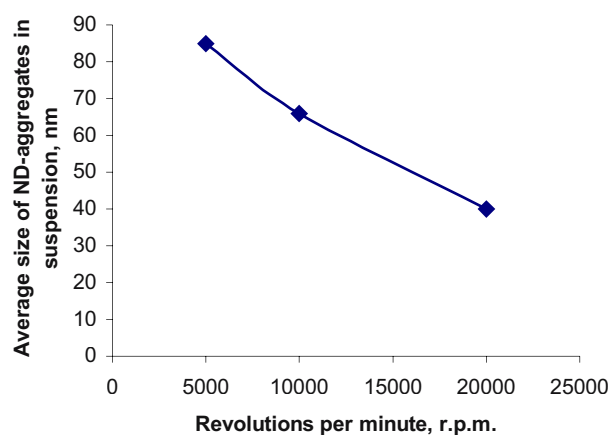


Figure 7. The average size of ND aggregates in a sedimentation-stable suspension (concentration ~0.7 wt.%) versus the centrifugation rate.

#### 4. CONCLUSIONS

(1) We have systematized the basic properties of nanodiamonds characterizing them as a new product combining every possible carbon hybridization into an all-in-one ensemble. Nanodiamonds can be considered as a transient inorganic-to-organic material.

(2) The removal of acids from the suspension by washing is a complex procedure. At  $\text{pH} > 3$ , most of the acidity of the aqueous suspension is due to that of the oxygen-containing groups on the nanodiamond surface. The pH of a medium containing well-washed nanodiamonds in a concentration of

1–10 wt.% is due to the nanodiamonds in themselves have pH between 4.4 and 4.5.

(3) The maximum concentration of a nanodiamond suspension thickened by the gravitational technique for 24 hours in a conventional washing cycle is 5–7 wt.%.

(4). We have offered a novel method to accelerate the nanodiamond purification, improving their quality and the suspension workability. It involves the treatment of acidic aqueous nanodiamond suspensions (pH = 2–2.5) with ammonia water, followed by heating to 200–240°C for 30 min. This procedure provides the following results: a complete desorption of poorly removable nitrogen oxides, their hydrolysis and the formation of ammonium salts; the decomposition of  $\text{NH}_4\text{NO}_3$  and  $\text{NH}_4\text{NO}_2$  into nitrogen and water; the disintegration of large aggregates of 350–500 nm in size into 10–100 nm clusters; a decrease in the suspension viscosity and an increase in its technological mobility; a 2-fold decrease in the impurity contents, including incombustible impurities, which is especially important; the production of stable nanodiamond suspensions after additional 2 or 3 water washing runs.

## REFERENCES

1. A.E. Alexensky, M.V. Baidakova, A.Ya. Vul', and V.I. Siklitsky. The structure of diamond nanocluster. *Phys. Solid State* **41**(4), 668–71 (1999).
2. V.Yu. Dolmatov, V.G. Sushev, and V.A. Marchukov. Method of isolation of synthetic diamonds Pat. 2109683 Russian Federation. Publ. 27.04.98, Bull. 1998/12.
3. T. Fujimura, M. Sone, V.Yu. Dolmatov, and S. Shiozaki. Stable aqueous liquid of finely divided diamond particles. Metallic film containing diamond particles and method of producing the same. Pat. 1 288 162 A2 EP. Publ. 05.03.2003, Bull.2003/10.

# 17

## DISINTEGRATION AND PURIFICATION OF CRUDE AGGREGATES OF DETONATION NANODIAMOND

### *A Few Remarks on Nano Methodology*

E. Osawa

*NanoCarbon Research Institute, Ltd. Rm 301, Toudai Kashiwa Venture Plaza 5-4-19  
Kashiwa-no-ha, Kashiwa, Chiba 277-0882, Japan*

**Abstract:** The long overdue disintegration/purification work of detonation nanodiamond (discovered 40 years ago) is in good progress. Here are described features of two novel processes adopted, stirred media milling and diamond carbon analysis. Contamination with bead material provides serious problem in the milling and preventive ways are discussed. Black color that appears as the disintegration proceeds is introduced. Necessity and principles of diamond analysis by integrated X-ray diffraction intensities and theoretically attainable highest purity are discussed.

**Keywords:** detonation nanodiamond; purification; de-aggregation; contamination of zirconia bead; black colloid; direct analysis of diamond carbon contents

## 1. INTRODUCTION

It is urgently requested to complete the method of releasing primary particles (Figure 1) from crude aggregates of detonation nanodiamond (CAND) and purify them to an acceptable level in order to meet great demands for ultra fine carbon particles having single-digit nano diameter that can be used as the standard material in the budding nanocarbon technology. 1) Having well-progressed towards the goal we report here a few features that we have encountered in the course of work. These features are peculiar to the nanoscience.

In view of its favorable cost, small diameter (av. 4.4 nm as measured by the width of X-ray diffraction peaks) [1] and above all its outstanding

properties, detonation nanodiamond will become one of the most useful nanomaterials in the nearest future.

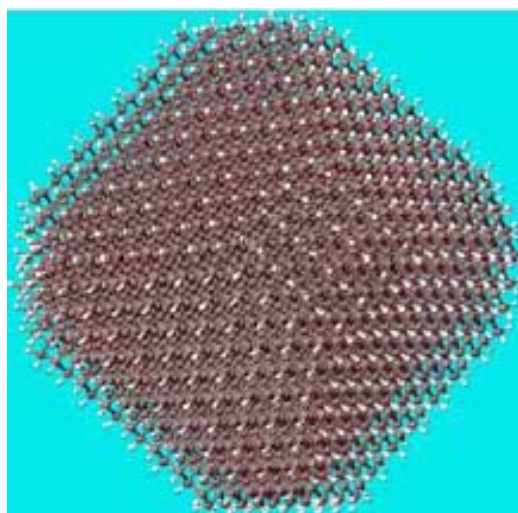


Figure 1. Geometry-optimized (MM3) model of truncated octahedral nanodiamond with the surface completely covered with hydrogen (white dots),  $C_{3450}H_{784}$ .

## 2. STIRRED MEDIA MILLING

One of the key techniques we developed in this work is to use so-called stirred media milling<sup>2)</sup> to destroy extremely tight core aggregates of nanodiamond to release primary particles. The use of such a novel comminuting method is suggested by adaptation of a model wherein primary particles of nanodiamond are incorporated in the well-known aggregated structure of flaming soot.<sup>3)</sup>

### 2.1 Contamination of Nanodiamond with Bead Materials

The milling conditions have to be adjusted to such mild levels that bead hits only the vulnerable, deformed graphitic portions that fill the space between diamond primary particles to disintegrate the core aggregates, but never touch diamond particles themselves in order to avoid destruction of bead, in our case zirconia bead with 30  $\mu\text{m}$  diameter. Nevertheless it is difficult to completely suppress contamination with bead as the latter is used in large excess, packed to 70% of the milling space. Analysis reveals that

milling time and agitation speed are the major factors for the destruction. Ad hoc means to remove broken pieces of bead such as centrifugation, absorption onto activated charcoal, and diffusion through osmotic membrane, are being attempted.

## **2.2 Dispersion Medium**

Either water or certain solvents that give stable slurry of CAND may be used as the wet medium in the stirred milling. Organic solvents are generally preferred to water due to higher efficiency in the following purification step. An interesting phenomenon is observed wherein apparent particle-size did not change during the milling under very mild conditions, but irradiation of the slurry after terminating the milling leads to perfect decrease in the particle-size to that of primary particles. We interpret this phenomenon as follows. It seems suffice to produce fatal 'cracks' in the weakest portion(s) of core aggregate during the mild milling, which will eventually lead to destruction of aggregate structure by intensive sonication. Developments of this type of mild milling will provide the uncontaminated primary particles of nanodiamond.

At least one common organic solvent was found that disintegrated core aggregates faster, gave highly stable colloids and proved more efficient in purifying the milled mixture. Colloids in these organic solvents are highly stable, and do not produce any precipitates upon standing in Argon atmosphere in stray light for months as we have observed when water was used as the dispersing medium.

## **2.3 Color of Colloids**

A convenient indicator on the progress of milling is the change in color of colloidal solution being circulated through the mill; the color changes from grey to surprising black (Figure 2). The origin of black color is still unknown at present, but we are sure that the color does not originate from impurities but is inherent to the presence of high concentration (up to 10%) of the first-digit nanoparticles. Color fades and eventually disappears upon dilution.





*Figure 2.* A milled colloid of CAND. Note deep black color.

It is likely that either or both of the following two reasons are responsible for the development of black color. One is a sort of black body effect, in which large number of highly reflective and dispersive nanodiamond scatter the incident light so efficiently that the light is practically lost. The other is to invoke abnormally high contents of nitrogen, up to 2.5%, in detonation nanodiamond, likely originating from high contents of N in the polynitro explosives used in detonation. It is well known that nitrogen impurities in the order of ppm, trapped in the lattice vacancy defect (NV), produce yellow color center in natural and artificial diamonds. Increased number of color centers will produce black color.

### **3. DIAMOND ANALYSIS**

Assessment of purity in the disaggregated detonation nanodiamond demands direct analysis of diamond carbon. It has, however, hardly been important to evaluate the contents of diamond carbon in natural and artificial micron-sized diamonds since the nature has done the best purification work to crystallize diamond. Furthermore, in these ‘visible’ particles, the contribution of surface impurities like carboxylic and hydroxyl groups (oxygenated complex) to the total number of atoms including tens of millions of bulk atoms is negligibly small. However, as will be mentioned below, situation changes in nanoparticles, and only in nanoparticles. Nanoparticles have significant contribution from the surface atoms, hence we need special care to assess their purities, and so do nanocarbons.

As the first step towards diamond analysis, we studied here quantitative diffraction intensity measurements using an internal standard [4]. When X-ray is irradiated upon a multiphase sample containing N-components, the intensity of X-ray diffracted by Thompson scattering of component  $J$  is given by the following equation derived from the Thompson scattering equation:

$$I_J = K_J \frac{V_J}{\bar{\mu}}, \quad (1)$$

where  $V_J$  denotes the volume component of  $J$  in the mixed sample,  $\bar{\mu}$  an average linear absorption coefficient of the mixed sample,  $K_J$  a constant peculiar to the component  $J$ . The average linear absorption coefficient is given by the following equation consisting of linear absorption coefficients of all components:

$$\bar{\mu} = \sum_{I=1}^N \mu_I V_I, \quad (2)$$

where  $\mu_I$  means the linear absorption coefficient of  $I$ -th component.

When dealing with powders, it is difficult to adjust volume, hence it is convenient to express mixing ratio in terms of weight fractions. When the density of component  $J$  is expressed by  $\rho_J$  (g/cm<sup>3</sup>), the weight fraction  $W_J$  of component  $J$  is given by Eq. 3:

$$W_J = \rho_J V_J \quad (3)$$

Substituting Eq. 3 into Eq. 1 leads to:

$$I_J = K_J \frac{W_J}{\rho_J} \frac{1}{\bar{\mu}} = \frac{K_J}{\rho_J} \frac{W_J}{\bar{\mu}} = L_J \frac{W_J}{\bar{\mu}}, \quad (4)$$

where

$$L_J = \frac{K_J}{\rho_J}.$$

Suppose the mixed sample consists of three components, diamond D, an internal standard substance S and a diluent W, then X-ray diffraction intensity of each component is given, according to Eq. 4, as follows:

$$I_D = L_D \frac{W_D}{\bar{\mu}} \quad (5)$$

$$I_S = L_S \frac{W_S}{\bar{\mu}} \quad (6)$$

$$I_w = L_J \frac{W_w}{\mu} \quad (7)$$

If we take an X-ray intensity ratio between diamond and internal standard, we obtain:

$$\frac{I_D}{I_S} = \frac{L_D}{L_S} \frac{W_D}{W_S} = M_{D,S} \frac{W_D}{W_S} \quad (8)$$

This intensity ratio does not depend on the amounts of diluent nor absorption coefficients, but is proportional only with the weight ratio of diamond and internal standard. Proportionality constant  $M_{D,S}$  is inherent to these two substances and can be obtained from the inclination of a linear plot between weight ratio and diffraction intensity ratio of several diamond-internal standard samples mixed in different proportions. Hence we can determine the weight of diamond by using the following equation:

$$W_D = \frac{1}{M_{D,S}} \frac{I_D}{I_S} W_S \quad (9)$$

### 3.1 Results and Discussion

Whereas we still have not optimized the analytical conditions, the weight-based purities (standard deviation of errors) of 61.3(5.1), 70.8(4.7) and 76.8(1.2) wt.% were obtained for the commercial CANDs imported in the year 1999 from Altai Co., Siberia, Russia, and in the years 2001 and 2003 from Gansu Lingyun Nano-Materials Co. Ltd., Lanzhao, China, respectively. Clearly we can recognize that the production technology is rapidly improving for the past few years. These results were, however, obtained by using the (111) diffraction peak alone. In the next step we will use the other two prominent diffraction peaks from (220) and (311) planes as well, in addition to a few other technical improvements. A drawback of the analysis of quantitative diffraction intensity with internal standard is that it needs large amounts of sample, unless exceptionally strong X-ray source is used, due to small X-ray absorption cross section of carbon.

### 3.2 Theoretically Attainable Purity

In nanoparticles the surface/bulk atomic ratio is significantly high. This characteristic feature has a couple of interesting consequences in the single-

digit nanodiamond. One is that active surface leads to very strong tendency of aggregate through particle-particle interactions, making it difficult to achieve good dispersion. This point is the reason for keeping the primary particles in colloidal solution<sup>1)</sup>. The other consequence is that, because surface atoms cannot be the diamond carbons but has to be something else, it is impossible to achieve 100% purity in diamond carbon. Then, in order to know the limit of purification, we must construct a series of model structures, in which all the surface carbon atoms are bound to surface (hetero)atoms to saturate the sp<sup>3</sup>-valence of internal carbon atoms.

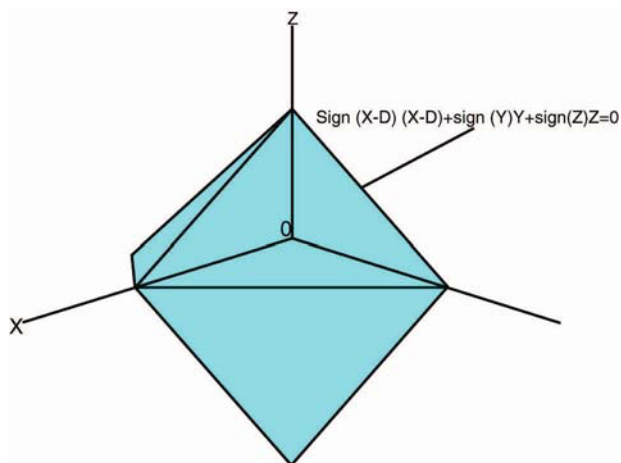


Figure 3. Illustration of octahedral diamond crystal with its central atom at the origin. Eight faces are oriented to  $[\pm 1 \pm 1 \pm 1]$  directions and given by the surface equation shown, where  $D=0$ , 'sign' is a simple function to return plus or minus of X, and Q is the length of vector between origin and a point on the surface in Å unit. Q is used as a measure of the size of octahedron in Table 1.

In order to evaluate surface/bulk ratio in various sizes of nanodiamond particles, we cut out octahedral crystals from the known diamond crystal structure [5] (Figure 3) and obtained atomic Cartesian coordinates of surface and bulk atoms with the central atom at the origin using a vector algorithm [6]. Surface atom is defined as those bound to one to three neighboring carbon atoms and attached with H or OH groups uniformly. Results of calculating various properties of these octahedral diamond crystals are given below:

Table 1. Computed properties of 40 octahedral diamond crystals with surface covered with either H or OH.

Q	Inter- apex dist., nm	Inter- plane dist., nm	Vol., nm <sup>3</sup>	Intern. atoms	Surface atoms	Diamond C, wt %	
						H	OH
1	0.000	0.000	0.000	1	4	75.000	15.000
2	0.177	0.100	0.001	1	4	75.000	15.000
3	0.354	0.200	0.007	1	4	75.000	15.000
4	0.531	0.299	0.025	5	12	83.333	22.727
5	0.708	0.399	0.059	17	60	77.273	25.000
6	0.885	0.499	0.116	35	36	92.105	40.698
7	1.062	0.599	0.200	35	36	92.105	40.698
8	1.239	0.699	0.317	59	84	89.394	40.972
9	1.416	0.799	0.473	119	180	88.806	45.652
10	1.593	0.898	0.674	165	100	95.192	53.804
11	1.770	0.998	0.924	165	100	95.192	53.804
12	1.947	1.098	1.230	225	220	92.466	53.150
13	2.124	1.198	1.597	365	364	92.327	56.795
14	2.301	1.298	2.030	455	196	96.535	62.102
15	2.478	1.397	2.536	455	196	96.535	62.102
16	2.655	1.497	3.119	567	420	94.186	61.364
17	2.832	1.597	3.786	819	612	94.138	64.085
18	3.009	1.697	4.541	969	324	97.289	67.857
19	3.186	1.797	5.390	969	324	97.289	67.857
20	3.363	1.897	6.339	1149	684	95.274	67.193
21	3.540	1.996	7.394	1545	924	95.253	69.262
22	3.717	2.096	8.559	1771	484	97.773	72.090
23	3.894	2.196	9.841	1771	484	97.773	72.090
24	4.071	2.296	11.245	2035	1012	96.021	71.521
25	4.248	2.396	12.776	2607	1300	96.010	73.134
26	4.425	2.495	14.441	2925	676	98.110	75.335
27	4.602	2.595	16.244	2925	676	98.110	75.335
28	4.779	2.695	18.191	3289	1404	96.565	74.852
29	4.956	2.795	20.288	4069	1740	96.559	76.141
30	5.133	2.895	22.540	4495	900	98.359	77.903
31	5.310	2.995	24.953	4495	900	98.359	77.903
32	5.487	3.094	27.533	4975	1860	96.979	77.492
33	5.664	3.194	30.284	5995	2244	96.975	78.544
34	5.841	3.294	33.213	6545	1156	98.549	79.986
35	6.018	3.394	36.325	6546	1156	98.550	79.989
36	6.195	3.494	39.625	7157	2380	97.304	79.634
37	6.372	3.593	43.119	8449	2812	97.301	80.508
38	6.549	3.693	46.814	9139	1444	98.700	81.710
39	6.726	3.793	50.713	9139	1444	98.700	81.710
40	6.903	3.893	54.823	9899	2964	97.566	81.406

This Table exhibits quite interesting facts. As the particle size (4.4 nm) given by X-ray diffraction intensities corresponds to inter-plane distance, we must look at the third column to estimate the average number of atoms contained in our nanodiamond crystal, which turned out to be about 20,000 for a H-terminated model by extrapolation. In the H-terminated model, theoretically attainable internal carbon content could reach to 99% level, but for a hydroxyl-terminated model, the highest diamond content is only slightly higher than 80%. For our nanodiamond covered by both H and OH, the highest purity we could reach would be somewhere near 85%.

#### **4. CONCLUSIONS**

The problem of contamination by bead material persists in the stirred milling technique, but may be eventually avoided through careful analysis. It is advantageous to use selected organic solvents as the dispersing medium rather than adhering to water. A good indicator on the progress of milling process is to watch black color to develop in the out coming slurry. The reason for the development of black color is still not understood but the color seems to be a property unique to nanodiamond or very small nanoparticles.

Necessity arises to analyze diamond content in order to evaluate a meaningful purity. Preliminary mathematical treatments of nano-sized octahedral fragments of nanodiamond lead to a prediction of surprisingly large number of atoms (about 20,000 inclusive of surface hetero-atoms) for the purified detonation nanodiamond having a maximum interplane distance of 4.4 nm.

Working with nanoparticles has so far given us a number of novel features and concepts never surfaced when working with molecules. More surprises will be seen on the other nanocarbons. Due to these new obstacles that must be overcome one by one, it will take more time to understand and control nanoparticles than optimistic businessmen thought initially when nanotechnology was proposed.

#### **Acknowledgments**

We are indebted to Professors A.Y. Vul', Dr. S. Kidalov, and Prof. R.S. Lewis for suggesting the possible reasons for black color in the colloids of fine nanoparticles of diamond. Experimental works were performed by research staffs of NanoCarbon Research Institute, including T. Fujino, Y. Suzuki. TEM picture was taken by the courtesy of Dr. M. Ozawa.

## REFERENCES

1. A.Krüger, F. Kataoka, A.E. Aleksenskii, A.Y. Vul', M. Baidakova, M. Ozawa, T. Fujino, Y. Suzuki, and E. Osawa. Unusually tight aggregation in detonation nanodiamond: identification and disintegration. *Carbon*, submitted for publication.
2. C.L. De Castro and Mitchell. The use of polymeric milling media in the reduction of contamination during mechanical attrition. *J. Mater. Res.* **17**, 2997-99 (2002).
3. M.Ozawa, H. Goto, M. Kusunoki, and E. Osawa. Continuously Growing Spiral Carbon Nanoparticles as the Intermediates in the Formation of Fullerenes and Nano-onions. *J. Phys. Chem.* **B 106**, 7135-38 (2002).
4. B.D. Cullity and S.R. Stock. *Elements of X-ray Diffraction*, 3rd Ed., Prentice Hall: New Jersey, 2001, Chapt. 12.
5. Cell constant of cubic lattice,  $a = 0.35667$  nm, JCPDS-International Centre for Diffraction Data, No. 06-0675 (1997).
6. This part of work done by Y. Suzuki.

# 18

## PURIFICATION AND FUNCTIONALIZATION OF NANODIAMOND

B.V. Spitsyn<sup>1</sup>, M.N. Gradoboev<sup>2</sup>, T.B. Galushko<sup>1</sup>, T.A. Karpukhina<sup>1</sup>,  
N.V. Serebryakova<sup>1</sup>, I.I. Kulakova<sup>2</sup>, and N.N. Melnik<sup>3</sup>

<sup>1</sup> *Institute of Physical Chemistry, RAS, Moscow, 119991, Russia*

<sup>2</sup> *M.V. Lomonosov State University, Moscow, 119992, Russia*

<sup>3</sup> *P.N. Lebedev Physical Institute, RAS, Moscow, 117924, Russia*

**Abstract:** This paper briefly discusses the advantages of commercial nanodiamond and analyses its structural and chemical impurities, polyfunctional surface termination, agglomeration, and other features that may restrict the ND application in academic research and industrial practice. We have designed and tested a novel approach to detonation nanodiamond purification and surface functionalization, using a high temperature treatment in gaseous media containing hydrogen and chlorine. A drastic change in the hydrophily (by a factor of 20) due to thermal treatment at 450°C in a CCl<sub>4</sub>/Ar mixture is demonstrated. The characterization techniques employed (chemical analyses; Raman, FTIR, and ESR spectroscopy; chromatomass spectrometry) can provide a profound nanodiamond modification and its prescribed functionalization.

**Keywords:** nanodiamond, detonation synthesis, low pressure synthesis, modification, functionalization, characterization

### 1. INTRODUCTION

The active and still increasing interest in nanodisperse and nanostructured materials is due to the fact that researchers expect special physical, physicochemical and chemical properties of these materials with, at least, one characteristic geometrical dimension lying in the range from several to hundreds of nanometers. Diamond with its excellent mechanical, physical and chemical characteristics is now available from natural deposits or it can be synthesized in one of the following three ways. One exploit static high pressure and temperature, *and second* - dynamic high pressure and



temperature (explosive and detonation methods). In the original explosive process suggested by DuPont (1970), the duration of the explosion was  $\sim 1$  ms and the size of the diamond crystal grains varied between 1 and 50  $\mu\text{m}$ . In the detonation process used initially by Russian researchers, these parameters were  $\sim 0.3$   $\mu\text{s}$  and  $\sim 4$  nm, respectively. Third way of producing diamond is the synthesis from the vapor phase under the conditions of thermodynamic metastability of diamond at low pressure [1, 2].

This NATO Workshop focuses on detonation nanodiamond (ND) synthesis. The product is born from a powerful explosion (with trinitrotoluene and a hexogene mixture) at the detonation wave front for 0.3  $\mu\text{s}$ .

The ND born at the detonation wave front seems to need a longer treatment, primarily by chemical and physical methods.

## 2. CHARACTERISTICS OF DETONATION ND

ND is produced on a commercial scale at a number of research and technical centers in Russia, NIS, China, Japan, and South Korea with an annual output of a several tons. The production technology was designed independently by a research team in the USSR in the 1960s and by two teams both the USSR and the USA in the 1980s [3–5]. All samples of detonation ND powders, irrespective of the supplier, have listed below characteristics. We will subdivide them, somewhat conventionally, into two groups.

One group of ND characteristics may be considered as its advantages. ND is among few commercially produced nanosize powders. It is genuine diamond, which does not undergo a transition to graphite in inert or reducing environments at temperatures as high as  $\sim 1000^\circ\text{C}$  and even higher. Individual ND particles are nearly spherical with not wide size range, from 2 to 10 nm.

The other, larger group of ND characteristics should be taken into account in researches and applications. Some of these characteristics do not permit considering ND as an individual nanosubstance, by V.B.Aleskovsky's definition. However, certain impurities and defects in ND may become advantageous in some applications.

The features that do not allow considering ND strictly as a substance in itself are the presence of the following foreign components: (1) non-diamond carbon impurities or non-carbon impurities (Fe, Cr, Ni, Al, Si, Ca, etc.) giving an ND sample a grey or dark grey appearance; (2) light elements mostly at the chemically bonded ND termination (oxygen  $\sim 10$  wt.%,

hydrogen ~1 wt.%) and nitrogen (~2 to 3 wt.%), mostly in the bulk; (3) well-defined chemical groups of C-H, C-OH, C-O-C, C=O, C=(O)H (aldehyde), C=O (OH) (acid), C-NH<sub>2</sub>, lactonic and other groups making the ND surface chemically multifunctional; (4) “ash-related” impurities (Fe, Cr, Al, Ca, Si etc.) with the total of several wt.% occurring as free elements, oxides or carbides, both on the ND particle surface and in the bulk; (5) intrinsic impurities and those with zero- and higher dimensionality defects in the particle’s bulk, producing an appreciable excess of enthalpy (up to 25 kcal/kg); (6) one or more twin boundaries in the fractions of ND particles [6]; (7) a fairly strong agglomeration (agglutination) of individual particles which form tightly packed structures of tens, hundred or thousands of nanometers in size; (8) not monodisperse distribution of particles with the size range of 2–10 nm.

Above listed features make it necessary to search for alternative ND production technologies which could control diamond metastability, using atmospheric and subatmospheric pressures. A successful attempt was the transformation of some carbides ( $\beta$ -SiC, TiC) by selective ‘leaching’ of the non-carbon fraction by chlorine vapor at a temperature of 900°C and lower [7]. ND self-nucleation and growth, both homogeneous [8,9] and heterogeneous [1], became feasible owing to the emergence of diamond CVD [1]. The homogeneous evolvement of nanosize diamond was achieved with the pulse high voltage DC in CH<sub>4</sub> and electrodeless mW discharges ignited in a CH<sub>4</sub>-O<sub>2</sub>-H<sub>2</sub> mixture [8]. The authors of this work observed both cubic diamond nanoparticles of 20–30 nm and polytype (4H and 6H) diamond due to a high supersaturation in the activated vapor. In early study [1] both single crystal cubic as well as doubly and multiply twinned cubic ND particles during the initial stages of diamond self-nucleation and growth on a non-diamond substrate have been found. In principle, the CVD process provides ND particles of a high chemical (e.g., no nitrogen) and phase (no non-diamond carbon) purity and a desired size range. Moreover, the CVD process may open the door to nanostructured carbon and other nanocomposite technologies [10]. Today, however, the most reliable ND technology is still the detonation synthesis. Therefore, our effort should be focused on improving some of the detonation ND characteristics and studying its structural, physical, physicochemical, and chemical properties.

### 3. THERMOCHEMISTRY OF SMALL DIAMOND PARTICLES

For diamond particles of  $> 10$  nm in diameter, the contribution of the surface energy to the total energy should be significant. The fraction of the surface energy increases with decreasing particle size. Several calculations have been made of the energies of small particles, using *ab initio* and semi-empirical methods [11], but the calculations are often time-consuming and their accuracy is not easy to estimate.

Consider the difference in the enthalpies of a small diamond particle and a bulk diamond crystal. Obviously, as the particle size increases, its enthalpy should approach asymptotically that of bulk diamond. On the assumption of the bond-breaking energy, it is more convenient to regard a diamond nanoparticle as a regular octahedron. Its size effect would be totally limited by the (111) surface completely covered with C-H bonds.

Shenderova *et al.* [4] suggested a general formula for a series of diamond octahedra as a function of the octahedron order.

Starting with adamantane ( $N = 2$ ), we have

$$N_{C2} = 6$$

$$N_{C3} = 4N^2 - 12$$

$$N_{Surface} = N_{C2} + N_{C3} = 4N^2 - 6$$

$$N_{total} = N(4N^2 - 1) / 3$$

Here C2 means 2-coordinated atoms (there are only 6, always at the vertices) and C3 means 3-coordinated atoms. These relations are summarized in Table 1.

Table 1. The number of dangling bonds and surface atoms in diamond octahedron.

N	2 adamantane	3	4	5	6	7	8	9	10
C2-coordinated	6	6	6	6	6	6	6	6	6
C3-coordinated	4	24	52	88	132	184	244	312	388
Number of surface atoms	10	30	58	94	138	190	250	318	394
Total number of atoms	10	35	84	165	286	455	680	969	1330

Note:  $N$  is the number of atoms along the octahedral edge (e.g., 2 for adamantane).

The thermochemical quantities estimated from the C-C and C-H bond energies in terms of the standard energy of formation (at 298K) suggest that, at least, the smallest 'diamond' octahedra, e.g.  $C_{10}H_{16}$  and  $C_{35}H_{36}$ , should be more energetically stable than graphite and that their stability should be comparable with bulk graphite at total number of atoms in diamond crystal equal to 33,000 [11]. But at high temperatures ( $\cong 1300K$ ), the thermochemical and thermodynamic stability may change dramatically due to the entropy effects.

## 4. EXPERIMENTAL

We used in two kinds of ND samples supplied by New Technology Co (by courtesy of P.Ya.Detkov and I.L.Petrov). Before supplying one type of samples was finally cleaned by ozone and another – in boiled mixture of sulfuric acid and potassium bichromate. The ash content in the {both types of} samples varied from 1.1 to 1.5 wt.%. Both samples were gray powders.

### 4.1. ND Modification and Functionalization

Liquid purification of ND commonly employed today involves the treatment of the initial powder with a strong acid or salt-containing mixtures. However, unburned impurities still remain in the ND sample in spite of a fairly good removal of nondiamond carbon. This and other disadvantages of the technique can be overcome by using gas and vapor reactive media. In the latter, the low-dimensional fraction of the powder is also purified; the penetration rate of a gas into the interparticle space is much higher than that of liquid. Moreover the equipment for vapor treatment is simpler in design and operation, making the technology less costly. The vapor treatment can be combined with controlled functionalization of the ND surface.

### 4.2. The Reactor Design

Our experiments were performed in a special reactor made from quartz glass (Figure 1).

This reactor design provided the treatment of ND samples which were placed in quartz boats into the reactor hot zone with a gas or vapor flow at temperatures from 400 to 1100°C and pressure of 1 atm. High purity Ar (5N) and  $NH_3$ (5N) gases were supplied from tanks and  $H_2$  was produced

electrochemically and dried in a silica-gel column. The gas flow rate was 1 - 3 NL per hour controlled by flow-meters. The duration of an experimental run was from 30 min to 5 h.

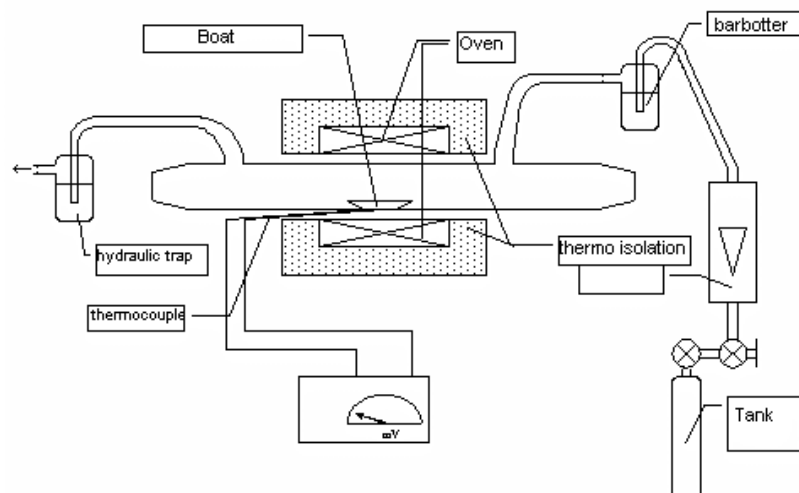


Figure 1. Set-up of reactor for ND treatment in-gas and vapor media.

### 4.3 Argon

The ND samples placed in pure Ar at 400°C demonstrated a remarkable, ~ 12 wt.% weight loss, but it was actively restored (within 1 hour) to the initial value in the laboratory atmosphere. The water vapor absorbance was controlled by the absence of weight change in a dry atmosphere in a dessicator filled with regenerated zeolite CaX.

### 4.4. Carbon Tetrachloride Vapor

Initial has grade “pure for chemical analysis”. The ND samples baked in an Ar/CCl<sub>4</sub> = 99/1 flow demonstrated an essential difference. First, the loss of weight was much less than in the comparable conditions in Ar. Secondly, the sample did not practically absorb water vapor from the air. The water reabsorbance was, at least, 20 times lower than in the ND samples treated in pure Ar. The FTIR spectra demonstrated a progressive C-Cl bonding in the ND. Therefore, the relative intensity of the C-Cl band at 709 cm<sup>-1</sup> progressively increased with the exposition in the Ar + CCl<sub>4</sub> flow at 450°C.

After the treatment for  $\frac{1}{2}$  to 3 hours, the C-Cl band intensity increased nearly 5-fold.

The chemical analysis of the ND samples was performed in a C-H-N analyzer of the CARLO ERBA type, model 1107. The Cl content was determined by titration. The results are presented in Table 2.

Table 2. Results of a chemical analysis of the samples.

ND sample	Initial, ozone treatment	CCl <sub>4</sub> treatment
C, wt.%	83.75	84.94
N, wt.%	2.09	2.34
H, wt.%	0	0
Cl, wt.%	0	6.84
O, wt.%(*)	~14	~7

\*) calculated by balance

The Raman spectra (Figure 2) demonstrate some improvement of the ‘diamond’ structure after a high temperature NH<sub>3</sub> and CCl<sub>4</sub> treatment of the ND powders. The peaks ratio D/G (diamond to graphite band) in the spectra markedly changed in favor of the ‘diamond’ *sp*<sup>3</sup>-structure.

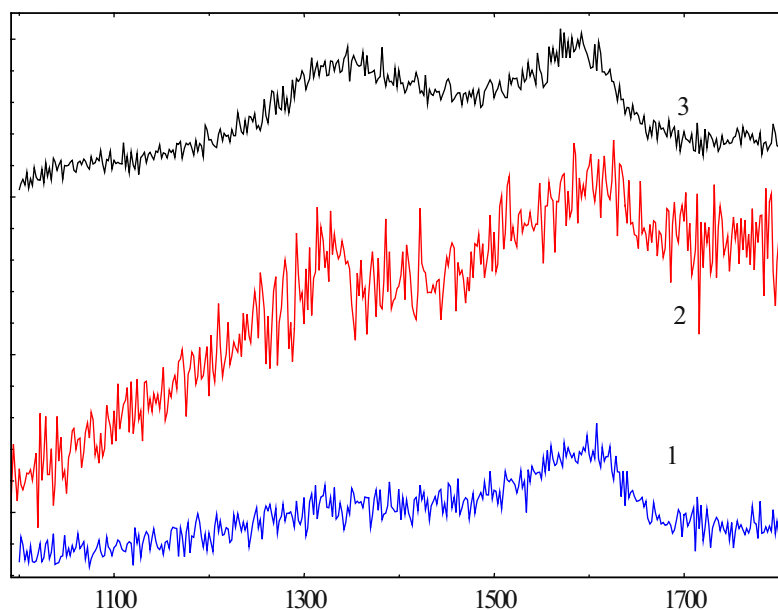


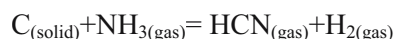
Figure 2. Raman spectra of the ND samples: 1 - initial powder, 2 - treated in ammonia at 900°C, 3 - treated in carbon tetrachloride at 1000°C. Intensity (a.u.) versus the wave number (cm<sup>-1</sup>).

## 4.5. Hydrogen

The above mentioned energy excess in ND immediately after the detonation synthesis required the measurement of the combustion energy change after the ND annealing in a hydrogen flow at 850°C for 5 h. The combustion heat was measured after the ignition of the samples in oxygen compressed to 30 atm. It is noteworthy that the combustion heat of ND samples annealed, on the average, by 5 ignitions was ~1000 cal/g lower than in the initial ND. The chemical composition of annealed ND changed slightly. The hydrogen content, however, increased from 0 wt.% to 0.95 wt.%. Note that the initial dangling bond density of  $\sim 1.16 \times 10^{20}$  spin/cm<sup>3</sup> was reduced 1.5 times after the hydrogen treatment.

## 4.6. Ammonia

In principle, the treatment with ammonia can change not only the ND surface termination but also remove some of the carbon through a thermodynamically permitted reaction:



After the treatment in a NH<sub>3</sub> flow at 600°C and 850°C for 70 min., the changes in the surface termination were clearly observable in the FTIR reflection spectra (Figure 3).

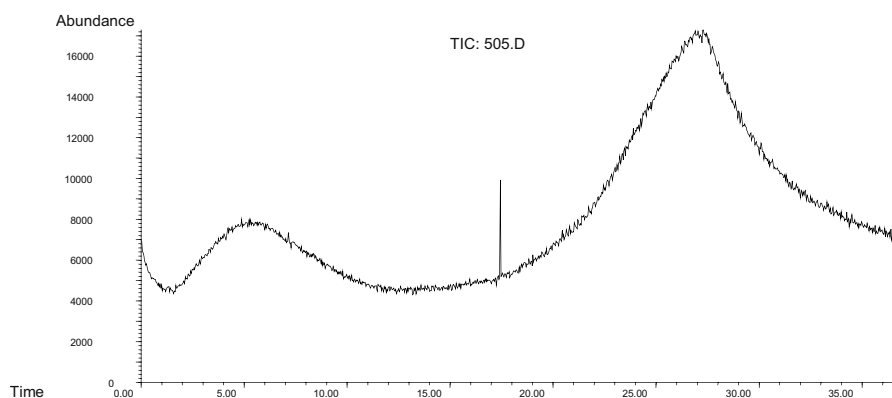


Figure 3. Sample after NH<sub>3</sub> treatment (850°C, 70 min).

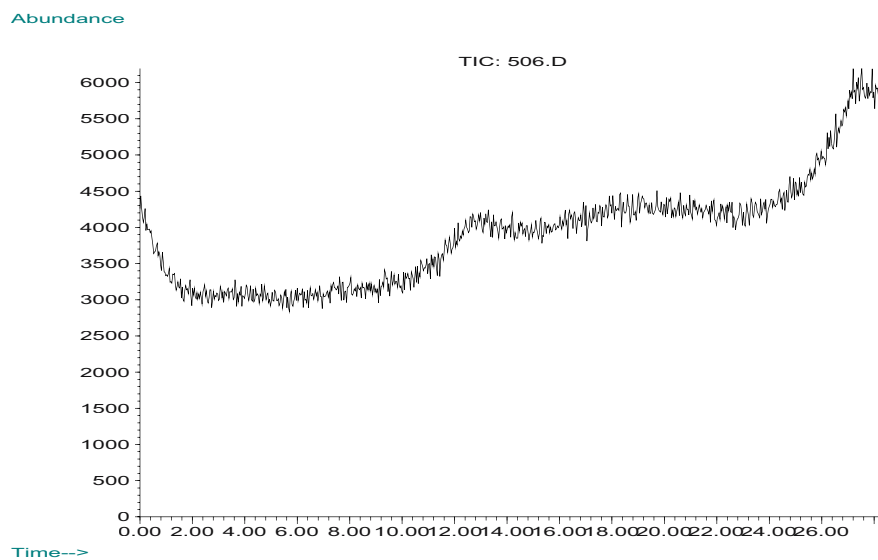


Figure 4. Initial sample.

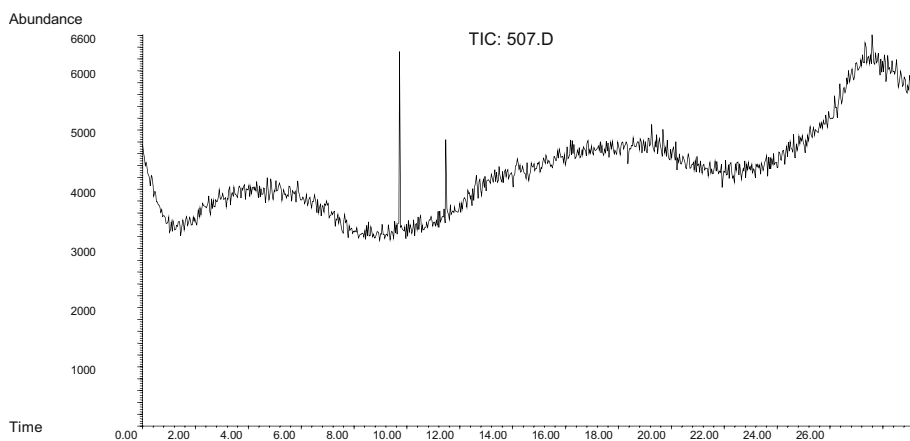


Figure 5. The ND sample after  $\text{NH}_3$  treatment ( $600^\circ\text{C}$ , 70 min).

One can see a smaller number of oxygen-containing groups with a simultaneous emergence of C-H stretching modes in the wavelength range from  $2870$  to  $2920\text{ cm}^{-1}$ . The multiple carbon-carbon bonding also



disappeared and the N-H bonding became observable. But the hydroxylic (O-H) and carboxylic (C=O) groups did not {seem to} disappear completely. This is indicated by some remaining hydrophilicity of the ammonia-treated samples, which is about 4 times lower than the original ND sample reabsorbance for atmospheric water vapor.

An independent support for the surface functionalization was provided by chromato-mass-spectrometry (Figures 4-6) successively used at 25–450°C.

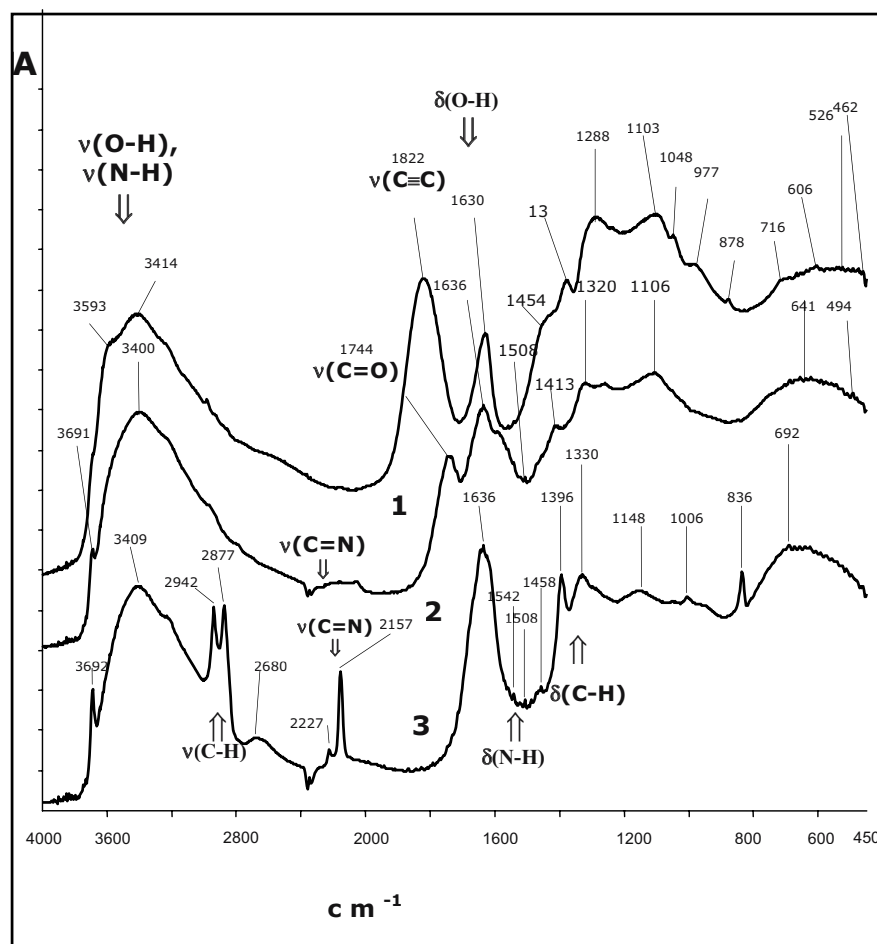


Figure 6. FTIR spectra of ND: 1 - initial; 2 - after  $\text{NH}_3$  treatment (600°C, 70 min); 3 - after  $\text{NH}_3$  treatment (850°C, 70 min).

However, the nitrogen-containing species thermally removed from the ND surface were masked by the oxygen-containing desorption products registered in the same 17–18 mass range. The presence of HCl molecules in the desorption species is quite typical and consistent with the ozone treatment regime of the ND samples.

## 5. CONCLUSION

We have suggested a simple and effective technique for vapor ND cleaning and functionalization. High temperature ND treatment allows the chemical agents to penetrate in nanoporous materials and functionalize the ND surface in a desired way. Hydrophilic/ hydrophobic or acid/base ND termination becomes feasible. We believe that this technique has a large potential in research and development projects.

## Acknowledgements

We are very thankful to P.Ya. Detkov and I.L. Petrov for supplying us with ND samples of high initial purity. The authors express their deep appreciation of the colleagues' assistance in ND characterization performed with their own facilities: A.K. Buryak - for chromato-mass-spectrometric measurements, Yu.N. Matyushin - for combustion calorimetry, N.N.Steparyova for XRD data, and A.I. Veinger - for ESR measurements.

The authors appreciate a partial support of this work through the Russian Foundation for Basic Research, grant # 04-03-32835.

## REFERENCES

1. B.V. Spitsyn, L.L. Bouilov, and B.V. Derjaguin. Vapor growth of diamond on diamond and other surfaces. *J. Cryst. Growth* **52**(1), 219-26 (1981).
2. B.V. Spitsyn, L.L. Bouilov, and A.E. Alexenko. Origin, state of the art and some prospects of diamond CVD. *Braz. J. Phys.* **30**, 471-81 (2000).
3. V.Y. Dolmatov. Detonation synthesis ultradispersed diamond: properties and applications. *Russian Chem. Reviews* **70**, 607-26 (2001).
4. O.A. Shenderova, V.V. Zhirnov, and D.W. Brenner. Carbon Nanostructures. *Critical Reviews in Solid State and Materials Sciences*, **27**, 227–356 (2002)
5. V.V. Danilenko. *Synthesis and sintering of diamond by detonation*. Energoatomizdat, 2003.
6. T.L. Daulton. Nanodiamonds in the Cosmos. this Proceedings, p. 49.
7. Yu.G. Gogotsi et al. Conversion of silicon carbide to crystalline diamond-structured carbonate ambient pressure. *Nature* **411**(6835), 283-87 (2001).
8. S. Mitura. Nucleation of diamond powder particles in an RF methane plasma. *J. Cryst. Growth* **80**, 417-24 (1987).

9. M. Frenklach, R. Kematick, D. Huang, W. Howard, K.E. Spear, R. Koba, and A.W. Phelps. *J. Appl. Phys.* **66**, 1247 (1989).
10. B.V. Spitsyn. Nanodiamond for science and practice. Repts. *Russian Acad. Sci.* **73**(5), 433-35 (2003).
11. O.A. Shenderova, Z. Hu, and D.Brenner. Carbon Family at the Nanoscale. This Proceedings, p. 1.

# 19

## INTERACTION OF CARBON ATOMS WITH NANODIAMOND SURFACE

A.P. Dementjev<sup>1</sup>, K.I. Maslakov<sup>1</sup>, and A.V. Naumkin<sup>2</sup>

<sup>1</sup>RRC "Kurchatov Institute", 1, Kurchatov sq., Moscow, 123182, Russia

<sup>2</sup>Institute of Elemento-Organic Compounds, Russian Academy of Sciences, 28 Vavilov Street, Moscow, 119991 GSP-1, Russia

**Abstract:** A combination of N(E) Auger spectroscopy, X-ray excitation (XAES), electron energy loss spectroscopy (EELS), and valence band (VB) XPS have been used to study nanodiamond (ND) particles. These methods have different information depths of 1–2, 5–7, and 10–12 monolayers (ML), respectively, and an inherent spectral structure in the identification of  $sp^2$ - $sp^3$  -bonds. Our data show that the upper 1–2 ML of a ND particle consists of carbon atoms with  $sp^2$ -bonds, which differ from those in well-known carbon compounds. The ND core is made up of diamond. Chemical reactions of the carbon atoms with the particle have been studied in-situ and ex-situ. The crucial role of the upper monolayer in the diamond growth has been established for both cases.

**Keywords:** nanodiamond, surface chemical interaction, growth mechanism

### 1. INTRODUCTION

At present, nanodiamonds (ND) can be synthesized from explosives by a variety of techniques. However, the growth mechanism is still a subject of much debate, so the understanding of nucleation phenomena appears to be essential for further progress in the growth technology.

In his review, Danilenko<sup>1</sup> considered some aspects of ND preparation and possible mechanisms of its formation in terms of the graphite-diamond diagrams and the detonation parameters of the explosives used. According to the data presented, the ND core is made up of diamond, while its surface contains adsorbed gases, graphite and onion-like graphite. The graphite may

be removed chemically. However, the results on the surface chemical states seem doubtful. Identification of the chemical states on a ND surface is a very important problem, because surface atoms play a great role in the nucleation during CVD diamond growth [2,3]. Besides, we must know the answers to, at least, two fundamental questions. What chemical and physical processes are responsible for ND nucleation and growth? Why the ND size is limited to 3–5 nm?

One cannot study the growth mechanism *in-situ*. Therefore, we must identify the chemical states of the surface carbon atoms analytically and try to understand the mechanisms of carbon formation from these data.

The aims of this work were to identify the chemical states on the ND particle surface and to study the interaction of the carbon atoms from gas phase with the ND surface.

To study the surface, we used a combination of N(E) Auger spectroscopy, X-ray excitation (XAES), electron energy loss spectroscopy (EELS), and valence band (VB) XPS. Our data show that these methods have different information depths: 1–2 ML, 5–7 ML, and 10–12 ML, respectively [4]. The EELS and VB XPS techniques provide a reliable ground for the identification of the  $sp^2$ - $sp^3$ -bonds [5], whereas the XAES technique is still under development [5-10].

## 2. EXPERIMENTAL

The XPS and XAES spectra were registered by a MK II VG Scientific spectrometer with a non-monochromatized Al  $K_\alpha$  X-ray source (1486.6 eV). The pressure in the major and preparation chambers was usually  $5 \cdot 10^{-10}$  mbar. All the spectra were charge-referenced to the C1s XPS peak (284.8 eV). The position of C1s was found with respect to the Ar  $2p_{3/2}$  XPS peak at 241.3 eV after implantation of a small dose of  $Ar^+$  into the ND.

The ND powders were prepared at the Kiev Institute of Superhard Materials, as well as in Snezhinsk and Krasnoyarsk. The powder was deposited on a Si wafer with native silicon dioxide by evaporating an alcohol suspension prepared in an ultrasonic bath. This method provides a continuous coverage of the substrate. The photoemission, the Auger process and the information depth of the analytical procedures are shown schematically in Figure 1.

A tungsten filament heated to 2300K was used to decompose  $H_2$  or  $CH_4$ ; its temperature was measured by a pyrometer. The distance between the hot filament and the sample was 10 mm. The temperatures of the diamond, ND and silicon samples were measured by a thermocouple mounted laterally. The surfaces of the ND and natural diamond were analyzed before and after

the atomic hydrogen treatment at  $10^{-6}$  mbar in the preparation chamber of the spectrometer. The sample was then deposited into the analytical chamber. The deposition rate was measured from the carbon deposition on a substrate under the same conditions and was found to be about 0.5–1 ML/min.

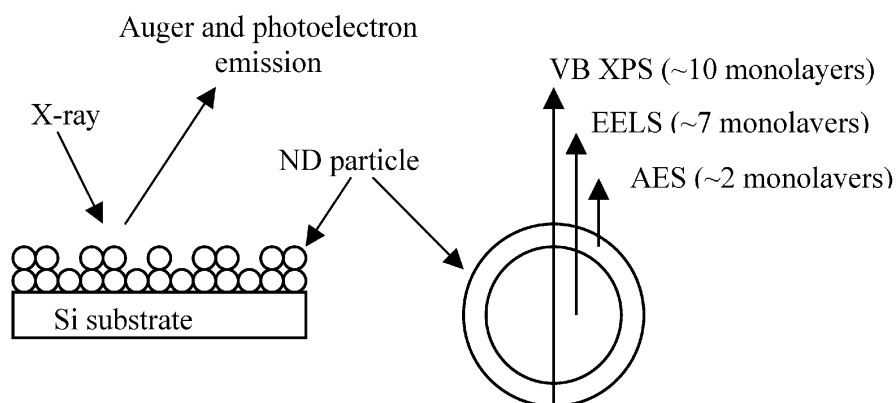


Figure 1. A schematic sample and the information depths of the electron spectroscopic techniques.

### 3. RESULTS

Figure 2 shows substantial differences between the CKVV Auger spectra of ND, HOPG, and natural diamond after the treatments in hydrogen and polyethylene. The latter served as a reference of the pure  $sp^3$  state. It is very difficult or nearly impossible to obtain a purely  $sp^3$  state of the diamond surface because the mechanical or chemical treatment breaks the chemical bonds irreversibly.

The XAES characterization of the (111) diamond surfaces after the H-treatment and the ND surface before and after the H-treatment shows the identity of the chemical states, which we denoted as  $C_d$ . Obviously, this fact cannot be accounted for by the same atomic structure of the top layers, so we suggest that this is due to Pandey's  $p$ -dimerization [11]. We have found that the  $C_d$  chemical state does not interact with an ambient like HOPG, because it was observed on all the ND samples and on the diamond surface after the *ex-situ* H-treatment.

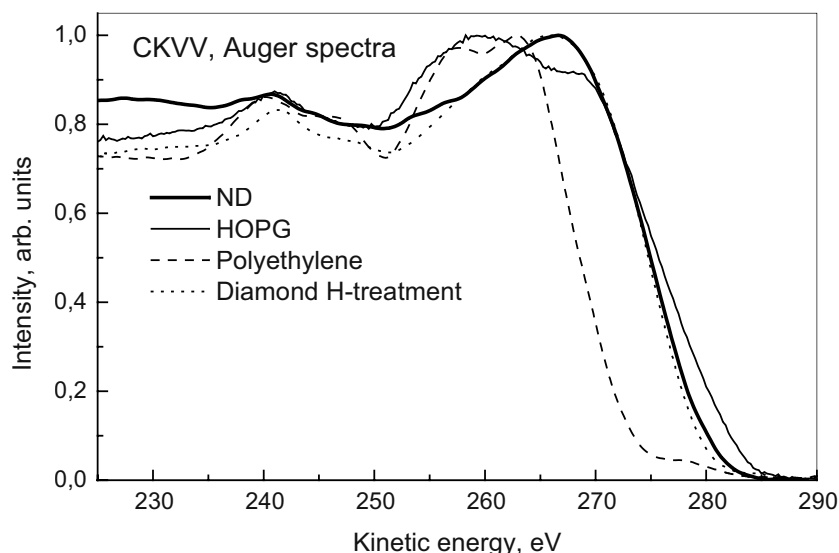


Figure 2. The CKVV Auger spectra of ND, HOPG, and natural diamond after the treatment in hydrogen and polyethylene.

The CKVV spectrum of the  $C_d$  state differs from that of carbon compounds such as  $C_{60}$ , adventitious carbon, nanotubes and has a “fingerprint” of its own. The XPS valence band spectra of the ND poorly coincide with the diamond spectrum. It is quite likely that the size of the ND particles is comparable with the information depth of the valence band photoelectrons, and the amount of the surface atoms is, at least, 25% of their total amount in a particle [1]. These atoms are not in the  $sp^3$ -hybridized state, so the difference in the ND and diamond spectra is clear.

To order to understand the details of the growth process, an elementary reaction of carbon atoms with a ND surface was studied *in-situ*. Carbon atoms were produced by decomposing  $CH_4$  (at  $10^{-6}$  mbar) on a tungsten filament heated to 2300K. The  $N(E)$  CKVV Auger spectra (Figure 3) show an insignificant amount of the  $sp^2$ -bonds on the ND surface after the deposition of about 8–10 ML, while the information depth of the Auger emission is found to be 1–2 ML.

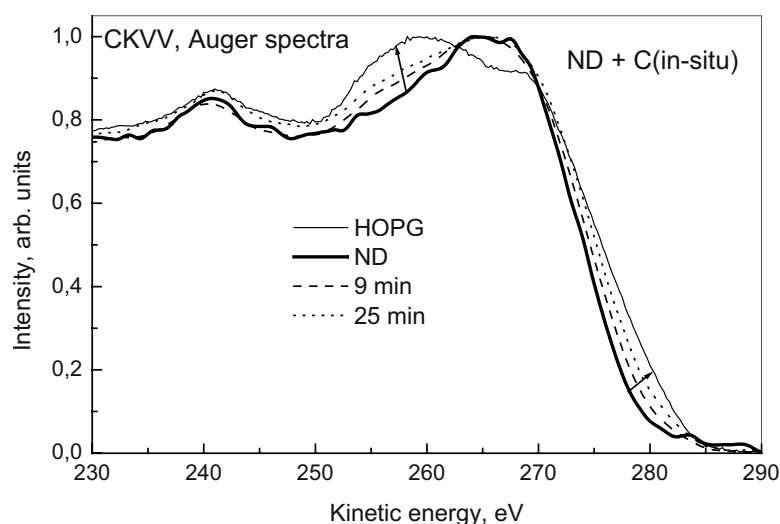


Figure 3. The CKVV Auger spectra of HOPG, ND, and the ND with deposited carbon atoms.

The observable modification of the C1s XPS (Figure 4) and EELS spectra (Figure 5) is an evidence for the atomic carbon deposition, while the broadening of the photoelectron C1s line indicates an increased dispersion after the carbon deposition. Figure 5 shows that no  $sp^2$ -bonds are formed in the bulk; their amount increases only on the top layer, as evidenced by the CKVV Auger spectra, suggesting that they are produced under the surface layer. So the  $C_d$  surface state may be thought to act as a catalyst of the  $sp^3$  bond production under the top layer.

The *ex-situ* interaction between carbon atoms and ND particles was studied in a CVD reactor at the General Physics Institute (Russia) under the conditions of diamond growth. The diamond growth can be analyzed from the energy loss of C1s electrons and the VB XPS spectra. In contrast to the *in-situ* study, the C1s line width is found to become narrow with atomic carbon deposition, indicating a powder→solid transformation. The major difference between the *in-situ* and *ex-situ* experiments is the concentration of hydrogen atoms. We believe that further comprehensive studies of differences between *in-situ* and *ex-situ* experiments may give a chance to understand the contribution of hydrogen atoms to the CVD process.

The *in-situ* results allow suggesting the following scenario of the ND production after the explosion: (1) the formation of a nucleus with the  $C_d$



state, resulting from the recombination of carbon atoms; (2) the catalysis of the ND growth stimulated by the  $C_d$  states; (3) the size of the ND particles is limited to either the termination of the  $C_d$ -state catalytic activity or to atomic carbon depletion.

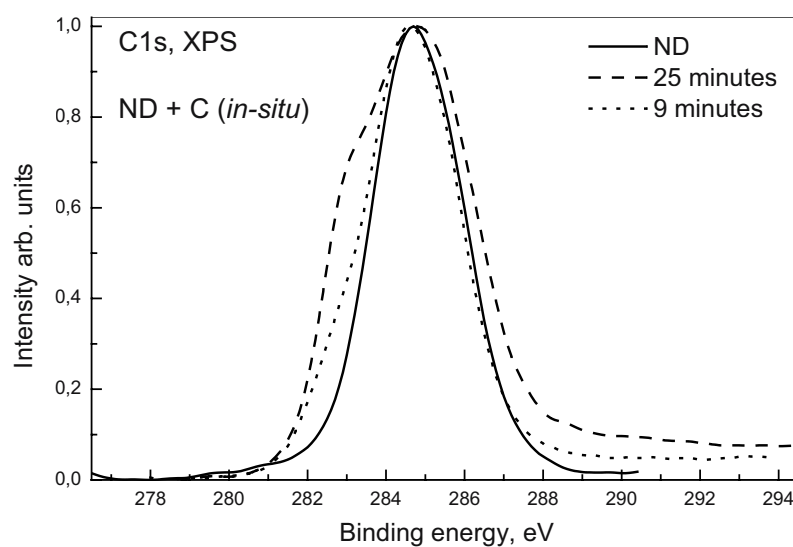


Figure 4. The C1s XPS spectra of ND before and after atomic carbon deposition.

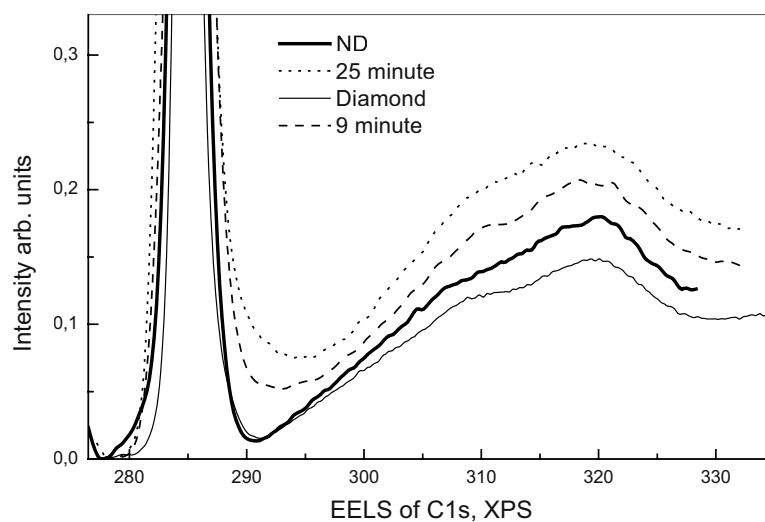


Figure 5. The C1s EELS spectra of diamond and ND before and after carbon deposition.

#### 4. CONCLUSION

We have shown an effective application of electron spectroscopic techniques in *in-situ* and *ex-situ* studies of the CVD process. The CKVV Auger spectra of ND and natural diamond treated by atomic hydrogen are found to be identical but they differ from the spectra of other  $sp^2$  and  $sp^3$  chemical compounds. This may indicate the presence of a new chemical state of carbon atoms ( $C_d$ ) on these surfaces. The  $C_d$  chemical state is inert to an ambient like HOPG. The role of the  $C_d$  state in the diamond growth is significant and seems to have a catalytic nature.

#### REFERENCES

1. V.V. Danilenko. *Sintetizing and sintering of diamond by explosion*. M.: Energoatomizdat, 2003 (in Russian).
2. A.A. Smolin, V.G. Ralchenko, S.M. Pimenov, T.V. Kononenko, and E.N. Loubnin. Optical monitoring of nucleation and growth of diamond films. *Appl. Phys. Lett.* **62** 3449-51 (1993).
3. V.I. Konov, A.A. Smolin, V.G. Ralchenko, S.M. Pimenov, E.D. Obraztsova, E.N. Loubnin, S.M. Metev, and G. Sepold. D.c. arc plasma deposition of smooth nanocrystalline diamond films. *Diamond and Related Materials* **4**, 1073-78 (1995).
4. C.J. Powell and A. Jablonski. NIST Electron Inelastic-Mean-Free-Path Database-Version 1.1, National Institute of Standards and Technology, Gaithersburg, MD, 2000.
5. F.R. McFeely, S.P. Kowalczyk, L. Ley, R.G. Cavell, R.A. Pollak, and D.A. Shirley. X-ray photoemission studies of diamond, graphite, and glassy carbon valence bands. *Phys. Rev. B* **9**, 5258 (1974).
6. J.S. Murday and B.I. Dunlap, F.L. Hutson, and P. Oelhafen. Carbon KVV Auger line shapes of graphite and stage-one cesium and lithium intercalated graphite. *Phys. Rev. B* **24**, 4764 (1981).
7. J.E. Houston, J.W. Rogers, Jr., and R.R. Rye, F.L. Hutson, and D.E. Ramaker. Relationship between the Auger line shape and the electronic properties of graphite. *Phys. Rev. B* **34**, 1215 (1986).
8. L. Calliari, G. Speranza, J.C. Lascovich, and A. Santoni. The graphite core-valence-valence Auger spectrum. *Surf. Sci.* **501**(3), 253 (2002).
9. A.P. Dement'ev and K.I. Maslakov. Chemical State of Carbon Atoms on the Surface of Nanodiamond Particles. *Physics of the Solid State* **46**(4), 678-80 (2004).
10. P.I. Belobrov, L.A. Bursill, K.I. Maslakov, and A.P. Dementjev. Electron spectroscopy of nanodiamond surface states. *Applied Surface Science* **215**, 169-77 (2003).
11. K.C. Pandey. New dimerized-chain model for reconstruction of the diamond (111)-(2×1) surface. *Phys. Rev. B* **25**, 4338 (1982).

## PHYSICAL AND CHEMICAL PROPERTIES OF MODIFIED NANODIAMONDS

A.P. Puzyr<sup>1</sup>, V.S. Bondar<sup>1</sup>, A.A. Bukayemsky<sup>2</sup>, G.E. Selyutin<sup>3</sup>, and V.F. Kargin<sup>3</sup>

<sup>1</sup> *Institute of Biophysics SB RAS, Krasnoyarsk 660036, Russia*

<sup>2</sup> *Research Institute of Physics and Engineering, Krasnoyarsk State University, Krasnoyarsk, 660070, Russia*

<sup>3</sup> *Institute of Chemistry and Chemical Technology SB RAS, Krasnoyarsk 660049, Russia*

**Abstract:** A unique technology of nanodiamond surface modification is suggested which allows to separation of commercial nanodiamond powders into two fractions (F1 and F2), each possessing absolutely new properties as compared to the initial powder. F1 and F2 differ in size characteristics. Initial and modified nanodiamonds contain iron impurities and two types of nondiamond carbon. The color of the powders and hydrosols does not correlate with the content of non-diamond carbon. According to the EPR data, modified nanodiamonds possess a high level of diamond matrix shielding, and the extracted fractions differ in width of the basic transition area and in the SHF energy adsorption ratio. Due to this, F1 can be applied as precursors for CVD growth of nanocrystalline diamond and as field electron emission tips.

**Keywords:** nanodiamond, modified nanodiamonds, hydrosols, colloidal stability, electrophoresis, powder fractioning, precursors for CVD, electron field emission

### 1. INTRODUCTION

There is a variety of technological procedures for stabilizing nanodiamond (ND) suspensions and preventing excessive particle aggregation, such as ultrasonic treatment [1,2], chemical surface modification and thermal treatment in vacuum [1], the use of cation and anion exchange resins [2], etc. However, additionally treated diamond sols preserve their stability only for a short time [1]. Moreover, subsequent

drying of a powder may lead to the loss of its ability to produce a stable suspension because of the formation of large aggregates.

It is generally believed that the color of a ND powder depends crucially on the content of non-diamond carbon and correlates with the product purity [3,4]. For example, experiments on ND fractionation have shown that a light-grey easily friable powder, a grey powder and a black filamentous crystal-like material can be produced with the nondiamond carbon content of 1.0, 1.5, and 1.9%, respectively [5], after the separation of the suspension particles.

We reported earlier [6,7] on a new method of ND modification, designed at the Institute of Biophysics (Krasnoyarsk, Russia), which allows the production of powders with new properties. A distinctive feature of the modified nanodiamonds (MND) is their ability to form stable hydrosols without additional treatment.

In this report, we describe our results on the physical and chemical properties of MND.

## **2. EXPERIMENTAL**

The MND used in our experiments was obtained from the original ND produced at the Department of Finely Dispersed Materials Physics (Krasnoyarsk Research Center, Russia). The MND powder was fractionated by centrifugation, using a Beckman J-21B centrifuge (USA) at 10,000 r.p.m. for 10 min. The X-ray phase analysis of the carbon content was performed with a DRON-3 (Russia). The X-ray spectra were analyzed for the iron content with a Spectroscan-004 (Russia). The EPR spectra of the samples were registered in the X-band at 300K with an RE 1307 spectrometer (Russia). We used an Eppendorf 5415D centrifuge (Germany) at an acceleration of 2.000–12.000 g for 2–30 min. to determine the sedimentation characteristics. (The optical density of the hydrosols was measured with a UV 300 spectrophotometer (Shimadzu, Japan). The specific surface of the powders was estimated from the argon adsorption, using a GH-1 gasometer (Russia).

## **3. RESULTS AND DISCUSSION**

### **3.1 The Powder Surface Morphology and Hydrosol Formation**

The modification technology described in [6,7] allows the separation of the initial ND powders into two fractions. One fraction F1 contains particles

with a maximum colloidal stability. When dried, F1 is a black powder (Figure 1) composed of crystal-like scaly structures. The other fraction F2 is a gray powder (Figure 1), whose colour is similar to that of the initial ND powder. The physical characteristics of the powders are as follows: the F1 specific surface is  $420 \text{ m}^2 \cdot \text{g}^{-1}$  and the bulk density is  $0.7 \div 0.5 \text{ g} \cdot \text{cm}^{-3}$ ; the F2 powder has  $300 \text{ m}^2 \cdot \text{g}^{-1}$  and  $0.5 \div 0.3 \text{ g} \cdot \text{cm}^{-3}$ , respectively.



Figure 1. The surfaces of the MND powders: F1 fraction (a), F2 fraction (b).

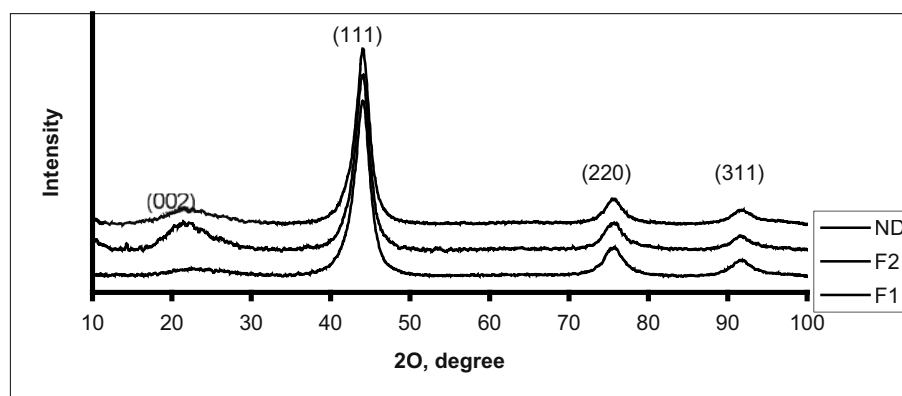
Dry MND powders form hydrosols without a conventional ultrasonic treatment, a property that the initial ND powder does not possess. The F1-based hydrosols are black, while the F2-based hydrosols are gray. The former exhibit a maximum colloidal stability, probably due to a higher  $\xi$ -potential, and can form stable hydrosols even after a multiple removal of the disperse medium [7]. Some other properties of the MND are listed in Table 1.

Table 1. Properties of the modified ND.

Characteristics	F1	F2
Stability of organosols in polar solutes	high	low
Agglomeration on hydrosol freezing and defrosting	-	+
Agglomeration on boiling or autoclaving	-	+
Possibility to get specified concentrations in hydrosols	+	+
Colloidal stability in oils (no sediment for 2 months)	+	-
Colloidal stability during AC/DC hydrosol electrophoresis (no indestructible aggregates).	+	-

### 3.2 X-Ray Analysis

Typical X-ray diffraction patterns of the initial ND powders and of the fractions F1 and F2 are shown in Figure 2.



*Figure 2.* The X-ray diffraction patterns of the initial ND and the F1 and F2 fractions. The diamond reflections from the (111), (220) and (311) planes at  $2\theta = 44.0^\circ$ ;  $75.7^\circ$  and  $91.6^\circ$  respectively, were registered from all the samples, which are found to contain nondiamond carbon that reflects from the (002) plane at  $2\theta = 17^\circ$ – $31^\circ$ .

A comparative X-ray analysis of the diamond showed that all the powders consisted of identical nanocrystallites with the size  $L = 3.5$  nm measured by the Hall -Williamson method [8] and that the microstress level was less than 0.06%. The lattice parameter was found to be  $0.3561 \pm 0.0007$  nm, a value corresponding to the theoretical ND density of  $3.56 \text{ g}\cdot\text{cm}^{-3}$ .

A comparison of the (002) reflections showed that the two fractions contained different amounts of nondiamond carbon, calculated as the area under the peak normalized against the area of 100% diamond reflection. According to these data, the amount of the nondiamond carbon in F1 is three times smaller than in F2 and two times smaller than in the initial powder. However, F1 is black (Figure 1a) and F2 is grey (Figure 1b). Therefore, the nondiamond carbon content does not always correlate with the powder colour and its hydrosols. Note that the reflection peak from the nondiamond carbon is asymmetrical and can be described with two Gaussian distributions (Figure 3). This suggests the existence of two types of nondiamond carbon in this material.

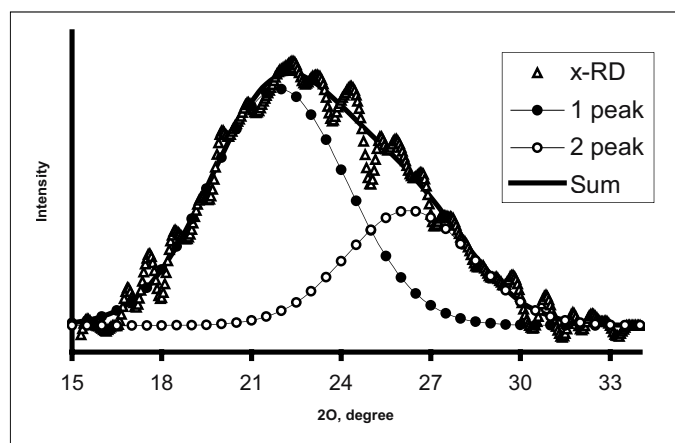


Figure 3. The X-ray diffraction patterns of nondiamond carbon, taken from the (022) plane.

One type of nondiamond carbon has the X-ray reflections at  $2\theta = 21\text{--}31^\circ$ . The peak reflections for F1 and F2 are  $2\theta = 26.26^\circ$  and  $25.39^\circ$ , which are close to the respective values in the JCPDS catalogue [9] for well-crystallized graphite ( $2\theta = 26.66^\circ$ ), but are shifted down by  $0.4^\circ$  and  $1.27^\circ$ , respectively. This appears to be turbostratic carbon. This conclusion can be supported by the following data: (a) the interplanar spacing  $a_c$  is 0.339 for F1 and 0.351 nm for F2; these values are close to the available data for turbostratic carbon ( $a_c = 0.344$  nm [10]); (b) the typical size of the nanocrystallites along the  $c$ -axis,  $L_c = 1.6$  nm, is 4–5 carbon layers for both MND fractions, as measured by Scherrer's method [11].

The values of  $a_c$  and  $L_c$  correlate with the results described in the paper [12] on finding the lattice parameter  $a_c$  and the nanocrystallite size  $L_c$  in turbostratic graphite.

The other type of nondiamond carbon shows the X-ray reflection at  $2\theta = 15\text{--}27^\circ$ , (Figure 3) and is characterized by a much larger interplanar spacing  $a_c$ , 0.406 and 0.419 nm for F1 and F2, respectively. However, the typical size of the nanocrystallites,  $L_c$ , is about 1.5–1.6 nm like that of the nondiamond carbon of the first type. This suggests that the larger interplanar spacing was not due to the crystallite downsizing but, rather, to (a) transverse bindings and complex substitutes on the graphite layer periphery [13] and to (b) the impurities, such as alkali metal ions, that can penetrate between the carbon layers, increasing the interplanar spacing [14].

### 3.3 Electron Paramagnetic Resonance (EPR) Study

The F1 and F2 powders show clear differences in the EPR spectra. The F1 spectrum (Figure 4) has an additional broadening in the area of basic transition. This can be interpreted as being due to the magnetic interaction between the unpaired electrons of the diamond matrix and the impurity paramagnetic ions distributed randomly.

The measurements made in vacuum (at  $\sim 10^{-2}$  Torr) and in the presence of air do not change the pattern of the EPR spectrum which indicates a high degree of the diamond matrix shielding. Otherwise the magnetic interaction between the molecular oxygen contained in the air and the unpaired electrons in the system would have caused the line broadening.

In contrast to F1, F2 absorbs the SHF energy more actively. Obviously, this is due to a higher content of the nondiamond carbon with free electrons.

The presence of an EPR signal with  $g_{\text{ef}} = 4.3$  (Figure 4) definitely indicates the existence of spin-uncorrelated  $\text{Fe}^{3+}$  ions in the system. The EPR data show that the MND fractions contain different amounts of iron impurities: F1 contains more iron impurities than F2 or the initial ND.

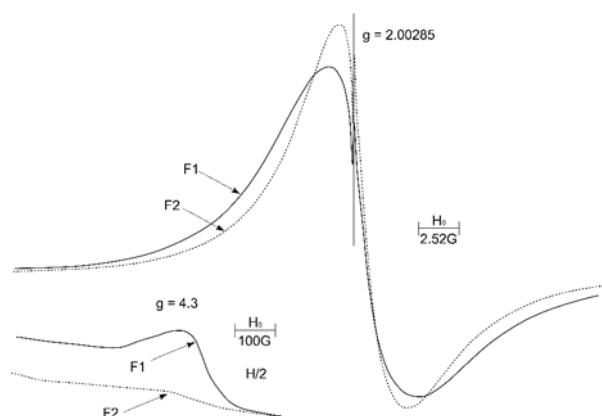


Figure 4. The EPR spectra of the F1 and F2 fractions.

Since EPR detects only signals from  $\text{Fe}^{3+}$  ions, we measured the iron content by a method insensitive to oxidation (Figure 5). The analysis showed that F1 contained three times more iron than F2.



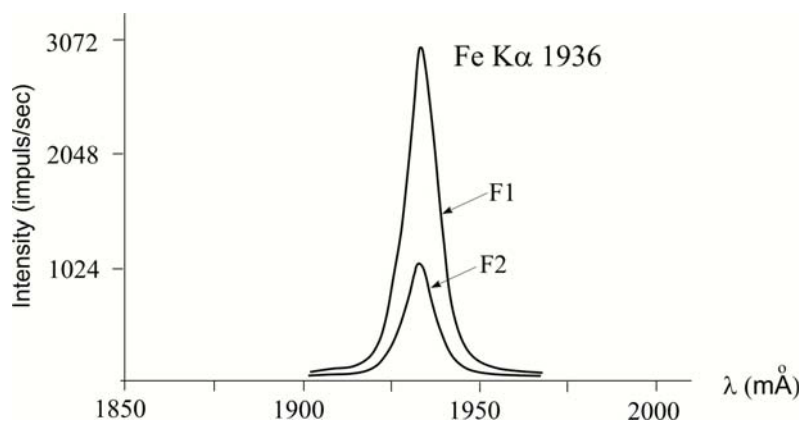


Figure 5. The iron contents in F1 and F2 samples of the same weight.

In our opinion, the source of iron ions in the powders is the chemical treatment used for the ND extraction from the diamond-graphite soot. This suggests that the ND crystallites did not contact the possible sources of iron, such as the fragments of the detonator or the explosion chamber, arising during the explosion that lasts for a few microseconds. The synthesis produces “pure” diamond-graphite particles. Pure iron and its compounds are found in the product as an individual phase or as phase formations, like well-crystallized magnetite  $\text{FeFe}_2\text{O}_4$  [13]. During the chemical purification, the soluble portion of the iron-containing phase is sorbed on the ND particles and then embedded into the near-surface graphite. The amount of the adsorbate varies with both the surface area of the particles and the surface functional groups.

### 3.4 Sedimentation Analysis

A high colloidal stability of MND particles in water allows application of sedimentation methods [15] for the size distribution analysis. Since the initial ND powder could not form stable suspensions without ultrasonic treatment, we did not study its sedimentation properties. The particle size distributions in the F1 and F2 powders are presented in Figures 6 and 7.

The calculations have given  $D_{05}^1 = 37.2 \text{ nm}$  and  $\sigma_1 = 1.95$  for F1;  $D_{05}^2 = 302 \text{ nm}$  and  $\sigma_2 = 1.95$  for F2. These are estimates because we used the particle density equal to the diamond density ( $\rho_d$ ). Since the diamond core is covered with a “radical shell” and the particles form aggregations (clusters), their actual weight-average diameters are larger than the calculated ones.

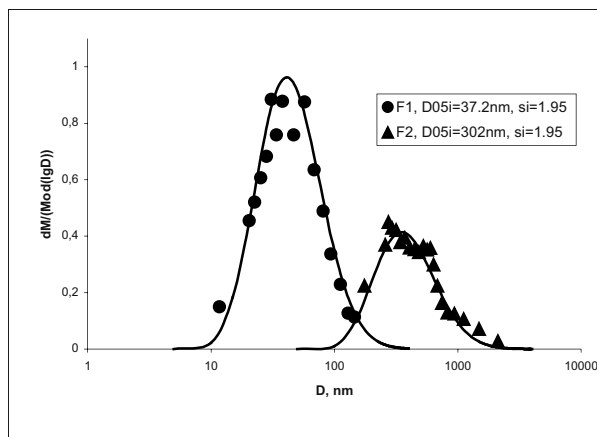


Figure 6. The size distribution of particles in F1 and F2 powders, calculated with the Stocks formula, where the particle effective diameter is inversely proportional to the square root of the difference between the densities of the dispersed material,  $\rho_m$ , and of the medium,  $\rho$ :  $D \sim (\rho_m - \rho)^{0.5}$ . The curves are in different size ranges and intersect in the D region from 100 to 150 nm. The amount of the powder for this experimental size range was less than 9%.

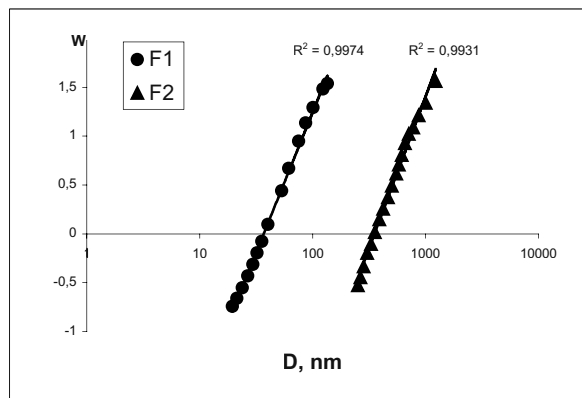


Figure 7. The linear dependences in the logarithmically probabilistic coordinates show the lognormal size distribution of particles [15].

The available data on the ND size characteristics are scanty and contradictory. The ND preserving a colloidal stability for 15 min is reported [1] to consist of 18–32 nm particles with their total amount of 90%. A bimodal size distribution is described in [16] with the parameters  $D_{05}^1 \sim 110$  nm and  $D_{05}^2 \sim 400$  nm.

The size characteristics of F1 and F2 can be compared to the respective characteristics of ND described in [2] since the sedimentation methods were used in both studies. After the ND powder was treated with ultrasound and anion-exchange resins, the size distribution showed three maxima at  $D_{05}^1 \sim 60$  nm,  $D_{05}^2 \sim 180$  nm, and  $D_{05}^3 \sim 280$  nm [2]. Note that the data on the F1 and F2 powders are in reasonable agreement with the mean values of fractions 1 and 3. Apparently, these size characteristics are most probable for stable hydrosols of MND or ND.

These data were obtained from the studies of F1 and F2 fractions of the initial ND produced at the Krasnoyarsk Research Center. However, our modification technique allows fractionation of ND powders from other manufacturers: the Altai Federal Research and Production Center (Biisk, Russia) [7, 17], “Elctrohimpribor” (Lesnoy, Russia) [17], The National Research Institute at the Federal Nuclear Center (Snezhinsk, Russia) (unpublished data). The fractions obtained from different ND sources possess some common properties: the ability to form hydrosols without ultrasonic treatment, similar colors of the powders and hydrosols, a high colloidal stability of the hydrosols, etc.). It is found that the content of modified F1 particles is 50–80% and that of F2 particles is 50–20%, depending on the characteristics of the initial material.

The presence of the two ND fractions differing in the particle size is a distinctive feature of the detonation products, which is typical of any ND powder obtained by purification methods under different conditions. A comparative study of the physical and chemical properties of the Krasnoyarsk fractions and those from other sources is a subject of additional research.

#### 4. SUMMARY

We have shown that our modification technique allows the separation of commercial ND powders into two fractions. The ND produced at the Krasnoyarsk Research Center exhibits a lognormal size distribution with the following parameters:  $D_{05}^1 = 37.2$  nm and  $\sigma_1 = 1.95$ ;  $D_{05}^2 = 302$  nm and  $\sigma_2 = 1.95$ . The initial and the modified NDs contain iron impurities and two types of nondiamond carbon: turbostrate-like carbon and carbon with a large lattice parameter. The nondiamond carbon and iron impurities are found to be distributed irregularly within the fractions. The color of the MND powders and hydrosols does not correlate with the content of nondiamond carbon. The EPR data show that the ND possesses a high level of diamond matrix shielding and that the fractions differ in the broadening in the region

of basic transition and the SHF energy adsorption ratio. The modified F1 powder is the most promising material for future researches and applications. It can be used, for example, as a precursor in the CVD growth of nanocrystalline diamond, in field electron emission tips, and some other areas.

## REFERENCES

1. A.Yu. Neverovskaya, A.P. Voznyakovsky, and V.Yu. Dolmatov. Structure of dispersion media and sediment stability of nano diamond suspensions. *Solid State Physics* **46**(4), 646-48 (2004).
2. S.I. Chukhrayeva. Fractionated nanodiamonds: obtaining, properties and application. *Solid State Physics* **46**(4), 610-13 (2004).
3. <http://www.newnanomaterial.com/production.htm>.
4. <http://www.nanoamor.com/home>
5. S.I. Chukhrayeva, P.Ya. Detkov, A.L. Tkachenko, and A.D. Toropov. Physicochemical properties of fractions extracted from the ultra disperse diamonds. *Superhard Materials*, No. 4, 29-36 (1998).
6. V.S. Bondar and A.P. Puzyr. Nanodiamonds for biological investigation. Abstracts from the I International Symposium «Detonation nanodiamonds: obtaining, properties and application», St.-Petersburg, p.109 (2003).
7. V.S. Bondar and A.P. Puzyr. Nanodiamonds for biological investigation. *Solid State Physics* **46**(4), 698-01 (2004).
8. G.K. Williamson and W.H. Hall. X-ray line broadening filed aluminium and wolfram. *Acta Metallurgica*, No.1, 22-31 (1953).
9. JCPDS N26-1076
10. Brian McEnaney. Structure and bonding in carbon materials. In: *Carbon Materials for advanced technologies*. Pergamon, New York. 1999, pp. 1-33.
11. H.P. Klug and L.E. Alexander. *X-ray diffraction procedures for polycrystalline and amorphous materials*. Wiley, New York, 1954, pp.491-95.
12. N. Iwashita and M. Inagaki. Relations between structural parameters obtained x-ray powder diffraction of various carbon materials. *Carbon*, **31**(7), 1107-13 (1993).
13. A.I. Shames, A.M. Panich, W. Kempinski et al. Defects and impurities in nanodiamond: EPR, NMR and TEM study. *Journal of Physics and Chemistry of Solids* **63**, 1993-01 (2002).
14. H. Shioyama The interaction of two chemical species in the interlayer spacing of graphite. *Synthetic Metals* **114**, 1-15 (2000).
15. P.A. Kouzov. *Principles of analysis of dispersion content of commercial powders and ground materials*. Leningrad: Chemistry, 1974, p. 280.
16. J. Chen, S.Z. Deng, J. Chen, Z.X. Yu, and N.S. Xu. Graphitization of nanodiamond powder annealed in argon ambient. *Applied Physics Letters* **74**(24), 3651-53 (1999).
17. A.P. Puzyr, K.V. Pourtov, and V.S. Bondar. Detonation materials with new properties. Abstracts from the All- Russia Scientific Conference "Ultra disperse powders, nanostructures, materials". 2003 October 23-24, Krasnoyarsk, pp.96-98.

## MAGNETIC RESONANCE STUDY OF NANODIAMONDS

A.I. Shames<sup>1</sup>, A.M. Panich<sup>1</sup>, W. Kempański<sup>2</sup>, M.V. Baidakova<sup>3,4</sup>,  
V.Yu. Osipov<sup>3,4</sup>, T. Enoki<sup>4</sup>, and A.Ya. Vul' <sup>3</sup>

<sup>1</sup> *Department of Physics, Ben-Gurion University of the Negev, P.O.Box 653, 84 105 Be'er-Sheva, Israel*

<sup>2</sup> *Institute of Molecular Physics, Polish Academy of Sciences, Smoluchowskiego 17, 60-179 Poznań, Poland*

<sup>3</sup> *Ioffe Physico-Technical Institute, 26 Polytechnicheskaya, St. Petersburg 194021, Russia*

<sup>4</sup> *Department of Chemistry, Tokyo Institute of Technology, 2-12-1, Ookayama, Meguro-ku, Tokyo 152-8551, Japan*

### Abstract:

Magnetic resonance techniques, namely Electron Paramagnetic Resonance (EPR) and solid state Nuclear Magnetic Resonance (NMR), are powerful non-destructive tools for studying electron-nuclear and crystalline structure, inherent electronic and magnetic properties and transformations in carbon-based nanomaterials. EPR allows to control purity of ultradispersed diamond (UDD) samples, to study the origin, location and spin-lattice relaxation of radical-type carbon-inherited paramagnetic centers (RPC) as well as their transformation during the process of temperature driven diamond-to-graphite conversion. Solid state NMR on <sup>1</sup>H and <sup>13</sup>C nuclei provide one with information on the crystalline quality, allows quantitative estimation of the number of different allotropic forms, and reveals electron-nuclear interactions within the UDD samples under study. Results of recent EPR and <sup>13</sup>C NMR study of pure and transition metal doped UDD samples, obtained by detonation technique, are reported and discussed. In addition to characteristic EPR signals, originated from para- and ferromagnetic impurities and doping ions, the UDD samples show a high concentration of RPC (up to 10<sup>20</sup> spin/gram), which are due to structural defects (dangling C-C bonds) on the diamond cluster surface. *In-situ* EPR sample's vacuumization experiment in conjunction with precise SQUID magnetization measurements allowed concluding that each UDD particle carries a single spin (dangling bond) per each from 8 crystal (111) facets bounded the particle.

### Keywords:

nanoparticle, diamond, nanodiamond, UDD, EPR, NMR, SQUID, metal impurity, free radical, dangling bond, spin-lattice relaxation, diamond-to-graphite transformation

## 1. INTRODUCTION

Nanodiamond, often called ultradispersed diamond (UDD), is one of the new carbon cluster substances that may be produced in large amounts by the detonation method [1,2]. The study of UDD properties was initiated in 1988, with the focus on its technology and mechanical properties. An unusual feature of UDD is the small size of clusters, with most particles varying between 40 and 50 Å [3–6]. This is attractive for using UDD as a polishing material and for seeding treatment of the substrate in CVD diamond film growth [7]. UDD powder can also be used as a starting material to produce onion-like carbon by heat treatment [8,9].

It was recently shown that a UDD cluster has a complex structure consisting of a diamond core of about 45 Å in size and a shell made up of  $sp^2$ -coordinated carbon atoms. The shell structure and thickness vary with the explosion conditions and chemical purification of UDD clusters from the soot produced by the detonation process [10,11].

A specific feature of clusters as nano-sized objects is the crucial effect of the surface on their structural and electronic properties, since the number of surface atoms becomes comparable with that of bulk atoms. In this connection, it is important to understand the structural differences between defect centers in nanodiamond and those in bulk diamond. Where are impurities and defects localized? May size-effects be detected in UDD? What are the parameters of defects and impurities in UDD? Magnetic resonance techniques, namely Electron Paramagnetic Resonance (EPR) and solid state Nuclear Magnetic Resonance (NMR), are well known as powerful non-destructive tools for studying electron-nuclear and crystalline structure, inherent electronic and magnetic properties and transformations in carbon-based nanomaterials. In this paper, we present the results obtained by EPR, NMR and SQUID techniques, which provide reliable answers to the most of these questions.

## 2. PRECEDING MAGNETIC RESONANCE STUDIES

### 2.1. EPR

EPR study of diamonds obtained by explosion synthesis started in the middle of 70-th. [12–14]. Then it was found that UDD show strong intrinsic paramagnetism originating from uncoupled spins localized at broken carbon-carbon bonds. All samples demonstrated the same typical EPR features: absence of characteristic triplet signals from spins located on doped nitrogen atoms; presence of a very intensive singlet signal with  $g = 2.003$  and line

width  $\Delta H_{pp} \sim 0.7\text{--}0.9$  mT, associated with carbon-centered defects; concentrations of these paramagnetic centers are of the order of  $10^{18}\text{--}10^{19}$  spin/g. Parameters of the EPR signal observed are most close to those of the EPR signal of broken bonds on the diamond surface ( $g = 2.0027$ ,  $\Delta H_{pp} = 0.55$  mT) [15]. Further EPR studies [16–18] of UDD, obtained by both wet and dry synthesis, justified the same EPR parameters, which were found to be practically independent (except of  $\Delta H_{pp}$ ) [18] on the preparation technique.

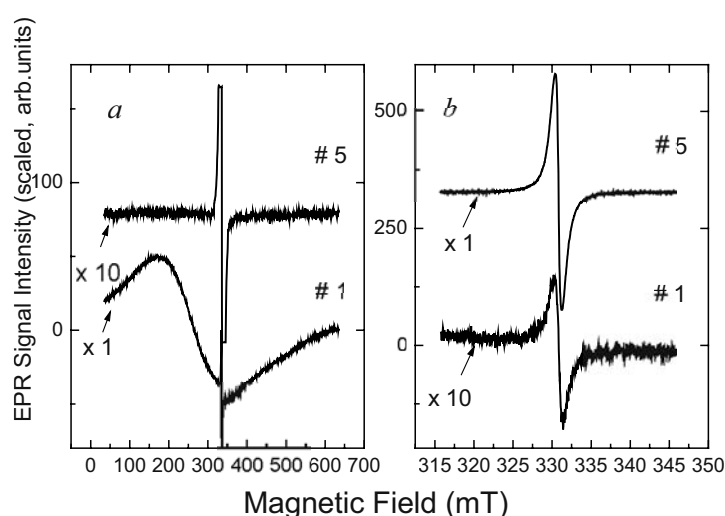


Figure 1. RT EPR spectra of  $\sim 1$  g of initial detonation soot UDD # 1, and well purified UDD #5: (a) general view,  $\nu = 9.38$  GHz; (b) free-radical region,  $\nu = 9.268$  GHz (# 1) and  $\nu = 9.272$  GHz (# 2). Spectra are plotted in the same scale using multiplication coefficients shown on the left of each spectrum.

The most comprehensive EPR, NMR and high-resolution transmission electron microscopy (HRTEM) study of purified detonation diamonds is reported in Ref. 19. It was shown [19] that EPR is a powerful tool for the control of para- and ferromagnetic impurities during the processes of UDD purification. Figure 1(a) demonstrates difference between room temperature (RT) EPR spectra of the initial detonation soot (UDD #1) containing a certain amount of magnetic impurities (Fe, Ni, Co, etc.) which are responsible for the intensive broad line, and well purified ( $\text{HNO}_3$  50%,  $200^\circ\text{C}$ ) UDD #5 sample, which demonstrates the only intensive narrow ( $\Delta H_{pp} = 0.97$  mT) Lorentzian-shaped singlet line in the  $g = 2.00$  region, attributed to radical-like paramagnetic centers (RPC). Figure 1(b) clearly shows, that specific density of RPC in detonation soot is of about an order of

magnitude lower, then in purified UDD samples which was found to be  $\sim 10^{20}$  spin/g disregarding the purification technique and quality. The  $g$ -factor of RPC was measured precisely and found to be  $g = 2.00282 \pm 0.00003$  within the temperature range of 4.2–300K. Temperature dependence of the RPC EPR line intensity, measured in the same temperature range, indicates that RPC obey the Curie law. The data obtained allowed to attribute these RPC to the non-interacting uncoupled spins, originating from defects of  $sp^3$  diamond-like system (dangling bonds). Moreover, the  $g$ -shift of RPC EPR line from the free electron  $g$ -value ( $g_e = 2.0023$ ), being interpreted in terms of uncoupled spins localized on a mesoscopic object (like nanodiamond), leads to UDD sizes of 20–60 Å which are in a good agreement with X-ray diffraction (XRD) and HRTEM data. Electron spin-lattice relaxation times, measured by the method of continuous saturation of RPC signals at RT, were found to be the same short for all UDD samples and estimated as  $T_{1e} < 10 \mu s$ .

EPR was successfully used for tracing nanodiamond to nanographite conversion due to the heat treatment (HT) in Ar atmosphere [20–21]. Starting material - nanodiamond - is known to be covered by functional groups on the surfaces, and HT easily reconstructs the diamond (111) planes into graphite (001) planes after stripping off the functional groups. XRD, HRTEM and Raman scattering studies show progressive development of graphite phase on increasing HT temperature (HTT), with the onset at  $T = 1200^\circ C$  and the complete diamond-to-graphite conversion at  $T = 1600^\circ C$ . RT EPR reflects these changes providing useful information on modifications in electronic subsystem. Thus, on heating, the following RPC EPR line parameters undergo remarkable changes:  $g$ -factor decreases from  $g = 2.0028$  for initial and HTT900 samples to 2.0013 for HTT1600 one; line width  $\Delta H_{pp}$  increases from  $\Delta H_{pp} = 0.9$  mT to 3.5 mT, correspondingly; electron spin-lattice relaxation time shortens for about an order of magnitude for HTT1600 sample. This evolution of the RT EPR signals, in conjunction with magnetization data, clearly evidence that initial UDD and HTT900 samples belong to  $sp^3$ -carbon-dominated diamond-like materials with all uncoupled electrons localized and negligible orbital susceptibility  $|\chi_{orb}|$ , whereas HTT1600 sample is  $sp^2$ -dominated complete graphitized system. Broad ( $\Delta H_{pp} = 3.5$  mT) RT EPR signal with  $g = 2.0013$  in HTT1600 sample may be credited to spins localized on the nonbonding  $\pi$ -electrons edge states (so-called Fujita's states). These states are caused by zigzag-type boundaries of randomly translated and rotated along the azimuth parallel graphitic sheets composing nanographite particle. Intermediate HTT1200 and HTT1400 samples are attributed to  $sp^2:sp^3$  mixed-phase systems.



## 2.2 NMR

Solid state NMR is a useful technique that may give an idea on crystalline quality of a defined structure, quantitative estimations of the abundance of different allotropic forms and electron-nuclear interactions (via relaxation times measurements). Two nuclei are suitable for NMR study of nanodiamonds:  $^{13}\text{C}$  isotope (natural abundance 1.1%) and  $^1\text{H}$  (abundance 99.99%). The former nuclei are inherent to all carbon-originating nanomaterials whereas the latter ones belong to impurities or proton-containing molecules adsorbed on the surface.  $^{13}\text{C}$  Magic Angle Spinning (MAS) NMR spectrum of purified UDD involved four signals regarded to diamond carbon atoms (main peak,  $\delta = 34.5$  ppm, here and further for  $^{13}\text{C}$  NMR - relative to TMS), defect diamond carbon atoms (broad peak,  $\delta \sim 30$  ppm) and partially oxidized structures (two weakly pronounced peaks with ( $\delta = 53$  and  $68$  ppm) [16]. Ref. 16 and 18 reported on  $^1\text{H}$  MAS NMR spectra of UDD samples, purified by various methods. Peaks located at  $\delta = 0, 0.5$  and  $2.5$  ppm, were ascribed to  $\text{CH}$ ,  $\text{CH}_2$  and  $\text{CH}_3$  groups at different configurations at the carbon site [18]. Signals with  $\delta = 3.8$  and  $6.7$  ppm were assigned to bound  $\text{C-OH}$  and  $\text{S-OH}$  groups formed on a surface of the particles during its chemical purification [16].

Ref. 22 presents thorough NMR study of samples obtained for various RDX/TNT charges.  $^{13}\text{C}$  MAS NMR spectrum of detonation soot obtained for RDX/TNT 65/35 charge reveals the presence of two contributions: the first at  $\delta = 37$  ppm is related to crystalline tetragonal carbon, i.e. to the diamond phase. The small shoulder at  $32$  ppm is attributed to  $sp^3$ -distorted system due to environmental perturbations, like crystal lattice defects. The second line, very broad and centered at  $\sim 120$  ppm, corresponds to  $sp^2$ -hybridized carbon.  $^{13}\text{C}$  MAS NMR spectrum of oxidized sample displays only the large  $sp^3$  peak at  $\delta = 37$  ppm, similar to that for untreated material, whereas broad  $120$  ppm peak has disappeared. Cross-polarization (CP) MAS NMR spectra reveal carbon atoms, neighboring protons. Thus, in detonation soot CP-MAS NMR technique reveals several peaks related to protonated tetragonal carbons: at  $38$  ppm (methylene carbons,  $\text{CH}_2$ ) and  $45$  ppm (methane carbons,  $\text{CH}$ ). Additional signals at  $71$  ppm appear in the oxidized sample evidencing  $\text{C-OH}$  group formation [22].

Low-resolution solid state  $^{13}\text{C}$  NMR study reported in Ref. 19. The  $^{13}\text{C}$  NMR spectrum of well purified UDD #5 sample shows a singlet Lorentzian-like resonance with the line width  $\Delta\nu = 2.1$  kHz and chemical shift  $\delta = 35 \pm 3$  ppm, the latter coinciding with that of both bulk and nanodiamond ( $35 \div 37$  ppm) [16,18,22]. The  $^{13}\text{C}$  NMR spectrum of detonation soot UDD #1 recorded at a slower repetition rate demonstrates a

superposition of two lines belonging to disordered graphite and diamond, respectively. The intensity of the diamond-like line in that NMR spectrum is about twenty times lower than in the spectrum of UDD #5.

The measurements of  $^{13}\text{C}$  nuclear spin-lattice relaxation  $T_{1n}$  in UDD #5 show magnetization decay well described by a stretched exponent

$$M(t) = M(0)\{1 - B\exp[-(t/T_1)^\alpha]\}, \quad (1)$$

with  $T_{1n} = 144 \pm 0$  ms,  $B = 1.91 \pm 0.04$ , and  $\alpha = 0.661 \pm 0.027$ . The relaxation time for the weak diamond-like line for UDD #1, obtained by the same method, was found to be  $T_{1n} = 173 \pm 45$  ms.

A diamond crystal is diluted in magnetic nuclei because of the low natural abundance of  $^{13}\text{C}$  isotope, 1.1%, which yields negligible nuclear dipole-dipole interactions. The cubic structure of diamond provides an isotropic chemical shift. Moreover, UDD #5 exhibits practically no magnetic impurities. Therefore, the NMR line is expected to show line width comparable with the instrumental broadening (about 100 Hz). However, the width of the NMR signal observed is 2.1 kHz. Nanoparticles usually show a behavior quite different from that of bulk material - due to significant contribution of surface atoms, which number, in the UDD case, is comparable with that of the bulk volume. Thus, surface may be considered as a distorted structure. Each nucleus "senses" different electronic environments, which causes a distribution of the chemical shifts revealing in a line broadening. The anomalous reduction in the spin-lattice relaxation time of  $^{13}\text{C}$  (from several hours in natural diamond to hundred milliseconds in UDD), as well as stretched exponential character of the magnetization decay, is attributed to the interaction between RPC and nuclear spins. The coefficient  $\alpha = 0.661 \pm 0.027$  is found to be in a good agreement with the model of non-uniform distributions of RPC and nuclei. The coefficient  $\alpha = 0.661 \pm 0.027$  is found to be in a good agreement with the model of non-uniform distributions of RPC and nuclei:  $\alpha = (D + d)/6$ , with  $D = 3$ , pointing out three-dimensional distribution of RPC in the sample, and  $d = 1$  which is typical for the high field NMR experiment, where the nuclear magnetization is confined to the direction of the external magnetic field [19].

### 3. RECENT DEVELOPMENTS

#### 3.1 EPR of Nanodiamonds Doped by Transition Metal Ions

RT EPR spectra of UDD samples intercalated by transition metal ions of Fe, Co, Ni, Cu show appearance of new signals in addition to signals belonging to RPC. Due to their spectroscopic properties just  $\text{Cu}^{2+}$  ions ( $d^9$ ,

$S = 1/2$ ,  $I = 3/2$ ) reveal some well-defined characteristic spectra and, therefore, indicate the penetration of metal ions into some graphite structures. Figure 2 demonstrate evolution of the additional EPR signals with increasing of the Cu doping level.

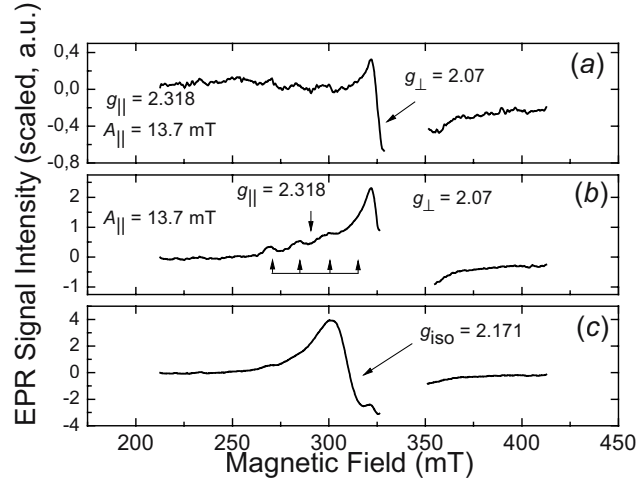


Figure 2. RT EPR spectra of UDD samples doped by  $\text{Cu}^{2+}$  ions in increasing level  $x$ : (a)  $x = 0.002\%$ ,  $\nu = 9.399$  GHz; (b)  $x = 0.01\%$ ,  $\nu = 9.409$  GHz; (c)  $x = 0.02\%$ ,  $\nu = 9.404$  GHz. Intensive RPC signals are subtracted.

At the lowest doping level ( $x = 0.002\%$ ) a polycrystalline pattern characteristic for  $\text{Cu}^{2+}$  ions in the crystal field of axial symmetry is observed. The spectrum may be described by the corresponding spin-Hamiltonian, which includes anisotropic Zeeman and electron-nuclear interactions:

$$H = g_{\parallel} S_z H_z + g_{\perp} (S_x H_x + S_y H_y) + A_{\parallel} S_z I_z + A_{\perp} (S_x I_x + S_y I_y), \quad (2)$$

with  $g_{\parallel} = 2.318 \pm 0.002$ ,  $g_{\perp} = 2.318 \pm 0.002$ ,  $A_{\parallel} = 13.7 \pm 0.3$  mT and  $A_{\perp} < 1.5$  mT. On increasing  $x$  to 0.01%  $\text{Cu}^{2+}$  spectrum becomes more pronounced but broadened keeping  $g$ -factors and hyperfine splittings unchanged. On further increase of the doping level an intensive singlet broad line with isotropic  $g_{\text{iso}} = 2.171 \pm 0.005$  is observed. Since copper does not produce carbides, it may be supposed that  $\text{Cu}^{2+}$  ions are located on the surface of UDD particles, possibly - on the graphene sheets. On increasing of the amount of  $\text{Cu}^{2+}$  surface centers the electron dipole-dipole and exchange interactions causes both averaging and broadening of the initially anisotropic ERP pattern.

### 3.2 Where are RPC located?

There are two very recent experiments, which results may give additional insight to precise number and location of uncoupled spins on the nanodiamond particle. Firstly, *in-situ* RT EPR kinetics during air exhaust from the well purified UDD #5 was studied for the elucidation of the effect of absorbed molecular oxygen on the RPC lines. Figure 3 shows the time dependence of RPC ERP line peak on various stages of pumping out (down to  $10^{-4}$  Torr) process. It is found that air exhaust abruptly increases the total amount of RPC observed for about 10% (determined by spectra double integration). No changes in the RPC line shape, position and width are detected. When pumping out is stopped and the sample is open to air, the RPC signal returns (in steps) to its initial value. Thus, molecular oxygen absorbed does not affect the line width of the RPC detected. On the other hand, 10% increase of the actual amount of detectable RPC may be explained just by the strong dipolar interaction of some RPC with paramagnetic  $O_2$ . In oxygen-containing sample part of RPC may be located in close vicinity of oxygen molecules. Dipolar interaction causes significant broadening of EPR lines just for these RPC, which reduces their contribution to the observed signal intensity, obtained by the integration within the limiting field range. When pumping out proceeds, the EPR signal of these RPC narrows and they contribute to the integral intensity again.

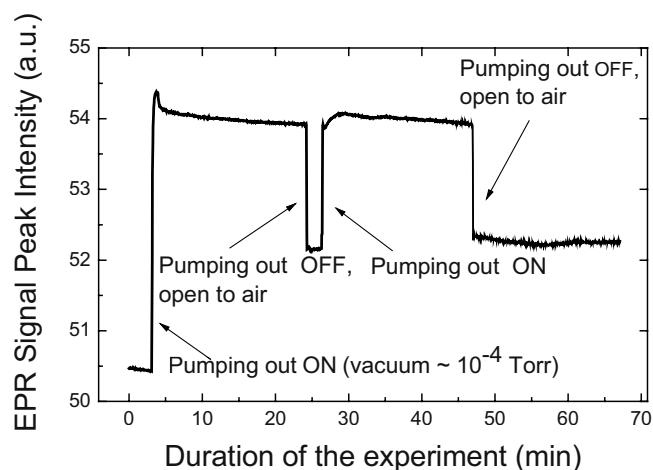


Figure 3. *In-situ* EPR kinetics during pumping out of UDD #5 sample at RT.

Secondly, the magnetic susceptibility and magnetization measurements on very pure UDD powder were carried out with a SQUID magnetometer (Quantum Design Co., MPMS-5) in the temperature range of 1.9–380K in magnetic fields up to 5.5 T in vacuum. In order to reduce remaining contamination of magnetic impurities, nitric acid treated nanodiamond sample (like UDD #5 above) was additionally purified.

Laboratory amount of UDD powder (0.95 g) was subjected to a repeated chemical treatment in 38% hydrochloric acid (5 treatments at forced-circulation boiling) and then washed in boiling water (repeating 5 times). Both magnetization curve measurements and EPR evidence that this additional treatment nearly totally removes remains of magnetic impurities. The samples for SQUID measurements were vacuum-sealed in the tubes after vacuum heat-treatment at 400°C for 3.5–4.5 hours and achieving the vacuum level of about  $(1.2\text{--}2.0)\times 10^{-6}$  Torr.

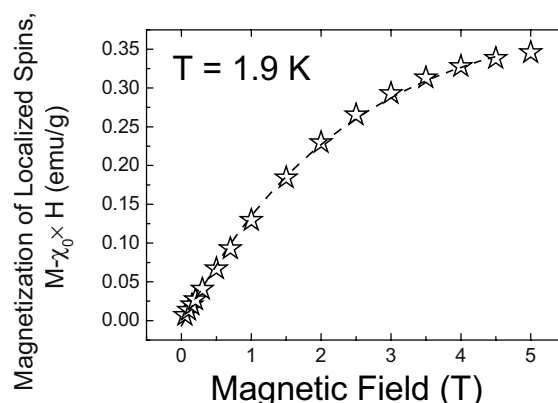


Figure 4. Magnetization curve at  $T = 1.9\text{K}$ . Saturating trend in the high magnetic field indicates the localized spin feature. The contribution of  $\chi_0 \times H$  has been subtracted. The dashed line shows a Brillouin type curve for the least square fit. Fitting parameters -  $N_s = 4.19 \times 10^{19}$  spins/g,  $S = 1/2$ . Sample weight - 20.2 mg.

Subsequent study of the magnetic properties on these samples shows that magnetic phenomena in pure UDD are associated only with the localized defects with  $S = 1/2$ . The magnetization ( $M$ - $H$ ) curve measured at  $T = 1.9\text{K}$  in magnetic fields  $H$  up to 5.5 T, may be interpreted as being a sum of the temperature-independent linear ( $M$ - $H$ ) curve with a negative slope  $\chi_0 \times H$  (here  $\chi_0 = -0.5 \times 10^{-6}$  emu/g is a core diamagnetic susceptibility of the carbon atoms) and the curve with a positive contribution of  $S = 1/2$  (Figure 4). The latter being fitted to the Brillouin curve yields a concentration of localized spins of  $4.19 \times 10^{19}$  spins/g. No contribution to the magnetization curve due to

transition metal ions impurities (spin value  $S > 1/2$ ) is observed. The absence of appreciable amounts of magnetic impurities is further confirmed by the measurements of the vanishing residual magnetization of powder at zero field  $H = 0$  at  $T = 1.9$  K. The local concentration of intrinsic paramagnetic centers, estimated from the value  $4.19 \times 10^{19}$  spins/g (assuming the average diameter and the density of UDD particles equal to 5.0 nm and  $3.52 \text{ g/cm}^3$ , respectively), is found to be only 9.7 spins per nanoparticle. Such a small number of dangling bonds, as compared with the total number (2400) of the surface atoms in a particle indicates that the surface bonds of a diamond core are almost totally terminated and RPC observed are due to the structural defects in the diamond core or at the interface between the core and the detached graphene layers, covered diamond core in a few places.

One can suppose that the full number of detached graphene flakes equals 8, because a single diamond nanoparticle is bounded by eight (111) crystal planes, which are readily graphitized. Because the total number of spins per nanoparticle is very close to the number of the (111) planes faceting the nanoparticle, it may be concluded that each spin, localized on the nanodiamond surface, is covered with its own detached graphene flake. The convincing argument in favor of attributing the RPC EPR signal to the structural defects in/on the diamond core is due to the width of narrow EPR line being independent of the ambient gas surrounding the sample. Both pumping out and increasing of the oxygen partial pressure up to 0.2 atm do not affect the line width. This means that there is no dipolar interaction between defect spins and paramagnetic  $\text{O}_2$ , and the absorbed oxygen molecules cannot draw near the defect pieces in/on the nanodiamond core through the protective covering of graphene flakes. On the other hand, at least 10% increase in the amount of detectable RPC on air exhausting occurs. It is reasonable to suppose that these 10% represents a difference between 8 spins, which are localized in/on the diamond core, and the total local spin concentration detected by SQUID (9–10 spins per particle). Thus, about 8 spins per particle are screened from the contact with paramagnetic  $\text{O}_2$ , but 1 or 2 spins belonging to the same nanoparticle are in direct contact with  $\text{O}_2$ . The latter spins are most probably localized on the outer side of graphene flakes and, therefore, their EPR signals are very sensitive to the presence of oxygen.

#### 4. CONCLUSIONS

Magnetic resonance techniques (both EPR and NMR) are powerful tools for studying structure and properties of nanodiamonds.

They allow:

- control of separation between graphite and nanodiamond phases as well as transition metal ion impurities and dopants;
- determine origin of paramagnetism in pure nanodiamonds and its mesoscopic-related features (like *g*-factor, NMR line width, relaxation times etc.);
- determine number of RPC (dangling bonds) per each particle and their precise location;
- track nanodiamond to nanographite transformation due to the heat treatment.

## Acknowledgements

V.Yu.O. and M.V.B. thank the Japanese Society for the Promotion of Science (JSPS) for the fellowship and financial support. V.Yu.O. thanks the Interactive Research Center of Science (Tokyo Institute of Technology) for the professorship. A.Ya.V. thanks the Russian State Program “Fullerenes and Atomic Clusters” for the financial support. M.V.B. thanks also INTAS project 0175wp.

## REFERENCES

1. A.M. Staver, N.V. Gubareva, A. I. Lyamkin, and E. A. Petrov. Synthesis of ultrafine diamond powders by explosion. *Physica Gorennya i Vzryva* **20**(5), 100-04 (1984).
2. N.R. Greiner, D.S. Phillips, J.D. Johnson, and F. Volk. Diamonds in detonation soot. *Nature* **333**(6172), 440-42 (1988).
3. V.I. Trefilov, V.S. Moskalenko, G.I. Savvakina, E.A. Tsapko, and D.G. Savvakina. Structural characteristics of ultrafine diamonds and hypothetical mechanism of their formation under highly nonequilibrium conditions of detonating carbon-containing explosives. *Dok. Akad. Nauk SSSR* **305**(1), 85-90 (1989).
4. V.L. Kuznetsov, A.L. Chuvilin, E.M. Moroz, V.N. Kolomiichuk, S.K. Shaikhutdinov, and Y.V. Butenko. Effect of explosion conditions on the structure of detonation soots: ultradisperse diamond and onion carbon. *Carbon* **32**(5), 873-82 (1994).
5. M. Yoshikawa, Y. Mori, H. Obata, M. Maegawa, G. Katagiri, H. Ishida, and A. Ishitani, Raman scattering from nanometer-sized diamond. *Appl. Phys. Lett.* **67**(5), 694-96 (1995).
6. A.E. Alexenskii, M.V. Baidakova, A.Ya. Vul', V.Yu. Davydov, and Yu.A. Pevtsova, Diamond-graphite phase transition in clusters of ultrafine diamond. *Phys. Solid State* **39**(6), 1007-15 (1997).

7. H. Makita, K. Nishimura, N. Jiang, A. Hatta, T. Ito, and A. Hiraki. Ultrahigh particle density seeding with nanocrystal diamond particles *Thin Solid Films* **281-282**(1-2), 279-81 (1996).
8. V.L. Kuznetsov, A.L. Chuvilin, Y.V. Butenko, I.Yu. Malkov, and V.M. Titov, Onion-like carbon from ultra-disperse diamond. *Chem. Phys. Lett.* 222(4), 343-48 (1994).
9. E.D. Obratsova, M. Fujii, S.Hayashi, V.L.Kuznetsov, and Y.V. Butenko. Raman identification of onion-like carbon. *Carbon* **36**(5-6), 821-26 (1998).
10. M.V. Baidakova, A.Ya. Vul', and V.I. Siklitski. Ultradisperse-diamond nanoclusters. Fractal structure and diamond-graphite phase transition. *Chaos, Solitons & Fractals* **10**(12), 2153-63 (1999).
11. A.E. Alexensky, M.V. Baidakova, A.Ya. Vul', and V.I. Siklitski. The structure of diamond nanoclusters. *Phys. Solid State* **41**(4), 668-71 (1999).
12. A.V. Belyankina, T.A. Nachal'naya, Yu.I. Sozin, and L.A. Shul'man. X-ray diffraction data and EPR spectra of explosion-formed diamonds. *Sint. Almazy* **5**, 5-7 (1975).
13. V.N. Bakul and V.D.Andreev. AV-type diamonds synthesized by explosion. *Sint. Almazy* **5**, 3-4 (1975).
14. M.V. Vlasova, N.G. Kakazei, and G. I. Savvakina. Some properties of ultradispersion diamonds prepared under high-temperature explosion synthesis conditions. *Izv. Akad. Nauk SSSR, Neorg. Mater.* **15**(7), 1303-04 (1979).
15. N.D. Samsonenko and E.V. Sobolev. Electron paramagnetic resonance caused by a diamond surface. *Pis'ma Zh. Eksp. Teor. Fiz.* **5**(9), 304-07 (1967).
16. A.L. Vereshchagin, V.F. Komarov, V.M. Mastikhin, V.V. Novoselov, L.A. Petrova, L.L. Zolotukhina, N.V. Vychin, K.S. Baraboshin, and A.E. Petrov. Proceedings of the Vth All-Union Meeting on Detonation, Krasnoyarsk 1991, **1**, 99 (1991).
17. K. Iakuobovskii, G.J. Adriaenssens, K. Meykens, M. Nesladek, A.Ya. Vul', and V.Yu. Osipov. Study of defects in CVD and ultradisperse diamond. *Diamonds and Rel. Mater.* **8**, 1476-79 (1999).
18. K. Iakuobovskii, M.V. Baidakova, B.H. Wouters, A. Stesmans, G.J. Adriaenssens, A.Ya. Vul', and P.J.Grobet. Structure and defects of detonation synthesis nanodiamond. *Diamonds and Rel. Mater.* **9**, 861-65 (2000).
19. A.I. Shames, A.M. Panich, W. Kempinski, A.E. Alexenskii, M.V. Baidakova, A.T. Dideikin, V.Yu. Osipov, V.I. Siklitski, E. Osawa, M. Ozawa, and A.Ya. Vul'. Defects and impurities in nanodiamonds: EPR, NMR and TEM study. *J. Phys. Chem. Solids* **63**(11), 1993-01 (2002).
20. O.E. Andersson, B.L.V. Prasad, H. Sato, T. Enoki, Y. Hishiyama, Y. Kaburagi, M. Yoshikawa, and S. Bandow. Structure and electronic properties of graphite nanoparticles. *Phys. Rev. B* **58**, 16387-95 (1998).
21. B.L.V. Prasad, H. Sato, T. Enoki, Y. Hishiyama, Y. Kaburagi, M. Yoshikawa, A.M. Rao, P.C. Eklund, and M. Endo. Heat treatment effect on the nanosized graphite  $\pi$ -electron system during diamond to graphite conversion. *Phys. Rev. B* **62**, 11209-18 (2000).
22. J.-B. Donnet, E. Fousson, L. Delmott, M. Samirant, C. Baras, T.K. Wang, and A. Eckhardt.  $^{13}\text{C}$  characterization of nanodiamonds. *C.R. Acad. Sci. Paris, Serie IIc, Chimie* **3**, 831-38 (2000).



## INFRARED SPECTRA OF EXPLOSION NANODIAMONDS: A COMPARISON WITH SPECTRA OF HYDROGENATED AMORPHOUS CARBON FILMS

W.W. Duley<sup>1</sup>, V.I. Grishko<sup>1</sup>, and O.A. Shenderova<sup>2</sup>

<sup>1</sup>*Department of Physics, University of Waterloo, Waterloo, Ontario, N2L 3G1, Canada*

<sup>2</sup>*International Technology Center, P.O. Box 13740, Research Triangle Park, NC 27709, USA*

**Abstract:** We report infrared absorption spectra of explosion nanodiamonds and compare these with spectra of *a*-C:H films prepared by laser ablation. Similarities between these spectra are discussed. In particular, we find that a feature near 1620 cm<sup>-1</sup> in nanodiamond particle spectra can be associated with the presence of C=C groups. This is supported by the observation of bands arising from CH<sub>2</sub>. We suggest that these groups are created by surface reconstruction on these extremely small particles that tends to de-emphasize tetrahedral bonding in the surface layer.

**Keywords:** nanodiamonds, *a*-C:H, infrared spectra

### 1 INTRODUCTION

Carbon nanoparticle clusters produced under the extreme conditions that exist during detonation at pressures of 30 GPa and  $T = 3000\text{K}$  are of mixed  $sp^3/sp^2$  hybridized bonding composition. Mixed composition arises because the small number of carbon atoms in typical nanoparticles (~several thousands of atoms) places a significant fraction of atoms at the surface where reconstruction can occur. Reconstruction can take the form of the formation of aromatic structures accompanied by the formation of defects [1–3]. Dangling bonds are also favored under certain conditions, leading to the possibility of enhanced adsorption of other chemical species. Infrared spectra of diamond nanoparticles are then strongly influenced by the vibrational spectra of functional groups such as C=O, C-O, C-N, C=C and C-C in ethers, esters and other carbonyl carbons. Nitrile and isonitrile groups are also commonly observed [4].

Many of these features can also be detected in infrared spectra of vapor-deposited hydrogenated amorphous carbon (*a*-C:H) films [5,6]. Specifically, the highly non-equilibrium conditions during laser ablation of *a*-C:H yield samples having a wide range of  $sp^2/sp^3$  bonding in a highly defected structure. As a result, these materials are effective in adsorbing a variety of other chemical species. These similarities suggest that further understanding of the structure of explosion nanodiamond particles might be obtained from a comparison between infrared spectra of these materials and those of *a*-C:H films. We report a preliminary comparison of this sort in this paper.

## 2 EXPERIMENTAL

Spectra were collected as average of 500, resolution  $1\text{ cm}^{-1}$ , 4% by weight of nanodiamonds in KBr pellet. Nanodiamond of detonation origin have average size 3–9 nm and total surface  $\sim 250\text{ m}^2/\text{g}$ . Characteristic formulae is  $[\text{C-}sp^3]_m\text{X}_n$ , where X are molecular groups with O, H, and N. X is about 10–20% of total. Three different samples were investigated [7]. One was the original soot after explosion without any treatment. Second sample of nanodiamond was obtained from a vendor using thermal oxidation with nitric acid under pressure to separate the diamond phase. The diamond should be flushed with water after separation from the acidic media. In the third sample nanodiamond was obtained from a vendor using ozon treatment for nanodiamond purification from soot. Thin film samples of amorphous hydrocarbon (*a*-C:H) were deposited on a 5 mm thick KBr optical window using excimer laser ablation of graphite in the presence of  $\text{H}_2$  or  $\text{H}_2/\text{NH}_3$ . Typical film thicknesses were 1–5  $\mu\text{m}$ . Spectra were obtained after exposure to air. The deposition chamber was continuously evacuated maintaining a slow flow of gas with a total pressure of gas kept at 1 Torr. Gases used: pure hydrogen, pure ammonia. The ablation source was a XeCl excimer laser, operating at 308 nm with average 70 mJ/pulse. Laser radiation was focused on the graphite target 4 cm from the substrate. The products of laser ablation react with hydrogen or ammonia to form *a*-C:H, which is deposited as an adherent layer on the surface of the substrate. At a pulse frequency of 10 Hz, a 1 micron-thick film layer can be deposited in the pure hydrogen gas flow in approximately 1 hour. Spectra were obtained after exposure to air.

### 3. RESULTS AND DISCUSSION

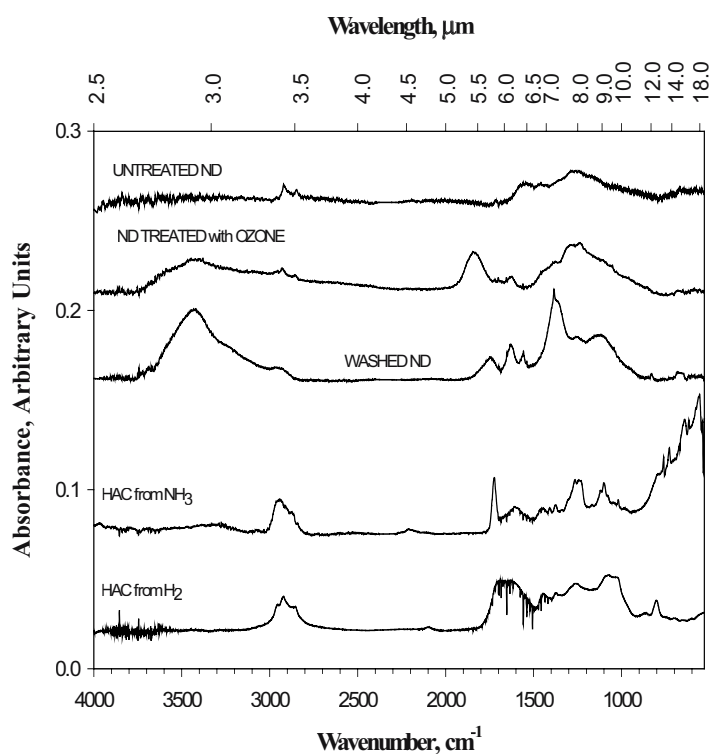


Figure 1. Infrared spectra of the nanodiamonds (untreated soot, washed in nitric acid, and treated with ozone) and thin films of amorphous hydrocarbon (deposited in hydrogen, or in ammonia)

Figure 1 shows infrared absorption spectra for soot deposits as obtained from the reactor and purified nanodiamond after treatment with ozone or nitric acid. These spectra are compared with the infrared spectrum of an  $\alpha$ -C:H sample prepared in hydrogen and one prepared in a mixture of hydrogen and ammonia. The energies of major spectral features observed in these samples are summarized in Table 1. Some notable differences and similarities between spectra of these samples is as follows:

- Absorption features at 2920 and 2850  $\text{cm}^{-1}$  attributable to  $\text{CH}_2$  hydrocarbon groups are most noticeable in untreated nanodiamond samples. These bands are similar to those seen in  $\alpha$ -C:H.
- An absorption feature at 1620  $\text{cm}^{-1}$ , assigned to the stretching vibration of C=C groups appears in nanodiamond samples treated with

O<sub>3</sub> or samples that have been purified with nitric acid. This suggests that surface reconstruction to form C=C bonded species has occurred as the result of chemical treatment. The 1620 cm<sup>-1</sup> band is commonly observed in the spectrum of *a*-C:H where it is identified with the presence of aromatic structures [8].

- A broad band associated with surface hydroxyl groups and adsorbed water is found near 3400 cm<sup>-1</sup> in samples treated with O<sub>3</sub> or exposed to H<sub>2</sub>O. This feature is not generally observed in spectra of *a*-C:H.
- A strong band arising from carbonate groups is found near 1840 cm<sup>-1</sup> in samples treated with O<sub>3</sub>. This band has not been detected in the spectrum of *a*-C:H.
- A strong absorption feature near 1260 cm<sup>-1</sup> likely arising from C-C groups appears in the spectrum of untreated and O<sub>3</sub>-treated nanodiamond samples. This band is also observed in the spectrum of *a*-C:H where it is identified with C-C groups in hydrocarbon bridging structures.

As expected, the stretching vibrations of CH<sub>2,3</sub> in laboratory samples of *a*-C:H are found to be much stronger than those observed in the ND samples. Spectra also show that CH<sub>3</sub> groups are present in *a*-C:H than but not in ND samples. The appearance of CH<sub>3</sub> reflects increased hydrogen saturation in *a*-C:H. We attribute CH<sub>2</sub> groups in ND samples to a strong surface reconstruction that tends to favor C=C bonds.

Table 1. Energies of spectral features in nanodiamond and *a*-C:H deposits (cm<sup>-1</sup>).

Untreated ND	ND treated with O <sub>3</sub>	ND purified in nitric acid	<i>a</i> -C:H from H <sub>2</sub>	<i>a</i> -C:H from NH <sub>3</sub>
	3417	3429		
	2959	2963	2961	2965
2920	2928	2937	2923	2928
			2886	
			2872	
2851	2855	2860	2851	2860
	1839			
		1744		1723
	1628	1632	1621	1608
1545		1558		
1459			1445	1453
	1373	1381	1375	1375
1260	1286	1256	1261	1260

## Acknowledgements

This research was supported by a grant from the NSERC of Canada. We acknowledge Dr.V. Dolmatov provided samples of soot for the investigation.

## REFERENCES

1. H.C. Chang, J.C. Lin, J.Y. Wu, and K.H. Chen. Infrared spectroscopy and vibrational relaxation of CH<sub>x</sub> and CD<sub>x</sub> on synthetic diamond nanocrystal surfaces. *J. Phys. Chem.* **99** (28), 11081-88 (1995).
2. C.L. Cheng, H.C. Chang, J.C. Lin, K.J. Song, and J.K. Wang. Direct observation of hydrogen etching anisotropy on diamond single crystal surfaces. *Phys. Rev. Letters* **78** (19), 3713-16 (1997).
3. C.F. Chen, C.C. Wu, C.L. Cheng, S.Y. Sheu, and H.C. Chang. The size of interstellar nanodiamonds revealed by infrared spectra of CH on synthetic diamond nanocrystal surfaces. *J. Chem. Phys.* **116** (4), 1211-14 (2002).
4. H.G.M. Hill, L.B. D'Hendecourt, C. Perron, and A.P. Jones. Infrared spectroscopy of interstellar nanodiamonds from the Orgueil meteorite. *Meteoritics and Planetary Science* **32**(5), 713-18 (1997).
5. V.I. Grishko and W.W. Duley. Detection of new infrared spectral features in hydrogenated amorphous carbon. *ApJ*, **543** (1, pt 2) 85-8 (2000).
6. V.I. Grishko and W.W. Duley. Infrared absorption and emission spectra of hydrogenated amorphous carbon prepared in the presence of oxygen, nitrogen, ammonia, and carbon monoxide. *ApJ*, **568** (1, pt 1), 448-53 (2002).
7. Samples of soot were obtained from 'Diamond Center', S.Petersburg (synthesized in 2003), as well as samples of nanodiamond purified with nitric acid (2002). Samples of nanodiamond purified with ozon treatment were synthesized by "New Technologies", Chelyabinsk (2000).
8. J. Robertson. and E.P. O'Reilly. Electronic and atomic structure of amorphous carbon. *Phys. Rev.* **B35** (6), 2946-57 (1987).

## CONVERSION OF ELEMENTAL SUBSTANCES AND INORGANIC COMPOUNDS TO CARBON NANOSTRUCTURES

V.G. Lutsenko

*V. I. Vernadskii Institute of General & Inorganic Chemistry, Ukrainian National Academy of Sciences, prospekt Palladina 32/34, 03680 Kiev 142, Ukraine*

**Abstract:** Chlorinated derivatives of methane were used for conversion of Si, Ge, Ti, Sn, Fe, SiC, GaSb, FeSi, and ZrN to microporous nanocarbons. The conversion represents the substitution of non-carbon atoms in the lattice by carbon atoms at 500–1100°C. Carbon nanofibers were produced from SiC whiskers, using both chlorine and chlorinated methane derivatives. The chlorination and the properties of the nanofibers were found to depend on the twinning and inversion of the type of SiC conductivity. We observed the formation of nanocrystalline diamond-like carbon. The conversion of carbides and other inorganic substances to carbon nanostructures was possible in the treatment with chlorinated methane derivatives.

**Keywords:** nanocarbon, silicon carbide, whiskers, microporosity, twinning, chlorination, nanofiber, diamond

### 1. INTRODUCTION

During the chlorination of  $E_xC_y$  carbides, carbide-forming elements (E) are extracted as volatile chlorides, with the carbon atoms remaining in the original lattice. The end products of this reaction are microporous carbon nanostructures of various phase composition. Their properties depend on the initial carbide and the chlorination conditions [1–5]. The presence of nanodiamond was found in carbon nanostructures produced from SiC [6,7], which is a remarkable representative of polytype material. Polycrystalline abrasive SiC powders contain a mixture of SiC polytypes and a large amount of donor and acceptor impurities [8]. So the twinning and conductivity inversion are characteristic of polycrystalline SiC particles. However, we are

unaware of studies that would analyse the effects of the two phenomena on the chlorination, composition and properties of the carbon structures obtained.

The rearrangement of the SiC lattice to the sphalerite or wurtzite type during the treatment with  $\text{Cl}_2$  leads to the formation of diamond structures. It is quite likely that  $sp^3$ -carbon having the diamond lattice is produced if the elements in a compound with the diamond lattice (Si) or the ZnS-type lattice ( $\text{A}^3\text{B}^5$ ) are replaced by carbon atoms. The replacement by carbon can be effected by a treatment with organic chlorinated derivatives. The use of chlorinating agents can provide the conversion of many simple substances and inorganic compounds (carbides, borides, silicides, nitrides, phosphides, etc.) to carbon materials. In this work we studied the process of chlorination of SiC, Si, Fe, Ti, Sn, GaSb, ZrN, and FeSi with chlorinated methane derivatives with the focus on the effect of nanosize twinning on the conversion of SiC whiskers to carbon nanostructures.

## 2. EXPERIMENTAL

We chlorinated Si powders and  $n$ -type single crystals, Sn melt, Ti wire, SiC whiskers and 6H single crystals, as well as Fe, FeSi, ZrN, and GaSb powders, using commercial 3C SiC whiskers made in Russia and Japan. The crystal diameter ranged between 10 and 400 nm. The average crystal length-to-diameter ratio was over 100. The specific surface area of the crystals was 5.3, 11.2 and 35  $\text{m}^2/\text{g}$ , values close to the average crystal diameter of 240, 110 and 35 nm, respectively. The SiC phase content was no less than 99.6%. In addition to 3C, the crystals contained less than 5% of  $\alpha$ -SiC polytypes (mostly 6H) [9]. The typical growth directions were  $\langle 111 \rangle$ ,  $\langle 110 \rangle$  and  $\langle 100 \rangle$ . The crystals were multiply twinned and contained thin twin interlayers of 3C and  $\alpha$ -SiC. The presence of donor (N) and acceptor (Fe, Al, Co) impurities lead to the formation of  $p$ - and  $n$ -type twin interlayers [10,11]. There were no micro- or mesopores on the crystal surface. Commercial whiskers always contain a thin surface layer of silicon dioxide, as indicated by the position of the Si line in the Auger spectrum at 82 eV. For this reason, the crystals were purified in a solution of hydrofluoric acid prior to chlorination. Then the suspension was filtered, and isotropic porous material was prepared. It was washed with distilled water and dried at 120°C. After drying, there were no silicon dioxide films detected on the crystal surface. The position of the Si line was at 92 eV, which corresponds to the silicon-carbon bond.

Isotropic porous whiskers of various shape and size can be produced which possess a considerable mechanical strength after drying. Their

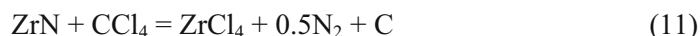
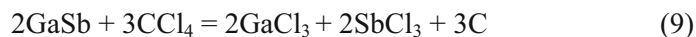
porosity can be varied from 75 to 95 vol.%, depending on the crystal length and diameter. For chlorination, we used isotropic cylinders and parallelepipeds with a 85–92 vol.% porosity. The chlorination was performed in a horizontal quartz tube, and chlorine was obtained by electrolysis of a  $\text{PbCl}_2$  -  $\text{KCl}$  melt. The chlorine flow rate was controlled by varying the electric current during the electrolysis. Argon was purified from oxygen (titanium sponge) and moisture (concentrated  $\text{H}_2\text{SO}_4$ ), using analytically pure  $\text{CCl}_4$  and  $\text{CHCl}_3$ . To deliver chlorinated methane derivatives to the chlorination zone, argon was passed through a vessel filled with  $\text{CCl}_4$  ( $\text{CHCl}_3$ ). The chlorination was performed in the temperature range of 500–1100°C for 15 min to 8 h. The samples were cooled by blowing argon through the tube. The mass of the samples was determined before and after the chlorination. The obtained carbon nanofibers were studied by X-ray phase analysis (Cu  $K_\alpha$ , DRON-3, Russia), scanning (Superpobor 733, Jeol) and transmission (JEM-100 CX, Jeol) microscopy, Auger spectroscopy (Jamp-10, Jeol) and thermogravimetry (Q-1500D, Hungary). The specific surface area was determined by the thermal desorption method ( $\text{N}_2$ ), and the micropore volume ( $\text{H}_2\text{O}$ ,  $\text{CCl}_4$ ,  $\text{C}_6\text{H}_6$ ) was found gravimetrically. The samples were pre-dried at 120–130°C for 5 h. The micro- and mesopore volume in the initial SiC whiskers was subtracted from the micropore volume of the carbon material. To remove the carbon from SiC-C composites, thermal treatment in air (480–650°C) or boiling in a mixture of concentrated acids ( $\text{HNO}_3$ ,  $\text{H}_2\text{SO}_4$ ) was used. The initial SiC whiskers were analysed according to [12].

### 3. RESULTS

The conversion of the elemental substances and inorganic compounds to carbon occurs as follows:







The chlorination of isotropic porous structures made up of SiC whiskers produces isotropic porous structures made up of carbon nanofibers. This does not affect the shape or size of the porous material or individual fibers. When SiC whiskers are treated with chlorine, carbon nanofibers are formed which contain a mixture of disordered carbon, graphite nanoclusters and stressed nanodiamond (Figure 1).

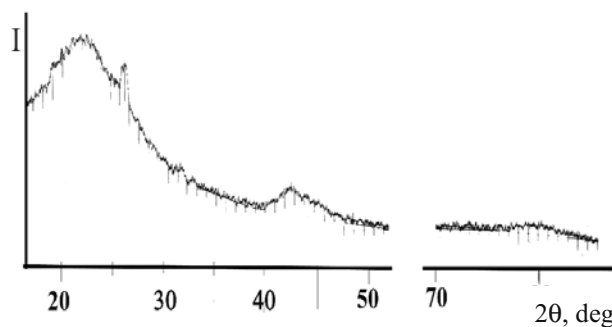


Figure 1. X-ray diffraction patterns of carbon nanofibers (840°C, Cl<sub>2</sub>).

The morphology of the carbon nanofibers is very diverse and varies with the fiber diameter and chlorination temperature (Figure 2). The fibers can be subdivided into four types: (a) tubular fibers with a continuous circular pore of less than 5–6 nm between the sheath and the core; (b) cylindrical or conical fibers with multi-phase carbon with a texture composed of loosely packed particles of the carbon modifications and a network of crevice-like pores of 1 nm in diameter; (c) tubular carbon with internal cavities and canals looking very much like carbon nanotubes; (d) cylindrical fibers similar to the type (b), which contain additionally a surface layer of carbon modifications with a lower packing density and a higher porosity (Figure 2). The specific surface of a carbon fiber ranges from 800 to 1650 m<sup>2</sup>/g, depending on the chlorination conditions. These nanofibers are fully oxidized in a boiling nitric acid – sulfuric acid mixture. Their oxidation in air begins at 380–400°C. The character of their combustion indicates the

presence of two carbon modifications, as evidenced by the extrema in the DT and DTG curves at 440 and 470°C. The volume of micropores in the nanofibers at 840°C is 0.62 cm<sup>3</sup>/g (CCl<sub>4</sub>) and 0.64 cm<sup>3</sup>/g (C<sub>6</sub>H<sub>6</sub>).

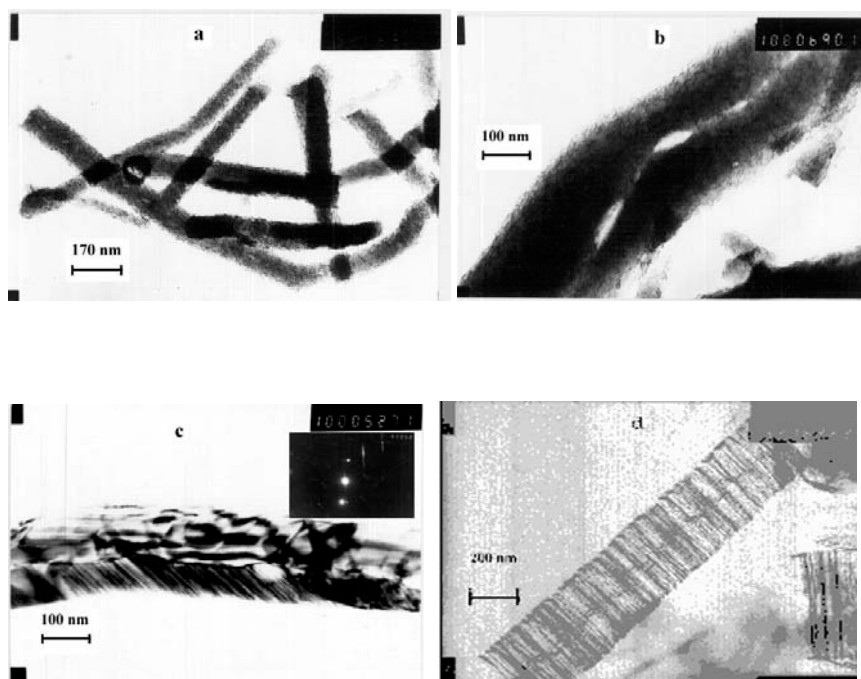


Figure 2. TEM images of carbon nanofibers and SiC whisker fragments: (a) carbon nanofibers (840°C, CHCl<sub>3</sub>); (b) carbon nanofiber with a crack (840°C, CCl<sub>4</sub>); (c) fragment of composite nanofiber after carbon removal (840°C, Cl<sub>2</sub>); (d) fragment of a composite nanofiber after carbon removal (72 % conversion of SiC to carbon).

When SiC whiskers are treated with chlorinated methane derivatives, there is no change in the shape or size of the original porous crystalline structures. The nanofibers contain carbon with  $2\theta = 9-9.5^\circ$  and  $2\theta = 21-22^\circ$ , nanographite, and probably nanodiamond. We also observed the presence of fibers with lower porosity than in the chlorine treatment. The carbon fibers may be subdivided into (a) curved and broken fibers and (b) fibers with an axial crack (Figure 3). The morphology of the carbon fibers treated with CCl<sub>4</sub> and CHCl<sub>3</sub> is found to be the same. They are fully oxidized in a mixture of boiling sulfuric and nitric acids. The oxidation in air begins at 460°C, and the temperature of maximum oxidation is 550°C. The specific

surface area depends on the chlorination temperature and ranges between 580 and 950 m<sup>2</sup>/g. The micropore volume varies with the treatment temperature and time. For fibers produced at 840°C, the micropore volume is found to be 0.10 (H<sub>2</sub>O), 0.145 (CCl<sub>4</sub>), and 0.28 (C<sub>6</sub>H<sub>6</sub>) cm<sup>3</sup>/g. The higher is the conversion temperature, the greater is the nanofiber microporosity, which is due to the sublimation of carbon nanoclusters.

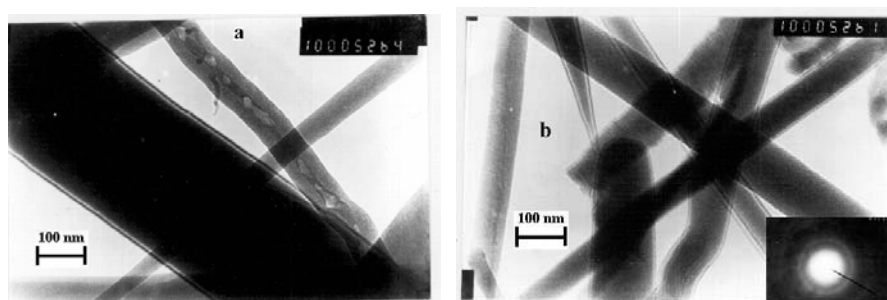


Figure 3. TEM images of carbon nanofibers (840°C, Cl<sub>2</sub>)

The chlorination of SiC whiskers at a temperature below 900°C for a period of time too short for carbide to transform to carbon completely gives rise to composite fibers containing a C-SiC mixture. Such fibers were obtained by chlorination with chlorine and chlorinated methane derivatives. After removing the carbon phases from the composite fibers by air oxidation or boiling in a sulfuric acid–nitric acid mixture, we observed pores on the surface of the crystals that remained (Figure 3). The pore volume in SiC whiskers with the conversion efficiency of 13.8% was 0.04 cm<sup>3</sup>/g (C<sub>6</sub>H<sub>6</sub>) and 0.03 cm<sup>3</sup>/g (CCl<sub>4</sub>). A greater conversion degree increases the porosity of the remnants SiC crystals (Figure 3). The micropores are either normal to the fiber surface (for the <111> growth direction) or inclined to it (for the other growth directions). The crystals with an over 50% conversion show an increased  $\alpha$ -SiC content. The character of the microdiffraction of the crystals and their fragments indicates the presence of multiple nanotwinning. Note that the use of a chlorinating agent promotes the sublimation of iron chloride even at the chlorination start. The Fe content of the crystals is found to be 0.36–0.47%.

The conversion of Si, Fe, Sn, Ti, FeSi, ZrN, and GaSb to porous carbon nanostructures was performed by chlorinating with CCl<sub>4</sub> (CHCl<sub>3</sub>). The structure and properties of the carbon nanomaterials are found to vary with the chlorination temperature and duration. The X-ray diffraction patterns

show peaks at  $2\Theta = 9\text{--}9.5^\circ$  (ZrN, Si, Fe, GaSb, FeSi),  $2\Theta = 12\text{--}13^\circ$  (Si),  $2\Theta = 17\text{--}18^\circ$  (plane  $\{0001\}$  6H SiC), and  $2\Theta = 21\text{--}22^\circ$  (Fe, the  $\{0001\}$  plane in 6H SiC). The nanocarbons obtained from chlorinated methane derivatives are microporous. For example, carbon from silicon produced at  $840^\circ\text{C}$  has a pore volume ( $V_s$ ) of  $0.23\text{ cm}^3/\text{g}$ :  $0.11\text{ cm}^3/\text{g}$  for  $\text{CCl}_4$  and  $0.23\text{ cm}^3/\text{g}$  for  $\text{C}_6\text{H}_6$ . The width of crevice-like pores in the carbon obtained from Si is over  $0.35\text{ nm}$ . The conversion of inorganic substances will be discussed in detail in other papers.

#### 4. DISCUSSION

The structure, morphology and properties of carbon nanofibers produced by chlorination of SiC whiskers vary with the chlorinating agent used (chlorine or chlorinated methane derivatives).

Chlorine extracts Si from the SiC lattice according to formula (1). As a result, half of the original atoms (carbon atoms) remain in the lattice. The lattice rearrangement gives rise to nanoclusters of misoriented carbon, graphite and stressed diamond (Figure 1). The cluster size is found from the diffraction line broadening to be  $5\text{ nm}$  or less. This value agrees with the chlorination data on polycrystalline SiC [2,3,4].

A chlorinated methane derivative replaces a Si atom in the SiC lattice with a C atom according to formulas (2) and (3). As a result, the total number of atoms in the lattice remains the same but these are only C atoms. The rearrangement of the new lattice mostly produces disordered carbon with a generally much lower nanographite content. The position of the diffraction peaks suggests that they may be attributed to fragments of a fullerite structure.

The morphological diversity of SiC fibers (Figures 2 and 3) is likely to be due to the multiple twinning of whiskers [10,11] because we observed thin nanosize twins along the crystal length (Figure 3). They are normal to the lateral crystal surface (the  $\langle 111 \rangle$  growth direction) or are at an angle to it (the other growth directions). The crystals contain donor (N) and acceptor (Fe, Co, Al) impurities. At the twin boundaries, these impurities are separated to produce *p*- and *n*-type interlayers (*p*-3C/*n*-3C) due to the polarity of the SiC structure along the  $\langle 111 \rangle$  direction. The crystals contain up to 5 % of  $\alpha$ -SiC polytypes. The (111) plane in 3C and the (0001) plane in 6H are parallel to each other, producing more junctions along the crystal length ( $\alpha$ -SiC/3C SiC). The band gap of 3C SiC is  $2.3\text{ eV}$  and that of 6H SiC is  $3.0\text{ eV}$ . The formation of quantum wells is also possible. During the initial treatment with chlorine or chlorinated methane derivatives, iron

chloride sublimates on the cold portions of the quartz tube, independent of the reaction temperature (600–1100°C). The crystals remaining after a partial conversion to carbon and their removal contain well-defined micro- and mesopores on the surface. In case of chlorination under mild conditions, the volume of these pores is slightly smaller than that of the SiC volume that has transformed to carbon. These pores are normal or inclined to the crystal surface. The  $\alpha$ -SiC content in the fragments of crystals subjected to partial conversion is always larger than that in the original crystals. As a result, the crystal surface is extremely inhomogeneous. The rate of conversion of *p*-type interlayers and quantum wells to carbon is much higher than that for *n*-type interlayers and  $\alpha$ -SiC. This structure of whiskers allows production of C-SiC composites by chlorination under “mild” conditions. This seems to be unfeasible in the case of polycrystalline SiC. Abrasive SiC powders contain a mixture of SiC polytypes [8] but there are no regularly oriented thin twin layers in them.

During the chlorination of whiskers, narrow microporous canals directed to the crystal axis are formed on their lateral surface. These micropores are filled with porous nanocarbon, whose thermal conductivity is much lower than that of SiC. As a result, the temperature in the narrow pores of the crystal bulk becomes higher than on the surface, leading to a still greater temperature rise and nanocarbon sublimation. The sublimate of the carbon nanoclusters crystallizes in the fiber sheath micropores and on the inner surface of the quartz tube. Chlorine molecules are capable to pass through the nanofiber carbon sheath but  $\text{SiCl}_4$  molecules are not, so silicon tetrachloride vapor accumulates in the micropores and its pressure rises. Eventually, the vapour compresses the fiber interior to make a circular pore between the sheath and the core.  $\text{SiCl}_4$  vapor diffuses from the fiber through the circular pore. However, we cannot create these conditions in the treatment with chlorinated methane derivatives because the diameter of a  $\text{SiCl}_4$  molecule is only slightly larger than that of a  $\text{CCl}_4$  molecule. But the local temperature rise in thin interlayers stimulates the nanocarbon sublimation and further crystallization in the micropores. Therefore, the conditions are created in SiC crystals larger than 50 nm, under which  $\text{CCl}_4$  molecules can pass through a micropore while  $\text{SiCl}_4$  molecules cannot. Owing to the  $\text{SiCl}_4$  pressure rise, the fiber is ruptured along its axis (Figure 3).

The micropores in carbon nanofibers produced by the chlorination of SiC whiskers have a crevice-like shape. The micropore width in nanofibers produced by  $\text{Cl}_2$  chlorination is over 0.6 nm, so they are accessible to  $\text{CCl}_4$  and  $\text{C}_6\text{H}_6$ . In addition to micropores, these fibers contain mesopores (Figure 2) with a width less than 5–6 nm. The carbon nanofibers produced by chlorination with methane derivatives have crevice-like micropores with

a width over 0.35 nm (about half of the micropore volume is inaccessible to  $\text{CCl}_4$ ).

The formation of nanocrystalline diamond-like carbon was detected in the treatment of SiC whiskers with  $\text{Cl}_2$  (Figures 1 and 2). In the treatment with  $\text{CCl}_4$  ( $\text{CHCl}_3$ ), the X-ray diffraction patterns show a peak at  $2\Theta \sim 43^\circ$ . However, we do not have a strong evidence that this peak is due to nanocrystalline diamond-like carbon.

## 5. CONCLUSION

Elemental substances and various inorganic compounds, including carbides, can be converted to porous nanocarbons by chlorination with methane derivatives. The carbons in this case have crevice-like micropores. The conversion of whiskers by treating them in chlorine and chlorinated derivatives of methane produce microporous carbon nanofibers which have an oriented micropore network due to the nanosize twinning and conductivity inversion along the crystal length.

## REFERENCES

1. Y. Gogotsi, A. Nikitin, H. Ye, W. Zhou, J.E. Fischer, B. Yi, H.C. Foley, and M.W. Barsoum. Nanoporous carbide-derived carbon with tunable pore size. *Nature materials* **2**, 591-94 (2003).
2. D.A. Ersoy, M.J. McNallan, and Y. Gogotsi. Carbon coatings produced by high temperature chlorination of silicon carbide ceramics. *Mat. Res. Innovat.* **5**, 55-62 (2001).
3. Y.G. Gogotsi, S. Welz, J. Daghfal, M.J. McNallan, I.D. Jeon, K.G. Nickel, and T. Kraft. Formation of carbon coatings on SiC fibers by selective etching in halogens and supercritical water. *Ceram. Eng. Sci. Proc.* **19**, 87-94 (1998).
4. R.N. Kyutt, E.A. Smorgonskaya, A.M. Danishevskii, S.K. Gordeev, and A.V. Grechinskaya. Structural study of nanoporous carbon produced from polycrystalline carbide materials: small-angle X-ray scattering. *Phys. Solid State* **41**, 1359-63 (1999).
5. J. Zheng, T.C. Exström, S.K. Gordeev, and M. Jacob. Carbon with onion-like structure obtained by chlorinating titanium carbide. *J. Mater. Chem.* **10**, 1039-41 (2000).
6. S. Welz, Y. Gogotsi, and M.J. McNallan. Nucleation, growth, and graphitization of diamond nanocrystals during chlorination of carbides. *Appl. Phys.* **93**, 4207-14 (2003).
7. GogotsiY, S. Welz, D.A. Ersoy, and M.J. McNallan. Conversion of silicon carbide to crystalline diamond-structured carbon at ambient pressure. *Nature* **411**, 283-87 (2001).
8. V.G. Lutsenko. Morphology and phase composition of silicon carbide powders. *Powder Metallurgy Metal Ceramics* **32**, 199-03 (1993).

9. V.M. Beletsky, V.G. Lutsenko, V.L. Milkov, D.D. Pokrovskii, A.N. Grybkov, E.V. Zagnitko, Y.V. Gniloshkurov, E.L. Umantsev, V.M. Gunchenko, and A.V. Polyakov. Phase composition and morphology of SiC whiskers. *Soviet Powder Metallurgy Metal Ceramics* **25**, 392-95 (1986).
10. V.G. Lutsenko. Acid - base and catalytic properties of powders, SiC 3C whiskers, and SiC 6 H single crystals (0001 planes) in aqueous electrolytes. Proceedings of 16<sup>th</sup> Europ. Conf. Chemistry at Interfaces, Vladimir, Russia, 2003 May 14-18, paper N 117 (2003).
11. V.G. Lutsenko. Formation of carbon with diamond structure on chlorination of abrasive powders, SiC whiskers and SiC single crystals. Proceedigs of 2<sup>nd</sup> Int. Conf."Carbon: Fundamental Problems of Science, Materials Science, and Technology", Moscow, 2003 Oct. 15-17, paper N 139 (2003).
12. V.M. Beletsky and V.G. Lutsenko. Chemical analysis of SiC whiskers. Proceedings of Int. Conf. Composite Materials, Moscow, 1990 Nov. 14-16, paper № 184 (1990).

## THE FINE AND FRACTAL STRUCTURE AND PROTONIC CONDUCTIVITY OF PHOSPHOSILICATE-DIAMOND SOL-GEL NANOCOMPOSITES

V.V. Shilov<sup>1</sup>, Yu.P. Gomza<sup>1</sup>, O.A. Shilova<sup>3</sup>, V.I. Padalko<sup>2</sup>, L.N. Efimova<sup>3</sup>, and S.D. Nesin<sup>1</sup>

<sup>1</sup> *Institute for Macromolecular Chemistry, Kharkivske Shaussee 48, Kiev, 02160, Ukraine*

<sup>2</sup> *JSC "Alit", Kiev, 03067, Ukraine*

<sup>3</sup> *Institute for Silicate Chemistry, RAS, Odоеvskogo 24/2, St. Petersburg, 199155, Russia*

**Abstract:** Composite xerogels based on a phosphosilicate matrix filled with nanodiamonds were synthesized by sol-gel processing. The crystalline and fractal characteristics of the initial nanopowders were obtained using wide-angle X-ray scattering (WAXS) and small-angle X-ray scattering (SAXS) techniques. Proton-conducting nanocomposite membranes of fuel cell applications were fabricated from the xerogels. The WAXS data on the nanodiamonds show diffraction patterns characteristic of graphitized ultradisperse nanodiamonds or pure nanodiamonds. The Beaucage plots of the phosphosilicate–nanodiamond composites show a multi-level fractal structure of the type of the surface fractal/mass fractal. The fractal characteristics such as the size and the gyration radius of the aggregates were calculated from the plots. The conductivity-frequency curves show that the conductivity is high and increases with the nanodiamond content in the composites.

**Keywords:** nanodiamond, sol-gel material, phosphosilicate, X-ray diffraction; small angle X-ray scattering, fractal structure, dielectric relaxation spectroscopy, proton conductor

### 1. INTRODUCTION

Polymer electrolyte membrane fuel cells (PEMFCs) have attracted interest as promising power sources for mobile electronic devices, electric vehicles, and stationary applications owing to their high efficiency [1,2]. One limitation of available PEMFCs operating at about 80°C is that even a



small CO amount in the H<sub>2</sub> feed gas is sufficient to poison the Pt anode electrocatalyst [3]. An effective way to increase the CO tolerance is to raise the operating temperature of PEMFC using inorganic polymer electrolyte membranes (PEMs) [3–5] prepared by the sol-gel process. It has recently been found that phosphosilicate gels produced by the sol-gel technique containing large amounts of phosphorus can preserve high conductivity of  $1 \times 10^{-2}$  S/cm above 100°C [6–12]. However, modification of the membrane material is needed to improve their protonic conduction and thermal resistance. One of the effective ways of modifying PEMs is to fill a protonically conductive polymer material with nanofillers of high surface activity. Recently, excellent surface properties of nanodiamonds have been demonstrated [13–15] functioning in electronic and electrochemical devices, conformal coatings, biosensors, bioactuators, retinal implants, IR transmitting windows and many other applications. In our study, we have used fillers containing raw and purified detonation nanodiamonds to modify phosphosilicate proton-conducting membranes [11,12]; their fractal structure and protonic conductivity have been examined.

## 2. EXPERIMENTAL

The protonically conductive xerogel matrix was synthesized using the sol-gel process, as described in [11,12]. Tetraethoxysilane Si(OEt)<sub>4</sub> (TEOS), ethanol (C<sub>2</sub>H<sub>5</sub>OH, 92% aqueous solution), a catalyst (HCl, 36.5% aqueous solution) and orthophosphoric acid (H<sub>3</sub>PO<sub>4</sub>, 85% aqueous solution) to be used as the starting components were taken as-received (all the chemicals were highly pure and conformed to the grade of the Federal Russian Standard). The molar ratio of the components in the initial solution was Si(OEt)<sub>4</sub>:EtOH:H<sub>2</sub>O:HCl:H<sub>3</sub>PO<sub>4</sub> = 1:4:2:0.01:1.5. TEOS was diluted with ethanol, hydrolyzed with HCl (aqueous solution) and stirred at room temperature for 1–2 min. The pH of the mixture was ~ 2. An appropriate amount of H<sub>3</sub>PO<sub>4</sub> was added to the hydrolyzed solution and then stirred at room temperature for 1–2 min. The sols were allowed to stay in sealed vessels to produce wet phosphosilicate (Si – P). All the wet gels were dried in an evacuated oven at 80°C for 5–8 h.

Graphitized ultradisperse diamond (UDDG) and purified ultradisperse diamond (UDD), both produced by ALIT Co, Ukraine, were used as nanofillers for phosphosilicate–nanodiamond composites. The UDDG and UDD powders were preliminarily mixed with ethanol and pulverized with an agate mortar for 15 min. To disaggregate the nanopowders, the ethanol–nanodiamond mixture was treated ultrasonically (22 kHz) for 30 min. The dispersion obtained was added to the initial TEOS–ethanol–water–HCl–H<sub>3</sub>PO<sub>4</sub>

solution to prepare phosphosilicate–UDDG/UDD xerogels containing 1, 3 or 10 wt.% of nanodiamond.

The dried xerogels were carefully crushed in an agate mortar and mixed with a polyurethane binder preliminarily dissolved in ethyl acetate (10 wt.% of the polymer). After drying for 2 hours at 80°C, the composites were placed between two stainless steel disks of 16 mm in diameter and 0.05 mm thick and subject to the pressure of 700 kg/cm<sup>2</sup>. Proton-conducting films of about 0.5 mm thick were used as specimens to be analysed in X-ray units and a dielectric spectrometer.

The WAXS patterns were obtained in a transmission mode in a DRON-2.0 diffractometer. Nickel-filtered Cu-K<sub>α</sub> radiation (wavelength,  $\lambda = 0.154$  nm) was produced by an IRIS-M7 high voltage generator operating at 30 kV and 30 mA. The scattered intensity was recorded by a scintillation detector operating in a step-scanning mode over the angular range of 3–5°. The intensity vs. wave vector curves were treated to reduce them to the equal primary beam intensity as well as to equal scattering volumes by a technique normally used in X-ray transmission experiments [16]. The curves were corrected for the contribution of the X-ray attenuation and the difference in the scattering effects.

The SAXS experiments were performed using a Kratky camera. The emission from the copper anode was monochromated by the total internal reflection and a nickel filter. The intensity curves were recorded in the step-scanning mode of the scintillation detector. The FFSAXS package [16,17] was used to smooth out the SAXS curves, to correct them for parasitic scattering and to make a desmearing procedure. The SAXS curves were recorded in the range of scattering angles from 0.03 to 4° corresponding to the wave vector,  $q$ , of 0.022–2.86 nm<sup>-1</sup> ( $q = 4\pi\sin\theta/\lambda$ ,  $\theta$  is one half of the scattering angle,  $\lambda$  is the wavelength of the X-ray radiation). So the range of the wave vector is as large as 30. The global unified equation of Beaucage [18–20] that describes the scattering by multi-level systems has been used to fit the measured SAXS intensity curves. Beaucage's equation for an arbitrary number of interrelated structural levels can be described as

$$I(q) = \sum_{i=1}^n (G_i \exp(-q^2 R_{gi}^2 / 3) + B_i \exp(-q^2 R_{g(i+1)}^2 / 3) \times \left\{ \left[ \text{erf}(q R_{gi} / 6^{1/2}) \right]^3 / q \right\}^{P_i} ) \quad (1)$$

Here  $G_i$  is the Guinier prefactor for level  $i$  and  $B_i$  is a prefactor specific to the type of power-law scattering. The quantity  $B_i$  is defined by a regime, in which the exponent  $P_i$  falls (for surface fractals  $4 > P > 3$ , for mass fractals  $P < 3$ ).

This unified approach can distinguish between Guinier regimes in a multi-level fractal structure to determine such characteristics as the type of the aggregate (mass or surface fractals), the fractal size ( $D_m$  for a mass fractal and  $D_s$  for a surface fractal), and the average gyration radius of the fractal aggregate,  $R_g$ .

The protonic conductivities of the samples were investigated at ambient temperatures by dielectric relaxation spectroscopy, using a home-made dielectric spectrometer operating in the frequency range from 100 to 100 000 Hz. The membrane samples of 14 mm in diameter were placed in the spectrometer cell between the blocking platinum electrodes.

### 3. RESULTS AND DISCUSSION

Figure 1 shows the WAXS curves for the UDD and UDDG powders. One can see that the UDD diffraction curve shows the (111) diamond crystal lattice at the scattering angle of  $44^\circ$  [21,22]. At the same time, the UDDG diffraction curve has the (0002) reflection at the angle of  $26^\circ$  characteristic of the graphite crystal lattice [22].

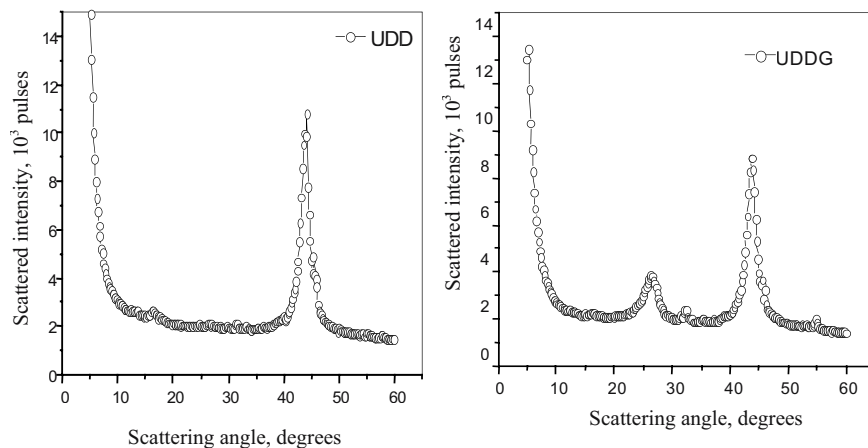


Figure .1 The WAXS curves of UDD and UDDG powders.

The SAXS curves of the UDD and UDDG powders are shown in Figure 2 on a double logarithmic scale. We can see a two-level fractal structure characteristic of both UDD and UDDG. Note that the respective intensity vs. wave vector dependences are very close to each other and that they are similar to those obtained by Ershov and Cupershtokh in their

well-known X-ray study of processes arising from some condensed explosives [23]. The similarity of the SAXS curve for UDDG would not be possible in the presence of a continuous graphite shell over the diamond granule. So the crystalline graphite producing the (0002) reflection in Figure 2 exists only as individual aggregates on the surface of the primary diamond particles. The fractal sizes and the average gyration radii of the samples  $R_g$  are presented in Table 1. We can see the fractal aggregations of UDD and UDDG, which can be considered in terms of the two-level scheme.

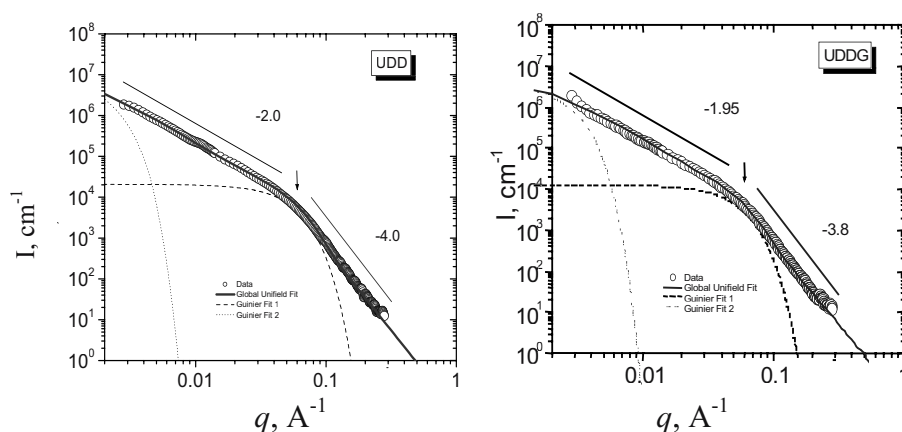


Figure 2. The SAXS curves of UDD and UDDG powders.

The WAXS curve of the initial protonically conductive phosphosilicate is shown in Figure 3. This curve reflects a completely disordered fine structure of phosphosilicate.

The WAXS curves for the phosphosilicate-based composites containing 1 and 10% wt. of UDD are presented in Figure 4 together with the UDDG curves. They indicate that the amorphous phosphosilicate matrix remains practically unchanged after introducing nanodiamonds and that the diamond (111) reflection appears in the diffraction patterns of samples containing only 10 wt.% of UDD and UDDG fillers.

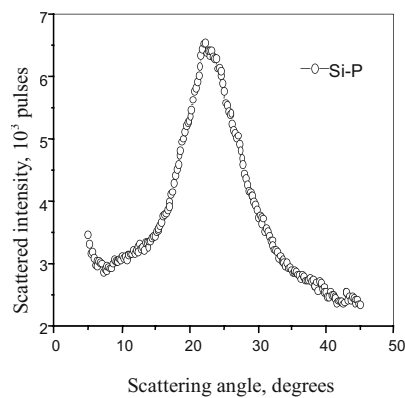


Figure 3. Normalized WAXS curve for the phosphorsilicate matrix.

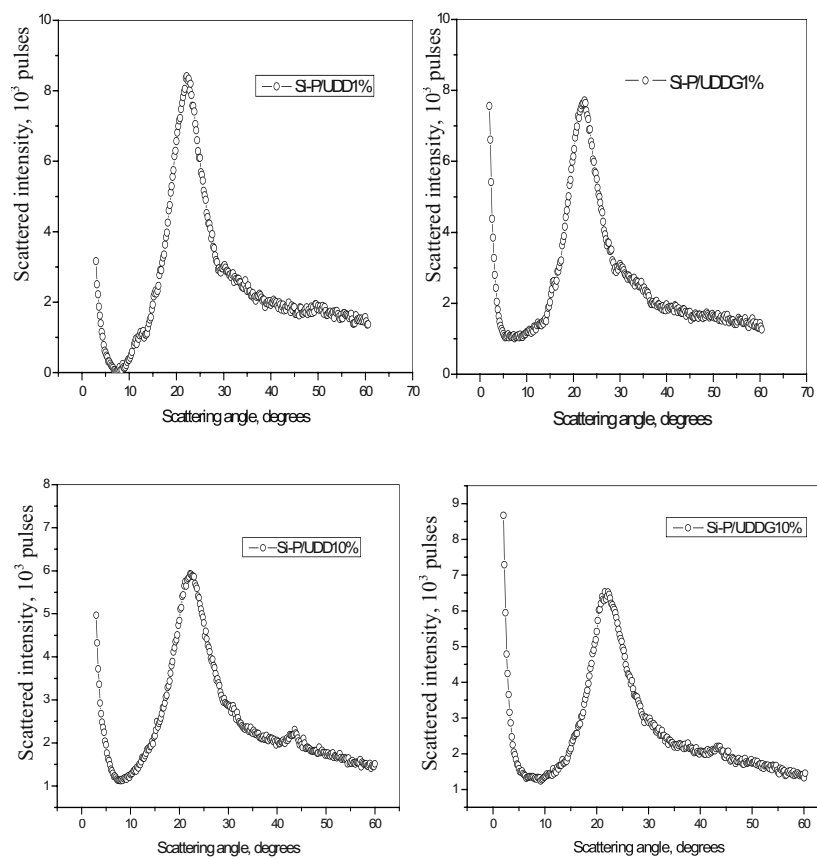


Figure 4. Normalized WAXS curves for phosphorsilicate-nanodiamond composites.

The log-log SAXS curve for the initial phosphosilicate matrix is presented in Figure 5. It displays three rectilinear regions of fractal behavior. The slope values are shown over the rectilinear curve segments above the experimental data and the fitted curve is shown by a solid line. The characteristics of the phosphosilicate fractal structure are given in Table 1.

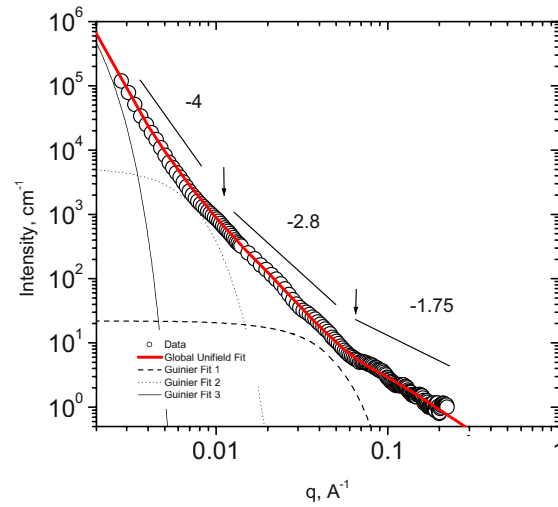


Figure 5. The SAXS curve for phosphorsilicate nanocomposite.

Table 1. The fractal behavior and the fitting curve parameters:  $D_m$  – the mass fractal size,  $D_s$  – the surface fractal size,  $R_g$  – gyration radius.

Sample coding	Regime I			Regime II		Regime III		
	$D_m$	$D_s$	$R_g, \text{\AA}$	$D_m$	$R_g, \text{\AA}$	$D_m$	$D_s$	$R_g, \text{\AA}$
Si-P (matrix)	1.75	–	42	2.8	270	–	2.0	1300
UDD	–	2	35	–	–	2	–	900
UDDG	–	2,2	35	–	–	1.95	–	700
Si-P/UDD1%	2.65	–	40	2.25	120	–	2.03	1300
Si-P/UDDG1%	2.65	–	27	2.5	160	–	2.1	1300
Si-P/UDD3%	–	2.4	50	2.5	140	–	2.2	1300
Si-P/UDDG3%	2.9	–	40	2.4	120	–	2.05	1300
Si-P/UDD10%	–	2.95	40	2.5	150	–	2.05	1300
Si-P/UDDG10%	–	2.7	40	2.5	150	–	2.05	1300

The SAXS curves for the phosphosilicate-nanodiamond composites are presented in Figure 6. Like the curve for pure phosphosilicate, these curves have three rectilinear regions indicating a three-level fractal aggregation in the composites. The slope value above the rectilinear curve segments shows a significant change in the fractal size of the primary particles. This behavior is reflected in the fractal characteristics of phosphosilicates filled with the UDD and UDDG powders that were presented in Table 1.

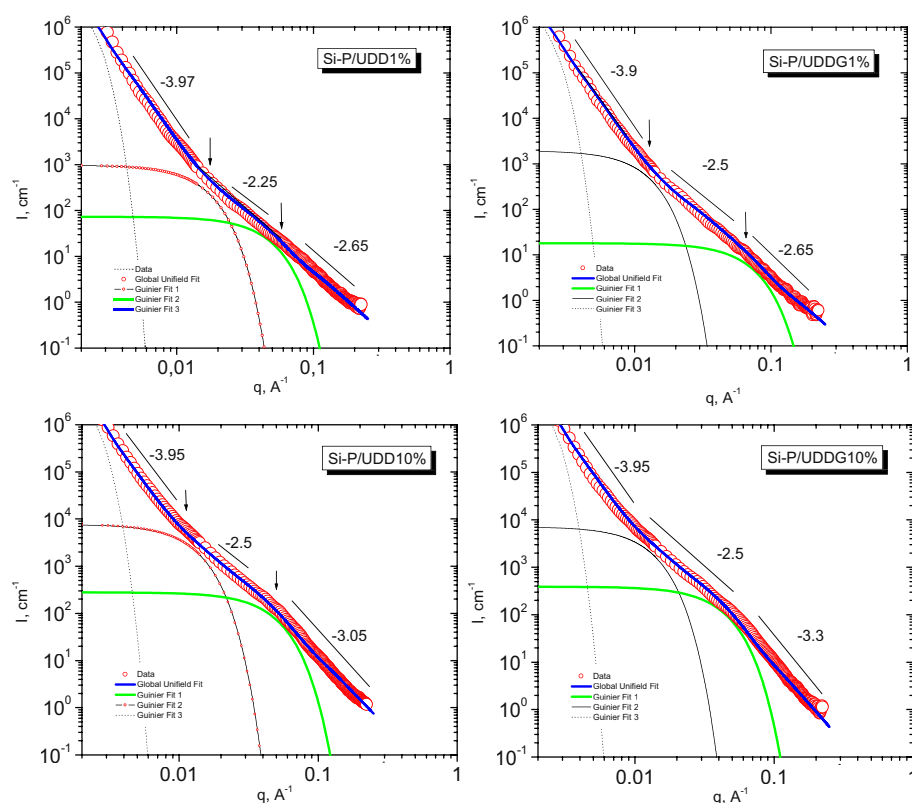


Figure 6. The normalized WAXS curves for phosphosilicate-nanodiamond composites.

Considering the fractal characteristics of phosphosilicate-nanodiamond systems, one should mention that despite the presence (or absence) of UDD or UDDG fillers, all the materials show the three regimes of fractal behavior. The first regime corresponds to the fractal behavior on the scale of several tens of angstroms, the second regime describes the fractal behavior for hundreds of angstroms and the third regime is for about a thousand of angstroms.

In the first regime, the initial phosphosilicate shows a small mass fractal size ( $D_m = 1.75$ ), indicating the formation of a fractal with low compact aggregation. The introduction of 1 wt.% of UDD or UDDG gives rise to more compact aggregates ( $D_m = 2.65$ ) of different sizes (the gyration radius for the UDD filler is 40 Å and for the UDDG filler it is 27 Å). The nanodiamond content increase to 3 wt.% produces totally compacted aggregates in the case of the UDD filler (a surface fractal with a rough surface,  $D_s = 2.4$ ) and nearly compacted aggregates in the case of the UDDG filler (a mass fractal of a large fractal size,  $D_m = 2.9$ ). The gyration radii of the aggregates increase to 50 and 40 Å, respectively. Larger nanodiamond contents (up to 10 wt.%) lead to the formation of compact particles similar to surface fractals with both UDD- and UDDG-based nanofillers ( $D_s = 2.95$  and 2.7, respectively) at practically the same gyration radius of 40 Å.

In the second regime of fractal behavior, the introduction of 1 wt.% of nanodiamond fillers decreases the mass fractal size from 2.8 to 2.25 for the UDD filler and to 2.5 for the UDDG filler, the radii decreasing in this case from 270 to 120 and 160 Å, respectively. Further increase in the filler contents to 10 wt.% leads to a nearly constant fractal size and radius of the fractal aggregate.

In the third regime, the introduction of nanodiamonds has no significant effect on the size or gyration radius.

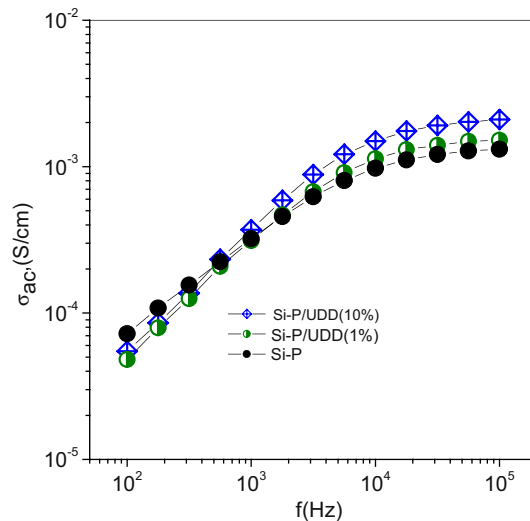


Figure 7a. The conductivity against the frequency for a phosphosilicate -UDD composite.



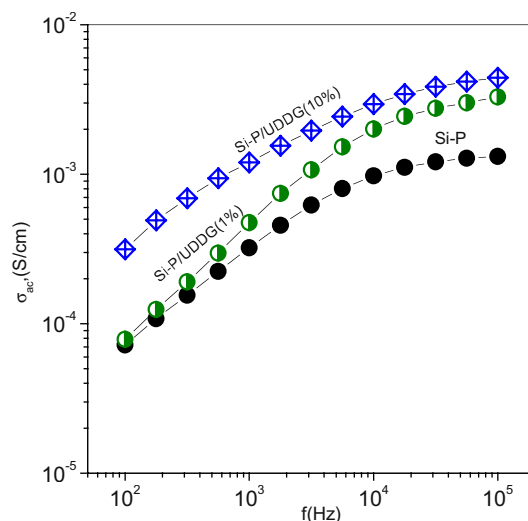


Figure 7b. The conductivity against the frequency for a phosphosilicate-UDDG composite.

The protonic conductivity vs. frequency curves for phosphosilicates filled with UDD and UDDG are compared in Figure 7 with the respective data on the matrix. We can see that the introduction of the composites normally increases the protonic conductivity. However, in the case of a UDDG filler, this effect is more pronounced.

#### 4. CONCLUSION

We have shown that UDD- and UDDG-based fillers demonstrate a similar fractal behavior. Crystalline graphite on the surface of primary diamond particles of UDDG exists as individual aggregates. The fractal structure of the initial phosphosilicate matrix has a three-level character. The introduction of UDD and UDDG powders into the phosphosilicate matrix is followed by a significant change in the fractal structure on the first and second level. The protonic conductivity of UDD and UDDG phosphosilicate composites increases with the filler content. However, this effect is more pronounced in the case of phosphosilicate-UDDG systems.

## Acknowledgements

The present work was supported by the Grant for Scientific Research on “Nanosystems, Nanomaterials, and Nanotechnologies” of the National Academy of Sciences of Ukraine.

## REFERENCES

1. C. Gavach and G. Pourcelly. “Applications of perfluorinated proton conductors (Nafions).” In: *Proton conductors. Solids, membranes and gels-materials and devices*. Ed. P. Colomban. Cambridge: University Press, 1992.
2. F.M. Gray. *Polymer electrolytes*. London: The Royal Society of Chemistry, 1997.
3. S.-H. Kwak, T.-H. Yang, C.-S. Kim, and K.H. Yoon. Nafion/mordenite hybrid membrane for high-temperature operation of polymer electrolyte membrane fuel cell. *Solid State Ionics* **160**, 309-15 (2003).
4. D. Carriere, M. Moreau, K. Lhalil, P. Barboux, and J.P. Boilot. Proton conductivity of colloidal nanometric zirconium phosphates. *Solid State Ionics* **162–163**, 185–90 (2003).
5. F. Damay and L.C. Klein. Transport properties of Nafion<sup>TM</sup> composite membranes for proton-exchange membranes fuel cells. *Solid State Ionics* **162–163**, 261–67 (2003).
6. A. Matsuda, H. Honjo, K. Hirata, M. Tatsumisago, T. Minami. Electric double-layer capacitor using composites composed of phosphoric acid-doped silica gel and styrene-ethylene-butylene-styrene elastomer as a solid electrolyte. *J. Power Sources* **77**, 12-6 (1999).
7. A. Matsuda, K. Hirata, M. Tatsumisago, and T. Minami. Proton- conductive composites composed of phosphoric acid-doped silica-gel and organic polymers with sulphogroups. *J. Ceram. Soc. Jap.* **108**, 40-5 (2000).
8. A. Matsuda, N. Nakamoto, K. Tadanaga, T. Minami, and M. Tatsumisago. Preparation and characterization of thermally stable proton-conducting composite sheets composed of phosphosilicate gel and polyimide. *Solid State Ionics* **162–163**, 247-52 (2003).
9. K. Hirata, A. Matsuda, T. Hirata, M. Tatsumisago, and T. Minami. Preparation and characterization of highly proton-conductive composites composed of phosphoric acid-doped silica-gel and styrene-ethylene-butylene-styrene elastomer. *J. Sol-Gel Sci Tech.* **17**, 61-9 (2000).
10. M. Nogami, Yu. Daiko, Y. Goto, Y. Acausui, and T. Kasuga. Sol-gel preparation of fast proton-conducting P<sub>2</sub>O<sub>5</sub>-SiO<sub>2</sub> glasses. *Sol-Gel Sci. Tech.* **24**, 1041-4 (2003).
11. V. Shilov, M. Burmistr, and O. Shilova. Solid Polymer Electrolyte fuel cells as ecologically acceptable power sources of clean energy. Perspectives and problems of applications. Proceedings of the 4<sup>th</sup> International Conference on Carpathian Euroregion Ecology “CERECO ’2003”; 2003 April 28–30; Miskolc. Miskolc: Miskolc-Tapolca, 2003.
12. V.V. Shilov, Yu.P. Gomza, O.A. Shilova, S.D. Nesin, and I.M. Kobylyak. Proton-conducting materials based on silicophosphate sol-gel nanocomposites. *Solid State Ionics* (submitted).

13. R.C. Mani, S. Sharma, M.K. Sunkara, J. Gullapalli, R.P. Baldwin, R. Rao, A.M. Rao, and J.M. Cowley. Synthesis and electrochemical characteristics of a nanocomposite diamond electrode. *Electrochem. & Solid-State Lett.* **5**, E32-5 (2002).
14. G.P. Bogatyreva, E.V. Ischenko, M.A. Marinich, A.V. Yatsymirsky, and V.L. Gvyazdovskaya. Catalytic properties of Pd, Pd-Ag, and Ag deposited on diamond submicropowders. *Superhard Materials*; **2**, 72-6 (2000).
15. D.M. Gruen. Ultrananocrystalline diamond films. Programme and Abstracts of NATO Advanced Research Workshop "Synthesis, Properties and Applications of Ultrananocrystalline Diamond", 2004 June 7–10; St. Petersburg, 2004.
16. Yu. Lipatov, V. Shilov, Yu. Gomza, and N. Kruglyak. *X-Ray Methods in Polymer Systems Analysis*. Kiev: Naukova Dumka, 1982 (in Russian).
17. C.G. Vonk. *FFSAXS's Program for the Processing of Small-Angle X-Ray Scattering Data*. Geleen: DSM, 1974.
18. G. Beaucage. Approximations leading to a unified experimental/power-law approach to small-angle scattering. *J. Appl. Crystallogr.* **28**, 717-28 (1995).
19. G. Beaucage. Small-angle scattering from polymeric mass-fractal of arbitrary mass-fractal dimension. *J. Appl. Crystallogr.* **29**, 134-46 (1996).
20. J. Hyeon-Lee, G. Beaucage, S.E. Prausnitz, and S. Vemury. Fractal analysis of flame-synthesized nanostructured silica and titania powders using small-angle X-ray scattering. *Langmuir* **14**, 5751-6 (1998).
21. A.E. Alexensky, M.V. Baidakova, A.Ya. Vul', V.Yu. Davidov, and Yu.A. Pebtsova. Diamond-graphite phase transition in ultradisperse-diamond clusters. *Phys.Solid State* **39**, 1007-15 (1997).
22. A.E. Alexensky, M.V. Baidakova, A.Ya. Vul', and V. Siklitsky. The structure of diamond nanocluster. *Phys.Solid State* **41**, 668-71 (1999).
23. A.P. Ershov and A.L. Cupershtokh. Formation of fractal structures under blast. *Fizika Gorenia i Vzryva* **27**, 111-17 (1991) (in Russian).

## FACILITIES FOR ULTRADISPERSE DIAMOND PRODUCTION

T.M. Gubarevich and D.N. Gamanovich

*Scientific Production Joint-Stock Company "Sinta" P.O. Box 59, Minsk, 220082, Belarus*

**Abstract:** We develop an industrial system for a large scale production of ultradispersed diamond (UDD). The system includes set-ups for synthesis and chemical purification of detonation soot as well as experimental shops for additional and deep purification and modification of UDD.

In detonation synthesis, we use "wet" and "dry" technologies when explosion is carrying out in water and gas atmosphere correspondingly. For purification of detonation soot we use the chemical treatment in bynitric-acid aqueous solution at high pressure and temperature in an autoclave. The process occurs in a continuous regime with a technological cycle of 4–6 days, providing large UDD batches of uniform and reproducible quality. The chemical treatment occurs in 5 temperature zones by varying the velocity of the reactive suspension in laminar and intermediary flow regimes. Non-carbon accumulation in the UDD powder and impurities in the waste acid have been studied. Methods for additional purification of UDD from soluble and insoluble impurities and admixtures are suggested, together with ways of decreasing titanium corrosion.

**Keywords:** ultradispersed diamond, detonation synthesis, chemical purification, diamond containing soot, oxidation, large scale UDD production

### 1. INTRODUCTION

The "Sinta" JS Company is producing ultradisperse diamonds (UDD) commercially with an annual diamond yield of 10 million carats. The production process includes a full work cycle of detonation synthesis, chemical purification, additional and deep purification, and modification of the diamond surface to obtain new properties. Nearly 10 years of the production experience and a regular improvement of the technological equipment have been a basis for large-scale experiments, reliable statistics

and, probably, a deeper insight into useful UDD properties and their «bad habits». Here we report on the technological facilities, the details of the technological cycle, and the production parameters, with emphasis on the diamond quality and ecological safety.

## 2. EXPERIMENTAL

Detonation synthesis of diamonds is carried out in special explosive chambers (EC) of 20 m<sup>3</sup> in volume each. The EC body is made from bimetal, with the interior surface plated with a corrosion-resistant alloy to reduce the pollution of soot and to produce powders with the ash content below 3% without chemical treatment. The ECs are designed for dry blasting of explosive charges and evacuation of the soot as a dust-gas flow. Blasting is carried out in the medium of gaseous products of the explosion; the quenching of the diamond phase is optimized due to a proper choice of the ratio between the explosive weight and the EC geometry.

The technology of dry diamond synthesis varies with the quality of the diamond-containing soot. The variability is provided by the following technological methods: series of explosions, the techniques for the detonation product evacuation, and the conditioning of dry soot.

In industrial UDD synthesis, the soot is evacuated after a series of explosions. The number of explosions in a series may vary from 5–10 to 100 and more, depending on the EC volume and details of the technological process. The condensed products accumulated in the EC are exposed to repeated shock processing. The shock load ranges between 0.4 and 15 MPa such that the frequency of the shock processing of each soot portion ranges from 0 to  $n-1$  in a series of  $n$  explosions. The physical and chemical properties, the structure and characteristics of the soot depend on the parameter  $n$ , as shown in Figure 1.

The soot yield (curve 1) and the UDD content (curve 2) vary with  $n$  only slightly. Nevertheless, we can identify an initial area within a blasting series, in which both characteristics can be increased by improving the gas atmosphere in the chamber. Then there is an extensive area of stability with a weak tendency for decreased yields of soot and UDD. As for diamond particles, we cannot exclude a partial graphitization under the action of shock waves. A decreased soot yield at  $n > 40$  may be due to a partial gasification of metastable carbon fragments and to powder aggregation at the bottom and on the walls, making the soot removal out of the dust-gas flow difficult. A 5–7% reduction in the soot surface area (curve 3 in Figure 1) also indicates a greater consolidation of ultradispersed carbon. The growth of ash impurities (curve 4) is associated with accumulation and dispersion of

technological pollutants throughout the chamber from blast to blast. The real problem here is not the large pollutant contents, which can be easily removed mechanically, but finely dispersed inclusions of metals, oxides and carbides, which form fairly strong agglomerates with the carbon powder.

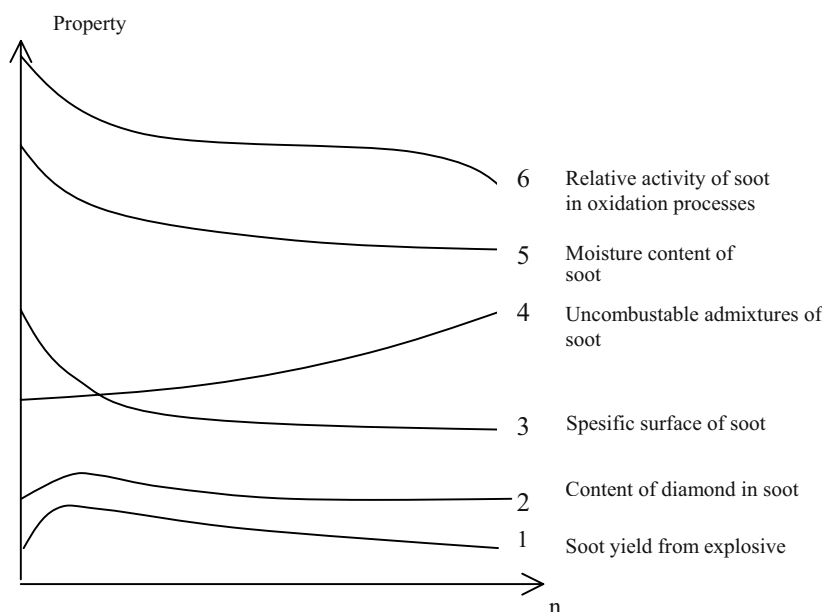


Figure 1. Some properties of soot as a function of the series of explosion  $n$ .

The soot humidity (curve 5) during dry synthesis depends on the temperatures in the chamber and along the dust-gas pathway. If the EC operates in the mode of self-heating, the first portions of soot contain up to 40% of condensed moisture. Thermostatic control of the equipment stabilizes the soot humidity at a level of 6–10%. It is an important point in the dry synthesis technology. To obtain an optimal hydrophilic-hydrophobic balance of the soot surface properties, it is necessary to prevent the condensation of the reaction water and to separate it from the soot together with the detonation gas products. One of the results of the  $(n-1)$ -fold shock processing of the soot is also the change in its reactivity during oxidation (curve 6, Figure 1); this is essential for the subsequent soot application for UDD chemical purification and for making compositions with oils, polymers and other materials. With increasing  $n$  in a serial explosion, the relative content of metastable carbon structures characteristic of "fresh" soot

produced in a single explosion is reduced. However, the partial loss of activity is compensated for by a better stability and higher technological parameters of the soot: the powder becomes less dusty, it contains less adsorbed gases, including toxic ones, and has a higher bulk density.

The regimes of detonation product evacuation from the EC allow varying the soot structure and quality within certain limits. The temperature profiles in the chamber and the pipelines determine the humidity of the carbon powder. Depending on the velocity of the dust-gas flow, they allow separating, more or less totally, the diamond-containing soot from noncarbon particles.

The detonation facilities for dry synthesis produce three sorts of soot according to the TS BELARUS standard 100056180.003-2003 (Figure 2). The stability and reproducibility of the soot properties in the industrial batch are of great value for barothermic UDD purification.

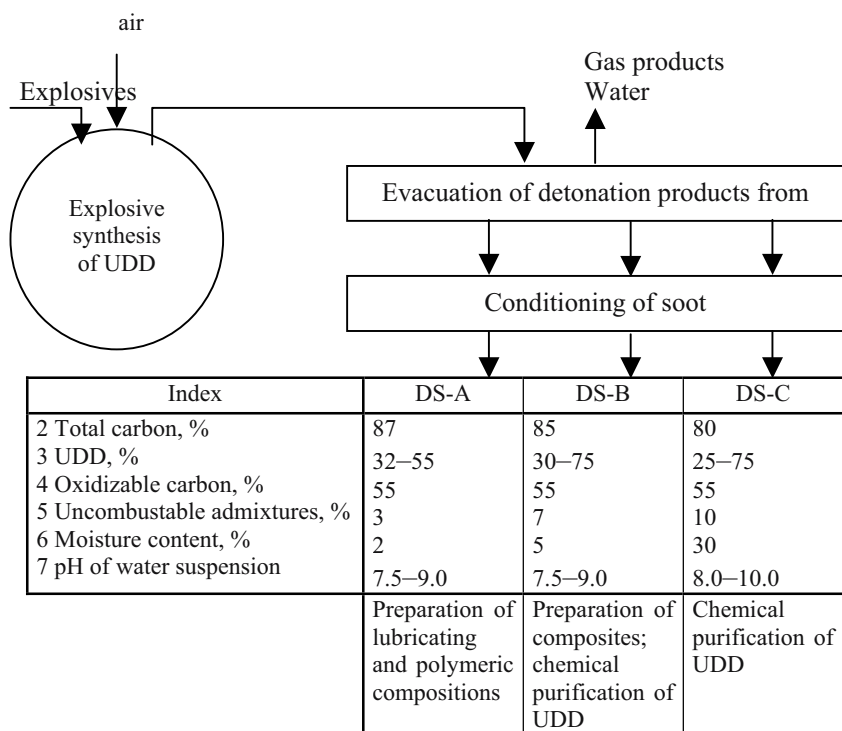
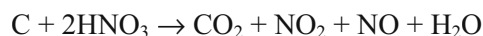


Figure 2. Production of diamond-containing soot.

Chemical purification of UDD is carried out by barothermic oxidation. The principle of this approach is to oxidize selectively the nondiamond modifications of carbon to get gaseous oxides under the action of nitric acid:



This reaction proceeds at a fairly high rate at temperatures above 280°C and pressures of 8–10 MPa. All the impurities in the soot (metallic particles, oxides, and most carbides) are nearly simultaneously dissolved.

The setup for barothermic UDD purification represents a cascade flow reactor with high pressure (HP) in the block including units for the preparation of the working suspensions, throttling down the liquid and gas products, accumulation and neutralization of exhaust gases, and UDD washing off (Figure 3).

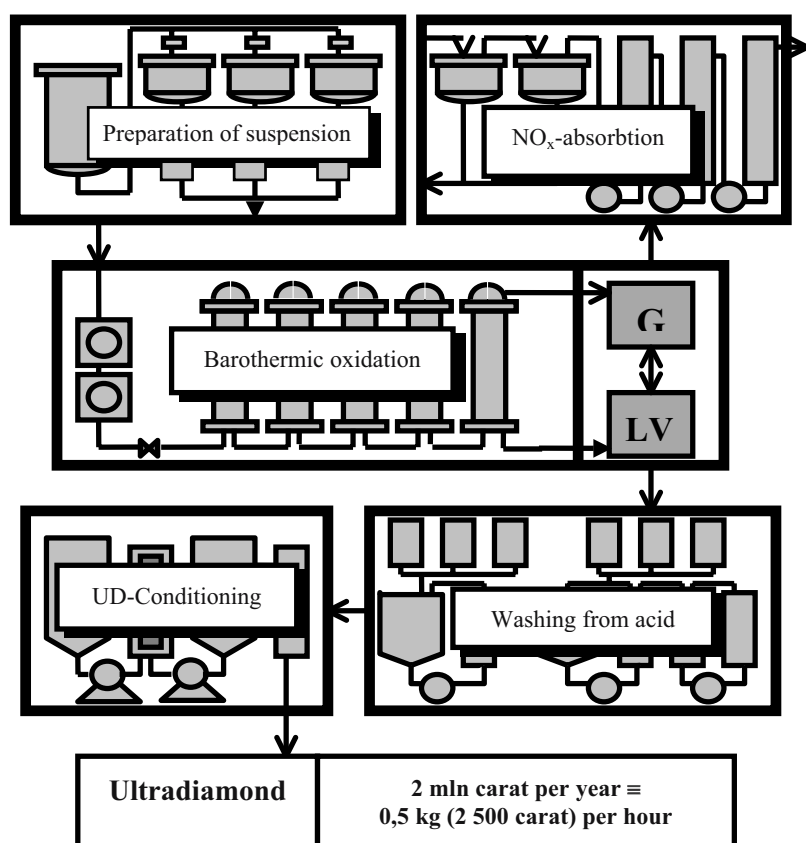


Figure 3. Schematic chemical purification of UDD.



The diamond-containing soot is vigorously mixed up with the acid and delivered to the reaction zone by high pressure pump feeders.. Passing through the cascade of electrically heated reactors, the acidic suspension is gradually heated, thermostatically controlled, then cooled down and delivered to a high pressure disposal unit. The heterophase mixture consisting of a liquid saturated with gases and containing up to 3 wt.% of diamond is removed. The suspension and the gas are separated in receiver devices by a purge of compressed air. The degassed UDD suspension is periodically subjected to washing off from the acid.

The nondiamond carbon in the soot is nonuniform in structure and chemical activity; therefore, the process of oxidation can be conveniently subdivided into three stages:

- |  |                             |
|--|-----------------------------|
| 1. Preliminary oxidation   | 10–20% of nondiamond carbon |
| 2. Oxidizing decomposition of<br>nondiamond carbon                               | 65–80% of nondiamond carbon |
| 3. After-burning of stable<br>nondiamond structures,<br>oxidation of UDD surface | 5–15% of nondiamond carbon  |

The preliminary oxidation is accompanied by a very intense gas evolution and self-heating, though the labile part of nondiamond carbon in the soot normally does not exceed 20%. At this stage, highly active intermediates are formed in the reaction mixture -- derivatives of nitric acid and nitrogen oxides, which initiate a fast and fully oxidizing decomposition of most of the nondiamond carbon at high temperatures. The final stage of the process is a thermostatic control of the suspensions at a temperature providing a full gasification of nondiamond carbon structures and the formation of a stable and homogeneous of oxygen-containing functional coverage on the diamond surface. The conditions for the thermostatic control determine the quality parameters such as the total carbon and the nondiamond carbon contents, the specific surface, and UDD adsorptivity.

The implementation of a continuous mode of the multiphase technology necessitated the solution of various design and technical problems. The experience has shown that it is necessary to control the heat supply in a large area of the reaction zone. This excludes the self-warming of the reaction mass and the loss of its chemical activity, thereby maintaining the rates of the process. As for the UDD quality, this means that the degree of nondiamond carbon decomposition and of the diamond surface oxidation will be constant and reproducible.

When designing the reaction space, it is necessary to account for the macrokinetics of soot oxidation, in particular, the intensity and non-uniformity of gasification, the exothermic and endothermic effects of the

interaction between ultradispersed carbon and the  $\text{HNO}_3$  solution. It is important to prevent an active corrosion of the equipment, especially at the waterline. The suspensive character of the reaction mass imposes restrictions on the flow pattern and rate in the pipelines and through the vessels. In view of these and some other factors, we have designed a system for multilevel zoning of the reaction space with respect to the temperature, linear flow velocity and the possibility of separating the liquid and the gaseous components. When passing through the cascade of HP reactors, the acid suspension is heated gradually in four temperature zones. The linear flow velocity changes cyclically from 0.5 to 50 m/min. The inner control units in the compact HP reactors provide the total length of the suspension pathway greater than 10 m. The reaction zones with maximum gasification are connected to air-cooled gas dampers, which reduce the pressure fluctuations along the HP line, increasing the technological safety. The high suspension flow velocity along the electrically heated reactor walls provides an effective heat removal and considerably reduces the risk of corrosion damage to the equipment.

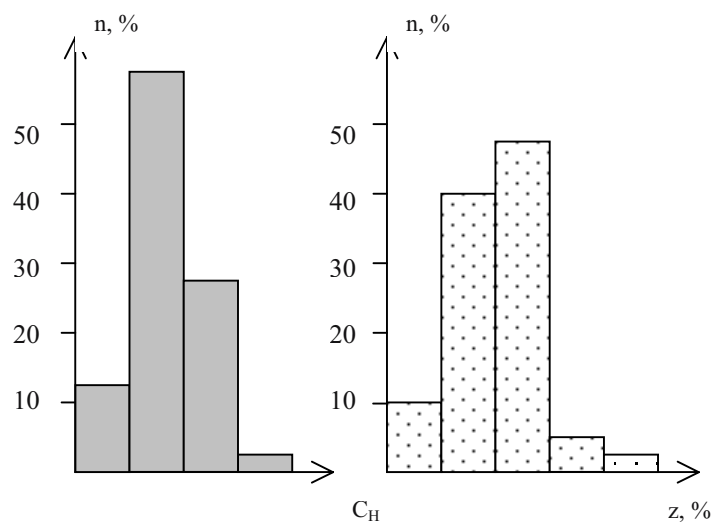


Figure 4. The distribution of industrial UDD as a function of the contents of nondiamond carbon (a) and incombustible noncarbon (b).

The alternation of the temperature, velocity and the reaction mass saturation with the gas, as is the case with the zoning, has some other important advantages: a continuous and deep disintegration of carbon

particles, the destruction of particle aggregations, a ready access of the oxidizer to the particle surface, and fewer diffusion restrictions on the product removal. As a result, a high and stable quality of purified UDD is achieved. Figure 4 shows a histogram of the distribution of industrial UDD (TS RB 28619110.001-95) with respect to the contents of nondiamond carbon and incombustible noncarbon impurities.

Intensive gasification requires effective measures for providing technological safety. The high pressure is controlled by a set of valves, throttling draw plates and chokes to maintain the pressure at about 8–9 MPa with an accuracy of  $\pm 0.05$  MPa in the mode of suspension feeding of 50 l/hour and more. During the processing, the gas volume is estimated to be 3.5–5 m<sup>3</sup>/hour.

Nitric acid and nitro-nitrogen oxides can be regenerated and re-used in the barothermic process. The acid recycling includes two flows, which can be termed the reaction HNO<sub>3</sub> and the absorption HNO<sub>3</sub> flows (Figure 5).

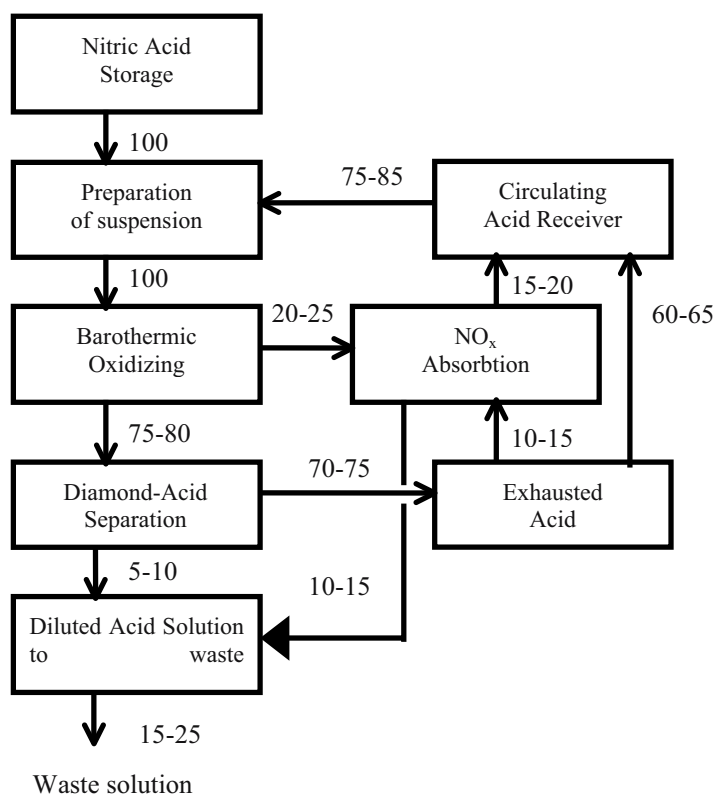


Figure 5. Nitric acid recycling.

The absorption acid is produced in the standard process of absorption of nitrore gases by water or acid solution. The kinetics of  $\text{HNO}_3$  accumulation to a 40–50% concentration is demonstrated in Figure 6.

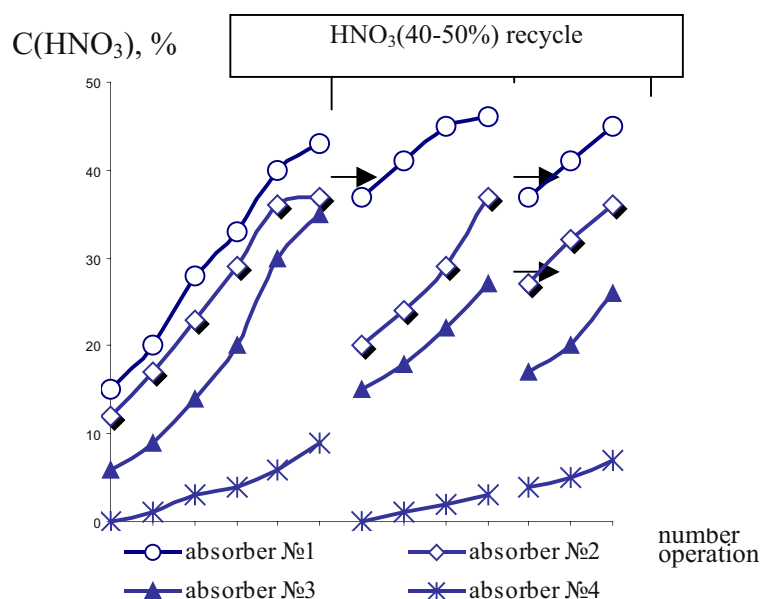


Figure 6. The accumulation of  $\text{HNO}_3$  in the absorption system during UDD purification.

A set of four absorbers, through which an absorbent solution moves via the countercurrent mechanism, provides a high degree of ecological safety. Simultaneously, up to 10 kg of strong and pure  $\text{HNO}_3$  per 1 kg of UDD are returned to the purification cycle.

The reaction acid makes up 70–75% of the recirculating acid, preserving a significant potential for the re-use in the UDD purification. Table 1 presents the results of seven consecutive UDD purification runs with the use of exhausted acid. As the concentration of  $\text{HNO}_3$  decreases from 50 to 29%, the oxidative activity of the acid with respect to nondiamond carbon remains practically the same. The acid does not absorb soluble salts of iron, which is the main impurity in the soot. However, the ash content in the UDD increases with each cycle, exceeding a technical threshold. The restriction on the multiple re-use of the exhausted acid at a concentration below 40% is due to the formation of finely dispersed oxide  $\text{Fe}_2\text{O}_3$  (hematite). This impurity is insoluble in the acid and presents a special problem during the basic, additional and deep purification of UDD.

Table 1. Utilization of exhausted nitric acid in barothermic UDD purification.

N	HNO <sub>3</sub> , %	Content of Fe		Content of oxidizable carbon in UDD, %
		in solution, g/l	in UDD, %	
1	50.1	0.92	0.4	1.5
2	46.4	1.35	0.7	1.6
3	43.4	1.52	0.9	1.5
4	38.8	1.95	1.5	1.7
5	34.9	1.70	1.9	1.8
6	31.5	1.28	5.3	1.4
7	29.7	1.20	5.7	1.6

Additional purification of UDD is made to improve the UDD composition. Deep purification provides powders and suspensions with low impurity contents and improved electrophysical characteristics. Both purification procedures and the modification of the diamonds surface are carried out at will to get a total of 5–10% of UDD.

The industrial UDD technology is developing along two lines: further increase in the stability of physical and chemical properties achieved in the basic production and the designing of new UDD modifications. We believe that these are the prerequisites and conditions for a successful application of nanodiamonds in various industries.

The present work was submitted at support of the Joint Chinese-Belarus-American enterprise “Shandong Gold Nano-Diamonds”, Jinan, People's Republic of China.

## REFERENCES

1. T.M. Gubarevich, A.P. Korzhenevsky, D.N. Gamanovich, V.Yu. Dolmatov. Method of chemical purification of ultradispersed diamond from impurities. Patent of Belarus No. 4533; 25.02.02. Priority date 20.10.95.
2. T.M. Gubarevich, D.N. Gamanovich, A.P. Korzhenevsky. S.M. Azarov, V.E. Romanenkov. *Method of isolation of UDD*. Patent of Belarus No.4532 of 25.02.02. Priority date 13.10.95.
3. T.M. Gubarevich, A.P. Korzhenevsky, D.N. Gamanovich. Industrial complex for ultradispersed diamond production. *Superhard Materials*, No. 1, 25-30 (1999) (in Russian).
4. T.M. Gubarevich and A.P. Korzhenevsky. *Method for treatment of Ultradisperse diamond*. Patent Application (Belarus) No. 19981035; Priority date 12.17.98.
5. T.M. Gubarevich and A.P. Korzhenevsky. *Method of producing of diamond-containing synthetic materials*. Application for a patent (Belarus) No. a20020330; Priority date 18.04.02.

# 26

## ULTRADISPERSE DIAMOND REGENERATION FROM COMPOSITE ELECTROLYTES OF CHROMIUM PLATING

T.M. Gubarevich, L.E. Chernukho, V.P. Kulik, and R.G. Shtempljuk  
*Scientific Production Joint-Stock Company "Sinta" P.O. Box 59, Minsk, 220082, Belarus*

**Abstract:** Composite chromium-diamond electroplating is one of the most UDD consuming technologies among UDD applications. The exploitation includes periodic cleaning of the chroming bath from accumulated anodic sludges and contaminants. During the cleaning, the UDD must be extracted from the sludges and regenerated for re-use. We have suggested technique for UDD regeneration from sludges containing up to 80% of insoluble Cr, Pb and Sb compounds. The process includes mechanic, colloidal-chemical and chemical treatments which provide a fairly pure material only with 1–3% of noncarbon; the calculated diamond yield is 85–90%. We have analyzed the contaminants in regenerated UDD for their dispersion, sedimentative and aggregative stability, adsorptive and structural characteristics of the surface. Regenerated diamond is applicable for re-use in electroplating technologies.

**Keywords:** ultradispersed diamond, compose electroplating, chromium-diamond codeposition, UDD regeneration, UDD purification, re-use of nanodiamonds

### 1. INTRODUCTION

Composite chromium-diamond plating is a technology consuming large amounts of ultradisperse diamonds (UDD). According to available technological developments [1–3], the UDD concentration in the electrolyte for chromium plating may be as high as 30 kg/m<sup>3</sup>. It is necessary to periodically clean the chromium plating baths from anodic sludge and contaminants, so there is the problem of UDD extraction from the sludge for reuse. Besides, the colloidal state of the UDD particles greatly changes because of the long presence in a working bath, which decreases the quality of composite electrochemical coatings (CEC). These factors limit the

applicability of the chromium-diamond plating technology in industries, which are focused on an intensive operation of chromic baths to achieve high and stable coating characteristics.

The present work was aimed at the study of UDD recovery from chromium plating sludge. We have suggested a method for UDD purification and activation, using a combination of physicochemical and chemical techniques. The study was focused on the impurity composition of regenerated UDD, their dispersity, aggregation and sedimentation stability, as well as on the adsorptive and structural characteristics of the surface. It is found that regenerated UDD can be successfully used for composite chromium plating.

## 2. EXPERIMENTAL

Diamond-containing sediments taken from pilot baths for composite chromium plating were used as the starting material. The electrolyte composition in g/l was  $\text{CrO}_3$  220–250;  $\text{H}_2\text{SO}_4$  2.2–2.5; UDD 5–7; temperature 53–57°C; the anodes were made from a lead-antimony alloy (5–10%). The other parameters of the bath operation are shown in Table 1.

Table 1. The operation parameters of baths for composite chromium plating

	Bath No. 1	Bath No. 2
Volume of electrolyte, m <sup>3</sup>	0.85	0.27
Concentration of UDD, kg/m <sup>3</sup>	6.2-7.0	8-10
Operation period, month	18	24
CEC area, m <sup>2</sup> (h = 10 μm)	707	1240
Calculated CEC mass, kg	50	88
UDD in CEC, kg	0.4	0.7
Operation loss of UDD, kg	0.1	0.2

The structure of the diamond-containing sediments was analyzed by chemical methods and X-ray spectroscopy. The mass fraction of the ashes was found from the weight of a sediment dose burned in air at 900°C; the total carbon was determined by burning the sediments and coatings in an oxygen flow at 900 and 1200°C with a subsequent coulometric detection of  $\text{CO}_2$  (AH 7560 and AH 7529 carbon analyzers, Gomel, Belarus). The elemental composition of noncarbon admixtures was studied using an X-ray microanalyzer (D 500 "Siemens"). Potentiometric titration of the UDD powders was carried out according to the method described in [4]. The Vickers microhardness of the coatings was measured at 100 g load.

### 3. RESULTS AND DISCUSSION

The diamond-containing sludge from composite chromium plating baths represents a grey-yellow mass with inclusions of black, brown and metallic particles. When suspended in water, the particles quickly settle down, leaving a transparent or slightly muddy liquid. A pre- processing of the sludge includes the wash-off of soluble admixtures, mainly  $\text{CrO}_3$ , and filtering through a sieve with a  $1\ \mu\text{m}$  cell diameter. In addition to UDD, the sludge includes as many as 20 components, mostly lead, chromium, antimony, iron, silicon, sulfur, and titanium compounds. Table 2 summarizes the qualitative composition of the major admixtures. The analysis of the sludge composition is a very hard task because of the complexity and heterogeneity of the material.

Table 2. The characteristics of the major admixtures in diamond-containing sludges.

Substances, formulare	Density, $\text{g/cm}^3$	Solubility			Colour
		Water	Acid	Base	
Chromates:					
$\text{PbCrO}_4$	6.12	-	+ ( $\text{HNO}_3$ )	+	yellow
$\text{PbCrO}_5$	6.27	-	-	+	
$(\text{SbO})_2\text{CrO}_4$		-	-	+ ( $\text{KOH}$ )	
$\text{CaCrO}_4$	3.12	0.79%	+	+	yellow
$\text{Fe}_2(\text{CrO}_4)_3$		-	-	-	red
Hydroxochromates					brown
$x\text{Cr}_2\text{O}_3 \cdot y\text{CrO}_3 \cdot n\text{H}_2\text{O}$	2.9-3.3	-	+ ( $\text{HNO}_3$ )	-	black
Oxydes:					
$\text{PbO}_2$	9.35	-	-	+	brown
$\text{SiO}_2$		-	-	+	white
$\text{Cr}_2\text{O}_3 \cdot \text{H}_2\text{O}$	4.12	-	-	-	red-brown
$\text{Fe}_2\text{O}_3$		-	+ ( $\text{HNO}_3$ )	-	red-brown
$\text{TiO}_2$	4.2	-	+	-	white
Hydroxydes:					
$\text{Cr}(\text{OH})_3 \cdot n\text{H}_2\text{O}$	1.64-2.9	-	+	+	black
$\text{Sb}(\text{OH})_3 \cdot n\text{H}_2\text{O}$					brown
Sulfates:					
$\text{Cr}_2(\text{SO}_4)_3 \cdot n\text{H}_2\text{O}$	3.01				
$\text{PbSO}_4$	6.35	$4.5 \cdot 10^{-3}$	+ ( $\text{HNO}_3$ )	+	colourless
$\text{Pb}(\text{OH})_2\text{SO}_4$		+	-	+	yellow
$(\text{SbO})_2\text{SO}_4$	3.27	-	-	+ ( $\text{KOH}$ )	red
$\text{Pb}_2\text{Sb}_2\text{O}_7$		-	-	-	orange-yellow



The elemental composition of the noncarbon in the mixture, recalculated for the respective oxides, is summarized in Table 3.

Table 3. Composition (C) and weight (M) of the major components of chromium plating sludges prior to processing.

Main components		PbO <sub>2</sub>	CrO <sub>3</sub>	Sb <sub>2</sub> O <sub>3</sub>	Fe <sub>2</sub> O <sub>3</sub>	SO <sub>3</sub>	SiO <sub>2</sub>	TiO <sub>2</sub>	CaO	Other
sample A	C, %	49.7	35.5	6.4	2.1	2.2	0.4	0.5	0.6	2.5
z = 47.6%	M, g	236.5	169.1	30.3	10.2	10.7	2.0	2.4	2.6	12.2
sample B	C, %	55.4	29.1	9.4	2.0	2.0	0.4	0.3	0.3	1.3
z = 70.5%	M, g	390.6	205.2	66.3	14.1	14.1	2.8	2.1	2.1	9.1

Chromates, oxides, sulphates and other derivatives of lead and antimony are the main products of electrochemical corrosion of the anodes. Iron finds its way to the electrolyte largely due to anodic activation of the parts. Silicon derivatives are accumulated in the chromium plating bath because of a poor washing after degreasing. The titanium sources are obviously the parts of the industrial equipment and the titanic bath case, which slowly corrode due to induced electric fields in the chromic acid medium. Poorly softened water (hard water) causes calcium pollution of the electrolyte. In addition to the above elements, the sludge contains Na, Al, Ni, P, V, Mo, and Cu. These impurities are not specific to chromium plating, and their origin is similar to that described above.

Direct chemical purification of UDD from such admixtures would present a significant difficulty because of the large amount of nondiamond components and the heterogeneity of their chemical properties. However, insoluble impurities have a much greater particle size and a higher density than UDD and their surface properties are different from those of diamond. Having these factors in mind, we have designed a way of UDD extraction from the sludge, based on the sedimentation separation of solid impurities and admixtures (Figure 1).

Previously, we reported on a method of UDD purification from coarsely dispersed oxide/ salt admixtures [5], which has been introduced with a high efficiency at an optimum ratio of UDD and surface-active substances in the aqueous medium with a fixed pH value. The treatment of a chromium plating sludge required substantial changes in the technological procedure and conditions of the method because of a specific chemical and disperse structure of the sludge.

A wet sludge sediment is a coagulated thixotropic material, in which UDD particles are tightly aggregated with polydisperse inorganic admixtures. They are surrounded by liquid, i.e. the aggregation is reversible. The liquid content in such deposits is about 70–80%; the liquid contains soluble constituents, which are difficult to wash off because of strong adsorption forces and diffusion restrictions characteristic of colloidal systems. The soluble impurities include polycharged cations having a strong coagulative action on UDD suspensions.

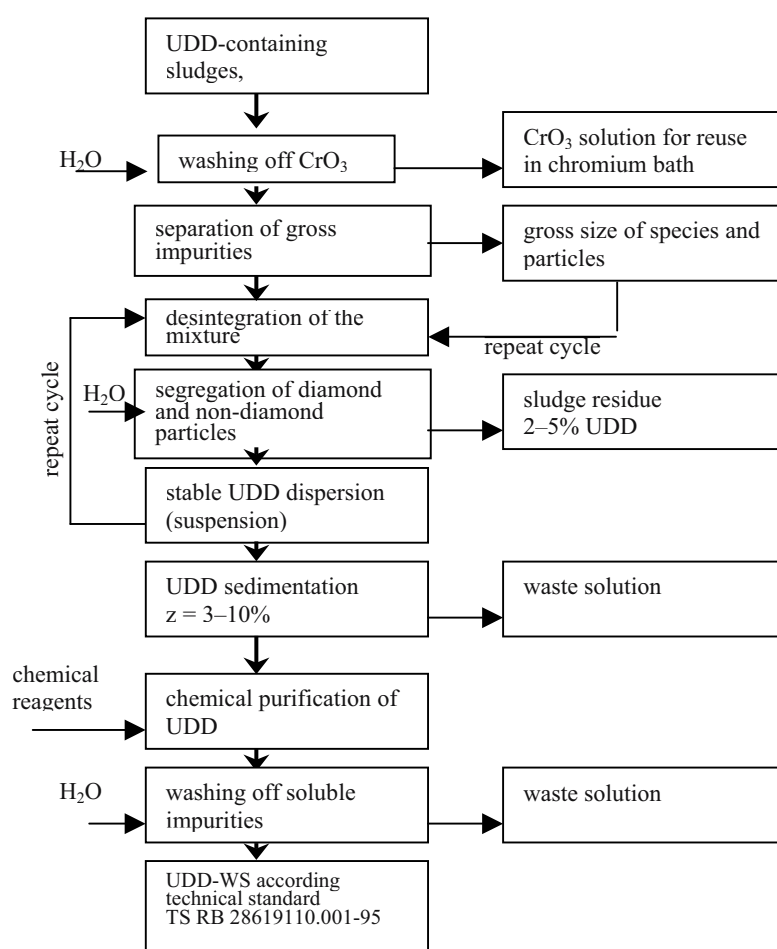


Figure 1. The process of UDD regeneration from chromium sludges

The conditions for the selective stabilization of UDD in the suspended layer are provided by the following factors: (a) disintegration of the

particles; (b) the composition of the active medium and the optimal concentration ratios of solid particles and liquid, water-soluble impurities and anticoagulants, UDD and surface-active substances; (c) the suspension pH; (d) the optimal duration and frequency rate of the sedimentation process.

The concentration of solid particles in an active aquatic medium may vary from 1–5 to 100 g/l, depending on the structure of the initial raw material. A high concentration raises the productivity but the UDD losses are also increased. Most of the diamond particles precipitates together with polydisperse admixture. A limiting factor here is the coagulation of UDD and the mechanical capture of diamond particles by the precipitating admixtures.

It is equally important to overcome the aggregation instability of diamond suspensions, which is due to the presence of substances causing a fast UDD coagulation. These are ions of the polyvalent metals  $\text{Cr}^{3+}$ ,  $\text{Fe}^{3+}$ ,  $\text{Ca}^{2+}$ , etc. They can not be totally removed by washing the initial mixture, but because of their presence, UDD cannot practically form stable suspensions. To deactivate these ions (coagulants), one or several chelating agents or heteropolyacids are introduced into the active aquatic medium. It is known that compounds of this class of agents are nonspecific and possess a chelating ability for a wide range of cations.

The concentration of the anticoagulants used should be high enough to bind completely polycharged cations. Moreover, one should not ignore the possible hydrolysis of some impurities and the hardness of the water used.

The efficiency of UDD separation increases with the use of surface-active substances, selectively stabilizing diamond particles. In our experiments, the most successful agents were found to be those of the non-ionic type. The UDD suspension stability in the presence of 0.1–10 g/l of surfactants varies from 6 to 30 hours; during this period the admixture particles with a size less than 5–10  $\mu\text{m}$  precipitate.

According to the UDD surface properties [6], an optimum pH range lies between 8 and 12.5. Here, UDD has the maximum surface charge and the highest adsorption of potential-determining ions. Both factors raise the aggregation stability of the diamond suspension.

The conditions in which UDD particles disintegrate are the most significant factor the deposit processing. The particle size distribution of the mixture is wide, from 0.5–1 mm to less than 1  $\mu\text{m}$ . A special problem is the products of hydrolysis and amorphous impurities (Table 2), which precipitate with difficulty. On ageing, the mixture of the substances is condensed to form highly concentrated thixotropic and coagulative structures. Destruction of such structures requires a vigorous treatment. The disintegration intensity affects the UDD yield, as shown in Figure 2. The best result is obtained with a combination of ultrasonic processing and

vigorous mixing. The disintegration by using tribomechanical devices provides highly dispersed homogeneous suspensions, whose admixture particles are, however, crumbled up and precipitate with difficulty.

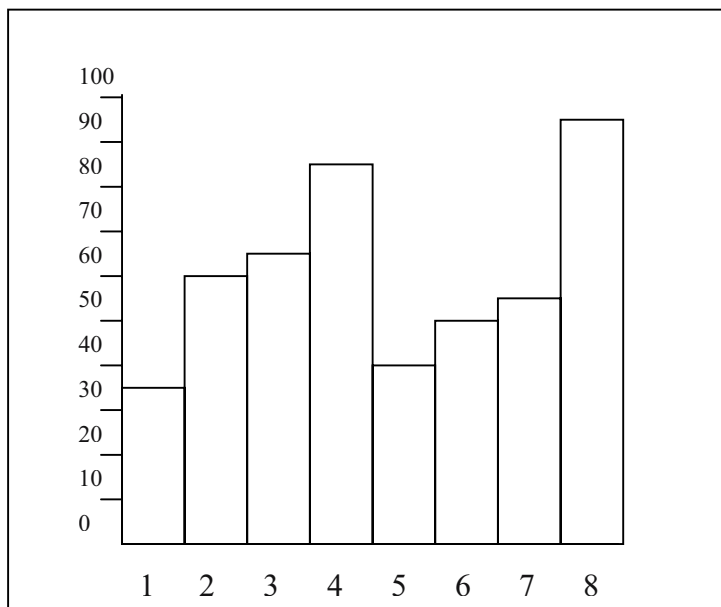


Figure 2. The dependence of UDD wt.-% after the separation from a pretreated sludge (sample A) on the disaggregation mode:

- 1 - slow stirring,
- 2-3 - intensive stirring (10 and 20 min, respectively),
- 4 - fast disintegration,
- 5-7 - ultrasonic treatment (10, 20 and 30 min, respectively),
- 8 - ultrasonic treatment and intensive stirring.

The admixtures are sedimented in one or several cycles. From a diamond-containing sludge with a low admixture content (20–25%), UDD can easily be extracted by a single sedimentation. A sludge containing a large amount of ashes should be subjected to a cyclic processing. Figure 3 shows the characteristic curves for a triple separation of the initial mixture (B). The total amount of impurities in a diamond-containing suspension prior to sedimentation is taken to be unity. The sedimentation was carried out in portions with a subsequent determination of the residual impurities in each UDD portion for a fixed period of time.

At the first stage, 80% of admixtures quickly settle down to form a deposit, and then the sedimentation is slowed down and is accompanied by a remarkable UDD co-deposition. The second sedimentation cycle includes mechanic and acoustic disaggregation with the necessary correction for the

chemical composition of the suspension. The settling of admixtures occurs more slowly, and a dense yellow-orange deposit is formed. The co-deposition of UDD is insignificant. The optimum time of repeated sedimentations is limited by the UDD coagulation and deposition. The coagulation stimulated by the polydisperse impurity particles with a size less than 50 microns. The third and the next cycles are effective when the colloidal stability time of the diamond suspension is longer than 8–10 hours. Then a significant reduction in the admixture content is observed with a still large UDD yield.

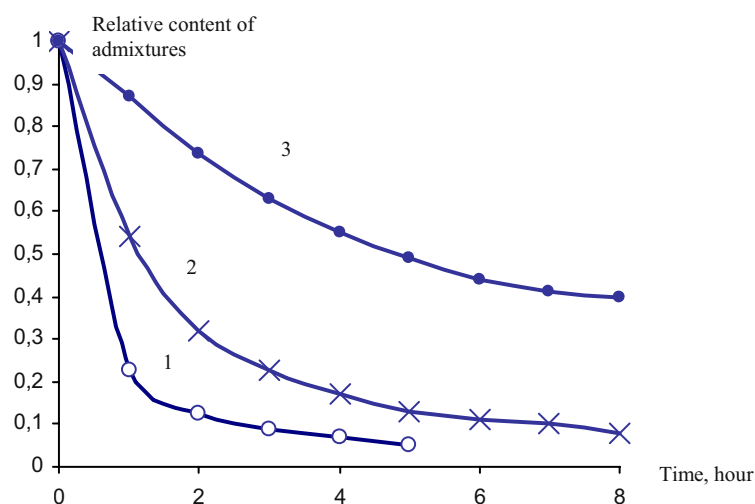


Figure 3. The residual impurity contents in the UDD suspension as a function of the sedimentation time during the first, second and third operation cycles.

The further treatment includes the coagulation of stable UDD suspensions and the washing of the diamond deposit from soluble impurities. The structure and amount of insoluble impurities are shown in Table 4.

The compounds of lead, chromium, and sulphur are removed nearly totally, because insoluble chromates and lead sulphates have a high density (Table 2). The amount of other impurities (Sb, Ca, Fe, Si, Ti) decreases 2–6 times, as compared with the initial content but their relative contents in the ashes are higher. This stage provides a UDD suspension with satisfactory parameters of free dispersiveness, aggregation and sedimentation stability; the average amount of incombustible impurities is  $5 \pm 2\%$ .

Table 4. The composition (C), weight (M) and yield (B) of the major components in the chromium plating sludge after the first processing stage.

Main components		PbO <sub>2</sub>	CrO <sub>3</sub>	Sb <sub>2</sub> O <sub>3</sub>	Fe <sub>2</sub> O <sub>3</sub>	SO <sub>3</sub>	SiO <sub>2</sub>	TiO <sub>2</sub>	CaO	Other
Sample A	C, %	35.6	23.0	13.8	8.9	1.7	2.6	3.4	4.0	7.0
z = 47.6%	M, g	12.4	8.0	4.8	3.1	0.6	0.9	1.2	1.4	2.4
	B <sub>1</sub> , %	5.2	4.7	15.8	30.4	5.6	45	50	53.8	19.7
Sample B	C, %	21.3	31.0	16.9	9.7	4.3	3.9	3.2	3.1	6.6
z = 70.5%	M, g	6.6	9.6	5.3	3.0	1.3	1.2	1.0	1.0	2.1
	B <sub>1</sub> , %	1.7	4.7	8.0	21.3	9.2	42.9	47.6	48.4	87.5

The further purification of UDD was carried out by chemical methods using the characteristics of the impurity composition. For practical reasons, the least expensive and readily available reagents were preferred together with a soft treatment. Alkaline treatment is considered to be one of the most effective and well-elaborate techniques for additional UDD purification. It uncludes boiling in an alkali solution with a 1–30% concentration. After an appropriate washing, the UDD characteristics totally meet the technical standard TC BELARUS 28619110.001-95 (Table 5).

Table 5. The composition (C), weight (M) and yield (B) of the major components of chromium plating sludges after the second processing stage.

Main components		PbO <sub>2</sub>	CrO <sub>3</sub>	Sb <sub>2</sub> O <sub>3</sub>	Fe <sub>2</sub> O <sub>3</sub>	SO <sub>3</sub>	SiO <sub>2</sub>	TiO <sub>2</sub>	CaO	Other
sample A	C, %	1.3	26.2	17.5	15.0	2.5	5.0	7.5	21.2	3,8
z=1.8%	M, g	0.1	2.1	1.4	1.2	0.2	0.4	0.6	1.7	0,3
C <sub>total</sub> =82.9%	B <sub>2</sub> , %	0.8	26.3	29.2	38.7	33.3	44.4	50.0	121.0	125
C <sub>ox</sub> =1.5%	B <sub>3</sub> , %	0.04	1.24	4.6	11.8	1.9	20.0	25.0	44.2	2,45
S <sub>spec.</sub> =238 m <sup>2</sup> /g										
sample B	C, %	2.9	19.4	14.6	2.4	5.3	8.3	4.8	12.0	11,3
z=3.6%	M, g	0.3	1.8	1.3	2.0	0.5	0.8	0.4	1.1	1,0
C <sub>total</sub> =81.7%	B <sub>2</sub> , %	3.9	18.4	25.1	65.0	36.9	63.3	44.0	110	47,6
C <sub>ox</sub> =1.8%	B <sub>3</sub> , %	0.07	0.9	2.0	13.8	3.4	27.1	21.0	52.3	76,9
S <sub>spec.</sub> =219 m <sup>2</sup> /g										

It was of special interest to estimate how the long stay in a strong oxidizer solution at raised temperatures (50–60°C) and permanent exposure to electric current (0.5–2 A/dm<sup>3</sup>) has affected the UDD physical and chemical properties. It is found that the average size of microcrystallites and the lattice parameter of the diamond remain practically unchanged; the specific surface decreases by 12–15%, in agreement with other data [6]. The content of the so-called oxidizable carbon determined by chemical methods is 1.5–1.8% for the regenerated diamond, which does not differ much from the values for the standard samples. The total carbon content of 81–83%

allows us to refer regenerated UDD to strongly oxidized modifications [6]; this is supported by the potentiometric titration data for powders in acid or alkali solutions in the NaCl background electrolyte (Figure 4).

The regenerated UDD in an aqueous suspension was tested in composite chromium plating. The structure and microhardness of the chromic coatings are compared with similar coatings in Figure 5. The regenerated UDD is practically the same as the standard "fresh" diamond, whereas the "old" diamond, which has worked in a chromium plating bath for over 6 months, is not as active.

#### 4. CONCLUSION

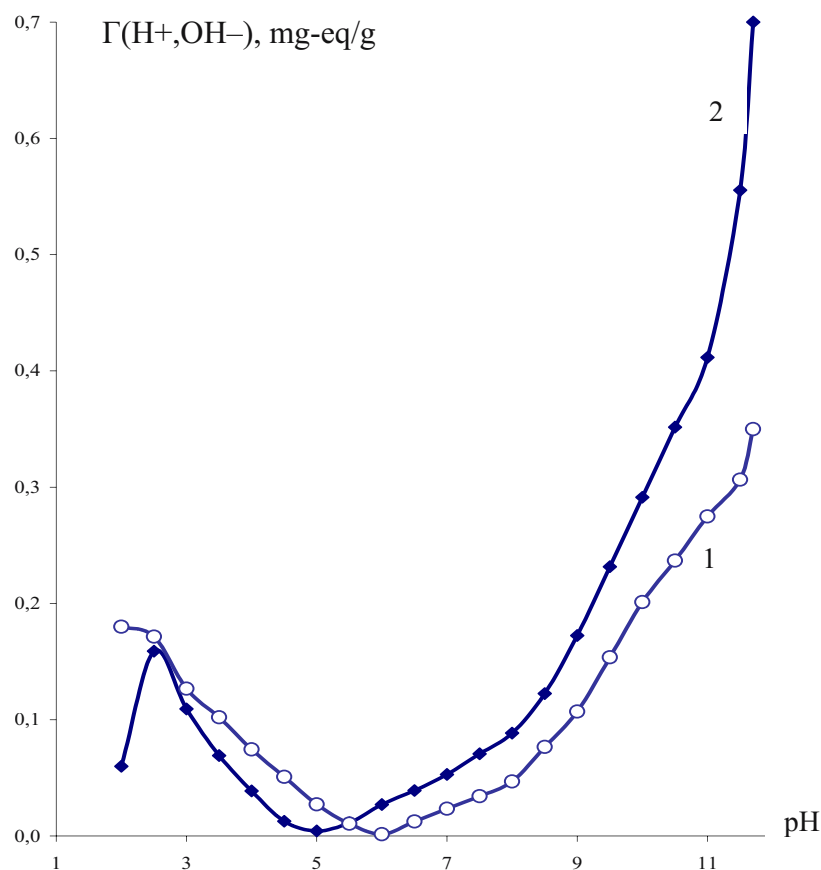


Figure 4. Potentiometric titration of UDD with an acid (0.1 N HCl) and base (0.1 N NaOH) solution. The background electrolyte is 0.1 N NaCl; 1 – standard UDD, 2 – regenerated UDD.

We have drawn the following conclusions from the above findings. First, a long-term operation of UDD-containing chromic electrolytes leads to deactivation of diamond particles, caused by the accumulation of sludge and pollution. Second, the method we have suggested for UDD regeneration by a combined physical and chemical treatment of a diamond-containing sludge is quite effective. Finally, the regenerated UDD preserves the basic physical and chemical characteristics of the standard UDD and can be successfully reused for making composite coatings.

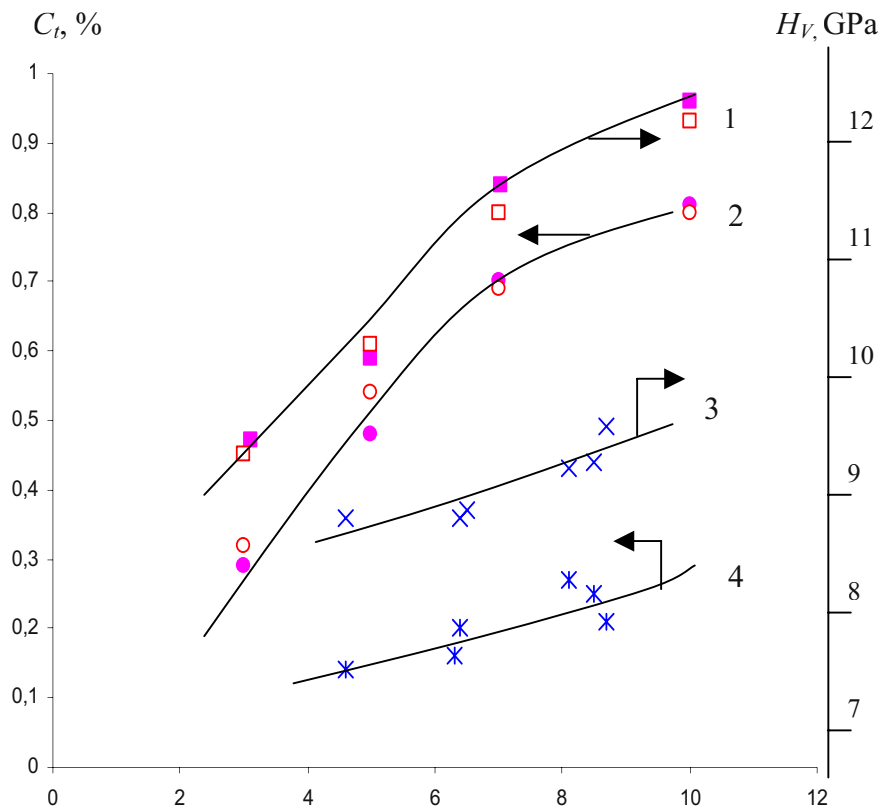


Figure 5. Weight percent of co-deposited UDD particles (2, 4) and the microhardness of composite chromium coatings (1, 3) versus the concentration of UDD particles suspended in a chromium plating bath:

- ■ - regenerated UDD,
- □ - "fresh" UDD,
- × ж - "old" UDD.



This work was submitted under support of the Joint Chinese-Belarus-American enterprise Shandong Gold Nanodiamonds, Jinan, People's Republic of China.

## REFERENCES

1. A.I. Shebalin, V.D. Gubarevich, P.M. Brylyakov, and G.V. Sakovich. Method for composite chromium electroplating. Author's certificate USSR No. 1694710, C25D15/00.
2. G.K. Burkat and V.Yu. Dolmatov. Ultradisperse diamonds in galvanotechnology. *Zhurnal Fiziki Tverdogo Tela* **46**(4), 685-93 (2004) (in Russian).
3. B.V. Litvinov, L.I. Filatov, P.Ya. Detkov, S.V. Samylov, A.N. Averin, Yu.I. Kramskoj, and S.I. Chukhaeva. Ultradisperse diamond powders. *Nov. Prom. Tehnologii*, No. 1, 30-2 (1994) (in Russian).
4. T.M. Gubarevich, N.M. Kostyukova, I.S. Larionova, and R.R. Sataev. Regularity changes of adsorption and structure characteristics of carbon diamond-containing materials of detonation nature. *Zhurnal Prikl. Khimii* **66**(1), 113-17 (1993) (in Russian).
5. T.M. Gubarevich and A.P. Korzhenevskii. Method for treatment of Ultradisperse diamond. Application for a patent (Belarus) No. 19981035; 12.17.98.
6. T.M. Gubarevich, Yu.V. Kulagina, and L.I. Poleva. Oxidizing of Ultradisperse diamonds in liquids. *Sverhtverdye Materiali*, No. 3, 34-40 (1993) (in Russian).

## SYNTHESIS AND PROCESSING OF THE CHELYABINSK DETONATION NANODIAMONDS

I.L. Petrov

*Scientific and Industrial Company "New technologies", Chelyabinsk, 454038, Russia*

**Abstract:** Technology of the synthesis of detonation soot, two alternative ways of their post-synthesis purification and related characteristics of the resulting detonation nanodiamond (DND) particulate are discussed.

**Keywords:** detonation nanodiamond, detonation soot, chemical purification, ozone treatment

The core technology of the DND synthesis used by our research group had been developed earlier at the Federal Nuclear Center in Chelyabinsk [1]; it had been further improved within years to follow.

For production of the detonation soot material according to the Chelyabinsk technology, an explosion chamber with a capacity of 2 m<sup>3</sup> and the amount of explosive material 1.2 kg is typically used. The explosion takes place in an icy coating, which plays the role of a coolant. By changing the conditions of preparation and synthesis one can get soot material with the required amount of diamond phase from 40% to 80%. A typical result of spectral analysis of the soot after magnetic separation is illustrated in Table 1.

A possibility to produce soot with the content of diamond phase of 75–80%, decreases the expenses of DND production since requires less extensive refining processes, as well as decreases the amount of non-carbon impurities. The method of soot processing being exploited at "New Technologies", allows producing DND of variable sizes and diamond-carbon amounts at the same equipment. The methods of DND purification

implemented at “New Technologies” are acid-chrome treatment, developed at the Federal Nuclear Center, and the ozone treatment, the proprietary method developed at “New Technologies”. The method of ozone treatment with ozone used as an oxidizer is more economical and environmentally friendly. This method allows producing powders with minimum content of non-diamond carbon. Recently, Zhirnov et al. characterized DND particles subjected to different post-processing treatments using field electron emission measurements by depositing small amount (0.2  $\mu\text{m}$  in thickness) of DND on metal or silicon tips by electrophoresis [2]. In these experiments, the field emission characteristics of tips with DND coatings were compared to characteristics of bare tips. The emission experiments showed that the emission characteristics differ significantly for different DND coatings (different fractions of ‘standard’ DND as well as ozone-treated DND had been studied). All types of nanodiamond coatings showed improvement in field emission threshold [2]. Additional hydrogen plasma treatment was used to modify surface properties of powders. In general, it was concluded that nanodiamond purified by ozone treatment followed by hydrogen plasma modification is most appealing for field emission applications. It demonstrates an importance of the application-specific DND modification.

*Table 1.* Physical and chemical properties of detonation soot produced by Chelyabinsk technology.

1	The quality of refinement	Unrefined
2	Mass portion of diamond carbon in solid phase, % mass, not less than	75.0
3	Mass portion of non-diamond carbon in solid phase, % mass, not more than	25.0
4	Mass portion of incombustible residuum in solid phase, % mass, not more than	2.8
5	Mass portion of moisture and volatilities, % mass, not more than	3.0
6	Pycnometric density, $\text{g}/\text{cm}^3$ , not less than	2.8
7	Average size of initial diamond particles, determined by the method of X-ray diffraction, nm	5 (3–30)
8	Specific surface area, $\text{m}^2/\text{g}$	250–350
9	Crystal structure of diamond particles	Cubic
10	pH of 10% suspense in the distilled water	5.5–6.5
11	Outward appearance	Black powder
12	Toxicity	Non toxic, chemically inert, radiation safe

Gradual increase of customers' requirements to the quality of the DND in the recent years made it necessary to develop technology of maximally refined powders using standard acid-chrome treatment equipment. As a result of optimization of a standard acid-chrome purification method in combination with other methods, we were able to produce laboratory quantity of "pure" DND of a light grayish-white color. The results of spectral elemental analysis of the powders produced by different purification methods are summarized in Table 2.

*Table 2.* The results of spectral analysis of incombustible elements in DND samples. 'Standard' means DND after acid-chrome treatment, 'Pure' – further modified standard powder, 'Ozone' – DND after ozone treatment. For a reference, content of impurities in the worse samples, ('defect' in the last column), is provided.

Chemical element	Content of elements, % mass., in DND			
	Standard	Pure	Ozone	Defect
Iron	0.1	–	0.05	–
	0.1	0.015	0.05	0.1
Chrome	0.5	–	–	0.9
	0.3–0.5	0.03	0.005	0.5–1
Silicon	0.15	0.01	0.15	0.1
Aluminium	0.01	0.003	0.005	0.003
Sodium	0.05	0.03	0.03	0.03
Potassium	0.002	0.002	0.002	0.002
Copper	0.003	0.005	0.01	0.01
Calcium	0.01	0.005	0.005	0.01
Magnesium	0.005	0.005	0.005	0.005
Manganese	0.001	0.0005	0.0005	0.003
Titan	0.002	0.002	0.002	0.002
$\Sigma$	0.85	0.11	0.26	1.165
$\Sigma$ in oxidized	1.15	0.16	0.47	1.73
Carbon ( T = 20°C in air)	0.2	0.05	0.4	0.5
$\Sigma$ in oxidized and Carbon	1.35	0.21	0.87	2.23
Incombustible residuum in solid phase, T = 800°C, % mass	1.4	0.2	0.9	2.2
pH of 10% suspension in the distilled water	4.0–5.0	3.5–4.5	1.6–1.8	5.5–6.0

Thus, depending on the required purity as well as specific applications demanding advanced properties of DND particles, it is recommended to use DND powders which were further modified (up to a purity level of ‘pure’ DND in Table 2).

For wide variety of applications, it is necessary to prepare DND suspensions or gels in a liquid. A method of DND dispersion for galvanic processes by means of an ultrasound was developed and patented in 1996 [3]. Since standard equipment for such processes was not efficient for obtaining suspensions stable for a long period of time, “New Technologies” developed an original ultrasound disperser. The proprietary method of dispersion of dry DND in water, butyl acetate, acetone, gas and other dissolving liquids resulting in long-lasting stable suspensions and gels had been successfully demonstrated.

In conclusion, ozone purification is considered to be the most optimum production process, since it is most ecologically pure and has optimum level of refining. The production technology of ozone-treated DND is relatively simple and correspondingly has a good balance of price and quality.

## REFERENCES

1. The Copyright Certificate N 2077476 of 20 April 1997, SU N 1833593 A3.
2. V.V. Zhirnov, , O.A. Shenderova, D.L. Jaeger et al. Electron emission properties of detonation nanodiamonds. *Phys. Solid State* **46**, 641 (2004).
3. Patent RU 2088689 C1 priority date 6 February 1996, registered 27 August 1997. The application N 96102094.

## CONVERSION RAW MATERIALS IN INDUSTRIAL PRODUCTION OF ULTRADISPERSE DIAMONDS

T.M. Gubarevich and D.N. Gamanovich

*Scientific Production Joint-Stock Company "Sinta" P.O. Box 59, Minsk, 220082, Belarus*

**Abstract:** A pilot process of UDD chemical purification UDD using a rocket oxidizer of “melange” type with expired storage term was developed and put into practice. The process is based on oxidation of diamond-containing blend by nitric acid solutions in the temperature range of 110–320°C and pressure up to 10 MPa. Methods of preliminary treatment and purification of the oxidizer are developed. The regimes of high-pressure and temperature treatment of diamond-containing mixture with the account of elevated chemical activity of the oxidizer are optimized. Specific impurities in the oxidizer and their behavior at high temperature and pressure are studied, and methods of impurity separation from the desired product are suggested. Corrosion effect of the oxidizer and its products on suggested high-pressure equipment is investigated.

**Keywords:** ultradispersed diamond, chemical purification, barothermic oxidizing, nitrate oxidize, utilization of conversion materials

### 1. INTRODUCTION

The early history of ultradisperse diamonds (UDD) was related to the research and developments for national defense projects [1,2]. Today the detonation synthesis of UDD is considered as an opportunity to utilize military explosives and shells for solving current problems of conversion and ecological safety [3]. In the present work, we have demonstrated that a rocket nitrate oxidizer known as melange can be used as a source of concentrated nitric acid for chemical UDD purification.

## 2. EXPERIMENTAL

The oxidizer includes nitric acid, nitrogen tetroxide  $N_2O_4$  and mixtures on their base. Additives, e.g. corrosion inhibitors, are introduced to improve the melange technological parameters. The additives include halogens and their derivatives, as well as orthophosphoric and sulfuric acids. Some standard compositions of melange are presented in Table 1.

Table 1. Nitrate mélanges.

Mark	$\rho$ , g.cm <sup>-3</sup>	Content, %					
		HNO <sub>3</sub>	N <sub>2</sub> O <sub>4</sub>	H <sub>3</sub> PO <sub>4</sub>	HF	I	H <sub>2</sub> O
27P	1.6105	71.1	27.6	0.10	0.47	-	0.7
20K	1.5942	75.1	21.6	1.25	0.64	-	1.45
20Φ	1.5683	71.6	20.5	0.84	-	-	7.0
H <sub>0</sub>	1.5887	75.2	18.8	-	-	0.11	5.9

As an oxidizer of nondiamond carbon in UDD purification, nitric acid is used in different ways: in high-boiling acid mixtures on the base of  $H_2SO_4$ , in aqueous solutions under barothermic conditions, and as a substance for activation, selective oxidation or additional treatment of diamond-containing soot in a wide range of concentrations and temperatures (up to 100°C) [4–5].

The "Sinta" JS Company has developed and implemented an industrial technology of barothermic UDD purification [6], which is based on the use of aqueous solutions of nitric acid at temperatures of 180–300°C and pressures up to 10 MPa. Nitric acid oxidizes nondiamond carbons to produce carbonic gas and dissolves most noncarbon impurities in the soot. The process of diamond purification at high temperatures takes a short time. The surplus of nitric acid necessary for completing the chemical processes is returned to the work cycle for reuse.

Nitric acid to be used as a raw material in UDD purification should meet two major requirements - a high initial concentration and the absence of limiting impurities. The working range of HNO<sub>3</sub> concentrations is quite wide, 20–90%, but in industrial practice an optimal concentration is about 50 ± 10%. The reaction consumption of nitric acid is 10–12 kg per 1 kg of UDD; the decrease in the HNO<sub>3</sub> concentration due to the reaction water and soot humidity (1.5–2.5 kg/kg of UDD) is 5–10%; the technological waste of the acid during diamond washing is 20–30% of the initial amount. For reuse, therefore, it is necessary to introduce an additional amount of concentrated HNO<sub>3</sub> to compensate for the consumption and to raise the total HNO<sub>3</sub> concentration. Naturally, the higher is the concentration of the initial nitric

acid, the greater are the opportunities for recycling of the solutions (Table 2.).

Table 2. The ratio of the initial (A) to worked out (B)  $\text{HNO}_3$  in the suspension versus the initial  $\text{HNO}_3$  concentration.

Initial concentration of $\text{HNO}_3$ , %		60	82	100
Relative contents in the reactionary suspension, %	A	40–60	30–45	10–30
	B	60–40	55–70	90–70

The nitric acid to be used for barothermic UDD purification should not contain the following impurities:

Table 3. Limitations for impurities in nitric acid.

Type of impurities	Undesirable effect
Halogens and their derivatives Sulphuric acid and sulphates	Corrosion of high pressure equipment
Surplus of higher nitrogen oxides	Risk of pyroforic reaction with titanium
Phosphoric acid, its salts and derivatives	Form insoluble salt with iron
Surplus of soluble nitrates of metals (iron, copper, etc.)	Danger of salt crystallization and clogging of pipelines; formation of insoluble oxides during nitrate thermolysis
Particles of sand, ceramics, silicates, etc.	Contamination of UDD, pipelines and filters

Nitrate oxidizers are corrosion-active substances for many metals and alloys. Aluminum and its alloys as like as ferro-silicon steels, high-alloy chrome-nickel and chromium steels are being considered as a tentatively corrosion-resisting materials. The most serious are the requirements on the corrosion safety of high pressure (HP) equipment made from titanium. Melanges are incompatible with titanium because of the danger of a pyroforic reaction. But when diluted with water down to a total acidity of 30–80%, melange does not cause a significant damage to titanium on moderate heating. Titanium activation in hot solutions of halogen-containing melange has been observed at 70°C and higher. Melange solutions inhibited



by sulphuric acid cause a moderate Ti corrosion at temperatures above 100°C; when inhibited by phosphoric acid, they become corrosion-inactive to Ti in the temperature range of interest (up to 300°C).

An estimation of the corrosion activity of melange solutions has shown that the phosphoric inhibitor and accompanying technological impurities are Ti-inactive in the range of 20–300°C. So the F-20 oxydizer was accepted for barothermic purification of UDD without its preliminary processing. A rated melange volume was mixed with water on cooling with a mild purge by air. The total acidity of the solution was determined, and the nitrate solution was then mixed with a rated doze of diamond-containing soot. The suspension was homogenized and delivered to a set of high pressure flow reactors. The UDD purification occurred at a rate of 40–50 l of suspension per hour at 110–280°C and 8 MPa. The UDD purified and washed from the acid was analyzed for quality. The conditions and the results of the UDD purification by melange solutions are given in Table 4.

Table 4. Barothermic purification of UDD with nitrate oxidizer solutions.

N	Purification conditions			Composition of UDD, %		
	(HNO <sub>3</sub> ), %	M=m(HNO <sub>3</sub> ): m(soot)	V <sub>max</sub> , l/hour	C <sub>tot</sub>	C <sub>ox</sub>	Incombustible admixture
1	70.2	23.4	50	87.4	1.3	8.7
2	61.3	20.6	50	89.0	1.5	8.3
3	55.4	19.8	50	91.2	1.8	7.4
4	50.9	20.5	45	92.2	1.8	7.6
5	47.7	22.1	40	91.4	2.1	6.9

C<sub>tot</sub> – total content of carbon, C<sub>ox</sub> – oxidable carbon

The purification with a melange solution proceeds in a complex way. Nondiamond carbon is oxidized quickly and completely; no etching or excessive oxidation of the diamond surface was observed. However, the content of incombustible impurities was unacceptably high, 6.9–8.7%. The analysis of the ashes showed that these impurities largely consisted of iron and titanium compounds. Insoluble impurities were separated from UDD by a method described in [7] and identified as basic phosphates of iron Fe<sup>II</sup>Fe<sup>III</sup>(OH)<sub>2</sub>(PO<sub>4</sub>) and rutile TiO<sub>2</sub>. The phosphates are formed in the hot zone of the HP reactor. A yellowish deposit is found partly on the vessel walls and the reactor bottom, and it accompanies diamond purification at all stages. Titanium dioxide TiO<sub>2</sub> is a product of corrosion of the titanite equipment. A high TiO<sub>2</sub> content necessitated a deeper insight into the

chemistry of the barothermic process. In particular, it was necessary to define the contribution of nitrose gases and their permissible contents in the mixture during UDD purification.

To control UDD contamination and equipment corrosion, we have designed a method of melange processing illustrated in Figure 1. This method normalizes the acid concentration and distills the concentrated  $\text{HNO}_3$  at atmospheric pressure. Some characteristics of the experimental batches of processed melange are listed in Table 5.

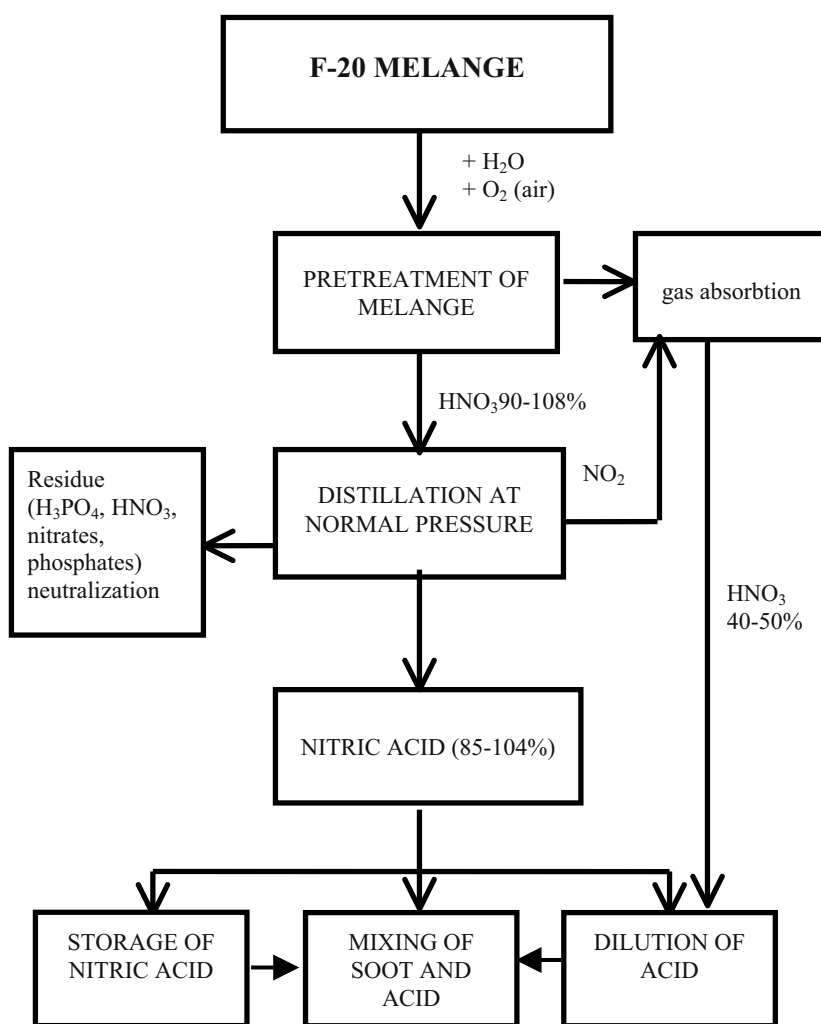


Figure 1. The basic scheme of F-2 melange processing.

Table 5 Characteristics of nitric acid obtained from F-20 melange processing.

Concentration, %	80–105
N <sub>2</sub> O <sub>4</sub> , %	2–8
Fe, g/l	0.001–0.02
PO <sup>4-</sup> , g/l	0.001–0.01
Dry residue, %	0.003–0.055

The experimental batches of HNO<sub>3</sub> obtained from the oxidizer processing were used for the UDD purification at high temperature and pressure. The results are summarized in Table 6.

Table 6. Characteristics of experimental batches of ultradisperse diamonds.

N Sets	Carbon, %			Ash content, %	Fe, %	Ti, %
	total	oxidizable	UDD			
1	84.3	2.1	82.2	4.3	0.6	2.8
2	87.6	1.8	85.8	2.7	0.6	1.7
3	85.9	2.0	83.9	3.1	0.4	2.3
4	87.5	0.4	87.1	3.2	1.9	1.0
5	90.1	2.2	87.9	0.9	0.4	0.04
6	91.2	0.8	90.4	2.3	1.1	0.03
7	87.8	2.3	85.5	1.7	1.0	0.04
8	87.5	1.3	86.2	1.2	0.2	0.04
9	87.1	1.7	85.4	1.2	0.3	0.04
10	84.1	1.8	82.3	1.4	0.4	0.05
11	88.1	1.8	86.3	1.4	0.4	0.04
12	89.2	1.9	87.3	1.5	0.2	0.03
13	87.9	2.3	85.6	1.4	0.3	0.04
14	87.6	0.9	86.7	1.0	0.1	0.03
15	86.6	2.5	84.1	1.7	0.5	0.05
16	87.8	3.4	84.4	1.4	0.5	0.05

The UDD purification of sets 1–4 showed an increased corrosion activity of the reaction mixture to the HP equipment made from titanium. The corrosion was localized in the hot reactor zones, which were in contact with gaseous products, especially at the "waterline". The reactor walls, which were in contact with the liquid, were not affected by additional corrosion. A detailed analysis has led us to the conclusion that corrosion is initiated by halogen derivatives, e.g. fluorine oxides produced in trace quantities from gas corrosion of the fluoroplastic seals.

To control corrosion, we suggested a new design of the HP reactor [8]. Owing to a controlling unit inside the reactor, the linear rate of the flow along the hot walls was increased and the temperature of the reactor wall at the waterline was reduced to a safe level. The seals were removed from the zone of hot gas products. As a result, the corrosive activity of the nitrate mixture was reduced almost by an order of magnitude. The condition of the HP equipment was found to be satisfactory. The content of  $\text{TiO}_2$  impurities in UDD did not exceed 0.05% (sets 5–16, Table 5).

Trace Ti contents of less than 0.05% are a chemical “label” of the barothermic method, no matter whether it uses standard  $\text{HNO}_3$  or processed melange. For the majority of UDD applications, e.g. galvanic cycle technologies, this impurity content is not an obstacle.

Thus, it has been found that surplus nitrogen dioxides in the reaction mixture cannot be a reason for increased corrosion of the equipment. Therefore, the requirements on the removal of oxides from the condensate during melange processing may not be too strict. A  $\text{NO}_2$  content up to 8–10% is technologically acceptable.

The saturation of nitrate solutions with higher oxides and active intermediate products has allowed improving some technological parameters of the barothermic UDD purification, as compared with standard  $\text{HNO}_3$  technologies. The working concentration of nitric acid can be reduced to 25–27%, preserving the UDD purification level at 97–98% during the removal of nondiamond carbon. The weight module of the suspension, i.e. the  $\text{HNO}_3$ : soot mass ratio, can be reduced to 15–17.5. These measures are of great importance for the acid circulation and the reduction in the waste products.

These experimental findings have been used to design a pilot plant for melange processing, meeting the requirements of an enterprise using nitric acid for UDD purification.

### 3. CONCLUSION

We have shown that the rocket oxidizer can be utilized as a source of nitric acid for barothermic purification of UDD to produce high quality diamonds. The process occurs in a standard manner; the presence of nitrogen oxides is not an obstacle because it does not increase the corrosion intensity.

This work was supported by the Joint Chinese-Belarus-American enterprise Shandong Gold Nanodiamonds, Jinan, People's Republic of China.

## REFERENCES

1. K.V. Volkov, V.V. Danilenko, and V.I. Elin. Diamond synthesis from the carbon of explosion products. *Fiz. Goren. Vzryva* **26**(3), 123-25 (1990) (in Russian).
2. G.V. Sakovich, P.M. Brylyakov, A.L. Verestchagin, V.F. Komarov, and V.D. Gubarevich. Production of diamond clusters by explosion and their application. *Zhyrnal Vses. Khim. Obschestva*. **35**(5), 600-02 (1990) (in Russian).
3. V.Y. Dolmatov, V.Y. Zhirkevich, and V.N. Postnov. Ammunition for diamonds. *Dvoine Tehnologii* No. 3, 71-8 (1998) (in Russian).
4. T.M. Gubarevich, I.S. Larionova, N.M. Kostyukova, G.A. Ryzhko, O.F. Turitsyna, L.I. Pleskach, and P.P. Sataev. A diamond purification technology. *Avt. Svid. USSR* No. 1770272 from 22.06.92.
5. T.M. Gubarevich, I.S. Larionova, G.A. Ryzhko, N.M. Kostyukova, and R.R. Sataev. Purification of diamond-containing mixtures. *Avt. Svid. USSR* No. 1830883 from 13.10.92.
6. T.M. Gubarevich, A.P. Korzhenevskii, and D.N. Gamanovich. A commercial system for production of ultradispersed diamonds. *Superhard Materials* No. 4, 14-19 (1998).
7. T.M. Gubarevich and A.P. Korzhenevskii. Method for treatment of Ultradisperse diamond. Application for a patent (Belarus) No. 19981035; 12.17.98.
8. T.M. Gubarevich, A.P. Korzhenevskii, and D.N. Gamanovich. Reactive vessel for purification of Ultradisperse diamond with oxidizers. Application for a patent (Belarus) No. a20020513; 13.06.02.

## ULTRADISPERSE DIAMOND MODIFICATIONS IN THE COMPOSITE GILDING PROCESS

T.M. Gubarevich and L.E. Chernukho

*Scientific Production Joint-Stock Company "Sinta" P.O. Box 59, Minsk, 220082, Belarus*

**Abstract:** Composite electrochemical coatings (CEC) deposited from three basic gilding solutions after addition of 0.1–10 g/l of three UDD modifications were studied. The UDD content of in the CEC was varied in the range of 0.2–0.8% depending on the electrolyte composition, the UDD concentration and modification. Microhardness of the CEC is found to increase by 50–70% due to UDD and the microhardness dependence on the UDD concentration may be monotonic or sharp, depending on the modification used. We suggest an effective electrolyte composition with less than 3 g/l of the best UDD modification. Composite electrolyte is characterized by high stability in exploitation, high colloid stability of UDD zol, and good physical, mechanical, protective, and decorative properties of CEC. The coating has a microhardness of 1.5–1.8 GPa, a relative wear resistance of 1.5–2.3, as compared to samples containing no diamond. An average thickness of the continuous layer (on polished substrate or a glance Ni interlayer) is 0.15–0.2  $\mu\text{m}$ .

**Keywords:** ultradispersed diamond, surface modifications, composite, electroplating, gold-diamond co-deposition, electrochemical coating.

### 1. INTRODUCTION

The use of ultradisperse diamonds (UDD) in electroplating technologies is an illustration of their successful application. Composite electrochemical coatings (CEC) with UDD have a high hardness, solidity, and resistance to wear, corrosion, and atmospheric influences. These properties are due to the changes in the CEC structure, caused by incorporation of nanoparticles in the range from 0.1 to 1%. It is obvious that CEC with uniformly distributed unaggregated diamond particles will have the optimal structure and properties. Both the behavior of UDD particles in electrolytes and the

interaction of the nanodiamond surface with the deposited matrix metal are of practical importance.

The influence of UDD surface properties on the co-deposition of metals and the coating characteristics was reported in [1,2]. Nanoparticles with various diamond-to-nondiamond ratios possess different abilities for co-deposition with nickel, and Ni-UDD CECs differ in the microstructure and physical characteristics, such as wear resistance and hardness. The effect of the surface charge of nanoparticles during the co-deposition with gold was studied in [3]. It was shown that diamond is co-deposited well with gold if the particles and the electrode are oppositely charged. Diamond particles which show essential advantages in electrodeposition with metals over polydisperse mixtures [4] can be separated by fractionation of UDD suspensions.

In the present work, we studied the co-deposition of gold and UDD of three modifications. The samples of UDD chosen for comparative tests differed in the acid-basic properties of the surface and, hence, in the sign and magnitude of the electrokinetic potential, the adsorption of potential-determining ions, and in the colloidal stability in various hydrosol pH ranges. Acidic gilding electrolytes are very convenient model systems for the analysis of diamond behavior in electroplating solutions, because they do not contain polycharged ions, having a strong coagulating effect on diamond particles, or functional organic additives that can be adsorbed on the diamond surface. In such electrolytes, the differences in the UDD surface properties become evident, and their influence on the composition and characteristics of composite coatings can be evaluated.

## **2. METHODS**

The electrodeposition of composite gold coatings containing UDD particles was performed from base electrolytes, whose composition is shown in Table 1. The UDD concentration ranged from 1 up to 10 g/l. The coating was deposited on a polished brass plate. The anodes were platinized titanium plates. The Vickers microhardness of coatings of over 10  $\mu\text{m}$  thick was measured with 25 g loading. The amount of co-deposited UDD particles in the coating was determined by an express integral Coulometric AH-7529 analyzer (Hemel, Republic of Belarus).

Table 1. The composition of experimental electrolytes.

Components of electrolytes	Electrolyte 1	Electrolyte 2	Electrolyte 3	Electrolyte 4
Kau(CN) <sub>2</sub> (on metal)	8–10	8–10	8–12	–
AuCl <sub>3</sub> ×HCl×4H <sub>2</sub> O (on metal)	–	–	–	3–5
K <sub>3</sub> Cyt	12–16	–	160–190	–
KH <sub>2</sub> Cyt	–	100–130	–	–
H <sub>3</sub> Cyt	35–37	–	8–10	–
K <sub>2</sub> HPO <sub>4</sub>	–	–	25–30	–
KH <sub>2</sub> PO <sub>4</sub>	–	–	8–10	–
Trilon B	–	40–60	–	–
K <sub>4</sub> Fe(CN) <sub>6</sub> ×3H <sub>2</sub> O	–	–	–	200
K <sub>2</sub> CO <sub>3</sub>	–	–	–	65
KCNS	–	–	–	100
T, °C	40	30	70	50
i <sub>k</sub> , A/dm <sup>2</sup>	0.5	0.4–1.5	0.4–1.5	0.4–0.5
pH	4.2–4.5	4–5	5.2	10–11

The structure and properties of aqueous suspensions of three UDD modifications are shown in Table 2.

Table 2. The characteristics of UDD aqueous suspensions.

Properties of UDD	UDD modification		
	UD-HP	UD-SO	UD-M
Total carbon C <sub>t</sub> , %	92.2	82.2	91.3
Oxidizable carbon, %	1	21.8	1.2
Ash, %	1.1	1.6	0.9
pH of suspension	6.9	6.3	7.5
Specific surface S <sub>уд</sub> , m <sup>2</sup> /g	246	183.6	292
Electrokinetic potential ζ, mB	-16	-87	+24.9

The electrokinetic and adsorption parameters of diamonds were studied by macroelectrophoresis and acid-basic potentiometric titration in the pH range of 2–12 [5].



### 3. RESULTS AND DISCUSSION

A detailed study of the UDD co-deposition with gold has shown that the structure and properties of the coatings vary nonmonotonically with the diamond concentration in the electrolyte. The total content of carbon  $C_t$  in the coating, which is the sum of the diamond content in the CEC and the background content of carbon in the gold deposit, was used as a characteristic of the composition, while the microhardness was taken to be a complex characteristic of the CEC properties. The relationships between the microhardness and the coating structure and texture, as well as their consumer properties, are well known in electrodeposition technology.

#### 3.1 The diamond content in a coating

The obtained dependences (Figure 1) have bimodal character in considered range of UDD concentration in electrolytes.

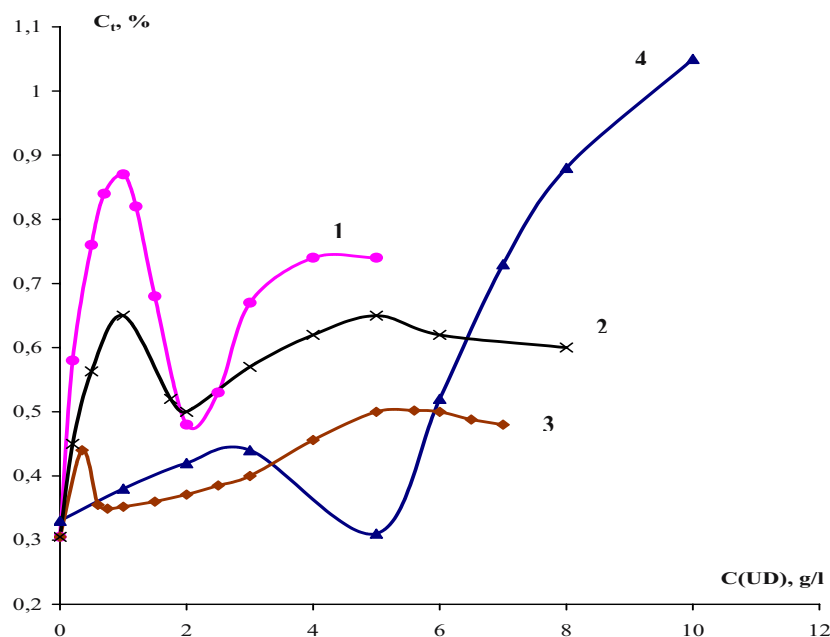


Figure 1. Weight percent of co-deposited particles *versus* the UDD concentration in the electrolyte: 1 - with UD-SO, 2 – with UD-HP, 3 – with UD-M, 4 - with UD-SO.

The first peak relates to the area of low concentrations, its intensity depends on both the electrolyte composition and the type of co-deposited diamond. The second peak is for higher UDD concentrations, whose range is wide. The valley between the two peaks may be deep and narrow (curves 1 and 2) or smeared (curves 3 and 4).

The co-deposition of UDD and gold occurs as a common electrochemical process including random acts of particle impact with the cathode, natural movement and regular embedding of particles in the metal matrix. Diamond nanoparticles may, in turn, be included in the coating as large aggregates or as individual particles, depending on their colloidal state in the electrolyte and at the electrode/electrolyte interface. The rate of the deposition from suspended electrolytes is generally proportional to the so-called particle concentration, which is the number of particles unit volume. Clearly, the UDD concentration will decrease if its nanoparticles aggregate, and then the mobility of the aggregates will become lower than that of individual particles. The way of the disperse phase incorporation in the deposit will change with the degree of UDD aggregation. The dependences shown in Figure 1 illustrate the phenomena of UDD aggregation and coagulation in gilding electrolytes.

In the area of low concentrations, there is no coagulation or it is minimal. The CEC include individual particles, mostly with high mobility. In acid electrolyte 1, the UD-HP and UD-SO particles, whose surfaces have acidic properties and a negative  $\xi$ -potential in the aquatic environment, actively participate in the plating process (curves 1 and 2). This indicates the re-charge of their surfaces due to the adsorption of cations.

The aggregation of UDD particles occurs with increasing electrolyte concentration. As a result, the statistical and kinetic conditions for particle incorporation in the electrocrystal deposit deteriorate, and the UDD content in the CEC is reduced nearly to the background level.

The area of the second peak described the co-deposition of gold largely with aggregated UDD. In this area, the process is sensitive to such factors as temperature, pH, mixing conditions, and some others, which affect the reversible aggregation of lyophobic sols. The stability of the aggregates is insignificant, and UDD is included in the deposit as polydisperse fractal clusters.

The further increase of the UDD concentration in the electrolyte normally decreases the diamond content in the coating. The reason is the formation of fairly strongly coagulated structures (3-D networks immobilizing the UDD particles). The UDD incorporated in the coating represent only fragments of the network destroyed by a continuous electrolyte mixing. In this concentration range, we observe a degradation of many technological

parameters of the gilding process, such as the sedimentation rate, the yield measured by current value, and the decorative properties of the deposit.

### 3.2 Microhardness

The dependence of the coating microhardness on the UDD concentration in the electrolyte supports the assumption about two modes of diamond particle incorporation in the coating. The curves in Figures 2 and 3 also show a bimodal behavior. We will try to understand whether there is a correlation between the CEC structure and hardness if we assume the UDD in the coating to be indeed a combination of individual particles and aggregates.

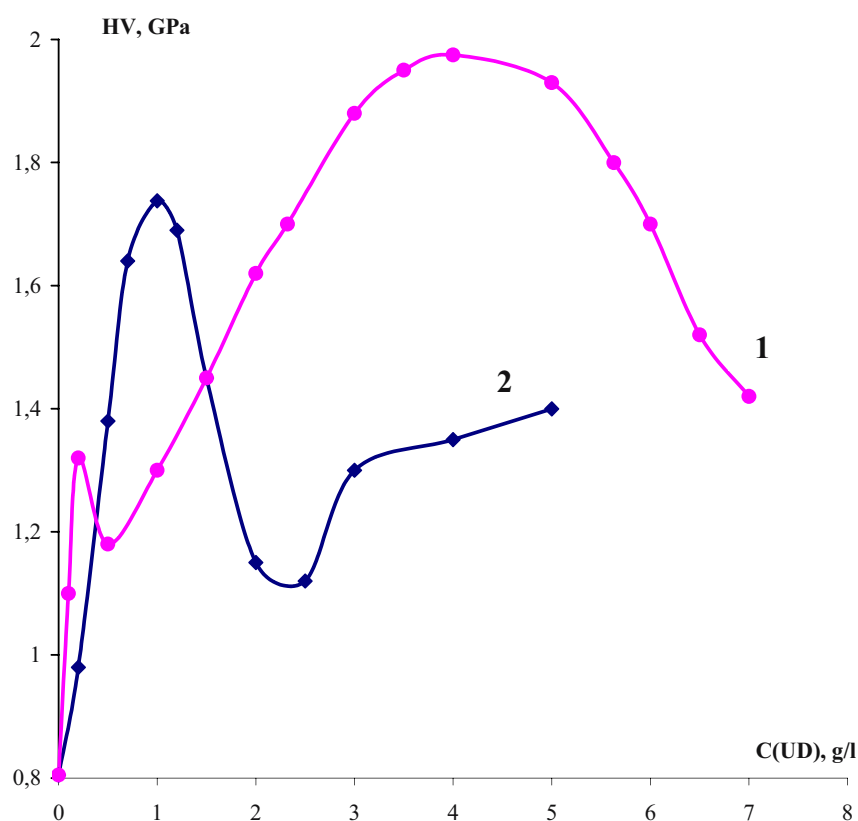


Figure 2. CEC microhardness versus the UDD concentration in the electrolyte: 1 - UD-M particles; 2 - UD-SO particles.

For UD-SO electrolyte 1 (Figure 2, curve 2), the microhardness curve is similar to the respective curve in Figure 1. At first ( $C_{\text{UDD}} \leq 1 \text{ g/l}$ ), there is an effective hardening of the coating. At the 0.5% diamond content in the coating, the microhardness increases by a factor of 2 as compared with the initial characteristic of the deposit in the same bath, indicating a high dispersiveness of the diamond inclusions. At UDD concentrations over 1 g/l, the coagulation deactivates the diamond particles, and the coating depleted in diamond loses most of its hardness properties. The further saturation of the electrolyte with UDD raises the statistical probability of co-deposition; however, the effect of CEC hardening due to aggregates is not as significant as for individual particles.

The coatings deposited from acid electrolytes containing UD-HP give the same microhardness dependences. This provides a high aggregate stability of UD-HP in electrolyte 2 and, hence, a higher microhardness than in electrolyte 3. Figure 3 illustrates the effect of the solution composition on CEC hardness. The same type of nanodiamond in electrolytes 2 and 3, which are compositionally related, shows a qualitative similarity but appreciably different quantitative results on the CEC hardening. For electrolyte 2, the microhardness increases by 0.7 GPa, while for electrolyte 3 the increase is only 0.35 GPa and the strengthening effect decreases fast with increasing UDD content in the electrolyte. There several reasons for this difference but the key ones are: (1) the presence of a strong nonspecific complexing agent, trilon, in solution 2 prevents a fast coagulation of disperse particles by cations; (2) a moderate concentration and a chemical uniformity of auxiliary salts together with low temperature (30° C), at which the deposition from electrolyte 2 occurs, promote the formation of a steady double electric layer of diamond particles.

The modification UD-M is characterized by a positive surface charge and is titrated as a base (Figure 4). In electrolyte 1, the anions act as potential-determining ions for UD-M particles. At low concentrations (0.1–0.2 g/l), they are positively charged and are actively involved in the coating process (Figure 2, curve 1). In the presence of polycharged anions, however, the coagulation processes occur quite actively. In the range of 0.3–3 g/l, the carbon content in the deposit increases only by 0.05% but we observe a fast and "smooth" increase in microhardness. In the 0.3–3 g/l range, the particle concentrations rise but slightly, so the number of individual particles in an average aggregate increases. The UD-M aggregates formed in this range are fragile and break down during the passage through the cathode double layer, increasing the percentage of individual particles and small aggregates over large clusters. Dispersed in the immediate vicinity of the cathode surface, the UDD particles are included in the CEC uniformly, thus providing high

physicomechanical properties of the deposit. The concentration range of 3–5 g/l is characterized by aggregate "hardening" and increased stability. The incorporation of the aggregates in the coating begins to compete with the co-deposition of small and individual diamond clusters. The microhardness growth is slowed down and then starts to decrease rapidly. The UD-M mass concentration of 5 g/l is already so high that the particles form a 3-D network. Under these conditions, the co-deposition of UDD with gold proceeds via the capture of a friable flocculent cluster with its subsequent overgrowth by the electrocrystallizing metal, thereby decreasing the coating strength.

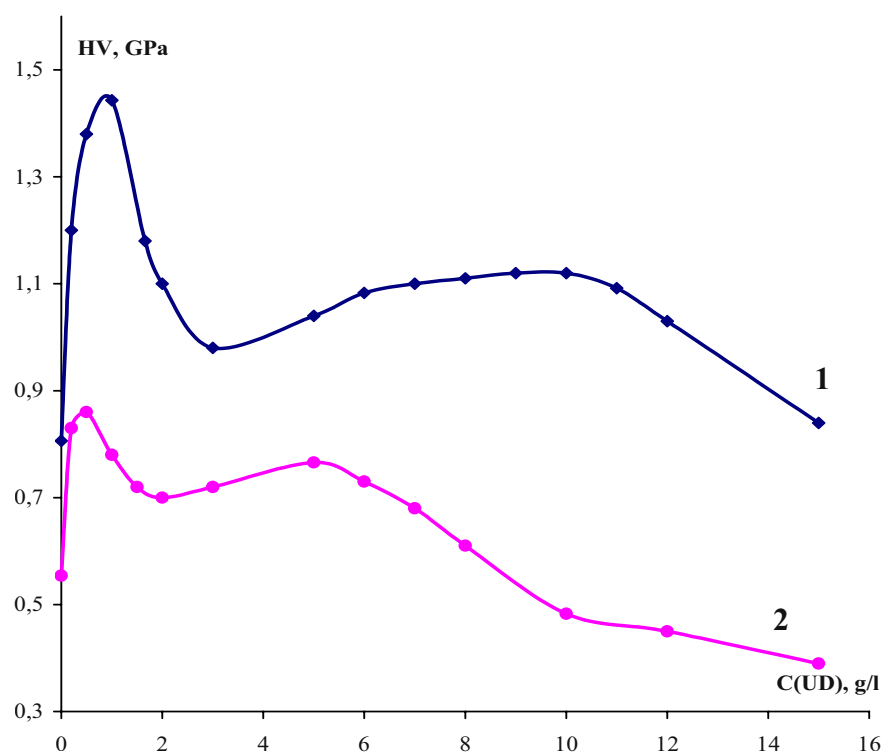


Figure 3. The coating microhardness versus the UD-HP concentration in electrolytes 2 (curve 1) and 3 (curve 2).

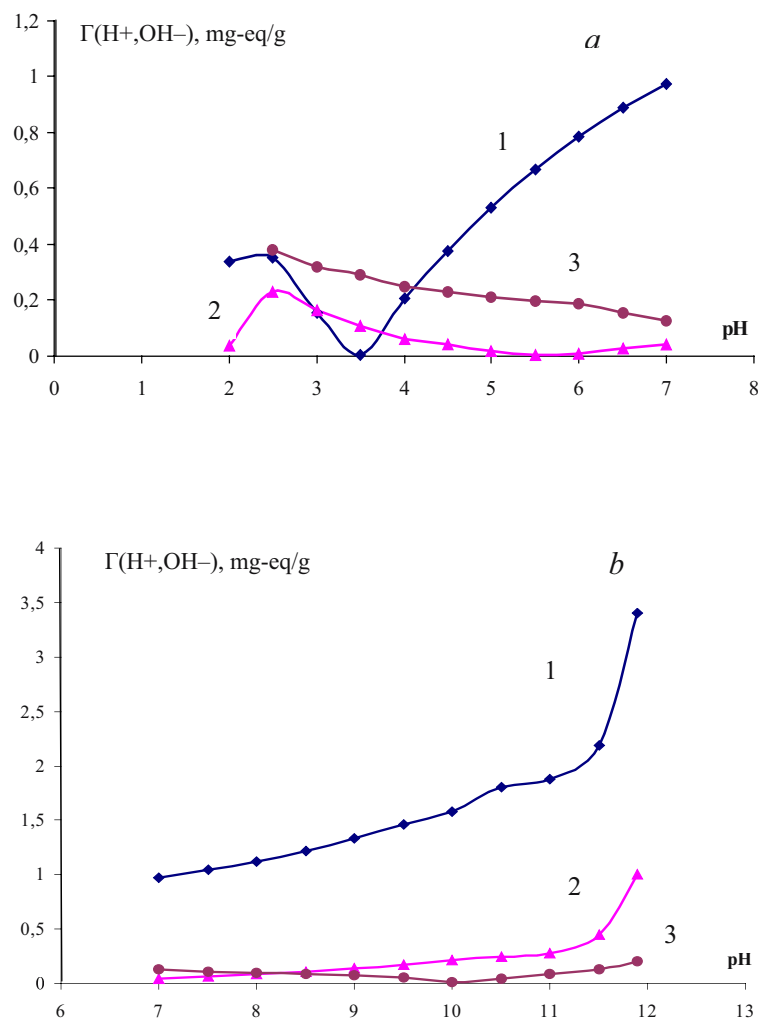


Figure 4. Sorption of potential-determining ions by the diamond surface in the acidic (a) and basic (b) areas for UD-SO (curve 1), UD-HP (curve 2), UD-M (curve 3).

The CEC obtained from solution 4 by using UD-SO give a special kind of dependences (Figure 5). This electrolyte has an alkaline reaction and contains a strong complexing agent, potassium thiocyanate; it is maintained at moderate heating. The UD-SO modification is aggregation-stable in the

pH range of 10-11 and has the  $\xi$ -potential of -87 mV. In the absence of the ion coagulants, the UDD particles are in a nondisperse state up to a concentration of about 3 g/l but their co-deposition with gold is insignificant, about 0.05%. As a result, the microhardness rises only by 0.02 GPa. With increasing UD-SO concentration, the particle aggregate and become incorporated in the deposit only accidentally, partly collapsing in the near-cathode layer, which provides the effect of deposit hardening at 5–7 g/l. Later, flocculent inclusions become dominant, and the coating properties deteriorate together with its appearance.

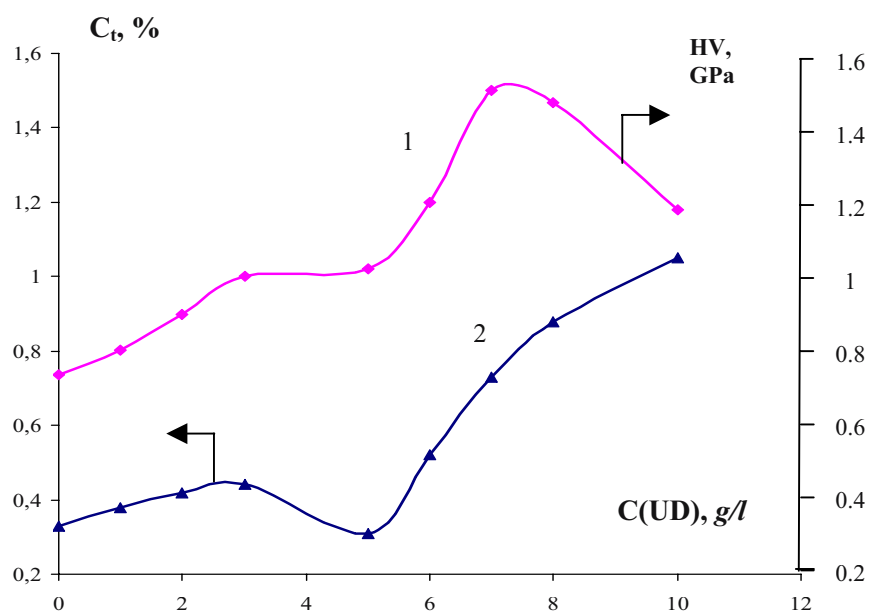


Figure 5. Microhardness (curve 1) and weight percent of co-deposited particles (curve 2) vs. the UD-SO concentration in electrolyte 4.

#### 4. CONCLUSION

The experimental results obtained in the present study allow the following conclusions to be made. First, the co-deposition of gold and nanodiamonds depends, in each electrolyte, on the properties of the UDD surface and the colloidal state. For each UDD modification, it also depends on the composition of the gilding electrolyte, from which a coating is co-deposited. Second, a common characteristic the UDD-gold co-deposition is a

bimodal character of the dependence of the coating structure and properties on the UDD mass concentration in the electrolyte. We believe that this fact reflects the processes of aggregation and concentration coagulation of nanoparticles occurring in actual electrolysis. Finally, the primary inclusion of nonaggregated particles in the coating, as is the case at low UDD concentrations in the electrolyte, is preferable for improving the physicalomechanical properties of the coating and is cost-effective for diamond applications.

This work was submitted under support of the Joint Chinese-Belarus-American enterprise Shandong Gold Nanodiamonds, Jinan, People's Republic of China.

## REFERENCES

1. Yu.V. Timoshkov, T.M. Gubarevich, and I.S. Molchan. Microstructure and wear behaviour of Ni-composite coatings with different types of ultra-dispersed diamond particles. *Surface Modification Technologies*, No. 11, 7-13 (1998).
2. J.V. Timoshkov, T.M. Gubarevich, T.I. Orehovskaja et.al. Properties of composite nickel coatings with various types of ultradisperse diamond particles. *Galvanotechnics and Processing of a Surface* 7(1), 20-26 (1999).
3. F. Wünsche, A. Bund, and W. Plieth. Investigations on the electrochemical preparation of gold-nanoparticle coatings. *J. of Solid State Electrochemistry* 8(3), 209-13 (2004).
4. A.D. Toropov, P.J. Detkov, and S.I. Chuhaeva. Reception and properties of composite nickel coatings with ultradisperse diamonds. *Galvanotechnics and processing of a surface*. 7 (1), 14-19 (1999).
5. T.M. Gubarevich, Z.A. Gotto, and L.E. Chernukho. New modifications of nanodiamonds for composite materials and coatings with given properties. Abstracts of the International symposium "Detonation nanodiamonds: synthesis, properties and application" 2003 July 7-9, St.-Petersburg, p. 84 (2003).



## APPLYING CVD DIAMOND AND PARTICULATE NANODIAMOND

J.L. Davidson and W.P. Kang

*Department of Electrical Engineering and Computer Science, Vanderbilt University, P.O.Box 99 Sta B, Nashville, Tennessee 37235, USA;*

**Abstract:** Nanometer scale diamond tip emitters for cold cathodes are being developed as (a) vertical and (b) lateral diamond vacuum field emission devices. These diamond field emission devices, diode and triode, were fabricated with a self-aligning gate formation technique from silicon-on-insulator wafers using variations of silicon micropatterning techniques. High emission current,  $> 0.1\text{A}$  was achieved from the vertical diamond field emission diode with an indented anode design. The gated diamond triode in vertical configuration displayed excellent transistor characteristics with high DC gain of  $\sim 800$  and large AC output voltage of  $\sim 100\text{ V p-p}$ . Lateral diamond field emission diodes with cathode-anode spacing less than  $2\text{ }\mu\text{m}$  were fabricated. The lateral diamond emitter exhibited a low turn-on voltage of  $\sim 5\text{ V}$  and a high emission current of  $6\text{ }\mu\text{A}$ . The low turn-on voltage (field  $\sim 3\text{ V}/\mu\text{m}$ ) and high emission characteristics are the best of reported lateral field emitter structures. We are also examining particulate nanodiamond for thermal conductivity enhancement of dielectric oils. We have observed that a dispersion of nanodiamond (particle size circa  $< 5\text{ nm}$ ) can increase the overall thermal conductivity of cooling oils such as used in power transformers by over 25%.

**Keywords:** nanodiamond, sensor, field emission devices, electron emission, thermal conductivity

## 1. DIAMOND VACUUM FIELD EMISSION DEVICES

### 1.1 Introduction

Chemical vapor deposited (CVD) diamond or related carbon materials are excellent materials for electron field emitters because of their low or negative affinity (NEA) [1–3] and excellent mechanical and chemical

properties like high hardness and ability to withstand ion bombardment. The NEA property of diamond, unlike other materials, is retained in a residual gas ambient [4–5]. In addition to these properties, diamond has the highest thermal conductivity and can have high electrical conductivity, enabling diamond devices to operate at high temperatures and high power. This makes diamond field emitters potentially advantageous in vacuum microelectronics.

We have fabricated micropatterned diamond pyramidal tips and edge emitters. In this paper we report the field emission characteristics of both types of emitter geometries in a diode configuration at high temperature. Both types of field emitters were fabricated from a silicon substrate utilizing conventional silicon micropatterning and etching techniques [6].

## 1.2 Experimental

The fabrication steps for diamond pyramidal tips and edge emitters are shown in Figure 1. The Si wafer was 500  $\mu\text{m}$  thick. A 0.2  $\mu\text{m}$  thick oxide was then grown on the wafer surfaces. Inverted pyramidal cavities were then etched into the Si substrate using photolithographic patterning and anisotropic etching of silicon with KOH solution. Next a  $\text{SiO}_2$  layer was grown into the mold to produce a well sharpened apex in the inverted pyramidal cavity. Diamond was then grown into the mold using plasma enhanced chemical vapor deposition (PECVD). The PECVD parameters were controlled so as to achieve small but deliberate  $sp^2$  content in the diamond film. Next the back-side silicon and  $\text{SiO}_2$  was etched away and sharpened diamond pyramidal geometries exposed. The diamond film was characterized using scanning electron microscopy (SEM) and Raman spectroscopy. The SEM image of an array of diamond pyramidal tips and edge emitters is shown in Figure 2 and 3 respectively. The tips had a base dimension of  $12 \times 12 \mu\text{m}$ , while the edges had a width of 2  $\mu\text{m}$  and length of 125  $\mu\text{m}$ .

Emission testing was carried out under vacuum at  $10^{-6}$  Torr. The sample, in a diode configuration, was placed on top of a button heater to perform emission measurements at elevated temperatures. A mica spacer 120  $\mu\text{m}$  thick provided the cathode-anode gap. Emission measurements at various temperatures were performed after the vacuum stabilized at  $10^{-6}$  Torr. The current-voltage behavior was recorded to a computer interfaced with the test chamber.

Fabrication of lateral diamond field emission arrays with co-built anode - The fabrication flow chart of the lateral diamond field emitter array with co-built anode is shown in Figure 4. A 1  $\mu\text{m}$  thick  $\text{SiO}_2$  layer was first grown onto the SOI wafer. Conventional photolithography was then performed to pattern

the anode and cathode structures onto the  $\text{SiO}_2$  layer. The exposed  $\text{SiO}_2$  was etched away using BOE exposing the Si below. Next, electrically conductive diamond was preferentially grown on Si using bias enhanced PECVD. Conductivity of diamond was achieved by introducing tri-methyl boron (TMB) gas in the plasma mixture for boron doping. The unwanted diamond that grew on  $\text{SiO}_2$  was lifted-off by etching the  $\text{SiO}_2$  using an HF etch in an ultrasonic bath. The patterned diamond layer was then used as a masking layer to etch Si to get the required spacing between the anode and cathode. The final structure consists of patterned diamond anode and cathode, supported by a Si layer underneath, sitting on the  $\text{SiO}_2$  layer on the Si substrate.

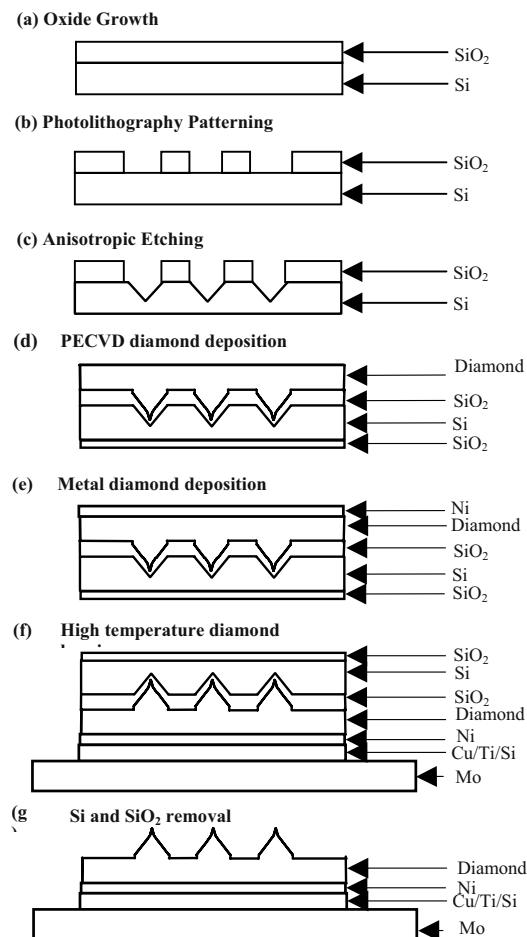


Figure 1 Fabrication sequence of diamond field emitter devices.

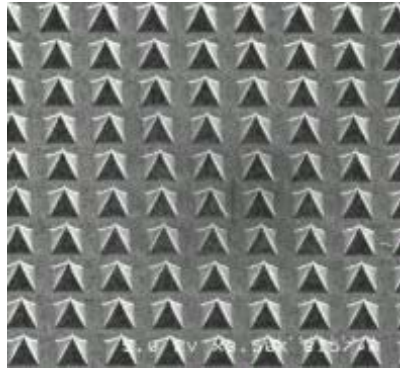


Figure 2 SEM of micropatterned diamond pyramidal tips.

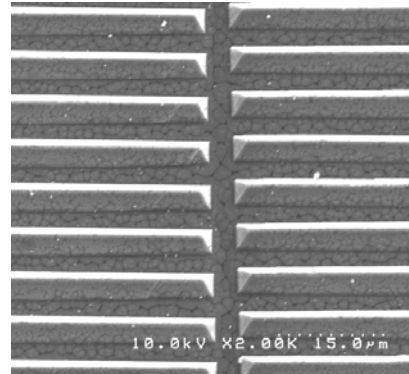


Figure 3 SEM of micropatterned diamond edge emitters.

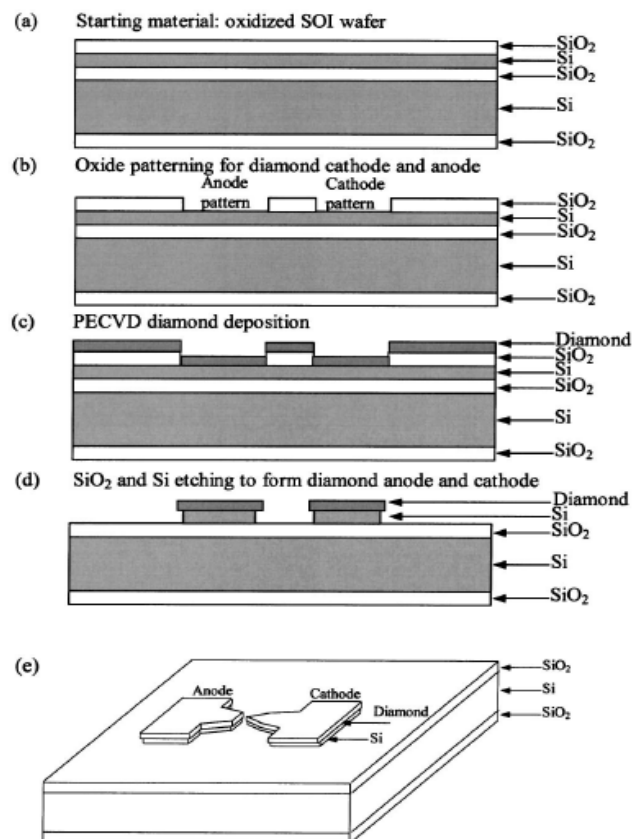


Figure 4 Fabrication sequence for lateral diamond emitter utilizing SOI wafer.

A SEM of the vertical diamond field emission triode is shown in Figure 5. The fabricated diamond emitter has a very sharp apex ( $\sim 5$  nm), surrounded by a self-aligned silicon gate. The diamond cathode is electrically insulated from silicon gate by a  $2\ \mu\text{m}$  thick  $\text{SiO}_2$  layer. Figure 6 shows an SEM of a lateral diamond field emission diode with a four diamond “fingers” configured as a field emission cathode and a diamond anode located  $2\ \mu\text{m}$  laterally away from the diamond fingertips.

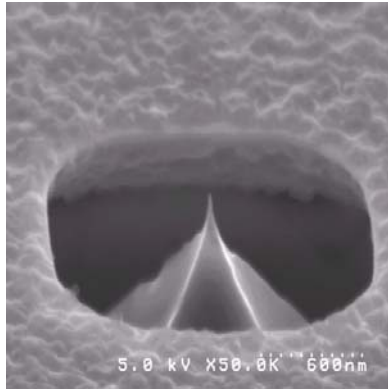


Figure 5 SEM of vertical diamond VFET

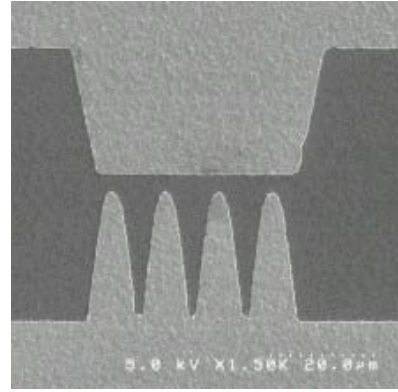


Figure 6 SEM of lateral diamond field emission diode

### 1.3 Results and Discussion

The fabricated diamond emission diodes and triodes were tested for electron emission under vacuum at  $10^{-6}$  Torr. The emission current was recorded as a function of applied voltages. Fowler-Nordheim (F-N) equation was used to analyze the diamond field emission data

$$\ln(I/E^2) = \ln(A \cdot K_1 \cdot \beta^2 / \Phi) - (K_2 \cdot \Phi^{1.5} / \beta)(1/E) \quad (1)$$

where  $K_1$  and  $K_2$  are constants:  $K_1 = 1.54 \times 10^{-6} \text{ A} \cdot \text{eV}/\text{V}^2$ ,  $K_2 = 6.83 \times 10^7 \text{ V}/(\text{cm} \cdot \text{eV}^{3/2})$ ,  $I$  is the emission current,  $\Phi$  is the work function of the emitting surface in eV,  $\beta$  is the geometrical field enhancement factor,  $A$  is the emitting area, and  $E$  is the applied electric field.

The field emission behavior of diamond edge emitter at different temperatures is shown in Figure 7 and the corresponding F-N plot in Figure 8. The emission current again shows insensitivity to temperature changes up to  $300^\circ\text{C}$ . The edge emitters show a turn-on voltage of  $7 \text{ V}/\mu\text{m}$ . The straight line F-N plot in Figure 8 demonstrates that the emission current of this diamond diode conforms to F-N behavior. Figure 9 shows the

emission current vs. temperature characteristic at various applied electric fields. The edge emitter diode reverse characteristics are similar to that observed in tip emitters.

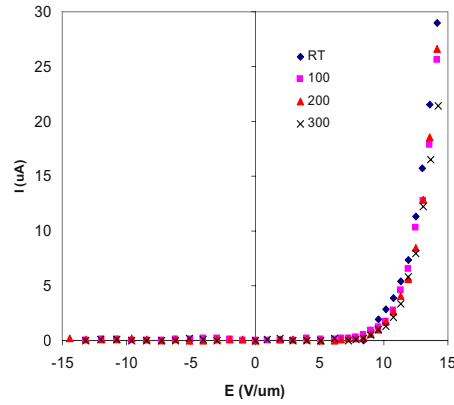


Figure 7  $I$  (microamps) vs.  $-E$  plot of diamond edge emitter for various temperatures.

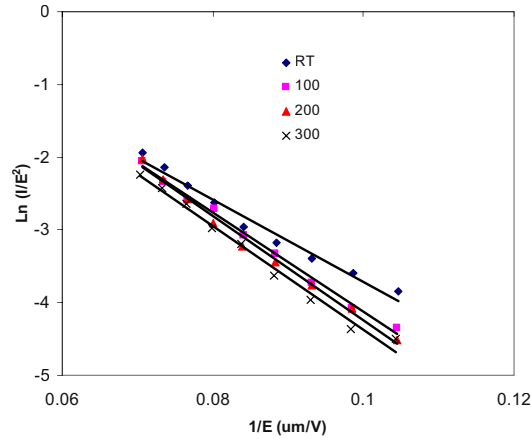


Figure 8  $F-N$  plot of field emission from diamond edge emitters for various temperatures.

The electron emission characteristics, anode emission current versus anode voltage ( $I_a$ - $V_a$  plots), of a self aligned gated diamond triode for various gate voltages ( $V_g$ ) is shown in Figure 10. The electrical characteristics of the diamond triode were characterized in a common emitter configuration. The plots demonstrate the linear and saturation behavior expected of a field-emission transistor. Saturation is seen for various gate voltages at anode voltage above 60 V. The corresponding anode emission current versus gate voltage plots of the diamond triode for various anode voltages is shown in Figure 11. The figure indicates a low turn-on gate voltage of 22 V and a high

emission current of 250  $\mu\text{A}$  at a gate voltage less than 32 V at an anode voltage of 500 V. The triode shows a high DC gain of 800. The DC gain of a triode is defined as

$$\mu = -\frac{dV_a}{dV_g}, \text{ at } I_a = \text{constant} \quad (2)$$

for which, the anode voltage  $V_a$  changes from 150 V to 400 V, while the gate voltage  $V_g$  has to change from 31.7 V to 31.4 V at a constant anode current  $I_a$  of 150  $\mu\text{A}$ . The AC characteristics of the field emission triode show a high AC voltage gain of  $\sim 65$  with a high output voltage of  $\sim 100\text{V}$  as shown in Figure 12. This indicates that the diamond field emission triode provides a high voltage gain when operated as an amplifier and is a very promising prospect for signal amplification applications.

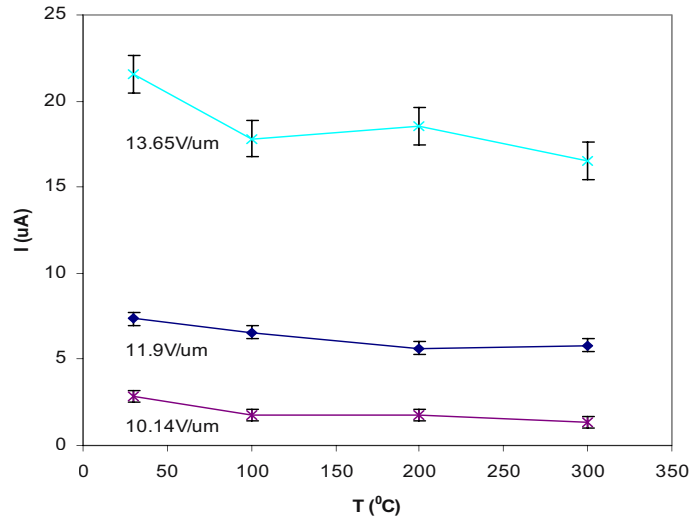


Figure 9 Current-temperature plot of field emission from diamond edges.

The emission characteristic of a lateral diamond field emission diode is shown in Figure 13. The figure shows that the lateral diamond field emitter has a very low turn-on voltage of  $\sim 5\text{ V}$  and a high emission current of 6  $\mu\text{A}$ , from the four diamond fingers, at an anode voltage of 25 V. The anode-cathode spacing is  $\sim 2\text{ }\mu\text{m}$ . Thus the lateral field emitter exhibits a very low turn-on field of  $\sim 3\text{ V}/\mu\text{m}$ , which is the lowest reported values for lateral field emitters [7–9]. Inset of Figure 13 shows the corresponding F-N plot for lateral field emitter. The linearity of this plot confirms the observed current to originate from electron field emission. The shallow slope ( $\sim 9\text{ V}/\mu\text{m}$ ) of

the F-N plot implies that the lateral diamond emitter diode has a high field enhancement factor. This high field enhancement factor is due to the fact that the diamond finger cathodes are made up of very small grain geometries with the smallest grain size of  $\sim 5$  to  $10$  nm as observed from high magnification SEM pictures. High field enhancement factor can also be attributed to the  $sp^2$  content of the film and presence of boron dopant in the diamond film. However it is clear that lateral diamond field emitters exhibit excellent field emission characteristics even prior to any application of special submicron photolithography patterning.

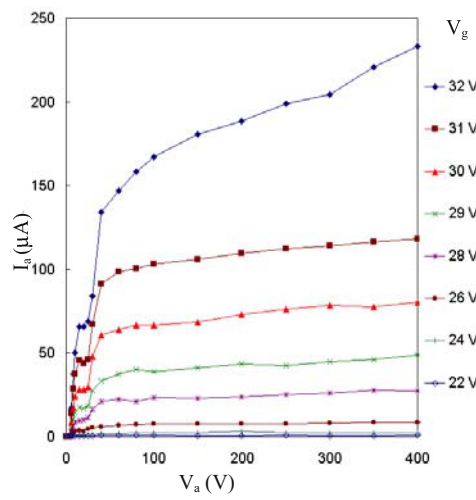


Figure 10.  $I_a$ - $V_g$  plot of self aligned gated diamond triode

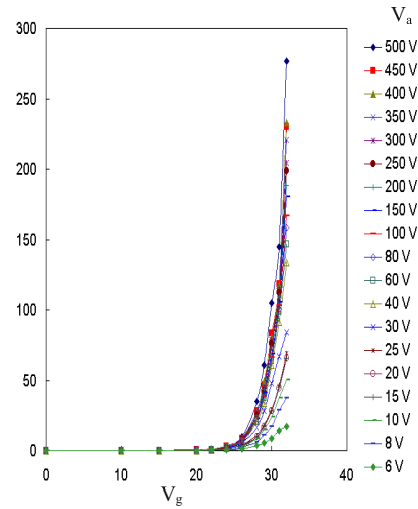


Figure 11.  $I_a$ - $V_g$  plot of self aligned diamond triode.

In summary, a diamond field emission diode operable at high emission current over  $0.1$  A in an indented anode vertical configuration has been demonstrated. A diamond field emission triode with excellent transistor characteristics of high dc voltage gain and large ac voltage amplification is achieved. A lateral diamond field emitter with the lowest turn-on voltage and high emission current has been realized. Diamond vacuum emission diode with high emission current offers great promise in high current and high power applications, while diamond field emission triodes exhibiting comparable characteristics with solid state MOSFETs have promise for potential integrated circuit compatible vacuum microelectronic applications. An efficient lateral diamond field emitter has potential applications in sensors and microelectromechanical systems.



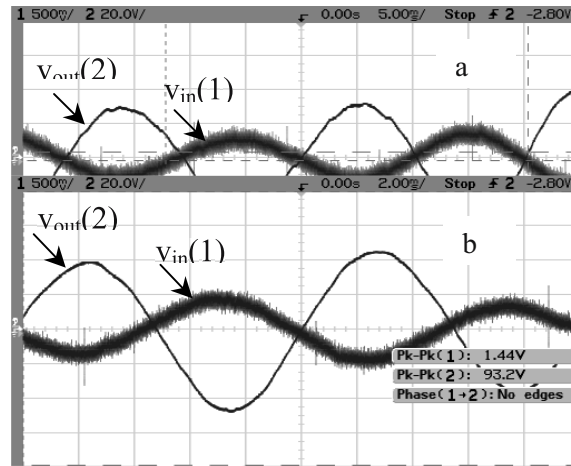


Figure 12 AC characteristics of self aligned vacuum triode: a) AC Characteristics of diamond triode amplifier at  $f = 50$  Hz; b) AC Characteristics of diamond triode amplifier at  $f = 100$  Hz

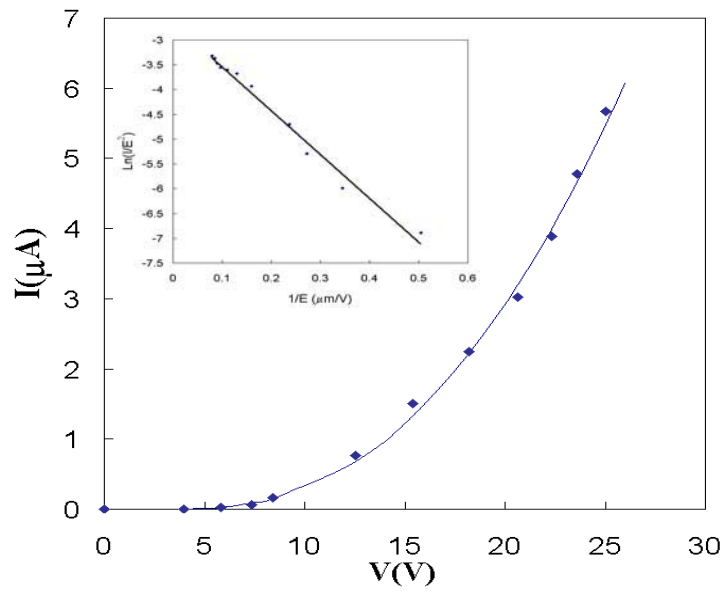


Figure 13  $I$ - $V$  plot of lateral diamond emitter diode. Inset shows the corresponding  $F$ - $N$  plot.

## 2. PARTICULATE NANODIAMOND FOR THERMAL CONDUCTIVITY ENHANCEMENT OF DIELECTRIC OILS

### 2.1 Introduction

The oil used to cool operating transformers has served the industry well, but suffers from excessive maintenance/replacement costs, environmental jeopardy and catastrophic failure incidence directly traceable to *overheating*. Transformer oil itself is a very poor thermal conductor; hence local hot spots lead to cracking of the oil's molecular composition and insulation collapse (corona).

It has long been known that nanosize particles suspended in liquids will increase the overall thermal conductivity (TC) and do so in much more than an additive manner. Several researchers have conducted tests on nanoparticle suspensions of alcohol and found, for example, a 40% increase in thermal conductivity with only 0.3% particle volume fraction—a result that is much higher than that predicted by traditional theory. These results demonstrate the potential of the effect and the shortcomings of macroscopic models applied to nanoscale materials.

In this program, we are using nanometer sized, low cost  $sp^3$  carbon (diamond matrix) particles, i.e., particulate nanodiamond (ND), as an additive to transformer mineral oil (XO) to enhance the TC and dielectric properties of the oil. With the addition of this property enhancing, cost effective dispersion, the TC can be directly raised, without compromising the oil's required electrical insulation, such that failures are suppressed, oil life greatly extended and load boundaries elevated. This could extend transformer life and allow increase to their MVA ratings.

Creating lab volume test mixtures of nanodiamond in transformer oil (NDXO) and conducting TC measurements in apparatus that will be described in the paper, we have observed TC enhancement > 20%. We have established a transformer test bed of two 25KW transformers, one with NDXO cooling fluid, the other a control, operated simultaneously and are collecting operational data, such as temperature-load profiles. The paper will discuss those results.

### 2.2 Discussion

Certainly the concept of additives to cooling media to enhance thermal conductivity (TC) is not new. "Anti-freeze" with water plus ethylene glycol enables cooling systems to be more efficient, not just protected from sub-freezing conditions. The idea that *particles* added to cooling media for cooling efficiency enhancement is less intuitive. Nevertheless, it is a

physically established fact [e.g. 10,11] that very small insoluble particles will significantly enhance the TC of the basic cooling liquid. The physics of this behavior is not the subject of this paper, but the effect arises from quantum principles wherein phonon transfer is enhanced by the “right” combination of particle size and concentration. As this work will show, not only is TC enhanced by particular additives, but the effect is significantly greater than a simple linear addition proportional to weight or volume.

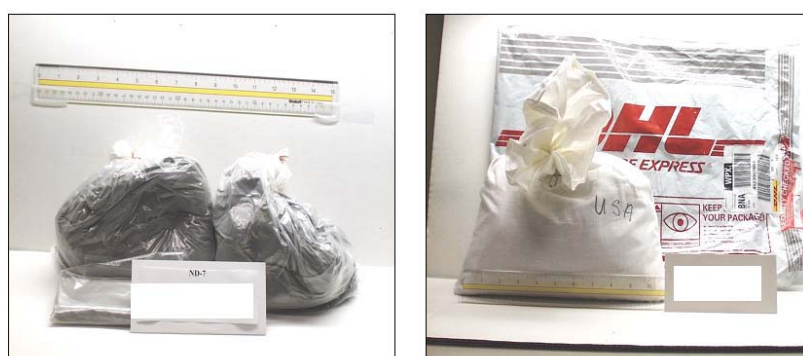


Figure 14 Photograph of nominally 2 Kg bags of nanodiamond.

On that basis, transformer oil is being evaluated for TC enhancement by particulate additives. Nanodiamond (ND) was chosen as the preferred material because it is:

- available in bulk quantities (Figure 14)
- comprised of inert, oil compatible carbon/diamond
- available in true nanoparticle (<20 nm) size distribution
- dispersible and suspendable in transformer oil
- enhances TC of transformer oil (XO)

As regards this latter point, the development program commenced with establishing a process adding the ND to XO such that it was suspended and designing a TC test cell to evaluate the NDXO mixture.

The TC test cell, with  $\sim 1 \text{ cm}^3$  sample volume is a temperature differential calorimeter described in Figure 15 and 16. Testing NDXO samples reveals a significant TC enhancement [13], Figure 17. Given that previous studies by EPRI indicated that TC enhancement of XO of < 5% would result in significant cost savings, these test results led to establishing a “test bed” of two 25KW GE line transformers for comparison purposes. The two transformer system is comprised of a control with only XO in it and an identical test transformer with bulk prepared NDXO in it. Specifics regarding the process for addition of ND to XO are not presented here but involve mixing, sonification and an optional surfactant. Figure 18 illustrates

the thermocouple placement strategy for load behavior evaluation. The system is intended to have the two transformers to load each other; hence the test bed was first characterized to determine there was no difference between the two transformers when they were identically filled with XO only and energized. This initialization test was profiled with time-temperature ( $t, T$ ) data. This directly determined that the same power loads resulted in the same temperature profile and thus the same thermal conductivity. Hence we were assured that when we added an NDXO mixture to one of the transformers (designated beta for NDXO additive and control designated alpha) we would be seeing the effect of the NDXO.

## Static Thermal Conductivity Experiments

- System design
  - Primary and guard heaters
  - High-precision thermistors
  - Cooling plate
- Dimensions
  - ~4 cm heater plate diameter
  - 1 mm liquid gap

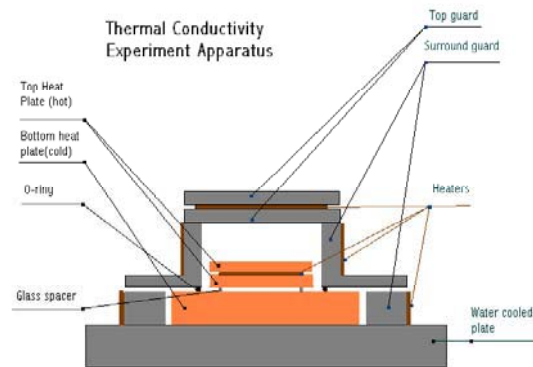


Figure 15 Schematic of thermal conductivity sample test cell.

Approximately 16 gallons of NDXO mixture (the transformer capacity) with ~ 1 % ND by weight, was prepared by “macro-extended” methods used to achieve the TC test samples. This was then added to the previously drained transformer. The control (alpha) and NDXO transformer (beta) were then energized to 15KW. Figure 19 shows the detail  $t, T$  curve of the two transformers, where there are several interesting observations, summarized in Figure 20.

Some striking observations are the significantly cooler lower interior of beta (where the core of these transformers is physically located) and its greater overall temperature differential. Obviously the ND additive has changed the thermal dynamics of that transformer.

### Thermal Conductivity Meter

- Aluminum outer (guard) surfaces
- Copper hot and cold plates
- Allows testing with no field, DC field, AC field



Figure 16 Photograph of thermal conductivity sample test cell.

### Experimental Results

- Have seen increased thermal conductivity up to 25% for suspensions
- Studying electric field effects
- Establishing in-situ substation testing capabilities

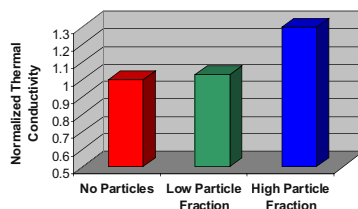


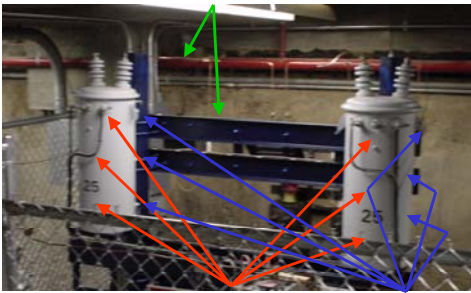
Figure 17 TC Enhancement of transformer oil from addition of nanodiamond.

We have begun thermal modeling of equivalent transformer/cooling fluid configurations. Figure 21 contrasts two hypothetical systems where the overall TC of one has been increased. The thermal profile simulations indicate, for example, a cooler bottom and greater thermal “mixing” than the control. This simulation is still in process and in this subject of a future paper.

In addition to the simulation, further operation and examination of the transformer test bed is proceeding, as is refinement of the NDXO bulk oil preparation process. Partial discharge testing, viscosity measurements and further TC improvement are in process.

Thermocouple Distribution and Layout

Ambient Temperature Thermocouples



Exterior Thermocouples

Interior Thermocouples

Figure 18 Thermocouple placement strategy.

# NDXO Thermal Testing

All Internal Thermocouples

Transformers  $\alpha$  &  $\beta$

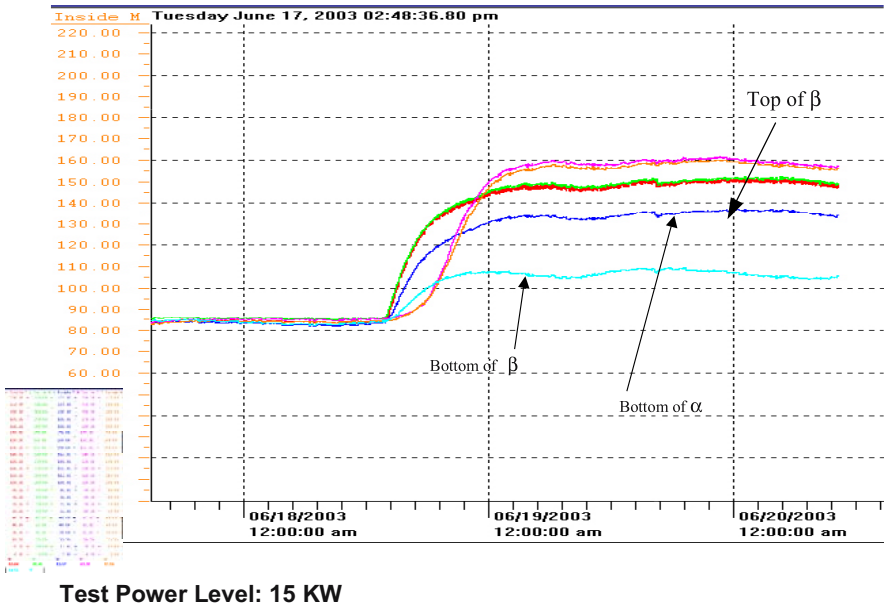


Figure 19  $t, T$  profile of two transformers, one standard, other with NDXO

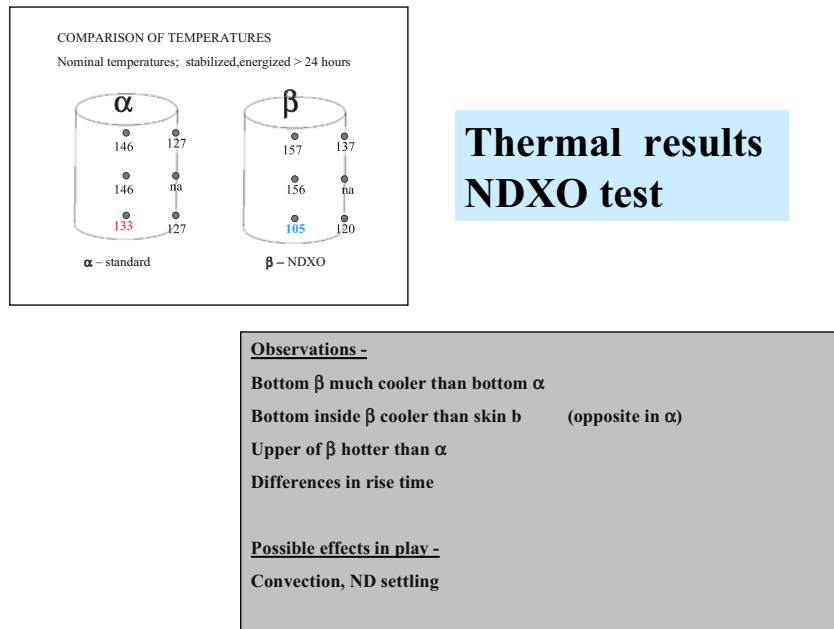


Figure 20 Thermal results of NDXO transformer test.

## Convection Analysis

Stream function formulation; constant temperature boundaries  
 NDXO modeled by increasing conductivity

- XO  
 –  $Pr = 200$ ,  $Ra = 1 \times 10^5$
  - NDXO  
 –  $Pr = 300$ ,  $Ra = 1.5 \times 10^5$
- 
- $Nu = 1.5$
  - $Nu = 1.6$  (more HX)

Prof. G. Walker

Figure 21 Thermal modeling of cooling behavior in transformers

## REFERENCES

1. J. van der Weide, Z. Zhang, P.K. Baumann, M.G. Wemnsell, J. Bernholc, and R.J. Nemanich. Negative-electron-affinity effects on the diamond (100) surface. *Phys. Rev. B* **50**, 5803-06 (1994).
2. I.L. Krainsky, V.M. Asnin, G.T. Mearini, and J.A. Dayton. Negative-electron-affinity effect on the surface of chemical-vapor-deposited diamond polycrystalline films. *Phys. Rev. B* **53**, 7650-53 (1996).
3. I.L. Krainsky and V.M. Asnin. Negative electron affinity mechanism for diamond surfaces. *Appl. Phys. Lett.* **72**, 2574-76 (1998).
4. M.W. Geis, J.C. Twichell, J. Macaulay, and K. Okano. Electron field emission from diamond and other carbon materials after H<sub>2</sub>, O<sub>2</sub>, and Cs treatment. *Appl. Phys. Lett.* **67**, 1328-30 (1995).
5. M.W. Geis, J. Gregory, and B.B. Pate. Capacitance-voltage measurements on metal-SiO<sub>2</sub>-diamond structures fabricated with (100)-oriented and (111)-oriented substrates. *IEEE Trans. Electron Devices* **38**, 619 (1991).
6. W.P. Kang, et al., "Mold Method for Forming Vacuum Field Emitters and Method for Forming Diamond Emitters", U.S. Patent 6,132,278, October 17, 2000.
7. C.S. Lee, J.D. Lee, and C.H. Han. A new lateral field emission device using chemical-mechanical polishing. *IEEE Electron Devices Lett.* **21**, 479 (2000).
8. M.Yun, A. Turner, R.J. Roedel, and M.N. Kozicki. Novel lateral field emission device fabricated on silicon-on-insulator material. *J. Vac. Sci. Technol. B* **17**, 1561 (1999).
9. S.S. Park, D.I. Park, S.H. Hahm, J.H. Lee, H.C. Choi, and J.H. Lee. Fabrication of a lateral field emission triode with a high current density and high transconductance using the local oxidation of the polysilicon layer. *IEEE Trans. Electron Devices* **46**, 1283 (1999).
10. X.W. Wang, et al. Thermal Conductivity of Nanoparticle-Fluid Mixtures. *Journal of Thermophysics and Heat Transfer* **13**(4), 474-80 (1999).
11. J.A. Eastman et al. Anomalous Increased Effective Thermal Conductivities of Ethylene Glycol-based Nanofluids Containing Copper Nanoparticles. *Applied Physics Letter* **78**(6), 718-20 (2001).
12. Yun Wang et al. Thermal conductivity of Nanoparticle Suspensions, Proceedings of the 8th AIAA (American Institute of Aeronautics and Astronautics)/ASME Joint Thermophysics and Heat Transfer Conference, St. Louis, Missouri, 24-26 June 2002, AIAA 2002-3345, p.1-6.



# 31

## ELECTRONIC PROPERTIES AND APPLICATIONS OF ULTRANANOCRYSTALLINE DIAMOND

O.A. Williams<sup>1</sup>, T. Zimmermann<sup>2</sup>, M. Kubovic<sup>2</sup>, A. Denisenko<sup>2</sup>, E. Kohn<sup>2</sup>, R.B. Jackman<sup>3</sup>, and D.M. Gruen<sup>4</sup>

<sup>1</sup> Center for Nanoscale Materials, Argonne National Laboratory, Argonne IL60439, USA

<sup>2</sup> Department of Electron Devices and Circuits, University of Ulm, Ulm, 89069, Germany

<sup>3</sup> Department of Electronic and Electrical Engineering, University College London, WC1E6BT, UK

<sup>4</sup> Materials Science Division, Argonne National Laboratory, Argonne IL60439, USA

**Abstract:** Ultrananocrystalline diamond (UNCD) is a 3–5 nm grain size material with many of the properties of diamond. Whilst intrinsic UNCD films display a mild *p*-type characteristic with high resistivity, the addition of nitrogen to the gas phase during deposition renders the material *n*-type with low resistivity and activation energy. Hall effect measurements as a function of temperature show that this conductivity mechanism is semi-metallic, with the carrier concentration decreasing very gradually with decreasing temperature. Increasing the nitrogen content in the gas phase during deposition results in higher carrier concentrations in the deposited films and lower activation energies. The carrier mobilities of the films are limited by the grain size of the films. A prototype heterostructure diode is demonstrated, combining single crystal and ultrananocrystalline diamond.

**Keywords:** Hall effect, *n*-type conductivity, diamond, nanocrystalline

### 1. INTRODUCTION

One of the key limitations in diamond electronics is the lack of a shallow electron donor. *N*-type doping has been achieved with phosphorus, and *p-n* junctions have been realized as proof of principle, but the resulting activation energy is 0.6 eV [1]. This activation energy results in highly

inefficient doping at room temperature. Phosphorus doping has only been achieved on {111} diamond substrates which are prohibitively expensive, of small size and difficult to polish. Ultrananocrystalline diamond (UNCD) films are grown from a hydrogen poor plasma, 99% Ar and 1% CH<sub>4</sub>, rather than the conventional 99% H<sub>2</sub>, 1% CH<sub>4</sub> plasmas associated with single crystal and microcrystalline diamond growth. These hydrogen poor plasmas contain a high concentration of carbon dimer (C<sub>2</sub>) and emit a strong green glow. The resulting films are nanocrystalline with no columnar structure due to very high re-nucleation rates [2]. This is in stark contrast to hydrogen based diamond growth plasmas, which grow columnar structured films with grain size proportional to thickness. By the addition of nitrogen into the plasma, the discharge glows white and then violet with increasing nitrogen, and the conductivity increases. This conductivity has been characterized as *n*-type and this is the topic of this paper.

## 2. EXPERIMENTAL METHODS

UNCD films were grown on {100} type Ib diamond in an microwave plasma enhanced chemical vapour deposition system with a 99% Ar and 1% CH<sub>4</sub> basic gas phase. The type Ib diamond was thoroughly oxidized before deposition and its resistivity exceeded the capabilities of the measuring apparatus. For the growth of conductive films, increasing amounts of nitrogen gas was exchanged for the argon precursor, i.e. for a 20% nitrogen concentration, the gas phase was 79% Ar, 20% N<sub>2</sub> and 1% CH<sub>4</sub>. UNCD films grown with 0 to 20% nitrogen in the gas phase were characterized.

For electrical conductivity and Hall measurements, Au contacts were thermally evaporated in the van der Pauw configuration at a base pressure lower than  $2 \times 10^{-7}$  mbar. The samples were then mounted into a He atmosphere based cryostat and wire bonded with silver paint onto the gold contacts. The air in the cryostat was then exchanged with high purity helium gas. The ohmic nature of the contacts was confirmed by I-V measurements at all temperatures before subsequent Hall effect and conductivity measurements.

Hall and resistivity measurements were performed in a Lakeshore 7504 Hall Measurement System. The magnetic field was swept between  $\pm 1$  T under a constant excitation current, the magnitude depending on the maximum possible obtainable within the current source compliance (Keithley 224), or limited to reduce sample heating. This procedure is essential when measuring samples with significant offset voltages, a result of low conductivity and uniformity. Figure 1 illustrates the problems associated with large offset voltages.

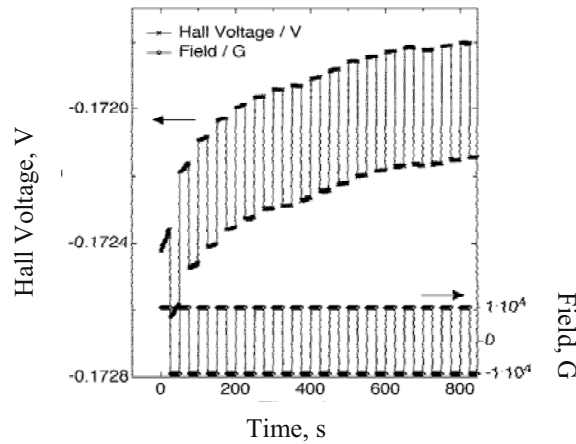


Figure 1. Example Hall measurement at 297K.

It can be seen that as the field is periodically reversed, the voltage is modulated around a non constant background. The magnitude of the oscillation generated in the voltage by the magnetic field periodicity is twice the Hall voltage. The background drift is due to the variation in the offset voltage against time. This is due to temperature fluctuations (which are generally small and of a low frequency), photo effects and contact drift. The background drift at the beginning of the measurement can be seen to be much greater than after  $t = 600$  s, this is due to the initial decrease in sample conductivity after placing the sample in the dark.

It should be noted that the field is in fact not reversed instantaneously as shown in the figure. Data points during the field reversal are discarded for clarity, thus a square wave in field and voltage is observed. The phase of this wave determines carrier type, i.e. voltage and field in phase as above signifies *n*-type conductivity whereas voltage and field  $180^\circ$  out of phase would constitute *p*-type conductivity. This was confirmed by measuring *n* and *p*-type silicon and boron doped, *p*-type diamond.

Amorphous and disordered materials have been known on occasion to yield the opposite carrier type by Hall effect rather than the true carrier type. This phenomenon is termed the “sign anomaly”, and is infamous in amorphous silicon [3]. In the above case, Hall polarities were confirmed by Seebeck or thermal power measurements. The sign anomaly is more often found in amorphous materials such as *a*-Si with grain sizes  $> 3$  nm and mobilities  $> 10^{-1} \text{ cm}^2 \text{ V}^{-1} \text{ s}^{-1}$  [4].

The above procedures were run at each temperature point between 40 and 350K for extended durations. The UNCD films conductivity values were measured by the van der Pauw method for conformal mapping.

A heterostructure diode was fabricated using single crystal *p*-type diamond and *n*-type UNCD. The mesa structure formed by RIE is detailed in the results section.

### 3. RESULTS

Figure 2 shows van der pauw conductivity as a function of temperature for the four UNCD films grown with systematic nitrogen concentrations. It can be seen that at room temperature, the conductivity values for each film increase with the nitrogen concentration in the gas phase. These values increase from  $< 10^{-1} \Omega^{-1}\text{cm}^{-1}$  for no nitrogen in the gas phase to  $> 10^2 \Omega^{-1}\text{cm}^{-1}$  for 20% in the gas phase. In fact the 0% Nitrogen sample has a higher conductivity than usual due to a high residual nitrogen concentration in this reactor. UNCD films can be grown orders of magnitude less conductive in reactors with lower base pressures.

As the films are cooled, all become less conductive. However, this effect is much more significant on the films grown with lower nitrogen concentrations. This effect has been seen before, and films grown with nitrogen concentration greater than 10% have conductivity values that are relatively temperature insensitive. The maximum conductivity measured here was  $400 \Omega^{-1}\text{cm}^{-1}$ .

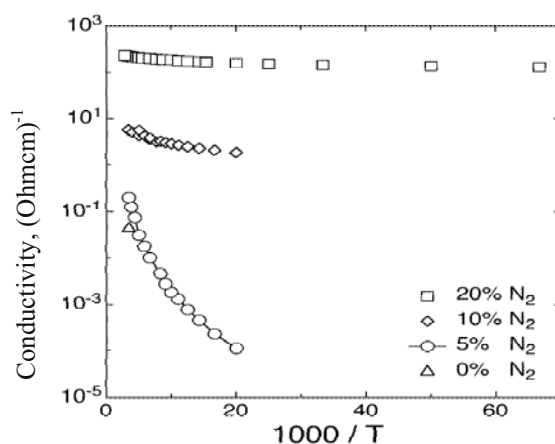


Figure 2. van der Pauw conductivity of UNCD films grown with nitrogen.

Figure 3 shows carrier concentration as a function of reciprocal temperature as determined from the aforementioned Hall effect procedure. It was only possible to determine the carrier concentration of the samples grown with 10% nitrogen in the gas phase and above. Below this critical concentration, no hall voltage was determinable from the hall offset background.

As the temperature is reduced, it can be seen that the carrier concentrations of both films reduce very gradually, with the 10% nitrogen sample decline being more pronounced than the 20% nitrogen sample. The 20% sample has a carrier concentration very near to  $10^{21} \text{ cm}^{-3}$  at room temperature, which indicates semi metallic behaviour. The carrier concentration of the 10% nitrogen sample is also very high, but almost two orders of magnitude lower at  $2 \times 10^{19} \text{ cm}^{-3}$ . Hence, both samples display very high carrier concentrations, the carrier concentration being higher for samples grown with higher nitrogen concentration within the gas phase.

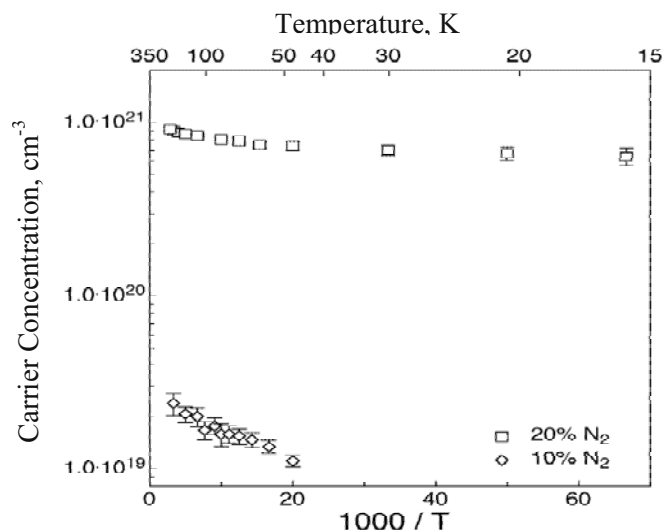


Figure 3. Carrier concentration as a function of reciprocal temperature.

This conductivity behaviour cannot be characterized by a single activation energy. From the above resistivity and conductivity data it is possible to derive the carrier mobility and this is plotted in Figure 4 as a function of reciprocal temperature. As expected, the mobility values are low and rather similar in both films.

Upon cooling, the mobility values reduce slightly in both samples, but more drastically in the 10% nitrogen sample. At 50K the mobility in the 10%

becomes too low to measure and Hall effect is not resolvable below this temperature.

A prototype diode has been fabricated by utilizing a heterostructure architecture. This device structure is shown in Figure 5. In this structure, a single crystal Type Ib diamond is used as a substrate. Highly conductive boron doped diamond is homoepitaxially grown on top to act as an electrical contact. Intrinsic single crystal diamond is homoepitaxially grown on top of this layer as the blocking region of the device. The last layer is highly conductive *n*-type UNCD.

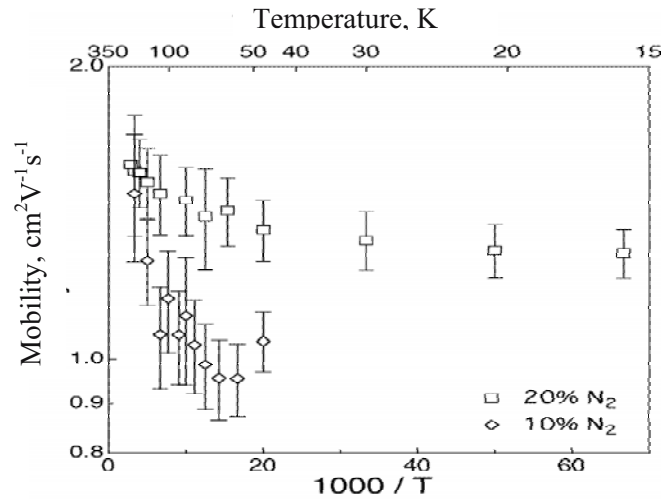


Figure 4 Carrier mobility as a function of reciprocal temperature.

This heterostructure sandwich was mesa etched to obtain access to the  $p^+$  layer via RIE, the final structure is pictured on the right of Figure 5. Thus the  $n^+$  UNCD formed one electrode and the  $p^+$  boron doped layer the other. The size and shape of the structure is a  $30\text{ }\mu\text{m}$  dot UNCD/intrinsic layer sandwich on the  $p^+$  layer.

The I-V characteristics of this device are shown in Figure 6. It can be seen that this device shows almost ten orders of rectification at 20 V. The reverse bias leakage is very low and the forward bias current is limited by the series resistance of the diode. This series resistance originates from the high resistance of the intrinsic diamond layer and this can be improved by reducing its thickness. The thickness of the UNCD also contributes to this resistance but the effect is less dramatic as it is highly conductive.

This device has been operated up to  $1000^\circ\text{C}$ , where the reverse bias current increases due to parasitics related to the quality of the intrinsic layer. At lower temperature ranges (around  $350^\circ\text{C}$ ), the device has similar

performance to room temperature, and hence the high temperature reverse leakage is due to activated defects in the single crystal intrinsic diamond. Due to the all carbon nature of the device, performance resists degradation as a function of time or temperature cycling.

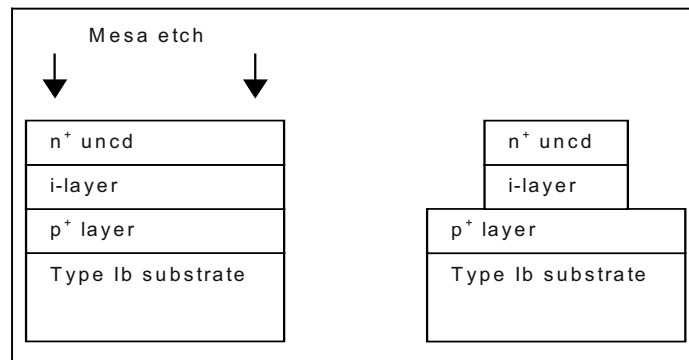


Figure 5. Heterostructure diode design.

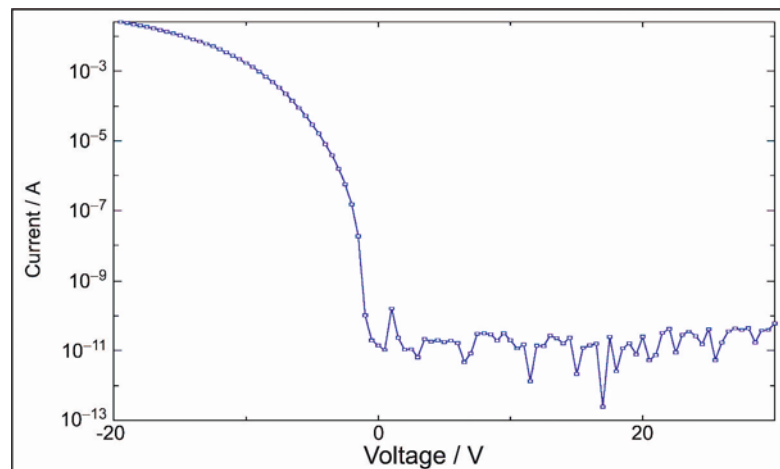


Figure 6. I-V characteristics of heterostructure diode discussion.

The above data shows that nitrogenated UNCD is *n*-type. However, it must be emphasized that the conductivity of this material is not due to a shallow donor beneath the conduction band minimum. Nitrogen forms a very deep donor level in single crystal diamond [5], and also forms complexes with vacancies [6]. None of these defects result in shallow donor levels in diamond, and nitrogen is generally considered detrimental to electronic grade diamond growth. The origin of the conductivity in *n*-type UNCD cannot be described by conventional dopant theory, and hence any

explanation of this effect must include the levels within the gap. In Figure 2, the conductivity behaviour observed has been reported before [7]. In both cases, the samples grown with less than 8% N<sub>2</sub> in the gas phase show a conductivity mechanism dominated by hopping. The conductivity of the films increase with nitrogen addition to the gas phase, and this behaviour is reminiscent of nitrogenated ta-C and other DLCs [8]. Undoped UNCD has a predicted Fermi level position near the valence band maximum [9], and this has been confirmed by Seebeck measurements. Undoped ta-C also shows slight *p*-type conductivity, and this is thought to be due to a structural defect in the carbon network [10]. The grain boundaries of UNCD represent a significant structural defect, and as they add up to 10% of the film, they could be responsible for the *p*-type nature of the as grown films. The activation energies of as deposited UNCD and ta-C are also similar, around 0.3eV for UNCD and 0.2–0.22 eV [11] for ta-C. Unlike single crystal diamond, UNCD has a high density of states within the bandgap due to  $\pi$  bonding at the grain boundaries. In ta-C, the electronic properties are dominated by  $\pi$  bonding as the energy spacing between  $\pi$  -  $\pi^*$  transitions is generally much lower than  $\sigma$  -  $\sigma^*$  transition [12]. Thus it is reasonable to assume a similar effect is the cause of what is observed here, that is, conductivity is increased by the increased  $sp^2$  fraction of nitrogenated films at the grain boundaries, and this has been predicted by density functional calculations [9]. Higher  $sp^2$  levels have been observed in films grown with nitrogen in the gas phase by NEXAFS [13]. It should however be noted that the carrier mobility of *n*-type UNCD is significantly higher than that of ta-C, and this may be related to the lower content of  $sp^2$  bonding and disorder in UNCD. The thermal stability of UNCD is also vastly superior to ta-C, which is again probably related to its higher crystallinity. In the case of ta-C, when nitrogen is added to the gas phase, the Fermi level shifts towards the conduction band, but the main cause of an increase in conductivity is the high density of states within the gap [11,14]. Thus, for low nitrogen levels, the conductivity mechanism can be explained by a hopping transport mechanism. At higher nitrogen levels (5-10%), a CN alloy is formed and the optical gap drops significantly. It is possible to correlate the conductivity of ta-C films with  $sp^2$  fraction, with conductivity increasing with increasing  $sp^2$ . Again, this is similar to UNCD where the transparency and conductivity are inversely related, conductivity and  $sp^2$  grain boundary concentration directly related. At high nitrogen content in the gas phase, the optical gap also drops considerably. Thus the conduction of UNCD is expected to be almost entirely within the grain boundary region. Higher nitrogen concentrations during growth lead to higher  $sp^2$  fractions at the grain boundaries due to increased widths. At very high concentrations this leads to a substantial morphology change where the grain boundaries expand [15]. These grain



boundaries show a higher conductivity from TEM contrast imaging, and thus are the dominant region of carrier transport within these films. Nitrogen is considerably more likely to be incorporated into the grain boundaries than the bulk [9]. From the nitrogen levels present from the gas phase and the volume fraction of grain boundary material ( $> 10\%$ ), it is possible that the grain boundary composition is some kind of amorphous CN or nitrogenated ta-C material. It must be emphasized that this does not mean that UNCD is fundamentally graphitic, and amorphous CN would not explain the high mobility recorded. Thus the conductivity mechanism of nitrogenated UNCD is a grain boundary mechanism involving states within the band gap. This results in a very high carrier concentration and low mobility. Thus this material is semi metallic and cannot be used in applications where modulation or depletion are required at reasonable voltages. This rules out most active device applications. However, this material has been shown to be a highly effective electrochemical electrode, and the heterostructure diode expands on this mode of operation. The heterostructure diode shown in figure 6, is the first all carbon schottky type contact. Whilst it is tempting to think of this device as a pn junction, from the above transport data it is obvious that this is not the case. The highly nitrogenated UNCD (15%) used in this case, has a very high carrier concentration and high density of states within the gap and is hence semi metallic. Thus, in the structure in Figure 5, the UNCD actually acts as though it was the metal in a metal semiconductor contact, or schottky contact. The principal advantage of this structure is that is an all carbon carbon interface, that is UNCD - single crystal diamond interface. This means that although there are likely to be many states at the interface due to the small grain size of the UNCD, the structure should be highly stable. The temperature stability of this device is highly impressive. Operation at  $1000^{\circ}\text{C}$ , and repeated temperature cycling show that this device has real application in harsh temperature environments. In fact, the principle problem utilizing this device will be in the packaging an electrical contacts to the outside world. As the material is fundamentally diamond, it will be able to withstand extreme environments such as high temperatures (as mentioned above), high radiation, acidic, basic etc, any condition which diamond is able to withstand. It would not be possible to achieve this with *n*-type ta-C, due to the low thermal stability of the material. The operating regime demonstrated here was unobtainable within the field of electronics until now.

#### 4. CONCLUSIONS

Ultrananocrystalline diamond is slightly *p*-type as grown. As nitrogen is added, this material becomes *n*-type with very shallow activation energy. The origin of this conductivity is related to disorder and  $\pi$  bonding at the grain boundaries, which introduce states within the gap and band tails, resulting in high carrier concentrations and low mobilities. High temperature operation of a heterostructure diode utilising *n*-type UNCD as an electrode has been demonstrated.

#### REFERENCES

1. S. Koizumi, et al. Growth and characterization of phosphorus doped *n*-type diamond thin film. *Diamond and Related Materials* **7**, 540 (1998).
2. D.M. Gruen. Nanocrystalline diamond films. *Annual Review of Materials Science* **29**, 211-59 (1999).
3. C.E. Nebel and R.A. Street. Hall Experiments and Interpretation in a-Si-H and a-SiC-H. *Journal of Non-Crystalline Solids* **166**, 449-52 (1993).
4. C.E. Nebel, et al. The sign of the Hall effect in hydrogenated amorphous and disordered crystalline silicon. *Philosophical Magazine Letters* **74**(6), 455-63 (1996).
5. G. Davies. *The Optical Properties of Diamond*. New York, USA: Marcel Dekker Inc, 1977.
6. G. Davies et al. Vacancy-Related Centers in Diamond. *Physical Review B* **46**(20), 13157-70 (1992).
7. S. Bhattacharyya et al. Synthesis and characterization of highly-conducting nitrogen- doped ultrananocrystalline diamond films. *Applied Physics Letters* **79**(10), 1441-43 (2001).
8. B. Kleinsorge, et al. Influence of nitrogen and temperature on the deposition of tetrahedrally bonded amorphous carbon. *Journal of Applied Physics* **88**(2), 1149-57 (2000).
9. P. Zapol et al. Tight-binding molecular-dynamics simulation of impurities in ultrananocrystalline diamond grain boundaries. *Physical Review B* **65**(4), 045403 (2002).
10. C. Arena et al. Electronic properties of tetrahedral amorphous carbon investigated by scanning tunneling microscopy. *Journal of Applied Physics* **85**(3), 1609-15 (1999).
11. V.S. Veerasamy et al. Nitrogen Doping of Highly Tetrahedral Amorphous-Carbon. *Physical Review B* **48**(24), 17954-59 (1993).
12. J. Robertson. Electronic and atomic structure of diamond-like carbon. *Semiconductor Science and Technology* **18**(3), S12-S19 (2003).
13. J. Birrell et al. Bonding structure in nitrogen doped ultrananocrystalline diamond. *Journal of Applied Physics* **93**(9), 5606-12 (2003).
14. V.S. Veerasamy et al. Electronic density of states in highly tetrahedral amorphous carbon. *Solid-State Electronics* **37**(2), 319-326 (1994).
15. J. Birrell et al. Morphology and electronic structure in nitrogen-doped ultrananocrystalline diamond. *Applied Physics Letters* **81**(12), 2235-37 (2002).

## THERMOELECTRIC EFFECT IN FIELD ELECTRON EMISSION FROM NANOCARBON

A.Ya. Vul', E.D. Eidelman, and A.T. Dideikin

*Ioffe Physico-Technical Institute, 26 Polytechnicheskaya st., St Petersburg 194021, Russia*

**Abstract:** We suggest a model of field emission from nanocarbon materials, which accounts for the electron drag by ballistic phonons through the temperature gradient region of the emission center. The model does not require additional assumptions of a special energy structure of the emission center. The numerical calculations made within this model agree well with available experimental data.

**Keywords:** nanocarbon, nanodiamond, nanographite, electron field emission, thermoelectric effect, drag effect, ballistic phonon

### 1. INTRODUCTION

In the past decade, there has been much interest in the study of field electron emission (FEE) in various carbon nanostructures in the hope to make a field-emission cathode which could provide an electron current density of about  $10^3 \text{ A}\cdot\text{cm}^{-2}$  at electric fields less than  $10^4 \text{ V}\cdot\text{cm}^{-1}$  and operate in a relatively low vacuum of  $10^{-6}$  Torr. However, the fundamental nature of FEE in carbon nanostructures still remains unclear, which is an obstacle to reaching these parameters and choosing an optimal carbon emitter design.

We suggest a novel approach to designing field electron emitters, based on a theory, which takes a proper account of the thermoelectric effect of phonon drag in a nanocarbon structure [1]. In this approach, the emission is considered to be due to processes occurring in the graphite-like ( $sp^2$ ) region of a few nanometers in size, which we call an emission center. The center is heated by the ohmic current passing through it. The diamond-like ( $sp^3$ ) region acts as a kind of a cooler removing the heat from the emission center. The electron emission current is responsible for the heating of the

$sp^2$ -regions of the emission center, while the high thermal conductivity of the  $sp^3$  (diamond)-regions produces a temperature gradient. The diamond grain must have a thermal contact with a massive conductive cathode. The temperature gradient between the emission center and the diamond regions creates a phonon flux. This induces an inner, local electric field at the emission center which, in turn, decreases the effective work function, providing a higher emission current.

The analytical theory based on this model is presented which explains the major experimental features observed in a diamond-like film, together with a microscopic theory of the quasi-ballistic phonon-electron drag effect. We believe that detonation nanodiamond clusters with a diamond region of 40 angstroms in size surrounded by a graphite-like shell may become a good basis for designing a carbon field emitter.

## 1.1 Model

Let us consider a carbon film consisting of two types of nanoregions, one containing carbon atoms in the  $sp^2$  state and the other in the  $sp^3$ -hybridized state, or graphite-like and diamond-like regions, respectively. The difference in the electrical and thermal conductivities of these regions may lead to a situation when the electric current passing through the film heats the  $sp^2$  regions to a high temperature  $T_h$ , while the  $sp^3$  regions have a relatively low temperature  $T_c$  (Figure 1).

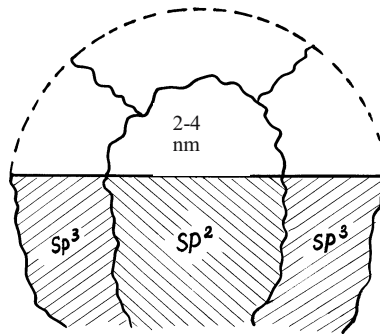


Figure 1. The model structure of an emission center.

The diamond-like regions act as coolers removing the heat from the graphite-like ones. The temperature gradient established between the two types of regions produces a phonon flux which drags the electron gas away, inducing a thermoelectric field in the graphite-like region. This local field

reduces the work function. The other details of the emission mechanism are the same as in the conventional model of field emission from a metal. What is important, however, is that the emission current heats the emission center, maintaining the local inner field. The arising positive feedback persists until the phonon flux heats up the whole system and the temperature gradient disappears. It is clear that a stationary mode will set up with a certain combination of parameters: (1) a certain ratio of the graphite-like and diamond-like region sizes, (2) a resistivity providing an adequate heat release, and (3) a certain thermoelectric coefficient determining the local inner field.

## 1.2 Emission Center

One can take it as a common knowledge that the electron emission area is small [2]. An evidence for this is provided by the current-voltage characteristics of carbon films on silicon tips [3]. If the resistance  $R$  and the conducting layer thickness  $d$  are known, we can calculate the ratio of the material resistivity  $\rho$  to the emission area  $S$ :

$$\frac{R}{d} = \frac{\rho}{S} = \text{const} \quad (1)$$

Therefore, the resistivity of the material of carbon structures used in [3] is proportional to the surface area of the structure, while the conductivity increases with decreasing area. It is obvious that the size of intensely emitting regions is indeed small, so an emission region may be termed as an emission center.

Since the emission current is accumulated at the emission centers, the current within them creates a temperature gradient. This induces a local inner electric field  $E_{in}$  at the emission center, which can significantly exceed the applied field. The local field reduces the effective work function.

In this model, the stability of emission centers is determined by the thermal and electrical conductivities of the emitter material. If the thermal conductivity is low, the local heating will eventually damage the material of the emission center. This effect has been observed in emitters based on carbon nanotubes but it is less pronounced in diamond-like films because of the high thermal conductivity of the diamond phase. On the other hand, the conductivity decrease with rising temperature can limit the heating.

We present some estimates made within our model for a diamond-like film containing  $sp^2$ -emission centers with a characteristic size  $d$ , surrounded by a shell, with the size of the diamond  $sp^3$ -region much larger than that of the  $sp^2$ -region (Figure 1).

To find a rough value of  $T_h$ , one can use the calculations for one-phase systems made, for example, in [4] on the assumption of zero heating of the  $sp^3$ -regions due to their high thermal conductivity.

The thermal conductivity equation for the time of establishing a stationary heat mode,  $\Delta t > 10^{-4} - 10^{-5} s$ , yields:

$$T_h = \frac{j^2 \Delta t}{\sigma \rho C} \quad (2)$$

Since the emission center is, at least, 20 times smaller than the total emitter area, we substitute into Eq.(2) the density of current through the center,  $j > 40 \text{ A/cm}^2$  (the value of  $j > 100 \text{ mA/cm}^2$  was given in [3]). For the material density of the  $sp^2$ -region equal to  $\rho \cong 2.0 \text{ g/cm}^3$  (graphite), the heat capacity  $C = 0.1 \text{ J} \cdot \text{kg}^{-1} \cdot \text{K}^{-1}$  and the specific electrical conductivity  $\sigma \cong 3 \cdot 10^4 - 1 \cdot 10^5 \text{ Ohm}^{-1} \cdot \text{m}^{-1}$ , we get  $T = 2 \cdot 10^2 - 2 \cdot 10^3 \text{ K}$ . This estimate agrees with the above experimental data on the temperature of nanotubes [5]. We assume that the temperature difference  $\Delta T$  on the outer emitter surface and at the boundary with the  $sp^3$ -region are an order of magnitude lower than  $T$ .

The field  $E_{in}$  induced in the  $sp^2$ -region due to the electron drag by the “phonon wind” is a thermoelectric field,  $E_{in} = \gamma \nabla T$  where  $\gamma$  is the thermo-emf coefficient. Clearly, this field becomes remarkable only at a sufficiently large temperature gradient which can be estimated as  $\Delta T/d$ . The thermo-emf coefficient can be expressed as  $\gamma = \alpha k_B/e$ ; here  $\alpha$  is a dimensionless thermo-emf coefficient;  $k_B$  and  $e$  are the Boltzmann constant and the electron charge, respectively. The estimations made in [1] show that the phonon path length is of the order of the emission center size. Therefore, the phonons move quasi-ballistically through the  $sp^2$ -region. Having the temperature of the emission center, the phonons travel through it in a collisionless mode. The result is that the value of  $\alpha$  is much larger than  $0.1 \div 1$  characteristic of, say, graphite [6], an issue discussed below.

We have shown in [1] that the local temperature difference defines the local electric field and the emission current, but it also determines the efficiency of the electron drag by phonons. In other words, the  $sp^2$ -region must be small enough to produce a sufficiently high electric field; on the other hand, the emission center should not be too small for the electrons to be dragged away by the phonon wind to induce a local electric field. With the phonon velocity  $c \cong (2-3) \cdot 10^3 \text{ m} \cdot \text{s}^{-1}$ , where  $h$  is the Plank constant, the optical size range can be written as

$$\alpha \frac{k_B \Delta T}{e E_{in}} \geq d \geq \sqrt{\frac{2\pi \hbar c}{e E_{in}}} \quad (3)$$

and is found to be quite narrow, 2–4 nm [1].

Let us define now the conditions for the phonon movement through the emission center. The path length of the phonons,  $l$ , must become of the order of the lattice constant  $a \cong 1 \text{ \AA}$  at temperatures providing the oscillation amplitude of the atoms,  $\zeta$ , equal to  $a$ . For a rough estimation, one can make use of the classical relation for the oscillations of carbon atoms with the mass  $M \cong 12 \text{ a.e.m.}$ , or for the energies  $M\omega^2 \xi^2 \approx k_B T$  and the characteristic frequency  $\omega \approx c/a$ . The quantity  $c$  is taken to be the velocity of longitudinal acoustic phonons which make the largest contribution to the electron drag [7]. Note that the electron-phonon interaction at temperatures above 10K occurs by absorbing longitudinal acoustic phonons [8].

Then we find

$$l \approx \frac{Mc^2 \alpha}{k_B T} \geq 5 \text{ nm} \quad (4)$$

This value was shown above to be larger than the emission center size, which means that phonons do travel in a collisionless mode through the  $sp^2$ -region ( $l > d$ ). Due to this quasi-ballistic mode of movement, allow one can calculate the intensity of the phonon flux as if it were emitted by an absolutely black body [8]:

$$r = \frac{4\pi \hbar c^2}{\lambda^5} \left[ \exp \left( \frac{2\pi \hbar c}{\lambda k_B T} \right) - 1 \right]^{-1} \quad (5)$$

Here  $\lambda$  is the wavelength and  $\hbar = h/2\pi$ .

### 1.3 Calculation of the Thermo-emf Coefficient in Quasi-Ballistic Phonon Drag

Return to the estimation of the dimensionless coefficient  $\alpha$  defined by the probability of interaction between an electron and a quasi-ballistic phonon. The electron drag represents a process (see [7] or [9]), in which an electron with the energy  $\epsilon_k$  absorbs a longwave phonon with the energy  $\hbar\omega_q$  to become an electron with the energy  $\epsilon_{k+q}$  (Figure 2). The latter then emits a phonon with the energy  $\hbar\omega_q$ . When the phonons are thermalized (the Debye temperature  $\theta < T$ ), the displacement of the electron which has emitted a phonon is subtracted from that of the electron which absorbed the phonon to yield a thermoelectric coefficient proportional to  $\theta/T$ .

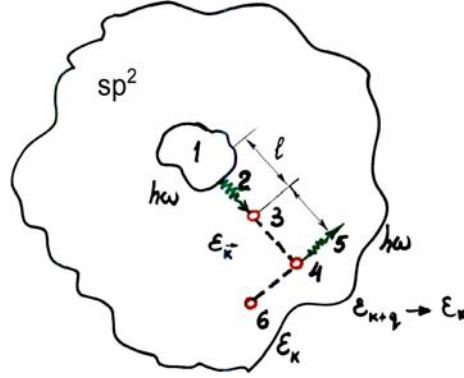


Figure 2. A schematic event of electron drag by a ballistic phonon. The distance 1-3 is the phonon path length and 3-6 is the drag path, or the displacement of the electron which has absorbed a phonon; 1 - the hottest area of the  $sp^2$ -region of the emission center; 2 - a ballistic photon of energy  $\hbar\omega_q$ ; 3 - the electron of energy  $\varepsilon_k$ , which has absorbed a phonon; 4 - an electron of energy  $\varepsilon_{k+q}$  emitting a phonon of energy  $\hbar\omega_q$ ; 5 - the emitted phonon with equally probable directions of motion; 6 - the electron which emitted a phonon after the recoil

The scenario is quite different for quasi-ballistic phonons. All of the absorbed phonons have a velocity component directed against the temperature gradient, whereas the emitted phonons are isotropic, and one may assume that the emission of quasi-ballistic phonons does not, on the average, affect the electron drag. As a result, the problem becomes much simpler: it is sufficient to find the probability of the phonon scattering by an electron. It has been found that the probability of interaction between an electron and a phonon for the time of the phonon travel through the emission center,  $d/c$ , is greater than 40%.

Turn now to the calculation of the thermoelectric coefficient. Generally,  $\alpha$  is determined by the interaction of electrons with random and quasi-ballistic phonons. For the region of random phonon motion, the thermo-emp coefficient is well known and can be described [7,9] as

$$\alpha_{ch} = \left( A_{dif} \frac{k_B T}{\varepsilon_F} + A_{dr} \frac{\theta}{T} \right), \quad (6)$$

where  $\varepsilon_F$  is the Fermi energy. The values of  $A_{dif}$  and  $A_{dr}$  are  $0.1 \div 10$ . The first term in Eq. (6) describes the diffusion processes and the second term describes the drag by the phonon wind.

It is known [9] that the Debye temperature, which, by definition, is expressed via the maximum phonon frequency  $\omega_m$ , in the random motion is related to the Fermi energy:



$$k_B \theta = \hbar \omega_m \approx \frac{\hbar c}{a} \approx p_F c \approx p_F v_F \left( \frac{m}{M} \right)^{\frac{1}{2}} \approx \varepsilon_F \left( \frac{m}{M} \right)^{\frac{1}{2}}, \quad (7)$$

where  $m$  is the mass of an electron,  $p_F$  is the Fermi momentum, and  $v_F$  is the velocity of the Fermi electrons.

The substitution of this result into Eq. (5) yields

$$\alpha_{ch} = \left( A_{dif} \frac{T}{\theta} \sqrt{\frac{m}{M}} + A_{dr} \frac{\theta}{T} \right). \quad (8)$$

At temperatures  $T = 2 \cdot 10^2 - 2 \cdot 10^3 K$ , the second term dominates in the whole range:  $A_{dr} \gg A_{dif}(m/M)^{1/2}$  and  $\theta/T \equiv T/\theta$ . Therefore, it is the electron drag rather than the electron diffusion that defines the thermo-e.m.f. in the phonon thermalization region.

In the region of ballistic movement of phonons, there is only the drag when an electron absorbs a phonon with the momentum directed against the temperature gradient. The thermo-emp coefficient for this process can be found using the concept of symmetry of kinetic coefficients (see, e.g., [10]). Due to this symmetry, the thermo-emp coefficient relates not only the field to the temperature gradient but also the amount of heat released by the system to the field. So we can generally write  $\alpha = \alpha_{bal} = A_{bal} C_V / k_B n_0$

Here,  $A_{bal}$  is another coefficient of the types  $A_{dif}$  and  $A_{dr}$  introduced above,  $C_V$  is the heat capacity per unit volume of the medium which releases the heat, and  $n_0$  is the concentration of electrons gaining this heat.

At the emission center, the heat is released by the flux of quasi-ballistic phonons:

$$C_V = \frac{16\pi^2 k_B^4 T^3}{60\hbar^3 c^3}. \quad (9)$$

This is the heat capacity of an absolutely black body. The electron concentration is as low as 10 to 20 electrons per emission center. In fact, this value was overestimated to avoid overestimation of the coefficient  $\alpha_{bal}$ . Then we have

$$\alpha_{bal} \approx \left( \frac{k_B T d}{\hbar c} \right)^3. \quad (10)$$

The numerical factor  $16\pi^2 A_{bal}/400$  is taken to be unity.

Our estimations show that the total thermo-emp coefficient is  $\alpha \equiv \alpha_{bal} = 50-500$  at the temperatures  $T = 2 \cdot 10^2 - 2 \cdot 10^3 K$ .

### 1.4 Emission with a Thermoelectric Field

In the conventional theory of field emission from a metal [11,12], the current density  $j$  is calculated from the Fowler-Nordheim formula

$$j = AE^2 \exp(-B/E). \quad (11)$$

The values of  $A$  and  $B$  are constant; they are expressed through the world constants and the work function  $A_e$ . Their calculation (see, e.g., [11]) yields

$$A = \frac{e^3}{8\pi\hbar A_e}; \quad B = \frac{8\pi}{3} \frac{\sqrt{2m}}{h} \frac{A_e^{3/2}}{e}. \quad (12)$$

The thermoelectric field at the emission center changes the band diagram. The electrons gain additional energy in the  $sp^2$ -region equal to the energy  $\alpha k_B(T_h - T_c) = \alpha k_B \Delta T$ , which has been given off by the thermoelectric field.

The emission center in a nanocarbon structure is a unique object, in which the temperature gradient is maintained by the passing electric current.

There are some experimental and theoretical studies (e.g., [13–18]) showing that the emission current from a nanocarbon structure can qualitatively obey Eq. (11). However, the experimental currents are several orders of magnitude greater than those calculated from this formula at a given field. This discrepancy cannot be explained by the tip effect (see [3], [16–18] and the references therein).

We believe that this can become clear if we assume that the change in the emission current results from the local inner thermoelectric field:

$$\gamma(T_h - T_c)/d = E_{in}. \quad (13)$$

The thermoelectric effect is responsible for the fact that the barrier, through which the electrons tunnel, decreases by the value  $\alpha k_B \Delta T$ .

Detailed calculations have shown that with the thermoelectric effect of Eq. (13) we get the following expression for the emission current:

$$j = A_T \exp(-B_T/E), \quad (14)$$

which differs from the Fowler-Nordheim formula only in the following coefficients:

$$A_T = \frac{e^3}{4\hbar A_e} \frac{\ln[1 + \exp(-\alpha(1-\beta)\Delta T/T_h)]}{\ln[1 + \exp(-\alpha\beta\Delta T/T_h)]} \quad (15)$$

$$B_T = \frac{4\sqrt{2m}}{3e\hbar} (A_e)^{3/2} \left[ 1 - \frac{\alpha(1-\beta)k_B\Delta T}{A_e} \right]^{3/2}. \quad (16)$$

The quantity  $\beta$  defines the characteristic energy of the tunneling electrons and is found to be  $0 < \beta < 1$ . At  $\beta < 0.5$ , we have  $A_T \ll A$  and at  $\beta > 0.5$  the coefficient becomes much larger,  $A_T \gg A$ .

Clearly, in the absence of thermoelectric effect,  $\alpha=0$ , the constants  $A_T$  and  $B_T$  change to the constants  $A$  и  $B$  from the Fowler-Nordheim formula (11). The work function in the exponential power decreases by the value of the energy gained from the thermoelectric field, as was expected.

## 2. COMPARISON WITH EXPERIMENTAL DATA

The comparison of the result obtained from Eq. (14) with the experimental data of [15,16] and [19–23] was made as follows. All the data were approximated by the straight lines:  $y = bx + y_0$ .

Eq. (14) for the emission current density  $j$  with the thermoelectric effect as a function of the applied field  $E$  was re-written in the conventional form:

$$\ln\left(\frac{j}{E^2}\right) = \ln(A_T) + \Gamma - \frac{B_T}{E} \quad (17)$$

where  $\Gamma = \ln\left(N_{ec} \frac{S_1}{S}\right)$  is defined by the number of emission centers  $N_{ec}$ ,

$S_1$  – mean surface area of one emission center,  $S$  – total surface area.

Obviously, Eq. (17) has  $x = 1/E$ ;  $|b| = B_T$ ;  $y_0 = \ln(A_T) + \Gamma$

Since the exact number of emission centers,  $N_{ec}$ , on the cathode is unknown (it is assumed to be  $N_{ec} \cong 10^3 - 10^7 \text{ cm}^{-2}$ ), the value of  $y_0$  cannot be found rigorously. The authors of [19–23] dealt with the currents rather than the current densities and we supposed that the emission was assumed to occur from the total surface area of  $S = 1 \text{ cm}^2$ .

Besides, in our calculations:  $\Delta T/T_h \cong 0.1$

The quantity  $\alpha(1-\beta)\Delta T/T_h$  is determined only by the slope of the straight line in Eq. (17), or the parameter  $b$ . Both  $\alpha$  and  $\beta$  were calculated using the values of  $y_0$  at  $\Gamma = 5$  and  $\Gamma = 15$ , respectively. Both parameters,  $b$  and  $y_0$ , are affected by the technology used for the emitting surface treatment.

The calculations and experimental data are compared in the Table 1 and in Figure 3. What is surprising is that a good agreement between the line

slopes for the theoretical and experimental results is achieved at the same value of  $\alpha(1-\beta)\Delta T/T_h \cong 32 \pm 0.6$  in all the cases.

*Table 1.* Parameters found from the comparison of experimental data and calculations with Eqs. (14) and (17). We did not give  $\alpha$  calculated from for experimental data [22,23] because values of  $\gamma_0$  needed for that calculations cannot be found rigorously.

Number of the lines on Figure 3	Reference	$ b $ $V/\mu m$	$\alpha(1-\beta)\frac{\Delta T}{T_h}$	$\gamma_0$	$\beta$	$\alpha$
					at $\Gamma = -2$ and $\Gamma = -6$ upper and lower values	
1	[19]	68	32.41	-10	0.6	800
					0.5	640
2	[20]	275	31.86	-7	0.7	1100
					0.5	640
3	[15]	16	32.62	-3	0.8	1600
					0.5	650
4	[16]	18	32.61	-1	0.8	1600
					0.5	650
5	[21]	25	32.52	-7	0.7	1100
					0.5	650
6	[22]	104	32.29	26	4	
					1	
7	[23]	420	31.56	24	4	
					1	

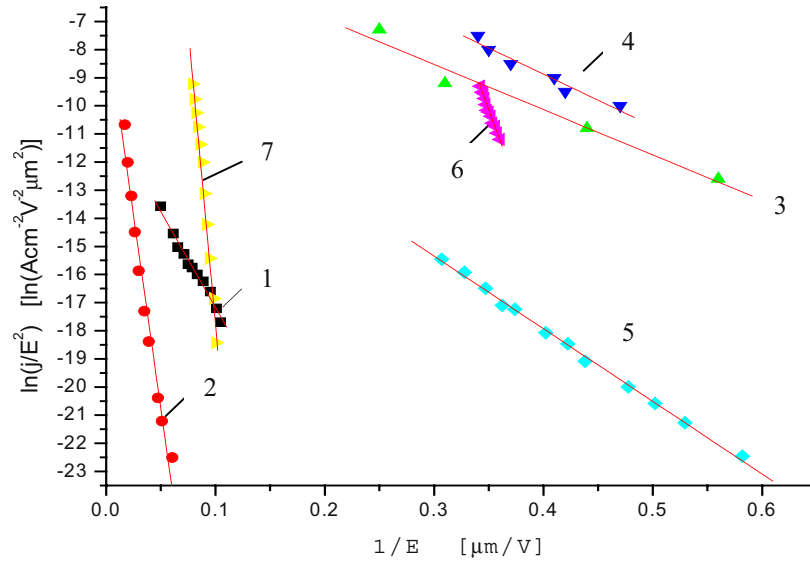


*Figure 3.* Experimental (points) and theoretical (straight lines) dependences of the emission current on the electric field in the Fowler-Nordheim coordinates.

### 3. CONCLUSION

Our study has shown that the observable behavior of field electron emission from nanocarbon structures can be interpreted satisfactorily on the assumption of the key role of the local inner electric field, which decreases the work function because of the thermoelectric effect. A unique property of nanocarbon structures, which represent a combination of the graphite-like phase ( $sp^2$ -hybridized carbon) and the diamond-like phase ( $sp^3$ -hybridized carbon), is that their thermal and electrical conductivities differ considerably. The temperature gradient produced by the current passing through the  $sp^2$  phase is due to a special role played by the  $sp^3$  phase which acts as a cooler. The large contribution of the thermoelectric effect arises from the electron drag by phonons which move quasi-ballistically because of the small size of the  $sp^2$  region.

We believe that ultrananocrystalline diamonds produced by detonation synthesis are a convenient material for making field emitters because they have a uniform size distribution in the nanometer range and the  $sp^2$ - $sp^3$  phase ratio in this material can be easily controlled by high temperature annealing.

### Acknowledgements

The authors are grateful to V. L. Gurevich who drew their attention to the electron drag by ballistic phonons when discussing the work [1], to E.L. Ivchenko who pointed out the importance of estimating the quantum-size effect, R.A. Suris and L.P. Mezhov-Deglin for stimulation discussion and suggestions.

This work was supported by the Russian Ministry for Education and Science (Contracts N 40.700.12.0117 and N40.012.11.1147) and by the Presidium of the Russian Academy of Sciences under the Project Quantum Nanostructures.

### REFERENCES

1. A.T. Dideykin, E.D. Eidelman, and A.Ya. Vul'. The mechanism of autoelectron emission in carbon nanostructures. *Solid State Communication*, **126**, 494-98 (2003).
2. A.V. Eletskii. Carbon nanotubes and their emission properties. *Phys. Uspekhi.*, **45** 369-02 (2002).

3. A.R. Krauss, O. Auciella, M.Q. Ding, D.M. Gruen, Y. Huang, V.V. Zhirnov, E.I. Givargizov, A. Breskin, R. Chechen, E. Shefer, V. Konov, S. Pimenov, A. Karabutov, A. Rakhimov, and N. Suetin. Electron field emission for ultrananocrystalline diamond films. *Journal of Applied Physics*, **89**, 2958-67 (2001).
4. P.H. Levin. Thermoelectric Phenomena Associated with Electron-Field Emission. *J. Appl. Phys.*, **33**, 582-87 (1962).
5. S.T. Pursell, P. Vinsent, C. Journet, and Vu Thien Binh. Hot Nanotubes: Stable Heating of Individual Multiwall Carbon Nanotubes to 2000 K Induced by Field Emission Current. *Physical Review Letters*, **88**, 105502 (2002).
6. Tables of Physical and Chemical Constants. By G.W. Kaye, T.H. Laby. Longmans Green & Co. 1958.
7. L.E. Gurevich. Thermoelectric properties of metals. *J. Phys. (USSR)* **9**, 4-26 (1946).
8. A. Zylbersztejn. Interaction of electrons with thermal pulses in semiconductors. *Journal de Physic*, **33** Suppl. C4, 85-91 (1972).
9. E.M. Livshits and L.P. Pitaevsky. *Physical Kinetics*. Moscow: Science, p 80, 1997.
10. J.M. Ziman. *Principles of the theory of Solids*. Cambridge: Univ. Press, 1964.
11. R.H. Fowler and L.W. Nordheim. Electron emission in intense electric field. *Proc. R. Soc. London.*, Ser. **A 119**, 173-86 (1928).
12. K. Yuasa, A. Shimoi, I. Ohba, and C. Oshina. Modified Fowler-Nordheim field emission formulae from a nonplanar emitter model. *Surface Science*, **520**, 18-28 (2002).
13. Z.-H. Huang, P.H. Cutler, N.M. Miskovsky, and T.E. Sullivan. Theoretical study of field emission from diamond. *Appl. Phys. Lett.* **65**, 2562-64 (1994).
14. A.N. Obraztsov, A.P. Volkov, and I.Yu. Pavlovskii. Cold electron emission mechanism for carbon materials. *Lett. Journ. Exp. Theor. Phys.*, **68**, 50-53 (1998).
15. W.Zhu, G.P. Kochanski, and S. Jin. Low-Field Electron Emission from Undoped Nanostructured Diamond. *Science*, **282**, 1471-73 (1998).
16. N. Obraztsov, A.P. Volkov, A.I. Boronin, and S.V. Koshcheev. Atomic orbitals rehybridization and field electron emission from nanostructural carbon. *Journ. Exp. Theor Phys.*, **93**, 846 -53 (2001).
17. V.D. Frolov, A.V. Karabutov, S.M. Pimeniv, V.I. Konov, and V.P. Ageev. Similarity in field electron emission from nanocrystalline diamond and related materials. *Diamond and Related Materials*, **10**, 1719-26 (2001).
18. F. Prins. The diamond - vacuum interface: I. A model of the interface between an *n*-type semiconductor, with negative electron affinity, and the vacuum. *Semiconductor Science and Technology*, **18**, 125-30 (2003).
19. K.-R. Lee, K.Y. Eun, S. Lee, D. -R. Jeon. Field emission behavior of nitrogen incorporated diamond-like carbon film. *Thin Solid Films*, **290-291**, 171-75 (1996).
20. W.J. Zhang, Y. Wu, W.K. Wong, X.M. Meng, C.Y. Chan, I. Bello, Y. Lifshitz and S.T. Lee. Structuring nanodiamond cone arrays for improved field emission. *Applied Physics Letters*, **83**, 3365-67 (2003).
21. R. Wächter, A. Cordery, S. Proffit, and J.S. Foord. Influence of film deposition parameters on the field emission properties of diamond-like carbon films. *Diamond and Related Materials*, **7**, 687-91 (1998).
22. M. Oliver, Küttel, O. Gröning, Ch. Emmenegger, L. Nilsson, E. Maillard, L. Diederich, L. Schlapbach. Field emission from diamond, diamond-like and nanostructured carbon films. *Carbon*, **37**, 745-52 (1999).
23. V. Ralchenko, A. Karabutov, I. Vlasov, V. Frolov, V. Konov, S. Gordeev, S. Zhukov, and A. Dementjev. Diamond-carbon nanocomposites: applications for diamond film deposition and field electron emission. *Diamond and Materials*, **8**, 1496-01 (1999).

## Author Index

Baidakova M.V.	271	Gruen D.M.	39, 373
Barnard A.	25	Gubarevich T. M.	311, 321, 337, 345
Bénédic F.	79, 93	Hassouni K.	79, 93
Bondar V.S.	261	Hoffman A.	125
Brenner D.	1	Horner D.A.	39
Bruno P.	79	Hu Z..	1
Buerki P.R.	63	Jackman R. B.	373
Bukayemsky A.A.	261	Kang W. P.	357
Butenko Yu.V.	199	Kargin V.F.	261
Carlson R.M.K.	63	Karpukhina T.A.	241
Chernukho L.E.	321, 345	Kempiński W.	271
Curtiss L.A.	39	Kohn E.	373
Dahl J.E.P.	63	Kubovic M.	373
Danilenko V.V.	181	Kulakova I.I.	241
Daulton T.L.	49	Kulik V.P.	321
Davidson J. L.	357	Kuznetsov V.L.	199
Dementjev A.P.	109, 253	Liu S.G.	63
Denisenko A.	373	Lombardi G.	79, 93
Dideikin A.T.	383	Lukyanchikov L.A.	169
Dolmatov V.Yu.	217	Lutsenko V.G.	289
Duley W.W.	283	Maslakov K.	109, 253
Efimova L.N.	299	Melnik N.N.	241
Eidelman E.D.	383	Milani P.	109
Enoki T.	271	Mohasseb F.	79, 93
Feoktistov N.A.	145	Nashchekin A.V.	145
Fujimura T.	217	Naumkin A.V.	253
Galli G.	15	Nesin S.D.	299
Galushko T.B.	241	Olmstead M.M.	63
Gamanovich D.N.	311, 337	Osawa E.	231
Gat R.	63	Osipov V.Yu.	271
Gicquel A.	79, 93	Padalko V.I.	299
Golubev V.G.	145	Panich A.M.	271
Gomza Yu.P.	299	Perova T.S.	145
Gradoboev M.N.	241	Petrov I.L.	333
Grishko V.I.	283	Podesta A.	109
Grudinkin S.A.	145	Puzyr A.P.	261

Ralchenko V.	109
Raty J.-Y.	15
Redfern P.C.	39
Salerno M.	109
Saveliev A.	109
Selyutin G.E.	261
Serebryakova N.V.	241
Shames A.I.	271
Shenderova O.A.	1, 283
Shilov V.V.	299
Shilova O.A.	299
Shtempljuk R.G.	321
Silva F.	79
Spitsyn B.V.	241
Sternberg M.	39
Ten K.A.	169
Titov V.M.	169
Tolochko B.P.	169
Voronina S.	109
Vul' A.Ya.	145, 271, 383
Williams O.A.	373
Zapol P.	39
Zavodinskii V.	157
Zimmermann T.	373
Zubkov P.I.	169



## Subject Index

- ab-initio* calculations, 15, 25, 157
- a*-C:H, 283
- adamantane, 63, 169
- ammonia water treatment, 217
- ballistic phonon, 383
- barothermic oxidizing, 337
- black colloid, 231
- bucky-diamond, 15
- carbon contents, 231
- Chapman – Jouguet, 181
- characterization, 241
- chemical purification, 217, 311, 333, 337
- chlorination, 289
- chromium-diamond codeposition, 321
- circumstellar grains, 49
- CN precursor, 39
- CO<sub>2</sub> laser, 63
- cohesive energy, 1
- colloidal stability, 261
- compose electroplating, 321
- composite, 345
- conductivity, 169
- contamination of zirconia bead, 231
- CVD, 63, 145
- CVD diamond film, 109
- CVD nanodiamonds, 49
- CVD process control, 79
- dangling bond, 271
- de-aggregation, 231
- density functional theory, 25
- detonation, 169
- detonation nanodiamond, 109, 181, 231, 333
- detonation nanodiamond structure, 217
- detonation soot, 181, 333
- detonation soot nanodiamonds, 49
- detonation synthesis, 241, 311
- detonation wave, 181
- diamond, 25, 39, 63, 157, 199, 271, 289, 373
- diamond containing soot, 311
- diamond-to-graphite transformation, 271
- dielectric relaxation spectroscopy, 299
- dislocations, 49
- drag effect, 383
- dynamic high pressure, 169
- electrochemical coating, 345
- electron emission, 357
- electron field emission, 261, 383
- electrophoresis, 261
- electroplating, 345
- epitaxial films, 157
- EPR, 271
- explosive charge, 181
- field emission devices, 357
- film characterization, 79
- fractal structure, 299
- free radical, 271
- functionalization, 241
- gold-diamond co-deposition, 345
- graphitization, 181, 199
- growth mechanism, 39, 253
- Hall effect, 373
- heat of formation, 1
- hydrogen content, 125
- hydrogenated carbon, 1
- hydrosols, 261
- infrared spectra, 283
- isolated nanodiamond, 15
- large scale UDD production, 311
- lonsdaleite, 49
- low pressure synthesis, 241
- mechanism of formation, 125
- melting, 181
- metal impurity, 271
- meteoritic nanodiamonds, 49
- microporosity, 289
- microwave plasma, 79, 93

- modeling, 93
- modification, 241
- modified nanodiamonds, 261
- molding, 109
- morphology, 25
- nanocarbon, 1, 181, 289, 383
- nanocrystalline, 373
- nanocrystalline diamond, 79, 93
- nanocrystalline diamond films, 145
- nanodiamond, 25, 125, 145, 169, 199, 241, 253, 261, 271, 283, 299, 357, 383
- nanofiber, 289
- nanographite, 383
- nanoparticle, 181, 271
- nanostucture, 157
- nanotechnology, 63
- nanowire, 25
- nitrate oxidize, 337
- NMR, 271
- non-ideal detonation, 181
- n*-type conductivity, 373
- nucleation, 109
- nucleation density, 145
- onion-like carbon, 199
- oxidation, 311
- ozone treatment, 333
- patterning, 109
- phase diagram, 181
- phosphosilicate, 299
- poly-aromatic hydrocarbons, 93
- polymantanes, 63
- powder fractioning, 261
- precursors for CVD, 261
- presolar nanodiamonds, 49
- proton conductor, 299
- purification, 231
- pyrometric interferometry, 79
- quantum chemical calculations, 39
- re-use of nanodiamonds, 321
- SAXS, 169
- sensor, 357
- shock wave, 169
- silicon carbide, 289
- small angle X-ray scattering, 299
- sol-gel material, 299
- soot particles, 93
- spin-lattice relaxation, 271
- SQUID, 271
- star dust, 49
- surface acoustic waves, 79
- surface chemical interaction, 253
- surface modification, 217, 345
- surface reactions, 39
- synchrotron radiation, 169
- thermal conductivity, 357
- thermodynamic balance, 181
- thermoelectric effect, 383
- thermolysis, 217
- twin microstructures, 49
- twinning, 289
- UDD, 271
- UDD purification, 321
- UDD regeneration, 321
- ultradispersed diamond, 311, 321, 337, 345
- ultrananocrystalline diamond, 1, 15
- utilization of conversion materials, 337
- whiskers, 289
- XAES, 109
- XPS, 109
- X-ray diffraction, 299
- 2H polytype, 49

## List of Participants

- |  |  |
|--|--|
| <p><b>Abramshe Ronald</b> USA<br/> Warren/Amplex Superabrasives<br/> Tel: (570) 383-3261<br/> Fax: (570) 383-6631<br/> E-mail: Ron.A.Abramshe@saint-gobain.com</p>   | <p><b>Daulton Tyrone</b> USA<br/> <i>Naval Research Laboratory</i><br/> Tel: (228) 688 48 77<br/> Fax: (228) 688 40 93<br/> E-mail: tdaulton@nrlssc.navy.mil,<br/> tld@howdy.wustl.edu</p> |
| <p><b>Baidakova Marina</b> Russia<br/> <i>Tokyo Institute of Technology,</i><br/> <i>Tokyo, Japan;</i><br/> Permanent Position:<br/> <i>Ioffe Physico-Technical Institute</i><br/> Fax: 812 - 247 00 73<br/> E-mail: baidakova@mail.ioffe.ru,<br/> baidakova@chem.titech.ac.jp</p> | <p><b>Davidson Jim</b> USA<br/> <i>Vanderbilt University</i><br/> Tel: 615-343-7804<br/> Fax: 615-343-6702<br/> E-mail: jld@vuse.vanderbilt.edu</p>  |
| <p><b>Barnard Amanda</b> USA<br/> <i>Argonne National Laboratory</i><br/> Tel: +1 630 252 8377<br/> Fax: +1 630 252 9555<br/> E-mail: amanda.barnard@anl.gov</p>   | <p><b>Dementjev Alexey</b> Russia<br/> <i>RRC "Kurchatov Institute"</i><br/> Tel: +7 095 196 72 86<br/> Fax: +7 095 196 72 86<br/> E-mail: a.dem@ru.net</p>                                |
| <p><b>B  n  dic Fabien</b> France<br/> <i>Universite Paris 13</i><br/> Tel: +(33) (0) 1 49 40 34 39<br/> Fax: +(33)(0) 1 49 40 34 14<br/> E-mail: benedic@limhp.univ-paris13.fr</p>  | <p><b>Dideikin Arthur</b> Russia<br/> <i>Ioffe Physico-Technical Institute</i><br/> Phone: +7 (812) 247 99 17<br/> Fax: +7 (812) 247 00 73<br/> E-mail: dideikin@mail.ioffe.ru</p>         |
| <p><b>Bogatyreva Galina</b> Ukraine<br/> <i>V.Bakul Institute for Superhard Materials</i><br/> <i>(ISM) of the NASU</i><br/> Tel: (+ 038 044 ) 468 - 85 - 99<br/> Fax: (+ 038 044 ) 468 - 85 - 99<br/> E-mail: bogatyreva@ism.kiev.ua</p>  | <p><b>Dolmatov Valery</b> Russia<br/> <i>JSC "Diamond Center"</i><br/> Phone: (812) 100 38 98<br/> E-mail: alcen@comset.net</p>  |
| <p><b>Chernukho Ludmila</b> Belarus<br/> <i>JSC "Sinta"</i><br/> Phone: +375 (17) 506-04-31<br/> Fax: +375 (17) 506-05-31<br/> E-mail: sinta92@yandex.ru</p>   | <p><b>Feoktistov Nikolay</b> Russia<br/> <i>Ioffe Physico-Technical Institute</i><br/> Tel: +7 (812) 247 93 93<br/> E-mail: Feokt@gvg.ioffe.ru</p>   |
| <p><b>Curtiss Larry</b> USA<br/> <i>Argonne National Laboratory</i><br/> Tel: 630-252-7380<br/> Fax: 630-252-9555<br/> E-mail: curtiss@anl.gov</p>   | <p><b>Fujimura Tadamasa</b> Japan<br/> <i>Vision Development Co., Ltd.</i><br/> Tel: +81 (3) 3561 3480<br/> Fax: +81 (3) 3561 3490<br/> E-mail: K-vision@rapid.ocn.ne.jp</p>               |
| <p><b>Danilenko Vyacheslav</b> Ukraine<br/> <i>JSC "ALIT"</i><br/> E-mail: vvdan@list.ru,<br/> listik99@mail.ru</p>  | <p><b>Galli Giulia</b> USA<br/> <i>Lawrence Livermore National Lab</i><br/> Tel: (925) 423-4223<br/> Fax: (925) 422-6594<br/> E-mail: galligygi1@llnl.gov</p>                              |
|  | <p><b>Gogotsi Yury</b> USA<br/> <i>Drexel University</i><br/> Tel: 1-215-895-6446<br/> Fax: 1-215-895-6760<br/> E-mail: Gogotsi@drexel.edu</p>   |

**Gruen Dieter** USA  
*Argonne National Laboratory*  
 Fax: 630 252 9555  
 E-mail: dmgruen@anl.gov

**Gubarevich Tatiana** Belarus  
*JSC "Sinta"*  
 Phone: +375 (17) 506 04 31  
 Fax: +375 (17) 506 05 31  
 E-mail: sinta92@yandex.ru,  
 TMGLab@yandex.ru

**Hamanovich Dmitriy** Belarus  
*JSC "Sinta"*  
 Tel: +375 (17) 506-04-31  
 Fax: +375 (17) 506-05-31  
 E-mail: sinta92@yandex.ru

**Hoffman Alon** Israel  
*Technion - Israel Institute of Technology*  
 Tel: 972 4 8293747  
 Fax: 972 4 8295703  
 E-mail: choffman@tx.technion.ac.il

**Korzhenevsky Alexander** Belarus  
*JSC "Sinta"*  
 Tel: +375 (17) 506-04-31  
 Fax: +375 (17) 506-05-31  
 E-mail: sinta92@yandex.ru

**Kuznetsov Vladimir** Russia  
*Boriskov Institute of Catalysis SB RAS*  
 Phone: (3832) 34 37 65  
 Fax: (3832) 34 30 56  
 E-mail: kuznet@catalysis.nsk.su

**Lutsenko Vadim** Ukraine  
*Vernadskii Institute of General & Inorganic Chemistry*  
 Tel: +(38044)4242130  
 Fax: +(038044)4243070  
 E-mail: lutsenko@ionc.kar.net

**Maslov Konstantin** Russia  
*RRC "Kurchatov Institute"*  
 Phone: +7 095 1967286  
 Fax: +7 095 1967286  
 E-mail: a.dem@ru.net

**Nakanishi Kaku** Japan  
*Vision Development Co., Ltd.*  
 Tel: +81-3-3561-3480  
 Fax: +81-3-3561-3490  
 E-mail: K-vision@rapid.ocn.ne.jp,

**Nedoluzhko Aleksey** Russia  
*Samsung Electronics Co Ltd*  
 Tel: +7 (095) 797-2471  
 Fax: +7 (095) 797-2503  
 nedol@src.samsung.ru

**Nikitin Yurii** Russia  
*Federal State Unitary Enterprise "Electrochimpribor"*  
 E-mail: main@chp-atom.lesnoy.ru

**Olesik Fedor** Russia  
*Department of Business Production, State Financial-Industrial Group*  
 Tel: (095) 927-51-26, 927-51-84  
 Fax: (095) 927-51-26, 927-51-84  
 E-mail: departamentfpg@mail.ru

**Osawa Eiji** Japan  
*Nanocarbon Research Co., Ltd.*  
 Tel/Fax + 81 267 45 8864  
 E-mail: OsawaEiji@aol.com,  
 osawa@nano-carbon.com

**Padalko Vladimir** Ukraine  
*JSC "ALIT"*  
 Phone: +38 044 457 5781  
 Fax: +38 044 457 5781  
 E-mail: alitex@mail.ru

**Patel Bhavik** UK  
*Imperial College London*  
 Tel: +44 20 7589 5111 ext 55172  
 Fax: +44 (0)20 7594 5177  
 E-mail: Bhavik.a.patel@imperial.ac.uk

**Petrov Igor** Russia  
*Scientific and Practical Company "New Technologies"*  
 Phone: (3512) 41 66 06, 24 06 21  
 Fax: (3512) 41 66 06, 24 06 21  
 E-mail: newtec@chel.surnet.ru

**Puzyr Alexey** Russia  
*Institute of Biophysics SB RAS*  
 Phone: (3912) 494430  
 Fax: (3912) 433400  
 E-mail: apuzyr@mail.ru

**Ral'chenko Victor** Russia  
*General Physics Institute RAS*  
 Tel: (095) 132-8229  
 Fax: (095) 135-7672  
 E-mail: ralchenko@nsc.gpi.ru;

**Rogozin George** Russia  
*Department of Business Production,  
State Financial-Industrial Group*  
+7 (095) 927-51-26, 927-51-84  
+7 (095) 927-51-26, 927-51-84  
departamentfpg@mail.ru

**Sciamanna Steven** USA  
*ChevronTexaco Technology Ventures*  
E-mail: BobCarlson@chevrontexaco.com

**Shames Alexander** Israel  
*Ben-Gurion University of the Negev*  
Tel: 972-7-647-25-81  
Fax: 972-7-647-29-03  
E-mail: sham@bgumail.bgu.ac.il

**Shenderova Olga** USA  
*International Technology Center*  
Tel: 919-881-0500 (ext.226)  
Fax: 919-881-0440  
E-mail: oshenderova@itc-inc.org

**Shilov Valer** Ukraine  
*Institute for Macromolecular Chemistry*  
Tel: +38 (044) 559-37-11  
Fax: +38 (044) 552-40-64  
E-mail: shilov@ukrpack.net,  
olgashilova@bk.ru

**Spitsyn Boris** Russia  
*Institute of Physical Chemistry RAS*  
Tel: 955-4475  
Fax: (095) 952 5308  
E-mail: lmm@phycs.ac.ru,  
bspitsyn@yahoo.com

**Swain Greg** USA  
*Michigan State University*  
Tel: (517)355-9715 x229  
Fax: (517) 353-1793  
E-mail: swain@chemistry.msu.edu

**Titov Vladimir** Russia  
*Lavrentiev Institute of Hydrodynamic RAS*  
Phone: 3832 33 28 43  
Fax: 3832 33 16 12  
E-mail: titov@hydro.nsc.ru

**Tolochko Boris** Russia  
*Institute of Solid State Chemistry and  
Mechanochemistry RAS*  
E-mail: titov@hydro.nsc.ru

**Tong Yi** China  
*Beijing Institute of Technology*  
Tel: 86-010-68914087-11  
Fax: 86-010-68461702  
E-mail: tongyi@bit.edu.cn

**Vul' Alexander** Russia  
*Ioffe Physico-Technical Institute*  
Tel: +7 (812) 247 91 07  
Fax: +7 (812) 247 10 17  
E-mail: AlexanderVul@mail.ioffe.ru

**Williams Oliver** USA  
*Argonne National Laboratory*  
Tel: 6302528471  
Fax: 6302529555  
E-mail: o.williams@anl.gov

**Zavodinsky Victor** Russia  
*Institute of Materials Sciences,  
Far East Branch of RAS*  
Tel: (4212)71-99-56  
Fax: (4212)71-99-56  
E-mail: vzavod@mail.ru

**Zhirnov Victor** USA  
*North Carolina State University*  
E-mail: [Victor.Zhirnov@src.org](mailto:Victor.Zhirnov@src.org)